Métamorphisme hydrothermal et réactions d'oxydo-réduction en contexte de marge passive et de zone de cisaillement ductile : genèse des concentrations Zn-Pb et graphite associées

Claire Ramboz

INSTITUT NATIONAL
POLYTECHNIQUE DE LORRAINE
(E.N.S.G.)

CENTRE DE RECHERCHES
PETROGRAPHIQUES ET GEOCHIMIQUES

METAMORPHISME HYDROTHERMAL ET REACTIONS D'OXYDO-REDUCTION EN CONTEXTE DE MARGE PASSIVE ET DE ZONE DE CISAILLEMENT DUCTILE:

GENESE DES CONCENTRATIONS ZN-PB ET GRAPHITE ASSOCIEES.

Claire RAMBOZ

Thèse soutenue publiquement le 08 Juillet 1988 devant la commission d'examen pour l'obtention du titre de Docteur d'Etat

MM. A. WEISBROD	Président
S.M.F. SHEPPARD	Directeur
G. CALAS J. SCHOTT J.C. TOURAY	Rapporteurs
F. ALBAREDE L.S. HOLLISTER	Examinateurs

A Joanna, je dédis ce mémoire,
l'un est déjà le passé,
l'autre va toujours de l'avant .

AVANT- PROPOS

Μετα γαρ των πολιτικων,
εα επι τους ποιετας...
Platon.

Après les thermodynamiciens,
je suis allée chez les chimistes...
Traduction libre.

Ce mémoire raconte l'histoire de cristaux et de roches dont je ne suis en aucun cas 'l'inventeur'. La barytine des Malines me fut présentée avec, malédiction!, son cortège de températures incroyables, par **A. Charef** qui consacrait sa thèse d'Etat à l'étude complète du gisement. Les anhydrites épigénétiques de la Mer Rouge, ce furent d'abord pour moi des points (déjà remarquables!) sur un diagramme présenté au hasard d'une rencontre à Paris par **E. Oudin**. Quant aux skarns à graphite des Jebilet, je suis allée les échantilloner avec **A. Bastoul** et S. M. F. Sheppard au Maroc en 1984. Ce n'est cependant pas ce court séjour sur le terrain qui m'a fait prendre conscience de l'intérêt exceptionnel de ces cailloux, mais bien les centaines de mesures microthermométriques qu' A. Bastoul avait déjà rassemblées dans sa thèse de 3e cycle, ainsi que les longues heures passées observer ces skarns sous le microscope. Merci, **B. Charoy**, pétrographe incomparable, de m'avoir aider à décripter chaque minéral, chaque texture, bref de m'avoir aider à acquérir un oeil intelligent.

Ce mémoire témoigne des nombreux échanges avec mes voisins immédiats. Je citerai d'abord **M. Arnold** avec qui j'ai partagé un bureau quelques années, et que j'ai constamment sollicité sur de multiples sujets. Parmi les 'géomathématiciens', c'est à **M. Danis** que revient l'initiative d'avoir considéré le problème de l'évolution thermique de la fosse d'Atlantis II. C'est lui qui m'a permis d'aborder les problèmes géologiques de thermométrie en Mer Rouge Centrale depuis l'échelle de l'inclusion fluide, quelques mm^3, jusqu'à l'échelle de la fosse, environ 3 km^3!. **J.J. Royer**, quant à lui, m'a dépanné de multiples fois dans des calculs rébarbatifs et m'a permis, avec **A. Mezgache**, d'explorer en un temps très court, toutes les possibilités du traitement statistique des données microthermométriques sur les anhydrites épigénétiques. A suivre...

Une grande partie des manuscripts rassemblés en annexe témoignent des contacts scientifiques étroits que j'ai liés avec le C.R.E.G.U.. Avec **J. Dubessy** tout d'abord, j'ai maintenu constamment, en dépit de la distance, un fructueux dialogue allant de l'histoire de l'azote protéïnique à la

structure de l'hydrate de gaz ou le rôle métallogénique des variations de la constante diélectrique de l'eau. Il me faut remercier tout particulièrement aussi **M. Cuney**, car ce fut lui qui initia et organisa les premiers travaux de A. Bastoul sur les skarns des Jebilet. Enfin, c'est **C. Kosztolanyi** qui effectua au C.R.E.G.U. les quelques analyses Raman présentées dans ce mémoire, ainsi que toutes celles mentionnées sur les skarns à graphite des Jebilet. Enfin, merci **A. Ploquin**, dont le nom figure aussi dans les publications rassemblées en annexe, de m'avoir permis de participer à la caractérisation géochimique des schistes de la Chataigneraie.

La plupart des analyses présentées dans ce mémoire ont été effectuées au C.R.P.G., dans le service de Mr. **K. Govindaraju**, dans le laboratoire de Chimie de Mr **M. Vernet**, dans le laboratoire des Rayons X de Mr. **F. Lhote**. Dans le service commun d'analyses de Nancy I, j'ai utilisé la microsonde électronique dirigée par Mrs. **Steinmetz** et **Claude** et le microscope à balayage sous la responsabilité de Mr. **Kohler**. Je tiens à remercier tous ces laboratoires pour la qualité remarquable des analyses qu'ils m'ont fournies.

Mer Rouge, Bassin Sud-Est, ce mémoire comporte un travail important de compilation bibliographique. C'est dire que j'ai usé et abusé des services de toutes les bibliothèques scientifiques de la place de Nancy. Au C.R.P.G., Mme **Protas** fut plus d'une fois sollicitée pour effectuer des demandes de références au centre de documentation du C.N.R.S.. A l'Ecole de Géologie, il m'a toujours suffit d'un simple coup de fil à Mmes **Matz** et **Leconte** pour obtenir aussitôt telle ou telle revue dont j'avais besoin. La Bibliothèque Universitaire a toujours satisfait mes demandes de prêts de livres auprès des bibliothèques en dehors de Nancy. Enfin, j'ai dérangé de nombreuses fois la bibliothécaire de l'E.N.S.I.C. pour retrouver telle table, tel article.

La réalisation de ce mémoire, c'est aussi l'envoi et le renvoi de nombreux articles, la préparation de conférences, avec des diapositives, des dessins et des proofs 10 fois recommencés, des tableaux modifiés...Tout cet obscur travail fut le lot de **A. Legros** pour le dessin, **J. Gorau** pour la photographie, Mmes **V. Embareck, J. Gerbaut, A.L. Monteragioni** et **M. Tailleur** pour la dactylograhie, et enfin Mme **Aubry** et de Mr **G. Chrétien** pour ce qui concerne le montage, collage et tirage.

Il me faut enfin remercier les éminents spécialistes dont le nom figure en ouverture de ce mémoire, appellés à en juger la qualité scientifique. Je commencerais par **A. Weisbrod**, à qui je dois ma formation dans le domaine des inclusions fluides. Bien des thèmes abordés dans ce travail sont les mêmes que ceux qui ont préoccupé l'Equipe des Fluides à Nancy depuis une quinzaine d'années. **S.M.F. Sheppard** fut un directeur de thèse tolérant. Il m'a laissé aborder les problèmes scientifiques comme je l'entendais, d'une façon pas forcément conforme à ce qu'il aurait

souhaité. J'espère qu'au travail minéralogique et cristallochimique présenté sur les skarns à graphite fera suite un travail de géochimie isotopique pointu, permettant de contraindre certaines hypothèses émises quant à la genèse des graphites. Enfin, S.M.F. Sheppard m'a appris à transformer un roman fleuve en une publication concise et claire; c'est en grande partie lui qui a inspiré la forme et la présentation du présent volume. **F. Albarède** est un juge averti en ce qui concerne les problèmes de prélèvement et d'analyse des fluides hydrothermaux sous-marins; il est à même d' apprécier la qualité des prélèvements qu'effectuent naturellement certains cristaux et la qualité des informations que l'on peut en tirer. Il a largement contribué à améliorer le fond des deux articles consacrés à la fosse d'Atlantis II, en acceptant en particulier de faire la revue détaillée des équations relatives au bilan de masse de cette fosse. G. Calas, J. Schott et J. C. Touray ont accepté d'être les rapporteurs de ce mémoire. Tâche d'autant plus méritoire que le manuscript fut tout d'abord un agglomérat de pièces détachées, qui ne se sont transformées en ce mémoire que quinze jours avant la soutenance. Je voudrais d'abord remercier **G. Calas** d'avoir pris le temps de venir discuter avec moi des problèmes posés par la minéralogie-cristallochimie des skarns à graphite des Jebilet. C'est à lui qu'échoit principalement la lecture détaillée de ce chapitre qui est, du point de vue de la forme, l'un des moins élaboré de ce volume. **J. Schott** se déplace de Toulouse via Paris et Marseille pour venir donner sur ce manuscript le point de vue du physico-chimiste. **J. C. Touray** a initié, quant à lui, les premiers travaux d'inclusions fluides à grande échelle sur le bassin Sud-Est ; il est donc à même d'apprécier les développements effectués dans ce manuscript sur certains épisodes de l'histoire du bassin. Enfin **L. Hollister**, venu de Suisse, pourra juger, outre l'ensemble du travail sur les inclusions fluides, l'interprétation qui est faite des textures des grenats des skarns des Jebilet. Il est en effet l'auteur de modéles relatifs à la genèse des zonages chimiques dans les cristaux de grenat et de staurotide.

A tous ceux dont les noms sont cités dans ce manuscript, à tous les gens que j'ai cotoyé quotidiennement au C.R.P.G. mais que je ne peux tous nommer, j'adresse donc mes remerciements les plus vifs.

RESUME

Ce mémoire comporte principalement cinq chapitres qui sont des publications originales, les manuscripts publiés par l'auteur entre 1980 et 1987 étant présentés en annexe.

Dans le **chapitre I** sont décrites les textures variées que présentent les grenats des skarns à graphite des Jebilet (Maroc) : dans les mines de graphite, grenats avec des inclusions à distribution de type chiastolite (type C) ou grenats ronds avec des inclusions présentant une distribution isotrope (type R); dans les niveaux carbonatés plus massifs en dehors des zones de mine, grenats englobant le graphite et les pyroxènes de la matrice (type M). Les grenats des types R et C présentent certains des caractères typiques des grenats formés au cours d'un métamorphisme prograde de bas degré (T< 550°C) : inclusions de quartz, teneurs en grossulaire décroissantes du coeur à la périphérie. Cependant, ils présentent aussi des compositions qui évoluent depuis des mélanites au coeur vers des titangrandites et des grandites à la périphérie. Les coeurs de composition mélanitique des cristaux de grenat de type R et C se sont formés dans des conditions de $fO_2 \leq 10^{-28}$ bar à 500°C, imposées par les quantités importantes d'hydrogène dégazées de la matière organique et des silicates ammoniés. L'eau et le CO_2 engendrés par les réactions de volatilization ont été presque totalement réduits, du fait que l'oxygène produit était fixé par les silicates de Fe^{3+} croissants simultanément : grenats et pyroxènes. On montre que les grenats des type R et C se sont formés de façon synchrone dans des environnements riches en matière organique où la teneur en fer du milieu, élévé pour les premiers, plus faible pour les autres, contrôlait l'intensité de la volatilisation du graphite en méthane. La transition vers des grenats de composition titangranditique a été synchrone de l'ouverture des veines et d'une augmentation de l'activité de la silice. C'est probablement l'entrée de l'eau dans le système qui a induit l'augmentation de l'activité de la silice, de même que l'augmentation de la fugacité d'oxygène. De telles conditions ont favorisé la cristallisation de grenats titangranditiques ou granditiques. On montre que les grenats déficitaires en silice (mélanites et titangrandites) ont pu se former parce qu'ils se sont développés à l'équilibre avec des pyroxènes supersiliciques riches en Fe^{3+}. Un algorithme est proposé qui permet de calculer une teneur en Fe^{3+} minimale des pyroxenes déficitaires en cations. On montre que, autour des mines dans les niveaux carbonatés plus massifs, riches en matière organique , les activités de l'eau, du CO_2, de la silice sont restées fortes, comme en témoigne la présence d'idocrase et de quartz en veinules. Les grenats de type M sont légèrement hyposiliceux et croissent à l'équilibre avec des pyroxènes supersiliciques qui n'incorporent pas le Fe^{3+}, mais sont essentiellement alumineux.

Le **chapitre II** présente l'étude, par microspectrométrie Raman et microthermométrie, des inclusions aqueuses dans les barytines à huile qui

sont caractéristiques des stades tardifs et postérieurs au stade fissural minéralisateur, du gisement Pb-Zn des Malines (bordure cévenole). Les variations corrélatives des températures d'homogénéisation (TH) et de fusion de la glace (Tfg) définissent trois stades dans l'évolution hydrothermale.

(1) Le premier stade est caractérisé par des inclusions à remplissage de gaz dominant, de salinité faible (≈5 % pds. eq. NaCl) et qui contiennent du CO_2 avec des traces de CH_4. En dépit de leurs TH élevées (180°≤TH≤380°C), ces inclusions ne peuvent avoir fui puisque leur contenu volatil est distinct de l'air. Ces inclusions sont interprétées comme ayant piégé un fluide carbonique de faible densité et chaud (≈300°C), qui s'est refroidi. C'est lui qui est responsable de la dégradation des huiles lors du piégeage dans la barytine et de la dissolution fissurale de la dolomie cambrienne du socle. Par sa composition et sa température, ce fluide traduit probablement un épisode volcanique contemporain de la surrection de la marge cévenole à la fin du Jurassique.

(2) Au cours du deuxième stade de l'évolution hydrothermale sont piégés à la fois des liquides et des vapeurs carboniques ayant la même teneur en sel et le même contenu en gaz qu'au stade précédant, mais qui s'homogénéisent cependant dans une gamme de température plus réduite : 160°-175°C. Ces inclusions résultent du mélange d'un fluide carbonique chaud avec les fluides de pore, lesquels avaient une température> 150°C avant tout mélange. On en déduit que des eaux de formation migraient avec les huiles depuis des niveaux profonds du bassin vers la marge le long de la faille E-W des Malines, sans se refroidir. Le fait que les cristaux aient piégé simultanément des liquides et des vapeurs lors du stade II traduit des conditions transitoires d'immiscibilité, ce qui est compatible avec la présence de calcite interstitielle dans la barytine. Les propriétés V-X d'une inclusion fluide du stade II (96.1 H_2O- 1.85 CO_2 mole %; V≈21.5 cm^3 / mole) fixent les conditions de l'immiscibilité autour de 175°C à une pression de 285±45 bars. Les propriétés TH-V-X des fluides carboniques piégés secondairement dans une barytine du stade fissural (Charef et Sheppard, 1988) impliquent que la pression fluide avait même atteint sur la marge des valeurs supérieures (≥365±45 bars). Les données relatives aux fluides carboniques témoignent donc que le socle cambrien aux Malines était transitoirement en surpression sous les marnes triassiques. C'est vraisemblablement l'addition de CO_2 à la phase fluide qui a fait que, en un temps très court, la pression a pu atteindre le pression lithostatique dans le horst des Malines. Ces surpressions fluides sont probablement contemporaines d'abord de la fin de la subsidence du Jurassique Moyen, où la couverture atteignait 1600±200 m d'épaisseur, puis du Jurassique Supérieur, alors que la couverture n'était déjà plus que 1200±200 m. La surpression fluide, ainsi que peut-être la poussée du magma, a induit la fracturation hydraulique du socle cambrien selon des fractures verticales postérieurement au dépôt des minéralisations fissurales.

(3) le stade final, représenté par des inclusions dont les TH décroissent

corrélativement avec les Tfg, traduit l'arrivée de fluides dilués et froids, alors que l'isolement du socle sous les marnes avait cessé après la fracturation hydraulique.

Le **chapitre III** décrit les cristaux d'anhydrite provenant de veines sécantes dans une carotte de sédiment du bassin SW de la fosse d'Atlantis II. Ils contiennent en leur coeur des inclusions aqueuses tubulaires primaires, à remplissage de liquide ou de vapeur dominant (type L et V, respectivement). Les inclusions de type L ont des températures de fusion de la glace (Tfg) comprises entre -20.4° et -4.4°C, et s'homogénéisent en phase liquide entre 55° et 420°C (Th LV(L)). Les inclusions de type V ont des TmI comprises entre -12° et -5°C et des Th LV(V) entre 324° et 430°C. Certains cristaux présentent des surcroissances avec des inclusions primaires isodiamétriques à cube de NaCl. Elles fournissent des températures de fusion de la halite et des Th LV(L) comprises entre 50°-283°C et 185°-405°C, respectivement; des inclusions sursaturées en NaCl ont fourni des valeurs de Th LV(L) comprises entre 84° et 404°C. Les inclusions de type L du coeur des cristaux, dont la salinité est < 19 % pds eq. NaCl, ont un contenu en NaCl qui décroit alors que leur volume molaire croit. De telles propriétés caractérisent des inclusions ayant piégé des mélanges mécaniques de liquide et de vapeur lors d'un processus d'ébullition; ces mélanges étaient déja refroidis lors du piégeage. Les inclusions de type L dont la salinité est comprise entre 19 et 23 % pds. ont piégé un fluide homogène. Elles regroupent 4 populations caractérisées par une distribution lognormale des Tfg et définissent dans le plan V-X 4 dérives verticales qui sont parallèles à celles définies par les inclusions saturées et sursaturées en NaCl. Deux inclusions appartenant à ces dérives, avec des Th maximales de 388° et 403°C et une salinité égale à 21.3 et 32.6 % pds, ont une pression interne à T=Th qui est à 10 bars près la pression du piégeage au fond de la mer, soit 223 ± 2 bars. Ces résultats démontrent que les fluides ont été piégés à l'ébullition. On peut en déduire que la saumure initiale avait une salinité de ≈ 19 % pds et une enthalpie de 1950 J/kg. Ce liquide s'est enrichi en NaCl jusqu'à ≈33 % pds par perte de vapeur. Une ébullition prolongée quasi isotherme implique que le fluide en profondeur a un volume limité et est réchauffé par un magma. Les liquides de salinité croissante ont été injectés de façon intermittente, et se sont refroidis sans mélange. Les données sur les fluides et les minéraux suggèrent que l'anhydrite épigénétique s'est formée par réaction entre le fluide et le sédiment hématitique, impliquant les couples rédox Fe^{2+}/ Fe^{3+} and $\Sigma S^{2-} / \Sigma SO_4^{2-}$.

Le **chapitre IV** est consacré à une ré-évaluation de la température moyenne de l'alimentation hydrothermale de la fosse d'Atlantis II, à partir du bilan des échanges de masse et de chaleur dans la fosse sur plusieurs années. Pour ce faire, est résumé l'ensemble des données hydrologiques, minéralogiques et géochimiques qui établissent que la fosse est alimentée de façon transitoire par une source de type geyser se déversant dans le bassin sud-ouest. De même, les arguments établissant que les saumures de la fosse d'Atlantis II constituent un système stratifié doublement diffusif

sont rappellés (Turner, 1969). Les données relatives aux fosses à saumures voisines, Discovery et Chain, sont également résumées puisqu'elles établissent que ces fosses se sont remplies par suite du déversement catastrophique de saumure hydrothermale provenant de la fosse d'Atlantis II.

Le bilan de masse établi à partir de la carte bathymétrique de la fosse (Bäcker et Richter, 1973) montre que le débit moyen des sources a été de 278±3 kg/s pour la période 1966-1977.

Le bilan de chaleur fait intervenir (1) le flux conductif à la base de la fosse, (2) les pertes de chaleur par conduction à travers l'interface entre la saumure inférieure et la saumure supérieure, (3) le flux de chaleur due à l'advection de saumure hydrothermale et (4) les pertes de chaleur liées à l'éventuelle advection de fluide vers les fosses voisines.

Les Cp du fluide hydrothermal salé ont été calculés en extrapolant au-delà de 300°C les valeurs proposées par Pitzer et al. (1984). Les valeurs ainsi obtenues n'augmentent que modérément au-dessus de 300°C. Avec ce dernier modèle pour estimer les Cp., la résolution des équations du bilan de masse et de chaleur conduit à une température de source de 470°C pour la période 1966-1977. Une telle température n'est pas réaliste car elle est supérieure d'environ 70°C à la température à laquelle le fluide bout, compte tenu de sa salinité et de la pression au fond de la fosse. L'équation de Born modifiée (Wood et al., 1981) prédit des valeurs de Cp du fluide hydrothermal qui croissent de façon exponentielle au-dessus de300°C. Une température de source de 354°C est obtenue en utilisant ce modèle pour les Cp. Cette température est cohérente avec la température moyenne de 330°C obtenue pour le piégeage des fluides dans des cristaux d'anhydrite épigénétiques des sédiments de la fosse (chapitre III). Les processus hydrothermaux observés dans la fosse d'Atlantis II ne peuvent donc s'expliquer de façon cohérente que si la capacité calorifique des fluides hydrothermaux augmente de façon importante au-dessus de 300°C. Le calcul montre que la température de la source hydrothermale a baissé d'environ 18°C entre 1972 et 1977 alors qu'elle est restée presque constante entre 1966 et 1972.

Enfin, les pertes de saumure de la fosse d'Atlantis vers la fosse Chain, démontrées entre 1972 et 1977, sont trop faibles pour influencer de façon significative le bilan de masse et de chaleur. Les données récentes sur l'évolution de la chimie des saumures inférieure et supérieure suggère cependant que des transferts de quantités inconnues de saumure inférieure vers la saumure supérieure se sont produits entre 1966 et 1972. Ceci implique que les températures calculées à l'aide du bilan de masse surestiment quelque peu les températures moyennes de l'alimentation de la fosse.

Le **chapitre V** s'attache enfin à dégager, à partir des deux exemples étudiés, Bordure Cévenole et Mer Rouge Centrale, les processus spécifiques qui régissent les circulations hydrothermales dans les contextes de marge passive. On insiste particulièrement sur le rôle

important des sédiments imperméables qui se déposent dans les environnements de rift (shales noires et/ou évaporites) parce qu'ils favorisent la genèse de pressions élevées et la décompression catastrophique des eaux de formation. Les failles de socle anciennes orientées selon des directions sécantes à la direction de l'extension sont les lieux privilégiés où cette décompression s'effectue. Ceci résulte du fait que de telles directions sont toujours réactivées au cours de l'extension crustale, et particulièrement lors des changements du régime des contraintes et/ou des mécanismes de l'extension. Des minéralisations Pb-Zn-F-Ba-U sont typiquement rencontrées dans de tels contextes géotectoniques. Les données thermométriques, chimiques et isotopiques établissent que les circulations, dont les mécanismes viennent d'être exposés, sont responsables de minéralisations, qu'elles soient situées dans l'axe du rift ou sur ses marges. On souligne que des évolutions à compositions constantes et températures d'homogénéisation variables sont enregistrées par les inclusions fluides et qu'elles sont symptômatiques de processus hydrothermaux à caractère pulsatoire; elles traduisent l'absence très générale de mélange de fluides et un refroidissement important des venues lors du dépôt. Ce dernier processus n'est cependant pas toujours enregistré par les cristaux. L'absence de mélanges de fluides lors de la précipitation des minerais est lié au fait que les sulfures s'accumulent en quantité importante seulement dans des zones abritées des eaux oxydantes (eau de mer ou eaux météoriques). Les saumures stratifiées en milieu marin (Mer Rouge) ou des marnes imperméables sur les marges (Malines) peuvent jouer ce rôle d'écran. Finalement, on souligne que les variations de pression fluides qui se produisent dans les zones source des gisements, ou dans les zones de dépôt, peuvent aider au lessivage des métaux ou à leur dépôt, selon que la chimie du fluide est contrôlée ou non par les minéraux.

ABSTRACT

The thesis mainly consists of five original manuscripts. The bulk of the papers published by the author from 1980 to 1987 are presented in Appendix (part III).

The main types of garnets in graphite-rich skarns from the Jebilet Mountains (Morrocco) are described in **Chapter I.** These are : garnets with chiastolite type distribution of the inclusions (type C), rounded garnets with isotropic inclusion patterns (type R) in graphite mines; in massive carbonated beds around mines, garnets overgrow the clinopyroxene-graphite-rich matrix (type M). R-type and C-type garnets display some typical features of garnets contemporaneous with low grade prograde metamorphism ($T \leq 550°C$) : presence of quartz inclusions, decreasing grossular-contents from cores to peripheries. They additionally show melanitic compositions in the cores and titangranditic to granditic compositions in peripheries. Melanitic cores in C-type and R-type garnets were probably formed at maximum fO_2-conditions of 10^{-28} bar at $\approx 500°C$, imposed by the large amounts of hydrogen degased out of the organic matter or from the ammonium-bearing silicates. Water and the CO_2 produced by volatilization reactions were almost totally reduced; this is because the oxygen was fixed by the Fe^{3+}-bearing silicates growing simultaneously : either the garnets or the pyroxenes. C-type and R-type garnets were cogenetic in graphite-rich beds. The iron-content of the sediment controlled the intensity of the volatilization of graphite to methane and hence, the type of the growing garnets : R-type garnets typically formed in iron-rich (chloritic) beds whereas C-type garnets developped in more Ca-rich layers. The change from melanitic to titangranditic compositions was accompanied by vein-opening and an increase in silica activity. Probably the influx of water to the system imposed the higher fO_2 and higher silica activities; this in turn favoured the titangranditic to granditic garnet compositions. It is shown that the silica-deficient garnets (the melanites and titangrandites) were formed only because they were at equilibrium with Fe^{3+}-bearing supersilicic pyroxenes. An equation is proposed which allows to calculate a minimum amount of Fe^{3+} in cation-deficient pyroxenes. It is shown that, in organic-rich massive limestones around mines, the activities of CO_2, H_2O and silica remained high, as shown by the presence of idocrase and quartz veinlets. M-type garnets are slightly silica-deficient and coexist with aluminous supersilicic pyroxenes; they do not contain significant amounts of Fe^{3+}.

Chapter II deals with oil-bearing vug-filling barite which postdates the karstic and fissural ore stages at Les Malines, one of the largest Mississipi Valley-type Zn-Pb deposits in Europe. Aqueous inclusions in barite have been studied by microthermometry and Raman spectrometry. The correlative variations of the melting points of ice

(Tm_{ice}) and of the homogenization temperatures (Th) define three main stages : (1) stage I, gas-rich inclusions characterized by Tm_{ice} = -7° ± 1°C and $Th_{L-V(V)}$ = 180° to 380°C, (2) stage II, liquid rich and gas-rich inclusions homogenized in the temperature range of 160° to 175°C, with Tm_{ice} = - 8.2° to - 4.1°C - stage I and stage II inclusions contain CO_2 and no CH_4, N_2, or H_2S detectable by Raman spectrometry, and (3) stage III, liquid rich inclusions, characterized by Tm_{ice} which increased from - 8° to - 1.7°C as their $Th_{L-V(L)}$ decreased from 160° to 130°C. They are essentially aqueous.

The H_2O-CO_2-NaCl vapor-dominant stage I inclusions in barite cannot have leaked because their gas-content is distinct from air. They are interpreted to have trapped a hot (T > 300°C), CO_2-bearing vapor which was cooling. Oil was thermally degraded during trapping in barite. The source of heat and CO_2 is considered to be volcanism contemporaneous with the major uplift of the horst during the Upper Jurassic. Dissolution of the carbonated wall rock is related to stage I. Stage II inclusions are interpreted to represent the end-product of the mixing of pore fluid with the hot vapor. The temperature of the pore fluid exceeded 150°C prior to the addition of magma-heated fluids. Such anomalous pore fluid temperatures are tentatively related to the steady dewatering of the Terres Noires shales from below, with the fluids moving up along the east-west fault of Les Malines near adiabatic conditions. The formation waters were probably responsible for the migration of the oil and for the recrystallization of the basement. Gas-rich and liquid-rich stage II inclusions are compatible with minor unmixing of the H_2O-CO_2-NaCl liquid with precipitation of calcite. The V-X properties calculated for a stage II liquid-rich inclusion (96.1 mole percent H_2O, 1.85 mole percent NaCl, and 2 ± 0.2 mole percent CO_2 ; V = 21.5 ± 1.3 cm3/mole) fix the pressure of unmixing at 175°C in the range 285 ± 45 bars. The Th - V-X properties of secondary CO_2-bearing inclusions in barite from the earlier fissural stage (Charef and Sheppard, in press) point to higher fluid pressures in the horst in the range of 365 ± 45 bars minimum. CO_2-rich inclusions in the two barite generations imply that the metamorphosed Cambrian basement at Les Malines has been transiently geopressured below the Triassic shales. The addition of a small amount of magma-derived CO_2 to the pore fluid probably accounts for the rapid increase of pressure. The fluid pressure in the horst reached near-lithostatic values repetitively, first at the end of the Middle Jurassic subsidence, when the burial depth was around 1.600 ±200 m, then at a later stage, probably during the Upper Jurassic, when the sedimentary cover was partly eroded to around 1.200 ± 200 m. The overpressuring, with a possible structural deformation resulting from the rising magma, probably caused the opening of the vertical late barite-filled veins by hydraulic fracturing. Stage III inclusions are interpreted to indicate the influx of colder diluted fluid to the horst under hydrostatic pressure conditions, i.e., after

decompression.

In **Chapter III** are studied anhydrite crystals in veins at the base of a drill core from SW Basin sediment These contain in their cores tubular primary two phase aqueous inclusions which are either liquid or vapor dominant (type L and V, respectively). Type L inclusions yield melting points of ice (TmI) comprised between -20.4° and -4.4°C, and homogenization temperatures to liquid (Th L-V(L)) in the range 55° to 420°C. Type V inclusions show TmI values between -12° and -5°C and Th LV(V) values between 324° and 430°C. Some crystal overgrowths contain more isometric NaCl-saturated primary inclusions. These are characterized by melting points of halite and Th LV(L) values ranging from 50° to 283°C and 185° to 405°C, respectively; some supersaturated inclusions are characterized by Th LV(L) values comprised between 84° and 404°C. Type L inclusions from crystal cores, with salinities <19 wt.% eq. NaCl, show decreasing salt content with increasing molar volume. Such V-X properties are characteristic of inclusions containing heterogenous mixtures of liquids and vapors generated by boiling; these inclusions were slighthly cooled before trapping. Type L inclusions with salinities in the range 19-23 wt.% eq. NaCl result from homogeneous trapping. They consist of four populations with lognormal distribution of the TmI values and define four vertical trends in a V-X plot which are parallel to those defined by saturated and supersaturated inclusions. Two inclusions from these trends with maximum Th values of 388° and 403°C and salinities of 21.3 and 32.6 wt.% eq. NaCl respectively, present an internal pressure at T=Th which is within 10 bars of the in situ hydrostatic pressure on the seafloor (i.e., 223±2 bars); this indicates that boiling took place. The fluid inclusion data are consistent with an initial brine of ≈ 19 wt. % eq. NaCl and with an enthalpy around 1950 J/kg, which became enriched in salt to ≈33 wt% eq. NaCl through loss of vapor. Near isothermal long duration boiling of solutions implies a deep fluid reservoir with a limited volume and heated by a magma. The salt-enriched liquids were injected intermittently on the seafloor, then cooled without mixing. These data and mineralogic observations suggest that epigenetic anhydrite is the product of interaction of the fluid and the hematitic sediment, i.e., redox reactions involving Fe^{2+}/Fe^{3+} and $\Sigma S^{2-} / \Sigma SO_4^{2-}$.

Chapter IV summarizes the data concerning the Central Red Sea Deeps. It is shown that Atlantis II is the only hydrothermally active of the four Central Red Sea Deeps filled with stratified anoxic brines. It is provided for hot new brine by a geyser spring. The other deeps are filled by brine overspill. Hydrological data show that some brine has overspilled from Atlantis II towards Chain A Deep between 1972 and 1977. The heat-mass balance of the lower brine of Atlantis II Deep between 1966 to 1977 is considered in order to estimate the mean temperature of the spring over that period.

Mass balance calculations are based on the published bathymetry of the Deep and on the measured rising rate of the interface between the lower and upper brines. The flow rate of brine discharge in Atlantis II Deep is

shown to have remained constant around 278± 3 kg/s between 1966 to 1977, assuming no loss of brine out of the considered system.
Heat balance equations involve (1) the conductive flow of heat at the bottom of the Deep, (2) the heat lost by conduction through the lower interface, (3) the flow of heat due to the advection of hot brine and (4) the heat lost by advection out of the lower brine. The evolution of the Deep is isobaric, therefore the heat balance only depends on the initial and final states chosen and not on whether the brine flow has been steady or discontinuous.
Cp values of the hydrothermal brine have been calculated on extrapolating the equation of Pitzer et al. (1984) above 300°C. These increase moderately above 300°C. A spring temperature of 470°C for the time range 1966-1977 is calculated using the latter model for the cp's; this temperature is unrealistic as it is ≈ 70°C higher than the boiling temperature of the lower brine at 220 bars. The modified equation of Born (Wood et al., 1981) predicts a near exponential increase of cp values of the brine above 300°C. A spring temperature of 354°C is obtained using the latter model for the cp's. This temperature compares favorably with the mean temperature of 330°C for the trapping of fluid inclusions in epigenetic anhydrite from sediments in discharge zones (Chapter III). Thermal processes in Atlantis II Deep are therefore consistent with highly increased heat capacities for the hydrothermal brine above 300°C. The temperature of the spring is shown to have dropped by ≈ 18°C between 1972 and 1977, compare to the near constant values of 352°±2°C obtained for the period 1966-1972.
The calculated spring temperature decreases and the flow rate increases if the rate of brine advection out of the pool increases. The amount of lower brine overspilled from Atlantis II towards Chain A Deep is small, therefore it has no influence on the calculated spring temperature. The changing chemistry of the lower and upper brines suggests that unknown amounts of lower brine have been supplied to the upper brine, particularly during the period of active discharge between 1966 and 1972. This implies that calculated spring temperatures are somewhat overestimated.

Finally, in **Chapter V,** an effort is made to identify the main mechanisms controlling hydrothermal processes in passive margin environments, based on a comparison between Central Red Sea and the Cévenole Border on the margin of the Subalpine Basin (France). It is emphasized that, in both environments, impermeable sediments (black shales and/or evaporites) have played a major role, as they have favoured high pore fluid pressures which were subsequently released by rock fracturing and brine expulsion related. Pore fluids were preferentially released along ancient basement fractures oblique on the direction of extension. This is because the latter directions were reactivated, particularly during periods when either the direction or the mechanisms of extension were modified. Pb-Zn-F-Ba-U mineralisations typically occur in passive margin environments. Chemical, isotopic and microthermometric

data support the interpretation that the above mentioned hydrothermal processes are responsible for them. It is emphasized that fluid inclusions most often record constant composition-variable Th variations, which indicate intermittent fluid circulations. Fluid inclusions point out to the absence of fluid mixing at the site of deposition and to important cooling; the latter process is not systematically recorded by crystals however. Sulfide preservation preferentially occurs in environments isolated from oxidizing waters (meteoric or sea-water). Either undercompacted clays (Les Malines) or anoxic brines (Red Sea) can act as seals preventing fluid mixing at the deposition site. Fluid pressure variations occur both in source areas and at the deposition site. It is suggested that these can favour either the leaching or the deposition of metals, depending on whether the fluid chemistry is buffered by the wall-rock or not.

TABLE DES MATIERES

INTRODUCTION GENERALE 1

PREMIERE PARTIE

INTRODUCTION 7

CHAPITRE I

Non-stoichiometric ferric garnets and pyroxenes in graphite-rich skarns from Sidi Bou Othmane (Morocco) : implications for graphite genesis (Claire Ramboz). 15

DEUXIEME PARTIE

INTRODUCTION 95

CHAPITRE II

Pressure-temperature-time-depth relations and paleohydrology at Les Malines Pb-Zn deposit (Ramboz and Charef, Econ. Geol., in press). 105

CHAPITRE III

Geyser-type discharge at the bottom of SW Basin of Atlantis II Deep, Red Sea: the evidence from fluid inclusions in epigenetic anhydrite (Ramboz, Oudin and Thisse, accepté pour publication dans Canadian Mineralogist). 165

CHAPITRE IV

The temperature of the inflowing brine at the bottom of Atlantis II Deep, Red Sea : the heat-mass balance revisited. (Ramboz et Danis, soumis à Earth Planetary Science Letters). 221

CHAPITRE V

Mécanismes des circulations hydrothermales en contexte de marge passive (Claire Ramboz). 275

CONCLUSIONS GENERALES 317

TROISIEME PARTIE

Publications annexes 323

INTRODUCTION GENERALE

Ce mémoire rassemble principalement cinq manuscripts originaux, dont certains sont soumis, acceptés ou sous presse dans des revues internationales. Tous ces manuscripts sont relatifs à la caractérisation des processus hydrothermaux et des interactions entre fluides et roches encaissantes.

La première partie comprend un seul manuscript. Celui-ci traite, principalement sous l'angle minéralogique et cristallochimique, de l'évolution dans un métamorphisme de contact prograde d'une roche pélitique et carbonatée interéagissant avec un fluide riche en hydrogène et s'équilibrant avec le graphite. Il s'agit de décrypter, par l'étude des textures des minéraux et de leur chimisme, et en utilisant les données relatives à la composition des fluides, les mécanismes par lesquels un tel système fluide-roche se transforme lorsqu'il est soumis à un déséquilibre brutal. Celui-ci résulte de la production à petite échelle de fluides de potentiels rédox très différent du fait des réactions de volatilisation au sein de roches de chimisme contrasté.

Les quatre articles rassemblés dans le seconde partie sont tous relatifs à la caractérisation, du point de vue de la température et de la pression, de processus hydrothermaux de haute température en contexte d'extension de type marge passive. Les fluides occlus sont étudiés dans la barytine ou l'anhydrite. Dans chacun des deux exemples choisis, on s'efforce de décrire les inclusions fluides à l'échelle du cristal et de quantifier leurs propriétés P-V-T-X. Les informations recueillies sont confrontées avec celles disponibles à une échelle plus large dans l'espace et le temps, en particulier l'échelle de la marge du bassin, ou de la fosse océanique.

Certains échantillons étudiés dans ce mémoire, que ce soient les cristaux d'anhydrite épigénétique de la Mer Rouge ou les skarns à grenat-pyroxene-graphite du Maroc, sont à bien des égards exceptionnels. Les premiers sont

des cristaux jeunes qui piègent presqu'exclusivement les fluides à l'ébullition à partir desquels ils poussent. Les seconds présentent des associations minéralogiques rares sur la Terre, particulièrement en contexte métamorphique. Les articles rassemblés en troisième partie de ce volume donnent un aperçu plus large de l'ensemble des préoccupations scientifiques qui ont conduit l'auteur à sélectionner de tels échantillons. Quant aux barytines des Malines, bien des caractéristiques qu'elles présentent sont communes aux barytines de phase tardive des gisements de Pb-Zn (e.g. Rife, 1971, Econ. Geol. 66, 1164-1167). Elles apparaissaient donc comme étant symptômatiques de processus très généraux dans l'histoire des bassins. C'est ce que l'auteur s'est attaché à révéler.

PREMIERE PARTIE

INTRODUCTION

La plupart des minéraux ou des liquides silicatés formés sur la Terre n'incorporent le Fe^{3+} dans leur réseau que dans des conditions de fugacité d'oxygène élevée. Le contenu en Fe^{2+} et Fe^{3+} des roches ou des magmas est donc le plus souvent le reflet fidèle du potentiel redox du milieu dans lequel ceux-ci se sont formés. Le contenu en Fe^{3+} d'une roche n'est en général susceptible d'augmenter que lorsque celle-ci interéagit avec d'importants volumes de fluide oxydant. Des pyroxènes ferriques peuvent ainsi se développer dans les magmas ou les roches sédimentaires exposés à la surface par réaction à température élevée avec l'oxygène de l'air (e.g. Foit et al., 1987). De même, les basaltes océaniques présentent souvent un contenu élévé en Fe^{3+} parce qu'ils ont interréagi avec de grands volumes d'eau de mer riche en sulfates (Spooner et al., 1977). C'est principalement la perméabilité des roches qui contrôle la convection des fluides dans la croûte. La convection dans la croûte océanique est facilitée parce que celle-ci est intensément fracturée (Lister, 1974). A l'inverse, les roches métamorphiques ont en général une perméabilité en grand qui est faible, elles évoluent donc le plus souvent en système chimique clos depuis la diagenèse jusqu'au métamorphisme de plus haut degré, en conservant un rapport Fe^{2+}/Fe^{3+} constant (Chinner, 1960).

Il existe cependant des roches ou des liquides silicatés terrestres riches en Fe^{3+} qui se sont formés à très basse fugacité d'oxygène. Ce sont les roches peralcalines, riches en amphiboles, pyroxènes et grenats ferriques (e.g. Huckenholz, 1969). Ces roches sont associées à des fluides riches en hydrogène (méthane et hydrocarbures : Konnerup-Madsen et al., 1979). Par ailleurs, les données expérimentales témoignent que les grenats riches en titane et Fe^{3+} qu'elles contiennent de façon caractéristique ne sont stables que dans des conditions de fugacité d'oxygène anormalement basses (Huckhenholz et al., 1976). Le problème reste posé de savoir dans quel environnement

terrestre particulier des roches ont pu acquérir une signature géochimique si particulière. C'est l'objet du chapitre qui suit que de décrire les mécanismes par lesquels un sédiment 'normal' du point de vue de la minéralogie des silicates et carbonates qu'il contient, mais anormal par son contenu élevé en élements volatils C, H et N, acquiert une minéralogie 'exotique' du fait de processus d'interaction fluides-minéraux complexes au cours du métamorphisme.

Références:

Chinner G.A. (1960). Pelitic gneisses with varying ferrous/ferric ratios from Glen Cova, Angus, Scotland. J. Petrol., 1, 178-217.

Foit F. F., Hooper R. L., and Rosenberg P. E. (1987). An unusual pyroxene, melilite and iron oxide mineral assemblage in a coal-fire buchite from Buffalo, Wyoming. Amer. Mineral. 72, 137-147.

Huckenholz H. G. (1969). Synthesis and stability of Ti-andradite. Amer. J. Sci. Schairer vol. 267A, 209-239.

Huckenholz H., Hölzl E., Huggins F. E. and Virgo D. (1976). A reconnaissance study of the Ti garnet stability field at defined oxygen fugacities. Ann. Rep. Director Geophys. Lab. 1975-1976, 711-720.

Konnerup-Madsen J., Larsen E. and Rose-Hansen J. (1979) Hydrocarbon-rich fluid inclusions in minerals from the alkaline Illimausaq intrusion, South Greenland. Bull. Minéral. 102, 642-653.

Lister C.R.B. (1974) On the penetration of water into hot rock. Geophys. J. Roy. Astron. Soc. 39, 465-509.

Spooner E.T.C., Chapman H.J. and Smewing J.D. (1977). Strontium isotopic contamination and oxidation during ocean floor hydrothermal metamorphism of the ophiolitic rocks of the Troodos Massif, Cyprus. Geochim. Cosmochim. Acta 41, 873-.

CHAPITRE I

NON STOICHIOMETRIC FERRIC GARNETS AND PYROXENES IN GRAPHITE-RICH SKARNS FROM SIDI BOU OTHMANE (MOROCCO) : IMPLICATIONS FOR GRAPHITE GENESIS

Claire RAMBOZ

C.R.P.G., B.P. 20, 54501-Vandoeuvre-lès-Nancy (France).

Introduction.

In the Sidi Bou Othmane area (Central Morocco), economic concentrations of graphite are associated with garnet and clinopyroxene-bearing skarns (Huvelin and Permingeat, 1980; Bastoul, 1983). They were formed after a stage of intense thermal metamorphism and ductile shearing related to the emplacement of post-Visean granites (Lagarde and Choukroune, 1982). Previous studies have shown the following concerning the genesis of the graphite. (1) Raman spectroscopic studies of the fluid inclusions have shown that the fluids in skarn areas are composed of N_2 and CH_4 and are devoid of CO_2 (Bastoul, 1983). (2) Geochemical studies have shown that the iron of the calcareous and argillaceous sediments in the ductile shear zone has been oxidized at the stage of the thermal metamorphism (Ramboz and Bastoul, 1985). Iron oxidation has been maximum in the graphite-bearing skarns where circulated the most reduced, CO_2-depleted fluids (Bastoul, 1983). Both these studies suggest that, in the Sidi Bou Othmane graphite-rich skarns, coupled oxido-reduction reactions occurred, which involved the following redox pairs : Fe^{2+}/Fe^{3+} from the silicates and CH_4/CO_2, NH_4^+/N_2 from the fluid (Ramboz and Bastoul, 1985), with possible volatilization of graphite (CH_4/C : Bastoul, 1983). The following points concerning skarn and graphite genesis remain to be precised : (1) in the lattice of which skarn silicate was the Fe^{3+} incorporated? (2) Was the growth of these skarn minerals indeed contemporaneous with volatilization reactions of the organic matter yielding the CH_4-N_2-bearing fluids? (3) What oxygen fugacity conditions were reached at the climax of volatilization reactions? It is worth noting that fluid inclusion studies only fix maximum fO_2-conditions of skarn formation at around 10^{-25} bars at 500°C and 2 kbar. This is because the water-content of the gas-rich inclusions cannot be estimated with higher precision than in the range 0-50 mole % (Bastoul, 1983).

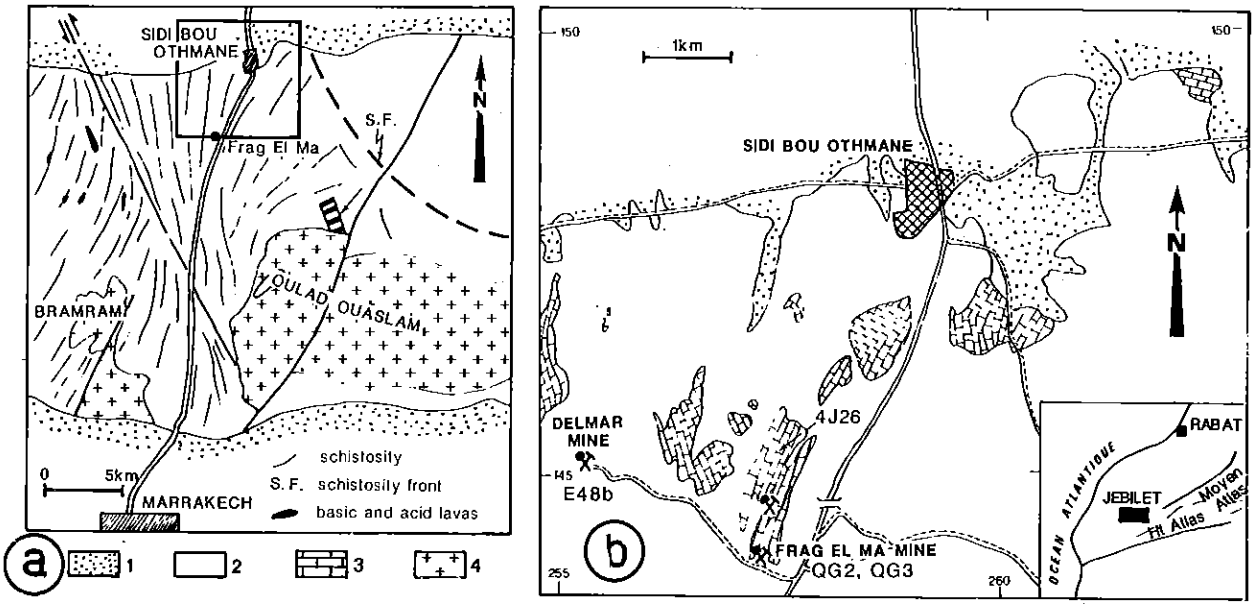

Fig. 1 : (a) Location map of graphite mine area (quadrangle) in Central Jebilet (after Lagarde and Choukroune, 1982).

(b) Detailed geological map of mine area, showing the location of graphite mines at the contact zone betwen shales and limestones (after Huvelin, 1977). E48b, QG2, QG3 and 4J26 are the studied samples (see Table I). 1 : Plio quaternary cover; 2 : Upper Visean to Namurian schists and shales; 3 : Upper Visean limestones; 4 : Granodiorite.

This paper is intended to answer to these questions by describing inclusion geometries in Sidi Bou Othmane garnets and by presenting the chemical variations shown by garnets and pyroxenes, based on wet chemical and electron microprobe analyses. Inclusion geometries in garnets are potential tools for ascertaining the metamorphic and tectonic regime prevailing during the mineral growth (Tracy, 1982). Besides, garnets and pyroxenes are recorders of bulk chemistry, fO_2 and growth kinetics (e.g., Huckenholz et al., 1976; Lindsley, 1980). The present work is therefore complementary to the fluid inclusion work to precise the fO_2-fH_2O-conditions of graphitization and skarnification at Sidi Bou Othmane. It is also a contribution based on crystal chemistry to understand 'mineral composition space and its limits' (Robinson, 1980, p.419), particularly that of clinopyroxenes, in a terrestrial environment where highly reducing conditions prevailed.

Geology.

Five kilometres north of Marrakech, the Jebilet Mountains are the southermost outcrop of Hercynian basement through the Mesozoic and Cenozoic terranes of the Moroccan Meseta Belt (Fig. 1a). (1) Western Jebilet are composed of Cambro-Ordovician rocks, with a rough schistosity and low-grade metamorphism. This block remained stable all over Hercynian time (Huvelin, 1977; Piqué, 1979). Further East, rocks of Upper Visean-Namurian age outcrop in tectonic contact with the Cambro-Ordovician basement (Huvelin, 1977). (2) East of the road from Marrakech to Sidi Bou Othmane, in Eastern Jebilet, the flysch of Kharrouba is at the base of the Visean series. It was affected by synsedimentary gravity tectonics, but was not deformed afterwards. (3) West of the road from Marrakech to Sidi Bou Othmane, in Central Jebilet, the schists of Sarlef are at the top of the Visean unit. They are composed of alternations of bioclastic carbonates, black shales and mica-

schists overlain by quartz-mica-bearing schists, with interstratified dykes of acid and basic lavas and massive sulfides related (Kettara deposit : Huvelin, 1977; Bordonaro, 1983). Central Jebilet exhibit a low-grade metamorphism (MT_1 = quartz, chlorite, muscovite I, biotite I), with rough schistosity related. However, a metamorphism of higher grade is visible in a 10 km-wide N-S area extending from Marrakech to Sidi Bou Othmane (MT_2 = cordierite - andalousite - muscovite II - biotite II- idocrase - garnet - clinopyroxene - chloritoïd - sillimanite) with strain slip cleavage (S2) related (El Hassani, 1980). Metamorphism MT_2 rapidly decreases westward and eastward, and is probably related to the syntectonic calc-alcaline granite magmatism (= contact metamorphism : Vogel et al., 1976). Granitic material outcrops only in the southern part of Central Jebilet (Ouled Ouaslam granodiorite; Bramram-Tabouchennt greisenized granite : Huvelin, 1977). Lagarde and Choukroune (1982) have shown that the limit between Central and Eastern Jebilet is a N160E sinistral ductile shear zone, 8.5 km-large, along which a horizontal movement of 22 km minimum took place. According to these authors, schistosity S_1 is related to the first stages of the shearing, whereas schistosity S_2, visible in the axial planes of curvilinear folds, was emplaced at the climax of deformation.

Graphite mines are located in a 4km-wide quadrangle southwest of Sidi Bou Othmane (Huvelin and Permingeat, 1980; Fig. 1b). They are within the northern part of the contact metamorphism aureole (MT2), 5 km east of the shear zone. The Oulad Ouaslam granodiorite outcrops 5 km south of graphite mines, however the mine area is crosscut by numerous dykes of pegmatite and dolerite (Huvelin, 1977), the latter being probably post-Hercynian (Mrini, 1985). Graphite concentrations occur in 10 m-wide pockets at the base of the schists of Sarlef, where carbonated lenses, 10-20 m-thick and a few hundred metre-wide, are interstratified in the organic-rich schists and shales (Fig. 1b). The regional N-S schistosity, slightly dipping west, is disturbed around the

graphite lenses. Graphite mines are systematically at the contact between carbonate lenses and schists, more rarely along faults within carbonates (Huvelin, 1977; Bastoul, 1983; Fig. 1b). No graphite concentration is enclosed within the massive limestones from the contact metamorphism aureole.

Petrography.

In and around graphite mines, primary calcite and argillaceous compounds are replaced by garnet, clinopyroxene and rarer wollastonite and epidote. The skarns associated with graphite concentrations are nearly devoid of hydroxyl-bearing silicates and are crosscut by numerous veinlets and veins. By contrast, massive carbonated levels a few metres away from mines contain calcite, garnet, zoned idocrase and clinopyroxene; they are crosscut by fewer veins. Skarn minerals in and around graphite mines, either in strata or in veins, are described below.

Skarn minerals along strata.

Anhydrous skarns. Garnets and clinopyroxenes are the main silicates associated with graphite. Pyroxene monocrystals are either isolated in the graphitic matrix or are included in garnet. In both occurrences, pyroxenes display either equidimensional shapes (type I) or are acicular (type II), with variable length (100 to 500 μm) and width (1 to 10 μm; Fig. 2b). Garnets growing along strata systematically contain silicate inclusions, mainly pyroxenes and minor quartz, epidote and/or K- or Ca- feldspars, identified optically or by electron or Raman microprobes. Two main types of garnets are identified in graphite mines based on contrasting inclusion geometries.

C-type garnets. Millimeter-wide rhombododecahedral garnet porphyroblasts with sector-zoned inclusions of the chiastolite-type are typically found in a matrix of abundant graphite with associated pyroxenes; these are mainly of type II. Figures 2a and 2b show the distribution of

inclusions observed in sections parallel with the basal plane of these porphyroblasts (see the sketch in Fig. 2, after Harker, 1939).

C-type garnets display up to three optical zones which often present variable thickness depending on the crystallographic orientation (Fig. 2a). (Zone 1) : Garnets have in their core relic textures of the graphitic matrix, with μm-wide type I clinopyroxenes. (Zone 2) : An intermediate garnet zone contains the sector silicate inclusions with rarer associated fluid inclusions. These consist of ≈ 5 μm-wide type I pyroxenes displayed both along crystal edges and along the planes perpendicular to the (110) crystal faces. Following the latter direction, sector inclusions tend to become acicular towards zone 3. Anorthite and quartz in that order have been found in the outer part of zone 2 towards zone 3; epidote is exceptional (Fig. 2b). Zone 2 commonly is the thickest along crystal edges and is the thinnest along axial planes perperdicular to the crystal faces. (Zone 3) : The outer part of C-type garnet, up to 500 μm-large, is usually inclusion free. Contrary to zone 2, zone 3 tends to disappear along crystal edges and is the thickest along axial planes perpendicular to the crystal faces. In some dissymetrical C-type crystals, zone 3 develops perpendicular to some of the crystal faces only. Zone 3 however can contain tubular calcite growing towards the crystal rim perpendicular to the (110) faces; this is only when samples are crosscut by microfolded calcite veinlets (Fig.3d; see below). Zone 3 frequently displays fractures perpendicular to the schistosity plane S_o/S_1.

Sidi Bou Othmane C-type garnets differ from those in the Magerøy metasediments (Andersen, 1984) by both the nature and shape of the inclusions they contain.

(i) Magerøy garnets only display two zones, equivalent in nature to zones 2 and 3 in Sidi Bou Othmane garnets, but the limits of which are parallel to the crystal faces. The inclusion free outer rim in Magerøy garnets is narrower

Fig. 2 : Photomicrographs of the different garnet types in Sidi Bou Othmane skarns (bar scale = 500 μm).

(a) C-type garnet porphyroblast with chiastolite-type distribution of the inclusions. C-type garnets typically occur in graphite-rich beds (sample QG2).

(b) Detail of inclusion patterns in growth planes perpendicular to the (110) crystal face of a C-type garnet (sample QG2). Note the presence of both equidimensional (type I) and tubular (type II) clinopyroxene inclusions.

(c) Rounded garnet porphyroblast (R-type), typical of silicate-rich beds with minor interstitial graphite (sample E48b). Note the numerous randomly distributed type I pyroxene inclusions and the spherically arranged quartz needles underlining a growth zone of the crystal (arrow).

(d) Contact zone between a graphite-free garnet vein and a R-type garnet-graphite-bearing bed (sample E48b). Note the fluid inclusion trails perpendicular to the contact.

(e) M-type garnet porphyroblast having incorporated the graphite-pyroxene matrix along preferential growth planes (sample 4J26). Such garnets typically occur in massive limestones around graphite mines. Note the quartz veinlet along the (110) crystal face.

(f) Zoned euhedral idocrase coexisting with M-type garnet in metamorphosed massive limestones (sample 4J26).

The upper sketch shows the arrangement of inclusions along preferential growth planes of a rhombododecahedral garnet porphyroblast (after Harker, 1939). The arrow indicates the sections shown in figures 2a and 2e.

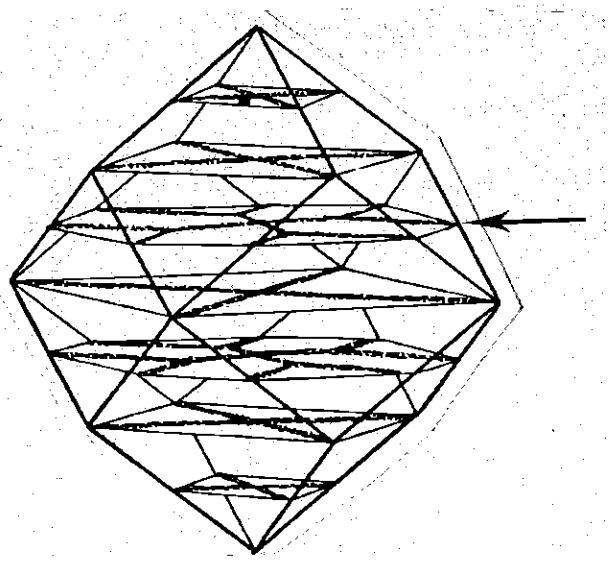

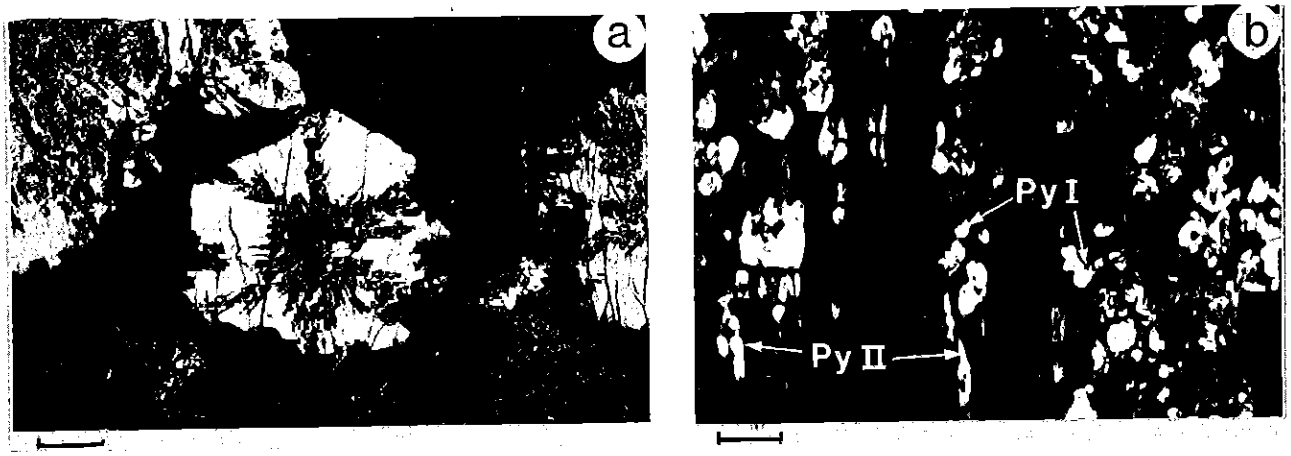
a
b
Py I
Py II

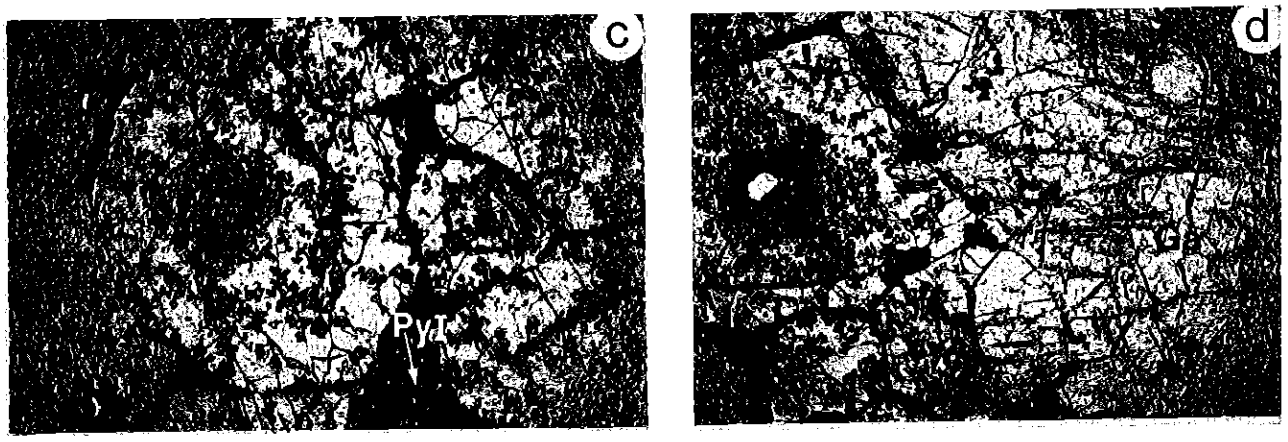
c
Py I
d


e
Q
f
Id
Py

(≈50 μm) and is separated from the inner zone by a graphite-rich, ≈50 μm-wide layer.

(ii) Magerøy garnets display type I inclusions along crystal edges and inclusions exclusively of type II along planes perpendicular to the faces of the porphyroblasts.

(iii) Sector inclusions in Magerøy garnets mainly consist of quartz and Fe-Ti oxides. Fe-Ti oxides have never been observed in Sidi Bou Othmane C-type garnets.

R-type garnets. Rounded garnet porphyroblasts are typically found in graphite-depleted zones from mine areas, where planar structures (S_o/S_1) tend to disappear (Fig. 2c). R-type garnets may either form an isotropic sheath at the periphery of garnet veins with a metric extent, or may be stratiform. In the latter case, they coexist with C-type garnets at the centimetric scale. R-type garnets are always cemented by minor interstitial graphite associated with type I pyroxenes. R-type garnets display three distinct zones. (Zone 1) : Their core contains relic textures of the fine-grained matrix, graphite and clinopyroxene, more seldom poecilitic calcite. (Zone 2) : An intermediate zone of the garnet, with rarer graphite, contains numerous equigranular (≈20 μm-wide) type I clinopyroxenes, randomly distributed. Zone 2 can often be sub-divided into an inner and an outer aureoles (zones 2A and 2B, respectively), separated by spherically arranged needles of quartz and sometimes anorthite. (Zone 3) : The clear rim devoid of silicate inclusions at the periphery of R-type garnets is either < 100 μm or absent, therefore it is less developped than in C-type garnets. The outer part of R-type garnet is frequently corroded by graphite. In strata where they are abundant, R-type garnets look as if they had been brechified and later cemented by graphite (Bastoul, 1983). Finally, the type I clinopyroxene inclusions in R-type garnets are frequently replaced in periphery by a red-coloured fibrous silicate, unidentified so far. The type I or type II clinopyroxenes in the graphitic

Fig. 3 : Microscopic aspects of vein stage minerals in Sidi Bou Othmane skarns and of the degassing related.

(a) Cm-wide vein filled with euhedral pyroxene and quartz crosscutting a graphite-pyroxene-rich bed.

(b) Cm-wide vein filled with euhedral garnet and quartz crosscutting a garnet-rich bed.

(c) Silicate-filled shear veinlet typically crosscutting graphite-rich beds in mine area. Note that the vein contains garnet when crosscutting a garnet-rich bed and pyroxene with crosscutting a pyroxene-rich bed.

(d) Sector zone inclusions of tubular calcite perpendicular to the (110) crystal faces in the outer part of a deformed M-type garnet porphyroblast.

(e) Detail of opaque and fluid inclusion trails in zone 3 of a C-type garnet.

(f) Gas-rich fluid inclusion (F.I.) attached to a type I clinopoxene in R-type garnet.

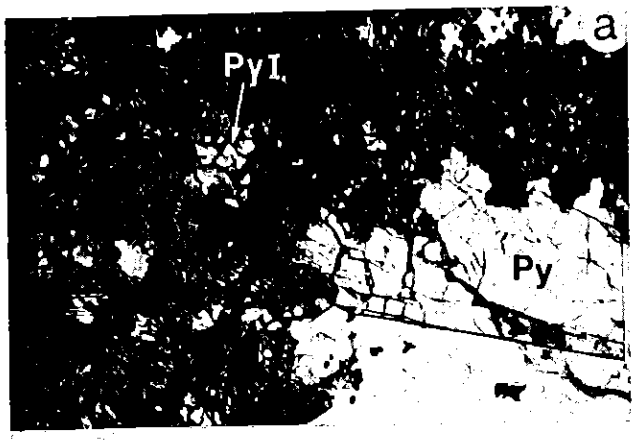

500 µm

500 µm

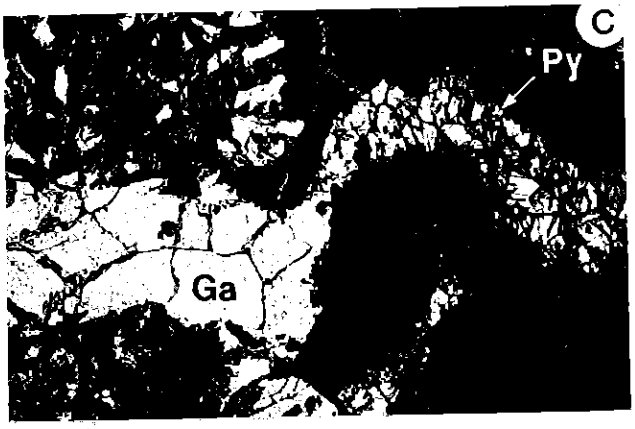

500 µm

500 µm

500 µm

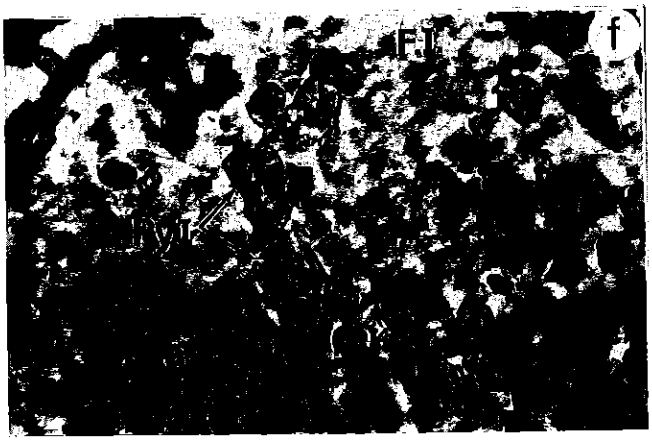

25 µm

matrix cementing both the C-type and R-type garnets are altered in a similar way. By contrast, type II clinopyroxenes included in C-type garnets are unaltered.

Hydrous skarns. A few meters outside graphite mines, carbonated levels coexist with garnet, pyroxene and idocrase-bearing skarnified layers. Garnets developping in massive carbonated beds are different from the previously described R-type and C-type garnets. These garnets are up to 1 or 2 cm-wide, larger than C-type and R-type garnets. They coexist with zoned idocrase, calcite or quartz in folded microveins (Figs. 2e and 2f). They have overgrown the graphitic and clinopyroxene-rich matrix, therefore they do not exhibit any specific inclusion geometry. These garnets are named M-type garnets hereafter.

The vein stages.

Millimeter wide veins in the graphite-rich zones. Millimiter-wide and centimeter-long calcite or clinopyroxene veins, and fewer garnet veins often crosscut the graphite-rich beds. They are microfolded and either parallel with S_o or oblique to it (Fig. 3c). Schistosity S_2 marked by microfolded clinopyroxene veins may totally replace S_o/S_1 in some intensely deformed samples. Graphite may be included in early calcite veins. Similarly, the outer part of C-type garnets, normally devoid of primary graphite, can contain some when it is crosscut by pyroxene microveins; some graphite is therefore precipitated during the latter vein stage. Graphite at the periphery of the clinopyroxene veinlets, whether it is primary or secondary, appears deep black and more shiny, probably because it is better crystallized.

Centimetric to metric veins in the graphite-rich zones. 1 to 10-cm wide, several meter-long veins filled with garnet, clinopyroxene and/or idocrase, or by calcite are ubiquitous in mines. The veins never underline folds and often present an inner filling of xenomorphic quartz. Garnet veins are the most

frequent ones. They locally contain green epidote. Idocrase is frequently associated with garnet or pyroxene in veins. The megaveins crosscutting C-type garnet graphite-rich beds are obviously connected with the folded garnet and/or clinopyroxene (calcite) microveins. The megaveins commonly widen to vugs filled with cm-wide euhedral crystals (Figs. 3a and 3b). Vein minerals may locally replace both R-type and C-type garnet-bearing facies.

Quartz-feldspar pegmatitic veins postdating the clinopyroxene-garnet-idocrase-quartz vein stage are present in the graphite-rich zone. K-feldspar frequently replaces idocrase or may coexist with it.

Chronology and factors controlling mineralogy. The large clinopyroxene-garnet-quartz veins often crosscut small microfolded clinopyroxene veins. Reversely, large idocrase-clinopyroxene-quartz veins are locally partially replaced by numerous microfolded clinopyroxene shear veins. These observations support the interpretation that the millimetric and the centimetric to metric vein stages were more or less contemporaneous.

Intense degassing accompanied skarn formation at Sidi Bou Othmane. This is shown by the numerous trails of small gas-filled fluid inclusions in the zones 2 and 3 of C-type garnets (Fig. 3e) and in the vuggy garnet and quartz (Fig. 2d). Obviously, silicate microveins in graphite were pathways along which fluids were collected from the sediments towards the megaveins. C-type and R-type garnets also contain isolated rounded gas-rich fluid inclusions at the contact with type I pyroxenes (Fig. 3f).

Both the microfolded veinlets and the centimeter-wide veins are filled with clinopyroxene when they crosscut a graphite-clinopyroxene-rich layer and with garnet when they crosscut a garnet-rich layer (Figs. 3a to 3c). This proves that the mineralogy of Sidi Bou Othmane silicate veins was mainly controlled by the chemistry of the immediate sedimentary wall-rock. Probably, R-type garnet-bearing levels, pyroxene enriched, formed from finely banded argillaceous, carbonated and/or plagioclase-bearing sediments,

Table 1 : Petrographic characters of the studied samples and characteristic minerals analysed in each of them.

SAMPLE (location)	PETROGRAPHY	ANALYSED MINERALS
QG2 (Frag El Ma)	Graphite-rich beds with 5mm-wide C-type garnets alternating with R type garnet-bearing graphite-depleted levels. Microfolded pyroxene and/or garnet veinlets.	C-type Ga;vuggy Ga; Py in C-type Ga; Py and Ga in veinlet.
QG3 (Frag El Ma)	Scattered C-type garnets in graphite-rich beds with acicular pyroxenes. Numerous calcite veinlets.	Py in graphite.
E48b (Delmar)	R-type Ga cemented by minor graphite around a garnet-quartz vein.	R-type Ga; Py in R-type Ga; vuggy Ga Py in graphite.
4J26 (Berger Prospect)	Cm-wide stratiform M-type garnets including the graphitic matrix with acicular pyroxenes.	M-type Ga Py in graphite

whereas C-type garnet-rich layers, with fewer clinopyroxenes, formed from more carbonated and/or plagioclase-rich beds. This suggests that mass transfers were restricted to the millimetric scale during the formation of Sidi Bou Othmane skarns, in spite of the intense degassing.

Four garnet and/or clinopyroxene-bearing samples from graphite mine areas were selected for analyses (Fig.1b). Their origin and petrography are summarized in Table I, together with the different types of minerals analysed in each sample.

Analytical techniques

Wet chemistry. (Chemistry Laboratory, CRPG, Nancy) The garnet-clinopyroxene skarns selected from graphite-rich zones were dissolved with a hot mixture of HF and $HClO_4$. Major elements were analysed by standard atomic absorption and colorimetry techniques with a precision $\leq$ 1wt.% (Vernet, 1968). Divalent iron was analysed by volumetry with $K_2 Cr_2 O_7$ with a precision of $\pm$ 0.5 wt.%. Organic carbon was measured as CO_2 by coulometry, after sintering in an oxygen furnace and titration with production of OH^- by electrolysis. The relative precision of the analyses is 5 10^{-3} wt.%.

X-Ray diffraction. Detailed X-Ray diffraction patterns were obtained using a Jobin Yvon Sigma 2800 apparatus (X-Ray Laboratory, C.R.P.G., Nancy). Experimental conditions were : Cu Kα1 radiation, scan rate of 4 mn/ degree, quartz as an internal standard.

Electron microprobe analyses were carried out with a Camebax electron microprobe (Nancy I University). Experimental conditions were : accelerating voltage 15 kV, sample current 6-8 nA, counting time 6s, beam diametre 2μm, crystalline silicate and oxides as standards. ZAF correction procedure was applied.

Crystal chemistry of garnets and clinopyroxenes in Sidi Bou Othmane skarns.

The stoichiometry of silicates has been defined for terrestrial minerals, mostly formed under average fO_2-conditions between HM and QFM buffers. However, much lower fO_2 values may locally prevail in the Earth'crust or are common in other planets. Minerals formed at very low fO_2-conditions are markedly distinct from the ones formed at higher fO_2. This is because some elements, like titanium or chromium, present a different oxidation state at low fO_2 (Lindsley, 1980; Anderson et al., 1981). The fO_2-conditions under which a mineral has crystallized also influence the coexistence of cations of different oxidation state at similar crystallographic positions (Huggins et al., 1977a). The growth of non-stoichiometric silicates can be suspected in the organic-rich CO_2-depleted skarns from Sidi Bou Othmane. The crystal chemical properties of both stoichiometric and non-stoichiometric garnets and pyroxenes are summarized below and used as an aid to characterize Sidi Bou Othmane silicates.

Garnets

Structure and stability conditions. Garnets formed under average crustal fO_2 conditions exhibit a regular crystal chemistry represented by the formula :

$$[M^{2+}]_3\,[M^{3+}]_2\,[M^{4+}]_3\,O_{12}$$ (Novak and Gibbs, 1971)

Most chemical analyses of Ti-free garnets do indicate an ideal filling of the tetrahedral, octahedral and dodecahedral sites of 3 : 2: 3, respectively (Huggins et al., 1977a). The divalent cations are located in dodecahedral site, the trivalent cations are found in octahedral site and Si^{4+} fills the tetrahedral site. Shimazaki (1977) has proposed the following procedure for recalculating the Fe^{2+}/Fe^{3+} ratio in garnet, based on the assumption of ideal filling of the three sites. (i) The cations are allocated to 12 oxygens. (ii) If Si is

< 3, then Al^{IV} = (3-Si) and Al^{VI} = (Al total - Al^{IV}). (iii) If Si≥3, then Al^{IV}=0 and Al^{VI}=(Al total). In both cases, (Al^{VI} + Ti + Cr + Fe^{3+}) = 2. The wt.% FeO and Fe_2O_3 yielding the Fe^{2+}/Fe^{3+} ratio satisfying conditions (i) to (iii) is adjusted using a computer program.

Natural titanium-bearing garnets contain Al, Fe^{3+}, Ti^{4+} and possibly Ti^{3+} and are commonly silica-deficient. They are therefore non-stoichiometric. Titanandradite solid solutions are characterized by Si≤3.00 and Si+Ti = 3.00. Their composition ranges between $Ca_3\ Fe^{3+}_2\ Si_3\ O_{12}$ and $Ca_3\ Fe^{3+}_2 Ti_{1.5}\ Si_{1.5}\ O_{12}$. The latter formula approximates the solubility limit of titanium in andradite (Huggins, 1969). Melanite and schorlomite are titanium-bearing garnets characterized by both Si < 3.00 and (Si+Ti) > 3.00. Their titanium-content ranges between 1 and 5 wt.% and 5 and 20 wt.% TiO_2 respectively.

Both natural and synthetic titanandradites, melanites and schorlomites have been studied by combined electron microprobe and Mössbauer spectrometry of Fe coexisting with Ti. These studies show that only a small fraction of Ti shares the tetrahedral site with Fe and Al (Dowty, 1971; Weber et al., 1975; Schwartz et al., 1980; Huggins et al., 1977a). This conclusion is confirmed by synchrotron radiation Xanes spectroscopy of Ti in garnet (Waychunas, 1987). Melanites and schorlomites present additional deviations from ideal site filling, apart from the presence of Ti in octahedral site. They contain more than 3.00 divalent cations and less than 2.00 trivalent cations. Huggings et al. (1977a and b) have precised the crystal chemistry of natural and synthetic melanites and schorlomites. (i) The dodecahedral site contains only divalent cations. (ii) The sum (Ca+Mn+Mg+Fe) exceeds 3.00, therefore divalent cations are also found in VI-fold site. (iii) Fe^{2+}, Fe^{3+}, Ti and Al can be found both in octahedral and tetrahedral sites. (iv) The relative preference for the tetrahedral site is in the order Al > Fe^{3+}> Ti, although Schwartz et al. (1980) found it to be Fe^{3+} > (Al, Ti) . Coupled electron microprobe analyses

and Mössbauer spectrometry of Fe in melanites and schorlomites, particularly in the most silica-deficient ones (Si<2.9), suggest that they may contain small amounts of Ti^{3+} (Manning and Harris, 1970; Dowty, 1971; Huggins et al., 1977a, 1977b; Amthauer et al., 1977; Schwartz et al., 1980). The latter conclusion is however denied by direct synchrotron radiation Xanes spectroscopy of Ti in natural garnets (Waychunas, 1987).

Huckenholz et al. (1976) and Huggins et al. (1977b) have shown that the following procedure is best adapted for recalculating the structural formulae of garnets of the melanite-schorlomite series. (i) The structural formula is calculated on the basis of 12 oxygens. (ii) The ferrous-ferric ratio is calculated in order that the cation to anion ratio is 8:12. (iii) The Fe^{2+}/Fe^{3+} ratio thus calculated includes contributions to the reduced state from both Ti^{3+} and Fe^{2+}.

Garnet stoichiometry is difficult to model unequivocally because there is a large number of end-member molecules and because the cations analysed are frequently in excess of the stoichiometry. Rickwood (1968) has proposed a standard scheme for modelling garnet analyses in terms of solid solutions, which is recommended by Deer et al. (1982). Rickwood's scheme fixes the ideal end-member molecules referred to. Titanium in the garnet lattice is allocated to the titanandradite of composition $Ca_3\ Fe^{3+}_2\ Ti_3\ O_{12}$ (= Rickwood's "schorlomite"; the term is used in that sense hereafter). Concerning the cations analysed in excess of the stoichiometry, Rickwood (1968) recommends to leave Ti^{4+}, Fe^{2+}, Fe^{3+} unallocated in preference to Al and Si. This is because Fe-Ti oxides and quartz are more frequent inclusions than alumino-silicates in garnets. Based on the work of Huggins et al. (1977a and b), Rickwood's scheme can be modified as follows as far as Ti-bearing garnets are concerned. (1) Titanium is only incorporated to the lattice of silica-deficient garnets. It appears therefore valid to left Ti systematically unallocated in preference to Al and Si only in analyses characterized by

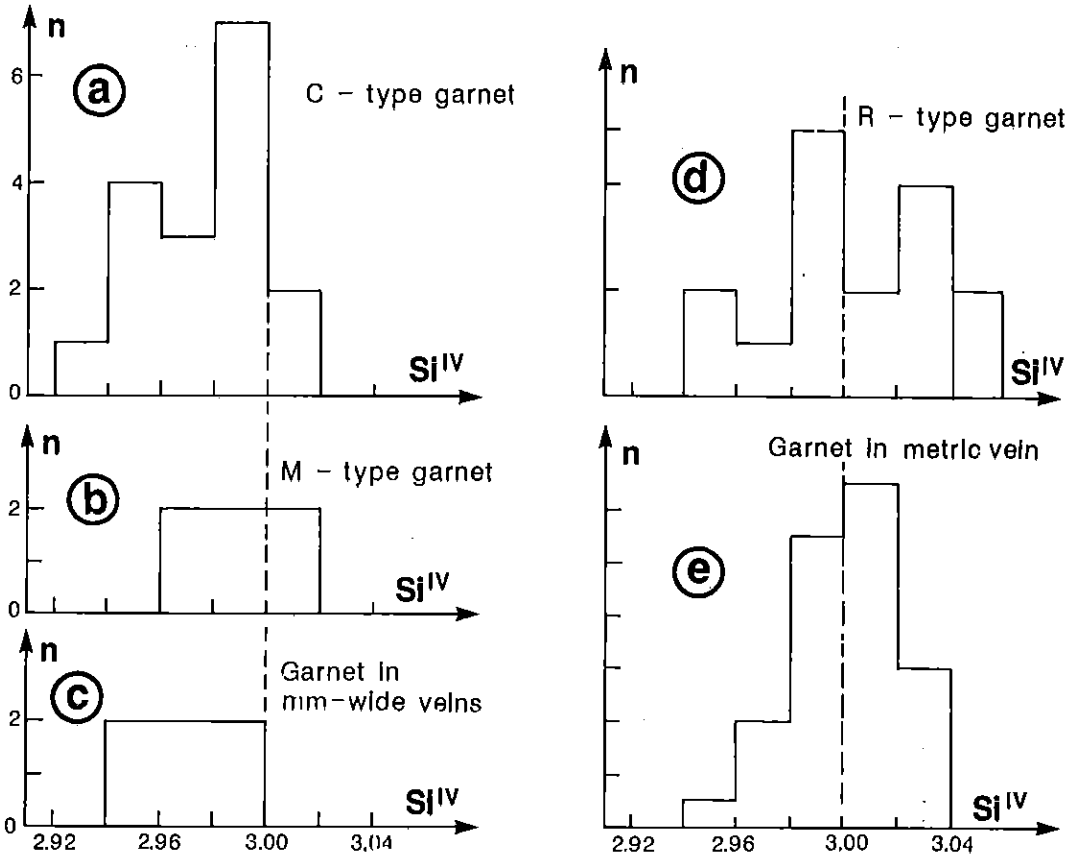

Fig. 4 : Frequency distribution of the amounts of Si^{IV} calculated to 6 oxygens in Sidi Bou Othmane garnet analyses (calculation scheme after Shimazaki, 1977).

Si≥3.00. (2) Because the structure of the Ti-bearing molecule referred to is $Ca_3\ Fe^{3+}_2\ Ti_3\ O_{12}$, Rickwood's scheme is appropriate for reconstructing titangrandite solid solutions only, i.e. solid solutions characterized by (Si+Ti) =3.00 and a sum of divalent cations close to 3.00. It is inappropriate to reconstruct melanite and schorlomite solid solutions, characterized by a sum of divalent cations > 3.00. The crystal-chemistry of these Ti-bearing garnets, however, cannot be simply modelled in terms of reference end-member molecules.

The stability of Fe^{3+} and/or Ti-bearing garnets varies little with pressure but is dependant on oxygen fugacity. Experiments at 2 kb in the presence of a CO_2-free fluid show that pure andradite is stable only at higher fO_2 values than those along a T-fO_2 line approximately between the Q-F-M and I-M I-W buffers below 800°C (Gustafson, 1974; Liou ,1974). Experimental studies at 1 kb show that silica-deficient garnets characterized by Si+Ti=3 (titanandradite) are unstable at low fO_2-conditions. Melanites and schorlomites in contrast, i.e. silica-deficient garnets characterized by (Si+Ti)>3, are stable only at very low fO_2 (e.g. below Q-F-M or W-M buffers at 700°C, depending on composition : Huckenholz et al., 1976). These very low fO_2 values are consitent with the presence of Ti^{3+} in their lattice. The stability field of titanandradite, melanite and schorlomite increases with temperature and is shifted towards lower fO_2 as the oxidation ratio $(Ti^{4+}+Fe^{3+})$/(total Fe+Ti) decreases. Finally, natural titanium-bearing garnets mainly occur in undersaturated alkaline rocks, therefore they are considered to be stable at low silica activity conditions.

Results and interpretation. The electron microprobe analyses of Sidi Bou Othmane Ti-bearing garnets have been treated using both the calculation schemes proposed by Shimazaki (1977) and Huckenholz et al. (1976). The calculated cations have then been compared to a solid solution of ideal

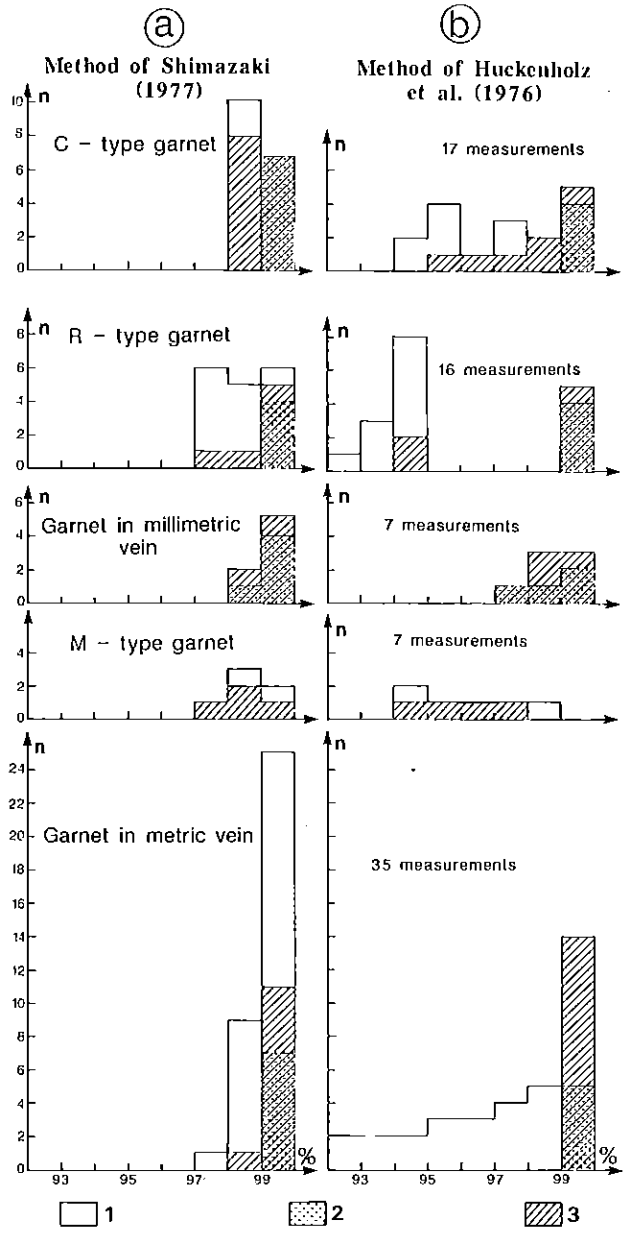

Fig. 5 : Sidi Bou Othmane garnet analyses : percentage of the calculated cations to 12 oxygens that can be allocated to ideal reference end member molecules, depending on the calculation scheme chosen. 1 : silica deficient analyses; 2 : Si + Ti ≈ 3.00; 3 : silica (super) saturated analyses.

molecules including schorlomite ($Ca_3\ Fe_2^{3+}\ Ti_3$) using Rickwood's procedure (1968).

The garnets analysed in the skarns from Sidi Bou Othmane are both silica-deficient ($Si^{IV}<3.00$) and silica-(super) saturated ($Si^{IV}\geq3.00$), except for the garnets in millimeter-wide veins which are essentially silica-deficient (Fig. 4).. In contrast, such analyses are only minor in C-type garnet (Fig. 4a). R-type, M-type and vuggy garnet yield silica-deficient and silica-saturated analyses in about equal proportions (Figs.4b, 4d and 4e).

Figure 5a shows that more than 97% of the cations calculated using the scheme of Shimazaki (1977) can be allocated to solid solutions of ideal molecules with schorlomite, whether the analyses are silica-deficient or not. Three groups of analyses can however be distinguished based on the compared results obtained using the procedure of Shimazaki (1977 : Fig. 5a) or that of Huckenholz et al. (1976 : Fig. 5b). (1) All analyses characterized by $Si \geq 300$, calculated after the scheme of Shimazaki (1977), can be modelled in terms of solid solutions of ideal molecules, with Ti systematically out of the lattice. They are therefore grandites. Many of them however contain silica in excess of 3 atoms per formula unit, which account for most of the unallocated cations. These garnets probably contain microinclusions of quartz. (2) Some silica-deficient analyses, and particularly all the ones in vuggy garnet, yield cations that can be modelled by more 99% in terms of solid solutions of ideal molecules with schorlomite, whathever the scheme is used to model the Fe^{2+}/Fe^{3+} ratio. These analyses are characterized by $Si\leq 3.00$ and $Si+Ti=3.00$ and a sum of divalent cations close to 3.00, they therefore correspond to titanandradite-bearing solid solutions. (3) Fewer silica-deficient analyses in C-type, R-type and M-type garnets yield cations that more strongly depart from a solid solution of ideal molecules with schorlomite, whatever the scheme is used to calculate the cations. These silica deficient analyses are

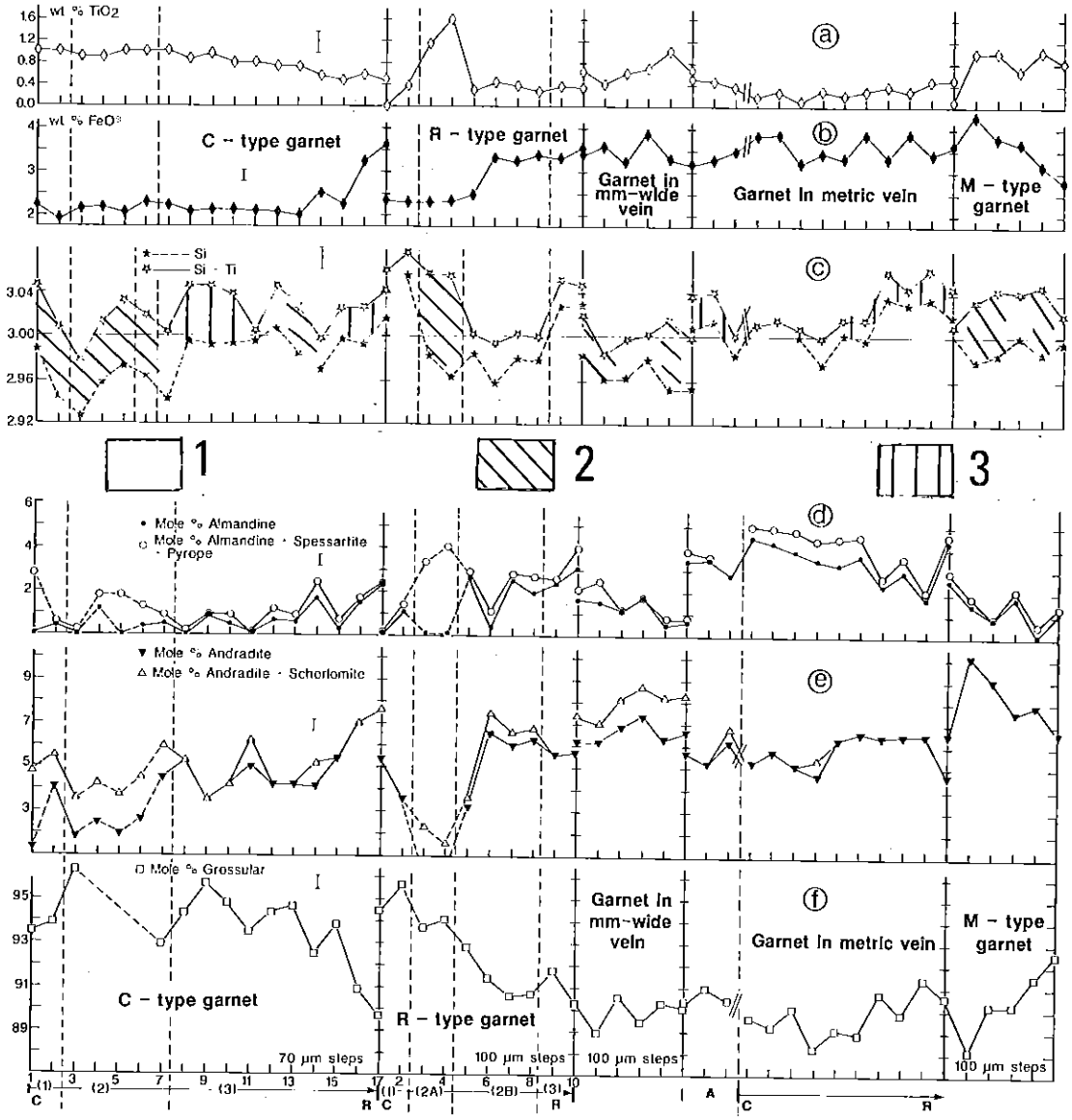

Fig. 6 : Compositional profiles through Sidi Bou Othmane garnets. The structural formulae of melanites are calculated after Huckenholz et al.'s procedure (1976) and that of titangrandites and grandites are calculated after Shimazaki (1977).

(a) and (b) : Profile analyses of TiO_2 and total Fe as FeO (Feo*; wt.%).
(c) Calculated tetrahedral Si and Ti to 12 O; 1: Si < 3.00 and Si+Ti≈ 3.00 (titangandite); 2: Si< 3.00 and Si+Ti> 3.00 (melanite); 3: Si≥ 3.00 (grandite).
(d) to (f) Interpreted structural formulae in terms of solid solutions of ideal molecules. Melanite analyses are shown for comparison, although they are non ideal solid solutions. Profiles through C-type, M-type and vuggy garnets are perpendicular to (110) crystal faces; the profile through a mm-wide vein is perpendicular to the vein axis. Bars are analytical errors (2σ) calculated after Ancey et al. (1978). Limits of zones 1 to 3 in C-type and R-type garnets are shown at the bottom. C: core; R: rim; A: contact zone between R-type and vuggy garnet.

characterized by Si+Ti≥3.00 and a sum of divalent cations in excess of 3.00, they are therefore melanites (Huggins et al., 1977a).

Granditic garnets may contain hydrogen substituting for Si (e.g. Onuki et al., 1982). More than 90% of the analyses from Sidi Bou Othmane garnets total 99±1.5 wt.% and 87% of them are characterized by (Si+Ti) > 3.00. The substitution $4H \rightarrow Si$ is probably of minor importance in Sidi Bou Othmane garnets.

All the structural formulae discussed hereafter are calculated using the scheme of Shimazaki (1977), except for the melanite analyses, which are calculated after Huckenholz et al. (1976). The analyses obtained are listed in Table 2. It is worth noting that the total FeO content and the average Fe^{3+}-content of vuggy garnet were determined to be 3.54 ± 0.28 wt.% and 0.57 ± 0.14 mole % on the basis of 34 microprobe analyses; these results compare favourably with the ones obtained by wet chemical analysis around 3.87± 0.5 wt.% and 0.52 mole % respectively. Figure 6 shows the compositional variations along profiles through the different types of garnet. The Si- and Ti-contents are shown in terms of calculated cations to 12 oxygens (Fig. 6c). The variations of Ca, Fe^{3+}, Mn and Fe^{2+} are shown as mole per cent of the corresponding end member molecules (grossular, andradite and "schorlomite", spessartine and almandine, respectively : Figs. 6d to 6f). The Fe^{2+}, Fe^{3+}, Ti and Mn-content of the melanites is also shown for comparison in terms of mole per cent of the corresponding end member molecules, although these garnets significantly depart from solutions of ideal molecules.

Each of the three zones identified optically in C-type and R-type garnets present a specific chemistry (Fig. 6). (1) Garnet cores, corresponding to zones 1 and 2 in C-type garnet,and to zones 1 and 2A in R-type garnets, have on average a characteristic composition of melanite (Si<3.00 and Si+Ti> 3.00). (2) The intermediate zone 2B in R-type garnet has approximately the composition of a titangrandite (Si<3.00 and Si+Ti≈3.00). In C-type garnet,

Table II : Average electron microprobe analyses of garnets from Sidi Bou Othmame graphite-rich skarns (Central Morocco). Atomic proportions are calculated using the scheme of Shimazaki (1977 for titangrandite and grandite, and using the procedure of Huckenholz et al. (1976) for melanite (indicate by the skar). Numbers in parentheses : 1σ.

	C-type garnet (QG2b)									R-type garnet						Vein garnet				Vuggy garnet			
	Zone 2* t ~ 300 n = 4		Zone 3A t ~ 700 n = 3		n = 5		Zone 3B t ~ 150 n = 2		Zone 2A* t ~ 300 n = 2	Zone 2B t ~ 400 n = 4		Zone 3 t ~ 200 n = 2		t ~ 800 n = 7					Core t ~ 1000 n = 6		Rim t ~ 1000 n = 4	
SiO_2	39.20		39.26		40.01		40.58		39.39	39.47		39.66		39.15					39.73		40.01	
TiO_2	0.95		0.82		0.76		0.53		1.38	0.36		0.36		0.70					0.23		0.40	
Al_2O_3	21.15		21.15		21.18		20.82		20.73	21.04		20.44		20.35					21.02		20.54	
Cr_2O_3	0.01		0.04		0.03		0.14		0.04	0.05		0.00		0.08					0.13		0.01	
FeO	2.19		2.30		2.14		3.45		2.31	3.13		3.44		3.38					3.71		3.61	
MnO	0.10		0.12		0.07		0.01		0.03	0.13		0.16		0.06					0.30		0.09	
MgO	0.07		0.03		0.04		0.02		0.01	0.04		0.06		0.09					0.06		0.05	
CaO	36.57		36.67		36.41		36.50		36.38	36.18		34.57		36.34					35.20		34.88	
Total	100.24		100.39		100.64		102.06		100.27	100.39		98.68		100.16					100.38		99.58	
Si	2.955	(0.021)	2.954	(0.012)	2.998	(0.059)	3.005	(0.016)	2.977	(0.019)	2.975	(0.013)	3.028	(0.007)	2.961	(0.014)	(0.010)	2.997	3.030	(0.008)			
Al	0.045	(0.027)	0.046	(0.016)	0.002	(0.016)	0.000	(0.013)	0.023	(0.013)	0.025	(0.031)	0.000	(0.006)	0.039	(0.021)	(0.027)	0.003	0.000	(0.027)			
Al	1.835		1.830		1.868		1.817		1.824		1.845		1.839		1.776			1.865	1.833				
Fe^{3+}	0.103	(0.016)	0.127	(0.010)	0.087	(0.016)	0.145	(0.013)	0.039	(0.015)	0.132	(0.043)	0.140	(0.005)	0.180	(0.016)	(0.012)	0.114	0.144	(0.030)			
Ti	0.054	(0.003)	0.046	(0.014)	0.043	(0.011)	0.030	(0.004)	0.078	(0.018)	0.020	(0.005)	0.021	(0.002)	0.040	(0.011)	(0.004)	0.013	0.023	(0.005)			
Cr	0.001	(0.001)	0.002	(0.003)	0.002	(0.002)	0.008	(0.001)	0.003	(0.004	0.003	(0.006)	0.000	0	0.005	(0.012)	(0.018)	0.008	0.001	(0.001)			
Mg	0.008	(0.006)	0.003	(0.003)	0.004	(0.002)	0.003	(0.004)	0.001	(0.001)	0.004	(0.002)	0.007	(0.008)	0.010	(0.009)	(0.004)	0.006	0.005	(0.003)			
Fe^{2+}	0.035	(0.013)	0.018	(0.023)	0.047	(0.016)	0.068	(0.002)	0.106	(0.013)	0.065	(0.022)	0.080	(0.014)	0.034	(0.027)	(0.014)	0.120	0.085	(0.034)			
Mn	0.006	(0.005)	0.008	(0.009)	0.004	(0.004)	0.001	(0.001)	0.002	(0.003)	0.008	(0.006)	0.010	(0.007)	0.004	(0.005)	(0.006)	0.019	0.006	(0.006)			
Ca	2.954	(0.014)	2.956	(0.033)	2.923	(0.021)	2.896	(0.023)	2.946	0.013	2.923	(0.020)	2.828	(0.017)	2.945	(0.048)	(0.012)	2.844	2.830	(0.015)			
Alm	-		0.6		0.2		1.9		-		2.0		2.7		1.1			3.9	2.9				
And	-		4.6		4.4		7.4		-		5.6		5.6		7.8			5.7	6.0				
Gro	-		93.3		94.9		90.2		-		91.2		91.1		89.4			89.1	90.7				
Py	-		0.1		0.1		0.1		-		0.1		0.2		0.3			0.2	0.2				
Sch	-		1.0		0.0		0.0		-		0.7		0.0		1.0			0.0	0.0				
Spe	-		0.3		0.2		0.0		-		0.3		0.3		0.1			0.6	0.2				
% Al	-		99.7		98.2		98.7		-		99.9		98.3		99.8			99.6	98.3				

t = thickness of the zone (μm); Alm = almandine, And = andradite, Gro = grossular; Py = pyrope; Sch = "schorlomite" ($Ca_3Fe^{3+}_2Ti_3O_{12}$); Spe = spessartine; n = number of analyses;

% Al = atomic proportion of cations allocated to end-member molecules.

the inner aurole of clear garnet beyond the chiastolite-like structure is mainly characterized by Si in near stoichiometric amount and all Ti in excess of the stoichiometry. A few analyses however are characterized by Si+Ti ≈ 3.00 (titangrandite). (3) The inclusion free outer rim in both C-type and R-type garnets has a granditic composition, with both Si and Ti in excess of the stoichiometry (Si>3.00). C-type and R-type garnets therefore record from core to rim the transition from melanite, to titangrandite and/or silica-saturated grandite, then to grandite with an excess of silica (Fig. 6c and Table II).

The grossular-content of R-type garnet progressively decreases from 95 to 90 mole% from core to periphery (Fig. 6f). R-type garnets however present a chemical discontinuity at the limit between zones 2 and 3, marked by the abrupt increase in total Fe from 2.4 ± 0.1 wt.% to 3.45 ± 0.15 wt.% (Fig. 6b).

C-type garnets also exhibit a chemical discontinuity in periphery, marked by a drop of the grossular-content (from 95 ± 1 to 90 ± 1 mole% : Fig. 6f) and an increase in total Fe as FeO from 2.20 ± 0.30 to 3.45 ± 0.20 wt.% (Fig. 6b).

Garnet in millimeter-wide veins mainly consists of titangrandite, with some analyses trending towards melanite (Fig.6c). It has a grossular-content of 89.7 ± 0.8 mole% (Fig. 6f), a titanium-content of 0.55 ± 0.15 wt.% (Fig. 6a) and total Fe as FeO in the range 3.55±0.35 wt% (Fig. 6b).

Profile analyses accross vuggy garnet show the following. A few analyses in the crystal core are characterized by Si+Ti≈3.00 (titangrandite) whereas most others present an excess of tetravalent cations, Si and Ti, relative to the stoichiometry (Fig. 6c). The grossular-content of vuggy garnet sligthly increases from core to periphery from 89±1 to 90.5±1 mole% (Fig. 6f). Vuggy garnet contains 0.3 ± 0.3 wt.% TiO_2 and 3.5 ± 0.4 wt.% FeO on average (Figs. 6a and 6b).

Finally, M-type garnet analyses are characterized either by Si ≈ 3.00 or are silica-deficient (3.00 < Si < 2.7 : Fig.6c). Both their titanium- and iron-contents are variable, in the range 0.15 - 1.05 and 2.8 - 4.3 wt.% respectively (Figs. 6a and 6b).

Pyroxenes.

Structure. The structural formula $[(M_1)_{1-x}\ (M_2)_x]^{VI}\ (Si,\ Al)^{IV}{}_2O_6]$ accounts for the regular crystal chemistry of pyroxenes (Deer et al., 1978). In calcic pyroxenes, calcium occupies more than two third of the M_2 site and Fe, Mg, Mn are mainly found in the M_1 site. Most naturally occurring pyroxenes, except for the sub calcic and jadeitic ones, are characterized by the sum of cations based on 6 oxygens close to the ideal value of 4.00 (Cawthorn and Collerson, 1974). The structural formulae of ideal clinopyroxenes containing Fe^{3+}, when calculated from electron microprobe analyses on the basis of 6 oxygens, yield a sum of cations > 4.00. The ferrous/ferric iron ratio of these clinopyroxenes can be satisfactorily approximated by introducing Fe_2O_3 in sufficient amounts to reduce the sum of cations to the ideal value of 4.00 (Mysen and Heier, 1972; Robinson, 1980). Papike et al. (1974) also proposed to estimate the Fe^{2+} / Fe^{3+}-content of pyroxenes on solving the charge balance equation :

$$Na + (Al + Fe^{3+})^{IV} = (Al + Cr + Fe^{3+})^{VI} + 2\ Ti \quad (1)$$

Non stoichiometric pyroxenes. Experimental studies show that the presence of large amounts of the $CaAl_2SiO_6$ component facilitates the solution of excess SiO_2 in clinopyroxene (Kushiro, 1969; Wood, 1976a; 1976b; Gasparik and Lindsley, 1980). Many eclogitic clinopyroxenes indeed present a cation sum which decreases progressively from 4.00 (calculated to 6 oxygens) as the Al^{VI} - content increases (Cawthorn and Collerson, 1974). Electron microprobe analyses of both synthetic and natural site-deficient pyroxenes

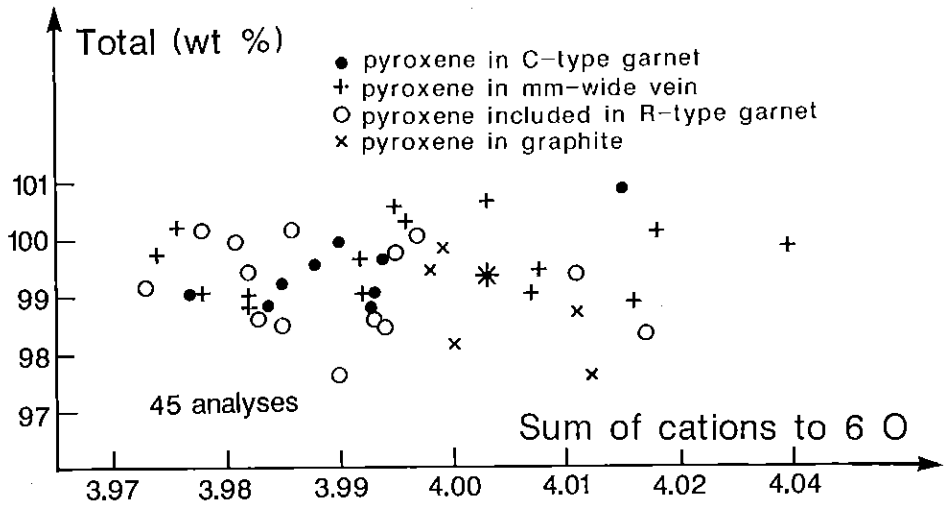

Fig. 7 : Electron microprobe analyses of Sidi Bou Othmane pyroxenes: totals obtained for 11 elements (wt.%) as a function of calculated cation sums to 6O (total Fe as FeO).

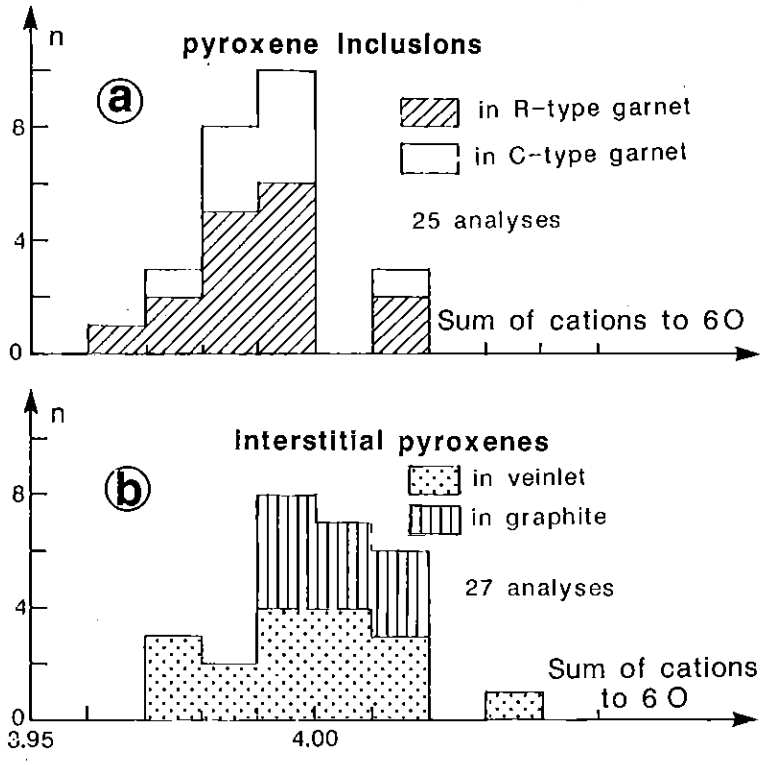

Fig. 8 : Frequency distribution of the calculated cation sums to 6O (total Fe as FeO) for the different types of pyroxenes in Sidi Bou Othmane skarns.

suggest that the solution mechanism probably involves coupled substitutions which produce vacancies in the M1 and M2 crystallographic sites (Cawthorn and Collerson, 1974; Wood, 1976; Wood and Henderson, 1978; Gasparik and Lindsley, 1980). These are, e.g. :

$$Ca^{M2} + 2Al^{T} \rightarrow \square^{M2} + 2\,Si^{T}$$

$$Mg^{M1} + 2Al^{T} \rightarrow \square^{M1} + 2\,Si^{T}$$

These mechanisms are preferred to the entry of Si in VI-fold site (e.g. Smith et al., 1982). $Ca_{0.5}AlSi_2O_6$ and $CaAl_{0.66}Si_2O_6$ have been proposed as hypothetical reference end member molecules for supersilicic pyroxenes with M2 and M1 vacancies respectively (Wood and Henderson, 1978). The vacancy is exclusively in the M2 site when anorthite and quartz coexist with the pyroxene (Wood and Henderson, 1978).

Natural aluminium-rich site-deficient pyroxenes, mainly eclogitic, appear favoured by increasing pressure. This is simply because the possibility of creating vacancies increases with the $CaAl_2SiO_6$ - content of the pyroxene, and the stability of $CaAl_2SiO_6$ increases at higher pressure (Wood and Henderson, 1978).

Results and interpretation. The pyroxenes from Sidi Bou Othmane skarns were analysed for the following elements : Na, K, Ca, Si, Al, Mn, Mg, Fe, Ni, Ti, Cr. 98% of chemical analyses total 98.5 ± 1.5 wt.% (Fig. 7). Three main populations of pyroxenes are identified in the skarns from Sidi Bou Othmane, based on electron microprobe analyses and calculated structural formulae.

(1) Pyroxene inclusions in garnets systematically yield analyses with a cation sum ≤ 3.993 (Fig. 8a).

(2) Pyroxene monocrystals isolated in graphite systematically yield formulae with a cation sum ≥ 3.998 p.f.u. (Fig. 8b).

(3) Pyroxene monocrystals in mm-wide veinlets are zoned. Analyses from crystal cores systematically yield cation sums ≤ 3.993. By contrast,

Table III = Average electron microprobe analyses of Sidi Bou Othmane pyroxenes.

Pyroxene inclusions in garnet

	in C-type garnet								in R type garnet								in M-type garnet	
	zone 1 n=2		zone 2 n=2		zone 2 n=4		zone 3 n=3		zone 1 n=3		zone 2 n=6		zone 2 n=2		zone 3 n=3			
SiO_2	52.54		52.60		52.62		52.29		53.13		52.41		51.55 •		53.09		51.98	
TiO_2	0.00		0.07		0.02		0.04		0.01		0.03		0.00		0.00		0.01	
Al_2O_3	0.50		0.79		0.43		0.41		0.43		0.28		0.13		0.15		0.99	
Cr_2O_3	0.01		0.04		0.04		0.02		0.05		0.02		0.00		0.02		0.01	
FeO*	10.62		9.53		11.00		9.28		10.34		10.30		10.82		11.01		11.69	
MnO	0.12		0.13		0.08		0.22		0.08		0.06		0.12		0.16		0.17	
MgO	10.68		11.72		10.30		11.43		11.16		11.11		10.98		10.93		9.88	
NiO	0.00		0.01		0.03		0.10		0.14		0.06		0.00		0.05		0.08	
CaO	24.71		24.91		24.64		25.60		23.87		24.41		25.16		24.58		24.21	
Na_2O	0.11		0.21		0.08		0.11		0.09		0.05		0.05		0.04		0.17	
K_2O	0.00		0.06		0.01		0.00		0.01		0.01		0.01		0.00		0.02	
Total*	99.29		100.27		99.27		99.50		99.31		98.72		98.83		100.04		99.18	
Smax	3.991		4.004		3.984		4.007		3.978		3.990		4.014		3.988		3.991	
Smin	3.881		4.000		3.871		4.000		3.872		3.883		4.000		3.876		3.871	
ORmin	0.039		0.045		0.164		0.074		0.277		0.117		0.124		0.164		0.000	
FeOc	10.21		9.10		9.20		8.59		7.47		9.09		9.48		9.21		11.69	
Fe_2O_3c	0.46		0.48		2.01		0.77		3.19		1.34		1.49		2.01		0.00	
Totalc	99.33		100.32		99.47		99.58		99.63		98.86		98.97		100.24		99.18	
Si	2.000	(0)	1.982	(0.013)	1.999	(0.002)	1.982	(0.005)	2.000	(0.008)	1.998	(0.004)	1.978	(0.008)	2.000	(0)	1.993	(0.002)
Al4	0.000		0.018		0.001		0.018		0.000		0.002		0.006		0.000		0.007	
Fe4	0.000		0.000		0.000		0.000		0.000		0.000		0.017		0.000		0.000	
Al8	0.023	(0.014)	0.017	(0.039)	0.018	(0.009)	0.001	(0.020)	0.019	(0.011)	0.11	(0.010)	0.000	(0.002)	0.007	(0.003	0.037	(0.008)
Fe8	0.013	(0.001)	0.013	(0.032)	0.057	(0.028)	0.022	(0.019)	0.090	(0.040)	0.038	(0.044)	0.026	(0.011)	0.057	(0.014)	0.000	(0)
Ti	0.000		0.002		0.001		0.001		0.000		0.001		0.000		0.000		0.000	
Cr^{3+}	0.000		0.001		0.001		0.001		0.002		0.000		0.000		0.000		0.000	
Mg	0.606	(0.113)	0.656	(0.064)	0.583	(0.069)	0.648	(0.032)	0.626	(0.027)	0.632	(0.025)	0.627	(0.020)	0.614	(0.021)	0.564	(0.015)
Fe^{2+}	0.325	(0.072)	0.286	(0.062)	0.292		0.272	(0.041)	0.235	0.040	0.290	(0.052)	0.304	(0.002)	0.290	(0.034)	0.375	(0.014)
Mn	0.004		0.004		0.003		0.007		0.003		0.002		0.004		0.005		0.005	
Ni	0.000		0.000		0.001		0.003		0.004		0.002		0.000		0.002		0.002	
Ca	1.008	(0.009)	1.002	(0.013)	1.003	(0.013)	1.040	(0.021)	0.963	(0.014)	0.997	(0.024)	1.034	(0.004)	0.992	(0.021)	0.994	(0.014)
Na	0.008		0.015		0.006		0.008		0.006		0.003		0.004		0.003		0.12	
K	0.000		0.003		0.000		0.000		0.000		0.000		0.000		0.000		0.001	
Scat	3.986		4.000		3.965		4.000		3.948		3.977		4.000		3.969		3.991	
AJd	0.8		1.7		0.5		0.7		0.5		0.3		0.4		0.2		1.3	
Fjd	0.0		0.0		0.0		0.0		0.0		0.0		0.0		0.0		0.0	
CATs	0.0		0.7		0.0		0.4		0.0		0.0		0.1		0.0		0.7	
CAFTs	-0.0		0.7		0.0		1.1		0.0		0.0		2.2		0.0		0.0	
M1sd	2.2		0.0		1.9		0.0		0.9		1.1		0.0		0.6		2.6	
FM1sd	2.0		0.0		8.6		0.0		5.6		5.8		0.0		7.1		0.0	
M2sd	0.0		0.0		0.0		0.0		0.8		0.0		0.0		0.1		0.0	
FM2sd	0.0		0.0		0.0		0.0		5.4		0.0		0.0		1.0		0.0	
En	30.3		33.0		29.3		32.5		31.4		31.7		31.4		30.8		28.3	
Fs	16.3		14.4		14.7		13.7		11.8		14.5		15.2		14.6		18.8	
Wo	48.4		49.6		45.0		51.5		43.6		46.5		50.7		45.7		48.3	

• in the quartz – needle zone

Atomic proportions are calculated following the scheme of Mysen and Heier (1977) from "ideal" pyroxenes. The minimum Fe^{3+} content of site-deficient pyroxenes is calculated following the scheme in Appendix.

Interstitial and vein pyroxenes

	Monocrystals in graphite								Protile through vein						Monocrystal in vein					
	4J26		Q63		E48b		Q62		C → R						R ← C → R					
	n=2		n=5		n=4		n=2		n=1	n=2		n=2			n=3	n=4		n=3		
SiO_2	51.89		52.45		52.46		51.88		53.24	52.21		52.43			52.22	52.64		51.71		
TiO_2	0.04		0.03		0.02		0.00		0.00	0.00		0.02			0.02	0.02		0.01		
Al_2O_3	0.81		0.47		0.17		0.16		0.15	0.21		0.13			0.15	0.16		0.15		
Cr_2O_3	0.02		0.01		0.00		0.00		0.00	0.06		0.00			0.00	0.01		0.00		
FeO*	11.50		8.42		10.04		12.88		12.49	12.87		10.62			11.99	12.12		12.32		
MnO	0.13		0.14		0.13		0.22		0.19	0.09		0.27			0.19	0.14		0.11		
MgO	10.21		12.06		11.33		9.91		9.80	9.57		11.31			10.26	9.72		10.24		
NiO	0.00		0.01		0.04		0.02		0.00	0.01		0.07			0.07	0.02		0.10		
CaO	24.24		25.60		25.26		25.81		24.37	24.53		24.90			24.72	24.26		24.92		
Na_2O	0.17		0.09		0.02		0.05		0.00	0.09		0.01			0.07	0.06		0.16		
K_2O	0.01		0.03		0.03		0.00		0.00	0.00		0.05			0.01	0.01		0.05		
Total*	99.00		99.32		99.50		100.91		100.23	99.64		99.81			99.71	99.16		99.78		
Smax	3.995		4.007		4.002		4.021		3.976	3.994		4.005			4.001	3.979		4.019		
Smin	3.876		4.000		4.000		4.000		3.848	3.861		4.000			4.000	3.854		4.000		
ORmin	0.000		0.76		0.020		0.157		0.320	0.055		0.047			0.006	0.316		0.146		
FeOc	11.50		7.78		9.84		10.85		8.49	12.04		10.12			11.92	8.29		10.53		
Fe_2O_3c	0.00		0.71		0.22		2.25		4.45	0.93		0.55			0.08	4.26		1.99		
Totalc	99.00		99.39		99.52		101.14		100.68	99.73		99.87			99.71	99.59		99.98		
Si	1.991	(0.013)	1.983	(0.012)	1.994	(0.008)	1.966	(0.008)	2.000	1.999	(0.000)	1.990	(0.005)		1.998	(0.002)	1.999	(0.002)	1.975	(0.010)
Al4	0.009		0.017		0.006		0.007		0.000	0.001		0.006			0.002		0.001		0.007	
Fe4	0.000		0.000		0.000		0.027		0.000	0.000		0.004			0.000	(0)	0.000		0.018	
Al8	0.028	(0.003)	0.004	(0.022)	0.002	(0.001)	0.000	(0.001)	0.006	0.009	(0.005)	0.000	(0.004)		0.004	(0.001)	0.006	(0.003)	0.000	(0.002)
Fe8	0.000	(0)	0.020	(0.015)	0.006	(0.018)	0.037	(0.021)	0.126	0.027	(0.006)	0.012	(0.008)		0.002		0.122	(0.028)	0.039	(0.051)
Ti	0.001		0.001		0.001		0.000		0.000	0.000		0.001			0.001		0.001		0.000	
Cr^{3+}	0.001		0.000		0.000		0.000		0.000	0.002		0.000			0.000		0.000		0.000	
Mg	0.584	(0.004)	0.679	(0.030)	0.642	(0.009)	0.560	(0.017)	0.548	0.546	(0.055)	0.640	(0.102)		0.585	(0.024)	0.550	(0.027)	0.583	(0.018)
Fe^{2+}	0.360	(0.012)	0.246	(0.019)	0.313	(0.018)	0.344	(0.006)	0.267	0.385	(0.055)	0.321	(0.082)		0.381	(0.009)	0.263	(0.044)	0.336	(0.064)
Mn	0.004		0.004		0.004		0.007		0.006	0.003		0.009			0.006		0.005		0.004	
Ni	0.000		0.000		0.001		0.001		0.000	0.000		0.002			0.002		0.001		0.003	
Ca	0.997	(0.003)	1.037	(0.010)	1.029	(0.009)	1.048	(0.004)	0.981	1.006	(0.004)	1.012	(0.011)		1.013	(0.037)	0.987	(0.027)	1.020	(0.026)
Na	0.012		0.007		0.001		0.003		0.000	0.007		0.001			0.005		0.005		0.012	
K	0.000		0.002		0.002		0.000		0.000	0.000		0.002			0.001		0.000		0.003	
Scat	3.995		4.000		4.000		4.000		3.934	3.985		4.000			4.000		3.939		4.000	
AJd	1.2		0.8		0.3		0.3		0.0	0.5		0.3			0.6		0.5		0.7	
Fjd	0.0		0.0		0.0		0.0		0.0	0.0		0.0			0.0		0.0		0.8	
CATs	0.6		0.6		0.2		0.2		0.0	0.1		0.1			0.0		0.0		0.0	
CAFTs	0.0		1.0		0.3		3.2		0.0	0.0		0.8			0.1		0.0		2.4	
Mlsd	1.4		0.0		0.0		0.0		0.7	0.5		0.0			0.0		0.2		0.0	
FM1sd	0.0		0.0		0.0		0.0		13.4	4.0		0.0			0.0		15.9		0.0	
M2sd	0.0		0.0		0.0		0.0		0.2	0.0		0.0			0.0		0.0		0.0	
FM2sd	0.0		0.0		0.0		0.0		3.7	0.0		0.0			0.0		1.6		0.0	
En	29.3		34.1		32.2		28.1		27.5	27.4		32.2			29.4		27.6		29.3	
Fs	18.5		12.3		15.7		17.3		13.4	19.3		16.2			19.2		13.2		16.9	
Wo	48.9		51.2		51.3		50.9		41.2	48.2		50.5			50.8		41.1		50.0	

Table III (continued)

analyses from crystal peripheries yield analyses with a cation sum > 4.00 (Fig. 8b).

Analyses yielding a cation sum to 6O ≥ 3.998 : stoichiometric pyroxenes. Pyroxene analyses with a cation sum ≥ 3.998, whether from the core of veinlet-forming crystals or from crystals included in graphite, were treated following the method of Mysen and Heier (1972) to recalculate the Fe^{2+} / Fe^{3+} ratio. The results obtained are listed in Table III. Calculated ferric iron -contents based on the assumption of ideal stoichiometry represent 0 to30 mole% of total iron. Figure 9 shows that the structural formulae thus obtained also verify the charge balance equation (1) to within 0.002 cations. In general, the structural formulae obtained for ideal pyroxenes from Sidi Bou Othmane skarns satisfy the requirements for acceptable analyses proposed by Cameron and Papike (1980), except for one. 70 % of them yield Ca cations in the range 1.020 - 1.057. These values contrast with the generally accepted maximum value of ≈ 1.020 for Ca in M2 site (1.016 : Robinson, 1980; 1.021 : Cameron and Papike, 1980). Besides, Ca-contents in M1 site > 0.010 were never observed (Robinson, 1980).

The calculated cations were allocated to the following reference ideal molecules in that order : jadeitic pyroxene ((Na, K)(Al, Cr) Si_2 O_6 = Jd) , Ti and Si Ca-Tschermak molecule (Ca (Al, Fe^{3+})$_2$ (Ti, Si) O_6, = Ti-CAFTs, CATs and CFTs), johannsenite (Ca Mn Si_2O_6, =Jo), clinoenstatite ($Mg_2Si_2O_6$, =En), clinoferrosilite ($Fe_2Si_2O_6$, = Fs), wollastonite ($Ca_2Si_2O_6$, = Wo). More than 99% of the calculated cations correspond to slightly tschermakitic and jadeitic salites. Observed compositions were in the range : 48.9-52 mole% Wo, 30.6-35.6 mole% En, 11-20 mole% Fs, 0-4.3 mole% CFTs, 0-2 CATs, 0.2-2.5 FJd and 0-1.6 mole% AJd.

Analyses yielding a cation sum to 6O ≤ 3.997 : non stoichiometric pyroxenes? Lindsley (1980) has discussed the problem of whether compositional deviations in lunar pyroxenes was significant of non

Table IV : Estimation of the Fe2+/Fe3+ ratio in pyroxenes based on a comparison of bulk rock wet chemical and electron microprobe analyses of the rock-forming garnets and pyroxenes (sample E48b).

	Wet chemistry			Electron microprobe data	
	bulk sample	silicate part [a]	reconstructed composition [b]	garnet	pyroxene
SiO_2	38.55	42.27	41.5	39.7	52.30
Al_2O_3	16.16	17.72	17.90	20.8	0.30
Fe_2O_3	2.28	2.50	2.50	1.90	6.13 [c]
FeO	2.40	2.63	1.91	1.40	5.00
MnO	0.13	0.14	0.14	0.15	0.09
MgO	1.46	1.60	1.60	0.04	11.06
CaO	30.22	32.03	33.90	35.5	24.44
Na_2O	0.03	-	–	–	–
K_2O	0.01	-	-	-	-
TiO_2	0.50	0.60	0.40	0.44	0.01
P_2O_5	0.06	-	–	–	–
CO_2*	0.73	-	–	–	–
C_{org}	6.47	-	–	–	–
H_2O	0.49	-	–	–	–
Total	99.49	99.49	99.85	99.75	99.83

*: decarbonation CO_2; Corg: organic carbon; (a): bulk sample minus (calcite + apatite + graphite); (b): garnet is almost Mg-free; the MgO-content of the silicate part therefore fixes the wt.% pyroxenes to ≈ 0.142; (c): deduced from total FeO and Fe_2O_3-content in the silicate part (wet chemistry) and in the garnet (interpreted electron microprobe data; see text).

stoichiometry or were due to analytical errors. The discussion was facilitated by the fact that lunar rocks contain very little Fe_2O_3, therefore representative structural formulae were calculated on taking total Fe as FeO. In contrast, Sidi Bou Othmane skarns contain some Fe as Fe_2O_3 (Ramboz and Bastoul, 1985). In particular, wet chemical analyses show that garnet-clinopyroxene-graphite-bearing samples contain ≈ 4-5 wt% FeO (total) and up to 70 mole % Fe as Fe^{3+}. Mass balance considerations based on bulk rock wet chemistry and on average estimates of Fe^{2+}/Fe^{3+} ratios in garnets from electron micropobe analyses, suggest that Sidi Bou Othmane pyroxenes contain significant amounts of Fe_2O_3 (≈ 50 wt.% : Table IV). This imply that cation sums obtained with total Fe as FeO are minimum values.

X-ray diffraction patterns obtained on hand picked pyroxenes from veinlets do not interpretably depart from that of hedenbergite. Despite that fact, calculated structural formulae with a cation sum ≤ 3.997 are thought to correspond to site-deficient (supersilicic) pyroxenes and not to analytical errors for the following reasons. (i) There is no positive correlation between the sum of cations calculated to 6 oxygens and the total wt.% oxides analysed (Fig. 7). The cation deficiencies observed p.f.u. therefore cannot be attributed to an element present in the crystals which is not analysed. (ii) Pyroxene yielding analyses with a cation sum to 6O both above and below 4.00 have been analysed within the same thin section and the same crystals, all experimental conditions being similar. (iii) The pyroxenes departing from an ideal stoichiometry are not randomly distributed in the sections. They systematically occur as inclusions in the core of R-type and C-type garnets and in the core of monocrystals in millimeter-thick veins. Site-deficient pyroxenes in particular systematically coexist with non stoichiometric garnet in the chiastolite-type structure of C-type garnets (zone 2) and in zones 1 and 2 of R-type garnets.

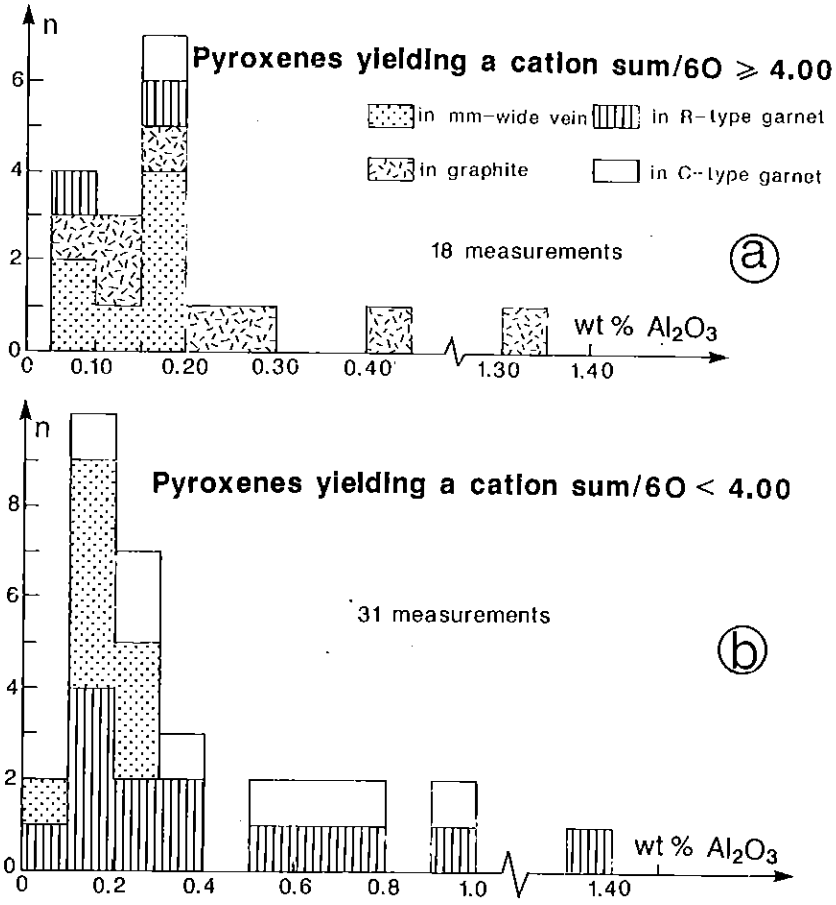

Fig. 9 : Frequency distribution of the Al_2O_3 - contents measured with electron microprobe analyses in the different types of pyroxenes in Sidi Bou Othmane skarns ($2\sigma \approx 0.1$ wt.%).

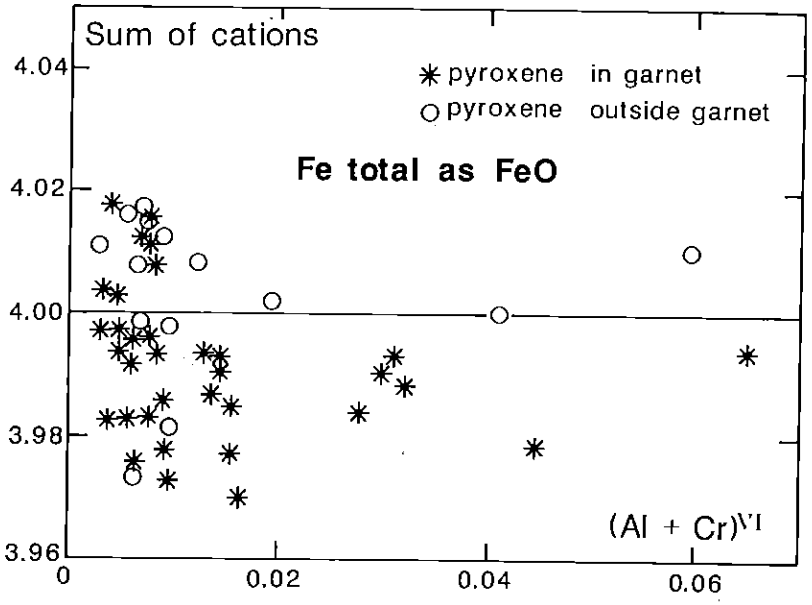

Fig. 10 : Sidi Bou Othmane pyroxene analyses : calculated cation sums to 6O as a function of the (Al+Cr) cation fillings in VI-fold site .

The presence of site-deficient pyroxenes in the skarns from Sidi Bou Othmane is most unusual. (1) All known synthetic and natural site-deficient pyroxenes were formed under high pressure conditions. In contrast, the skarns from Sidi Bou Othmane are formed below 4 kb, as shown by the presence of $(Fe_{0.5}Mg_{0.5})$-cordierite in the near-by metamorphic schists (Holdaway and Lee, 1977; Ramboz, unpubl. analyses). (2) All natural site-deficient pyroxenes are aluminium-rich whereas the Sidi Bou Othmane pyroxenes do not contain more than 1.40 wt.% Al_2O_3, whether they are site-deficient or not (Fig. 9). (3) Unlike what is observed in eclogitic pyroxenes, the amount of observed cation deficiencies is unrelated to the presence of Al in octahedral site.(Fig. 10).

By analogy with the formation of Al-rich non stoichiometric pyroxenes in high pressure environments being linked with increasing amounts of $CaAl_2SiO_6$ molecule, the possibility of creating vacancies in the low pressure pyroxenes from Sidi Bou Othmane is tentatively related to increasing amounts of $CaFe^{3+}{}_2SiO_6$ molecule. (1) Ferri-tschermakitic pyroxenes are stable at low pressure. Esseneite, a clinopyroxene with ideal formula $Ca(Fe^{3+}Al)SiO_6$, has been recently found in partially fused rocks resulting from near surface combustion of coal (Cosca and Peacor, 1987; Foit et al., 1987). It can be argued that esseneite is stable at high fO_2-conditions (Oba and Onuma, 1978; Onuma, 1983; Cosca and Peacor, 1987), in contrast to the Sidi Bou Othmane pyroxenes, which are associated with fluids and silicates typical of reducing environments. This is probably because the former pyroxenes mainly contain Fe^{3+} whereas the latter contain both Fe^{2+} and Fe^{3+}.

Bases for the interpretation of cation deficient pyroxene microprobe analyses in terms of end member molecules, including the site deficient ones, is given in Appendix. These show that the proper characterization of the composition of site-deficient pyroxenes requires an independant determination of the Fe^{2+}/ Fe^{3+} ratio in complement to the electron

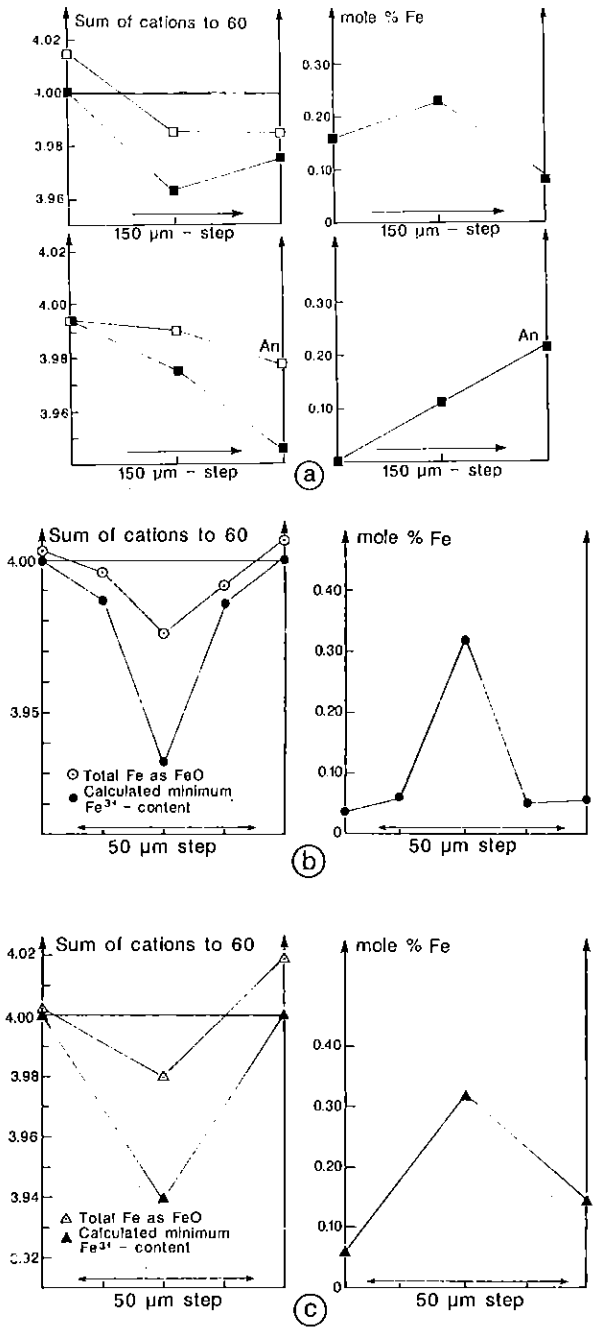

Fig . 11 : Compositional variations shown by (a) pyroxene inclusions in a C-type garnet, (b) across a mm-wide veinlet and (c) through veinlet-forming pyroxene monocrystals (averages values for 3 or 4 analyses) . The arrow indicates the growth direction of the host garnet or of the pyroxene. The method for calculating minimum Fe^{3+}-contents in pyroxene analyses yielding less than 4 cations / 6O (total Fe as FeO) is given in Appendix.

micropobe analysis. Only a minimum Fe^{3+}-content can be deduced from latter data, in order to satisfy the modified charge balance equation

$$(Na + K) + (Al+Fe^{3+})^{IV} = 2\,Ti + (Al.\ Fe^{3+} + Cr)^{VI} + 2\,(p+q) \qquad (2).$$

A minimum Fe^{3+}-content in the range 4- 45 mole% is required for most cation deficient pyroxene analyses at Sidi Bou Othmane to satisfy equation (2). Figure 11 shows interpreted profile analyses of pyroxenes included along growth planes of C-type garnets, or in section across veinlets or veinlet-forming crystals. Calculated cation deficiencies increase in sector zoned pyroxenes included in C-type garnet, corresponding to increasing calculated mole fractions of M1-site deficient molecule to around 11 mole% (Fig. 11a). In contrast, calculated cation deficiencies in veinlets or veinlet-forming monocrystals decrease from cores to peripheries, corresponding to decreasing contents in M1 site-deficient component from 15 to 0 mole % (Figs. 11b and 11c). Cation deficiencies in M2 site are generally zero, except in the core of vein pyroxenes where they systematically reach 2 to 7 mole% $Ca_{0.5}Fe^{3+}_2SiO_6$.

It is worth noting that four preliminary analyses of pyroxenes associated with M-type garnets in sample 4J26, either included in garnet or as needles in the graphitic matrix, showed Al_2O_3-contents in the range 0.76-1.11 wt.%, i. e. higher than average values measured in anhydrous skarn pyroxenes. For three of them, structural formulae calculated with total Fe as FeO yielded cation deficiencies ranging from 3.994 to 3.985. These analyses, like two other ones of Al_2O_3-enriched pyroxenes included in C-type and R-type garnets, verified the modified charge balance equation (2) to within .002 cations, all Fe being taken as Fe^{2+} (Fig.12). This suggests that pyroxenes associated with M-type garnets have a lower Fe_2O_3-content than those associated with C-type and R-type garnets, a conclusion supported by bulk rock wet chemical analyses. Sample 4J26 has a FeO-content ≈ 5wt.% FeO, similar to that of sample E48b but it presents an oxidation ratio of iron of 0.24

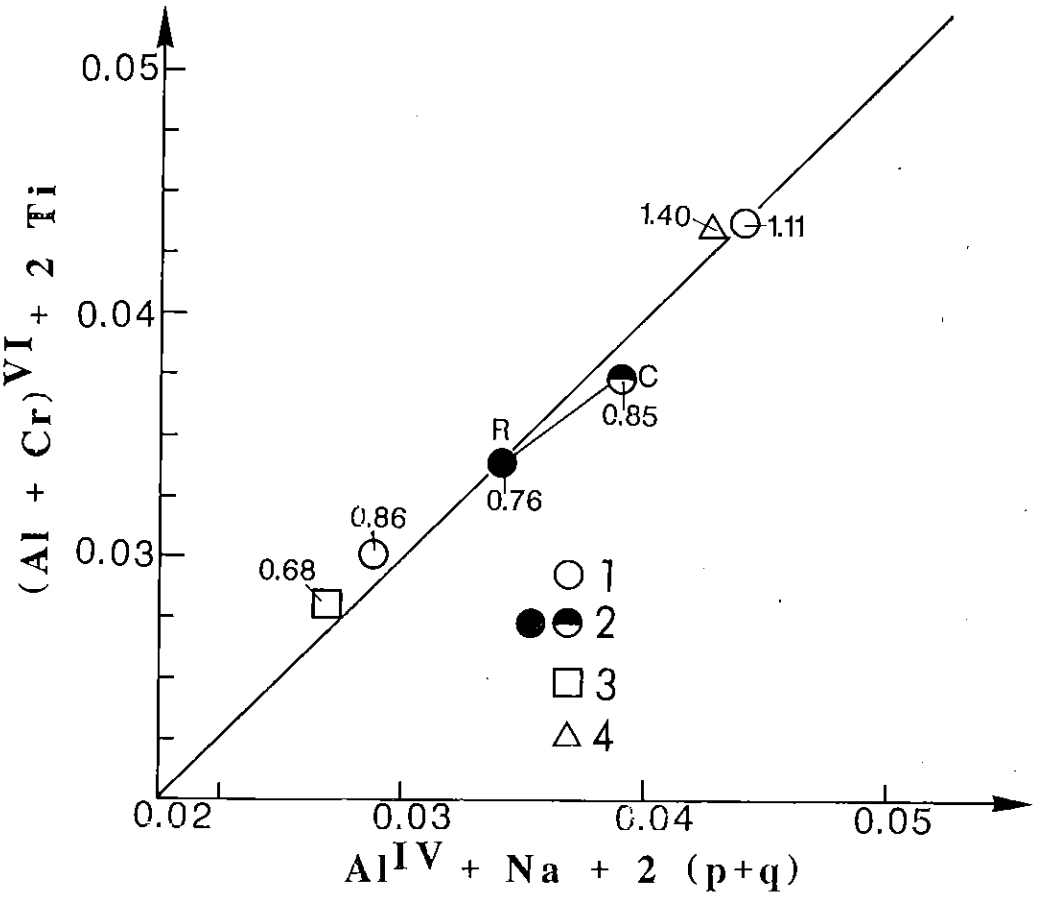

Fig. 12 : (Al + Cr)^{VI} + 2 Ti versus Al^{IV} + Na + 2 (p + q) diagram for 6 Al_2O_3-rich pyroxene analyses, where p and q are the cation deficiencies in M1 and M2 sites, respectively (see Appendix). 1 : Pyroxene inclusions in M-type garnet. 2 : Needle-like pyroxene in the graphitic matrix (C = core; R = rim). 1 and 2 refer to sample 4J26. 3 : Pyroxene inclusion in R-type garnet. 4 :Pyroxene inclusion in C-type garnet. The numbers above data points are Al_2O_3-contents in wt.%.

% (mole),lower than that of sample E48b ≈ 0.46 % (Ramboz and Bastoul, 1985).

Discussion.

Sidi Bou Othmane skarns are remarkable by the different types of garnet they display at the metric scale. C-type and R-type garnets show similar compositional zoning but specific inclusion geometries. By contrast, M-type garnets are devoid of specific inclusion patterns and well characterized chemical zoning. Compositional zoning and inclusion patterns in R-type and C-type garnets are somewhat similar to the ones that low grade garnets develop during their growth, but also present some characteristic features, to be examined below.

Growth zoning and inclusion formation in minerals are disequilibrium features, the preservation of which depends on the kinetics of prograde and retrograde metamorphic reactions. The fact that such features are commonly observed in low grade garnet proves that later bulk volume re-equilibration of the crystals are precluded at any reasonable growth rate below 550°C, implying very low diffusivities in this mineral under such conditions (Tracy, 1982).

C-type and R-type garnets.

Inclusion geometries. Chiastolite-type distribution of graphite in andalousite or staurolite is frequent, however silicate and/or oxide inclusions with chiastolite-type patterns in garnet, as observed in C-type porphyroblasts, are uncommon; they have been mainly observed in manganese garnets from contact metamorphism aureoles (in the Ardennes and the Urals : Harker, 1939; in Magerøy, Norway : Andersen, 1984). C-type garnets at Sidi Bou Othmane coexist with abundant graphite, but their Mn-content is low (< 0.30 wt.%). The latter character, like the richness in Al_2O_3 and Fe_2O_3, reflects

bulk rock chemistry. To account for the chiastolite-type distribution of graphite in andalousite or staurolite, it has been proposed that graphite was excluded from growing crystal faces and concentrated at the crystal edges, thereby poisoning the growth of the latter surfaces (Penfield and Pratt, 1894). The accumulation of graphite along edges has in fact been observed in some Sidi Bou Othmane C-type garnets; however, it was exclusive of the presence of associated clinopyroxenes along these preferential growth planes. It is worth noting that, in Magerøy garnets, graphite is also distributed along distinct crystallographic planes from that where quartz or Fe-Ti oxides are found (Andersen, 1984). This suggests that distinct (if not antagonist) mechanisms rule the incorporation of graphite and silicate or oxide inclusions in garnets.

Silicate or oxide inclusions in garnets can either be matrix minerals or minerals which are not found in the matrix outside garnet. In the latter case, inclusions likely represent unreacted phases, which testify of otherwise non preserved intermediate reaction stages (Thompson et al., 1977). This interpretation probably applies to poecilitic calcite observed once in the core of a R-type garnet. As for matrix minerals, they are thought either to have been incorporated mechanically in garnet or to have formed simultaneously with it. The fact that all garnet-forming reactions in low grade conditions are quartz-producing (Thompson, 1976) and that quartz is the most frequent inclusion mineral in low grade garnets comes in support of the latter hypothesis (Tracy, 1982). In Magerøy garnets however, Andersen (1984) proposed that type I quartz or Fe-Ti oxide inclusions displayed along crystal edges represented relics of the matrix, whereas type II inclusions displayed along planes perpendicular to crystal faces were newly-formed with garnet. At Sidi Bou Othmane, R-type garnets contain mainly type I pyroxene inclusions and C-type garnets contain both type I and type II pyroxenes along growth planes. Pyroxene inclusions in R-type and C-type garnets are almost

graphite-free, whereas the matrix outside garnet consists of associated graphite and pyroxene. This suggests that pyroxenes were formed simultaneously with the garnet and do not represent relics of the matrix.

In both C-type and R-type garnets, quartz is only included at an intermediate stage of the crystal growth. In C-type garnets, type II pyroxene inclusions occur at the limit between zone 2 and zone 3 along planes perpendicular to crystal faces. In R-type garnets by contrast, it occurs as spherically arranged needles. Ilmenite inclusions arranged in a similar tridimensional spherical pattern have been interpreted to have formed during static growth of the garnets (Harvey and Ferguson, 1973). At Sidi Bou Othmane, there is abundant evidence that C-type and R-type garnets were formed simultaneously, as shown by their similar chemical zoning (Fig. 6), and by the fact they contain inclusions similar in nature, although dissimilar in shape, and that they coexist at the centimetric scale in strata. As there is both textural and chemical evidence that C-type garnets were contemporaneous with shear veins, it is therefore concluded that R-type garnets were syntectonic like C-type garnets, and not post-tectonic.

One way to explain how silicates growing in a regional shear stress field can locally develop isotropically (as shown by rounded shapes and spherical inclusion geometries) and obliterate previous schistosities, is to assume that the fluid pressure locally exceeded σ_3. Coupled micothermometric and Raman spectrometric studies of fluid inclusions in Sidi Bou Othmane skarns in fact point out to variable fluid pressures at the centimetric scale at Sidi Bou Othmane (Bastoul, 1983). Probably, the cause of enhanced fluid pressure during R-type garnet growth was the simultaneous intense volatilization of graphite, consistent with the fact that R-type garnet-rich facies are graphite-depleted and associated with CH_4-enriched fluids compare to C-type bearing facies. This implies that R-type garnets have grown in a gas-rich, higher energy environment than C-type garnets; this is

consistent with the former crystals containing larger amounts of clinopyroxene inclusions than the latter (Spry, 1969).

During the growth of C-type garnets, magnesium (which was not incorporated to the garnet lattice in the considered conditions) and silica were transported towards crystal edges through the graphitic matrix, due to lower growth rate and lower nucleation rates (e.g. Kretz, 1973). This therefore favoured the nucleation of clinopyroxenes and quartz along crystal edges. It is worth noting that staurolite from contact metamorphism aureoles also show systematic preferential enrichment in Si and Fe, Mg along (010) sectors compare to (001) sectors; this compositional zoning was interpreted to result from different atomic configuration of the surface layers (Hollister, 1970).

The compositional zoning displayed by Sidi Bou Othmane C-type and R-type garnets is somewhat different from that commonly observed in low grade garnets. These typically display bell-shaped profiles of Mn, corresponding to decreasing Mn-content from core to peripheries, with antipathetic variations of Fe. Such variations are interpreted to reflect the progressive depression of Mn in Fe-Mg-Mn reactants of the rock under prograde conditions ('reaction partitioning model' : Harte and Henley, 1966; Hollister, 1966; Kretz, 1973). At Sidi Bou Othmane, garnets have a low Mn-content, and profile analyses of Fe do not simply reflect variable almandine-contents, because Fe shows variable oxidation state. Only the bell-shaped profile of Ca through C-type and R-type garnets is typical of low grade garnets formed under prograde conditions (see references in Tracy, 1982; Andersen, 1984).

The most uncommon characteristic feature of the compositional zoning in C-type and R-type garnets is the progressive transition from melanite to titangrandite and grandite from cores to peripheries (Fig. 6c). Experimental data show that silica-deficient garnet characterized by (Si + Ti) > 3.00, as observed in C-type and R-type crystal cores, require very low fO_2-conditions

to form, whereas later crystallized titangranditic and granditic garnet does not (Huckenholz et al. 1976; Liou, 1974; Gustafson, 1974). FO_2-conditions at an early growth stage of C-type and R-type garnets can be tentatively estimated to have been around 10^{-28} bar maximum at 550°C, i.e. at or below I-W buffer conditions. These estimations are based on the experimentally determined stabilities of some melanite and titangrandite samples (HGH1 and GTA7 : Huckenholz et al., 1976). These samples are poorer in Al_2O_3 and richer in TiO_2 than the studied garnets; however experimentally studied samples with dissimilar Al_2O_3, Fe_2O_3 and TiO_2-contents have yeilded comparable fO_2 stability fields below 600°C. At 500°C and 2 kbar, a fO_2 value of 10^{-28} bar fixes the mole fraction of water to around $3\ 10^{-3}$ in a fluid at equilibrium with graphite and containing about 80 mole% N_2 (Bastoul, 1983). This implies that near total reduction of water took place at an early stage of R-type and C-type garnet growth.

The cause of unusually low fO_2-conditions at an early stage of skarn development was probably the decay of some major rock - forming components : the organic derived compounds, whether they resulted from the breakdown of organic matter or from the destabilization of NH_4^+-bearing micas or feldspars. It is worth noting that the release of NH_4^+ from micas to the fluid has been experimentally determined to occur at 550°-600°C (Hallam and Eugster, 1976). At Sidi Bou Othmane by contrast, the chemistry of the garnets and the nature of the inclusions they contain fix the temperature of garnet formation and NH_4^+-release related to maximum values of ≈ 550°C (Tracy, 1982). Volatilization reactions at Sidi Bou Othmane were probably shifted to lower temperatures because H_2O and CO_2 activities were lowered in the nitrogen and carbon-rich fluids (Dubessy and Ramboz, 1986).

Both veinlet garnet and the core of vein garnet have titangranditic compositions on average, suggesting they were formed at about the same time as the zone 2-zone 3 transition in C-type garnets or the zone 2A-zone 2B

transition in R-type garnets. The increase in fO_2 marked by the transition from melanitic to titangranditic garnet was therefore contemporaneous with vein opening. Hence it probably corresponded to a discontinuity in the evolution, compatible with the influx of water-rich fluids from the surrounding pelites and limestones towards the graphite-rich areas. R-type garnets in fact record a drop of TiO_2 and an increase in FeO at about the latter growth stage (Figs. 6a and 6b).

The association of silica-deficient melanitic and titangranditic garnets with supersilicic pyroxenes at Sidi Bou Othmane is now considered. This association is somewhat puzzling as, at the magmatic stage, the formers develop from low silica activity melts whereas the latters commonly grow from high silica activity ones (e. g. Huckenholz, 1969; Wood and Anderson, 1978). In R-type garnet, the intermediate zone between the inner silica-deficient core and the outer silica-supersaturated rim shows near perfect titangranditic composition (Fig. 6c); the latter garnet coexists with supersilicic pyroxenes. By contrast, the equivalent intermediate zone in C-type garnet is devoid of pyroxenes and shows silica-saturated compositions with all Ti in excess of the stoichiometry (Fig. 6c). It is concluded that, at Sidi bou Othmane, although fO_2-conditions were appropriate and Fe^{3+} and Ti were available, the overall silica activity was too high for melanites and titangrandites to form. In spite of that, Fe^{3+}-Ti-bearing garnets developped because locally, the excess silica was uptaken by the supersilicic pyroxenes growing simultaneously. Based on the stability of the coexisting garnets, Fe^{3+}- Fe^{2+}-bearing supersilicic pyroxenes appear stable over a wide range of fO_2-values, overlapping T-fO_2 stability conditions of melanitic and titangranditic garnet (Huckenholz et al. 1976; Liou, 1974; Gustafson, 1974).

An abrupt increase in silica activity also occurs at the transition between melanitic and titangranditic garnet, as shown by the change from supersilicic pyroxene to anorthite and quartz inclusions along sectors of C-

type garnet, and by the quarz needle ring in R-type garnet. The latter increase is unrelated to the progressive depletion in Fe-Mg components (probably chlorite-derived) in the environment as, in R-type garnet, Fe-Mg-bearing pyroxenes are found on both parts of the quartz ring. It is tentatively proposed that, at an early stage of garnet growth, solutions were both alcaline and with low dielectric constant due to the decay of organic matter and/or the release of NH_4^+-bearing silicates; this favoured the complexation of silica as the neutral species $Si(OH)_4$. These complexes were probably destabilized by the abrupt influx of more acidic H_2O-rich fluids coming from the pelitic environment at the beginning of the vein stage.

M-type garnets.

Preliminary data suggest that M-type garnets and associated pyroxenes in massive carbonated beds are different from the ones formed in the nearby more pelitic levels. M-type garnets do not display marked compositional zoning. They are slightly silica-deficient, however they show some similarities with syn-to post-vein stage garnet from mines : high bulk FeO content (Fig. 6a) and andradite-content > 6mole%. (Fig. 6d). This probably resulted from the fact that associated pyroxenes have high Al_2O_3-content and low Fe_2O_3-content (Fig. 12). Probably, the higher activity of water controlled the specific chemistry of M-type garnets and associated pyroxenes, as implied by the presence of idocrase at equilibrium (Fig. 2f; Ito and Arem, 1970). In parallel, silica activities were higher as shown by the presence of quartz in veinlets instead of pyroxene or garnet (Fig. 2e)

Conclusions.

The garnets growing in graphite mines at Sidi Bou Othmane display quartz inclusions and prograde compositional zoning (in particular decreasing grossular-contents from cores to peripheries) which are

characteristic of porphyroblasts formed under prograde greenschist facies metamorphic conditions (≈T≤ 550°C).

Garnet also present changing compositions from melanitic in the cores to titangranditic and granditic in peripheries. The formation of Ti-bearing-garnets (melanites and titangrandites) at an early stage of skarn formation in graphite mines required (1) that ferric iron was available, (2) that silica activities were low and (3) that fO_2-conditions had dropped to very low values (e.g., below I-W buffer at 550°C), at least for the melanite to form. The transition from melanitic compositions to titangranditic ones was discontinuous, marked by vein-opening and abrupt increase in silica activity. Probably, this part of the evolution was controlled by the influx of water in the system, which destabilized $Si(OH)_4$ complexes in the fluids controlled by organic derived compounds.

It is proposed that all three previously mentioned conditions were verifiéd at an early stage of skarn formation as a consequence of fluid-rock interactions, the driving force of which were the chemical equilibration of the C-O-H-N fluid with graphite. In a hydrogen-dominated fluid system, the latter process implies all the more intense reduction of CO_2 and H_2O, as the environment is more hydrogen-dominated. The presence of CO_2 and H_2O-depleted CH_4-N_2-enriched fluids trapped in quartz from mine areas (Bastoul, 1983), and of associated melanitic garnets, point out to the fact that reduction of CO_2 and H_2O was near complete. The reason for that is that oxygen-producing reactions at Sidi Bou Othmane were coupled with the oxidation of Fe^{2+} from the wall-rock to Fe^{3+} (Ramboz and Bastoul, 1985), which was incorporated into the garnets and pyroxenes formed simultaneously.

Crystal chemical data suggest that the pyroxenes included in silica-deficient garnets are supersilicic. The presence of large amounts of $CaFe_2SiO_6$ component probably facilitated the solution of excess SiO_2 into the lattice of clinopyroxenes in that context. This induced the creation of small

scale silica-deficient environments in which the Ti-bearing garnets could develop. Hence crystal chemical data on garnets and clinopyroxenes point out to the absence of bulk chemical equilibration of the silicates formed at an early stage of skarn formation.

There are petrographic and chemical evidences that the Fe-content of the wall-rock controlled the metamorphic textures at a very local scale in graphite mines. Garnets formed in Fe-rich facies, i.e., in initially chlorite-rich beds, are rounded and display numerous randomly distributed clinopyroxene inclusions. These probably formed under hydrostatic pressure regime for the following reasons. The reduction of water and the volatilization of graphite following the reaction : $C + 2H_2O \rightarrow CH_4 + O_2$ could be completed because the oxygen produced reacted with Fe in the wall-rock. Hence nucleation rates were enhanced in such a gas-producing high energy environment. By contrast, garnets with chiastolite-type distribution of the inclusions developped in more calcic beds. Nucleation of pyroxenes and volatilization of graphite related preferentially occurred along crystal edges in that case, because graphite, excess Si and Fe-Mg were transported towards these growth planes. This was favoured by slower nuleation rates due to less active volatilization of graphite in the Fe-poor environment.

Finally, both silica and water activities were high in massive organic-rich limestones outside the graphite mines. This shows that reduction reactions could not be completed in that context, due to the fact that CO_2 activities were high and that insufficient amounts of Fe^{2+} reducing agent were available in the wall-rock.

Acknowledgments. The samples studied in this paper were either collected by A. Bastoul, or with the help of A. Bastoul and S.M.F. Shepard. Many thanks to both of them. This paper took benefit of fruitful discussions with J.

Dubessy, M. Cuney and P. Landais. Present work was supported by A.T.P. 'Géochimie et Métallogénie 1983'.

References

Amthauer G., Annersten H. and Hafner S. S. (1977) - The Mössbauer spectrum of ^{57}Fe in titanium-bearing andradite. Phys. Chem. Minerals 1, 399-413.

Ancey M., Bastenaire F. and Tixier R. (1978) - Application des méthodes statistiques en microanalyse. In Microanalyse, Microscopie Electronique à Balayage, (Maurice F., Meny L. and Tixier R. eds.), Les Editions de Physique, Orsay, France, p. 327-347.

Andersen T. B. (1984) - Inclusion patterns in zoned garnets from Magerøy, North Norway. Mineral. Mag. 48, 21-26.

Andersen D. J. and Lindsley D. H. (1981) - Compositional deviations in lunar pyroxenes : analytical error or non-stoichiometry?. Lunar and Planetary Science XII, 19-21.

Anderson A. T. Jr., Crewe A. V., Goldsmith J. R., Moore P. B., Newton R. C., Olsen E. J., Smith J. V. and Wyllie P. J. (1970) - Petrologic history of Moon suggested by petrography, minerology, and crystallography. Science 167, 587-590.

Bastoul A. (1983) - Etude des fluides carbo-azotés associés au métamorphisme de contact des schistes noirs sur l'exemple des Jebilet Centrales (Maroc). Comparaison avec la région des Bondons et de Pen Ar Ran (France). Unpubl. Thesis Univ. Nancy I, 190 p.

Bordonaro M. (1983) - Tectonique et pétrographie du district à pyrrhotine de Kettara (Paléozoïque des Jebilet, Maroc). Unpubl. Thesis Univ. Louis Pasteur, Strasbourg, 132 p.

Cameron M. and Papike J.J. (1980) - Crystal chemistry of silicate pyroxenes. In Reviews in Mineralogy, vol. 7 : Pyroxenes, (C.T. Prewitt ed.), p. 5-92.

Cawthorn R. G. and Collerson K. D. (1974) - The recalculation of pyroxene end-member parameters and the estimation of ferrous and ferric iron content from electron microprobe analyses. Amer. Mineral. 59, 1203-1208.

Cosca M. A., and Peacor D. R. (1987) - Chemistry and structure of esseneite (Ca Fe^{3+} Al SiO_6), as new pyroxene produced by pyrometamorphism. Amer. Mineral. 72, 148-156.

Deer W. A., Howie R. A., and Zussman J. (1978) - Rock-forming minerals, vol. 2A, Single-chain silicates, 2nd. ed., Wiley, New-York.

Deer W. A., Howie R. A. and Zussman J. (1982) - Rock-forming minerals, vol.1A, Orthosilicates, 2nd ed., Wiley, New-York.

Dowty E. (1971) - Crystal chemistry of titanium and zirconian garnet. I, Review and spectral studies. Amer. Mineral. 56, 1983-2009.

Dubessy J. and Ramboz C. (1986) - The history of organic nitrogen from early diagenesis to amphibolite facies : mineralogical, chemical, mechanical and isotopic implications. 5th Water-Rock-Interaction Congress, Reijkavik, 171-175 (publication n° 13).

El Hassani A. (1980) - Etude lithostratigraphique, tectonique et pétrographique de la région de Sidi Bou Othmane (Maroc), Unpubl. Thesis Univ. Aix Marseille, 110 p..

Foit F. F., Hooper R. L., and Rosenberg P. E. (1987) - An unusual pyroxene, melilite and iron oxide mineral assemblage in a coal-fire buchite from Buffalo, Wyoming. Amer. Mineral. 72, 137-147.

Gasparik T. and Lindsley D. H. (1980) - Experimental study of pyroxenes in the system Ca Mg $Si_2 O_6$-Ca Al_2 Si O_6 - Ca $_{0.5}$ Al $Si_2 O_6$. E.O.S. 61, p. 402-403.

Gustafson W. I. (1971) - The stability of andradite, hedenbergite, and related minerals in the system Ca - Fe - Si - O - H. J. Petrol. 15, 455-496.

Haldaway M. J. and Lee S. M. (1977) - Fe-Mg cordierite stability in high-grade pelitic rocks based on experimental, theoritical and natural observations. Contrib. Mineral. Petrol. 63, 175-198.

Hallam and Eugster (1978) - Ammonium silicate stability relations. Contrib. Mineral. Petrol. 57, 227-244.

Harker A. (1939) - Metamorphism. 2nd Ed., Methuen, London.

Harte B. and Henley K. J. (1966) - Occurrence of compositionally zoned almanditic garnets in regionally metamorphosed rocks. Nature 210, 689.

Harvey P. K and Ferguson C. C. (1973) - Spherically arranged inclusions in post-tectonic garnet porphyroblasts. Mineral. Mag. 39, 85-88.

Hollister L. S. (1966) - Garnet zoning : an interpretation based on the Rayleigh fractionation model. Science 154, 1647-1651.

Hollister L. S. (1970) - Origin, mechanism, and consequence of compositional sector-zoning in staurolite. Amer. Mineralogist 55, 742-766.

Huckenholz H. G. (1969) - Synthesis and stability of Ti-andradite. Amer. J. Sci. Schairer vol. 267A, 209-239.

Huckenholz H., Hölzl E., Huggins F. E. and Virgo D. (1976) - A reconnaissance study of the Ti garnet stability field at defined oxygen fugacities. Ann. Rep. Dir. Geophys. Lab., 1975-1976, 711-720.

Huggins F.E. (1969) - Synthesis and stability of Ti-andradite, Amer. J. Sci. 267A, 209-232.

Huggins F. E., Virgo D. and Huckenholz H. G. (1977) - Titanium-containing silicate garnets. II. The crystal chemistry of melanites and schorlomites. Amer. Mineral. 62, 646-665.

Huggins F. E., Virgo D. and Huckenholz H. G. (1977) - Titanium-containing silicate garnets. I. The distribution of Al, Fe^{3+} and Ti^{4+} between octahedral and tetrahedral sites. Amer. Mineral. 62, 475-490.

Huvelin P. (1977) - Etude géologique et gitologique du Massif hercynien des Jebilet (Maroc occidental). Notes Mém. Serv. géol. Maroc 232 bis, 308 p.

Huvelin P. and Permingeat F. (1980) - Graphite. Notes Mém. Serv. Géol. Maroc 276, 245-256.

Ito J. and Arem J.E. (1970) - Idocrase : synthesis, phase relations and crystal chemistry. Amer. Mineral. 55, 880-912.

Kerrick D. M. (1970) - Contact metamorphism in some areas of the Sierra Nevada, California. Bull. Geol. Soc. Amer. 81, 2913-2938.

Kretz R. (1973) - Kinetics of the crystallization of garnet at two localities near Yellowknife. Canad. Mineral. 12, 1-20.

Kushiro I. (1969) - Clinopyroxene solide solutions formed by reactions between diopside and plagioclase at high presures. Mineral. Soc. America, Spec. Pap. 2, 179-191.

Lagarde J. L. and Choukroune P. (1982) - Cisaillement ductile et granitoïdes syntectoniques : l'exemple du massif hercynien des Jebilet (Maroc). Bull.Soc. Geol. Fr. XXIV, 299-307.

Lindsley D.H. (1980) - Phase equilibria of pyroxenes at pressures > 1 atmosphere. In Reviews in Mineralogy, vol. 7 : Pyroxenes, (C.T. Prewitt ed.), p. 289-339.

Liou J. G. (1974) - Stability relation of andradite-quartz in the system Ca-Fe-Si-O-H. Amer. Mineral. 59 1016-1025.

MacQueen J. A. and Powell D. (1977) - Relationship between deformation and garnet growth in Moine (Precambrian) rocks of western Scotland. Geol. Soc. America Bull. 88, 235-240.

Manning P. G. and Harris D. C. (1970) - Optical absorption and electron microprobe studies of some high Ti-garnets. Canad. Mineral. 10, 260-271.

Mrini Z. (1985) - Age et origine des granitoïdes hercyniens du Maroc : apport de la géochronologie et de la géochimie isotopique (Sr, Nd, Pb). Thèse Univ. Clermont II, 166 p.

Mysen B. O. and Heier K. S. (1972) - Petrogenesis of eclogites in high grade metamorphic gneisses, examplified by the Hareidland eclogite, Western Norway. Contrib. Mineral. Petrol. 36, 73-94.

Novak G. A. and Gibbs. G. V. (1971) - The crystal chemistry of silicate garnets. Amer. Mineral. 56, 791-825.

Oba T. and Onuma K. (1978) - Prelimary report on the joint Ca Mg $Si_2 O_6$ - Ca Fe^{3+} Al SiO_6 at low oxygen fugacity. J. Fac. Sci. Hokkaïdo Univ. Ser. IV, 18, 433-444.

Onuki H., Akasaka M., Yoshida T. and Nedachi M. (1982) - Ti-rich hydroandrandites from the Sandagawa metamorphic rocks of the Shibukawa area, Central Japan. Contrib. Mineral. Petrol. 80, 183-188.

Onuma K. (1983) - Effect of oxygen fugacity on fassaitic pyroxene. J. Fac. Sci. Hokkaido Univ. Ser. IV, 20, 185-194.

Papike J. J., Cameron K. L. and Baldwin K. (1974)- Amphiboles and pyroxenes : characterization of other than quadrilateral components and estimates of ferric iron from microprobe data. Geol. Soc. Amer. Abstr. Programs 6, 1053-1054.

Penfield S. L. and Pratt J. H. (1894) - On the chemical composition of staurolite and the regular arrangement of its carbonaceous inclusions, Amer. J. Sci. 47, 81-89.

Piqué A. (1979) - Evolution structurale d'un segment de la chaine hercynienne : la Meseta marocaine nord-occidentale. Sci. Géol. Mém., Strasbourg, 253 p.

Ramboz C. and Bastoul A. (1985) - Oxydation du fer dans les skarns et les schistes à graphite des Jebilet Centrales (Maroc) : un indicateur de transfert de matière par les fluides dans une zone de cisaillement ductile. C. R. Acad. Sci. Paris 301, 931-936 (publication n° 13).

Rickwood P. C. (1968) - On recasting analyses of garnet into end-member molecules. Contrib. Mineral. Petrol. 18, 175-198.

Robinson P. (1980) - The composition space of terrestrial pyroxenes. Internal and external limits. In Reviews in Mineralogy, vol .7 : Pyroxenes, (C. T. Prewitt ed.) , 419-466.

Schwartz K.B., Nolet D.A. and Burns R.G. (1980) - Mössbauer spectroscopy and crystal chemistry of natural Fe-Ti garnets, Amer. Mineral. 65, 142-153.

Shimazaki H. (1977) - Grossular-spessartine-almandine garnet from some Japanese scheelite skarns, Canad. Mineral. 15, 74-80.

Smith D. C., Domeneghetti C., Rossi G., and Ungaretti L. (1982) - Single crystal structure refinements of supersilicic clinopyroxenes from the Zagdochnaya kimberlite pipe, Yakutia, U.S.S.R.. Terra Cognita, 2, 223.

Spry A. (1969) - Metamorphic tectures. Pergamon Press., Amsterdam.

Thompson A. B. (1976) - Mineral reactions in pelitic rocks. Amer. J. Sci. 276, 401-454.

Thompson A. B., Tracy R. J., Lyttle P. and Thompson J. B. Jr (1977) - Prograde reaction histories deduced from compositional zonation and mineral inclusions in garnet from the Gassett schists, Vermont. Amer. J. Sci. 277, 1152-1167.

Tracy R. J. (1982) - Compositional zoning and inclusions in metamorphic minerals. In Reviews in Mineralogy, vol. 10 : Characterization of Metamporphism through Mineral Equilibria, (J. M. Ferry ed.), 355-397.

Vernet M. (1968) - Annual Report, Centre Recherches Pétrographiques et Géochimiques.

Vogel T., Williams E., Preston J. and Walker B. (1976) - Origin of the late

plutonic massifs in Morrocco, Geol. Soc. Amer. Bull. 87, 1753-1762.

Waychunas G. A. (1987) - Synchrotron radiation Xanes spectroscopy of Ti in minerals : effects of Ti bonding distances, Ti valence, and site geometry on absorption edge structure. Amer. Mineral. 72, 89-101.

Weber H. P., Virgo D. and Huggins F. E. (1975) - A neutron diffraction and ^{57}Fe Mössbauer study of a synthetic Ti-rich garnet. Ann. Rept. Dir. Geophys. Lab. 74, 575-579.

Wood B. J. (1976a) - Mixing properties of tshermakitic chinopyroxenes., Amer. Mineral. 61, 599-602.

Wood B. J. (1976b) - On the stoichiometry of clinopyroxenes in the system $CaO - MgO - Al_2O_3 - SiO_2$. Ann. Rept. Dir. Geophys. Lab. 1975-76, 741-742.

Wood B. J. and Henderson C. M. B. (1978) - Compositions and unit cell parameters of synthetic non-stoichiometric tschermakitic clinopyroxenes, Amer. Mineral. 63, 66-72.

Appendix : On recasting non stoichiometric analyses of pyroxenes to end-member molecules.

Let us consider a pyroxene analysis yielding a sum of cations to 6 oxygens (Σ cat) < 4.00. The Fe^{3+}/Fe^{2+} ratio is first assumed to be fixed by an independant method. Let Si, Ti, Al, Fe^3, Ca^{M2}, $\Sigma(X^{2+})^{M1}$ ...be the number of cations calculated p.f.u.; $\Sigma\ (X^{2+})^{M1}$ is the sum of divalent cations in M1 site, Ca^{M2} is the amount of Ca cations in M2 site.

Natural stoichiometric pyroxenes correspond to the general formula :

$$X^{M1}_{1-x}\ Y^{M2}_{1+x}\ Z_2\ O_6$$

where x is < ≈0.02 (Robinson, 1980).

The substitution $^{VI}(Ti^{4+}) - 2\ (^{IV}Al^{3+})$ is the major one in natural pyroxenes (Papike, 1980), therefore Ti is assumed to enter pyroxene structure following the latter mechanism only. Hence the amount of silica ions which is in excess of the ideal stoichiometry p.f.u. is :

$$Si_{ex} = Si + Ti - [\ 2\ (Na + K) + \Sigma(X^{2+})^{M1} + Ca^{M2}] \qquad (a)$$

The vacancies in M1 and M2 sites p.f.u., p and q, are respectively :

$$p = 1 - (\Sigma(X^{2+}) + (Al, Fe, Cr)^{3+} + Ti)^{M1} \qquad (b)$$

$$q = 1 - (K+Na+Ca)^{M2} \qquad (c)$$

if $(K+Na+Ca)^{M2} < 1$, and

$$p = 1 - (x + \Sigma(X^{2+}) + (Al, Fe, Cr)^{3+} + Ti)^{M1} \qquad (b')$$

$$q = 1 \qquad (c')$$

if $(K+Na+Ca)^{M2} > 1$ ($x = (K+Na+Ca) - 1$).

Charge balance constraints imply :

$$Si_{ex} = 3\ [4 - \Sigma\ cat\ ] = 3\ (p+q) \qquad (d)$$

100 % of the analysed cations can be modelled in terms of the molecular proportions of the different end member molecules, including the site-deficient ones, as follows.

(1) All cations are first allocated to reference ideal molecules following standard procedures (e.g. Cawthorn and Collerson, 1974), except for the Si_{ex} amounts of silica ions which are unallocated.

(2) Let Ca (Al, $Fe)^{3+}_{0.66}$ Si_2 O_6 and $Ca_{0.5}$ (Al, $Fe)^{3+}$ Si_2 O_6 be the site-deficient molecules referred to, with vacancies in the M1 and M2 sites respectively (Wood and Henderson, 1984).

3 p amounts of Ca (Al, $Fe^3)_{0.66}$ Si_2 O_6 molecule are formed at the expense of p amounts of Ca-Tschermak molecule (Ca (Al, $Fe^{3+})_2$ Si O_6) plus wollastonite (Ca_2 Si_2 O_6) and of 3 p amounts of silica ions.

2 q amounts of $Ca_{0.5}$ (Al, Fe^{3+}) Si_2 O_6 are formed at the expense of q amounts of Ca-Tschermak molecule (Ca (Al, $Fe^{3+})_2$ Si O_6) and of 3q amounts of silica ions.

The modified charge balance equation for site-deficient pyroxenes is

$$(Na + K) + (Al+Fe^{3+})^{IV} = 2\ Ti + (Al, Fe^{3+} + Cr)^{VI} + 2\ (p+q) \qquad (e)$$

The minimum value of Fe^{3+} for which equation (e) is verified corresponds to zero amount of CaFTs 'molecule'. Higher Fe^{3+}-contents correspond to increasing amounts of CaFTs end member.

Hence it is concluded that the Fe^{3+} - content of site-deficient pyroxenes, unlike that of ideal pyroxenes, cannot be roughly estimated using electron microprobe analyses but must be fixed by independant methods such as wet chemistry or Mössbauer spectrometry.

ANNEXES

Electron microprobe analyses of Sidi Bou Othmane skarn pyroxenes and garnets with calculated structural formulae and interpretations in terms of end-member molecules. Minimum Fe^{3+}-content in site-deficient pyroxene analyses is calculated as indicated in Appendix.

TABLE CAPTION

FeO* : Total Fe as FeO (wt.%)
Total * : Total wt.% oxides with bulk Fe as FeO

Garnets

Allocated : cations allocated to end-member molecules (mole %) .

Alm : $(Fe^{2+})_3\ Al_2\ Si_3\ O_{12}$

And : $(Ca)_3\ (Fe^{3+})_2\ Si_3\ O_{12}$ Sch : $(Ca)_3\ (Fe^{3+})_2\ Ti_3\ O_{12}$

Gro : $(Ca)_3\ (Al)_2\ Si_3\ O_{12}$ Spe : $(Mn)_3\ (Al)_2\ Si_3\ O_{12}$

Py : $(Mg)_3\ (Al)_2\ Si_3\ O_{12}$ Uva : $(Ca)_3\ (Cr)_2\ Si_3\ O_{12}$

Pyroxenes

FeOc (Fe_2O_3c, Totalc) : wt.% FeO (Fe_2O_3, Total) obtained on calculating the minimum Fe^{3+}-content required by the modifies charge balance equation (see Appendix).

Smax : sum of cations to 6O with total Fe as FeO.

Smin : sum of cations to 6O with total Fe as Fe_2O_3.

Ormin : minimum calculated $Fe^{3+}/(Fe^{2+} + Fe^{3+})$ ratio (mole).

Scat : sum of cations to 6O with adjusted minimum Fe_2O_3-content.

Ajd : $Na\ Al\ Si_2\ O_6$ Fjd : $Na\ (Fe^{3+})\ Si_2\ O_6$

CATs : $Ca\ Al_2\ Si\ O_6$ CFTs : $Ca\ (Fe^{3+})_2\ Si\ O_6$

M1sd : $Ca\ Al_{0.66}\ Si_2\ O_6$ FM1sd : $Ca\ (Fe^{3+})_{0.66}\ Si_2\ O_6$

M2sd : $Ca_{0.50}\ Al\ Si_2\ O_6$ FM2sd : $Ca_{0.50}\ (Fe^{3+})\ Si_2\ O_6$

En : $Mg_2\ Si_2\ O_6$ Fs : $Fe_2\ Si_2\ O_6$

Wo : $Ca_2\ Si_2\ O_6$

Profile through C-type garnet - sample QG2b

	Core																Rim
	Zone 1		Zone 2				Zone 3A									Zone 3B	
	42	43	44	45	46	47	48	49	50	51	52	53	54	55	56	57	72
SiO_2	39.59	38.89	38.71	39.30	39.13	39.65	39.20	39.84	39.72	40.10	39.12	40.38	39.37	39.45	40.00	40.41	40.75
TiO_2	1.02	1.07	0.89	0.92	1.01	0.99	1.08	0.86	0.94	0.79	0.81	0.75	0.73	0.56	0.45	0.58	0.48
Al_2O_3	20.75	21.09	21.49	21.27	20.81	21.04	21.10	20.85	21.24	21.34	20.97	21.33	21.13	21.40	21.14	20.91	20.73
Cr_2O_3	0.00	0.00	0.00	0.00	0.00	0.04	0.08	0.07	0.00	0.02	0.04	0.07	0.04	0.00	0.00	0.16	0.12
FeO*	2.26	1.91	2.18	2.22	2.06	2.29	2.24	2.08	2.14	2.15	2.11	2.10	2.01	2.54	2.24	3.26	3.63
MnO	0.19	0.01	0.00	0.12	0.19	0.08	0.10	0.00	0.00	0.13	0.00	0.13	0.15	0.27	0.09	0.00	0.03
MgO	0.00	0.05	0.05	0.02	0.08	0.14	0.05	0.05	0.02	0.02	0.00	0.06	0.00	0.03	0.05	0.05	0.00
CaO	36.49	36.60	36.72	36.42	36.23	36.91	36.77	36.56	36.00	36.48	36.91	36.35	36.09	36.33	36.64	36.69	36.32
Total	100.31	99.62	100.04	100.28	99.51	101.14	100.62	100.32	100.06	101.02	99.96	101.18	99.54	100.58	100.60	102.06	102.06
Si	2.988	2.946	2.926	2.961	2.974	2.964	2.942	2.996	2.992	2.994	2.958	3.007	2.985	2.965	2.999	2.994	3.016
Al	0.012	0.054	0.074	0.039	0.026	0.036	0.058	0.004	0.008	0.006	0.042	0.000	0.015	0.035	0.001	0.006	0.000
Al	1.834	1.830	1.840	1.850	1.838	1.818	1.808	1.843	1.878	1.872	1.827	1.872	1.874	1.860	1.868	1.820	1.808
Fe^{3+}	0.063	0.109	0.110	0.085	0.076	0.105	0.126	0.104	0.068	0.083	0.125	0.082	0.082	0.108	0.107	0.139	0.158
Ti	0.058	0.061	0.051	0.052	0.058	0.055	0.061	0.049	0.053	0.044	0.046	0.042	0.042	0.032	0.025	0.032	0.027
Cr	0.000	0.000	0.000	0.000	0.000	0.002	0.005	0.004	0.000	0.001	0.002	0.004	0.002	0.000	0.000	0.009	0.007
Mg	0.000	0.005	0.006	0.003	0.009	0.015	0.006	0.006	0.002	0.002	0.000	0.007	0.001	0.003	0.005	0.005	0.000
Fe^{2+}	0.079	0.012	0.028	0.055	0.055	0.038	0.015	0.027	0.068	0.051	0.009	0.049	0.046	0.052	0.034	0.064	0.067
Mn	0.012	0.001	0.000	0.008	0.012	0.005	0.006	0.000	0.000	0.009	0.000	0.008	0.010	0.017	0.006	0.000	0.002
Ca	2.951	2.971	2.974	2.940	2.950	2.956	2.957	2.945	2.906	2.918	2.990	2.900	2.932	2.925	2.944	2.912	2.879
Alm	2.8	0.4	0.0	1.8	1.8	1.3	0.5	0.0	0.8	0.5	0.1	0.7	0.6	1.7	0.3	1.5	2.3
And	1.3	4.1	1.8	2.5	1.9	2.6	4.5	5.3	3.5	4.2	5.1	4.2	4.2	4.1	5.4	7.0	7.6
Gro	93.5	93.9	96.3	91.3	89.7	93.4	92.9	94.3	95.7	94.8	93.5	94.4	94.7	92.5	93.9	90.9	89.7
Py	0.0	0.2	0.2	0.1	0.3	0.5	0.2	0.2	0.1	0.1	0.0	0.2	0.0	0.1	0.2	0.2	0.0
Sch	2.0	1.4	1.7	1.7	1.9	1.9	1.4	0.0	0.0	0.0	1.2	0.0	0.0	1.1	0.0	0.0	0.0
Spe	0.4	0.0	0.0	0.3	0.4	0.2	0.2	0.0	0.0	0.3	0.0	0.3	0.3	0.6	0.2	0.0	0.1
Uva	0.0	0.0	0.0	0.0	0.0	0.1	0.3	0.2	0.0	0.1	0.1	0.2	0.1	0.0	0.0	0.5	0.3
ALLOCATED	95.5	99.7	99.6	98.7	97.0	99.1	99.5	98.05	98.0	98.3	99.8	98.2	98.8	99.9	98.9	98.8	98.7
O.R.	.44	.90	.89	.61	.58	.73	.90	.79	.50	.62	.93	.63	.64	.68	.76	.68	.70

(1) Centre with relics of graphite-bearing matrix; (2) pyroxene-bearing chiastotite type structure; (3) clear garnet devoid of silicate or graphite inclusions; (4) rim of the crystal.

R-type garnet - sample E48b

	Core → (A) → Rim										(B)	(A)			
	Zone 1		Zone 2A		Zone 2B				Zone 3			Zone 3			
	33	35	55	54	53	52	50	49	46	43	58(1)	39	40	41	42
SiO_2	40.23	40.39	39.47	39.31	39.59	39.35	39.05	39.87	39.73	39.58	39.27	39.47	39.97	39.78	40.14
TiO_2	0.00	0.38	1.15	1.60	0.30	0.47	0.38	0.29	0.38	0.34	0.34	1.16	0.50	0.44	1.32
Al_2O_3	20.45	20.88	20.58	20.89	21.53	20.77	20.73	21.12	20.42	20.45	20.48	20.66	20.84	20.71	20.80
Cr_2O_3	0.01	0.07	0.00	0.09	0.20	0.00	0.00	0.00	0.00	0.00	0.00	0.12	0.00	0.00	0.00
FeO*	2.34	2.30	2.31	2.30	2.49	3.35	3.29	3.38	3.35	3.54	3.64	2.57	3.23	2.64	2.18
MnO	0.05	0.04	0.07	0.00	0.00	0.22	0.12	0.18	0.08	0.23	0.20	0.19	0.14	0.13	0.20
MgO	0.00	0.05	0.00	0.02	0.06	0.05	0.01	0.04	0.01	0.10	0.00	0.03	0.08	0.05	0.02
CaO	35.63	34.96	36.40	36.35	36.01	36.67	35.57	36.48	34.77	34.36	35.52	34.59	33.84	34.14	35.17
Total	98.71	99.07	99.98	100.57	100.18	100.88	99.15	101.35	98.74	98.61	99.46	98.80	98.59	97.90	99.82
Si	3.060	3.056	2.991	2.964	2.985	2.957	2.981	2.979	3.029	3.028	2.989	3.009	3.046	3.051	3.024
Al	0.000	0.000	0.009	0.036	0.015	0.043	0.019	0.021	0.000	0.000	0.011	0.000	0.000	0.000	0.000
Al	1.833	1.862	1.829	1.820	1.898	1.797	1.845	1.839	1.835	1.844	1.825	1.856	1.872	1.871	1.846
Fe^{3+}	0.149	0.113	0.050	0.029	0.073	0.177	0.133	0.145	0.143	0.136	0.155	0.070	0.099	0.103	0.079
Ti	0.000	0.021	0.066	0.091	0.017	0.027	0.022	0.016	0.022	0.019	0.020	0.067	0.029	0.026	0.075
Cr	0.001	0.004	0.000	0.005	0.012	0.000	0.000	0.000	0.000	0.000	0.000	0.007	0.000	0.000	0.000
Mg	0.000	0.006	0.000	0.002	0.006	0.005	0.001	0.004	0.001	0.012	0.000	0.004	0.009	0.006	0.002
Fe^{2+}	0.000	0.032	0.097	0.116	0.084	0.034	0.077	0.066	0.070	0.090	0.077	0.093	0.107	0.066	0.058
Mn	0.003	0.002	0.004	0.000	0.000	0.014	0.007	0.012	0.005	0.015	0.013	0.012	0.009	0.008	0.013
Ca	2.903	2.833	2.955	2.936	2.909	2.952	2.908	2.921	2.840	2.816	2.896	2.825	2.763	2.805	2.838
Alm	0.0	1.1	0.0	4.1	2.7	0.4	2.6	2.0	2.4	3.1	2.6	2.1	3.7	2.3	1.2
And	5.1	2.6	3.38	0.0	3.2	6.6	6.0	6.3	5.6	5.7	7.7	3.6	2.8	2.7	4.1
Gro	94.5	95.7	93.8	94.1	92.8	91.4	90.6	90.7	91.8	90.3	89.3	93.3	92.9	94.5	94.2
Py	0.0	0.2	0.0	0.1	0.2	0.2	0.0	0.1	0.0	0.4	0.0	0.1	0.3	0.2	0.1
Sch	0.0	0.0	2.3	1.5	0.4	0.9	0.6	0.5	0.0	0.0	0.0	0.0	0.0	0.0	0.0
Spe	0.1	0.1	0.1	0.0	0.0	0.5	0.2	0.4	0.2	0.5	0.4	0.4	0.3	0.3	0.4
Uva	0.0	0.2	0.0	0.3	0.6	0.0	0.0	0.0	0.0	0.0	0.0	0.4	0.0	0.0	0.0
ALLOCATED	98.0	97.4	94.4	94.5	99.9	99.7	99.8	99.9	98.1	98.5	99.6	97.2	97.5	97.6	97.0

(A) profile analyses; (B) isolated analysis; *quartz needles.

M type garnet - 4J26

	Rim ←		Core		→ Rim	
	13	14	15	16	17	18
SiO_2	39.63	39.13	39.17	39.35	39.38	39.54
TiO_2	0.14	0.97	1.03	0.66	1.05	0.83
Al_2O_3	20.86	19.71	19.83	20.13	20.13	20.89
Cr_2O_3	0.00	0.00	0.00	0.04	0.00	0.00
FeO	3.33	4.32	3.81	3.65	3.15	2.82
MnO	0.09	0.08	0.02	0.06	0.11	0.01
MgO	0.02	0.02	0.00	0.04	0.09	0.05
CaO	35.76	35.57	35.64	35.26	35.85	36.45
Total	99.83	99.80	99.50	99.19	99.76	100.59
Si	3.002	2.978	2.985	3.003	2.987	2.972
Al	0.000	0.022	0.015	0.000	0.013	0.028
Al	1.862	1.745	1.766	1.810	1.786	1.822
Fe^{3+}	0.130	0.199	0.175	0.149	0.154	0.131
Ti	0.008	0.056	0.059	0.038	0.060	0.047
Cr	0.000	0.000	0.000	0.002	0.000	0.000
Mg	0.002	0.002	0.000	0.005	0.010	0.006
Fe^{2+}	0.081	0.075	0.067	0.083	0.046	0.046
Mn	0.006	0.005	0.001	0.004	0.007	0.001
Ce	2.902	2.900	2.909	2.882	2.913	2.935
Alm	2.6	1.5	0.8	1.8	0.0	1.1
And	6.5	8.2	7.0	7.6	5.9	5.0
Gro	90.6	88.1	90.2	90.2	91.5	92.1
Py	0.1	0.1	0.0	0.2	0.3	0.2
Sch	0.0	1.9	2.0	0.0	2.0	1.6
Spe	0.2	0.2	0.0	0.1	0.2	0.0
Uve	0.0	0.0	0.0	0.1	0.0	0.0
ALLOCATED	99.7	98.5	98.1	98.4	97.9	99.2

Profile through a mm-wide garnet vein (sample QG2b)

	32• R		33	34	35		36	38		37• R
	←				C					→
SiO_2	39.60		39.52	39.05	39.65		38.15	39.37		38.73
TiO_2	0.65		0.43	0.63	0.71		0.73	1.12		0.64
Al_2O_3	20.65		20.59	20.54	20.40		19.49	20.47		20.33
Cr_2O_3	0.00		0.55	0.00	0.00		0.01	0.00		0.00
FeO*	3.42		3.60	3.19	3.89		3.06	3.30		3.18
MnO	0.10		0.01	0.00	0.00		0.19	0.00		0.10
MgO	0.07		0.26	0.01	0.01		0.11	0.08		0.07
CaO	36.03		36.27	36.44	36.21		36.76	36.37		36.32
Total	100.52		101.25	99.87	100.88		98.50	100.71		99.38
Si	2.983		2.961	2.962	2.980		2.945	2.952		2.953
Al	0.017		0.039	0.038	0.020		0.055	0.048		0.047
Al	1.816		1.779	1.798	1.787		1.718	1.761		1.779
Fe^{3+}	0.147		0.164	0.166	0.173		0.198	0.176		0.184
Ti	0.037		0.024	0.036	0.040		0.042	0.063		0.037
Cr	0.000		0.033	0.000	0.000		0.001	0.000		0.000
Mg	0.008		0.029	0.001	0.001		0.012	0.009		0.007
Fe^{2+}	0.069		0.062	0.036	0.072		0.000	0.031		0.019
Mn	0.006		0.001	0.000	0.000		0.012	0.000		0.007
Ca	2.908		2.910	2.961	2.915		3.041	2.921		2.967
Alm	1.6		1.5	1.2	1.8		0.0	0.5		0.6
And	7.4	(6.2)	6.2	6.9	8.7	(7.4)	10.1	7.9	(6.3)	6.6
Gro	90.5		88.9	90.6	89.4		89.1	91.3		91.1
Py	0.3		1.0	0.0	0.0		0.4	0.3		0.3
Sch	0.0	(1.24)	0.8	1.2	0.0	(1.3)	0.0	0.3	(1.9)	1.2
Spe	0.2		0.0	0.0	0.0		0.4	0.0		0.2
Uva	0.0		1.6	0.0	0.0		0.0	0.0		0.0
ALLOCATED	99.1		99.7	99.9	99.1		98.5	98.9		99.8

• in contact with graphite. R = rim, C = core of the vein

Vuggy garnet (samples E48b and QG2b) (continued)

	Core ←					(B)				→ Rim		(D)	
	18	19	20	10	23	24	25	26	27	28	29	30	31
SiO_2	39.77	39.81	40.00	39.66	39.79	39.36	39.51	40.30	40.16	40.06	39.97	40.08	39.39
TiO_2	0.18	0.27	0.10	0.29	0.22	0.31	0.39	0.27	0.46	0.46	0.17	0.27	0.12
Al_2O_3	21.21	21.03	21.39	20.86	20.93	20.67	20.08	20.66	20.32	21.08	21.12	20.72	21.18
Cr_2O_3	0.00	0.00	0.02	0.76	0.00	0.00	0.00	0.00	0.00	0.06	0.00	0.00	0.00
FeO	3.83	3.87	3.46	3.69	3.54	3.89	3.53	3.89	3.41	3.62	3.60	3.21	3.89
MnO	0.21	0.23	0.31	0.21	0.44	0.39	0.11	0.21	0.04	0.00	0.51	0.37	0.24
MgO	0.04	0.06	0.06	0.10	0.09	0.00	0.06	0.03	0.02	0.07	0.07	0.07	0.06
CaO	35.04	35.04	35.45	35.63	35.19	34.84	34.39	35.15	35.16	34.82	34.78	34.71	34.79
Total	100.28	100.32	100.79	101.20	100.20	99.46	98.06	100.50	99.59	100.17	100.22	99.44	99.67
Si	3.001	3.001	3.001	2.976	3.003	2.997	3.037	3.029	3.035	3.018	3.014	3.037	2.994
Al	0.000	0.000	0.000	0.024	0.000	0.003	0.000	0.000	0.000	0.000	0.000	0.000	0.006
Al	1.886	1.869	1.892	1.822	1.862	1.852	1.819	1.830	1.810	1.872	1.877	1.850	1.890
Fe^{3+}	0.103	0.116	0.101	0.117	0.126	0.131	0.158	0.155	0.163	0.099	0.114	0.134	0.103
Ti	0.010	0.015	0.006	0.017	0.013	0.018	0.023	0.015	0.026	0.026	0.010	0.015	0.007
Cr	0.000	0.000	0.001	0.045	0.000	0.000	0.000	0.000	0.000	0.003	0.000	0.000	0.000
Mg	0.004	0.006	0.006	0.011	0.010	0.000	0.007	0.003	0.002	0.008	0.008	0.008	0.007
Fe^{2+}	0.139	0.128	0.116	0.115	0.098	0.117	0.068	0.009	0.052	0.130	0.113	0.069	0.145
Mn	0.013	0.015	0.020	0.014	0.028	0.025	0.007	0.013	0.002	0.000	0.033	0.024	0.015
Ce	2.833	2.830	2.849	2.864	2.845	2.842	2.832	2.830	2.847	2.811	2.810	2.818	2.832
Alm	4.5	4.2	3.9	3.5	3.3	3.7	2.3	3.0	1.8	4.4	3.8	2.4	4.8
And	5.2	5.8	5.1	4.7	6.3	6.6	6.4	6.5	6.5	4.6	5.0	4.9	5.0
Gro	89.7	89.2	90.1	88.2	89.1	88.9	90.8	89.9	91.5	90.6	89.8	91.6	89.3
Py	0.1	0.2	0.2	0.4	0.3	0.0	0.2	0.1	0.1	0.3	0.3	0.3	0.2
Sch	0.0	0.0	0.0	0.6	0.0	0.0	0.0	0.0	0.0	0.0	0.0	0.0	0.2
Spe	0.4	0.5	0.7	0.5	0.9	0.9	0.2	0.5	0.1	0.0	1.1	0.8	0.5
Uve	0.0	0.0	0.1	2.3	0.0	0.0	0.0	0.0	0.0	0.2	0.0	0.0	0.0
ALLOCATED	99.6	99.3	99.7	99.9	99.5	99.4	98.1	98.6	97.9	98.7	99.2	98.3	100.0

B = profile through the crystal; (D) vuggy garnet.

Vuggy garnet (samples E48b and QG2b)

	(A)			Rim ←		(B)			→ Core	Rim ←					(C)						→ Rim
	1	3	5	76	77	75	79	80	81	6	7	8	9	12	11	10	13	14	15	16	17
SiO_2	40.45	39.95	39.43	39.71	39.54	39.95	39.23	40.11	39.40	39.80	40.22	39.97	40.32	39.51	39.84	39.66	39.53	40.21	39.56	39.94	39.83
TiO_2	0.51	0.47	0.35	0.52	0.40	0.46	0.39	0.38	0.47	0.06	0.12	0.27	0.18	0.20	0.18	0.29	0.04	0.32	0.27	0.18	0.12
Al_2O_3	21.20	20.98	20.91	20.70	20.47	20.99	20.66	20.35	20.66	20.81	21.19	21.48	21.51	20.96	21.24	20.86	20.97	21.29	21.05	21.29	21.50
Cr_2O_3	0.00	0.04	0.00	0.00	0.04	0.04	0.00	0.00	0.00	0.00	0.00	0.00	0.04	0.00	0.05	0.76	0.00	0.02	0.00	0.00	0.00
FeO	3.57	3.30	3.49	3.53	3.18	2.66	3.66	3.09	3.65	3.50	3.80	3.13	3.58	3.47	3.83	3.69	3.61	3.71	3.64	3.06	3.86
MnO	0.15	0.02	0.00	0.22	0.07	0.00	0.04	1.37	0.20	0.25	0.15	0.33	0.14	0.30	0.24	0.21	0.20	0.40	0.38	0.24	0.24
MgO	0.05	0.03	0.0	0.04	0.12	0.10	0.13	0.13	0.00	0.00	0.00	0.09	0.06	0.02	0.07	0.10	0.00	0.09	0.08	0.01	0.00
CaO	35.65	35.26	36.01	36.94	35.92	36.28	35.83	36.03	36.34	35.39	35.39	35.67	35.23	34.39	35.19	35.63	35.41	34.92	35.29	34.81	35.61
Total	01.58	100.06	100.20	101.67	99.74	100.47	99.93	101.46	100.71	99.81	100.87	100.93	101.06	98.84	100.64	101.20	99.76	100.95	100.25	98.52	101.17
Si	3.009	3.014	2.981	2.958	2.998	2.998	2.969	2.998	2.968	3.012	3.014	2.994	3.014	3.019	2.997	2.976	3.000	3.010	2.909	3.024	2.983
Al	0.000	0.000	0.019	0.042	0.002	0.002	0.031	0.002	0.032	0.000	0.000	0.006	0.000	0.000	0.003	0.024	0.000	0.000	0.011	0.000	0.017
Al	1.859	1.866	1.843	1.775	1.827	1.854	1.812	1.790	1.802	1.856	1.872	1.890	1.894	1.887	1.881	1.822	1.875	1.879	1.863	1.900	1.882
Fe^{3+}	0.113	0.105	0.137	0.196	0.148	0.118	0.166	0.189	0.172	0.141	0.121	0.095	0.093	0.101	0.106	0.117	0.123	0.102	0.122	0.090	0.112
Ti	0.028	0.027	0.020	0.029	0.023	0.026	0.022	0.021	0.026	0.003	0.007	0.015	0.010	0.011	0.010	0.017	0.002	0.018	0.015	0.010	0.007
Cr	0.000	0.003	0.000	0.000	0.002	0.002	0.000	0.000	0.000	0.000	0.000	0.000	0.002	0.000	0.003	0.045	0.000	0.001	0.000	0.000	0.000
Mg	0.006	0.003	0.000	0.004	0.014	0.011	0.014	0.014	0.000	0.000	0.000	0.009	0.007	0.002	0.008	0.011	0.000	0.010	0.009	0.001	0.000
Fe^{2+}	0.109	0.103	0.084	0.024	0.053	0.049	0.066	0.005	0.058	0.081	0.117	0.101	0.131	0.120	0.135	0.115	0.107	0.130	0.109	0.104	0.130
Mn	0.009	0.001	0.000	0.014	0.004	0.000	0.002	0.087	0.012	0.016	0.009	0.021	0.009	0.020	0.015	0.014	0.013	0.025	0.024	0.015	0.016
Ca	2.841	2.849	2.916	2.947	2.918	2.916	2.905	2.885	2.932	2.869	2.842	2.863	2.821	2.815	2.837	2.864	2.879	2.800	2.856	2.824	2.857
Alm	3.4	3.5	2.8	0.7	1.1	1.3	2.2	0.0	1.6	2.7	3.9	3.1	4.4	4.1	4.3	3.5	3.5	4.4	3.5	3.5	3.9
And	5.7	5.2	6.2	7.8	7.5	6.0	6.9	9.5	7.3	6.1	5.4	4.8	4.1	4.3	5.3	4.7	6.1	4.9	5.9	3.2	4.6
Gro	90.3	91.0	90.4	99.9	90.7	92.3	89.8	87.1	89.8	90.6	90.3	91.1	90.8	90.9	89.4	88.2	89.9	89.4	89.3	92.7	90.8
Py	0.2	0.1	0.0	0.1	0.5	0.4	0.5	0.5	0.0	0.0	0.0	0.3	0.2	0.1	0.3	0.4	0.0	0.3	0.3	0.0	0.0
Sch	0.0	0.0	0.6	1.0	0.0	0.0	0.6	0.0	0.9	0.0	0.0	0.0	0.0	0.0	0.0	0.6	0.0	0.0	0.2	0.0	0.2
Spe	0.3	0.0	0.0	0.5	0.1	0.0	0.1	2.9	0.4	0.5	0.3	0.7	0.3	0.7	0.5	0.5	0.4	0.9	0.8	0.5	0.5
Uva	0.0	0.1	0.0	0.0	0.1	0.1	0.0	0.0	0.0	0.0	0.0	0.0	0.1	0.0	0.2	2.3	0.0	0.1	0.0	0.0	0.0
ALLOCATED	98.8	98.9	100.0	99.6	9931	98.9	99.7	99.2	99.9	99.3	99.3	99.6	99.3	99.1	99.7	99.9	99.9	99.1	99.8	98.8	99.8

(A) Rtype garnet (1) in contact with vuggy garnet (3,5); B = profile through the crystal; (C) profile parallel to the [110] crystal faces.

Pyroxenes included in C-type garnets (sample QG2)

Site-deficient molecules calculated with minimum Fe^{3+} content

	Zone 1		Zone 2							Zone 3		
	62	61	60	59	58A	64	66	67B	71A	33	34	27
SiO_2	52.82	52.26	53.64	53.24	52.33	51.96	52.70	52.22	52.71	52.13	51.97	52.78
TiO_2	0.00	0.00	0.00	0.00	0.06	0.15	0.04	0.00	0.00	0.00	0.13	0.00
Al_2O_3	0.29	0.72	0.18	0.21	0.53	1.40	0.65	0.34	0.17	0.15	0.92	0.16
Cr_2O_3	0.01	0.00	0.00	0.00	0.13	0.07	0.03	0.00	0.04	0.00	0.00	0.07
FeO*	9.04	12.20	8.97	8.73	10.01	10.09	11.99	13.29	8.47	10.47	8.84	8.52
MnO	0.00	0.23	0.00	0.09	0.13	0.27	0.05	0.05	0.19	0.35	0.18	0.14
MgO	12.15	9.21	12.65	11.95	10.61	10.78	9.65	8.98	11.84	10.74	11.50	12.05
NiO	0.00	0.00	0.00	0.00	0.10	0.02	0.04	0.00	0.00	0.08	0.21	0.00
CaO	24.69	24.74	24.96	24.97	24.94	24.86	24.52	24.15	25.34	25.46	24.92	26.42
Na_2O	0.04	0.18	0.36	0.03	0.00	0.05	0.29	0.00	0.03	0.10	0.14	0.08
K_2O	0.00	0.00	0.12	0.00	0.00	0.00	0.03	0.00	0.00	0.00	0.00	0.00
Total*	99.04	99.54	100.90	99.22	98.83	99.65	99.98	99.03	98.79	99.48	98.81	100.22
Smax	3.983	3.960	4.015	3.985	3.984	3.994	3.990	3.977	3.993	4.008	4.000	4.013
Smin	3.900	3.962	4.000	3.896	3.880	3.890	3.867	3.840	3.905	4.000	4.000	4.000
ORmin	0.039	0.039	0.162	0.246	0.078	0.000	0.117	0.215	0.086	0.074	0.004	0.145
FeOc	8.59	11.73	7.52	6.58	9.23	10.09	10.58	10.44	7.75	9.69	8.81	7.29
Fe_2O_3c	0.49	0.53	1.62	2.39	0.87	0.00	1.56	3.17	0.81	0.86	0.04	1.37
Totalc	99.08	99.59	101.06	99.46	98.92	99.65	100.13	99.35	98.87	99.57	98.81	100.36
Si	2.000	2.000	1.990	2.000	1.997	1.971	1.998	2.000	2.000	1.988	1.980	1.979
Al4	0.000	0.000	0.008	0.000	0.003	0.029	0.002	0.000	0.0000	0.007	0.020	0.007
Fe4	0.000	0.000	0.002	0.000	0.000	0.000	0.000	0.000	0.000	0.005	0.000	0.014
Al8	0.012	0.032	0.000	0.009	0.020	0.034	0.027	0.016	0.007	0.000	0.022	0.000
Fe8	0.014	0.015	0.043	0.067	0.025	0.000	0.045	0.091	0.023	0.019	0.001	0.025
Ti	0.000	0.000	0.000	0.000	0.002	0.004	0.001	0.000	0.000	0.000	0.004	0.000
Cr^{3+}	0.000	0.000	0.000	0.000	0.004	0.002	0.001	0.000	0.001	0.000	0.000	0.00^2
Mg	0.685	0.525	0.700	0.669	0.603	0.610	0.545	0.513	0.670	0.610	0.653	0.673
Fe^{2+}	0.272	0.375	0.233	0.207	0.294	0.320	0.335	0.334	0.246	0.309	0.281	0.22^9
Mn	0.000	0.008	0.000	0.003	0.004	0.009	0.002	0.001	0.006	0.011	0.006	0.004
Ni	0.000	0.000	0.000	0.000	0.003	0.001	0.001	0.000	0.000	0.002	0.006	0.000
Ca	1.001	1.014	0.992	1.005	1.020	1.010	0.996	0.991	1.030	1.040	1.017	1.061
Na	0.003	0.013	0.027	0.002	0.000	0.004	0.022	0.000	0.002	0.007	0.010	0.006
K	0.000	0.000	0.006	0.000	0.000	0.000	0.001	0.000	0.000	0.000	0.000	0.000
Scat	3.988	3.983	4.000	3.963	3.975	3.994	3.975	3.946	3.985	4.000	4.000	4.000
AJd	0.3	1.3	0.8	0.2	0.0	0.1	2.2	0.0	0.1	0.7	1.0	0.4
Fjd	0.0	0.0	2.5	0.0	0.0	0.0	0.0	0.0	0.0	0.1	0.0	0.0
CATs	0.0	0.0	0.0	0.0	0.2	2.0	0.0	0.0	0.0	0.0	1.2	0.2
CAFTs	0.0	0.0	1.0	0.0	0.0	0.0	0.0	0.0	0.0	1.2	0.1	1.9
Mlsd	1.4	2.8	0.0	1.0	3.7	1.9	0.7	1.9	0.9	0.0	0.0	0.0
FMlsd	2.1	2.3	0.0	10.1	3.8	0.0	6.7	11.4	3.5	0.0	0.0	0.0
M2sd	0.0	0.0	0.0	0.0	0.0	0.0	0.0	0.3	0.0	0.0	0.0	0.0
FM2sd	0.0	0.0	0.0	0.0	0.0	0.0	0.0	1.6	0.0	0.0	0.0	0.0
En	34.3	26.4	35.0	33.5	30.2	30.8	27.3	25.7	33.6	30.7	33.0	33.8
Fs	13.6	18.8	11.7	10.4	14.8	16.2	16.8	16.7	12.3	15.6	14.2	11.5
Wo	48.3	48.3	49.1	44.7	47.4	48.9	46.2	42.5	49.5	51.7	50.6	52.2

(1) zone 1; (2) zone 2; (3) zone 3. The arrow indicates the growth direction of the garnet. The outermost pyroxene is in contact with clear garnet (A) or with tubular anorthite (B) towards the rim.

Pyroxenes included in R-type garnet (sample E48b)

	(1)			Core → Rim (2)											
	36	37	38	59	60	70	67	68	63	62	66	51	56	4*
SiO_2	53.31	52.64	53.45	52.58	51.92	51.19	52.10	51.68	51.94	52.84	53.30	53.18	53.28	52.82
TiO_2	0.02	0.00	0.00	0.00	0.00	0.00	0.10	0.01	0.00	0.00	0.05	0.00	0.00	0.00
Al_2O_3	0.93	0.15	0.22	0.32	0.17	0.09	0.68	0.32	0.11	0.12	0.11	0.11	0.28	0.07
Cr_2O_3	0.12	0.04	0.00	0.04	0.00	0.00	0.02	0.00	0.00	0.00	0.03	0.00	0.05	0.00
FeO*	9.95	10.85	10.23	9.79	11.07	10.58	9.57	10.15	11.45	10.60	10.22	11.35	10.74	10.95
MnO	0.00	0.05	0.19	0.02	0.11	0.13	0.12	0.05	0.04	0.14	0.00	0.17	0.12	0.18
MgO	11.74	10.54	11.19	10.99	10.77	11.18	11.52	10.83	10.25	11.38	11.70	10.54	11.27	10.99
NiO	0.20	0.20	0.01	0.00	0.00	0.00	0.17	0.00	0.04	0.00	0.16	0.00	0.15	0.00
CaO	23.86	23.97	23.79	24.67	25.20	25.13	24.23	24.52	24.58	24.75	23.72	24.59	24.16	25.00
Na_2O	0.01	0.15	0.10	0.08	0.10	0.00	0.06	0.00	0.05	0.00	0.09	0.00	0.08	0.03
K_2O	0.00	0.02	0.00	0.02	0.01	0.00	0.00	0.00	0.00	0.00	0.03	0.00	0.00	0.00
Total*	100.14	98.61	99.18	98.51	99.35	98.30	98.57	97.56	98.46	99.83	99.41	99.94	100.13	100.04
Smax	3.978	3.983	3.973	3.985	4.011	4.017	3.993	3.990	3.994	3.995	3.982	3.981	3.986	3.997
Smin	3.877	3.871	3.868	3.883	4.000	4.000	3.893	3.884	3.874	3.886	3.878	3.865	3.877	3.885
ORmin	0.251	0.332	0.484	0.211	0.096	0.152	0.000	0.047	0.094	0.039	0.371	0.273	0.172	0.043
FeOc	7.46	7.25	5.17	7.72	10.01	8.97	9.57	9.67	10.38	10.19	6.43	8.25	8.89	10.48
Fe_2O_3c	2.76	4.00	5.62	2.30	1.18	1.79	0.00	0.53	1.19	0.46	4.21	3.45	2.05	0.52
Totalc	100.42	99.01	99.74	98.74	99.47	98.48	98.57	97.61	98.58	99.88	99.83	100.29	100.34	100.09
Si	1.986	2.000	2.000	2.000	1.983	1.972	1.991	1.999	2.000	2.000	1.997	2.000	2.000	2.000
Al4	0.014	0.000	0.000	0.000	0.008	0.004	0.009	0.001	0.000	0.000	0.003	0.000	0.000	0.000
Fe4	0.000	0.000	0.000	0.000	0.009	0.024	0.000	0.000	0.000	0.000	0.000	0.000	0.000	0.000
Al8	0.027	0.007	0.009	0.014	0.000	0.000	0.022	0.014	0.005	0.005	0.002	0.005	0.012	0.003
Fe8	0.078	0.114	0.158	0.066	0.025	0.028	0.000	0.015	0.035	0.013	0.119	0.098	0.058	0.015
Ti	0.001	0.000	0.000	0.000	0.000	0.000	0.003	0.000	0.000	0.000	0.001	0.000	0.000	0.000
Cr^{3+}	0.004	0.001	0.000	0.001	0.000	0.000	0.001	0.000	0.000	0.000	0.001	0.000	0.001	0.000
Mg	0.652	0.597	0.624	0.623	0.613	0.642	0.656	0.625	0.588	0.642	0.653	0.591	0.631	0.620
Fe^{2+}	0.233	0.230	0.162	0.246	0.320	0.289	0.306	0.313	0.334	0.322	0.201	0.259	0.279	0.332
Mn	0.000	0.002	0.006	0.001	0.004	0.004	0.004	0.002	0.001	0.004	0.000	0.005	0.004	0.006
Ni	0.006	0.006	0.000	0.000	0.000	0.000	0.005	0.000	0.001	0.000	0.005	0.000	0.005	0.000
Ca	0.952	0.976	0.953	1.005	1.031	1.037	0.992	1.016	1.014	1.004	0.952	0.991	0.972	1.014
Na	0.001	0.011	0.007	0.006	0.007	0.000	0.004	0.000	0.004	0.000	0.007	0.000	0.006	0.002
K	0.000	0.001	0.000	0.001	0.000	0.000	0.000	0.000	0.000	0.000	0.001	0.000	0.000	0.000
Scat	3.952	3.945	3.920	3.963	4.000	4.000	3.993	3.985	3.982	3.991	3.943	3.949	3.967	3.992
AJd	0.0	0.7	0.7	0.6	0.8	0.0	0.4	0.0	0.4	0.0	0.5	0.0	0.4	0.2
Fjd	0.0	0.4	0.0	0.0	0.0	0.0	0.0	0.0	0.0	0.0	0.2	0.0	0.0	0.0
CATs	1.1	0.0	0.0	0.0	0.0	0.2	0.3	0.0	0.0	0.0	0.0	0.0	0.0	0.0
CAFTs	0.0	0.0	0.0	0.0	1.7	2.6	0.0	0.0	0.0	0.0	0.0	0.0	0.0	0.0
M1sd	0.0	0.0	0.1	1.3	0.0	0.0	1.1	2.1	0.2	0.8	0.0	0.6	0.4	0.1
FM1sd	0.2	12.9	12.1	9.9	0.0	0.0	0.0	2.3	5.2	2.0	5.2	12.0	2.7	2.2
M2sd	1.7	0.0	0.1	0.0	0.0	0.0	0.7	0.0	0.0	0.0	0.0	0.1	0.5	0.0
FM2sd	7.7	2.5	7.8	0.0	0.0	0.0	0.0	0.0	0.0	0.0	8.0	1.8	4.0	0.0
En	32.8	30.0	31.3	31.2	30.7	32.2	33.1	31.3	29.5	32.2	32.8	29.6	31.7	31.1
Fs	11.7	11.6	8.1	12.3	16.0	14.5	15.4	15.7	16.7	16.2	10.1	13.0	14.0	16.6
Wo	44.8	42.0	39.7	44.8	50.8	50.6	48.9	48.6	48.1	48.9	43.2	42.9	46.2	49.7

(1) Pyroxene from zone 1 (with relics of the graphitic matrix); (2) pyroxene monocrystals form zone 2 (the arrow indicate the growth direction of the crystal;) * in contact with vuggy garnet; O : close to quartz needle inclusion.

site-deficient molecules calculated with minimum Fe^{3+} content

Pyroxene monocrystals in interstitial graphite

	QG3a					E48b				QG2b	
	9*	15	16	22	13•	3*	4*	7	47	63	66
SiO_2	52.35	52.55	53.48	51.54	52.35	52.52	53.40	52.75	51.16	51.35	52.40
TiO_2	0.00	0.13	0.00	0.01	0.00	0.00	0.03	0.00	0.04	0.00	0.00
Al_2O_3	0.26	0.44	0.07	1.33	0.26	0.22	0.16	0.16	0.15	0.18	0.13
Cr_2O_3	0.03	0.00	0.00	0.00	0.03	0.00	0.00	0.00	0.00	0.00	0.00
FeO*	7.99	8.33	9.87	8.77	7.16	10.12	10.16	9.98	9.89	13.09	12.66
MnO	0.11	0.04	0.24	0.18	0.11	0.00	0.16	0.24	0.12	0.23	0.20
MgO	12.56	11.99	11.76	11.44	12.56	11.18	11.69	11.23	11.24	9.64	10.19
NiO	0.00	0.00	0.04	0.00	0.00	0.00	0.01	0.02	0.11	0.00	0.04
CaO	25.65	25.79	25.70	25.21	25.65	25.45	25.47	25.46	24.66	25.71	25.91
Na_2O	0.01	0.09	0.13	0.22	0.01	0.00	0.00	0.00	0.07	0.09	0.00
K_2O	0.01	0.00	0.14	0.00	0.01	0.00	0.01	0.03	0.09	0.00	0.00
Total*	98.97	99.36	101.43	98.70	98.14	99.49	101.09	99.87	97.53	00.29	101.53
Smax	4.009	4.003	4.012	4.011	4.000	3.998	3.999	3.999	4.012	4.026	4.017
Smin	4.000	4.000	4.000	4.000	4.000	3.894	3.896	3.896	4.000	4.000	4.000
ORmin	0.104	0.029	0.113	0.115	0.000	0.000	0.000	0.000	0.113	0.188	0.126
FeOc	7.16	8.09	8.75	7.76	7.16	10.12	10.16	9.98	8.77	10.64	11.07
Fe_2O_3c	0.92	0.27	1.24	1.12	0.00	0.00	0.00	0.00	1.25	2.73	1.77
Totalc	99.06	99.39	101.55	98.81	98.14	99.49	101.09	99.87	97.65	100.56	101.71
Si	1.981	1.986	1.989	1.962	1.994	1.997	1.996	1.998	1.982	1.960	1.972
Al4	0.012	0.014	0.003	0.038	0.006	0.003	0.004	0.002	0.007	0.008	0.006
Fe4	0.007	0.000	0.008	0.000	0.000	0.000	0.000	0.000	0.011	0.032	0.022
Al8	0.000	0.006	0.000	0.022	0.006	0.007	0.004	0.005	0.000	0.000	0.000
Fe8	0.019	0.008	0.027	0.032	0.000	0.000	0.000	0.000	0.025	0.047	0.028
Ti	0.000	0.004	0.000	0.000	0.000	0.000	0.001	0.000	0.001	0.000	0.000
Cr^{3+}	0.001	0.000	0.000	0.000	0.001	0.000	0.000	0.000	0.000	0.000	0.000
Mg	0.709	0.675	0.652	0.649	0.713	0.634	0.651	0.634	0.649	0.548	0.572
Fe^{2+}	0.227	0.256	0.272	0.247	0.228	0.322	0.318	0.316	0.284	0.339	0.348
Mn	0.004	0.001	0.008	0.006	0.004	0.000	0.005	0.008	0.004	0.007	0.006
Ni	0.000	0.000	0.001	0.000	0.000	0.000	0.000	0.001	0.003	0.000	0.001
Ca	1.040	1.044	1.024	1.028	1.047	1.037	1.020	1.033	1.024	1.051	1.045
Na	0.001	0.007	0.009	0.016	0.001	0.000	0.000	0.000	0.005	0.007	0.000
K	0.000	0.000	0.007	0.000	0.000	0.000	0.000	0.001	0.004	0.000	0.000
Scat	4.000	4.000	4.000	4.000	4.000	3.998	3.999	3.999	4.000	4.000	4.000
AJd	0.0	0.7	0.3	1.6	0.0	0.0	0.0	0.1	0.7	0.7	0.0
Fjd	0.0	0.0	1.3	0.0	0.0	0.0	0.0	0.0	0.3	0.0	0.0
CATs	0.6	0.3	0.0	2.1	0.6	0.3	0.2	0.2	0.0	0.1	0.3
CAFTs	1.3	0.4	1.1	1.6	0.0	0.0	0.0	0.0	1.6	3.9	2.5
En	35.5	33.9	32.7	32.6	35.8	31.7	32.7	31.8	32.6	27.5	28.7
Fs	11.4	12.8	13.7	12.4	11.4	16.1	15.9	15.9	14.3	17.0	17.5
Wo	51.2	51.9	50.9	49.7	52.2	51.4	51.1	51.6	50.6	50.8	51.0

* in contact with graphite; • in contact with calcite; clear garnet. site-deficient molecules calculated with minimum Fe^{3+} content

Vein pyroxenes (sample QG2)

(site-deficient molecules calculated with minimum Fe^{3+}-content)

	(1) R←C→R					(2) R←C→R			(2) R←C→R			(2) C→R		(2) C→R	
	25*	26	27	28	29*	39*	40	41	*23-1	22+1	24-1	29	28	24-2	23-2
SiO_2	53.42	52.26	53.24	52.17	51.45	52.50	52.40	51.96	53.00	52.61	51.49	53.28	51.17	52.26	51.69
TiO_2	0.04	0.00	0.00	0.00	0.00	0.00	0.00	0.03	0.07	0.01	0.00	0.08	0.00	0.00	0.00
Al_2O_3	0.08	0.14	0.15	0.28	0.18	0.13	0.21	0.10	0.14	0.09	0.17	0.12	0.17	0.22	0.16
Cr_2O_3	0.00	0.05	0.00	0.06	0.00	0.00	0.00	0.00	0.00	0.00	0.00	0.04	0.00	0.00	0.00
FeO*	8.79	14.24	12.49	11.50	12.45	12.47	13.16	12.64	11.53	11.01	11.90	11.78	11.99	12.54	12.41
MnO	0.30	0.08	0.19	0.10	0.24	0.23	0.15	0.00	0.14	0.00	0.23	0.10	0.21	0.32	0.11
MgO	12.77	8.69	9.80	10.24	9.84	10.06	9.14	10.16	10.82	10.00	10.65	10.36	9.89	9.36	9.91
NiO	0.00	0.00	0.00	0.01	0.14	0.09	0.00	0.06	0.05	0.00	0.17	0.00	0.06	0.08	0.07
CaO	25.13	24.49	24.37	24.57	24.66	24.06	23.92	24.28	24.75	25.19	24.75	23.97	25.35	23.97	25.73
Na_2O	0.00	0.11	0.00	0.06	0.03	0.08	0.07	0.08	0.06	0.03	0.35	0.05	0.06	0.09	0.06
K_2O	0.06	0.00	0.00	0.00	0.04	0.03	0.00	0.04	0.00	0.00	0.12	0.01	0.00	0.02	0.00
Total*	100.59	100.28	100.23	99.00	99.04	99.64	99.04	99.36	100.58	98.96	99.84	99.79	98.90	98.86	100.14
Smax	4.003	3.996	3.976	3.992	4.007	3.992	3.978	4.003	3.995	3.982	4.037	3.974	4.016	3.982	4.018
Smin	4.000	3.849	3.848	3.873	4.000	3.863	3.842	4.000	3.878	3.869	4.000	3.854	4.000	3.852	4.000
ORmin	0.037	0.061	0.320	0.051	0.56	0.137	0.289	0.020	0.098	0.295	0.289	0.438	0.121	0.252	0.135
FeOc	8.46	13.38	8.49	10.91	11.76	10.76	9.36	12.40	10.40	7.76	8.46	6.63	10.54	9.38	10.74
Fe_2O_3c	0.36	0.96	4.45	0.65	0.77	1.89	4.23	0.27	1.25	3.61	3.82	5.73	1.61	3.51	1.86
Totalc	100.62	100.37	100.68	99.06	99.12	99.83	99.47	99.39	100.70	99.32	100.22	100.36	99.06	99.21	100.33
Si	1.994	2.000	2.000	2.000	1.987	2.000	2.000	1.997	1.996	1.999	1.958	1.995	1.975	2.000	1.972
Al4	0.003	0.000	0.000	0.000	0.008	0.000	0.000	0.003	0.004	0.001	0.008	0.005	0.008	0.000	0.007
Fe4	0.003	0.000	0.000	0.000	0.005	0.000	0.000	0.000	0.000	0.0000	0.035	0.000	0.017	0.000	0.021
Al8	0.000	0.006	0.006	0.013	0.000	0.006	0.009	0.001	0.002	0.003	0.000	0.001	0.000	0.010	0.000
Fe8	0.007	0.028	0.126	0.019	0.017	0.054	0.121	0.008	0.035	0.103	0.075	0.161	0.030	0.101	0.032
Ti	0.001	0.000	0.000	0.000	0.000	0.000	0.000	0.001	0.002	0.000	0.000	0.002	0.000	0.000	0.000
Cr^{3+}	0.000	0.002	0.000	0.002	0.000	0.000	0.000	0.000	0.000	0.000	0.000	0.001	0.000	0.000	0.000
Mg	0.710	0.507	0.548	0.585	0.566	0.571	0.520	0.582	0.607	0.567	0.604	0.578	0.569	0.534	0.563
Fe^{2+}	0.264	0.428	0.267	0.350	0.380	0.343	0.299	0.398	0.328	0.247	0.269	0.208	0.340	0.300	0.343
Mn	0.010	0.003	0.006	0.003	0.008	0.007	0.005	0.000	0.005	0.000	0.007	0.003	0.007	0.010	0.004
Ni	0.000	0.000	0.000	0.000	0.004	0.003	0.000	0.002	0.002	0.000	0.005	0.000	0.002	0.002	0.002
Ca	1.005	1.004	0.981	1.009	1.020	0.982	0.978	1.000	0.998	1.026	1.008	0.962	1.048	0.983	1.052
Na	0.000	0.008	0.000	0.005	0.002	0.006	0.005	0.006	0.005	0.002	0.026	0.004	0.004	0.007	0.004
K	0.003	0.000	0.000	0.000	0.002	0.002	0.000	0.002	0.000	0.000	0.006	0.000	0.000	0.001	0.000
Scat	4.000	3.987	3.934	3.986	4.000	3.974	3.937	4.000	3.984	3.948	4.000	3.920	4.000	3.948	4.000
AJd	0.3	0.6	0.0	0.3	0.4	0.6	0.5	0.5	0.5	0.2	0.8	0.3	0.5	0.8	0.4
Fjd	0.0	0.1	0.0	0.0	0.0	0.2	0.0	0.3	0.0	0.0	2.5	0.0	0.0	0.0	0.0
CATs	0.0	0.0	0.0	0.0	0.2	0.0	0.0	0.0	0.0	0.0	0.0	0.0	0.2	0.0	0.1
CAFTs	0.4	0.0	0.0	0.0	1.1	0.0	0.0	0.1	0.0	0.0	4.3	0.0	2.4	0.0	2.7
M1sd	0.0	0.0	0.7	1.5	0.0	0.0	0.4	0.0	0.0	0.1	0.0	0.0	0.0	0.3	0.0
FM1sd	0.0	4.0	13.4	2.8	0.0	4.7	13.5	0.0	4.9	15.5	0.0	13.7	0.0	12.4	0.0
M2sd	0.0	0.0	0.2	0.0	0.0	0.0	0.1	0.0	0.0	0.0	0.0	0.0	0.0	0.0	0.0
FM2sd	0.0	0.0	3.7	0.0	0.0	2.1	3.2	0.0	0.0	0.0	0.0	6.9	0.0	1.9	0.0
En	35.7	25.4	27.5	29.4	28.5	28.7	26.0	29.2	30.5	28.3	30.4	29.1	28.6	26.9	28.3
Fs	13.3	21.5	13.4	17.6	19.1	17.2	15.0	20.0	16.5	12.3	13.5	10.4	17.1	15.1	17.2
Wo	50.3	48.4	41.2	48.5	50.7	46.4	41.2	49.9	47.6	43.5	48.6	39.6	51.4	42.6	51.3

*in contact with graphite. (1) Profile through a veinlet; (2) Profile through a monocrystal.

Pyroxenes associated with M-type garnets (sample 4J26)
(site-deficient molecules calculated with minimum Fe^{3+} content)

	inclusions in garnet		interstitial C ——→ R	
	11	12	19	20
SiO_2	51.91	52.05	52.15	51.62
TiO_2	0.01	0.00	0.04	0.05
Al_2O_3	1.11	0.86	0.85	0.76
Cr_2O_3	0.00	0.02	0.02	0.02
FeO*	11.97	11.40	10.99	12.01
MnO	0.19	0.14	0.12	0.13
MgO	9.67	10.09	10.25	10.16
NiO	0.00	0.16	0.00	0.00
CaO	23.90	24.51	24.20	24.28
Na_2O	0.21	0.12	0.14	0.19
K_2O	0.00	0.03	0.00	0.01
Total*	98.97	99.38	98.76	99.23
Smax	3.988	3.994	3.985	4.005
Smin	3.864	3.877	3.872	4.000
ORmin	0.000	0.000	0.000	0.041
FeOc	11.97	11.40	10.99	11.52
Fe_2O_3c	0.00	0.00	0.00	0.55
Totalc	98.97	99.38	98.76	99.28
Si	1.994	1.991	1.999	1.980
Al4	0.006	0.009	0.001	0.020
Fe4	0.000	0.000	0.000	0.000
Al8	0.044	0.030	0.038	0.015
Fe8	0.000	0.000	0.000	0.016
Ti	0.000	0.000	0.001	0.001
Cr^{3+}	0.000	0.001	0.001	0.001
Mg	0.554	0.575	0.586	0.581
Fe^{2+}	0.385	0.365	0.352	0.369
Mn	0.006	0.005	0.004	0.004
Ni	0.000	0.005	0.000	0.000
Ca	0.984	1.004	0.994	0.998
Na	0.016	0.009	0.010	0.014
K	0.000	0.001	0.000	0.000
Scat	3.988	3.994	3.985	4.000
AJd	1.6	1.0	1.0	1.4
Fjd	0.0	0.0	0.0	0.0
CATs	0.5	0.9	0.0	0.9
CAFTs	0.0	0.0	-.1	0.8
M1sd	3.3	1.7	4.0	0.0
FM1sd	0.0	0.0	0.4	0.0
M2sd	0.2	0.0	0.0	0.0
FM2sd	0.0	0.0	0.0	0.0
En	27.8	28.9	29.4	29.2
Fs	19.3	18.3	17.7	18.6
Wo	47.4	49.2	47.7	49.2

C = core; R = rim

DEUXIEME PARTIE

INTRODUCTION

Cette deuxième partie regroupe trois articles écrits avec divers collaborateurs : A. Charef dans le cadre de sa thèse d'état consacrée à des gisements Pb-Zn de la Bordure Cévenole et associés aux diapirs de sel de Tunisie ainsi que des auteurs de différentes spécialités, notamment dans les domaines de la minéralogie (E. Oudin) et de l'hydrodynamique (M. Danis). Par ailleurs, le problème posé par le bilan thermique de la fosse d'Atlantis II a été résolu à l'aide de spécialistes de la thermodynamique des solutions (J.P. Grolier et ses collaborateurs), qui ont mis au point un modèle pour calculer les capacités calorifiques de la saumure fortement chlorurée dans les conditions P-T proches du point critique de l'eau pure. Les articles qui suivent s'attachent à l'identification et à la quantification, du point de vue de **la température et de la pression,** des processus hydrothermaux dans les contextes d'extension crustale étudiés. Ils s'efforcent d'expliquer les **paragenèses minérales** observées et les processus de **croissance cristalline** des minéraux dans le cadre de l'évolution thermobarométrique et chimique proposée. Les deux exemples étudiés sont associés à des minéralisations économiques essentiellement zincifères. Il s'agit :

-(1) du gisement Zn-Pb des Malines sur la Bordure Cévenole (Massif Central Français). Le travail fait suite aux publications récentes de Verraes, 1983; Charef, 1983; 1986; Charef et Sheppard, 1983; 1988). Dans ce qui suit, la formation d'une partie du gisement est replacée dans le contexte de la marge passive bordant la Mer Mésozoique Subalpine, à l'extrêmité nord-ouest de la Téthys. Cette partie du gisement des Malines s'est formée lors des processus

d'extension crustale diffuse, qui n'ont pas été suivi d'une expansion océanique marquée (rift avorté : Boillot et al., 1979).

-(2) des boues métallifères déposées depuis l'Holocène jusqu'à nos jours au fond de la fosse à saumures stratifiées d'Atlantis II (Mer Rouge). L'article ci-joint, écrit en collaboration avec E. Oudin et Y.Thisse, reprend essentiellement les données d'inclusions fluides obtenues par Y.Thisse (1982) et contient des observations nouvelles sur la croissance des cristaux. Le contexte tectonique dans lequel se développent les minéralisations de la fosse d'Atlantis II fait encore l'objet de débats : sont-elles synchrones des premiers stades d'expansion océanique faisant suite à plusieurs millions d'années d'extension diffuse (Cochran, 1983) ou se sont-elles développées dans un contexte océanique franc (Le Pichon et Gaulier, 1987) ? Les deux articles qui suivent traitent de problèmes essentiels à la compréhension des processus hydrothermaux dans la fosse d'Atlantis II : (i) à quelle température se sont formés les minéraux épigénétiques au voisinage des évents?; (ii) par quel mecanisme (et à quelle température) s'est déposée l'anhydrite hydrothermale?. Il faut noter qu'au moment où se termine le présent travail, M.F. Le Quentrec (IFREMER, Brest) achève la mise en forme de nouvelles mesures de magnétisme effectuées à petite échelle sur la fosse d'Atlantis II, tandis que Marc Urvoy (BRGM, Orléans) termine une thèse consacrée à l'établissement de cartes bathymétriques et de cartes de faciès des boues métallifères de la fosse.

La méthode utilisée dans les deux premiers articles (chapitres II et III) est l'étude maintenant classique d'inclusions fluides par les techniques de la microthermométrie. L'originalité du travail présenté tient principalement à l'interprétation quantitative qui est faite des mesures d'inclusions fluides. Au premier stade, l'interprétation est conduite par référence aux données

expérimentales en utilisant des plans de projection appropriés. On trouvera notamment une illustration supplémentaire de la pertinence des projections V-X pour le traitement des données microthermométriques, ici appliquées à l'identification quantitative du processus de piégeage hétérogène (Ramboz et al.,1982 : publication 6; Ramboz, 1983 : publication 7). Dans un deuxième stade de l'interprétation, les contraintes essentiellement thermobarométriques obtenues par les inclusions fluides sont confrontées aux multiples faits établis par la géophysique, la géologie et la géochronologie Il convient de remarquer que, pour les deux contextes géologiques étudiés, cette étape interprétative a été facilitée par les nombreux travaux de synthèse disponibles. Les mémoires du BRGM n^{os}125 et 126 font le point des connaissances acquises sur le bassin Sud-Est en France (Debrand-Passard, 1984). En ce qui concerne la Mer Rouge, on citera par exemple le livre classique de Degens et Ross (1969), et les articles de Cochran (1983) et Guennoc et Pouit (1988) qui font le point des données géophysiques et structurales acquises sur la Mer Rouge.

Les études d'inclusions fluides présentées ci-après sont relatives à deux sulfates (barytine et l'anhydrite) typiques des gisements de Pb-Zn en environnements carbonatés (en partie de type Mississipi Valley) et associés aux dépôts de sulfures sous-marins. Les spécialistes d'inclusions fluides manifestent beaucoup de suspicion à l'égard de ces minéraux en raison de leur fragilité (Bodnar et Bethke, 1984; Roedder, 1984) . Les chapitres II à IV constituent de fait un plaidoyer montrant que les sulfates qui peuvent être, dans certains cas, des minéraux hôtes fiables pour les fluides. Loin de conduire à des conclusions erronées du point de vue de la géologie, les études microthermométriques réalisées sur les sulfates conduisent à quantifier des paramètres peu accessibles, même dans des systèmes géothermiques actuels :

-mise en évidence de pressions fluides fossiles anormales sur la marge cévenole et estimation de l'âge de mise en place des barytines étudiées.

-mise en place de jets de saumures de salinité variable au fond de la fosse d'Atlantis II. On remarquera que grâce aux inclusions fluides, la température maximale de la saumure hydrothermale alimentant la fosse d'Atlantis II est à présent mieux connue que la température des évents hydrothermaux émergeant le long de la dorsale Est Pacifique (cf la synthèse proposée par Roedder, 1984): pourtant, les saumures chaudes se déversant au fond de la fosse d'Atlantis n'ont jamais été prélevées directement alors que le fluide hydrothermal a été échantillonné au fond du Pacifique!

Dans le cas de la fosse d'Atlantis II, il a été possible de pousser plus loin la démonstration de la pertinence des interprétations thermobarométriques tirées des inclusions fluides. Le chapitre IV présente un calcul de bilan thermique réalisé à partir des données hydrographiques disponibles sur la fosse. Les calculs montrent que les données thermométriques tirées des inclusions fluides dans l'anhydrite s'intègrent de façon cohérente avec les autres mesures caractérisant ces systèmes actuels. Une propriété remarquable des solutions salées au-dessus de 300°C apparaît être leur capacité calorifique accrue. Les données thermiques disponibles pour la fosse d'Atlantis II permettent de vérifier le bien-fondé de certaines prédictions des modèles thermodynamiques (Quint et al., 1987).

Le lecteur courageux pourra lire dans le chapitre V la réfléxion synthétique condensée que suggère la comparaison de l'ensemble des données rassemblées sur les deux gisements étudiés : Les Malines et la fosse d'Atlantis II. Une première étape de la démonstration consiste à mettre en évidence les contextes géotectonique et structural similaires dans lequel se développe l'hydrothermalisme en Mer Rouge et sur la Bordure Cévenole, dont le

gisement des Malines est partie intégrante. Puis un modèle est proposé qui met en évidence les mécanismes structuraux et sédimentaires qui sont à l'origine des circulations conduisant à la mise en place de minéralisations Pb-Zn-F-Ba-U au cours de l'évolution spatio-temporelle d'une croûte continentale au cours du rifting. Ce travail s'achève donc par l'élaboration d'un modèle pour les circulations hydrothermales dans le contexte des marges passives.

Bibliographie :

Bodnar R.J., et Bethke P.M., 1984, Systematics of stretching of fluid inclusions. I : Fluorite and sphalerite at 1 atmosphere confining pressure, Econ. Geol., 79, 141-161.

Boillot G., Montadert L., Lemoine M., et Biju-Duval B., 1979. La marge occidentale de la Téthys Ligure, 157-248, in 'Les marges continentales actuelles et fossiles autour de la France', Masson.

Charef A., 1986, La nature et le rôle des phases fluides associées à la minéralisation Pb-Zn dans les formations carbonatées et leurs conséquences métallogéniques : études des inclusions fluides et des isotopes (H, C, O, S, Pb) des gisements des Malines (France), Jbel Hallouf, Sidi Bou Aouane et Fedj-et-Adoum (Tunisie), Thèse I.N.P.L., Fr., non publié, 291 p..

Charef A., 1983, Les minéralisations cambriennes et karstiques Zn-Pb du district des Malines (Gard, France) : géochimie isotopique, pétrographie et phases fluides : unpub., Thèse spéc. I.N.P.L., Nancy, Fr., non publié, 285 p..

Charef A., et Sheppard S.M.F., 1983, Sources of aqueous fluids and sulphur in the Malines carbonate-hosted Pb-Zn deposit, France : Terra Cognita, 3, 171.

Charef A., et Sheppard S.M.F., 1985, Le gisement des Malines (Gard) Zn-Pb : contribution isotopique (D/H) au rattachement de la minéralisation karstique KII à la minéralisation hydrothermale F. : C.R. Acad. Sci., Paris, 301, 39-42.

Charef A., et Sheppard S.M.F., 1988, Les Malines Cambrian shale-hosted Pb-Zn deposit, France : Thermometric and isotopic (H_2O) evidence for pulsating hydrothermal mineralization : accepté pour publication dans Mineralium Deposita.

Cochran J.R., 1983, A model for development of Red Sea. Am. Assoc. Petroleum Geologists Bull., 67, 41-69.

Debrand-Passard (Ed), 1984, Synthèse géologique du Sud-Est de la France. Mém. B.R.G.M. 125 et 126, 615p. et 28p. et 65 cartes, respectivement.

Degens E.T., et Ross R.A., 1969, Hot brine and recent heavy metal deposits from the Red Sea, Springer-Verlag, New-York, 600 p.

Le Pichon X., et Gaulier J.M., 1987, Oceanic nature of Northern Red Sea crust : implications of seismic measurements made during Minos cruise, Terra Cognita, 7, 201.

Guennoc P., and Pouit G., 1988, The Red Sea : history and associated mineralization, accepté pour publication dans A.A.P.G. Bull.

Quint J.R., Coxam J.Y., et Grolier J.P.E., 1987, Détermination expérimentale et corrélation des capacités calorifiques des solutions aqueuses salines pour une modélisation des fluides géothermiques. Colloque "Minéraux argileux et géothermie", E. N. S. Paris, 17-19 nov. 1987.

Ramboz C., 1983. Application of V-X projections to the quantitative interpretation of heterogeneous trapping from fluid inclusion study. Terra Cognita, 3 , 164.

Ramboz C., Pichavant M., et Weisbrod A., 1982. Fluid immiscibility in natural processes : use and misuse of fluid inclusion data. Part II : interpretation of fluid inclusion data in terms of immiscibility. Chem. Geol., 37, 29-48.

Roedder E., 1984, Extrusive rocks and volcanic environments, in 'Fluid Inclusions', Mineralogical Society of America, v. 12, 473-501.

Thisse Y., 1982, Sédiments métallifères de la fosse d'Atlantis II (Mer rouge)- Contribution à l'étude de leur contexte morpho-structural et de leurs caractéristiques minéralogiques et géochimiques. Thèse Univ. Orléans et B.R.G.M., Fr., non publié, 155 p.

Verraes G., 1983, Etude monographique du district minier des Malines et de ses environs (province sous-cévenole, France) : Thèse d'Etat, Univ. Montpellier, non publié, vols. 1 and 2, 591 p.

CHAPITRE II

TEMPERATURE, PRESSURE, BURIAL HISTORY AND PALEOHYDROLOGY OF THE LES MALINES PB-ZN DEPOSIT : RECONSTRUCTION FROM AQUEOUS INCLUSIONS IN BARITE+

Claire RAMBOZ° and Abdelkrim CHAREF°⁺

°Centre de Recherches Pétrographiques et Géochimiques, B.P. 20, 54 501- Vandoeuvre-lès- Nancy (FRANCE).

⁺Present address : Office National des Mines, 26 rue d'Angleterre, Tunis (TUNISIE)

Running title : Late barite at Les Malines

+ Economic Geology, v. 83, 1988, in press.
Contribution C.R.P.G. n° 755.

INTRODUCTION

It is now widely accepted that many Mississippi Valley Type deposits are formed in the margins of sedimentary basins from the superimposition in space and time of static and dynamic processes related to the normal evolution of the basin (e.g., Anderson and Macqueen, 1982). Fluid inclusion data have demonstrated the existence of a hydrothermal stage ($65° < T < 175°C$) superimposed upon early diagenetic and supergene processes at the sites of ore deposition (Roedder, 1976). In addition, they have shown that the hydrothermal fluids were Na-Ca-Cl brines with > 5-15 % dissolved salt and similar in composition and in deuterium-content to subsurface formation waters (Hall and Friedman, 1963 ; Clayton et al., 1966; Hanor, 1979). It has therefore been proposed that the hydrothermal stage in MVT deposits resulted from the centrifugal migration of fluids in sedimentary basins (e.g., Noble, 1963), either by gravity- driven flow (Garven and Freeze, 1984; Bethke, 1986) or by pulsatory dewatering of sediments (Cathles and Smith, 1983).

Among the problems still to be solved in the generation of MVT deposits are the timing of ore deposition, the relation between the ore stage and hydrocarbons, and the mechanism of porosity generation (Anderson and MacQueen, 1982). In addition, the processes of formation of carbonates, barite, or fluorite during the late stage of MVT deposits are also still under debate. Late stage minerals frequently contain monophase inclusions with dilute fluids (< 5 wt. % chloride), and their potassium content is systematically higher than that of subsurface waters or of MVT hydrothermal ore stage fluids (Hanor, 1979). Late stage barite may also contain fluid inclusions with high and variable homogenization temperatures (Rife, 1971). The late stage of MVT deposits is therefore markedly distinct from the

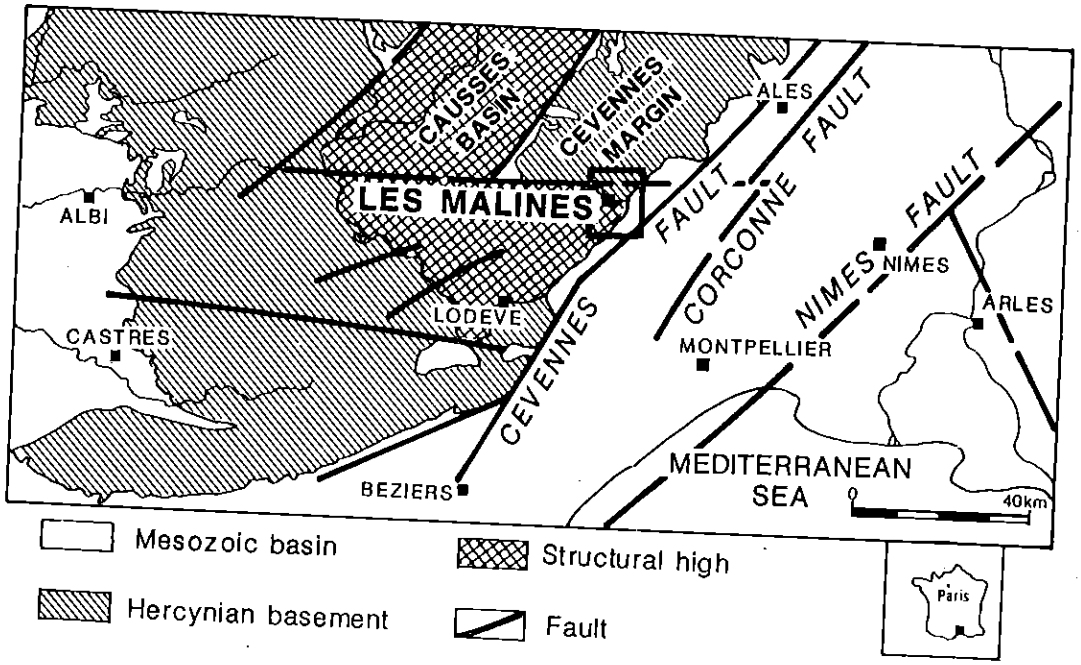

Fig. 1 - Location map of the Les Malines deposit in the structural map of the Subalpine Basin (after Baudrimont and Dubois, 1977).

earlier ones.

The Les Malines Pb-Zn deposit, on the western margin of the Mesozoic Subalpine Basin (France) is one of the largest Pb-Zn deposits in Europe (Fig.1). It is a Mississippi Valley type deposit, with an early karstic ore stage followed by hydrothermal stages including a late barite-forming stage (Charef, 1983 ; Charef and Sheppard, in press). The major part of the mineralization at Les Malines is hosted in the Cambrian basement below the Mesozoic sediments. Late barites at Les Malines are particularly rich in oil (Verraes, 1983). Late barite crystals contain a complex association of CO_2-bearing aqueous inclusions, oil, and hydrocarbon inclusions. This paper presents microthermometric and Raman spectrometric data on the aqueous inclusions in the late Les Malines barite. Barometric implications derived from the presence of CO_2 in inclusions postdating the Main Stage are discussed. The data on the hydrocarbon and oil inclusions will be presented elsewhere (C. Ramboz and C. Kosztolanyi, in preparation). This paper therefore complements the paper by Charef and Sheppard (in press), which deals with the thermometric and isotopic characters of the essentially aqueous inclusions contemporary with Main Stage mineralization.

GEOLOGY

The Les Malines district is situated in the south-eastern part of the French Massif Central (the Cévenole Border) where the sediments deposited in the Mesozoic Subalpine Basin lie unconformably on Paleozoic formations (Fig.1). In the Les Malines district, this basement is composed of Cambrian dolomitic limestones and shales (Demay, 1952; Michaud, 1970). They were metamorphosed to greenschist facies during the Hercynian orogeny and were subsequently karstified

during a pre-Lower Triassic emersion period (Bernard, 1958; Orgeval, 1976).

From the end of the Lias to the end of the Middle Jurassic, the Cévenole Border was the north-western continental margin of the Tethys Ocean (Laubscher and Bernoulli, 1977), which separated the highly mobile Subalpine Basin to the East from the Causses Basin, its projection to the West (Baudrimont and Dubois, 1977; Fig.1). This margin was very similar to the present day passive margins of the Atlantic Ocean, Galicia and the Bay of Biscay (Graciansky et al., 1979). The period ranging from the Rhaetian to the beginning of the Callovian corresponded to a major E-W extensional episode (Elmi, 1984; Bonijoly and Delpont, 1982). Active rifting was controlled by the structure of the basement and, in particular, by the N 50° E Hercynian faults, and to a lesser extent by the E-W faults of Stephanian age (Macquar, 1973; Baudrimont and Dubois, 1977; Triat and Truc, 1983; Mouterde, 1984; Fig.1). The Cévenole Border was composed of a mosaic of blocks, tilted and uplifted separately, whereas the Subalpine Basin to the East consisted of deeps and rises limited by antithetic faults (Artru, 1968; Mouterde, 1984; Elmi, 1984). Two sequences of shales and limestones were deposited during the major E-W Mesozoic extension : from the end of the Lias to the Lower Bajocian, then from the Middle-Upper Bajocian to the Oxfordian (Baudrimont and Dubois, 1977; Elmi, 1984). The later cycle included the Jurassic Terres Noires, 2000 m-thick on average (Artru, 1968).

From the Lower Callovian on, the rifting process became attenuated: the Terres Noires sedimentation became more active and homogeneous over the whole Basin. The Cévenole Border subsided and became flooded: the Subalpine Sea then reached its maximum E-W extension. The Upper Jurassic marked a change in the mechanism of the subsidence in the Subalpine Basin from active rifting to passive

conductive cooling (Boillot et al., 1979). Progressive regression started during the Upper Callovian, particularly at Les Malines (Elmi, 1984). During the Cretaceous, the Subalpine Basin progressively filled up, the Subalpine Sea receded from the Causses basin and from the Cévenole Border, and both regions underwent intense erosion (Demay, 1931, 1952 ; Lesage, 1972 ; Verraes, 1983).

In the Les Malines district, Pb-Zn mineralization occurs both below the Triassic unconformity (stratoid ores, karstic deposits = KI, and fissure-related mineralizations = KII and F), and above the Triassic unconformity (veinlets crosscutting the Triassic shales, and bedded ores within the Bathonian dolomites). KII and F mineralization consists of banded sphalerite, dolomite, barite and quartz cementing fractures crosscutting karstic fillings and Cambrian dolomites. Both stages were formed from hydrothermal (~140°C) formation waters (Charef and Sheppard, 1983, 1985 and in press). The latest vein stage at Les Malines consists of barite and recrystallized Cambrian dolomites in large vertical fractures crosscutting the Cambrian basement and Mesozoic, including Jurassic, sediments (Verraes, 1983). This generation of barite will be named "late barite" or "late stage barite" further in the text. Earlier fissural barites are found in a complex network of veins, vugs and breccias croscutting the Cambrian dolomites; they never affect Mesozoic sediments. Late barite and recrystallized dolomite may be found in the same fractures or in independent veins, suggesting they were formed by two distinct but contemporaneous processes. Minor sulfur ores are formed at that stage, with only few euhedral galena crystals in vug-fill barite. Many authors have emphasized the ubiquitous presence of hydrocarbons and bitumen below the Paleozoic and Bathonian unconformities, either in sphalerite, barite and dolomite from the ore stage or in barren zones. Connan and Orgeval (1977) studied the organic matter in the basement

at Les Malines and concluded that the carbonaceous substances were derived from Triassic oil through migration and biodegradation at low temperatures. The reader is referred to the papers by Macquar (1968), Foglierini and Bernard (1967), Foglierini et al. (1980), Verraes (1983) for detailed descriptions of the ore stages at Les Malines.

SAMPLES

Late barite was sampled from the central part of the district in the Ratonneau Mine (1 km south of Les Malines) and 70 m deep within the Cambrian basement. The mineralization and related bitumen in Ratonneau have been described by Orgeval (1976), Connan and Orgeval (1977), Foglierini et al. (1980), Verraes (1983) and Charef (1983). The barite occurs as decimetre-long milky white to beige or translucent crystals flattened in the plane (001). Sometimes the cleavages are curved, and micrometre-long inclusions of calcite and quartz are observed within the barite blades (identification confirmed by micro-Raman spectrometry). Some other solid microinclusions are also observed. They have lower relief than barite and present a common crystallographic orientation. No Raman signal other than that of the host barite was obtained from these solid inclusions in the range 500-1500 cm^{-1}. They therefore remain unidentified. A complex association of sulfides and sulfosalts is observed between the barite blades: chalcopyrite, covellite replacing chalcopyrite, bournonite, galena, tennantite-tetrahedrite and pyrite, with minor Pb-Zn oxides. Yellow colloform sphalerite covers the apex of the barite crystals.

ANALYTICAL TECHNIQUES

Microthermometric studies of fluid inclusions were performed

Table 1. List of symbols.

C	clathrate
d	bulk density of the inclusion ($g cm^{-3}$)
df	density of the fluid phase ($g cm^{-3}$)
dl(dv)	density of the aqueous part (of the non-aqueous part) of the inclusion ($g cm^{-3}$)
Flw	degree of filling of the inclusion (= volumetric fraction of the aqueous liquid in the inclusion) at room temperature
z	depth below the water-table
L	aqueous liquid
ni	number of moles of species i in 1 cm^3 of the fluid in the inclusion
P	total pressure (bar)
Pf	fluid pressure
Ph	hydrostatic pressure
Pi	partial pressure of the species i (bar)
Pl	lithostatic pressure = total vertical pressure produced at any specific depth by the weight of the superincumbent strata
T	temperature (°C)
TH	temperature of total homogenization of the inclusion (°C) (TH L-V(L) : to the liquid ; TH L-V(V) : to the vapor)
TmC	melting temperature of clathrate (°C)
TmI	melting temperature of ice (°C)
V	vapor
$\bar{V}$	molar volume ($cm^3 mole^{-1}$)
Xi	mole fraction of the species i in the inclusion
ZNaCl	mole fraction of NaCl in the aqueous part
$Z'CO_2$	mole fraction of CO_2 dissolved into the aqueous part at TmC
$\delta^{34}S$	isotopic composition of sulfur of the sample in per mil relative to the Canon Diablo Troilite
λ	ratio of the fluid pressure to the lithostatic pressure (=geostatic ratio).

on 200 µm-thick plates using a microscope equipped with a UMK 50 Leitz objective and a Chaix-Meca cooling and heating stage properly calibrated for temperature (Poty et al., 1976). The low-temperature measurements below 0°C were achieved with a precision of 0.3°C on regularly warming the inclusions at a rate of 5°C per minute. The high-T measurements were performed by heating the inclusions at a rate of 1°C per minute, with a relative precision of 5 %.

Raman spectrometric measurements were made at room temperature using a M.O.L.E. type microprobe (Jobin Yvon; Dhamelincourt et al., 1979). The exciting radiation was the 514.5 nm green line from a 5W Spectra Physics ionized argon laser. The photomultiplier was a RCA 31034 type cooled to -20°C. The presence of CO_2, CH_4, N_2, H_2S in the gas part of the aqueous inclusions was checked using a 1W laser beam, referring to the following lines respectively : 1388 cm^{-1}, 2915 cm^{-1}, 2331 cm^{-1}, 2611 cm^{-1}.

For **sulfur isotopic measurements**, barite, separated under a binocular microscope, was reacted in the presence of excess silica in a vacuum line to give SO_2. The $\delta^{34}S$ value in per mil relative to the Cañon Diablo troilite was measured with a VG 602 type mass spectrometer with a precision of 0.2 ‰.

RESULTS

The symbols used in the text and figures are listed in Table 1.

Description.

Fluid inclusions in barite were observed at a magnification of up to x2000. The crystals were found to contain a complex

juxtaposition of oil, hydrocarbon (colorless) and aqueous inclusions. Red waxy globules which were either scattered within the crystals or coated the wall of some inclusions were tentatively identified as asphaltenes. Oil inclusions were easily recognizable because they contained a yellow or a brown liquid, sometimes with a vapor bubble. The aqueous inclusions were difficult to discriminate from the hydrocarbon inclusions using only microscopic observations. This is because both of them were either monophased (filled with a colorless liquid or gas) or two-phased (filled with a colorless liquid and gas). Only at high magnification could some hydrocarbon inclusions be identified : an outer liquid meniscus (= water) clearly surrounded the inner hydrocarbon liquid and gas.

Classification.

Criteria were established to discriminate between aqueous and hydrocarbon inclusions on the basis of the behavior of the inclusion on heating and cooling. Aqueous inclusions verified the following : (1) Low-temperature behavior of the colorless liquid strictly consistent with the H_2O-NaCl system (freezing of the colorless liquid above -100°C, first melting above -55°C ; no increase of the volume of the gas part on cooling). (2) Strict reproducibility of the liquid-vapor (L-V) homogenization on heating.

Aqueous inclusions often had a regular oval shape. Their size ranged from 5 to 25 µm. About 5 % of them, either liquid- or vapor-dominant, contained a round birefringent solid filling up to 10 % of the cavity volume. This solid did not dissolve on heating to 400°C; it therefore was not a chloride. No Raman signal other than that of the host barite was derived from it in the range 400-1240 cm^{-1}. However, it was observed that the Raman spectrum derived from the solid in the inclusion presented the same Raman lines as the ones derived from the

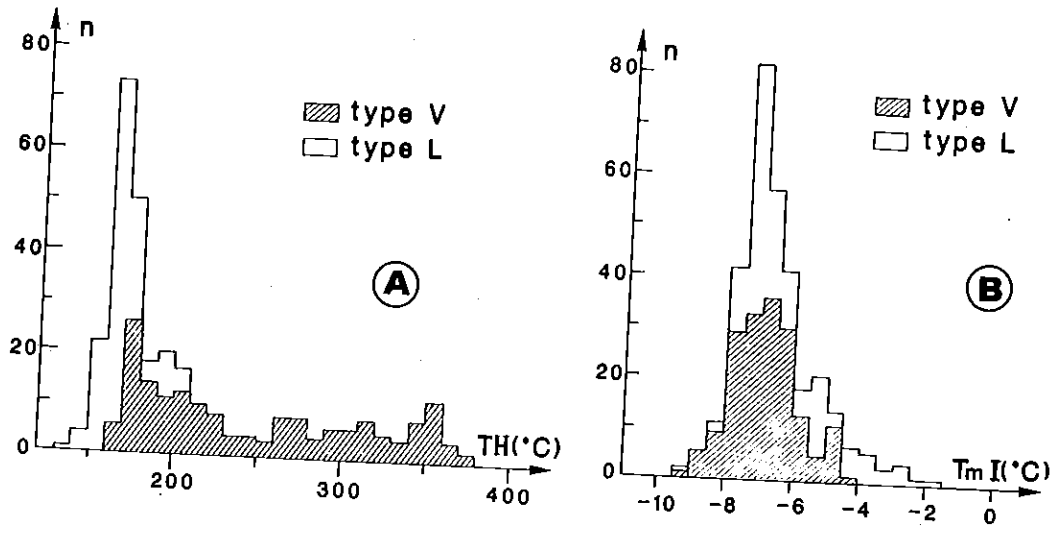

Fig. 2 - Histograms of the homogenization temperatures (A) and of the melting points of ice (B) in all type V and type L inclusions studied in barite. n = number of measurements.

immediate host barite, but with different intensities. This suggests that the round solid in the aqueous inclusions is a barite, distinct from the host crystal by a different crystallographic orientation. Aqueous inclusions presented highly variable gas volumes with the volumetric fraction of the liquid of the inclusion (= degree of filling = Flw) ranging from 0.1 to 0.9. For clarity, all aqueous inclusions with Flw < 0.5 and homogenizing to the vapor were classified as type V (= vapor-rich). All inclusions with a degree of filling greater than 0.5 and homogenizing to liquid were classified as type L (= liquid rich). The melting points of clathrate (= TmC) were not systematically measured because they were difficult to observe. However, Raman microprobe analysis of the non-aqueous part of two type L inclusions and of two type V inclusions demonstrated that they contained CO_2 in significant quantities and no detectable CH_4, N_2 or H_2S (< 0.2 mole%). For the purpose of a quantitative interpretation of the measurements on the type L inclusions, TmC was found to be 4.7 °C in one selected type L inclusion.

Figure 2 summarizes the microthermometric data collected in type V and in type L inclusions. Both melting points of ice and homogenization temperatures (TmI and TH) have a wide range of values in type V and type L inclusions : -9.2° < TmI < -4.1°C and 180° < TH L-V(V) < 380°C for type V inclusions ; -9.2° < TmI < - 1.7°C and 130° < TH L-V(L) < 190°C for type L inclusions.

INTERPRETATION

Is barite a reliable host mineral for fluid inclusion studies ?

Larson et al. (1973) have presented analytical evidence that fluid inclusions in soft cleavable minerals can stretch on heating and thus yield erroneous density determinations. Fluid

inclusions in barite are thought to be particularly susceptible to necking down (Roedder, 1972), to yield frequently scattered homogenization temperatures (Rife, 1971) and non-systematic behavior on heating (Bodnar and Bethke, 1983). Many consider barite to be "...a very unreliable host mineral for fluid inclusion studies...", in which, at least for some inclusions, "...it is not possible to obtain valid homogenization temperatures..." (Bodnar and Bethke, 1984).

Both anhydrite and barite are cleavable non-plastic minerals and their hardness is comparable (Tugarimov and Naumov, 1970). They should therefore exhibit a similar capacity to stretch or to decrepitate under comparable P and T. Roedder (1984a) has stated that inclusions in anhydrite might provide good thermometric data. Recent studies on modern submarine anhydrites associated with sulfides at 21°N E.P.R., and on anhydrites and barites from SW basin of Atlantis II Deep, Red Sea, have given interpretable results. At 21° N E.P.R., the temperature deduced from fluid inclusions in anhydrite is consistent with the temperature measured directly at the thermal vents (Le Bel and Oudin, 1981). In the Red Sea case, the P-T conditions of submarine fluid discharge deduced from fluid inclusion studies in anhydrite and/or barite (Thisse et al., 1983; Oudin et al., 1984) agree with the presence of cubic cubanite, chalcopyrite and pyrite at equilibrium with the hydrothermal fluid (Pottorf and Barnes, 1983). The thermometric conclusions based on fluid inclusions in sulfates are additionally consistent with the heat-mass balance of Atlantis II Deep over the past 15 years (Ramboz and Danis, 1987). Finally, the boiling of a 22 ± 1 wt % eq. NaCl solution at the bottom of Atlantis II Deep has been documented from fluid inclusions in anhydrite (Thisse et al., 1983), consistent with the two-phase field boundaries of the H_2O-NaCl system (e.g. Parisot and Plattner, 1981) and with the burial depth of the crystals at the sea-floor. On account of these results, the above

authors have concluded that fluid inclusions in anhydrite and in barite can be good thermobarometers, at least in certain situations.

Concerning the late barite at Les Malines, the large range from 180°C to 380°C of TH of type V inclusions cannot result from leakage. CO_2 gas without N_2 was detected with the Raman probe in two type V inclusions after heating. The gas part of these inclusions is markedly distinct from air because atmospheric N_2 is readily detectable with the Raman probe and atmospheric CO_2 is below the detection level of the probe. It is also possible that CO_2 may have been generated in situ after the formation of the inclusions from the breakdown of organic products. This hypothesis can readily be discarded for the following reasons. (1) CO_2-bearing inclusions placed under the laser beam have yielded a ground noise which was 10 to more than 100 times lower than the one observed when focusing on gaseous and liquid hydrocarbon inclusions. This low level of fluorescence of the aqueous CO_2-bearing inclusions under the laser beam is consistent with their organic content being negligible. (2) The kerogen and the oil in the Cambrian basement at Les Malines, rich in hydrogen and in carbon and with a low oxygen content, are derived from biodegradation of migrated oil (Connan and Orgeval, 1977). Breakdown products of such matter should be mainly composed of CH_4 and higher hydrocarbons with minor CO_2. This is in strong contrast with the gas-content of aqueous inclusions in late barite, CO_2 dominant and without detectable CH_4 or higher hydrocarbons. (3) Secondary inclusions presenting a meniscus of liquid CO_2 at low temperature, with no or only minor CH_4 and/or H_2S detectable with the Raman probe, were also observed in barite crystals characteristic of the end of the Fissural Stage (Charef and Sheppard, in press). These crystals are devoid of organic products. They therefore provide additional evidence that a CO_2-bearing aqueous fluid circulated after the Main Stage in the Les Malines horst.

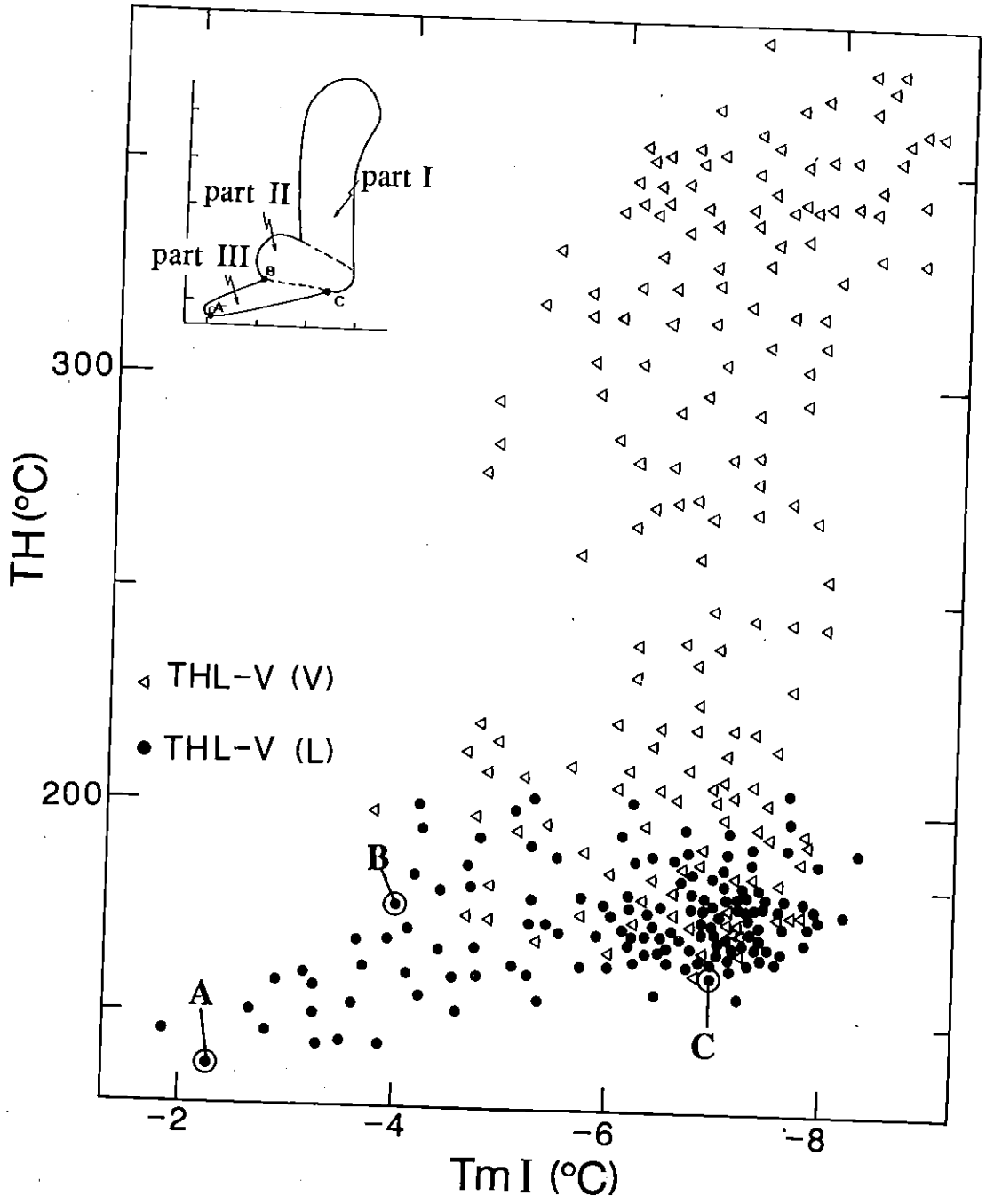

Fig. 3 - Correlative variations of the melting points of ice and of the bulk homogenization temperatures of type V and type L inclusions in barite. On the inset, the microthermometric trend is divided into three main parts (see text). Points A, B and C are three particular inclusions discussed in the text. n = number of measurements.

We cannot exclude that the high TH values of some type V inclusions are in excess by some tens of degrees because of overheating. However, homogenizations to the vapor above 300°C for H_2O-CO_2-NaCl inclusions with Flw < 0.20 are realistic (Gehrig, 1980 ; Pichavant et al., 1982). The point whether these high TH values indicate minimum trapping temperatures for the fluid in the inclusion or result from heterogeneous trapping of liquid and vapor must now be established.

Reconstruction of the fluid and mineralogical evolution

Chronology. The type V and the type L inclusions plot on a complex but continous surface of the TH-TmI plane (Fig. 3). For clarity, the TmI-TH trend has been divided into three parts (inset, Fig. 3) : part I with type V inclusions only, part II where type V and type L inclusions overlap, part III with type L inclusions only. The existence of a continuum between type V and type L inclusions is demonstrated by the continuity of their microthermometric properties and is confirmed by the presence of CO_2, detected with the Raman probe, in both type L and type V inclusions. Their trapping must have occurred during the course of a single continuous hydrothermal evolution with no evidence for a repetitive process.

The identification of primary inclusions in barite is often difficult and open to criticism (e.g., Roedder, 1972). In the present case, no definite criteria for the primary or secondary character of either type V or type L inclusions can be derived from the microscopic observations, partly because the relations between the aqueous inclusions are obscured by abundant hydrocarbon inclusions. The identification by Raman spectrometry of barite crystals in both type V and type L inclusions is the only argument that the aqueous inclusions as a whole are associated with the barite formation, i.e. are primary.

Two chronologies of inclusions must be envisaged : part I followed by part II and then part III inclusions or the reverse sequence.

Do type V part I inclusions result from heterogeneous trapping ? The homogenization temperatures of type V inclusions approach 380°C. They are out of thermal equilibrium with the shallow environment. We must consider the possibility that these inclusions contain mechanical mixtures of immiscible fluids at the temperature of trapping, Tt : this would account for homogenization temperatures systematically in excess of Tt. According to this interpretation, the large range of homogenization temperatures results from the trapping of variable proportions of the immiscible liquid and vapor (Ramboz et al., 1982). This hypothesis can be rejected for the present case based on two arguments. (1) No type L inclusion was found with high TH comparable to the TH values of type V inclusions. Hence, we must conclude that heterogeneous trapping of variable amounts of vapor with the pure unmixed liquid seldom occurred. This conclusion appears very unlikely because the probability of trapping minor vapor with the unmixed liquid is certainly not zero. (2) From an analysis of the H_2O-NaCl system using a $\bar{V}$-X projection, it can be established that heterogeneous trapping of minor liquid with the vapor has resulted in inclusions with values of homogenization temperatures to vapor (TH L-V(V)) all higher than the predicted unmixing temperature; these inclusions additionally show a negative correlation between TmI and TH L-V(V) (Ramboz, 1983). When unmixing occurs in the H_2O-CO_2-NaCl system, CO_2 is preferentially partitioned into the vapor and NaCl goes into the liquid. Therefore, in the case where inclusions are generated by trapping increasing amounts of liquid with the unmixed vapor in this system, they exhibit increasing mole fractions of NaCl and decreasing concentrations of CO_2. Although such changes in the bulk composition of the inclusions have opposite effects on TmI because

both dissolved CO_2 and NaCl depress TmI (Takenouchi and Kennedy, 1965), such inclusions are expected to exhibit decreasing TmI with increasing TH L-V(V). This is because NaCl is far more soluble in water than CO_2 below 30°C, whatever the pressure. Therefore increasing the NaCl-content of the fluid is the dominant effect on TmI. The TmI of type V part I inclusions remain roughly constant (-7° ± 1°C, Fig. 3) whatever their TH in the range 180°-380°C. Such a TmI-TH pattern is incompatible with heterogeneous trapping.

Hence we must conclude that the measured TH L-V(V) in part I inclusions are minimum trapping temperatures for the CO_2-bearing fluid. The most likely inclusion chronology compatible with this interpretation is as follows : trapping of part I, then part II, then part III inclusions.

Type V part I inclusions : cooling of a high-T fluid. It is likely that the variable TH of part I inclusions with roughly constant TmI corresponds to the cooling of a hot CO_2-bearing vapor. (1) Oil inclusions in barite present a wide variety of colors ranging from ligth yellow to deep brown : this is consistent with the oil having undergone thermal degradation as it was trapped in barite (Burruss, pers.com.). This probably implies transient fluid temperatures in excess of 200°C during barite formation. (2) The interpretation that type V inclusions are primary relative to the host barite and indicate cooling is consistent with the mineralogy of the veins. Experimental data show that the solubility of barite is prograde at least up to 300°C in solutions with NaCl concentrations above 1 molal (Blount, 1977). This suggests that barite can precipitate by simple cooling of a hot brine (Holland and Malinin, 1979). Because the solubility of calcite is retrograde at constant PCO_2 (Ellis, 1959), the cooling of a CO_2-bearing fluid can explain the formation of vugs and fissures by dissolution of the carbonated wall-rock. Although large amounts of

calcium were thus freed to the solution, anhydrite was not precipitated during the cooling because its solubility is also retrograde in low to moderately saline fluids (Blount and Dickson, 1969) and because the concentration of dissolved SO_4^{2-} was depressed by the presence of dissolved barium.

Part III type L inclusions : mixing with a cooler liquid. Part III inclusions are characterized by values of TH L-V(L) which decrease as the TmI approach zero (Fig. 3). This evolution corresponds to the cooling of the saline CO_2-bearing fluid by mixing with a more dilute aqueous liquid. The type L inclusion with the highest TmI and the lowest TH (point A on Fig. 3) represents most closely the coolest end-member in the mixing process : a 3 wt % eq. NaCl solution (Potter et al., 1978), with a density of 0.96 gcm^{-3} and a minimum temperature around 130°C (Potter, 1977). This last stage of mixing and dilution can also have favored barite precipitation (Hall and Friedman, 1963 ; Chukhrov et al., 1977).

Part II type L and type V inclusions : unmixing. Part II inclusions, both of type L and V (Fig. 3), probably indicate minor unmixing in the H_2O-CO_2-NaCl system due to the following reasons. (1) The dilution of a low-density CO_2-bearing vapor by liquid water favors unmixing. As both the H_2O-content and the density of the H_2O-CO_2-NaCl liquid increase, the two-phase field boundary of the fluid is progressively shifted towards higher pressure, thereby making fluid unmixing more probable. (2) As unmixing in a shallow environment is expected to be adiabatic, it is probably short-lived and with no important related loss of vapor. This is consistent with the fact that no marked increase in the NaCl-content of the liquid is recorded. (3) The few calcite crystals observed in barite may have precipitated due to unmixing of the H_2O-CO_2-NaCl fluid (Ellis and Mahon, 1977). (4) The lowest T-range in which both type V and type L part II inclusions

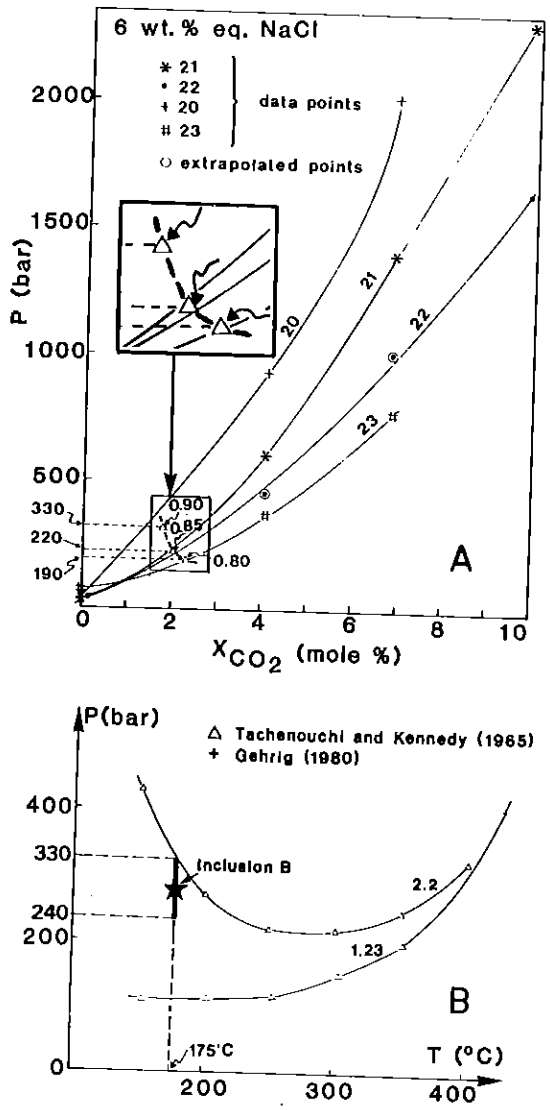

Fig. 4 - Estimation of the P-T conditions of trapping of inclusion B referring to the liquid-vapor equilibrium curves of the system (H_2O-6 wt% NaCl)-CO_2). 4A : Isochoric P-XCO_2 projections. Numbers above the curves are molar volumes in cm^3 $mole^{-1}$. 4B : Isocomposition P-T projections. On account of its V-X properties calculated for a degree of filling ranging from 0.8 to 0.9 (Table 2), inclusion B plots along the dotted line from the P-XCO_2 plane (Fig. 4A). For a degree of filling of 0.87, the V-X properties of inclusion B are consistent with the fact that the inclusion homogenizes to the liquid at T = 175°C (Fig.4B). Both the P-T and the P-XCO_2 projections show that the internal pressure in inclusion B at TH=175°C is in the range 240-330 bar.

homogenize is along line BC (inset, Fig. 3). Because no type L or type V inclusions homogenize below that line, the TH-range along the line BC (160°-175°C) probably represents the T-range of the unmixing event (Ramboz et al., 1982). The composition of the fluid was probably changing during unmixing because, in a solution with fixed $\bar{V}$-X properties, phase separation occurs under fixed P and T conditions.

Thermobarometry. The bulk volume and composition of inclusion B in late barite were estimated using microthermometric and Raman spectrometric data, as detailed in the Appendix. The principal uncertainties in the calculations arise from a poor estimate of the degree of filling of the inclusion at room temperature ($0.80 < Flw < 0.90$; Table 2) and from a poor knowledge of the salt-content of the fluid due to insufficient experimental data. On Figures 4A and 4B, the TH-$\bar{V}$-X properties of inclusion B are compared to the P-$\bar{V}$-T-X properties of the two-phase field boundary of the H_2O-NaCl-CO_2 system. Figure 4A illustrates that the $\bar{V}$-X properties of inclusion B calculated on the basis of microthermometric measurements below 25°C only (Table 2), fix the internal pressure in inclusion B in the range 190-330 bars. On the other hand, the range of compositions calculated for inclusion B (Table 2) fixes the internal pressure in the inclusion at TH = 175°C between 240 and 330 bars. Comparison between figures 4A and 4B therefore establishes that the pressure conditions of unmixing at 175°C were in the range 285±45 bars. It also shows that, if any TH-increase has occurred because of overheating inclusion B, the uncertainty introduced in the barometric interpretation is small compared with the one which results from poor precision on the degree of filling of the inclusion.

According to Charef (1983) and Charef and Sheppard (in press), CO_2-rich fluids trapped secondarily in barite from the end of the Fissural Stage have the following characteristics :- $57.2° < TmCO_2 <$-

Table 2. Analytical data and calculated bulk $\overline{V}$-X properties for CO_2-bearing inclusions : secondary inclusion in a fissural stage barite (Charef and Sheppard, in press) and primary inclusion B in a late stage barite (see Fig.3).

	(1)	(2)	(3)	(4)
Fissural Stage	$TmCO_2$ = - 56.6° TmC = + 6° $ThCO_2LV(V)$ = + 5° THLV(L) = 120° Flw = 0.80 ± 0.05	CO_2 no N_2 no H_2S no CH_4	ZNaCl = 0.7 $Z'CO_2$ = 1.0 dl = 1.03 dv = 0.113	XH_2O = 95.25 (94.91 - 95.6) XNaCl = 1.224 (1.219 -1.228) XCO_2 = 3.53 (3.87 - 3.19) $\overline{V}$ = 22.95 (24.4 - 21.7)
Late Stage	TmI = - 4.0° TmC = + 4.6° TH = 175° Flw = 0.85 ± 0.05	CO_2 no N_2 no H_2S no CH_4	Z NaCl = 1.93 $Z'CO_2$ = 1.5 dl = 1 dv = 0.08	XH_2O = 96.13 (95.9 - 96.3) XNaCl = 1.855 (1.85 -1.86) XCO_2 = 2.01 (2.21 - 1.80) $\overline{V}$ = 21.6 (22.9 - 20.4)

(1) Microthermometric data. (2) Raman spectrometric data. (3) Interpreted density-composition parameters of the aqueous and the non-aqueous parts. (4) Composition -density parameters calculated for the bulk inclusion (see Appendix; mole fractions x100).

56.6°C, -5.3°<TmI< -2.0 °C, $ThCO_2$ LV(V)↷5°C, 6.5°<TmC<8.1°C, 0.75<Flw<0. 9 and 90°<TH LV(L) <155°C. Table 2 shows that an inclusion representative of the CO_2-bearing secondary stage in fissural barite contains 3.3±0.3 mole% CO_2 dissolved in a .7 molal eq. NaCl solution and has a molar volume around 23±1.3 $cm^3 mole^{-1}$. Using calculated fugacities for pure CO_2 in the tables by I.U.P.A.C. (1976), solubility data by Ellis and Golding (1963) show that a pressure range of 365±45 bar is required to dissolve 3.3±0.3 mole% CO_2 in a 0.7 molal H_2O-NaCl solution. As there is no evidence of boiling at that stage, CO_2-bearing inclusions in fissural barite therefore imply minimum fluid pressures of 365±45 bars in the basement at Les Malines. This pressure range is higher than the one fixed by primary CO_2-rich inclusions in later barite.

Relations between fluid, hydrostatic and lithostatic pressure : evidence for geopressuring

In sedimentary basins (e.g. Price, 1975; Graf, 1982), the fluid pressure (Pf) is related to burial depth (z) and commonly varies between hydrostatic values (Ph) and lithostatic values (Pl). Normal pressure regime is hydrostatic i.e. it is characterized by Pf = Ph. Fluid pressures in excess of Ph characterize geopressured or overpressured zones. The excess fluid pressure at a given depth is conveniently expressed in terms of the geostatic ratioλ(λ = Pf/Pl). In the upper part of the crust, the pore fluid is commonly water or brine, of density close to 1 gcm^{-3} and the density of sediments is 2.2 gcm^{-3}. Therefore, hydrostatic pressures are equivalent to a geostatic ratio of around 0.45. High pressure zones are commonly characterized by 0.45 <λ< 0.9 (e.g. Watts, 1948) : geostatic ratios approaching 0.87 maximum characterize high pressure zones in Gulf Coast Louisiana (Dickinson, 1953). However, fluid pressures in excess of lithostatic

values ("superpressures") have also been encountered in sedimentary basins, as summarized by Hedberg (1974, p.665). In particular, Matthews et al. (1971) report that, in volcanic areas from the northwest coast of the U.S., from Southeast Asia and eastern Central America, a mud weight equal to or in excess of overburden pressure was required to completely cut off physical expansion occurring when penetrating CO_2-CH_4-bearing sediments. These authors also mention that a fluid pressure 1.5 times greater than the overburden pressure was required to initiate fracturing in dolomites and limestones in Kentucky.

CO_2-rich inclusions in fissural and in late barite imply that the fluid pressure 70m deep within the Cambrian limestones was 365±45 bars and 285±45 bars successively. During the Mesozoïc, the water depth over the Cévenole Border is estimated to have been always less than 100 m (Baudrimont and Dubois, 1977). Its contribution, therefore, to the pressure in the underlying sediments and basement was negligible. Referring to the crossection of the Triassic and Jurassic series in the Cévenole Border around Les Malines (Macquar, 1970 ; Palut and Bernier, 1970), the thickness of Mesozoic sediments currently present at Ratonneau is 450 m. However, this is a minimum estimate because the Kimmeridgian sediments have been partly eroded. It is difficult to reconstruct the burial depth of the Les Malines basement during Mesozoic, at the end of the Middle Jurassic and at the beginning of the Upper Jurassic in particular, as the horst was highly mobile and partly flooded by the Subalpine Sea. Geologists consider that the burial at the base of the Oxfordian never exceeded 600 m in the Cévenole Border (e.g. Boichard-Morin, 1983). A thickness of 1000 m can be tentatively proposed for the maximum overburden on the basement at Les Malines, based on present-day geology.

Hydrostatic pressure conditions. Assuming a hydrostatic pressure

regime, pressures of 365±45 and 285±45 bars are equivalent to 3950±500m and 3050±500 m of Mesozoic sediments respectively, given a fluid density of 0.91 gcm^{-3} (Table 2). Such thicknesses of sediments were never attained here during the Mesozoic. Hence, the basement at Les Malines has been geopressured.

Geopressured conditions. The extent of geopressuring at the time the barite formed is not known. The degree of compaction and hence the density of the Mesozoic sediments at that time is also unknown. Although it is not possible to derive the precise depth of burial of the two generations of barite from the fluid pressures of 365±45 bars and 285±45 bars, average values can be estimated. Taking 2.2 gcm^{-3} as the typical density of non-metamorphosed sediments and 2.7 gcm^{-3} as the average density of metamorphosed limestones (Daly et al., 1966), 1600±200m, then 1200±200m of sediment above the Cambrian limestones are required to achieve fluid pressures of 365±45 and 285±45 bar successively under lithostatic conditions. Geostatic ratios in undercompacted sediments are commonly $\leq$ 0.90 because sedimentary strain rates do not exceed $10^{-16}s^{-1}$. A geostatic ratio around 1 at Les Malines can however be expected if the metamorphosed basement was submitted to faster strain rates (Price, 1975; see below).

The following implications are derived from the interpretation of the TH-$\bar{V}$-X properties of CO_2-rich inclusions in barite in terms of near lithostatic pressure conditions. (1) The burial depth of the Les Malines horst during the Upper Jurassic was larger than commonly estimated on the basis of the present-day geology. (2) A burial depth around 1600m over the Cambrian limestones can have been reached only at the end of the major subsidence period of the Cévenole Border, i.e. at the end of the Lower Callovian (Elmi, 1984). Late stage barite at a burial depth of 1200m probably formed during the Upper Jurassic, as the horst had started rising up and as the Mesozoic sediments were

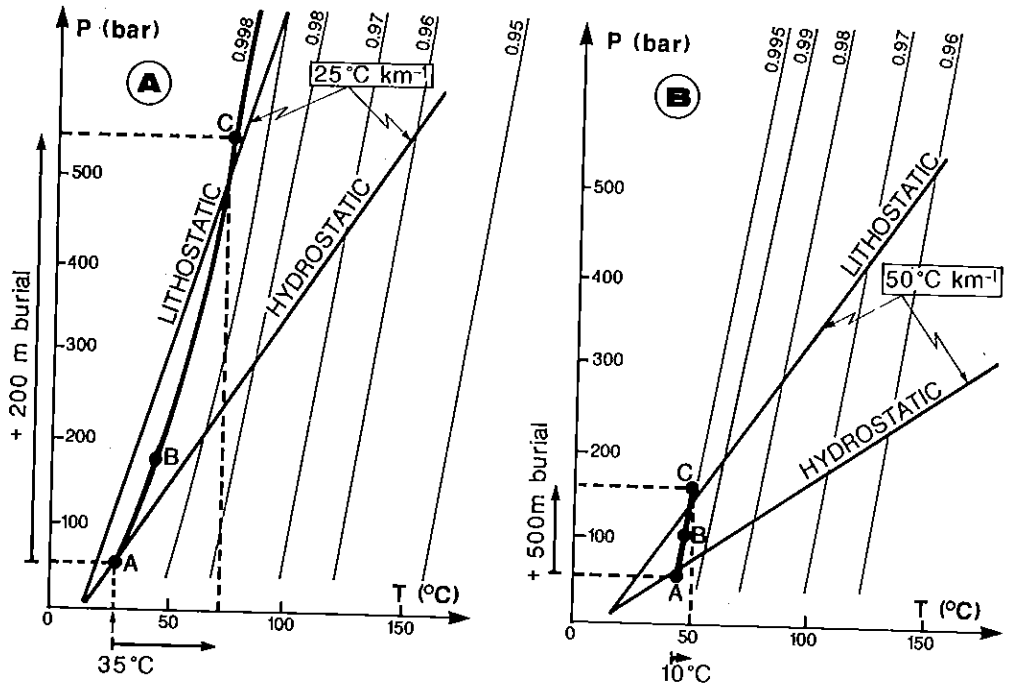

Fig. 5 - Mechanisms of generation of high pressure zones in an isolated compartment. 5A and 5B = Aquathermal pressuring (after Barker, 1972). Normal fluids follow hydrostatic P-T paths (=lowermost heavy lines) depending on the local geothermal gradient (5A : 25°C Km^{-1}; 5B : 50°C Km^{-1}). In a rigid isolated compartment that is buried, fluids follow isodensity lines of water(=light lines), therefore the fluid pressure may rise above hydrostatic pressure (point B) and possibly above lithostatic pressure (point C). Figures 5A and 5B show that the burial depth required to generate abnormal pressures is all the smaller as the geothermal gradient is larger. Lithostatic P-T paths = uppermost heavy lines.

already partly eroded.

Let us examine the mechanisms that can have accounted for a fluid pressure near lithostatic values in the basement at the Les Malines dome.

Mechanisms of generation of abnormal fluid pressures

The pressure seal. Abnormal pressure zones develop in compartments that are isolated from overlying strata by a pressure seal, commonly a fault or a layer of impermeable sediments (Watts, 1948). At Les Malines, there are Triassic shales which lie unconformably over the Cambrian basement (Macquar, 1970), particularly in Ratonneau (figure 9 in Fogglierini et al., 1980). It is realistic to propose that the Triassic shales have been undercompacted at the end of the Middle Jurassic subsidence because the overburden was more than 1000m-thick and the heat flow was anomalous (see below). The normal faults active during the Jurassic at Les Malines may also have contributed to the isolation of a small compartment in the dome.

At least 15 distinct causes of the generation of high pore fluid pressures in young basinal sediments have been proposed so far (e.g. Hedberg, 1974, p.666). Only two mechanisms appear applicable to the late barite stage at Les Malines and are discussed below.

Aquathermal pressuring. Barker (1972) assumed that geopressured reservoirs behave as closed isochoric systems. He concluded therefore that, in a H_2O-NaCl reservoir that is isolated and then moved down a normal geothermal gradient, the P-T regime follows the isodensity lines of the considered fluid system (line AC, Figs.5A and 5B). The rate of increase of the fluid pressure in such a reservoir is expected to be 400 bar km^{-1}, significantly higher than that of the overburden pressure (220 bar km^{-1}). Figure 5A illustrates that, to raise the fluid pressure above the lithostatic pressure in a compartment that

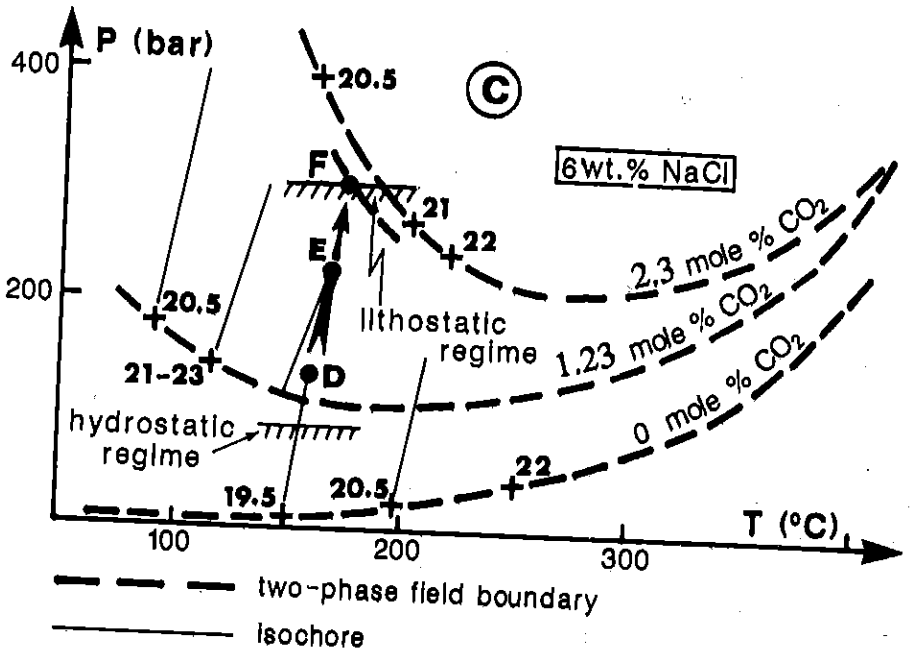

5C = Addition of CO_2 to the pore fluids.

Sources of data for solubility curves of CO_2 in a H_2O-6 wt.% NaCl liquid as in Fig.4. Numbers above the crosses are the molar volumes of the solution in cm^3 $mole^{-1}$. At Les Malines, as CO_2 was added to the fluid and as the temperature increased, the fluid pressure raised to near lithostatic pressure. The fluid remained homogeneous first , then, with CO_2 increasing, the solution became saturated with respect to CO_2 (point F).

has become isolated at 35°C and has moved down a normal geothermal gradient, a 2000 m-thick overburden is required. The required overburden thickness decreases if isolation begins at lower temperatures and if the geothermal gradient is greater (Fig.5B).

Chapman (1980) argued that undercompacted shales can neither be near perfect seals nor maintain constant pore volume in the geopressured zone since they have measurable permeability. At Les Malines, it is very unlikely that a pore fluid pressure in excess of 250 bars has been generated by aquathermal pressuring because the abnormal pressure was maintained as the pore volume was increasing by wall-rock dissolution.

The role of gases. In a medium with constant porosity, the generation of CH_4 and low molecular weight hydrocarbons from organic matter or from petroleum through bacterial or thermal maturation increases the volume of the pore fluid and induces overpressuring (Hedberg, 1974). At the late stage at Les Malines, the hot CO_2-bearing vapor degraded the oil to alcanes (C. Ramboz and C. Kosztolanyi, unpublished data). The related expansion of the fluid undoubtly contributed to compensate the increase in pore volume due to the dissolution of the wall-rock. Figure 5C illustrates that the addition of 2 mole% CO_2 at 175°C to the pore fluid of a compartment isolated below shales can also raise Pf above Pl. Note the increase in the volume of the solution resulting from the addition of CO_2. At Les Malines, the fluid pressure probably increased until the solution became saturated with respect to CO_2, the later parameter being strictly controlled by temperature. Figure 5C shows that the P-T conditions in the Les Malines horst below an overburden around 1200m are incompatible with a normal geothermal gradient. Such conditions were probably the result of the influx of hot fluids to the horst, to be examined below.

Volcanism and probable timing

The occurrence of fluids at $T > 300°C$ in a sedimentary environment probably implies the presence of a magma as the heat source. Arguments in favor of an alkali basalt as a source for both heat and CO_2 are as follows : (1) Verraes (1983) observed pieces of altered basalt associated with the late barite in fractures at Les Malines. (2) A sill of alkali basalt dated at 155 ± 6 m.y. (Baubron et al., 1978) has been found interstratified in the Jurassic limestones and dolomites from the Causses Basin at Les Vignes. (3) Alkali basalt magmatism is known to occur in passive continental margins (e.g. Carmichaël et al., 1974) and particularly during periods of uplift (Lemoine, 1982). The volcanism and the related high fluid pressures probably occurred repetitively at the end of the Middle Jurassic subsidence of the margin and later during the Upper Jurassic uplift. (4) CO_2 is a volatile component characteristic of alkali basalts (e.g. Roedder, 1984b). (5) Oil inclusions with colors ranging from light yellow to deep brown indicates that thermal degradation of oil was contemporaneous with late barite formation (Burruss, pers. com.). The liquid-dominant and the gas-dominant hydrocarbon inclusions in barite, associated with solid organic products (asphaltenes?), can result from the degradation of oil in the sediments by the high-T fluids (C. Ramboz and C. Kosztolanyi, unpublished data).

The relative chronology of hydrothermal events at Les Malines is as follows : first, the KII and F mineralizations resulting from episodic dewatering of sediments (Charef and Sheppard, 1983; 1985), then, at the beginning of the Upper Jurassic, the oil-bearing late barite synchronous with volcanism. Apparently, there is a continuum between the end of the fissural stage and the late barite-forming stage because the barite synchronous with the end of the Fissural Stage contains secondary three-phased CO_2-bearing inclusions (Charef,

1983) and the late vug-fill barite contains primary CO_2-bearing inclusions (this work). In addition, based on micro-Raman analyses, CO_2-rich inclusions in both generations of barite present a similar gas-content, with only trace amounts of CH_4 and H_2S (Charef, 1983; Charef and Sheppard, in press; Table 2). Several levels of shales were deposited in the Subalpine Basin : first, during the Lower Jurassic, then the Terres Noires during the Middle Jurassic (Fig. 6A). These levels may have dewatered prior to the Callovian. In the western part of the basin, unaffected by the alpine orogenesis, the Terres Noires still contain 25%-45% interstratified illite-montmorillonite (Barlier et al., 1974), the swelling fraction essential to the generation of high pore fluid pressures (Powers, 1967). The sedimentation rate during the deposition of the Terres Noires and of the superincumbent limestones was ranging from 200 to 300 m per million years in the deeper parts of the basin (Baudrimont and Dubois, 1977). It was high enough for high pressure zones to have existed in the Liassic shales and in the Terres Noires under 1000 to 1600 m of burial prior to the end of the Middle Jurassic (Burst, 1969; Magara, 1975). Montmorillonite dehydration may have occurred at the base of the Liassic shales during the Bajocian (175 m.y.) and at the base of the Terres Noires during the Bathonian (165 m.y.).

Evidence for a steady convective heat flow to the pressurized Les Malines horst

Part II type L inclusions along line BC (Fig.3) are interpreted to have been trapped at around 170°C. They probably represent the end product of the mixing of the hot CO_2 vapor with a physically stable cooler reservoir of fluids, i.e. the pore fluid. On account of the low CO_2-content of part II liquid inclusions and of their high density, we can estimate that the amount of hot CO_2-bearing

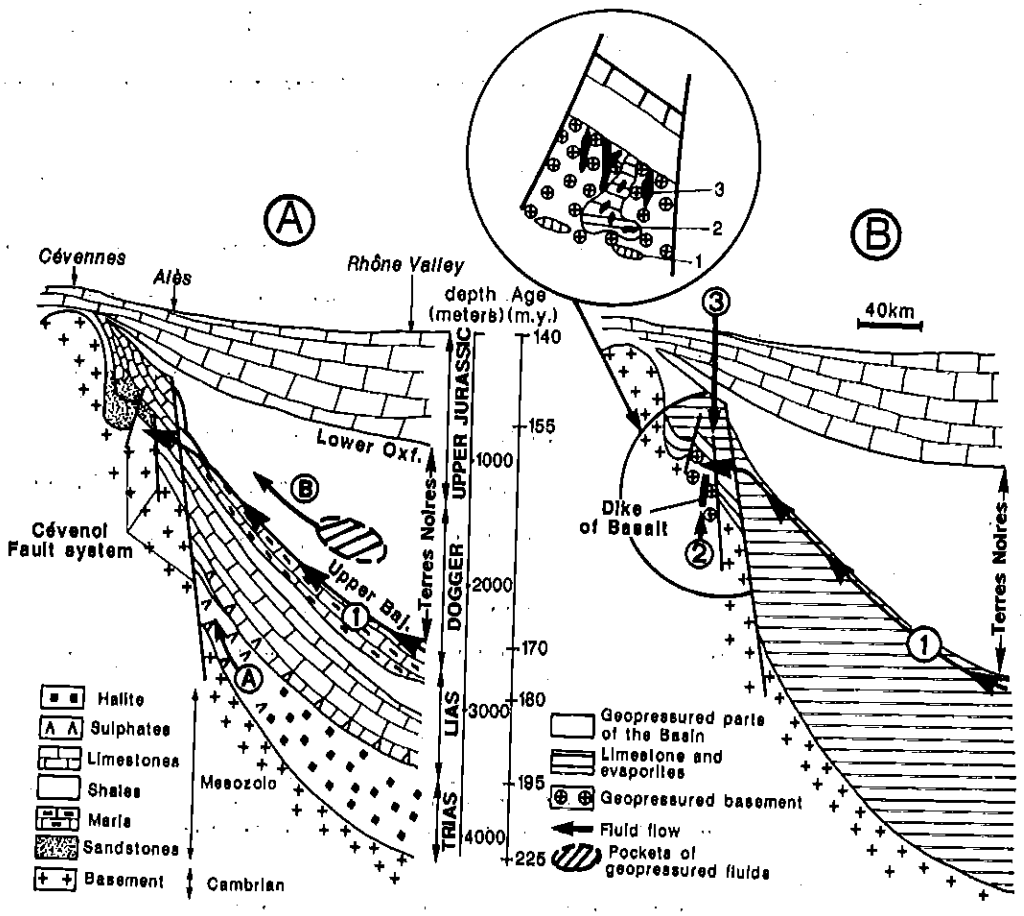

Fig. 6 - Possible fluid flows from the Subalpine Basin to the Les Malines horst. The schematic cross section of the Subalpine Basin is modified after Macquar (unpublished), in Routhier (1980). The different types of mineralisations are schematized on the inset (ores in karst: KI=2, KII=1; ores in fissures: F=3; after Charef and Sheppard, in press). Vertical dimensions are exaggerated. Figure 6A = Flows accounting for the KII and F mineralizations (Charef and Sheppard, 1983; 1985). A = flow of dehydration water of gypsum, probably involved in KI mineralizations (Charef, 1983). B = adiabatic fluid flow resulting from the decompression of geopressured pockets of dehydration water in shales (e.g. Cathles and Smith, 1983) and accounting for the Fissural Stage. Figure 6B = Fluid flows involved in the generation of late vug-fill barite, numbered 1 as in Table 3. 1 = steady dewatering of the "Terres Noires" shales from below. The exact position of the aquifer is unknown and it is tentatively located in normally pressured limestones below the shales. 2 = influx of hot CO_2-bearing fluids, tentatively related to volcanism in the horst. 3 = influx of cold diluted waters. The centrifugal flows (A, B, 1) were probably channelled towards the horst along the E-W fault of Les Malines, in the figure plane. Baj.= Bajocian; Oxf.= Oxfordian.

fluid added to the system did not exceed 10 % by volume. Assuming that the heat lost by conduction was negligible, the temperature of the pore fluid was not increased by more than 25°C by this mixing process. It is therefore concluded that the temperature of the pore fluid after the Fissural Stage at Les Malines was greater than 150°C and possibly approached 160°C, apart from the volcanic episode and any transient reheating due to catastrophic pulsatory dewatering of the basin (Fig.5C). Only a slow steady outward flow of formation waters can have accounted for stable pore fluid temperatures above 150°C at Les Malines.

The reconstructed hydrology of the Tertiary Niger Basin (Robert, 1985) is used as an aid to understand the possible hydrology of the Subalpine Basin during the Middle Jurassic. The Niger Basin contains a thick bowl-shaped layer of undercompacted shales, the Akata, quite similar in size, shape and burial thickness to the Jurassic Terres Noires in the Subalpine Basin. The margins of the Niger Basin are limited by vertical faults and are characterized by a high geothermal gradient and an advanced degree of diagenesis of organic matter. The situation at Les Malines was probably similar during the Middle Jurassic, based on fluid inclusion data (Charef and Sheppard, in press) and organic geochemical data. In the Cévenole Border at large, kerogens (i.e. the non-migrated organic matter) in Mesozoic sediments present an anomalous degree of evolution on account of their burial depth (Boichard-Morin, 1983). In the margins of the Niger Basin, it is interpreted that the heat flow and the organic diagenesis are enhanced and anomalous because of the combined effects of the thermal insulation of the impermeable Akata shales and of a centrifugal flow of hot formation waters in a permeable level below the Akata and moving up along the growth faults. By analogy, it can be proposed that, during the Upper Jurassic, normally pressured fluids

(basinal brines and oil) moved up down the pressure gradient from the deeper parts of the basin to the Les Malines Horst (Fig.6B), where they induced the recrystallization of the Cambrian dolomites. Such a steady dewatering process clearly implies that the high pressure episodes recorded by CO_2-rich inclusions in barite were necessarily transient: steady dewatering would have been precluded if the fluid pressure in the horst had markedly departed from hydrostatic values.

Calculations by Cathles and Smith (1983) show that, in bowl shaped basins with a typical slope < 1%, slow centrifugal flows of formation waters are not adiabatic, therefore they cannot account for near-surface temperatures in excess of 100°C. The Subalpine Basin abruptly deepens along the Cévenole fault system, therefore it presents a slope markedly smaller than 1%. The Les Malines deposit is located 15 km west of the N 50 E Cévenole fault system : the only possible avenue which can have driven the fluids from the deeper parts of the basin to the horst with minimum loss of heat is therefore the E-W fault of Les Malines (Fig.1). This fault is indeed locally mineralized in barite and sulfides (Macquar, pers. com.).

The oil associated with late barite probably migrated to the margin with basinal brines from a section of the basin near the 160°C-isotherm : this section was probably below the principal zone of oil formation (Tissot and Welte, 1978; Milliken et al., 1981).

Release of fluid overpressure by hydraulic fracturing

High pore fluid pressure and in particular fluid pressure in excess of lithostatic values is a transient, geologically unstable condition which is relieved by hydraulic fracturing (Goguel, 1963; Phillips, 1972; Barker, 1972). It is proposed that the pressure dropped to hydrostatic values of less than 100 bars and that the hot (>150°C) H_2O-CO_2-NaCl fluid was diluted by water and cooled to less

than 135°C (Fig.7B). The hydrocarbon inclusions, with degrees of filling ranging from 1 (i.e. liquid hydrocarbon inclusions) to 0 (gaseous hydrocarbon inclusions) are compatible with the inferred decompression (C.Ramboz and C. Kosztolanyi, unpublished data).

The vertical fractures hosting the late barite are compatible with resulting from hydraulic fracturing during uplift and at high pore fluid pressure (Bredehoeft et al., 1976). The rising basaltic magma may also have contributed in optimizing the fracture formation below a Mesozoic cover of 1200m (Watts, 1983). According to that model, the orientation of the veins should be parallel to the maximum principal stress of the extension stress field prevailing in the basin during the Upper Jurassic. The direction of the late barite fractures is not well characterized. Precise knowledge of the orientation of the late barite veins could provide some more arguments in favor of Upper Jurassic age for the veins.

Origin of sulfates in late barite

Two late barites from Ratonneau have $\delta^{34}S$ values of 35.2 and 42.1 ‰. These values are 15 per mil or more enriched in ^{34}S relative to barite associated with the earlier hydrothermal vein or F mineralization at 16 ± 4 ‰ (Charef, 1983). The $\delta^{34}S$ values of the late barite are completely different from all other generations of barite at Les Malines. They are also enriched in ^{34}S compared to sea water sulfates of Cambrian or younger age (Claypool et al., 1980).

The earlier vein mineralization with barite formed from hydrothermal formation waters at about 110°C and the sulfate sulfur was interpreted to have come from the leaching of Triassic evaporitic sulfates.

During the early diagenesis of sediments, bacterial sulfate reduction is a common process in the presence of organic matter.

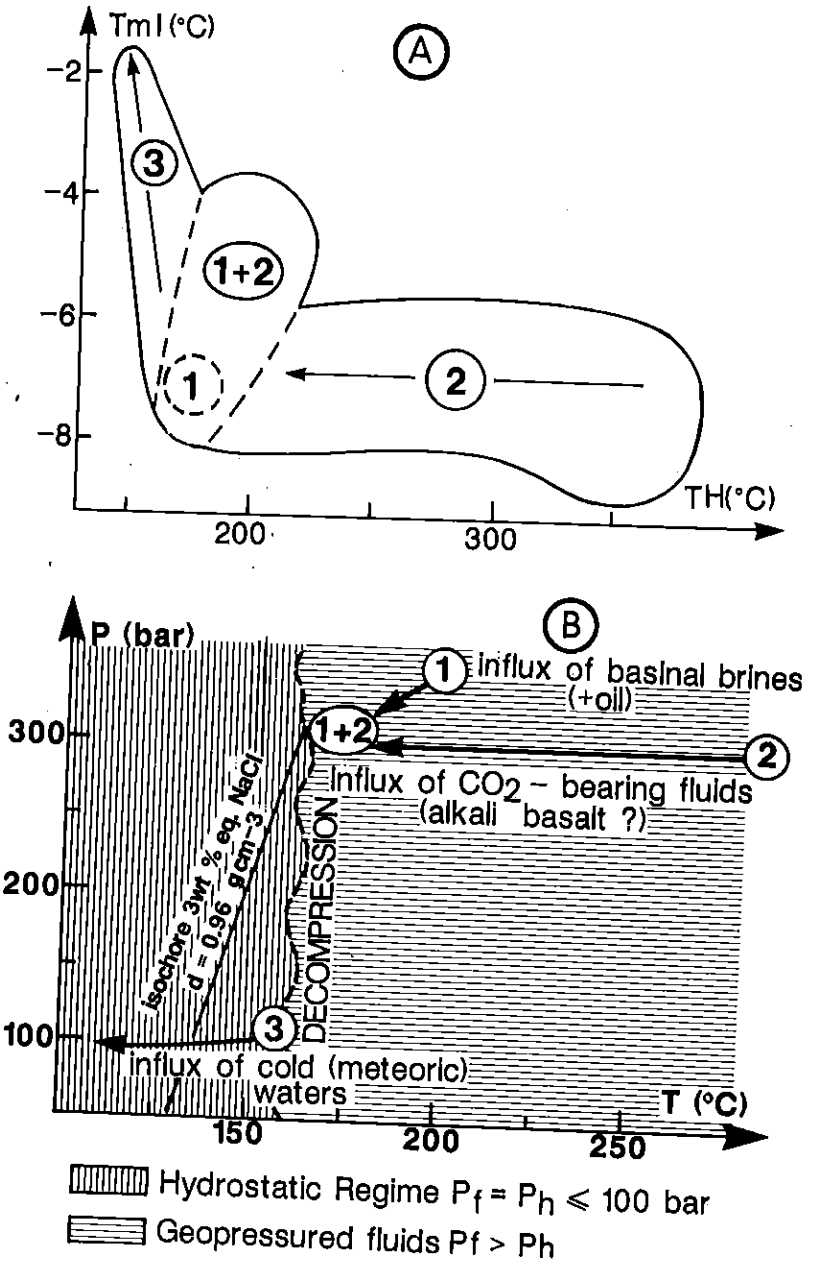

Fig. 7 - Interpretation of the TmI-TH trend (7A) in terms of the P-T trapping conditions of the different fluids (7B). The isochore for inclusion A (see text and Fig. 3) is calculated after Potter (1977).

Because the reduced sulfur is depleted in ^{34}S, the residual sulfate can become markedly enriched in ^{34}S during the Rayleigh distillation process unless the ratio of sulfate to sulfide remains high.

Thus, the high $\delta^{34}S$ values of barite probably originate from the leaching of residual sulfate in sediments where sulfate reduction reactions had been extensive and the sulfate was transported by formation waters. This implies that the sedimentary formations supplying this sulfur were different from those that supplied sulfate sulfur for the earlier generations of barite at Les Malines. The precise formations cannot be identified but it could be Lower or Middle Jurassic sequences in the deep basin. No arguments are known to suggest that the magmatic fluids supplied the necessary sulfur.

CONCLUSIONS

Unlike dominantly aqueous inclusions, gas-rich inclusions provide evidence for abnormal fossil fluid pressures in sediments. This is because minimum P-T conditions of trapping deduced from the measurement of liquid-vapor phase transitions in gas-rich inclusions overlap the P-T range corresponding to geopressuring in sediments. At les Malines, CO_2-rich inclusions in barite from the end of the Fissural Ore Stage and from the Late Stage have been used to demonstrate that the basement hosting the ores has been repetitively geopressured below the Triassic shales at the end of the Middle Jurassic and during the Upper Jurassic. They establish that the mechanism of open space creation in the Cambrian basement was hydraulic fracturing at near lithostatic pressure conditions. Figure 7 and Table 3 summarize microthermometric data on aqueous inclusions in late barite and their interpretation in terms of the fluid evolution and related mineralogy.

Table 3 - Summary of the interpretation proposed for the P-T-X fluid evolution recorded in the vug-fill barite and of their bearing on the mineralogy.

P = 285 ± 45 bars GEOPRESSURED SYSTEM			DECOMPRESSION	P > 100 bar HYDROSTATIC SYSTEM
Pf = Ph	Pf ≥ Pl			Pf = Ph
1	2	1 + 2		3
- brines (T >150°C) originating from the basin	- CO_2-bearing vapor (T >300°C) probably derived from an alkali basalt and contaminated by the aqueous pore fluid	- end product of the mixing between the aqueous pore fluid and the hot vapor - undergoing minor boiling		- cold diluted water marking the end of the isolation of the Les Malines Horst from the surface
- bringing oil to the horst	- responsible for the thermal degradation of oil			
- bringing SO_4^{2-}	- precipitating barite by cooling			
- inducing recrystallization of the Cambrian dolomites	- dissolving the limestones	- precipitating minor calcite		

It is emphasized that the Les Malines Zn-Pb deposit, hosted in a metamorphosed limestone-shale basement acting as the continental margin of an elongate Mesozoic basin once comparable to the present day Red Sea (Artru, 1968), is not directly equivalent to classical MVT deposits from the U.S., hosted in sediments in the margin of large (200km-wide) bowl-shaped basins. All the mineralisation episodes at Les Malines (KI, KII and F : Fig.6) occurred at a stage when the basin evolution was strictly controlled by thermal subsidence and active rifting. In that context, the E-W fault of Les Malines, parallel to the direction of the major Mesozoic extention, channeled both the pulsatory and the steady flows of formation waters to the horst.

This work characterizes the nature of the thermal event, of speculative origin, which is responsible for many Pb-Zn-Ba-U mineralizations in and around the Cévennes and elsewhere in Western Europe at 170 m.y. (e.g. Bonhomme et al., 1983 ; Lancelot et al., 1984). At Les Malines, geochemical and geological data support the interpretation that the end of the Zn-Pb Fissural Ore Stage occurred at the end of the Middle Jurassic as a result of the rapid centrifugal flow of formation waters originating from undercompacted shale levels in the deep basin. By contrast, subsequent hydrothermal mineralisation related to volcanism in the basin margin contributed minor barite and very little sulfide mineralization.

Finally, this work defines some important processes involved in the history of sedimentary basins. (1) Concerning the timing between upflift and volcanism in passive continental margins (e.g. Bott,1980), it has been established that, in the shelf of a basin submitted to discrete volcanism and major uplift, volcanism has occurred at an early stage of uplift and after the pulsatory dewatering of shales in the deep basin. (2) It has been shown that

the addition of small amounts of gas to the interstitial brine of an isolated compartment is an effective mechanism of rapidly increasing the fluid pressure to near lithostatic pressure, any time after the beginning of the isolation and with no constraint of constant pore volume evolution.

Acknowledgments : The samples studied were collected by G. Verraes whom we sincerely thank for his help. We are grateful to J. J. Guilloux and G. Dagallier for their assitance in mineralogy, to C. Kosztolanyi for Raman spectrometric measurements and to B. Jacquier for sulfur isotopic measurements. We thank M. Arnold, A.M. Boullier, M. Pagel, S.M.F. Sheppard and A. Weisbrod for fruitful discussions and advices concerning earlier versions of the paper. We wish to thank A. Legros, Ch. Lehman, J. Gorau and M. Tailleur for aid in preparing the manuscript.

REFERENCES

Anderson, G.M., and Macqueen, R.W., 1982, Ore deposit models, 6 - Mississippi Valley type lead-zinc deposits : Geoscience Canada, v. 9, p. 108-117.

Artru, P., 1968, Répartition du bore et de quelques éléments-traces dans des bassins semi-euxiniques du miogéosynclinal alpin (Terres Noires jurassiques, France sud-est) : Bull. Centres Rech. Explor.-Prod. Elf Aquitaine, Fr., v.2, p. 83-100.

Barker, C., 1972, Aquathermal pressuring - Role of temperature in development of abnormal pressure zones : Am. Assoc. Petroleum Geologists Bull., v. 56, p. 2068-2071.

Barlier, J., Ragot, J.P., and Touray, J.C., 1974, L'évolution des Terres Noires Méridionales d'après l'analyse minéralogique des argiles et la réflectométrie des particules carbonées : Bull. B.R.G.M., Fr., II, v.6, p. 533-548.

Baubron, J.C., Defaut, B., Demange, J., and Maury, R.C., 1978, Une coulée sous-marine d'âge jurassique moyen dans les Causses : le basalte alcalin des Vignes (Massif Central Français) : C. R. Acad. Sci., Paris, v. 287, p. 225-227.

Baudrimont, A.F., and Dubois, P., 1977, Un bassin mésogéen du domaine péri-alpin : le sud-est de la France : Bull. Centres Rech. Explor.-Prod. Elf Aquitaine, Fr., v. 1, p. 261-308.

Bernard, A.J., 1958, Contribution à l'étude de la province métallifère sous-cévenole : Mém. Sci. Terre, Nancy, Fr., v. 7, p. 123-403.

Bethke, C.M., 1986, Hydrologic constraints and the genesis of Upper Mississipi Valley District from Illinois Basin brines : Econ.

Geol., 81, p. 233-249.

Blount, C.W., 1977, Barite solubilities and thermodynamic quantities up to 300°C and 1400 bars : Am. Mineral., v. 62, p. 942-957.

Blount, C.W., and Dickson, F.W., 1969, Solubility of anhydrite ($CaSO_4$) in NaCl-H_2O from 100 to 450°C and 1 to 1000 bar : Geochim. Cosmochim. Acta, v. 33, p. 227-245.

Bodnar, R.J., and Bethke, P.M., 1983, Data on stretching of fluid inclusions in fluorite and sphalerite : U. S. Geol. Survey Open-File Rept., v. 83-790, 20 p.

Bodnar, R.J., and Bethke, P.M., 1984, Systematics of stretching of fluid inclusions. I : Fluorite and sphalerite at 1 atmosphere confining pressure : Econ. Geol., v. 79, p. 141-161.

Boichard-Morin, E., 1983, Contribution à l'étude du degré d'évolution des kérogènes et des argiles de quelques niveaux jurassiques (pourtour Sud-Ouest et Sud-Est du Massif Central). Approche paléogéothermique : unpub., Thèse Spéc. Univ. Bordeaux III, Fr., 168 p.

Boillot, G., Montadert, L., Lemoine, M., and Biju-Duval, B., 1979, La marge occidentale de la Téthys Ligure, in "Les marges continentales actuelles et fossiles autour de la France", Masson Paris, Chap. 3, p. 157-248.

Bonhomme, M.G., Bühmann, D., and Besnus Y., 1983, Reliability of K-Ar dating of clays and silicifications associated with vein mineralizations in Western Europe : Geologische Rundschau, v. 72, p. 105-117.

Bonijoly, D., and Delpont, G., 1982, Etude du Bassin des Causses et de la Bordure Cévenole par la télédetection et la géologie structurale : Documents B.R.G.M., Fr., v. 46, 40 p.

Bott, M.D.H., 1980, Problems of passive margins from the viewpoint of the geodynamic project : Phil. Trans. R. Soc. London, Ser. A,

v. 294, p. 5-14.

Bozzo, A.T., Chen, H.S., Kass, J., and Barduhn, A.J., 1973, The properties of the hydrates of chlorine and carbon dioxide : International Symposium of Fresh Water from the Sea, v. 3, p. 437-451.

Bredehoeft, J.D., Wolff, R.G., Keys, W.S., and Shuter, E., 1976, Hydraulic fracturing to determine in situ stress field, Piceance Basin, Colorado : Geol. Soc. America Bull., v. 87, p. 250-258.

Burst, J.F., 1969, Diagenesis of Gulf Coast clayey sediments and its possible relation to petroleum migration : Am. Assoc. Petroleum Geologists Bull., v. 53, p. 73-93.

Carmichaël, I.S.E., Turner, F.J., and Verhoogen, J., 1974, Continental tholeiitic provinces, in Igneous Petrology : McGraw Hill, New-York, Chap. 9, p. 427-486.

Cathles, L.M., and Smith, A.T., 1983, Thermal constraints on the formation of Mississippi Valley type lead-zinc deposits and their implications for episodic basin dewatering and deposit genesis : Econ. Geol., v. 78, p. 983-1002.

Chapman, R.E., 1980, Mechanical versus thermal causes of abnormally high pore pressures in shales : Am. Assoc. Petroleum Geologists Bull., v. 64, p. 2179-2183.

Charef, A., 1983, Les minéralisations cambriennes et karstiques Zn-Pb du district des Malines (Gard, France) : Géochimie isotopique, pétrographie et phases fluides : unpub., Thèse Spéc. I.N.P.L., Nancy, Fr., 285 p.

Charef, A., and Sheppard, S.M.F., 1983, Sources of aqueous fluids and sulphur in the Les Malines carbonate-hosted Pb-Zn deposit, France : Terra Cognita, v. 3, p. 171.

Charef, A. and Sheppard, S.M.F., 1985, Le gisement des Malines (Gard) Zn-Pb : contribution isotopique (D/H) au rattachement de

la minéralisation karstique KII à la minéralisation hydrothermale F. : C.R. Acad. Sci. Paris, v. 301, p. 39-42.

Charef, A., and Sheppard, S.M.F., Les Malines Cambrian shale-hosted Pb-Zn deposit, France : Thermometric and isotopic (H,O) evidence for pulsating hydrothermal mineralization : Mineralium Deposita, in press.

Chen, C.T.A., Chen, J.H., and Millero, F.J., 1980, Densities of NaCl, $MgCl_2$, Na_2SO_4 and $MgSO_4$ aqueous solutions at 1 atm from 0 to 50°C and from 0.001 to 1.5 M : J. Chem. Eng. Data, v. 25, p. 307-320.

Chukhrov, F.V., Ermilova, L.P., and Nosik, L.P., 1977, Isotopic composition of sulphur and the genesis of hydrothermal sulphates, in Klemm D.D., and, Schneider, H.J., eds, Time and Strata-Bound Deposits : Springer Verlag, Berlin, p. 334-395.

Claypool, G.E., Holser, W.T., Kaplan, I.R., Sakai, H., and Zak, I., 1980, The age curves of sulfur and oxygen isotopes in marine sulfate and their mutual interpretations : Chem. Geol., v. 28, p. 199-260.

Clayton, R.N., Friedman, D.L., Graf, D.L., Mayeda, T.K., Meents, W.F., and Shimp, N.F., 1966, The origin of saline formation waters. I. Isotopic composition : J. Geophys. Res., v. 71, p. 3869-3882.

Connan, J., and Orgeval, J.J., 1977, Un exemple d'application de la géochimie organique en métallogénie : la mine des Malines (Gard, France) : Bull. Centres Rech. Explor.-Prod. Elf-Aquitaine, Fr., v. 1, p. 59-105.

Daly, R.A., Manger, G.E., and Clark, S.P. Jr., 1966, Density of rocks, in Clark Jr., S.P., ed., Handbook of Physical Constants, revised edition, Geol. Soc. America, Mem. 97, Section 4, p. 19-26.

Demay, A., 1931, Contribution à l'étude de la tectonique hercynienne anté-stéphanienne dans les Cévennes méridionales et dans le Rouergue : Bull. Soc. Géol. France, v. 1, p. 663-696.

Demay, A., 1952, Sur les relations stratigraphiques entre les calcaires Géorgiens ou Acadiens et les grès Acadiens près de Saint-Laurent-le-Minier dans les Cévennes méridionales : Bull. Soc. Géol. France, v. 2, p. 9-12.

Dhamelincourt, P., Bény, J.M., Dubessy, J., and Poty, B., 1979, Analyse d'inclusions fluides à la microsonde Mole à effet Raman : Bull. Minéral., Fr., v. 102, p. 9-12.

Dickinson, G., 1953, Geological aspects of abnormal reservoir pressures in Gulf Coast Louisiana : Am. Assoc. Petroleum. Geologists Bull., v. 37, p. 410-432

Ellis, A.J., 1959, The solubility of calcite in carbon dioxide solutions : Am. J. Sci, v. 257, p. 354-365.

Ellis, A.J., and Golding, R.M., 1963, The solubility of carbon dioxide above 100°C in water and in sodium chloride solutions, Am. J. Sci., v.261, 47-60.

Ellis, A.J., and Mahon, W.A.J., 1977, Chemistry and geothermal systems : New York, Academic Press, 392 p.

Elmi, S., 1984, Jurassique Moyen : Dogger in "Synthèse géologique du sud-est de la France" : Mém. B.R.G.M., 125, p. 177-221.

Foglierini, F., and Bernard, A., 1967, L'histoire géologique d'un gisement stratiforme plombo-zincifère : Les Malines (Gard, France) : Econ. Geol., v. 3, p. 294-307.

Foglierini, F., Bernard, A., and Verraes, G., 1980, Le gisement des Malines (Gard) Zn, Pb : 26e C.G.I., Paris, Fasc. sur les gisements français, E5, 56 p.

Garven, G., and Freeze, A., 1984, Theoretical analysis of the role of ground water flow in the genesis of stratabound ore deposit.

II. Quantitative results : Am. J. Sci., v. 284, p. 1125-1174.

Gehrig, M., 1980, Phasengleichgewichte und PVT - daten ternärer Mischungen aus Wasser, Kohlendioxid und Natriumchlorid bis 3 kbar und 550°C: unpub. Thesis, Institute of Physical Chemistry, Univ. Karlsruhe, 109 p.

Goguel, J., 1963, A hypothesis on the origin of the "cryptovolcanic structures" of the central platform of North America: Am. J. Sci., v. 261, 665-667.

Graciansky (de), P.C., Bourbon, M., Charpal (de), O., Chenet, P.Y., and Lemoine, M., 1979, Genèse et évolution comparées de deux marges continentales passives : marge ibérique de l'Océan Atlantique et marge européenne de la Téthys dans les Alpes occidentales : Bull. Soc. Géol. France, v. 7, p. 663-674.

Graf, D.L., 1982, Chemical osmosis, reverse chemical osmosis, and the origin of subsurface brines: Geochim. Cosmochim. Acta, v. 46, p. 1431-1448.

Hall, W.E., and Friedman, I., 1963, Composition of fluid inclusions, Cave-in-Rock fluorite district, Illinois, and Upper Mississippi Valley zinc-lead district : Econ. Geol., v. 58, p. 886-911.

Hanor, J.S., 1979, The sedimentary genesis of hydrothermal fluids, in Barnes, H.L., ed., 2nd edition, Geochemistry of Hydrothermal Ore Deposits : New-York, Wiley, p. 137-172.

Hedberg, H.D., 1974, Relation of methane generation to undercompacted shales, shales diapirs, and mud volcanoes: Am. Assoc. Petroleum Geologists Bull., v. 58, p.661-673.

Holland, H.D., and Malinin, S.D., 1979, The solubility and occurrence of non-ore minerals, in Barnes, H.L., ed., 2nd edition, Geochemistry of Hydrothermal Ore Deposits: New York, Wiley, p. 461-508.

I.U.P.A.C., 1976, International Thermodynamic Tables of the Fluid

State. 3- Carbon Dioxide, in, Angus, S., Armstrong, B., and de Reuck, K.M., eds: Pergamon Press, 385p.

Lancelot, J.R., Saint André (de), B., and Boisse (de la), H., 1984, Systématique U-Pb et évolution du gisement d'uranium de Lodève (France) : Mineralium Deposita, v. 19, p. 44-62.

Larson, L.T., Miller, J.D., Nadeau, J.E., and Roedder, E., 1973, Sources of error in low-temperature inclusion homogenization determination and corrections on published temperatures for the East Tennessee and Laiswall deposits : Econ. Geol., v. 68, p. 113-116.

Laubscher, H., and Bernoulli, D., 1977, Mediterranean and Tethys, in, Nairn, A.E.M., Kanes, W.H., and Stehli, F.G., eds, The Ocean Basins and Margins : Plenum Publishing Company, New-York, vol.4A, p.1-27.

Le Bel, L., and Oudin, E., 1981, Temperature evolution at deep-sea hydrothermal vents at 21°N (East Pacific Rise) recorded by fluid inclusions : Chem. Geol., v. 37, p. 129-136.

Lemoine, M., 1982, Tectonique synsédimentaire mésozoique dans les Alpes Occidentales : naissance et évolution d'une marge continentale passive : Mémoires Géologiques Univ. Dijon, Fr., 7, Livre jubilaire Gabriel Lucas, p. 347-361

Lesage, J.L., 1972, Tectonique et microtectonique de la partie méridionale des monts de Saint-Bresson: unpub. D.E.A. Report, Univ. Montpellier, 26 p..

Macquar, J.C., 1968, Contribution à l'étude géologique et métallogénique de la bordure méridionale des Cévennes. Le Trias de la région des Malines, relations entre les minéralisations plombo-zincifères, la lithologie et les structures : Unpub. Thesis, Paris VI, Fr., v.1, 122 p.

Macquar, J.C., 1970, Le Trias, in Contribution à la recherche de

gisements métallifères cachés (district des Malines, Cévennes): Bull. B.R.G.M., Fr., II, v. 1, p. 27-65.

Macquar, J.C., 1973, Evolution tectonique post-hercynienne du domaine pericévenol. Incidences sur les filons de couverture. Exemple des bordures ouest et sud des Cévennes : Bull. B.R.G.M., Fr., II, v. 1, p.45-68.

Magara, K., 1975, Reevaluation of montmorillonite dehydration as cause of abnormal pressure and hydrocarbon migration : Am. Assoc. Petroleum Geologists Bull., v. 59, p. 292-302.

Matthews, W.R., Rehm, W.A., and Louden, L.R., 1971, Understanding origin of pressure is a key to better well planning, Oil and Gas J., November 15, p. 141-144.

Michaud, J.G., 1970, Le Paléozoïque de la partie méridionale du Horst du Saint Bresson, in Contribution à la recherche de gisements métallifères cachés (district des Malines, Cévennes) : Bull. B.R.G.M., Fr., II, v. 1, p. 17-26.

Milliken, K.L., Land, L.S., and Loucks, R.G., 1981, History of burial diagenesis determined from isotopic geochemistry, Frio formation, Brazoria County, Texas, Am. Assoc. Petroleum Geologists Bull., v. 67, 1397-1413.

Mouterde, R., 1984, Jurassique Inférieur : Lias, in "Synthèse géologique du sud-est de la France" : Mém. B.R.G.M., n° 125, p. 119-176.

Newitt, D.M., Pai, M.U., Kuloor, J.A.W., and Huggill, J.A.W., 1961, Carbon dioxide, in Thermodynamic functions of gases, F. Din Ed., v. 1 : Butterworths, London, p. 102-135.

Noble, E.A., 1963, Formation of ore deposits by waters of compaction : Econ. Geol., v. 58, p. 1145-1156.

Orgeval, J.C., 1976, Les remplissages karstiques minéralisés : exemple de la mine des Malines (Gard, France) : Mém. hors série

Soc. Géol. France, v. 7, p. 77-83.

Oudin, E., Thisse, Y., and Ramboz, C., 1984, Fluid inclusion and mineralogical evidence for high-temperature saline hydrothermal circulation in the Red Sea metalliferous sediments : preliminary results : Marine Mining, v. 5, p. 3-31.

Palut, J.P., and Bernier, P., 1970, Le Jurassique, in Contribution à la recherche de gisements métallifères cachés (district des Malines, Cévennes) : Bull. B.R.G.M., Fr., II, v. 1, p. 67-95.

Parisot, C.J., and Plattner, E., 1981, Vapor-liquid equilibria of the $NaCl-H_2O$ system in the temperature range 300-400°C : J. Chem. Eng. Data, v. 26, p. 16-20.

Pichavant, M. Ramboz, C., and Weisbrod, A., 1982, Fluid immiscibility in natural processes : use and misuse of fluid inclusion data. I. Phase equilibria analysis. A theoretical and geometrical approach : Chem. Geol., v. 37, p. 1-27.

Phillips, J.W., 1972, Hydraulic fracuring and mineralization : J. Geol. Soc. London, v. 128, p. 337-359.

Potter, R.W., 1977, Pressure corrections for fluid inclusion homogenizatiuon temperature based on the volumetric properties of the system $NaCl-H_2O$: J. Res. U.S. Geol. Survey, v. 5, p. 603-607.

Potter, R.W., Clynne, M.A., and Brown, D.L., 1978, Freezing point depression of aqueous sodium chloride solutions : Econ. Geol., v. 73, p. 284-285.

Pottorf, R.J. and Barnes, H.L., 1983, Mineralogy, geochemistry and ore genesis of hydrothermal sediments from the Atlantis II Deep, Red Sea : Econ. Geol., Monograph 5, 198-223.

Poty, B., Leroy, J. and Jachimowicz, L., 1976, Un nouvel appareil pour la mesure des températures sous le microscope : l'installation de microthermométrie Chaix-Meca : Bull. Soc. Fr.

Minéral. Cristallogr., v. 99, p. 182-186.

Powers, M.C., 1967, Fluid-release mechanisms in compacting marine rocks and their importance in oil exploration : Am. Assoc. Petroleum Geologists Bull., v. 51, p. 1240-1254.

Price, N.J., 1975, Fluids in the crust of the Earth : Sci. Prog., Oxford, G.B., v. 62, p. 59-87.

Ramboz, C., 1983, Application of V-X projections to the quantitative interpretation of heterogeneous trapping from fluid inclusion study : Terra Cognita, v. 3, p. 164.

Ramboz, C., Pichavant, M. and Weisbrod, A., 1982, Fluid immiscibility in natural processes : use and misuse of fluid inclusion data. Part II : interpretation of fluid inclusion data in terms of immiscibility : Chem. Geol., v. 37, p. 29-48.

Ramboz, C., Schnapper, D., and Dubessy, J., 1985, The P-V-T-X-fO_2 evolution of H_2O-CO_2-CH_4-bearing fluid in a wolframite vein : reconstruction from fluid inclusion studies : Geochim. Cosmochim. Acta, v. 49, p. 205-219.

Ramboz, C., and Danis, M., 1987, The temperature of the inflowing brine at the bottom of Atlantis II Deep, Red Sea : Terra Cognita, v.7, n. 2-3, p. 187.

Rife, D.L., 1971, Barite fluid inclusion geothermometry, Cartersville Mining district, Northwest Georgia : Econ. Geol., v. 66, p. 1164-1167.

Robert, P., 1985, Histoire géothermique et diagénèse organique : Bull. Centres Rech. Explor-Prod. Elf-Aquatiaine, Fr. : Mém. 8, Pau, 345 p.

Roedder, E., 1972, Barite fluid inclusion geothermometry, Cartersville Mining district, Northwest Georgia : Econ. Geol., v. 67, p. 821-822.

Roedder, E., 1976, Fluid inclusion evidence on the genesis of ores

in sedimentary and volcanic rocks, in Wolf, K., H., ed., Ores in sediments, sedimentary and volcanic rocks, v. 2 : Elsevier, Amsterdam, p. 67-110.

Roedder, E., 1984a, The fluids in salts: Am. Mineral., v. 69, p.413-439.

Roedder, E., 1984b, Extrusive rocks and volcanic environments, in Ribbe, P.H., ed., Fluid Inclusions : Review in Mineralogy, v. 12, p. 473-501.

Routhier, P., 1980, Où sont les métaux pour l'avenir ? : Mém. B.R.G.M., Fr., v. 105, 409 p.

Takenouchi, S., and Kennedy, G.C., 1965, Dissociation pressures of the phase CO_2, 5 3/4 H_2O : J. Geol., v. 73, p. 383-390.

Thisse, Y., Oudin, E., and Ramboz, C., 1983, Boiling fluids in the Red-Sea metalliferous sediments : E.C.R.F.I., Orléans, Fr., p. 58.

Tissot B.P., and Welte, D.H., 1978, Petroleum formation and occurrence : Springer Verlag, Berlin, 538 p.

Triat, J.M., and Truc, G., 1983, Le rôle des failles N 50 dans la sédimentation des temps méso et cénozoïques et dans l'évolution tectonique du bassin sud-est (France) : Bull. Centres Rech. Explor.-Prod. Elf Aquitaine, Fr., v. 7, p. 409-424.

Tugarimov, A.I., and Naumov, V.B., 1970, Dependence of the decrepitation temperature of minerals on the composition of their gas-liquid inclusions and hardness : Akad. Nauk SSSR Doklady, v. 195, p. 112-114.

Verraes, G., 1983, Etude monographique du district minier des Malines et de ses environs (province sous-cévenole, France) : unpub., Thèse d'Etat, Univ. Montpellier, vols. 1 and 2, 591 p.

Watts, E.V., 1948, Some aspects of high pressures in the D7-zone of the Ventura avenue field: Am. Inst. Min.Metall. Engin. Trans.,

v. 174, p. 191-205.

Watts, N.L., 1983, Microfractures in chalks of Albuskjell Field, Norwegian Sector, North Sea: possible origin and distribution: Am. Assoc. Petroleum Geologists Bull., v.67, p.201-234.

Calculation of the bulk composition and bulk density of inclusion B in the H_2O-CO_2-NaCl system.

The principles of the calculation of the bulk V-X properties of fluid inclusions, recalled in Ramboz et al. (1985), can be extended to the H_2O-CO_2-NaCl system as follows :

$$nH_2O = \frac{Flw \cdot dl \ (1-ZNaCl)}{18 \ (1-ZNaCl) + 58.5 \cdot ZNaCl}$$

$$nNaCl = \frac{Flw \cdot dl \cdot ZNaCl}{18(1-ZNaCl) + 58.5 \cdot ZNaCl}$$

$$nCO_2 = \frac{(1-Flw) \cdot dv}{44} + Z'CO_2 \cdot nH_2O$$

$$Xi = \frac{ni}{nH_2O + nCO_2 + nNaCl}$$

$$d = Flw \cdot dl + (1- Flw) \cdot dv$$

ZNaCl was estimated to be 0.02 (6 wt. eq. NaCl) based on

the overestimated value obtained on interpreting Tml referring to the H_2O-NaCl system (Potter et al., 1976) and neglecting CO_2.

dl at T = TmC was estimated using the data by Chen et al. (1980).

The internal pressure in inclusion B at T = TmC was estimated to be 30 bar, referring to the P-T conditions of the equilibrium C+L+V at T = 4.6 °C in the system CO_2 - (H_2-6 wt.% NaCl) (Bozzo et al., 1973).

dv was taken as the density of pure CO_2 vapour at 4.6°C, 30 bar (Newitt et al., 1961).

CHAPITRE III

Geyser-type discharge in Atlantis II Deep (Red Sea) : evidence from fluid inclusions in epigenetic anhydrite.*

CLAIRE RAMBOZ

Centre de Recherches Pétrographiques et Géochimiques,
B.P.20, 54501-Vandoeuvre-lès-Nancy (France).

ELISABETH OUDIN AND YVES THISSE**
B.R.G.M., avenue de Concyr, BP 6009, 45060-Orléans Cedex (France)

* Accepted for publication in Canadian Mineralogist Special Issue, v. 26/3, 1988. (Contribution C.R.P.G. N°749).

** Present address : La Touche, Sambin, 41120-Les Montils (France)

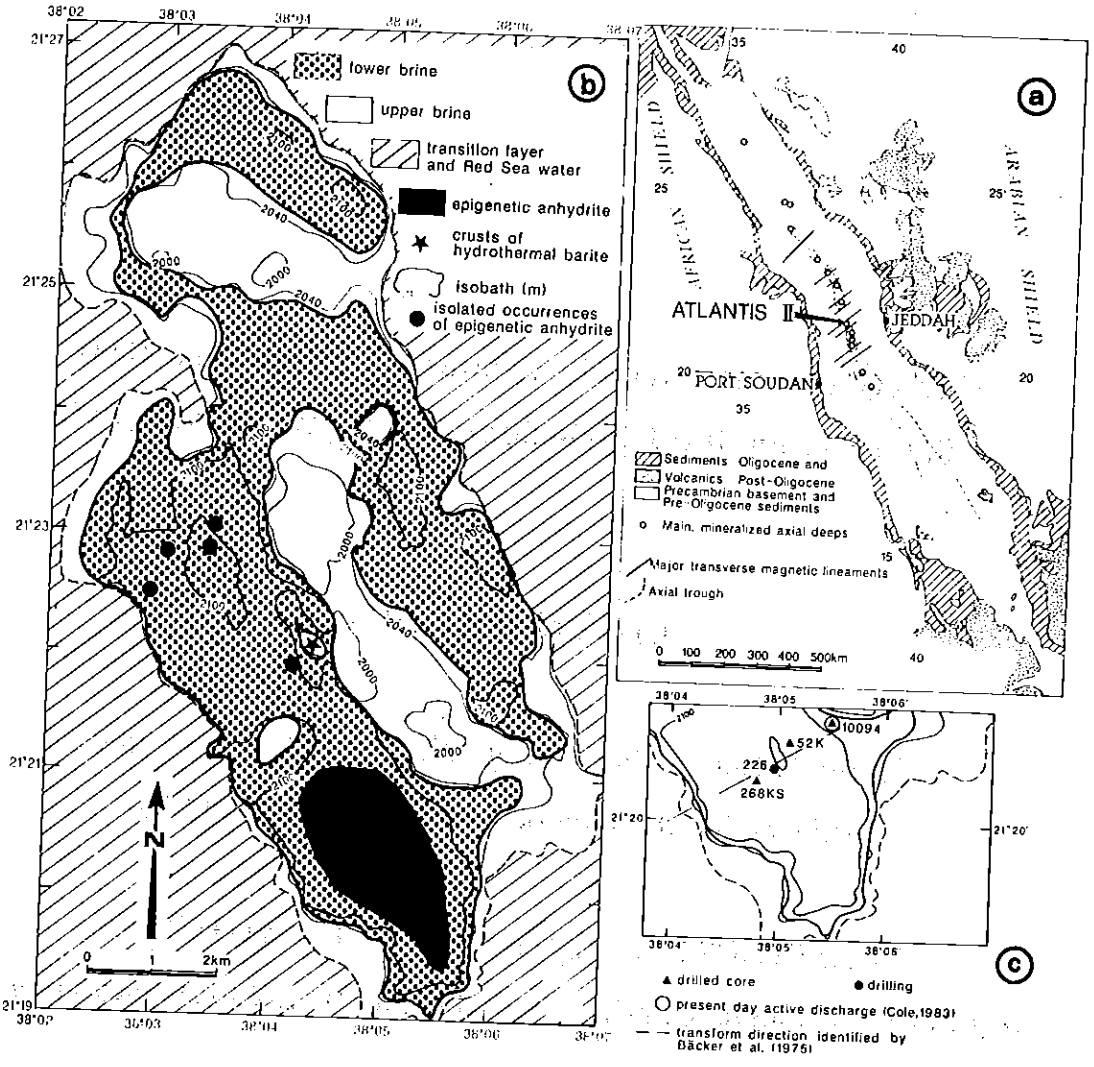

FIG. 1 : (a) Schematic Red Sea map showing the mineralized Deeps close to transverse faults crosscutting the Axial Trough (after Bertin et al. 1979 and an unpublished compilation by Guennoc in Oudin et al. 1984).

(b) Bathymetric map of Atlantis II Deep (depths are uncorrected for higher sound velocity in brines), showing surface areas covered by the lower and upper brines (situation in 1971; after Bäcker & Richter 1973). Sediments presenting epigenetic anhydrite veins are indicated after Zierenberg & Shanks (1983). Hydrothermal banded barite crusts after Sval'nov et al. (1984).

(c) Location of the studied 268 KS core and of some other drilling sites in SW Basin. 52K: core sample presenting numerous epigenetic features (Zierenberg & Shanks 1983); 226: shallow basalt sequence (Ross et al. 1973); 10094: core showing evidences of present day discharge (Cole 1983); 268 KS: core sampled at 21° 20.45' N, 38° 04.67' E: (Thisse 1982; Oudin et al. 1984; this study).

INTRODUCTION

In the Atlantis II Deep, Red Sea (Fig.1a), ≈10 to 30 m of metalliferous sediments have accumulated below anoxic stratified brines over the past 25,000 years. These form a potentially economic deposit of Zn, Ag, Au and Cd (Shanks 1983, Bäcker & Lange 1987). The brine pool in Atlantis II Deep is 14 km long, 5 km wide and ~200 m thick (Fig. 1b). The pool consists of two convecting brine layers of nearly constant composition and temperature, separated by a 1m-thick fluid interface, and overlain by a transition layer which approaches the composition of deep Red Sea waters at the top (Turner 1969, Hartmann 1980; Fig. 2). Experimental studies on double diffusive layered brines show that such a density-stratified structure is stable. Exchange through the lower interface is much more efficient for heat than for particulate matter (Turner 1969). Hydrological studies show that a vent source at the bottom of the SW Basin provides the whole Deep with hot brine, which homogenizes by convection (Schoell & Hartmann 1973; Fig.1a). This accounts for the gradual increase in the temperature and volume of the lower brine observed for the past 15 years (Hartmann 1980). The lower brine is injected at the bottom of the Deep with little or no mixing with seawater (Craig 1969, Turner 1969, Hartmann 1985). The upper brine, however, is a mixture of this lower brine with seawater (Craig 1969, Hartmann 1985).

Based on 300 cores collected in the Deep and its surroundings, the lithostratigraphy of the finely layered metalliferous sediments is from bottom to top: detritic-oxidic pyritic zone (DOP), lower sulfidic zone (SU1), central oxidic zone (CO), upper sulfidic zone (SU2) and amorphous silicate zone (AM)(Bäcker & Richter 1973). All the units were deposited through rapid chemical sedimentation, with a small component of detrital material (Hackett & Bischoff 1973, Bäcker & Richter 1973, Shanks & Bischoff 1977). SW Basin core samples present a specific lithostratigraphy, due to intense brecciation, resedimentation and volcanic activity. These features are caused

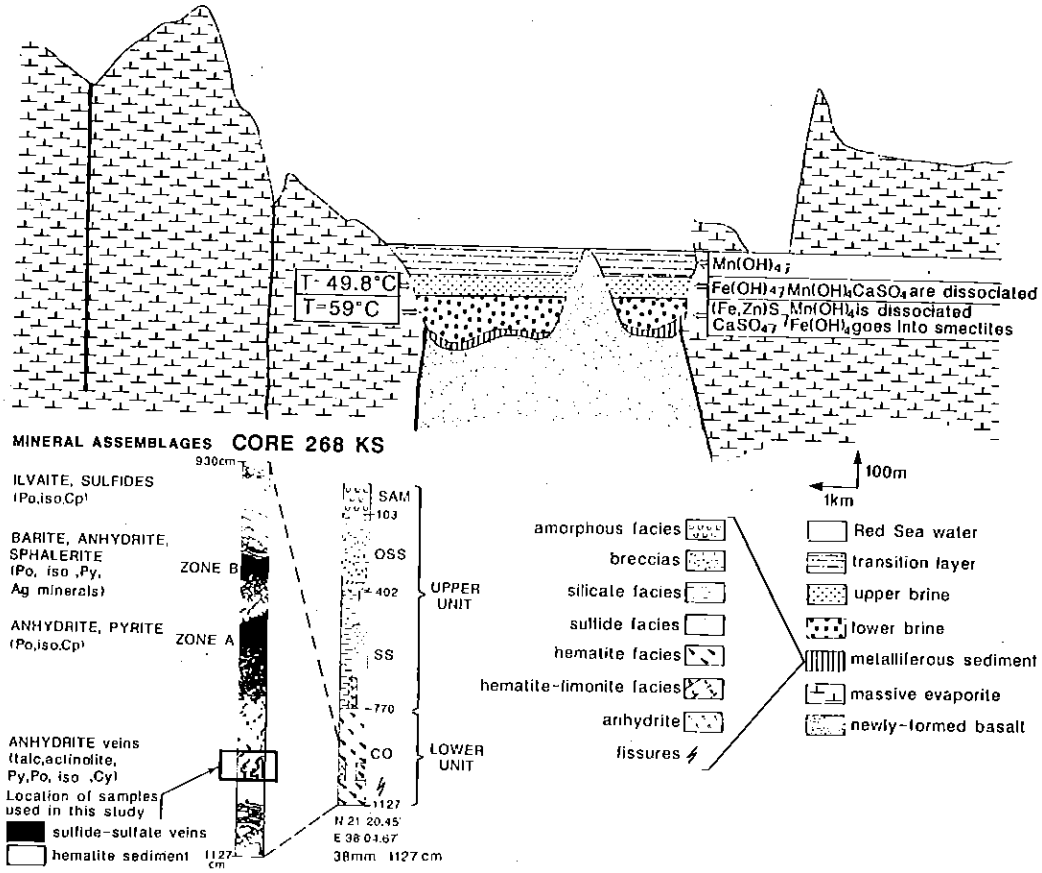

FIG. 2 : Schematic cross-section of Atlantis II Deep (after Bäcker et al. 1975). The temperature of the stratified brines (situation in 1971) and the nature of the particulate matter they contain are schematic after Hartmann (1973, 1985), Cole (1983) and Zierenberg & Shanks (1986). The simplified stratigraphy of the core 268 KS is shown at the bottom left. Epigenetic anhydrite crystals examined in this study are from near the base of the core, which is expanded to the right side (after Thisse 1982 and Oudin et al. 1984). (Po: pyrrhotite; Py: pyrite; Iso: isocubanite (cubic); Cp: chalcopyrite).

by the venting of hydrothermal sources in the SW Basin. This process started ≈11,000 years ago and still continues today (Bäcker & Richter 1973). Numerous epigenetic veinlets or pseudoconformable beds indicate movement of hydrothermal solutions through the sediments (Bäcker & Richter 1973, Zierenberg & Shanks 1983). These veins contain a complex assemblage of sulfides and anhydrite, similar to the high temperature assemblages forming hydrothermal chimneys along the EPR (Oudin 1983, Oudin et al. 1984). The veins are associated with talc, ilvaite, actinolite, pyroxene and garnet, which are either primary (i.e. directly precipitated from the fluid) or secondary (i.e. resulting from metamorphism of the sediment) (Weiss et al. 1980, Pottorf & Barnes 1983; Oudin 1983, Zierenberg & Shanks 1983, Oudin et al. 1984). Figures 1 and 2 summarize bathymetric, hydrographic, geological and geochemical conditions in the Atlantis II Deep.

The conditions of hydrothermal discharge in Atlantis II Deep are not fully understood because the hot discharging brine has never been directly sampled. Hydrothermal activity in Atlantis II Deep is intermittent. This is shown by annual changes in the temperature of the lower and upper brines (Schoell & Hartmann 1978, Hartmann 1980). Barite crusts on basalts from the flank of the Central Sill near the SW Basin (star in Fig.1b), with rhythmic sulfur and oxygen isotopic compositions, also imply episodic venting at around 140°-180°C in the Deep (Sval'nov et al. 1984). Hydrothermal discharge in Atlantis II Deep is turbulent (Schoell & Hartmann 1978, Voorhis & Dorson 1975) and characterized by high flow rate around 278 kgs^{-1} (Hartmann 1980). Present hydrothermal activity in Atlantis II Deep is therefore similar to that of surface geysers (Ross 1972, Schoell & Hartmann 1978). Subaerial geyser discharge is commonly accomplished by a vapor phase (White 1968). It has, however, never been demonstrated so far that the brines discharging in Atlantis II Deep were boiling.

The temperature of brine venting in Atlantis II Deep is poorly constrained. A wide range of values has been obtained from mineral and isotopic geothermometers, and from heat-mass balance calculations (see reviews by Shanks & Bischoff 1977, Pottorf 1980). The former methods may lead to erroneous results if mineralogical and isotopic disequilibria prevailed. However the changes in the temperature and volume of the lower brine over the past 15 years should provide accurate estimates of brine temperatures.

The distribution of dissolved sulfides and sulfates in the stratified brine pool is not presently understood. The lower brine contains no detectable H_2S (Brewer & Spencer 1969) although the sulfide content of the sediment is greatest in brine-venting areas. Anhydrite is stable in the lower brine, as indicated by its presence as an authigenic mineral in the youngest sediments (Hartmann 1985). Detailed calculations using Pitzer's equations confirm that the lower brine is anhydrite saturated (Monnin, pers. com.). During the period of increasing hydrothermal activity, the sulfate content of the lower brine, which is controlled by the solubility product of anhydrite, decreased from 840 to 683 ppm (Hartmann 1985). It remains to be explained how the anoxic lower brine has a low H_2S content and is saturated with respect to anhydrite, whereas the upper brine, which contains $\approx$ 55% of a sulfate-bearing seawater component (Hartmann 1985, Zierenberg & Shanks 1986), is undersaturated.

Bäcker and Richter (1973) first examined the distribution of anhydrite in Atlantis II Deep sediments in relation to the anomalous distribution of dissolved sulfates and sulfides in the stratified brine pool. Epigenetic anhydrite is abundant in the W and SW basins (Zierenberg & Shanks 1983; Fig.1b) but is insignificant in sediments from the periphery of the lower brine pool, which are directly precipitated from the upper brine (Fig.1b). As the lower brine is representative of the hydrothermal fluid discharging in the Deep, the spatial distribution of anhydrite over the Deep suggests that it

precipitates directly from the Ca and sulfates in the hydrothermal fluid, and seawater is not a source of these elements. The increasing SO_4-content with depth of interstitial waters from one SW Basin core suggests a deep source of sulfates (Blanc 1987).

Fluid inclusions in seafloor hydrothermal deposits (e.g. Le Bel & Oudin 1982; Kusakabe et al. 1982) can provide information on the temperature of formation and on the role of fluid mixing or unmixing during mineral precipitation. However, inclusions are rare in minerals from Atlantis II Deep sediments. Pottorf (1980) first reported several (liquid+vapor)-filled inclusions in anhydrite from the SW Basin. Most inclusions leaked during heating runs, but three, filled with a $\approx$ 25 wt.% eq. NaCl-rich solution, homogenized into the liquid phase, implying a minimum temperature of formation of around 238°C at 200 bars. Later, Zierenberg & Shanks (1983) noted the presence of NaCl-saturated (liquid+vapor)-filled inclusions in addition to two-phase inclusions in the epigenetic anhydrites.

This paper presents extensive data on fluid inclusions in epigenetic anhydrites from one core typical of SW Basin sediments. The present work is intended to further constrain the temperature of brine discharge in the Atlantis II Deep and to explain the formation of epigenetic anhydrite in brine-venting areas.

DESCRIPTION OF THE CORE.

The anhydrites studied were selected from core 268 KS, collected in the center of the SW Basin (Figs. 1b & 1c) during the Valdivia cruise Va 29 in 1980. Since then, the core has been stored at 2°C. The core consists of 11 m of sediments; it does not penetrate the basaltic basement. Sediments are enriched in hematite, are intensely brecciated and crosscut by veins (Thisse 1982). The lithostatigraphy and mineralogy of the core are summarized in Figure 2. The upper part of the core is enriched in clays and Zn, Fe, Pb and Cu sulfides

relative to the lower part, which is dominated by hematite (Oudin et al. 1984). The 3 m-thick Lower Unit (Fig. 2) is crosscut by numerous epigenetic veins and unconformable beds of well-crystallized sulfides and sulfates. Millimeter-long anhydrite and barite crystals, which are rich in fluid inclusions, are all located in the lower 2 m of the core. The sediment adjacent to the veins has been intensely thermally metamorphosed. Metamorphic minerals include ilvaite, mushketovite, actinolite and talc (Oudin et al. 1984; Fig.2). The studied anhydrites are from veins that crosscut hematitic sediments at a depth of 1085±5 cm (Fig.2). The crystals are associated with talc, actinolite, pyrite, pyrrhotite, isocubanite (cubic $CuFe_2S_3$) and chalcopyrite. Barite was not observed and the surrounding sediment contains only ≈ 420 ppm barium (Thisse 1982). The chemistry of the layer 1085 sediment is representative of the bulk of Lower Unit: SiO_2, Cu, Zn, and Pb are depleted relative to the Upper Unit.

ANALYTICAL PROCEDURE.

About 100 platy anhydrite crystals were hand-picked from the core at 2°C, then kept at room temperature for up to 8 months. Reliable microthermometric data were obtained for 182 inclusions from 16 selected anhydrite crystals, using a Chaix-Meca heating-freezing stage (Poty et al. 1976). Inclusions without NaCl daughter crystals were cooled to -120°C, then warmed at a rate of 4° to 10°C per minute. Measurements included temperature at which the first liquid formed in the frozen inclusion (eutectic temperature=Te), and the temperature of final ice disappearance (TmI). Inclusions were also sequentially heated and then immediately frozen. Many inclusions more than 50 μm long burst when quickly heated to a high temperature. Therefore, the temperature of halite disappearance (Ts), of vapor (Th L-V (V)) and liquid (Th L-V(L)) disappearance were always measured on heating the inclusions at a rate of 1° to 5°C per minute up to

250°C, then at a rate of 0.5° to 1°C per minute above 250°C. About 80% of the measurements were duplicated to characterize and recognize leaking and stretching problems (e.g., Roedder 1981; see Appendix). Measurements of some liquid-filled inclusions were repeated after storage at room temperature for 3 to 12 months. Reproductibility was always within the limit of experimental error and inclusion morphologies were apparently unchanged. The precision of the phase change temperatures are: ± 0.2°C for TmI, ± 2°C for both Th L-V (L) and Ts. The precision of the Th L-V (V) is probably no better than 20°C, due to the difficulty in observing the presence of very small amounts of liquid in gas-filled inclusions.

CO_2, CH_4, H_2S, N_2 and SO_2 were looked for in the vapor phase of all inclusion types using a M.O.L.E. Raman microprobe (Delhaye & Dhamelincourt 1975, Dhamelincourt et al. 1979). However, these species were all below the detection level of ≈0.5 mole%.

DESCRIPTION OF THE ANHYDRITE AND INCLUSIONS.

Most anhydrite crystals are usually platy and euhedral with (001) cleavages. They often show 20 μm-wide negative crystal vacancies in surface. Anhydrite contains opaque inclusions of hematite from the sediments or, more typically, sector-zoned inclusions of fine-grained (≈5 μm wide) euhedral sulfides or oxides (Figs. 3a & 3c). In the latter case, crystals may display a bow-tie structure (see Fig. 11a of Oudin et al. 1984). Inclusions of magnetite, pyrrhotite, isocubanite, chalcopyrite and pyrite were identified in epigenetic anhydrites from level 1085, using reflected-light microscopy and scanning electron microscopy.

Fluid inclusions are uniformly distributed throughout the anhydrites but cannot be observed where opaque inclusions are too abundant. Most inclusions are parallel with the c-axis of the crystal. Fluid inclusions in anhydrite are either monophase and filled with a liquid (type L), or two-phase

FIG. 3 : Microphotographs of fluid inclusions in anhydrite from level 1085 cm in core 268 KS.

(a) Part of a polygenic anhydrite crystal with, in its core, numerous opaque inclusions (oxides and sulfides) and associated tubular two-phase inclusions (liquid-dominant and vapor-dominant); isometric NaCl-saturated inclusions are trapped in crystal overgrowth.

(b) Slender tubular two phase liquid dominant inclusions in an anhydrite crystal. The inclusion length exceeds 1mm.

(c) Primary tubular two phase inclusions initiated by opaque inclusions.

(d) Three phase type L inclusion containing a liquid (L), a vapor (V) and an opaque phase.

(e) Primary cogenetic fluid inclusions showing various liquid to vapor ratios as evidence of boiling. The inclusion in the upper right hand side is vapor filled and the one at the bottom left side is empty.

(f) Primary type S inclusions in an overgrowth zone of anhydrite (same legend as Fig. 3d). Note the characteristic isometric shape of inclusions. The inclusion at the top right hand side is metastable for lack of halite nucleation .


a
200 µm


b
200 µm

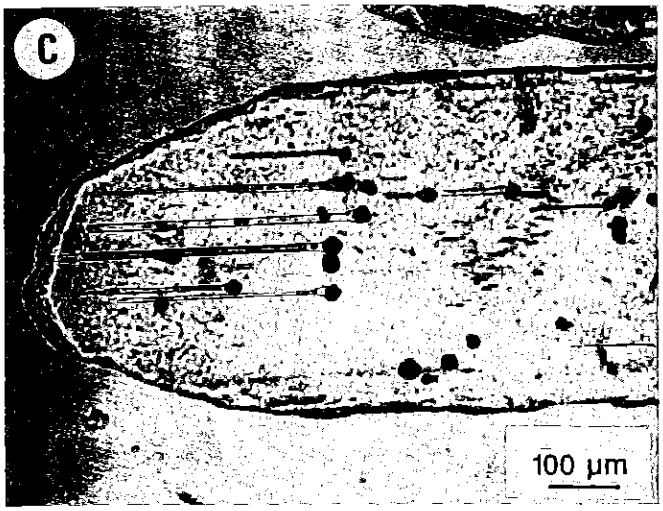
c
100 µm

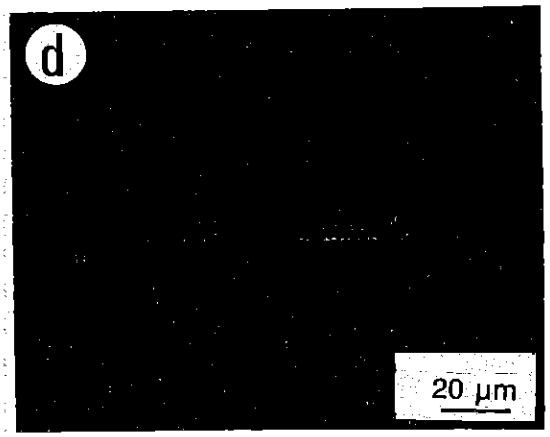
d
20 µm

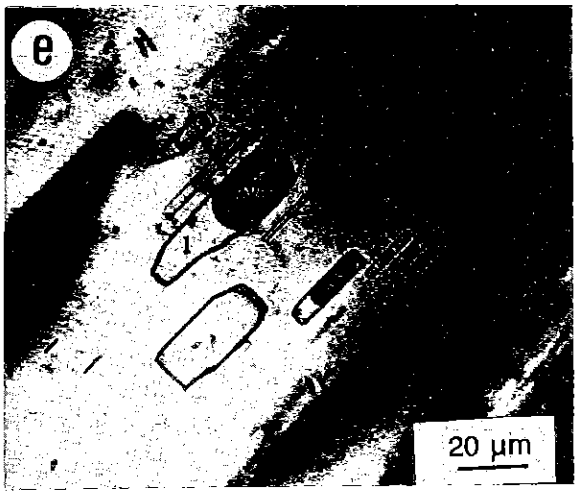
e
20 µm


f
20 µm

and either liquid-dominant (type L) or vapor-dominant (type V), or three-phase, i.e. filled with liquid, vapor and a halite cube (type S). Most type L, all type V and S inclusions are randomly distributed, and therefore grew simultaneously with the host anhydrite as primary inclusions (cf. Roedder 1976). Less than 10% of the type L inclusions appear secondary; these are concentrated along ≈200 μm-long fractures. All anhydrite crystals contain type L inclusions and about two thirds of them contain liquid+vapor-filled aqueous inclusions and no type S inclusions. One third of the crystals contains both NaCl-undersaturated and NaCl-saturated inclusions. No crystals in which all the inclusions were NaCl-saturated were observed.

Type L and type V inclusions differ in morphologies and distributions from type S inclusions. Type S inclusions are in overgrowths a few hundred μm wide at the periphery of the crystals but never in the cores (Fig. 3a). In contrast, type L inclusions, some of which are associated with type V inclusions (Fig. 3e), are characteristically in the cores of crystals (Fig. 3a). Type S inclusions typically are rectangular with sharp angles, about 20 μm long and 5 μm wide (Figs. 3a & 3f). Type L and type V inclusions often have round ends, and vary from 50 μm to a few mm in length and from 1 to 15 μm in width (Figs. 3b to 3d). Type S inclusions never contain opaque solids. Type L and V inclusions can contain one or more opaques. Most commonly, such opaque inclusions are at one end of the elongate inclusions (Figs 3c & 3d). Opaque inclusions have acted as defects in the anhydrite crystal structure which have initiated the vacancies favorable for the trapping of fluid. Crystal growth has been parallel to the long axis of the inclusion and away from the opaque inclusions. In particular, crystals with a bow-tie distribution of opaque solid inclusions grew symetrically from the center. Fine-grained hematite is less commonly trapped with the fluid in 30 μm long type L inclusions. Most type S inclusions contain constant liquid:vapor ratios over a scale of a few hundred square microns. In contrast, many adjacent type L and

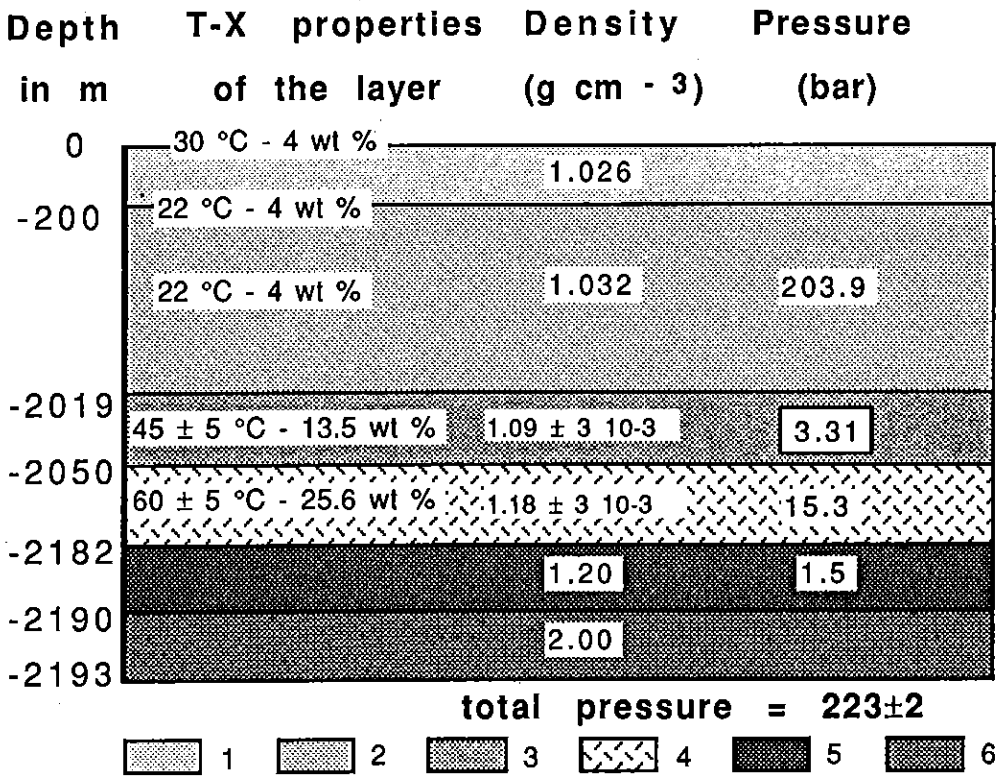

Table 1 : Reconstructed hydrostatic pressure regime over the anhydrite veins in core 268 KS, level 1085cm. Data on Red Sea water and brines are from Brewer et al. (1969) and Hartmann (1980). Data on the core are from Thisse (1982). Fluid densities are calculated after Pitzer et al. (1984). 1 and 2: Surficial and deep Red Sea water, respectively. 3: Upper brine. 4: Lower brine. 5: Shaly sediment. 6: Hematitic sediment.

V inclusions have different liquid:vapor degrees of filling (ratio of liquid volume to total volume; Fig. 3e). Portions of anhydrite crystals can contain only type L inclusions with variable degrees of filling in the range of 0.10 to 0.40 (i.e. primary azonal fluid inclusions: Sobolev & Kostyuk 1975). Type L inclusions underlining a growth zone in the anhydrite are uncommon; in the latter case, they are homogeneously filled and yield very constant microthermometric data (primary zonal fluid inclusions: Sobolev & Kostyuk 1975).

Most fluid inclusions in the clearer parts of the crystals have the regular shape described above and show no evidence for necking or reequilibration. However, fluid inclusions of variable size and irregular shape can occur in the outer part of crystals and some of these show evidence of necking. All analytical data presented below are for inclusions with a regular shape in clear sections of anhydrite crystals.

METASTABILITY.

Many monophase, two-phase and three-phase inclusions exhibited metastable behavior in the range -120° to +550°C. In most monophase liquid-filled inclusions distributed among two-phase inclusions, a vapor bubble nucleated on cooling. Conversely, some type L inclusions did not nucleate a vapor bubble on cooling after homogenization. Some primary two-phase inclusions (filled with a liquid and either a vapor or a halite cube), located among saturated three-phase inclusions, showed metastable behavior and nucleated a gas or a halite cube on abrupt cooling (Fig. 3f). Some two-phase liquid + vapor-filled inclusions were supersaturated: they contained hydrohalite at low temperatures and never nucleated halite in the course of normal cooling-heating cycles. During warming of frozen type V and L inclusions, the first drop of liquid appeared at around -21°C and reproducible melting points of ice were measured. Liquid-dominant two-phase inclusions

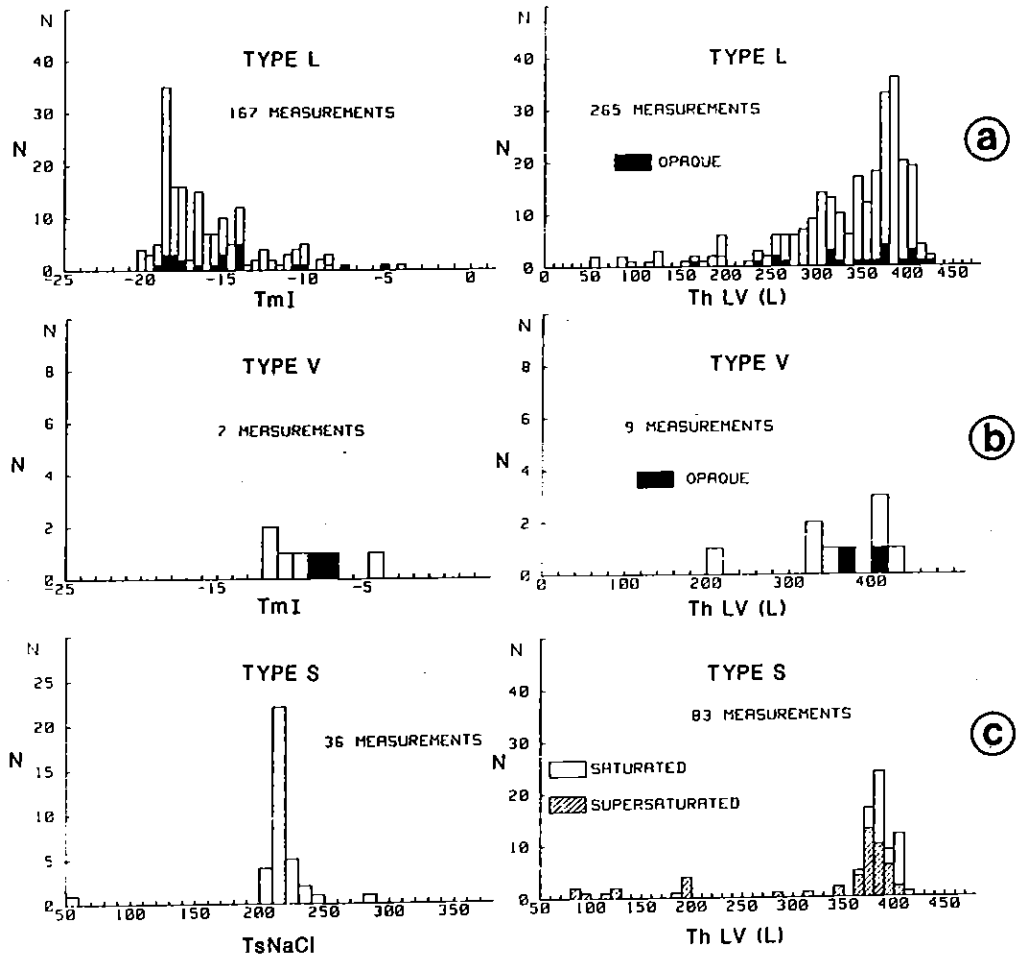

FIG. 4 : Histograms of the microthermometric measurements (°C) obtained on 16 anhydrite crystals from level 1085 cm. (a) type L, (b) type V and (c) type S inclusions. TmI: melting point of ice; Th LV: homogenization temperature (L: to liquid; V: to vapor); TsNaCl: temperature of disappearance of halite. N: number of measurements.

however also exhibited a metastable behavior during low-temperature runs. Highly birefringent yellow, green and uncolored salt hydrates were randomly formed. Up to three distinct salt-hydrates were seen to melt successively in a given inclusion. These salt-hydrates have not been identified.

ANALYTICAL DATA.

The microthermometric data obtained mainly on primary type L, V and S inclusions are shown in Figure 4.

Type L inclusions. At room temperature, these contain a liquid occupying at least 50% of the inclusion volume. Frequency distribution of the melting points of ice (TmI) and homogenization temperatures (Th LV(L)) are skewed. TmI values are between -4.4° and -20.4°C, with a marked mode of -18.5°C. Most measurements are in the range -18.5° - -4.4°C (Fig. 4a). Inclusions homogenized to liquid between 55° and 420°C with a mode of around 390°C. Secondary type L inclusions were not studied systematically. Most such small inclusions homogenized below 100°C.

Type V inclusions . At room temperature, these contain a liquid occupying at least 50% of the inclusion volume.TmI values in 7 inclusions are between - 12.0° and - 5.0°C and homogenisation temperatures from 9 inclusions are in the range 324° to 430°C (Fig. 4b). However, due to the difficulty in observing the disappearance of the vapor bubble, the precision of the homogenization measurements is very poor.

Type S inclusions. At room temperature, these contain a halite cube, liquid and vapor. All but one of the 36 inclusions analysed contained a halite cube occupying about 30 to 40 % of the inclusion and yielded Ts values in the range 201° to 283°C. Supersaturated type S inclusions contain no NaCl cube but nucleated hydrohalite on cooling. One initially supersaturated inclusion nucleated a small halite cube which dissolved at 50°C. Saturated and supersaturated type S inclusions always homogenized to liquid through

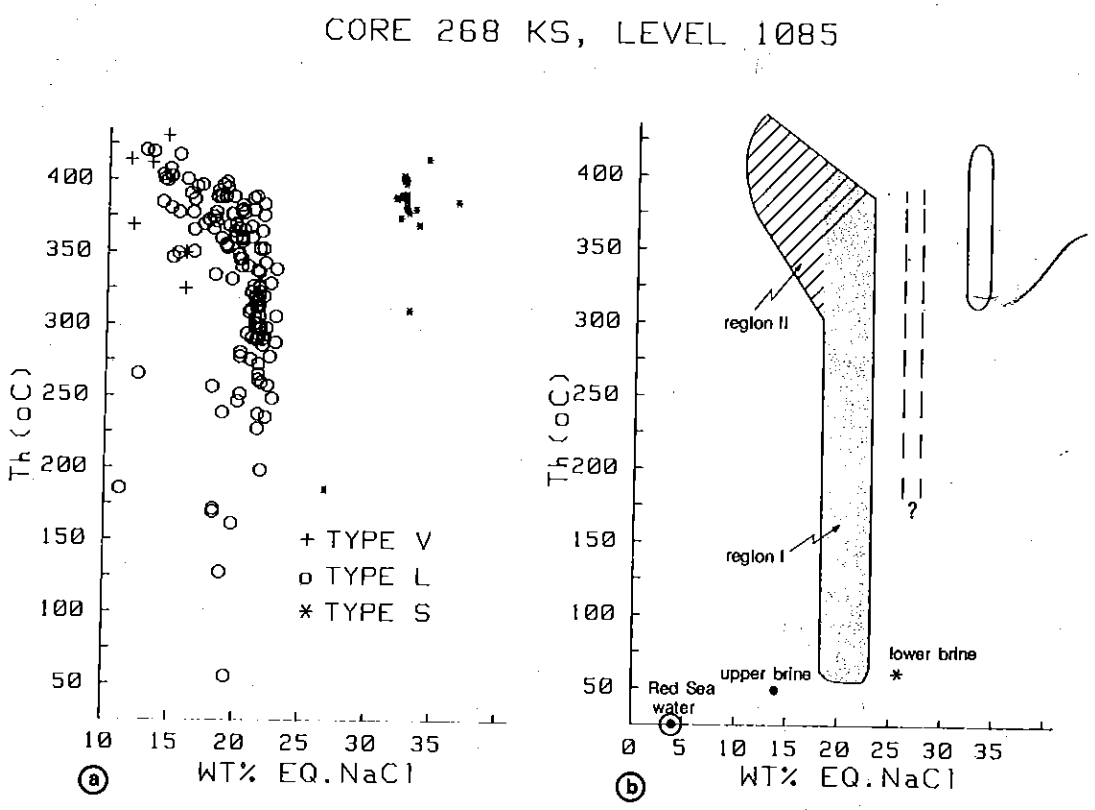

FIG. 5 : (a) Homogenization temperatures for type L and S inclusions as a function of salt content (Xw in wt.% eq. NaCl, after Potter et al. 1978, 1977). (182 inclusions from 16 crystals).
(b) Summary of Th-Xw data: all the type L and V inclusions with Xw< 23 wt% eq. NaCl are grouped in two distinct regions, the limits of which become unclear at high temperature. The projected field of type S inclusions is shown on the right; the datched lines mark the projected field inferred for supersaturated inclusions (see text).

disappearance of the vapor bubble. Homogenization temperatures for saturated inclusions are in the range 185° to 415°C, with most values above 340°C (Fig.4c). Th values in supersaturated inclusions are in the range 84° to 404°C, with a larger number of lower temperatures than for NaCl-saturated inclusions (Fig.4c).

THE H_2O-NaCl SYSTEM AS AN ANALOG.

The fluids in primary and secondary inclusions in anhydrite are complex Na-Ca-Fe-Zn...-Cl-SO_4 brines, because the fluids are saturated with respect to $CaSO_4$ and precipitated oxides and sulfides. Numerous salt-hydrates nucleated in type L inclusions during low temperature "cycling" experiments. NaCl is certainly the dominant salt in solution. The first drop of liquid always appeared close to the eutectic point of the system H_2O-NaCl (-20.8°C: Potter et al. 1978). A halite cube formed in some supersaturated inclusions. The lower brine, which is representative of the hydrothermal brine, contains ≈ 15.6 wt.% Na^+ and only 0.5 wt. % Ca^{2+} and 80 ppm Fe^{2+} (Brewer et al. 1969, Hartmann 1985). TmI values in type L and V inclusions therefore were interpreted in terms of eq. NaCl content (Potter et al. 1978). The dissolution of halite was determined from the data by Potter et al. (1977). Two-phase field boundaries for the H_2O-NaCl system are from the experimental studies of Khaibullin & Borisov (1966) and Parisod & Plattner (1981). Molar volumes are from Khaibullin & Borisov (1966) along the two-phase boundaries, and from Zhang & Frantz (1987) and Pitzer et al. (1984) in the liquid stability field.

PRESSURE CONDITIONS IN THE SEDIMENT.

The sediments in the Deep are unconsolidated muds which are occasionnally indurated due to hydrothermal metamorphism (Bäcker & Richter 1973). The SW Basin sediments are crosscut by numerous sulfate and

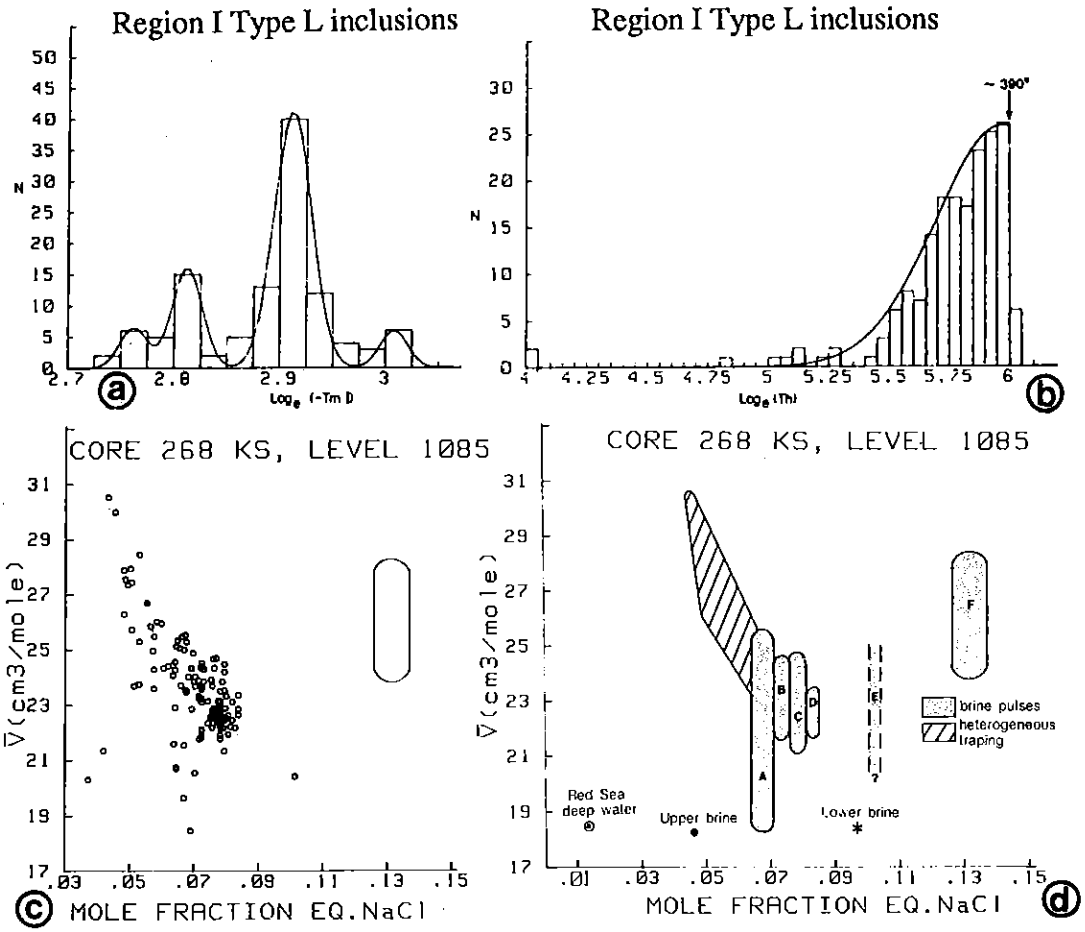

FIG. 6 : Region I type L inclusions. (a): Interpreted histogram of the TmI values in terms of four populations with lognormal distribution.

(b) Discontinuous distribution of the Th values, which approximates twice a lognormal law below ≈390°C and zero above 390°C.

(c) Variations of the molar volume (V) of all type L inclusions as a function of mole fraction eq. NaCl (derived from the TmI values as in Fig. 5; 176 inclusions from 16 crystals). The molar volumes of type L inclusions are calculated using a fit of the V-T-X experimental data for the two-phase field boundaries in the H_2O-NaCl system of Khaibullin & Borisov (1966; regression program by M. Danis, C.R.P.G.). The field of type S inclusions is approximated based on experimental data of Gehrig et al. (1983).

(d) Summary of V-X relations. Dotted elongate area: constant composition-variable volume trends corresponding to brine pulses injected at decreasing temperatures on the sea-floor and evolving without mixing, in particular with the lower brine (A to D: pulses corresponding to the four populations in region I type L inclusions (Fig. 6a); E: projection field inferred for supersaturated inclusions: see text; F: pulse defined by type S inclusions). Hatched area: inclusions resulting from L/V heterogeneous trapping (see also Fig. 9).

sulfide-bearing veinlets, indicating that they are consolidated enough to fracture. However it is unlikely that the strength of such a sediment has exceeded one bar. Fluids in Atlantis II Deep anhydrites were therefore probably trapped under hydrostatic pressure conditions.

Microfaunal studies of Red Sea sediments show that the level of the Red Sea has not varied significantly since the beginning of the Holocene (Bourdillon & Gideiri 1983). Hydrothermal processes in the SW Basin of the Deep are no older than the Holocene (Bäcker and Richter 1973), therefore this is the maximum age of the crystals. The hydrostatic pressure at which the fluids have been trapped in anhydrites can be estimated at 223 ± 2 bars, taking into account the present column of water and sediments over the veins. The main cause of error in pressure determination arises from the fact that the temperature and hence the density of the lower and upper brines at the time the crystal formed is unknown (Table 1).

Data on geothermal systems show that brines can be superheated, i.e. they can exist at a temperature in excess of the boiling temperature at the pressure considered (Elder 1981). This results from the metastable suppression of vapor nucleation. It cannot be excluded therefore, that the crystals have trapped small amounts of superheated brine. The fluid inclusions therefore may indicate a minimum trapping pressure exceeding by a few bars the hydrostatic value.

INTERPRETATION OF FLUID INCLUSION DATA.

Figure 5a shows homogenization temperatures (Th) versus salt content for 182 type L, V and S inclusions. On the Th-Xw plane, type L and V inclusion fluids plot on a linear trend distinct from type S inclusion fluids. The magnitude of the salinity gap separating type L and V inclusions from type S inclusions is exaggerated due to metastability, as mentioned previously. Halite fails to nucleate at low temperatures from inclusion fluids with a

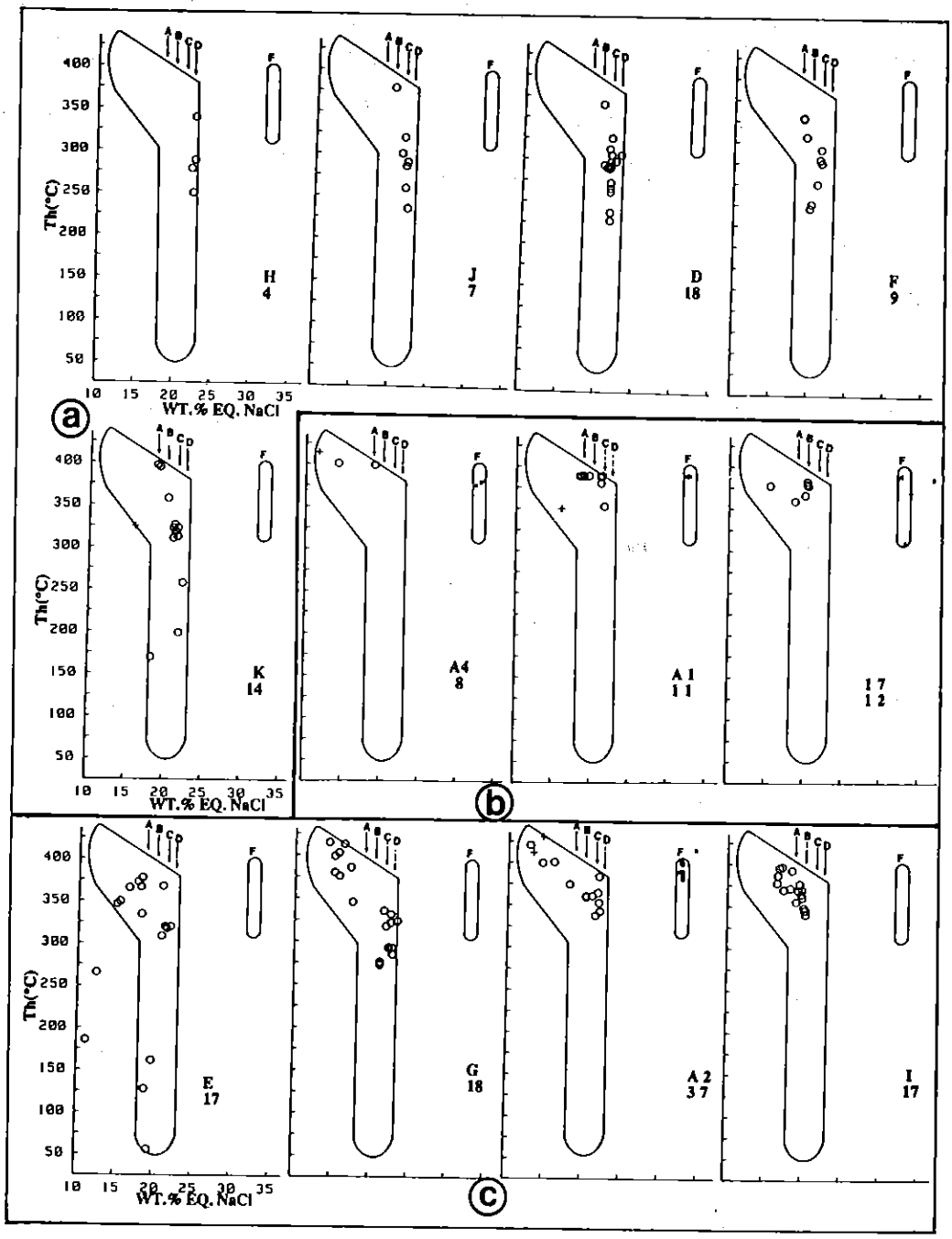

FIG. 7 : Th-Xw plot of inclusions measured in individual anhydrite crystals (the name of the crystal and the number of data points are indicated in the lower right hand side). Type L and S inclusions define three main fluid inclusion patterns: (a) isochemical cooling; (b) isochemical isothermal process; (c) overprint of heterogeneous trapping on the previous patterns (see text). Numbers 1 to 6 are individual inclusions discussed in the text (Table 2). A to D and F are the brine pulses identified in Fig. 6d.

salinity close to saturation at 25°C, i.e. ≈ 23 wt.% NaCl (cf. Yajima & Touray 1967). Although only one NaCl-saturated inclusion yielded a salinity of 27 wt.% eq. NaCl, it is likely that a large number of inclusions exhibiting metastable behavior have similar salinities. On Figure 5b, type S inclusions with metastable behavior are therefore shown on a roughly vertical trend centered about 27 wt.% NaCl.

The region within which type L and V inclusions plot can be subdivided into two parts (Fig. 5b). Type L inclusions of 18 - 23 salinity outline a vertical trend (region I) parallel to that defined by saturated and supersaturated inclusions. Region II includes type V inclusions and the less saline type L inclusions. Two distinct processes are recorded by region I and region II inclusions, which are discussed separately hereafter.

On Figure 5b, all type L inclusions with $18 < Xw < 23$ wt.% are grouped in a single population. However, the histogram of the TmI values of region I type L inclusions consists of four populations with lognormal distribution (Fig. 6a). In contrast, the Th values of these inclusions present an unimodal distribution, with very few values higher than the mode ≈ 390°C (Fig. 6b). Figure 6c shows that a larger scatter exists for all region I inclusions in a $\overline{V}$-X plot compared to a Th-Xw plot. Four vertical trends are outlined in the $\overline{V}$-X plot (trends IA to I D, Fig. 6d) which are parallel to those marked by saturated and supersaturated inclusions (trends IE and IF, Fig. 6d). These are equivalent to the four populations of inclusions identified within region I type L inclusions based on the TmI values (Fig. 6a). Trends A to F are vertical. It therefore implies that each brine pulse underwent cooling and did not mix on the seafloor, in particular with the lower brine (Fig. 6d). Individual anhydrite crystals in fact contain type L inclusions with a restricted salinity range. They yield the vertical Th-Xw trends identified based on the statistical analysis of all inclusions from 16 crystals (Fig. 7a). In conclusion, the trends shown in Figure 6d indicate that brine pulses progressively

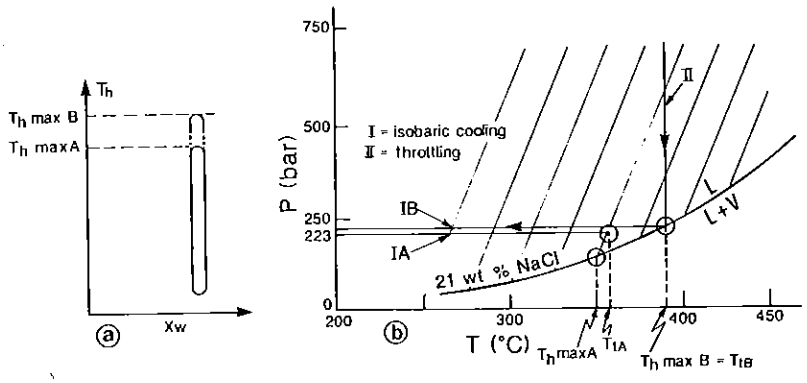

FIG. 8 : Brine influxes on the seafloor under conditions of boiling (path IA) and non boiling (path IB). (a) Schematic microthermometric signature on a Th-Xw plot. (b) Interpreted P-T trapping conditions of a 21 wt. NaCl brine pulse venting on the sea floor at a pressure of 223 bars (after Parisod & Plattner 1981). Brine venting in an unconsolidated sediment is necessarily isobaric (path I), which excludes throttling (path II). Tt A and Tt B are the trapping temperatures of the brine, in the liquid field and under boiling conditions, respectively.

enriched in salts were injected intermittently at the bottom of Atlantis II Deep and cooled without mixing.

It is possible to determine the P-T conditions of trapping on the seafloor for inclusions with a vertical Th-Xw trend at ≈ 21 eq.wt. NaCl at a hydrostatic pressure of 223 bars (Fig. 8a). Figure 8b shows that, at a pressure of 223 bars, the maximum homogenization temperatures for inclusions of a given composition is fixed by the temperature of the two-phase boundary (Bischoff et al. 1986). A 21 wt.% NaCl solution undergoes phase separation at ≈ 390°C, close to maximum values recorded by inclusions of that composition in level 1085 cm anhydrites (Fig.5a).

Region II contains type L and V inclusions with salinities ≈<19 wt.% eq. NaCl. Th values negatively correlate with salt-contents (Fig. 5a). This trend is obvious in some individual crystals (Fig. 7c). Such a pattern is expected to characterize H_2O-NaCl inclusions which have trapped mechanical mixtures of immiscible liquid and vapor (e.g. Ramboz et al. 1982, Ramboz 1983). On a $\overline{V}$-X projection, the nearly pure H_2O vapor (point V) and the 21 wt.% NaCl brine (point L) coexisting at 390°C and 223 bars have been plotted (Fig. 9). The straight line (L-V) represents mechanical mixtures of the pure end-member phases. This plot shows that region II inclusions cannot contain mixtures of the pure end-members as they plot markedly below line L-V. More likely, region II inclusions contain mechanical mixtures of liquid L with a cooled condensed vapor at point C (Fig. 9). All type V inclusions have salinities >10 wt.% eq.NaCl which are far in excess of the salinity of the pure unmixed vapor at around 390°C and 223 bars (≈ 0.5 wt. % NaCl: Khaibullin & Borisov 1966; Pitzer & Pabalan 1986). Therefore, all type V inclusions are interpreted to have trapped a vapor and a significant fraction of brine. Some region II type L inclusions have both salinities and Th-values comparable to those of vapor-rich inclusions (Fig. 5a). Liquid-rich and vapor-rich inclusions plotting in the same portions of the Th-Xw plot must necessarily

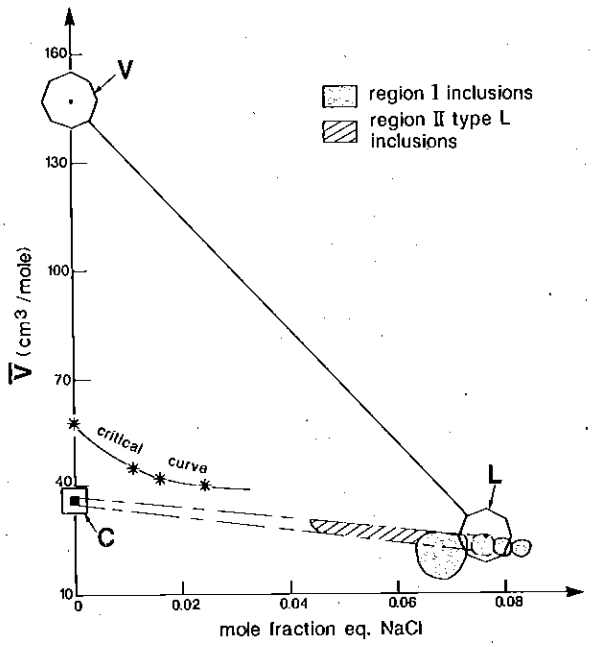

FIG. 9 : Interpretative diagram showing properties of inclusions resulting from L/V heterogeneous trapping. The hexagons represent coexisting liquid (L) and vapor (V) in the H_2O-NaCl system at 390°C and 223 bars (conditions fixed by inclusion 3, Table 2, and Fig. 10; data of Khaibullin & Borisov 1966). Mechanical mixtures of these phases will plot on a straight line. Region II type L inclusions (hatched area) probably represent mixtures of the cooled liquid and a cooled and/or condensed vapor (point C). Region II inclusions are close to the critical curve of the H_2O-NaCl system. Critical curve after Keenan et al. (1969) and Khaibullin & Borisov (1966).

have been trapped at near critical $\bar{V}$-X conditions. The mixing line L-C in fact is close to the critical curve of the H_2O-NaCl system (Fig. 9).

Figure 10a is a $\bar{V}$-Xw plot showing the five major "isochemical cooling" trends identified in Figure 6. The maximum Th in each trend has been outlined (points 1 to 5). Table 2 lists microthermometric data and interpreted composition-volume parameters of these five inclusions. Figure 10b shows the locations of these inclusions on a P-X projection in the H_2O-NaCl system as well as liquid+vapor-liquid boundaries at 380°, 400° and 420°C from Parisod & Plattner (1981). Within the error limits of the field boundaries and microthermometric measurements, the minimum trapping pressures of inclusions 3 and 5 are compatible with the calculated in situ pressure. Brine pulses with compositions of 21.3 and 32.6 wt.% eq. NaCl were undergoing phase separation on venting in the Atlantis II Deep sediment. By contrast, inclusions 2 and 4 respectively plot 30 and 100 bars below the pressure of 223 bars. Microthermometric data for the remainder of the crystal which hosts inclusion 2 (crystal I, Fig. 7c) suggest heterogeneous trapping, implying boiling. Type L inclusion 4 has the highest salinity around 23 wt.% eq. NaCl. The latter brine pulse was recorded only in crystal H (Fig. 7a), therefore the data required to prove boiling for that pulse are insufficient. Inclusion 1 fluid plots 18 bars above the calculated in situ pressure for the anhydrite veins. This probably implies that this inclusion contains a mechanical mixture of liquid and vapor (Ramboz 1983), consistent with its location close to the "heterogeneous trapping" trend (Figs. 5 & 6).

DISCUSSION

Boiling on and below the seafloor has long been invoked in the formation of certain ancient base metal deposits (Ridge 1973, Finlow-Bates & Large 1978, Spooner 1980, Anderson 1983). Fluids of variable salinities in present day active subaerial geothermal systems are known to result from

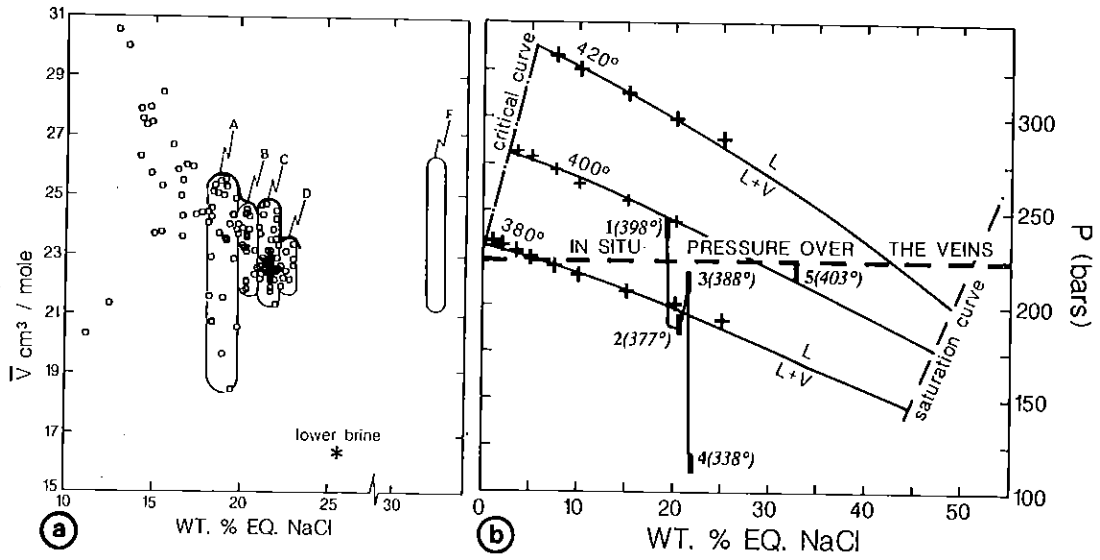

FIG. 10 : Estimated P-T-X conditions of boiling at the bottom of the Atlantis II Deep. (a) V-Xw plot of the type L, V and S inclusions with superimposed trends inferred for brine pulses (Fig. 6d). The highest V in each trend is outlined (inclusions 1 to 5).

(b) Comparison of the minimum trapping pressure of inclusions 1 to 5 (i.e., the internal pressure at Th) with the in situ pressure at the bottom of the Deep (Table 1). Microthermometric data for inclusions 1 to 5 are given in Table 2. Two phase boundaries at 380°, 400° and 420°C after Parisod & Plattner 1981; experimental points from Khaibullin & Borisov (1966). Critical and saturation curves after Keenan et al. (1969), Bischoff et al. (1986), Bischoff & Rosenbauer (1984) and Chou (1987).

different degrees of boiling at depth (e.g. Fournier 1981). Fluids enriched or depleted in chlorine relative to sea-water circulate in the oceanic crust (Jehl et al. 1977, Vanko1984, Dubois 1984, Dubois et al. 1984) or are discharged at vents and/or trapped in hydrothermal minerals on 23°N EPR (Cosens Gallinatti 1984), 21°N EPR (Le Bel & Oudin 1982, Von Damm et al. 1985), 13°N EPR (Michard et al. 1984), and on the Southern Juan de Fuca Ridge (Bischoff & Pitzer 1985). However, the Cl-content of the fluid alone does not provide any definite indication of boiling on or near the sea floor, as it is partly controlled by hydration processes and the formation of Fe-hydroxy chlorides during basalt-seawater interaction (Seyfried et al. 1986). Liquid-rich and vapor-rich inclusions coexisting in the same mineral have been seldom reported in oceanic settings (e.g., Spooner 1980).

Fluid inclusion data from Atlantis II Deep anhydrites provide direct evidence for boiling near the seafloor in the SW Basin. They therefore support previous conclusions based on hydrological observations that hydrothermal discharge in Atlantis II Deep, being accomplished by a vapor phase, is of geyser-type (Ross 1972, Schoell & Hartmann 1978). Complementary geochemical studies on core 268 KS ascertain that gold precipitates ≈ 1 m above the boiling zone (Oudin 1987). The history of the brines can be reconstructed as follows. As boiling of the ≈19 wt.% eq. NaCl fluid proceeded at depth, liquids progressively enriched in salt ascended towards the seafloor under the P-T conditions defined by boiling curves. Data from type L and S inclusions suggest that these liquids were separated from initially coexisting vapor (open-system boiling) and were injected intermittently. The brine influxes in the Deep were probably controlled by tectonics.

At 21°N E.P.R., it is now established that a magma chamber exists 1 to 4 km deep below the vents (e. g. McClain et al. 1985) and that the hydrothermal fluid has acquired its chemical characters near the top of the

magma chamber at around 400°C and 400 bars (e.g., Bischoff 1980, Seyfried & Janecky 1985). In contrast, the nature of the seafloor underlying the Atlantis II Deep is uncertain (Le Quentrec et al. 1987). The fact that hydrothermal solutions discharged at the Deep bottom have undergone long duration boiling implies that the deep fluid reservoir has a limited volume. Besides, the near isothermal boiling observed in surface requires a large heat supply and hence probably a magma in the source area. The P-T conditions in the reservoir were, at least transiently, below critical (i.e., ≈540°C and 700 bars for a 19 wt% NaCl solution: Urusova 1974). The enthalpy of the fluid in the reservoir can be estimated around 1950 J g^{-1} (Hass 1976, Bischoff & Pitzer 1985), assuming isenthalpic boiling during ascent and using enthalpy-salinity projections of Fournier (1981).

Hedenquist & Henley (1985) suggested that "...boiling of a hydrothermal fluid flowing rapidly through a fracture may not always be preserved in fluid inclusions". The vapour resulting from fluid boiling at low pressure (P < 200 bars) is in fact rarely trapped in inclusions (Ramboz et al 1982, Weisbrod 1984, Aissa et al. 1987). In the Atlantis II geothermal system, evidence for boiling is provided by heterogeneous trapping of liquid and vapor in early-formed anhydrite. The histogram of Th values of region I type L inclusions resulting from homogeneous trapping is skewed, with a marked discontinuity near the temperature of the boiling; the distribution equals twice a lognormal law below 390°C and zero above 390°C (Fig. 6b). If the liquids trapped in crystals under boiling conditions are perfectly separated from the vapor and there is no superheating, the probability of trapping inclusions yielding homogenization temperatures higher than the boiling temperature is zero. Boiling conditions, therefore, could have been reconstructed even in the absence of L/V heterogeneous trapping.

Present data allow an estimate of the minimum temperature which has prevailed in SW Basin sediments. Inclusion 6 in Figure 10a implies a

No	TmI (°C) (±0.2)	Ts (°C) (±2)	Th(°C) (±2)	XNaCl wt%	$\bar{V}$ (cm^3/mol)	Trapping tempe-rature (°C) at 223 bar
1	-15.3	-	398	19.04	25.6	-[1]
2	-17	-	377	20.43	24.3	379[3]
3	-18.2	-	388	21.35	24.7	388[2]
4	-20.4	-	338	22.94	23.4	345[3]
5	-	213	403	32.56.	25.6[4]	403[2]
6	-15.8	-	55	19.4	18.5[5]	64[3], 69[5]

1: inclusion resulting from heterogeneous L/V trapping; 2 : inclusion fluid on the two-phase field boundary at 223 bars; 3 : pressure correction after Zhang & Frantz (1987); 4 : after Gehrig et al. (1983); 5 : after Pitzer et al.(1984)

Table 2 : Microthermometric data and interpreted composition, volume and trapping temperature of the six inclusions shown in Figure 10a (sources of experimental data as in Fig. 10).

minimum trapping temperature of 69°C for the fluids in level 1085 anhydrites (Table 2). This temperature is 7°C higher than the maximum value measured in the Deep sediments (Erickson & Simmons 1969). However, these measurements were at no depths greater than 3 m below the seafloor whereas the value of 69°C is for a depth of 11 m.

All salinity variations recorded by primary inclusions in anhydrite can be attributed either to variable degrees of boiling at depth or to heterogeneous trapping. In situ mixing with the lower brine is unlikely as it is not supported by a relevant mixing trend (Figs. 6c & 6d); the linear trends of constant salinity and variable molar volumes identified in the crystals (Figs. 5 & 6) correspond to brine pulses undergoing "isochemical cooling". Anhydrite has a prograde solubility above 250°C in solutions with more than ≈15 wt.% NaCl (Blount & Dickson 1973), and therefore it can precipitate from a cooling, high temperature saline solution. However, cooling is not the main mechanism in the formation of epigenetic anhydrites, as 8 of the crystals examined had a very narrow range in both homogenization temperatures and salinity for both type L inclusions in region I and type S inclusions (Fig. 7b). In the growth zones of these crystals, type L and S inclusions with homogeneous morphologies and fillings yielded well constrained microthermometric data. Calculations at and below 350°C show that boiling does not favor anhydrite precipitation. Anhydrite is more likely to precipate last from boiling hydrothermal solutions (Drummond & Ohmoto 1985). This in in contrast to the nature of the crystals and fluid inclusions from the cores to peripheries. These suggest that, as the fluids became more saline after prolonged sub-seafloor boiling, they became less saturated with respect to anhydrite. Anhydrite crystals initially grew too quickly for a vapor phase to separate; the fluid was trapped in elongate tubular cavities with disequilibrium morphologies. Saline residual brines were finally trapped in 500 μm-wide crystal overgrowths.

Hydrothermal vein minerals in the SW Basin are thought to have formed mainly by precipitation from hydrothermal brines, with only limited reaction with the sediment (Hackett & Bischoff 1973, Zierenberg & Shanks 1983, Pottorf & Barnes 1983). The Fe^{2+}-bearing minerals, ilvaite and magnetite formed after hematite (mushketovite) , which precipitated around the vents are considered to have formed by incorporation of the Fe^{2+} from the fluid, exclusive of any in situ reduction of ferric iron from the sediment. A careful examination of epigenetic veins in SW Basin cores shows that both magnetite and ilvaite occur under two distinctive mineralogical forms (Oudin et al. 1984, Oudin unpubl.data). Euhedral crystals are apparently precipitated directly from the fluid whereas poikilitic aggregates are suggestive of replacement (see Figs. 8c and 10a in Oudin et al. 1984).

In the SW Basin sediments, lateral mineralogical changes around the vents include: (1) the development of ferrous silicates and oxides; (2) the progressive change from dioctahedral nontronite to trioctahedral chamosite or ferroan saponite (Pottorf 1980, Zierenberg & Shanks 1983); (3) the appearance of minor ilvaite (Pottorf 1980, Oudin et al. 1984); (4) a progressive transition from goethite to hematite to magnetite towards the SW Basin (Bischoff 1969, Hackett & Bischoff 1973); (5) the presence near the vents of mushketovite (Oudin et al. 1984). Badaut et al. (1985) also described a trioctahedral Fe^{2+}-bearing clay of minnesotaite type associated with sulfides in the upper part of a SW Basin core, above the sulfate-enriched layer. By analogy with contact metamorphic aureoles (Thompson 1972), the bulk mineralogical changes marking the thermal metamorphism of SW Basin sediment around the vents are best explained in terms of dehydration, (de)carbonation and/or sulfidation/sulfatation reactions. The latter are initiated by the diffusion of hydrothermal H_2S through the sediment. Anhydrite and Fe^{2+}-bearing minerals with replacement textures around brine

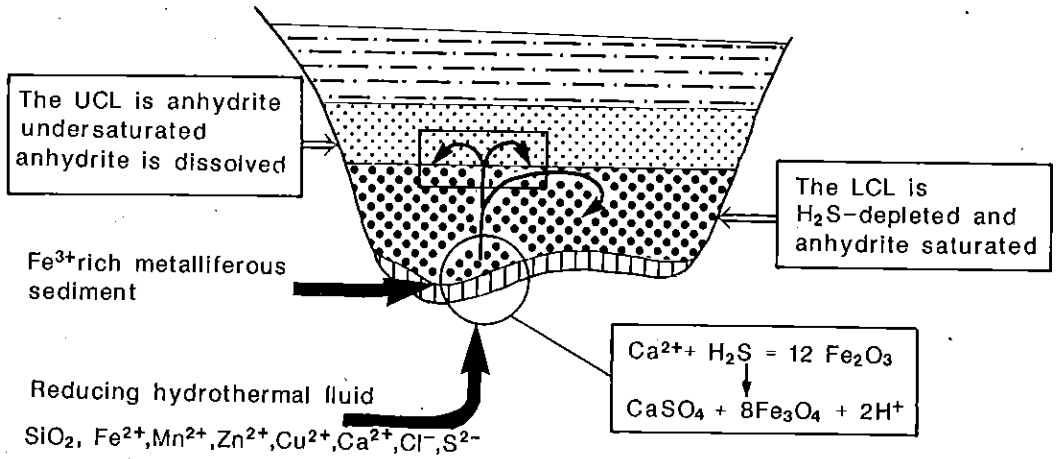

FIG. 11 : Schematic representation of anhydrite deposition in Atlantis II Deep sediments as a result of redox reactions between the hydrothermal fluid and the Fe^{3+}-bearing sediment (modified after Hartmann 1973 and Cole 1983). The distribution of sulfates and sulfides in the lower (LCL) and upper (UCL) brines is also shown (after Hartmann 1985, Zierenberg & Shanks 1986 and unpublished calculations by Monnin).

vents are probably the end products of redox reactions. An anhydrite-magnetite-forming reaction can be written as:

$$Ca^{2+} + H_2S + 12\,Fe_2O_3 \rightarrow CaSO_4 + 8\,Fe_3O_4 + 2H^+ \qquad (1)$$

The formation of magnetite after hematite following that reaction implies a volume reduction by ≈25% of the solids which can account for the porous aspect of the mushketovite. Anhydrite formation is induced by the contrast in redox potential between the hydrothermal fluid and the sediment. Reaction (1) explains why the earlier sulfide-enriched fluid became catastrophically saturated with respect to anhydrite on venting through the sediment, whereas the residual, salt-enriched oxidized brine did not. Hartmann (1985) noted that, during the period of increasing hydrothermal activity from 1966 to 1977, the dissolved sulfate of the upper brine increased compared to the theoretical value based on conservative mixing of the lower brine with Red Sea water. Because more suspended sulfides were supplied to the lower brine, Hartmann (1985) proposed that the excess sulfate in the upper brine resulted from the oxidation of lower brine sulfides in the transition zone at the contact with the upper brine. Zierenberg & Shanks (1986) showed, however, that the calculated isotopic composition of the excess sulfate in the upper brine was incompatible with the later origin, and favored the presence of particulate anhydrite in the lower brine itself. Zierenberg & Shanks (1986) therefore suggested that the excess sulfate was supplied through the interface to the upper brine and subsequently was redissolved. These latter results support our interpretation that the H_2S from the hydrothermal fluid venting in Atlantis II Deep was oxidized through reaction with the sediment and now occurs as sulfate in the lower brine (Fig. 11).

In contrast to the anhydrite crystals from level 1085 in core 268 KS, very few fluid inclusions have been observed in epigenetic anhydrites from other SW Basin cores. Epigenetic anhydrite crystals from the cores described by Zierenberg & Shanks (1983) are fibrous in comparison to the essentially

euhedral anhydrites from level 1085 (Oudin et al. 1984). They contain slender fluid inclusions (<5 μm), with a small to non-existent vapor bubble. The anhydrite crystals from core 268 KS are thought to be very recent for the following reasons. The core 268 KS was collected along a presently hydrothermally active transform fault in the SW Basin (Fig. 1c). Indeed, many authors have stated that hydrothermal activity in the Red Sea is related to transform fault activity (Bäcker et al. 1975, Bignell 1975, Bertin et al. 1979, Pautot, 1983). The episodic nature of activity inferred from the anhydrite crystals is in good agreement with the recorded recent fluctuations of the hydrothermal activity (Hartmann 1980). The average temperature of brine discharge implied by fluid inclusions in level 1085 anhydrites is consistent with that obtained from revised estimations of the exchanges of heat and mass in Atlantis II Deep for the past 15 years (Ramboz & Danis 1987; submitted).

CONCLUSIONS

Epigenetic anhydrites from level 1085 cm in core 268KS have trapped liquid-rich inclusions which either contain mechanical mixtures of liquid and vapor or result from homogeneous trapping. These are distinguished using composition-volume projections (Ramboz 1983). Anhydrite was precipitated from successive boiling brine pulses with salinities progressively increasing from 19 to 32 wt.% eq. NaCl. The maximum homogenization temperatures of the pure liquids trapped in anhydrite are in the range 390°-403°C and are compatible with boiling of the brines on the seafloor at a hydrostatic pressure fixed by overlying water and sediment column (i.e., 223 bars). This study confirms previous conclusions based on hydrological studies that the hydrothermal activity in the Atlantis II Deep is of geyser-type (Ross 1972, Schoell and Hartmann 1978). The vapor was already cooled and partly mixed

with the coexisting liquid at the time of trapping. The present data set therefore supports the suggestion by Bischoff and Pitzer (1985) that the low salinity fluids (around 1.9 wt.% NaCl) collected from differents vents at 11°N-13°N EPR represent fluids which underwent phase separation, then cooled and/or mixed during ascent. Finally, the present data set shows that boiling of natural complex brines is best represented by liquid-rich inclusions referring to the system H_2O-NaCl (Haas 1971, Bischoff et al. 1986). The distribution of Th values of type L inclusions resulting from homogeneous trapping is diagnostic of unmixing and the P-T boiling conditions could therefore have been reconstructed even in the absence of L/V heterogeneous trapping.

Anhydrite crystals are polygenic. (1) Crystal cores grew from less saline, sulfide-bearing fluids. During this process, mechanical mixtures of the coexisting liquid and vapor were trapped in tubular fluid inclusions with disequilibrium morphologies.(2) In contrast, later crystal growth was from the residual solutions which had boiled longer. Liquids devoid of vapor were trapped in small isometric cavities. The formation mechanism which best accounts for the contrasting nature of the crystals and their fluid inclusions from cores to peripheries is as follows. The fluid reached anhydrite saturation on venting on the sea floor because the hydrothermal sulfides were rapidly oxidized to sulfates. This reaction was coupled with the reduction of iron from Fe^{III}-bearing oxides and silicates in the sediment. Anhydrite, like mushketovite and part of ilvaite, is considered to be the product of intereaction of the fluid and the sediment.

The anhydrites were probably formed recently from brines discharged at about 400°C along ≈1 km length of the active transform fault crosscutting the SW Basin (Bäcker et al. 1975, Cole 1983; Fig. 1c). For the past 15 years, the mass discharge flow rate in the Atlantis II Deep has been around 278 kg s^{-1}. By comparison at 21°N EPR, the vents along 1km of the ridge have yielded

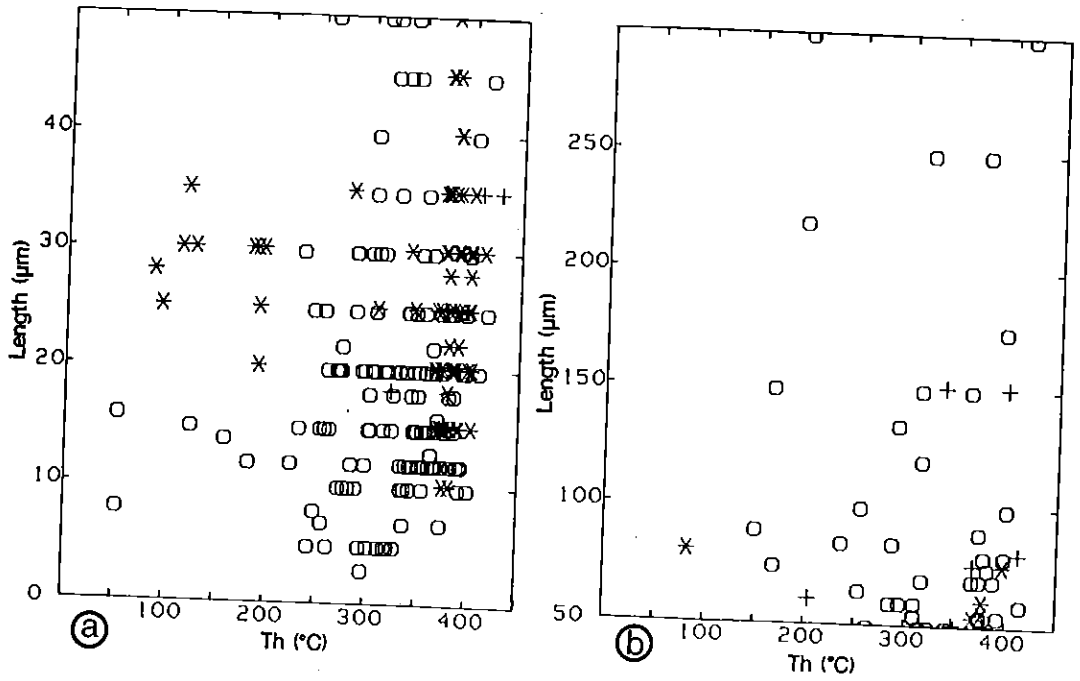

FIG. 12 : Variations of homogenization temperatures (Th) versus inclusion length (mm) for type L, V and S inclusions (symbols as in Fig. 3).(a) 0-50 µm long inclusions. (b) 50-350 µm long inclusions. Symbols as in Fig. 5a.

an instantaneous outflow of 150 ± 60 kg s^{-1}, with vent temperatures ≤358°C (Converse et al. 1984).

The fact that the brines in the Atlantis II Deep discharge at higer temperature and undergo near isothermal boiling implies that there is a fluid reservoir with a limited volume at depth, which is heated by a magma. Maximum discharge temperatures on the seafloor are fixed by unmixing conditions. These increase with increase in pressure or depth and salinity. Although the hydrostatic pressure is lower, the hydrothermal fluid in Atlantis II Deep discharges at a higher temperature than the one at 21°N, because it is more than 4 times richer in salt.

APPENDIX

Significance of fluid inclusion data in anhydrite

Anhydrite, like all soft, cleaved minerals, is susceptible to stretching (Larson et al. 1973). Fluid inclusions in anhydrite often yield high and scattered Th. Similar distributions in barite have been attributed to non-systematic behavior of the inclusions during heating runs (Roedder 1972). Many analytical problems were encountered on studying fluid inclusions in the Red Sea anhydrites. Inclusions often burst prior to homogenizing. Inclusions that changed shape by precipitating anhydrite on heating were observed once. Nevertheless, we believe that stretching problems have been minimized in this study. 80% of the phase changes were measured twice. About 5% of the microthermometric measurements were also repeated after the samples had been stored for one year at room temperature. As reprodicible measurements were determined, the crystals had therefore remained unchanged although anhydrite in contact with the ≈ 6 molal NaCl solution from the inclusions is unstable and should transform to gypsum at room temperature (Marshall & Slusher 1968). Figure 12 shows that inclusions in anhydrite present high and scattered Th values, whatever their

size. This implies that stretching alone cannot account for all the high Th values obtained because, in the latter case, the largest inclusions should exhibit the highest Th values (Bodnar & Bethke 1984).

Re-equilibration of the Red Sea anhydrites can also complicate the interpretation of the microthermometric data. Brine venting has been active from the Holocene to the present in the SW Basin of Atlantis II Deep. Anhydrite crystals in sediments from that part of the basin may therefore have been repeatedly reheated, even if they are very young (e.g. Cole 1983). Both the tubular inclusions with round ends in the cores of the anhydrites and the more isometric type S inclusions with sharp angles near the crystal margins are sensitive to re-equilibration (Gratier & Jenatton 1984, Doukhan & Trépied 1985). Type L and V inclusions often root on solid microinclusions; such associations may act as defects in the lattice along which re-equilibration processes are initiated (Wilkins & Sverjensky 1977). Nevertheless, the shape of the inclusions in the Red Sea anhydrites indicate that the crystals have not been re-equilibrated at the temperature of the surrounding sediments. Besides, the anhydrite has trapped boiling fluids, i.e. fluids on the liquid-vapour cexistence curve. The trapping pressure indicated by fluid inclusions is consistent with the depth of the crystals beneath sea level.

ACKNOWLEGMENT

We wish to thank H.E.Z. Mustapha and Z.A. Nawab, respectively Secretary General and Deputy of the Saudi Sudanese Red Sea Joint Commission, for allowing us to study the core sample. The manuscript was improved thanks to the many suggestions from F. Albarède, M. Arnold, J. J. Royer, A. Mezgache, S.M.F. Sheppard and A. Weisbrod. Reviews by T. J. B. Barrett, R. Linne and an anonymous person were greatly appreciated. We wish to thank V. Embareck, J. Gorau, A. Legros for technical assistance in

REFERENCES

Aissa, M. Weisbrod, A. & Marignac, C. (1987): Caractéristiques chimiques et thermodynamiques des circulations hydrothermales du site d'Echassières. In Géologie Profonde de la France (M. Cuney and A. Autran, eds.). Tome 1, p. 241-271.

Bäcker, H. & Richter, H. (1973): Die Rezente Hydrothermal-Sedimentäre Lagerstätte Atlantis II-Tief im Roten Meer. Geol. Rundsch. 3, 697-741.

____ , Lange, K. & Richter, H. (1975): Morphology of the Red Sea central graben between Subair Islands and Abul Kizzan. Geol. Jahrb. 13, 79-123.

____ & ____ (1987): Recent hydrothermal metal accumulation, products and conditions of formation . In Marine Minerals (P.G. Teleki.et al., eds.). Reidel Publishing Company, p. 317-337.

Badaut, D. Besson, G. Decarreau, A. & Rautureau, R. (1985): Occurrence of a ferrous, trioctahedral smectite in recent sediments of Atlantis II Deep, Red Sea. Clay Minerals. 20, 389-404.

Bertin, J. Pedeux, J.P. & Magenham, J.C. (1979): Contribution de la géophysique et de l'océanographie physique à la recherche et à l'exploration des boues métallifères de la Mer Rouge. In Ressources Minérales Sous-Marines. Documents B.R.G.M. 7, 339-366.

Bignell, R.D. (1975): Timing, distribution and origin of submarine mineralization in the Red Sea . Trans. Inst. Mining. Metall. 84, 1-6.

Bischoff, J.L. (1969): Goethite-hematite stability relations with relevance to sea water and the Red Sea brine system. In Hot Brines and Recent Heavy Metal Deposits in the Red Sea (E.T. Degens and R.A. Ross eds.). Springer-Verlag, Berlin, 402-406.

_____ (1980) : Geothermal system at 21°N, East Pacific Rise : physical limits on geothermal fluid and role of adiabatic expansion. Science 207, 1465-1469.

_____ & Rosenbauer, R.J. (1984): The critical point and two-phase boundary of seawater, 200-500°C. Earth Planet. Sci. Lett. 68, 172-180.

_____ & Pitzer, K.S. (1985): Phase relations and adiabats in boiling seafloor geothermal systems. Earth Planet. Sci. Lett. 75, 327-338.

——— Rosenbauer, R.J. & Pitzer, K.S. (1986): The system H_2O-NaCl : Relations of vapor-liquid near the critical temperature of water and vapor-liquid-halite from 300° to 500°C. Geochim. Cosmochim. Acta 50, 1437-1444.

Blanc, G. (1987): Géochimie de la fosse Atlantis II (Mer Rouge): Evolution spatio-temporelle et rôle de l'hydrothermalisme. Ph. Thesis, Univ. Pierre et Marie Curie, Paris France.

Blount, C.W. & Dickson, F.W. (1973): Gypsum-anhydrite equilibria in systems $CaSO_4$-H_2O and $CaSO_4$-NaCl -H_2O. Amer. Mineral. 58, 323-331.

Bodnar, R.J. & Bethke, P.M. (1984): Systematics of stretching of fluid inclusions I : Fluorite and sphalerite at 1 atmosphere confining pressure. Econ. Geol. 79, 141-161.

Bourdillon, C. & Gideiri, V.A. (1983): Etude micropaléontologique de deux carottes prélevées dans la fosse Atlantis II (Mer Rouge): âge de la mise en place et milieu de dépôt des boues métallifères. C. R. Acad. Sci., Paris 296, 1271-1274.

Brewer, P.G. & Spencer, D.W. (1969): A note on the chemical composition of the Red Sea brines. In Hot brines and Recent Heavy Metal Deposits in the Red Sea. (E.T. Degens and D.A. Ross, eds). Springer-Verlag, Berlin, p. 174-179.

———, Densmore, C.D. Munns, R. & Stanley, R.J. (1969): Hydrography of the Red Sea brines. In Hot brines and Recent Heavy Metal Deposits in the Red Sea (E.T. Degens and D.A. Ross, eds). Springer-Verlag, Berlin, p. 138-147.

Chou, I.-Ming (1987): Phase relation in the system NaCl-KCl-H_2O: III: Solubilities of halite in vapor-saturated liquids above 445°C and redetermination of phase equilibrium properties to 1000°C and 1500 bars. Geochim. Cosmochim. Acta 51, 1965-1975.

Cole, T.G. (1983): Oxygen isotope geothermometry and origin of smectites in the Atlantis II Deep, Red Sea. Earth. Planet. Sci. Lett. 66, 166-176.

Converse, D.R. Holland, H.D. & Edmond, J.M. (1984): Flow rates in the axial hot springs of the East Pacific Rise (21°N) : implications for

the heat budget and the formation of massive sulfide deposits. Earth Planet. Sci. Lett. 69, 159-175.

Cosens Gallinatti, B. (1984): Initiation and collapse of active circulation in a hydrothermal system at the Mid Atlantic Ridge, 23°N. J. Geophys. Res. 89, 3275-3289.

Craig, H. (1969): Geochemistry and origin of the Red Sea brines. In Hot Brines and Recent Heavy Metal Deposits in the Red Sea (E.T.Degens and R.A. Ross, eds.). Springer-Verlag, Berlin, p. 208-242.

Delhaye, M. & Dhamelincourt, P. (1975): Raman microprobe and microscope laser excitation. J. Raman Spectrosc. 3, 33-43.

Dhamelincourt, P. Bény, J.M. Dubessy, J. & Poty, B. (1979): Analyse d'inclusions fluides à la microsonde Mole à effet Raman. Bull. Minéral. 102, 600-610.

Doukhan, J.C. & Trépied, L. (1985): Plastic deformation of quartz single crystals. Bull. Minéral. 108, 97-123.

Drummond, S.E. & Ohmoto, H. (1985): Chemical evolution and mineral deposition in boiling hydrothermal systems. Econ. Geol. 80, 126-147.

Dubois, M. (1984): Plagiogranites et Hydrothermalisme : Une Approche à Partir des Complexes Ophiolitiques de Chypre et d'Oman. Ph. D. Thesis, Univ. Nancy I, France.

_____ Charoy, B. & Onnenstetter, M. (1984): The importance of fluid phases in the genesis and alteration of the ophiolitic "plagiogranites" of Cyprus and Oman. Ofioliti 9, 688-689.

Elder, J. (1981): Particular discharge mechanisms. In Geothermal systems. Academic Press, London, p.382-417.

Erickson, A.J. & Simmons, G. (1969): Thermal measurements in the Red Sea hot brine pools. In Hot Brines and Recent Heavy Metal Deposits in the Red Sea (E.T. Degens and D.A. Ross, eds). Springer Verlag, Berlin, p.114-121.

Finlow-Bates, T. & Large, D.E. (1978): Water depth as major control on the formation of submarine exalative ore deposits. Geol. Jahrb. 30, 27-30.

Fournier, R.O. (1981): Application of water geochemistry to geothermal exploration and reservoir engineering. In Geothermal systems : principles and case histories (L. Rybach and J.P. Muffler, eds.). Wiley, New York, p. 109-143.

Gehrig, M. Lentz, H. & Franck, E.U. (1983): Concentrated aqueous sodium chloride solutions from 200 to 600°C and to 3000 bar. Phase equilibria and PVT-Data. Ber. Bunsenges Phys. Chem. 87, 597-600.

Gratier, J.P. & Jenatton, L. (1984): Deformation by solution-deposition and re-equilibration of fluid inclusions in crystals depending on temperature, internal pressure and stress. J. Struct. Geol. 6, 189-200.

Hackett, J.P. Jr & Bischoff, J.L. (1973): New data and the stratigraphy, extent, and geologic history of the Red Sea geothermal deposits. Econ. Geol. 68, 553-564.

Hartmann, M. (1972): Sound velocity data for the hot brines and corrected depth of interfaces in the Atlantis II Deep. Marine Geol. 12, 1116-1120.

--------- (1973): Untersuchung von suspendierten Material in der Hydrothermalaugen des Atlantis II Tiefs. Geol. Rundschau 62, 742-754.

--------- (1980): Atlantis II Deep geothermal brine system. Hydrographic situation in 1977 and changes since 1965. Deep-Sea Research 279, 141-161.

--------- (1985): Atlantis II Deep geothermal brine system. Chemical processes between hydrothermal brines and Red Sea deep water. Marine Geol. 64, 157-177.

Haas, J.L. Jr (1971): The effect of salinity on the maximum thermal gradient of a hydrothermal system at a hydrostatic pressure.Econ. Geol. 66, 940-946.

--------- (1976): Thermodynamic properties of the coexisting phases and thermochemical properties of the NaCl component in boiling NaCl solutions. U.S. Geol. Surv. Bull., 1421-B.

Hedenquist, J.W. & Henley, R.W. (1985): The importance of CO_2 on the freezing point measurements of fluid inclusions: evidence from

active geothermal systems and implications for epithermal ore deposition. Econ. Geol. 80, 1379-1406.

Jehl, V. Poty, B. & Weisbrod, A. (1977): Hydrothermal metamorphism of the oceanic crust in the North Atlanctic Ocean. Bull. Soc.Géol. Fr. 6, 1213-1221.

Keenan, J.H. Keyes, F.G. Hill, P.G. & Moore, J.G. (1969): Steam Tables. Wiley, New York.

Khaibullin, K. & Borisov, N.M. (1966): Experimental investigation of the thermal properties of aqueous and vapor solutions of sodium and potassium chlorides at phase equilibrium.Teplofizika Vysokikh Temperatur 4, 518-523. (English translation, 489-494).

Kim, K.R. Welhan, J.A. & Craig, H. (1984): The hydrothermal vent fields at 13°N and 11°N on the East Pacific Rise : Alvin 1984 results (abstract). E.O.S. 65, 973.

Kusakabe, M. Chiba, H. & Ohmoto, H. (1982): Stable isotopes and fluid inclusion study of anhydrite from the East Pacific Rise at 21°N. Geoch. J. 16, 89-95.

Larson, L.T. Miller, J.D. Nadeau, J.E. & Roedder, E. (1973): Source of error in low-temperature inclusion homogenization determination and correction on published temperature fo the East Tennessee and Laisvall deposits. Econ. Geol. 68, 113-116.

Le Bel, L.& Oudin, E. (1982): Fluid inclusion studies of deep-sea hydrothermal sulfide deposits on the East Pacific Rise near 21°N. Chem. Geol.37, 129-136.

Le Quentrec, M.F. Sichler, B. & Bayer, R. (1987): Magnétisme profond au fond de la fosse d'Atlantis II (Mer Rouge). Réunion Spécilisée de la Société Géologique de France, Paris, (abstract).

Marshall, W.L. & Slusher, R. (1968): Solubility to 200°C of calcium sulfate and its hydrates in sea water concentrates and temperatures-concentrations limits. Chem. Eng. Data 13, 83-91.

McClain, J.S. Orcutt, J.A. & Burnett, M. (1985): The East Pacific Rise in cross section : a seismic model. J. Geophys. Res. 90, 8627-8639.

Michard, G. Albarède, A. Michard, A. Minster, J.F., Charlou, J.L. & Tan, N. (1984): Chemistry of solutions from the 13°N East Pacific Rise hydrothermal site. Earth Planet. Sci. Lett. 67, 297-307.

Oudin, E. (1983): Minéralogie de gisements et indices liés à des zones d'accrétion océaniques actuelles (ride Est-Pacifique et Mer Rouge) et fossiles (Chypre). Chronique Rech. Minière 470, 43-55.

———— (1987): Trace elements and precious metal concentrations in East Pacific Rise, Cyprus and Red Sea submarine sulfide deposits. In Marine Minerals (P.G. Teleki et al., eds.). Reidel Publishing Company, p. 349-362.

———— Thisse, Y. & Ramboz, C. (1984): Fluid inclusion and mineralogical evidence for high-temperature saline hydrothermal circulation in the Red Sea metalliferous sediments : preliminary results. Marine Mining 5, 3-31.

Parisod, C.J. & Plattner, E. (1981): Vapor-liquid equilibria of the NaCl-H_2O system in the temperature range 300 - 440°C . J. Chem. Eng. Data 26, 16-20.

Pautot, G. (1983): Les fosses de la Mer Rouge : approche géomorphologique d'un stade initial d'ouverture océanique réalisée à l'aide du seabeam. Oceanol. Acta 6, 235-244.

Pécher, A. & Boullier, A.M. (1984): Evolution à pression et température élevées d'inclusions fluids dans un quartz synthétique. Bull. Minéral. 107, 139-153.

Pitzer, K.S. & Pabalan, R.T. (1986): Thermodynamics of NaCl in steam. Geochim. Cosmochim. Acta 50, 1445-1454.

———, Peiper, J.C. & Busey, R.H. (1984): Thermodynamic properties of aqueous sodium chloride solutions. J. Phys. Chem. Ref. Data 13, 1-102.

Potter, R.W. II, Babcock, R.S. & Brown, D.L. (1977): A new method for determining the solubility of salts in aqueous solutions at elevated temperatures. J. Res. U.S. Geol. Survey 5, 389-395.

——— Clynne, M.A. & Brown, D.L. (1978): Freezing point depression of aqueous sodium chloride solutions. Econ. Geol. 73, 284-285.

Pottorf, R.J. (1980): Hydrothermal Sediments of the Red Sea, Atlantis II Deep - A Model for Massive Sulfide Type Ore Deposits. Ph. D. thesis, The Pennsylvania State Univ., University Park.

_____ & Barnes, H.L.(1983): Mineralogy, geochemistry and ore genesis of hytrothermal sediments from the Atlantis II deep, Red Sea. Econ. Geol. Mono.5, 198-223.

Poty, B. Leroy, J. & Jachimowicz, L. (1976) : Un nouvel appareil pour la mesure des températures sous le microscope : l'installation de microthermométrie Chaix-Meca. Bull. Soc. Fr. Minéral. Cristallog. 99, 182-186.

Ramboz, C. (1983): Application of V-X projections to the quantitative interpretation of heterogeneous trapping from fluid inclusion study. Terra Cognita 3, 164.

_____ & Danis, M. 1987: The temperature of the inflowing brine at the bottom of Atlantis II Deep, Red Sea. Terra cognita 7, n.° 2-3, 187.

_____: The temperature of the inflowing brine at the bottom of Atlantis II Deep, Red Sea: the heat-mass balance of the Deep revisited. Submitted to Earth Planet. Sci. Let.

_____ Pichavant, M. & Weisbrod, A. (1982): Fluid immiscibility in natural processes : use and misuse of fluid inclusion data. Part II : interpretation of fluid inclusion data in terms of immiscibility. Chem. Geol. 37, 29-48.

Ridge, J.D. (1973): Volcanic exhalations and ore deposition in the vicinity of the sea floor. Mineral. Deposita. 8, 332-348.

Roedder, E. (1972): Barite fluid inclusion geothermometry, Cartersville Mining District, Northwest Georgia. Econ. Geol. 67, 821-822.

_____ (1976): Fluid inclusion evidence on the genesis of ores in sedimentary and volcanic rocks. In Ore in sediments. Sedimentary and volcanic rocks (K.H.Wolf, ed.). Elsevier. 2, 67-110.

_____ (1981): Origin of fluid inclusions and changes that occur after trapping. In Short course in fluid inclusions : applications to petrology (L.S. Hollister and M.L. Crawford, eds.). Mineral. Assoc. Can. 6, 101-137.

Ross, D.A. (1972): Red Sea hot brine area : revisited. Science 175, 1455-1457.

——, Whitmarsh, R.B. Ali, S.A. Boudreaux, J.E. Coleman, R. Fleisher, R.L. Girdler, R. Manheim, F. Matter, A. Nigrini, C. Stoffers, P. & Supko, P.R. (1973). Red Sea drillings. Science. 179, 377-380.

Schoell, M. (1976): Heating and convection within the Atlantis II Deep geothermal system of the Red Sea. Proceedings second United Nations Symposium on the development and use of geothermal resources, San Francisco 20-29 May 1975 2, 583-590.

———— & Hartmann, M. (1973): Detailed temperature structure of the hot brines in the Atlantis II deep area (Red Sea). Marine Geol. 14, 1-14.

———— &———— (1978): Changing hydrothermal activity in the Atlantis II Deep geothermal system. Nature 274, 784-785.

Seyfried, W.E. Jr. & Janecky, D.R. (1985): Heavy metal and sulfur transport during subcritical and supercritical hydrothermal alteration of basalt : influence of fluid pressure and basalt composition and crystallinity. Geochim. Cosmochim. Acta. 49, 2545-2561.

---------- Berndt, M.E. & Janecky, D.R. (1986): Chloride depletions and enrichments in seafloor hydrothermal fluids : Constraints from experimental basalt alteration studies. Geochim. Cosmochim. Acta. 50, 469-475.

Shanks, W.C. II (1983): Economic and exploration significance of Red Sea metalliferous brine deposits. In Cameron Volume on Unconventional Mineral Deposits (W.C. Shanks, ed.). Amer.Inst. Mining. Eng. Mono., 157-171.

———— & Bischoff, J.L. (1977): Ore transport and deposition in the Red Sea geothermal system : a geochemical model. Geochim. Cosmochim. Acta. 43, 1507-1519.

Sobolev, V.S. & Kostyuk, V.P. eds., (1975): Melt inclusions, their types, and thermometric methods of investigations. In Magmatic Crystallization based on a Study of Melt Inclusions, Novosibirsk, Nauka Press (In Russian), Translated in Fluid Inclusion Research, Proc. of COFFI. 9, 182-218.

Spooner, E.T.C. (1980): Cu-pyrite mineralization and sea water convection in oceanic crust. the ophiolitic ore deposits of Cyprus. Geol. Assoc.of Can., Spec. Pap. 20, 685-704.

Sval'nov, N. Strizhov, V.P. Bogdanov, Y.A. & Isayeva, A.B. (1984): Hydrothermal barite crust on basalts in Atlantis II Deep (Red Sea). Oceanology 24, 716-720 .

Thisse, Y. (1982) : Sédiments Métallifères de la Fosse d'Atlantis II (Mer Rouge). Contribution à l'Etude de Leur Contexte Morpho-Structural et de Leurs Caractéristiques Minéralogiques et Géochimiques. Ph. D. Thesis, Université Orléans et B.R.G.M., Orléans, France.

Thompson, J.B. Jr. (1972): Oxides and sulfides in regional metamorphism of pelitic schists. 24 th Int.Geol.Congress, section 10, 27-35.

Turner, J.S. (1969): A physical interpretation of the observations of hot brine layers in the Red Sea. In Hot Brines and Recent Heavy Metal Deposits in the Red Sea (E.T. Degens and D.A. Ross, eds). Springer Verlag, Berlin, 164-173.

Urusova, M. (1974): Phase equilibria in the sodium hydroxide-water and sodium chloride-water systems at 350-550°C. Russian J. Inorg. Chem. 19, 450-454.

Vanko, D.A. (1984): Chlorine-rich amphiboles and chlorine-rich fluid inclusions in quartz : evidence for high salinity oceanic hydrothermal systems (abstr.). Geol. Soc. Amer. Abstr. Prog. 16, 682.

Voorhis, A.D. & Dorson, D.L. (1975): Thermal convection in the Atlantis II hot brine pool. Deep-Sea Research. 22, 167-175.

Von Damm, K.L. Edmond, J.M. Measures, C.I. Grant, B.C. Trull, T. Walden, B. & Weiss, R. (1985): Chemistry of submarine hydrothermal solutions at 21°N East Pacific Rise. Geochim. Cosmochim. Acta. 49, 2197-2221.

Weisbrod, A. (1984): Utilisation des inclusions fluides en geothermobarométrie. In Thermométrie et Barométrie Géologiques (M. Lagache ed.). Soc. Française Minéral. Cristallogr., v. 2, p.1016-1027.

Weiss, H.M Nölltner, T. & Stoffers, P. (1980): Occurrence of ilvaite in metalliferous brine muds from the Red Sea. Neues Jahrb. Mineral. Abh. 139, 239-253.

Wilkins, R.W.T. & Sverjensky, D.A. (1977): The role of fluid inclusions in the exsolution of clinopyroxene in bustamite from Broken Hill, New South Wales, Australia. Amer. Mineral. 62, 465-474.

White, D.E. (1968): Hydrology, activity, and heat flow of the Steamboat springs thermal system, Washoe County, Nevada. U.S. Geol. Surv. Prof. Pap. 458-C, 109.

Yajima, J. & Touray, J.C. (1967): Observation sur la sursaturation des liquides inclus dans les cristaux de fluorite. C.R. Acad. Sci., Paris 264, 1129-1132.

Zhang, Y.G. & Frantz, J.D. (1987): Determination of the homogenization temperatures and densities of supercritical fluids in the system NaCl-KCl-H_2O using synthetic fluid inclusions. Chem. Geol. 64, 335-350.

Zierenberg, P.A. & Shanks, W.C. (1983): Mineralogy and geochemistry of epigenetic features in metalliferous sediments, Atlantis II Deep, Red Sea. Econ. Geol. 78, 57-72.

———— & Shanks, W.C. (1986): Isotopic constraints on the origin of the Atlantis II, Suakin and Valdivia brines, Red Sea. Geochim. Cosmochim. Acta 50, 2205-2214.

CHAPITRE IV

The temperature of the inflowing brine at the bottom of Atlantis II Deep, Red Sea : the heat-mass balance of the Deep revisited.*

C. Ramboz [1] and M. Danis [1,2]

1 Centre de Recherches Pétrographiques et Géochimiques, B.P. 20, 54501-Vandoeuvre- lès-Nancy, France.

2 Present address : Université de Bordeaux I, Institut de Technologie A, Génie Mécanique, 33405 - Talence Cedex.

* Submitted to Earth and Planetary Science Letters, 6th May 1988.

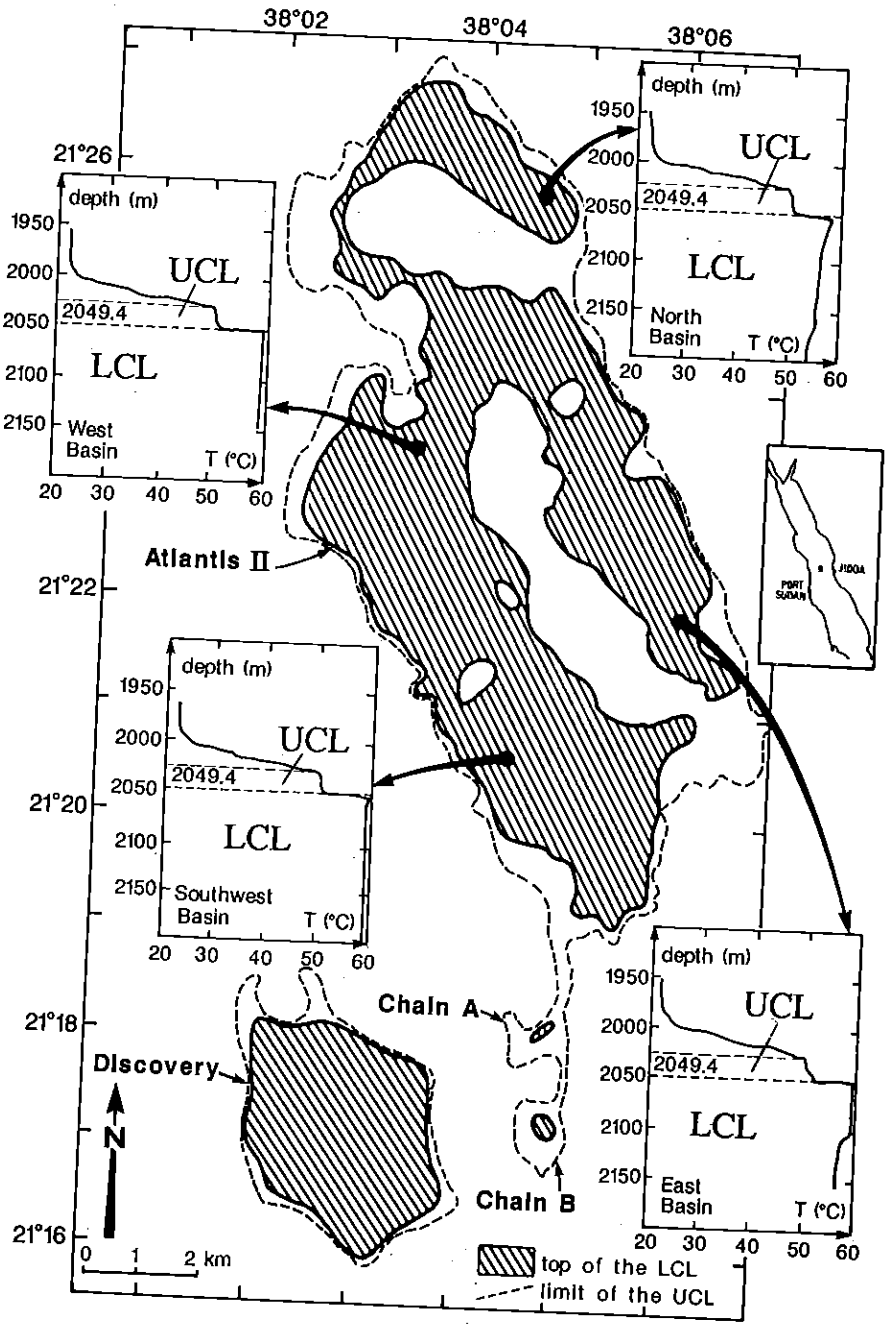

Fig. 1 : Simplified bathymetric map of the brine pools in Atlantis II Deep area (after [39]) and characteristic temperature-depth profiles of the four basins of Atlantis II Deep (after [24] : stations N° 50, 61, 75, 89, April 1971). Depths are corrected for higher sound velocity in brines [62].

1-Introduction

The sediments at the bottom of Atlantis II Deep form one of the largest known submarine deposits of Zn, Cu, Ag and Au [1]. They have been forming there for the past 11,000 years.They have been preserved because Atlantis II Deep, like the other Central Red Sea Deeps (Discovery, Valdivia, Chain A and Chain B Deeps), is filled with anoxic stratified brines which separate the underlying sulfides from the overlying oxidizing oceanic waters of the Red Sea. In contrast, most sulfides deposited in the open ocean are later dispersed, dissolved or oxidized [2]. Stratified hot brine pools are one way that aids the formation and preservation of economic base metal sulfide deposits in oceanic environments.

Geochemical studies have established that, at 13°N and 21°N E.P.R. and in the five Central Red Sea Deeps, metals are deposited from hydrothermal fluids enriched in Ca and depleted in Mg, O_2 and SO_4 relative to sea water [3 to 5]. Along the E.P.R., the mineralizing fluid is modified sea water having acquired its chemical and isotopic characters by interacting with basalts at high temperature [6 to 8]. Temperatures of the discharging brine of up to 358°C at 21°N E.P.R. have been measured directly [9]. In contrast, the conditions of hydrothermal feeding of the hot brine pools from the Central Red Sea, and particularly that of Atlantis II Deep, are still debated in spite of 30 years of oceanographic studies. Although there is no doubt that the brines in Atlantis II Deep have exchanged with the Miocene evaporites deposited on the flanks of the rift [10 to 12], it is still debated whether their reducing and metalliferous potentials result from the interaction with newly-formed basalt [13, 14] or with organic-rich shales within or above the evaporites [15]. The

Table 1 : Changes in the temperature and volume of the lower brine and of the upper brine in Atlantis II Deep from 1965 to 1980 and their interpretation in terms of the temperature and flow rate of the hydrothermal source feeding the Deep.

REF.	SYSTEM			CHANGES					
		Δt	ΔT	ΔD	Φ_c^i	Φ_c^o	M_e	Ts	Qs
[34]	UCL + LCL	II-65 X-66		0.34	15-20	39[1]	0	-	-
[48]	UCL + LCL S=49.3[4] xu=47[4]; xl=33[4]	X-66 II-71	UCL: +1.3 LCL: +0.6	0 1.4	0 0	0 0	0 0	>114 <360	-
[46]	"	"	"	"	0	0	0	>104	3.1
[37]	UCL + LCL S=42 xu+xl=61.9	IV-71 III-72	0.75	0.3	0	0	0	210	0.19
[23]	LCL S=43.5 xl=69	V-65 XI-77	0.48	0.22 0 0	0 0 0	0 0 230	0 + +	215 140 280	0.28 0.56 0.56
[47]	LCL S = 40 xu=30; xl=78	IV-65 XI-77	UCL: +1.3 LCL: +0.6	0.22	20[5]	150	0	490	0.35
This work	LCL S = 43-43.4 xl = 63.3-64.6	II-65 XI-77	0.40 0.40	0.22 0.22	20[5] 20[5]	120[2] 177[3]	0 0	343 354	0.33 0.33

Δt = time length; ΔT = heating rate (°C/year); ΔD = rising rate of the lower interface (m/year); Φ_c^i (Φ_c^o) = conductive input (output) of heat (HFU); M_e = mass of fluid expelled out of the system; Ts and Qs = calculated temperature (°C) and rate of flow (10^3 kg /s) of the inflowing brine respectively; xu and xl = thickness (m) of the upper and lower brines respectively; S = surface of the system (km^2); [1], [2] and [3] = heat lost by pure conduction through the lower interface, the thickness of which is taken as 5 m, 1.5 m and 1 m respectively; [4] = after [31]; [5] = after [34]; + = considering that half the mass of the injected brine is lost through the lower interface.

temperature of brine discharge at the bottom of the Atlantis II Deep has never been measured directly. Mean temperatures have been indirectly estimated to be in the range 115°-250°C, based on mineral equilibria, geochemistry of the brines and heat-mass balance calculations (see the reviews in [14, 16] and Table 1). These temperatures are much lower than those based on recent mineralogical and/or fluid inclusion data on high temperature sulfide assemblages in epigenetic anhydrite veins crosscutting the sediment of the SW basin of Atlantis II Deep [16 to 20]. Fluid inclusions in the epigenetic barites and anhydrites show that the crystals were precipitated directly from boiling hydrothermal solutions at temperatures up to 390°-403°C [21]. It is worth noting that Kaplan et al. [15] measured isotopic fractionation factors between interstitial sulfates and total sulfides from the same stratigraphic level of the sediment in the range 1.011 to 1.017, compatible with an isotopic temperature, assuming equilibrium, of between 400° and 550°C. Oudin et al. [20] showed that these veins are equivalent to the high temperature hydrothermal assemblages at 21°N E.P.R.

The recent directly observed fluctuations of the temperature and volume of the lower brine provide one of the best way of averaging the heat flux over Atlantis II Deep, and hence to calculate mean hydrothermal discharge temperatures [22]. The many generations of fluid inclusions in anhydrite and barite, with different temperatures and salinities [20, 21], are compatible with fluctuations of the temperature and salinity of the lower brine as presently observed [23]. Geochemical studies of the various sulfide-bearing levels demonstrate that the conditions of the hydrothermal feeding (temperature, chemistry of the brine) have been relatively uniform over the past 15,000 years up to present [14].

This paper reconsiders the temperature of the Atlantis II Deep hydrothermal spring using heat-mass balance calculations and explains the

wide range of discharge temperatures in the Deep derived from mineralogical, isotopic or fluid inclusion thermometry in barite-anhydrite-sulfide veins. Data on the structure and hydrology of Atlantis II, Discovery, Chain A and Chain B Deeps over the past 15 years provide the bases for reconstructing the processes accounting for the geothermal activity in Atlantis II Deep, they are therefore summarized below. A table listing references on oceanographic expeditions having contributed to the knowledge of the structure of Central Red Sea Deeps is given in Appendix. Revised equations for the heat-mass balance of Atlantis II Deep, which include the possibility of a loss of heat and mass out of Atlantis II Deep towards the near-by Deeps, are proposed. The equations are solved in terms of the temperature and the flow rate of brine discharge in Atlantis II Deep. Special attention is given to the problem of properly estimating heat capacities of concentrated brines above 300°C.

2. Notation.

c_p : specific heat of the fluid (J /K/kg).
c_{po} : mean specific heat of the lower brine at 220 bars in the temperature range 56°-62°C (taken as a constant).
h_i : depth of the lower interface of Atlantis II Deep at time t_i.
H_i (Q_i) : enthalpy per mass unit (quantity of heat) of the lower brine in Atlantis II Deep at time t_i.
LCL : lower convective layer of Atlantis II Deep.
M_e : mass of lower brine expelled out of Atlantis II Deep.
M_{to} (M_{te}, M_{tf}) : mass of the lower brine pool at time t_o (t_e, t_f).
M_s : mass of hydrothermal fluid added to the lower brine over the time range (t_o, t_f).
S : mean area of the lower interface in the time range (t_o, t_f).
t_e : time at which some lower brine was expelled from Atlantis II Deep.
t_i : unspecified time.
t_o (t_f) : initial (final) time.
T_e : temperature of the lower brine expelled out of Atlantis II Deep.
T_o (T_f) : temperature of the lower brine at time t_o (t_f).
T_{ref} : reference temperature.

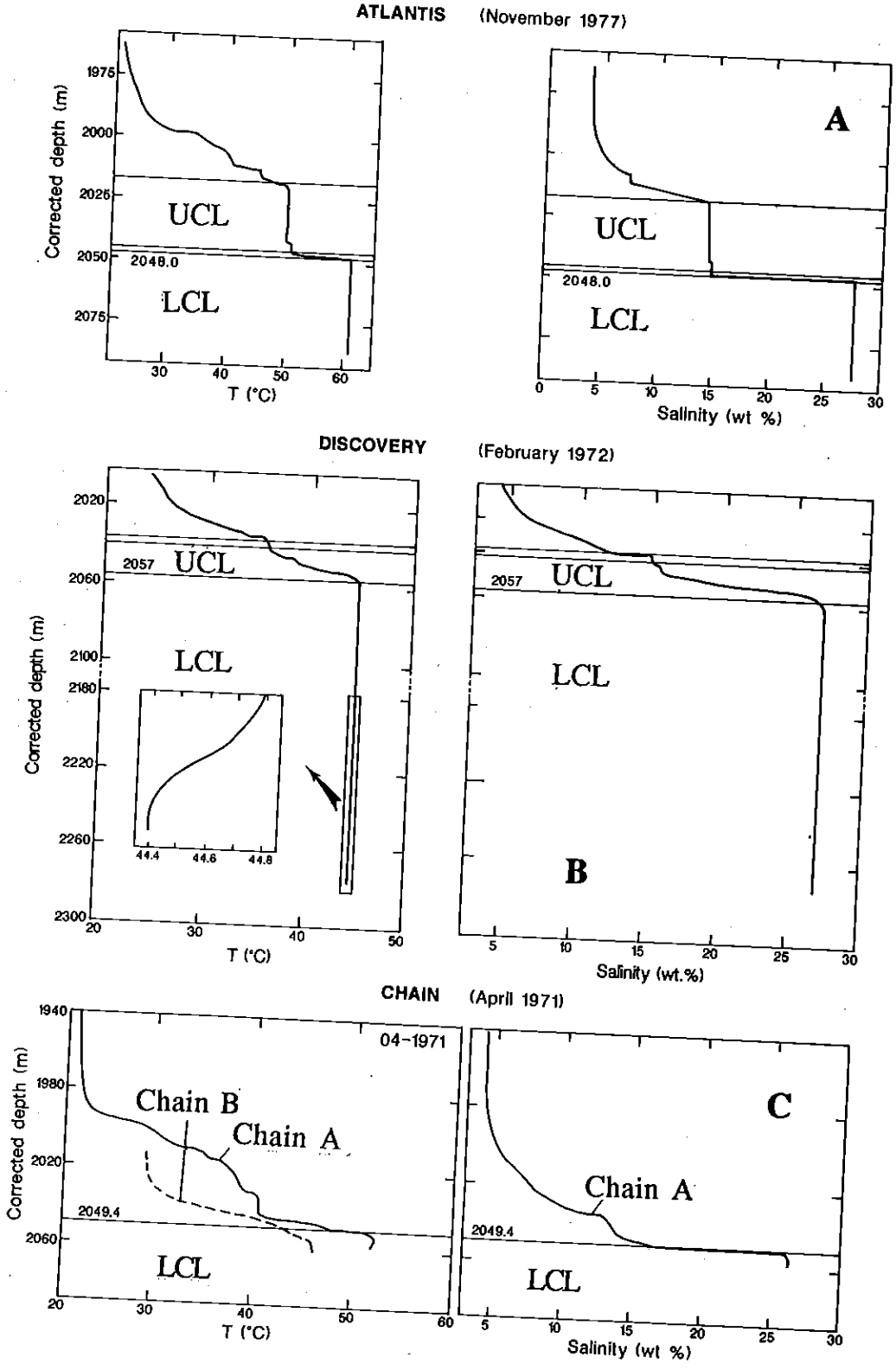

Fig. 2 : Temperature-depth (left) and salinity-depth profiles (right) in Atlantis II Deep (=A), Discovery Deep(=B), Chain A and B Deeps (=C), Central Red Sea. The temperature profiles, corrected for higher sound velocity in brines [62], are drawn after [24]. Salinity profiles are tentatively reconstructed after chlorosity, salinity and chlorinity data (Atlantis II Deep : [23], Discovery Deep : [35], Chain A Deep : [29], respectively).

T_s : mean temperature of the spring at the bottom of Atlantis II Deep over the time range (t_o, t_f).
UCL : upper convective layer of Atlantis II Deep.
V_i : volume of the lower brine at time t_i.
x_{li} : thickness of the lower interface of Atlantis II Deep.
z_{li} : depth of the lower interface of Atlantis II Deep.
$\Delta H_{o\text{-}f}$ ($\Delta Q_{o\text{-}f}$): variation of the enthalpy (of the quantity of heat) of the lower brine in the time range (t_o, t_f).
$\Delta Q_c{}^i$ ($\Delta Q_c{}^o$) : conductive input (output) of heat through the bottom (the top) of the lower brine pool over the time range (t_o, t_f).
$\Delta Q_s{}^i$: heat brought by the geyser spring to the lower brine in the time range (t_o, t_f).
Δt : time length (t_f-t_o).
$\Delta T_{li}(t)$: temperature difference across the lower interface of Atlantis II Deep at time t.
λ : thermal conductivity of the lower brine at 57°C.
$\Phi_c{}^i$ ($\Phi_c{}^o$): conductive heat flux at the bottom (at the top) of the lower brine.
ρ_o: mean density of the lower brine in the range 56°-62°C (taken as a constant).

3. The hot brine pools in Atlantis II Deep area.

The Central Red Sea Deeps (Discovery, Atlantis II, Valdivia, Chain A and Chain B Deeps) have in common a stratified structure characterized by well mixed layers with, both horizontally and vertically, nearly constant composition and temperature, alternating with interfaces which concentrate the largest gradient of temperature [24]. Only the structure of Atlantis II, Discovery, Chain A and Chain B Deeps are discussed below (Figs. 1 to 3; Tables 1 and 2). The Valdivia Deep is unrelated to Atlantis II Deep because, unlike other Central Red Sea Deeps, it is formed by dissolution of Miocene evaporites [25, 26].

Table 2 : Temperature-depth structure of Atlantis II and Discovery Deeps in February 1972 (after [23, 24]) and in October 1966 (numbers in brackets, after [22]). Only the 1972 depth data are corrected for higher sound velocity in brines [62].

	ATLANTIS II DEEP (SW BASIN)				DISCOVERY DEEP			
	Depth range	X	T	ΔT/Δx	Depth range	X	T	ΔT/Δx
Normal Sea Water	< 1992(1984)		<23		< 1987(1986)		<23	
Upper interface	1992(1984)	30(25)		0.9(0.9)	1987(1986)	48(37)		0.3(0.4)
UCL	2019(2009)	23(28)	50.8(44)		2035(2023)	3(4)	35.75(36)	
Lower Interface	2049(2037)	1 (5)		9(2.4)	2038(2027)	22(15)		0.4(0.6)
LCL	2050(2042)		59.8(56)		2057(2042)		44.8(45)	
	>2050(2042)				> 2057(2042)			

T= temperature (°C); X= thickness (m); ΔT/Δx= temperature gradient accross the interface; UCL (LCL)= upper (lower) convective layer.

3.1. Physical interpretation of the Deeps.

The physical interpretation of the observations on the stratified hot brine pools from the Central Red Sea as established by Turner [22; 27] are summarized below. Stratified fluid layers with sharp interfaces have been obtained in the laboratory on heating uniformly a tank from below under conditions of high heating rate and low salinity gradients. The stability of the layers depends on the ratio of the separate contribution of salinity and temperature to the density difference at the interface. As this ratio increases, the stratified layers become increasingly stable with sharper interfaces. The transfer of heat and salt through sharp interfaces occurs mainly by molecular diffusion compared to mixing in the layer.The stratified systems from the Central Red Sea are rather different from the experimentally studied ones. They have formed under conditions of low heating rate and comparatively high salinity gradients. Only the lower interface of Atlantis II Deep, about 1m-thick [23], is equivalent to the sharp interfaces studied experimentally. Despite these differences, the following qualitative conclusions concerning the Central Red Sea stratified pools can be inferred from the experimental studies .

The two interfaces in Atlantis II Deep are quite stable due to the low heating rate of the Deep compared to the salinity gradient. The two interfaces in Discovery Deep are even more stable due to a smaller contribution of temperature to the density difference through the interfaces (Table 2). The composition and temperature are maintained constant in the two layers of Atlantis II Deep by convection. The transfer of salt and heat through the sharp lower interface of Atlantis II Deep proceeds mainly by molecular diffusion. It can be neglected, on account of the low molecular diffusivity of salt compare to that of heat. Brewer (in [28]) interpreted an increase of 2.2‰ of the salinity of the upper brine

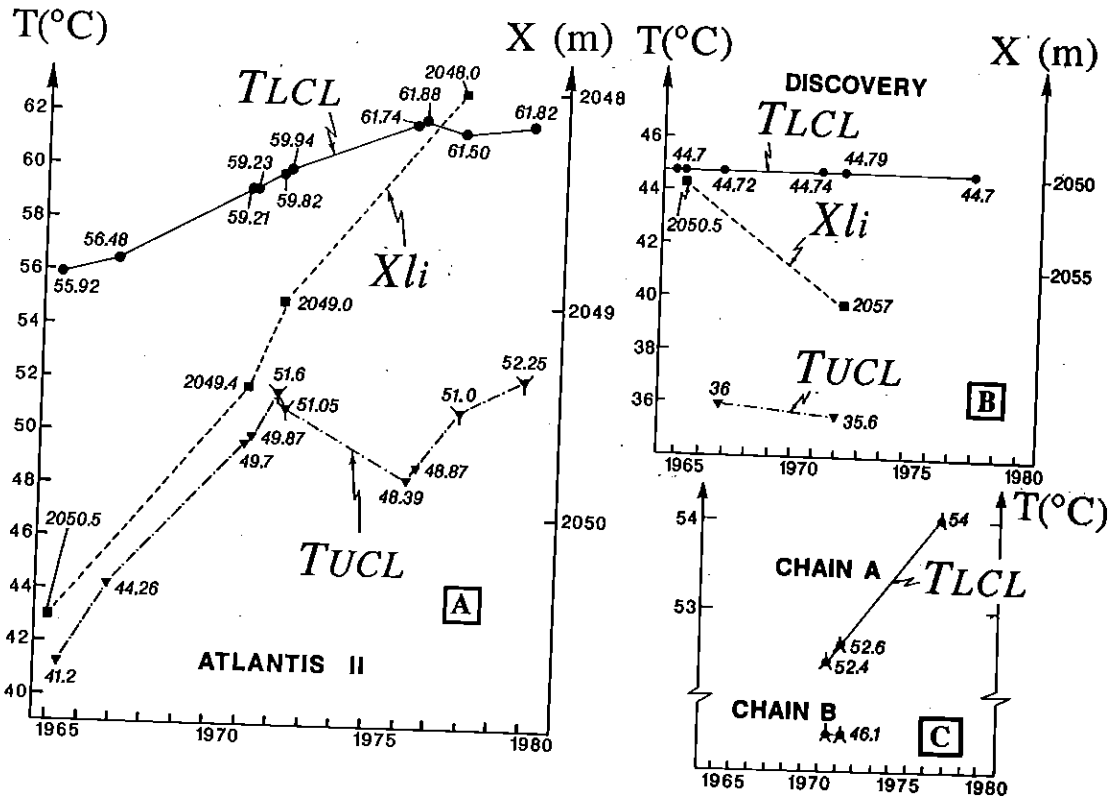

Fig. 3 : Temperature of the lower brine (circles), of the upper brine (triangles) and depth of the lower interface (squares) in (A) Atlantis II, (B) Discovery and (C) Chain A and B Deeps from 1965 to 1979. The ticks on the triangles correspond to the maximum temperature measured in the convective layer (data after [23, 24, 32, 35, 41, 47, 48, 63]).

from 1966 to 1971 in terms of a mean net flux of salt through the lower interface of around 6 10^{-8} g $cm^{-2}s^{-1}$.

3.2.Contrasting structure and origin of the Deeps.

The convective layer in contact with the sediment, i.e. the Lower Convective Layer (=LCL), has a similar chlorinity in Atlantis II, Discovery, Chain A and Chain B Deeps [29]. Except for that fact, the four Deeps have many dissimilarities. (i) The temperature of the LCL is different from one Deep to another, and is highest in Atlantis II Deep (Fig.2). In addition, the temperature gradient across both the upper and the lower interfaces is steeper in Atlantis II than in Discovery Deep (Table 2), due to thinner interfaces and the higher temperature of the convective layers in the former Deep. (ii) The LCL is found at greater depth in Discovery and Chain B Deeps than in Atlantis II and Chain A Deeps (Fig. 2). (iii) The temperature of the LCL in the SW basin of Atlantis II Deep remains constant down to the surface of the sediment whereas a 50m-thick cooler layer is identified at the bottom of the Discovery Deep ([24,30], Fig. 2B). (iv). The Atlantis II Deep Upper Convective Layer (=UCL) is 7 times thicker than that in Discovery Deep and is found at greater depth (Table 2; Fig.2; [23, 31]). (v) Many authors have noted that the temperature of the Atlantis II Deep brines changes over periods of a few minutes to a day [32 to 34] due to small scale convection currents [28]. The structure of Atlantis II Deep is also highly changeable over the longer term : the temperature of the UCL and of the LCL has evolved continuously over 15 years and the volume of the LCL has increased simultaneously (Fig. 3A). From 1972 to 1977, Chain A Deep has presented a more limited activity, marked by an increase of 1.4°C in the temperature of the lower brine layer (Fig. 3C). The maximum temperature of the LCL in Chain B Deep is only known from April 1971

to February 1972 : it has remained constant during this period (Fig.3C). Similarly, Discovery Deep has been essentially inactive, as the temperature of both convective layers has remained unchanged. The volume of the LCL has slightly decreased over the same period (Fig. 3B). The Preussag data summarized in Figure 3B do not support the statement by Bubnov et al. [35] that the lower interface in the Discovery Deep has deepened by 18 m from October 1966 to June 1976.

The difference between the Atlantis II Deep structure and that of the other Deeps (Figs. 2 and 3; Table 2) point out to more active convection in the former Deep and also suggests a distinct origin for them. The very high measured heat flows of up to 60 HFU (2500mW) in the SW basin of Atlantis II Deep [34], and the high flow rate implied by the hydrological data over 15 years [23] confirm that Atlantis II Deep is presently an active submarine geothermal system [37]. Pugh [30, 36] and Turner [22] first suggested that the layering in Atlantis II Deep could not be maintained by conductive heat transfer through the sediment and that the large temperature increase of the LCL had resulted from convection. Schoell and Hartmann [29] showed that there is no direct connection between the pools of lower brine in Discovery, Chain A and Atlantis II Deeps. Bäcker et al. [25] suggested the possibility of a subsurface connection between the lower brines in these Deeps. However, the similar chemistry of the lower brine in Discovery, Chain A, Chain B and Atlantis II Deeps [29; 38], the very high measured heat flows in and out of Atlantis II Deep compare to those in Discovery Deep [34], and the cooler layer at the bottom of the latter Deep suggest that the lower brine in Atlantis II Deep may have overspilled by some catastrophic process towards Discovery and Chain Deeps (Fig.1; [22, 30, 34]). According to this interpretation, the recent temperature evolution of the four Deeps (Fig.3) suggests that some brine

has overflowed from Atlantis II towards Chain A between 1972 and 1977 but none towards Discovery over the past 15 years.

3.3. Localized feeding of Atlantis II Deep.

Although Erickson and Simmons [34] proposed that the supply of heat at the bottom of Atlantis II Deep was uniform, Turner [22] ruled out this hypothesis based on laboratory experiments. If the lower brine in Atlantis II Deep had formed by uniform heating, it should be thinner than actually observed, given the low heating rate. Turner [22] suggested that both heating from below and local injection of brine at the bottom of the Deep was the cause of the observed layering. The most direct line of evidence for a local and still active influx of hot brine in the SW basin is provided by the continuous survey of the temperature-depth structure of Atlantis II Deep from 1965 to 1980.

The Preussag group has studied in detail the horizontal and lateral variations of the brine temperature of Atlantis II Deep from 1965 to 1977 [23, 29, 41, 42]. The hydrology of the Deep can thus be reconstructed [37]. Schoell and Hartmann [29] were the first to demonstrate that Atlantis II Deep presently contains a single layer of upper brine with a homogeneous composition and temperature and four basins of lower brine characterized by regional differences in their temperature structure (Fig.1). The circulation within the lower brine pool is limited by topographic highs emerging from the top of the lower brine. A specific feature of the temperature profiles in the lower brine of the SW basin is a transition zone, below the lower interface, which is a few meters-thick and characterized by temperatures higher and more scattered than at greater depth ([29, 42], Fig.1). This high temperature zone provides evidence that, as predicted by Turner [22], a hot brine is injected directly into the bottom of the SW basin. It rises as a plume above the vents, spreads out below the

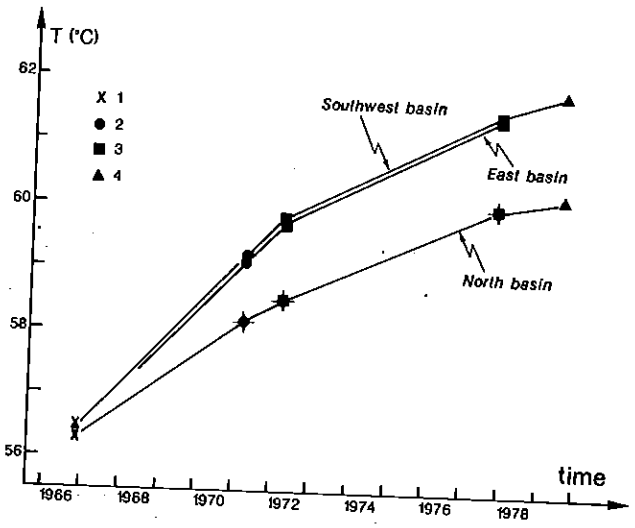

Fig. 4 : Evolution of the temperature of the lower brine with time in three basins of Atlantis II Deep (1= [34]; 2= [29]; 3= [42]; 4= [47]. Ticks as in Figure 3.

interface and then mixes turbulently with the lower brine. The mixing process is complete, as shown by the negligible scatter of the temperatures below the high temperature zone down to the surface of the sediment [29].

In 1966, Erickson and Simmons [34] measured large temperature gradients in the sediment at the bottom of the SW basin. The perturbation of the temperature resulting from brine injection apparently has dissipated more slowly in the sediment, due to the more sluggish rates of conductive heat transfer through solids. The W basin is supplied by new hot brine on top of the lower convective layer, as shown by the attenuated transition zone on the temperature profiles from this basin in 1971 and 1977 [24, 42]. Both the maximum temperature in the transition zone and the mean temperature in the underlying layer are lower than in the SW basin due to the greater distance from the brine vents. Finally, the temperatures of the lower brine below the transition zone are more scattered than in the SW basin, indicating a lower degree of mixing of the injected hot brine and less active convection.

Temperature profiles in the lower brine from the E and N basins present large temperature gradients (Fig.1). In the E basin and in an isolated depression in the W basin, a sublayer of lower brine is visible in contact with the sediment, characterized by a constant temperature 2° to 3°C lower than that in the overlying lower brine. This structure was interpreted to result from the recent influx of hotter newly-formed brine coming from the W part of the Deep and trapping relics of the older and colder brine at the bottom of isolated basins [29]. Constant temperature profiles in the colder layer [29] and in the underlying sediments of the E basin [34] prove that no heat was transiently lost or gained through the bottom of this basin. In the N basin, the temperature of the lower brine typically decreases with depth and the maximum temperature is systematically lower than the mean value measured in the other basins

Table 3 : Summary of main mineralogical-geochemical characteristics of SW basin sediments consistent with direct localized injection of brine at the bottom of Atlantis II Deep (after [17, 19, 20, 39, 43 to 45]).

(1)	- specific stratigraphy - thickest metalliferous sediments (up to 30m) - covariation of Fe, Zn,Cu Ag,Cd,Ba with S - intense brecciation and resedimentation -numerous basaltic glasses as interstratified pieces or in larger sills	
(2)		-anhydrite, barite, magnetite, ilvaite, cpy, sph, po,py -large size crystals in veins and vugs (up to 4mm)
(3)		- increased grain size after recrystalization(up to 250μm) - magnetite, ilvaite, trioctahedral clays

(1)=bulk stratigraphy and geochemistry ; (2)=epigenetic minerals ; (3)=hydrothermal metamorphism; cpy=chalcopyrite; sph=sphalerite; po=pyrrhotite; py=pyrite

(Fig.4). These features are the result of the very restricted communication between the N basin and the lower brine in the W basin.

Table 3 summarizes the evidence for a localized influx of brine in the SW basin based on the mineralogy and geochemistry of the sediments at the bottom of Atlantis II Deep. (i) Epigenetic magnetite-sulfate-sulfide-bearing veins and vugs typical of the SW basin are directly precipitated from the hydrothermal brine at around 400°C [21].(ii) Both the mineralogy of the veins and the specific geochemistry of the sediment in the SW basin (particularly the covariations of the metals including Ag and Zn, with S : [43]) indicate that the reduced venting brine in Atlantis II Deep supplies the metals and sulfur. This conclusion is in agreement with the observation by Hartmann [23] that the increase in the reducing conditions and heavy metal supply has accompanied the increase in the temperature of the lower brine from 1966 to 1971. (iii) The hydrothermal-chemical sediments in the SW basin are recrystallized and metamorphosed where the hot brines are venting. A temperature anomaly is marked at a larger scale by the transformation of goethite to hematite in the W and SW basins [39, 44] and, on a more restricted scale, by the transformation of hematite to magnetite in the SW basin [45]. Similarly, dioctahedral clays become trioctahedral [16, 19]. (iv) The hydrothermal-chemical sedimentation at the interface between the lower and the upper brines is enhanced in the SW basin because hot brine upwelling is more active immediately above the brine vents [45]. (v) Intense magmatic activity and bottom instability accompany brine venting in the SW basin [39], agrees with the inferred episodic and catastrophic overspill of brine from Atlantis II towards the near-by Deeps to the South. Finally, because the sediments in Chain A, Chain B and Discovery Deeps are a marginal facies of Atlantis II and are characteristically differenciated from those in

the SW basin of Atlantis II Deep [39], no brine is considered to be venting at the bottom of these three Deeps.

3.4. Geyser-type activity.

Ross [46] first suggested that the feeding of Atlantis II Deep was of geyser-type, given the high flow rate of brine discharge calculated over 52 months from October 1966 to February 1972. Based on bathysonde measurements [23], a precise estimate of 0.28 m^3/s for the flow rate of the brine over a period of about 12 years was calculated from the increase in the volume of the lower brine; this value is about 20 times the flow rate of Old Faithful Geyser in Yellowstone National Park. The changes in the temperature of the UCL and of the LCL in Atlantis II Deep over 15 years (Fig.3A) confirm that the hydrothermal activity in Atlantis II Deep is discontinuous and changing yearly [23, 42, 46 to 48].

Mineralogy provides additional evidence that the hydrothermal activity in Atlantis II Deep is intermittent : (i) Sval'nov et al. [49] described barite crusts on basalts from the Central Sill of Atlantis II Deep which presented a rythmic isotopic composition of oxygen and sulfur. Some epigenetic anhydrite and barite crystals from the SW basin are polygenic, being formed from brine pulses with a progressively increasing salinity [21]. These crystals contain liquid-rich and vapor-rich inclusions which prove that the discharging spring from which they formed was boiling on the sea floor [21]. According to White [50], this is evidence for geyser-type activity.

4. The heat-mass balance of Atlantis II Deep.

4.1. Reference system.

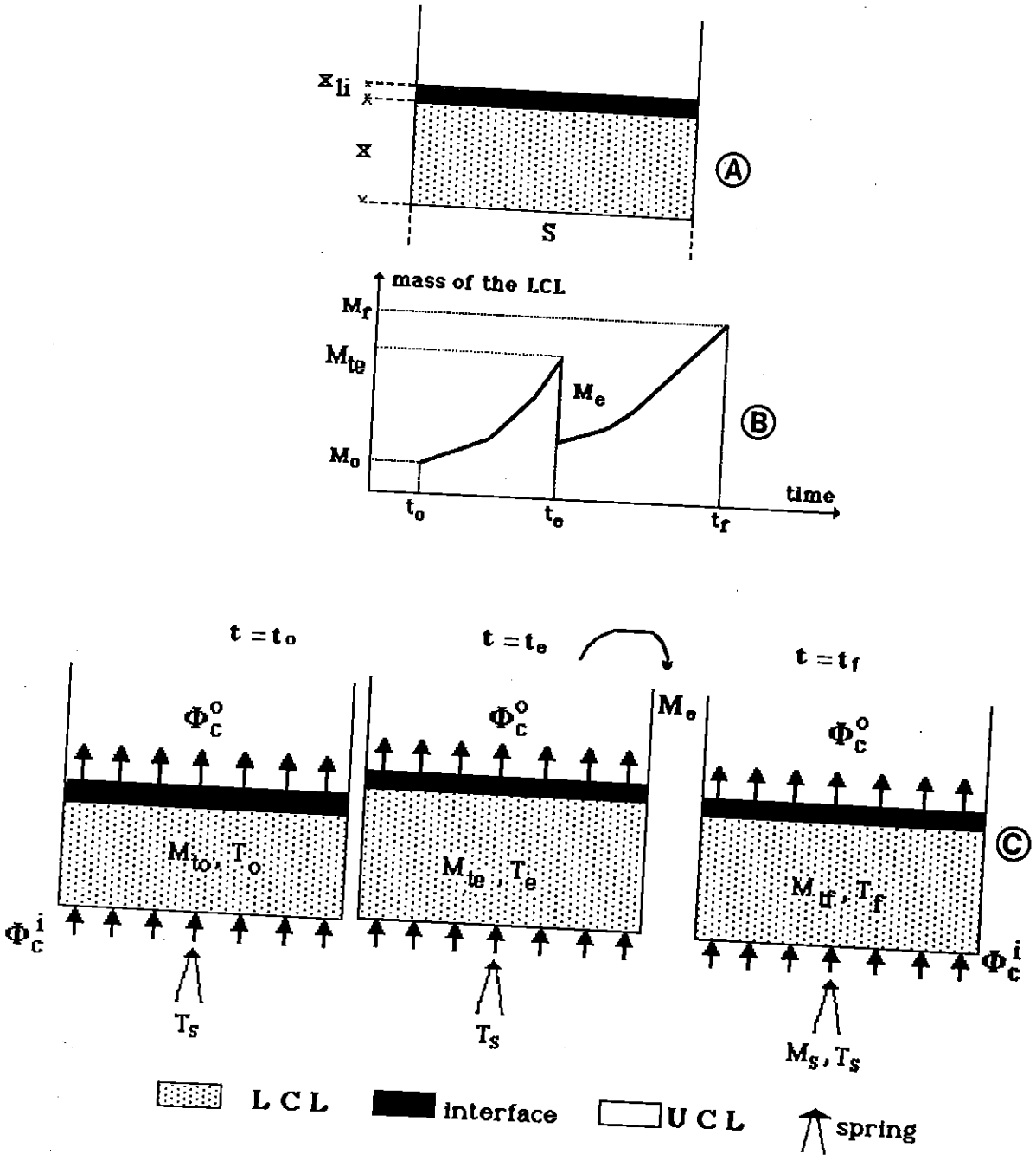

Fig. 5 : The heat-mass balance of the lower brine pool in Atlantis II Deep : (A) schematic geometric model for the deep, and (B and C) exchanges of mass and heat taken in account in the calculations, including the possibility of brine expulsion out of the pool at $t=t_e$.

In Atlantis II Deep, the transition layer between the UCL and the normal Red Sea water is very thick (25-30 m : Table 2) and characterized by highly changeable temperature profiles [23]. The heat transfer through such a complex upper interface cannot be predicted by referring to a standard model. A precise estimate of this parameter would require detailed knowledge of the changes in the temperature structure of the layer with time. As this information is not available, the lower brine pool is chosen as the reference system for the heat-mass balance calculation in preference to a system including both the UCL and the LCL (Table 1). The lower interface of Atlantis II Deep has been very sharp over the past 15 years. The heat exchanges through it have been therefore essentially conductive with, as a first approximation, negligible diffusive transfer of mass (section 3-1).

4.2. Equations.

The heat-mass balance calculation applies to a time length $\Delta t = (t_f - t_o)$. The LCL is modelled as a prismatic box with an area S and a heigth x (Fig.5A).The heat-mass balance of the lower brine in Atlantis II Deep over the time range (t_o, t_f) can be expressed as a function of three unknown parameters (Figs. 5A and 5B) : M_e = the mass of fluid expelled out of Atlantis II Deep over Δt; T_S = the temperature of the hydrothermal brine; M_S = the mass of the hydrothermal brine discharged over Δt into the LCL. Highly changeable chemical gradients in interstitial waters from the sediments show that the flux of pore water to the LCL is small [51].

Over the time length Δt, all the mass brought by the spring (i.e. M_S) accounts for (i) the observed increase in the mass of the lower brine (i.e. $M_{tf}-M_{to}$), and (ii) the mass of brine overflowed towards Chain A Deep (i.e. M_e; Fig. 5B):

$$M_{tf} - M_{to} + M_e = M_s \qquad (1)$$

We shall assume that, in the time range (t_o, t_f), only one catastrophic expulsion of brine from Atlantis II Deep has occurred at time $t=t_e$. The variations of the enthalpy of the system over Δt are :

$$\Delta H_{o-f} = H_f - H_o = (H_f - H(t_e-dt)) + (H(t_e+dt) - H_o) \qquad (2)$$

Let (M_{to},T_o), (M_{te},T_e), (M_{tf},T_f) be the mass and the temperature of the system at time $t= t_o$, $t= t_e$ and $t= t_f$ respectively (Figs.5A and 5B), let T_{ref} be a reference temperature. As the evolution of the system is isobaric, it follows :

$$\Delta H_{o-f} = \Delta Q_{o-f} = (Q_f - Q(t_e-dt)) + (Q(t_e+dt) - Q_o) =$$

$$\int_{Tref}^{Tf} M_{tf}\, c_p(T)\, dT - \int_{Tref}^{Te} (M_{te} - M_e)\, c_p(T)\, dT$$

$$+ \int_{Tref}^{Te} M_{te}\, c_p\,(T)\, dT - \int_{Tref}^{To} M_{to}\, c_p\,(T)\, dT \qquad (3)$$

Over the time range Δt, the system exchanges heat by three processes (Fig. 5C) :

(i) conductive input of heat through the sediments :

$$\Delta Q_c^i = \int_{to}^{tf} S\, \Phi_c^i\, dt \qquad (4)$$

(ii) heat lost on top of the system :

$$\Delta Q_c^o = -\int_{to}^{tf} S\, \Phi_c^o dt = -\int_{to}^{tf} \lambda\, S\, (\Delta T_{li}(t) / x_{li})\, dt \qquad (5)$$

where λ is the thermal conductivity of the lower brine and $\Delta T_{li}(t) / x_{li}$ is the temperature gradient across the lower interface of the Deep;

(iii) heat brought by the geyser spring :

$$\Delta Q_s^i = +\int_{Tref}^{Ts} M_s\, c_p(T)\, dT \qquad (6)$$

The conductive exchange through the lateral walls of the box is negligible because the lower brine in Atlantis II Deep is about three orders of magnitude longer or wider than thick.

The heat balance equation for the system is:

$$\Delta Q_{o\text{-}f} = \Delta Q_c{}^i + \Delta Q_c{}^o + \Delta Q_s{}^i$$

or, combining equations (3) to (6) :

$$\int_{Tref}^{Tf} M_{tf}\, c_p(T)\, dT - \int_{Tref}^{Te} (M_{te} - M_e)\, c_p(T)\, dT + \int_{Tref}^{Te} M_{te} c_p(T)\, dT$$

$$-\int_{Tref}^{To} M_{to}\, c_p(T)\, dT = \int_{to}^{tf} S\, \Phi_c^i\, dt - \int_{to}^{tf} \lambda\, S\, (\Delta T_{li}(t) / x_{li})\, dt + \int_{Tref}^{Ts} M_s\, c_p(T)\, dT \qquad (7)$$

Replacing T_{ref} by T_e in equations (1) and (7), it follows :

$$\int_{Te}^{Tf} M_{tf}\, c_p(T)\, dT + \int_{To}^{Te} M_{to}\, c_p(T)\, dT = \int_{to}^{tf} S\, \Phi_c^i\, dt - \int_{to}^{tf} \lambda\, S\, (\Delta T_{li}(t) / x_{li})\, dt + \int_{Te}^{Ts} M_S\, c_p(T)\, dT \qquad (8)$$

4.3. Solution.

- z_{li} , **S, V** : Hartmann [23] determined to within ±0.5m the depth of the lower interface in 1965, 1971, 1972 and 1977; the values are given in Figure 3. The area of the lower interface (S) from 1965-1980 has been estimated from new planimetric measurements of the bathymetric map by Bäcker and Richter [39]. Hence, the volume of the lower brine (V) was determined, taking into account the changing depth of the lower interface (Fig.3A, [23]). For example, in 1965, S and V were estimated to have been 43 km^2 and 2.7 km^3 respectively, the lower interface being at a depth of -2050.5 m in 1965. The volumes are 10 % lower than those published by Hartmann [23].

-x_{li}: The transition between the UCl and the LCL takes place over a vertical distance of 1± 0.2 m [23]. As the fluctuations of the thickness of

the lower interface with time are not known precisely, x_{li} is taken constant in the time range from 1965 to 1980.

-Φ_c^i : In 1966, Erickson and Simmons [34] estimated that the heat flux through the sediment was in the range 0.63-0.84 Wm^{-2} (15 to 20 HFU), by interpreting the temperature profiles measured at that date in the sediments all over the Deep. Obviously, the measured thermal gradients were transient, as discontinuous convection is the dominant process in Atlantis II Deep. The conductive influx of heat to Atlantis II Deep has therefore probably changed with time. It is worth noting that Erickson and Simmons [34] interpreted a composite temperature profile of all the 1966 thermal data in terms of the cooling of a 10 m-thick layer of sediment from 74°C to 56°C in 6 to 7 years. In the absence of data enabling changes in the conductive influx of heat to the Deep to be estimated, Φ_c^i will be taken constant both in time and space over the Deep and equal to 0.67 Wm^{-2} (16 HFU).

- λ: In the temperature range (T_o, T_f), λ is considered constant and equal to the thermal conductivity of liquid water at 57°C [22] i.e., 0.648 W/m/K [52].

- ρ : As the salinity of the LCL has not significantly departed from 26 wt % eq. NaCl from 1965 to 1980 [23; 53], both the lower brine and the hydrothermal fluid over the time range Δt are modelled in terms of a 26 wt % NaCl (6M) solution. (T_f - T_o) has not exceeded 10°C from 1965 to 1980 therefore, in the temperature range (T_o,T_f), ρ is considered constant and taken equal to ρ_o = 1.18154 g/cm^3 [54]. It follows :

$$M_{to} = \rho_o V_o \quad (9)$$

$$M_{tf} = \rho_o V_f \quad (10)$$

where V_o and V_f are the volume of the LCL at t_o and t_f respectively.

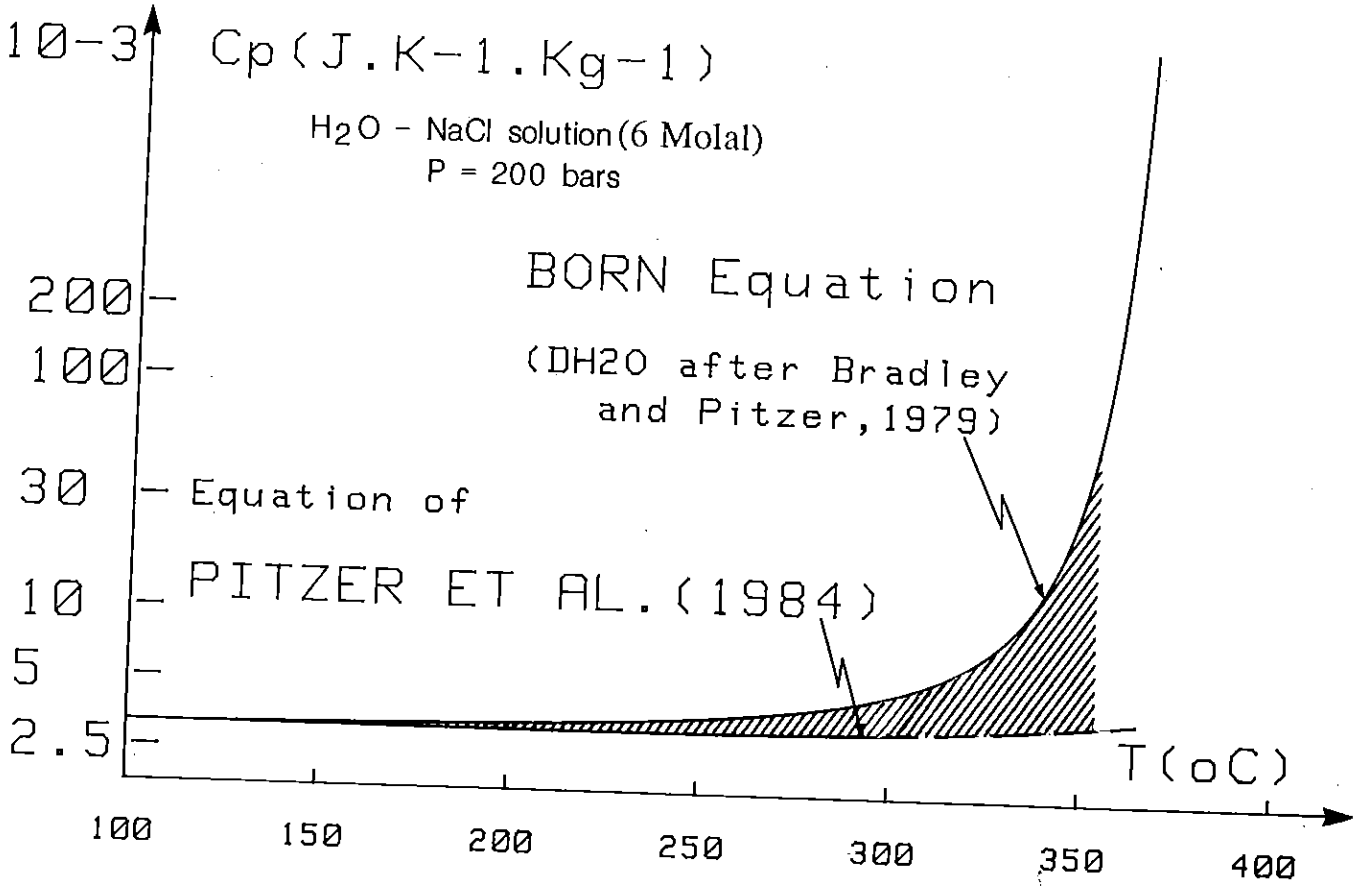

Fig. 6 : Calculated isobaric heat capacities of a 6 M H_2O-NaCl solution under pressure as a function of temperature, using the equation of Pitzer et al. [54] extrapolated above 300°C, and the equation of Born [56] modified after Wood et al. [57] (calculations after Quint, Groslier and Coxham).

-T_e : Brine expulsion from Atlantis II Deep is arbitrarily assumed to have occurred when the temperature of the LCL was $T_e = (T_f + T_o)/2$.

- $c_p(T)$: In the temperature range (T_o, T_f), the heat capacity of the lower brine can be taken as constant and equal to $c_{po} = 3.2044\ 10^3\ J\ kg^{-1}K^{-1}$ [54]. In the temperature range 200°-300°C, the cp's of pure water and of moderately saline solutions increase by ≈ 10% [54, 55]. Calculations by Pitzer et al. [54] and Helgeson [55] predict that the specific heat of 3 to 6 molal H_2O-NaCl solutions under pressure also increase moderately between 200° to 300°C (Fig. 6). In the following calculations, two models have been used to calculate the cp's of the hydrothermal brine taken as a 6 molal H_2O-NaCl solution :

(i) the values predicted by the equation of Pitzer et al. [54] below 300°C have been fitted by a least square method and extrapolated to higher temperatures. Figure 6 shows that the cp's thus extrapolated increase by≈ 15% in the range 100°-350°C.

(ii) The cp's of pure water near its critical point can be calculated using the equation of Born [56]. This equation, with additional terms to take into account the compressibility of the fluid [57], and with the equation of Bradley and Pitzer [58] to model the dielectric constant of pure water, have been used to predict the cp's of the hydrothermal brine at 200 bars (Quint, Grolier and Coxham, unpublished). Figure 6 shows that the cp's thus predicted for the brine increase exponentially above 300°C. On account of the above approximations, and depending on the model chosen for the cp's (i.e. cp(T)), equation (8) combined with equations (9) and (10) becomes :

$$c_{po}\,\rho_o\,(V_f + V_o)\,(T_f - T_o)/2 - \int_{(T_f+T_o)/2}^{T_s} M_s\,c_p(T)\,dT = +0.67\,S\,(t_f - t_o) - \lambda\,S\int_{to}^{tf}(\Delta T_{li}(t)/x_{li})\,dt \quad (11)$$

Equations (1) and (11) express the heat-mass balance of Atlantis II Deep as a function of the three unknown parameters T_S, M_S, M_e. These simplified

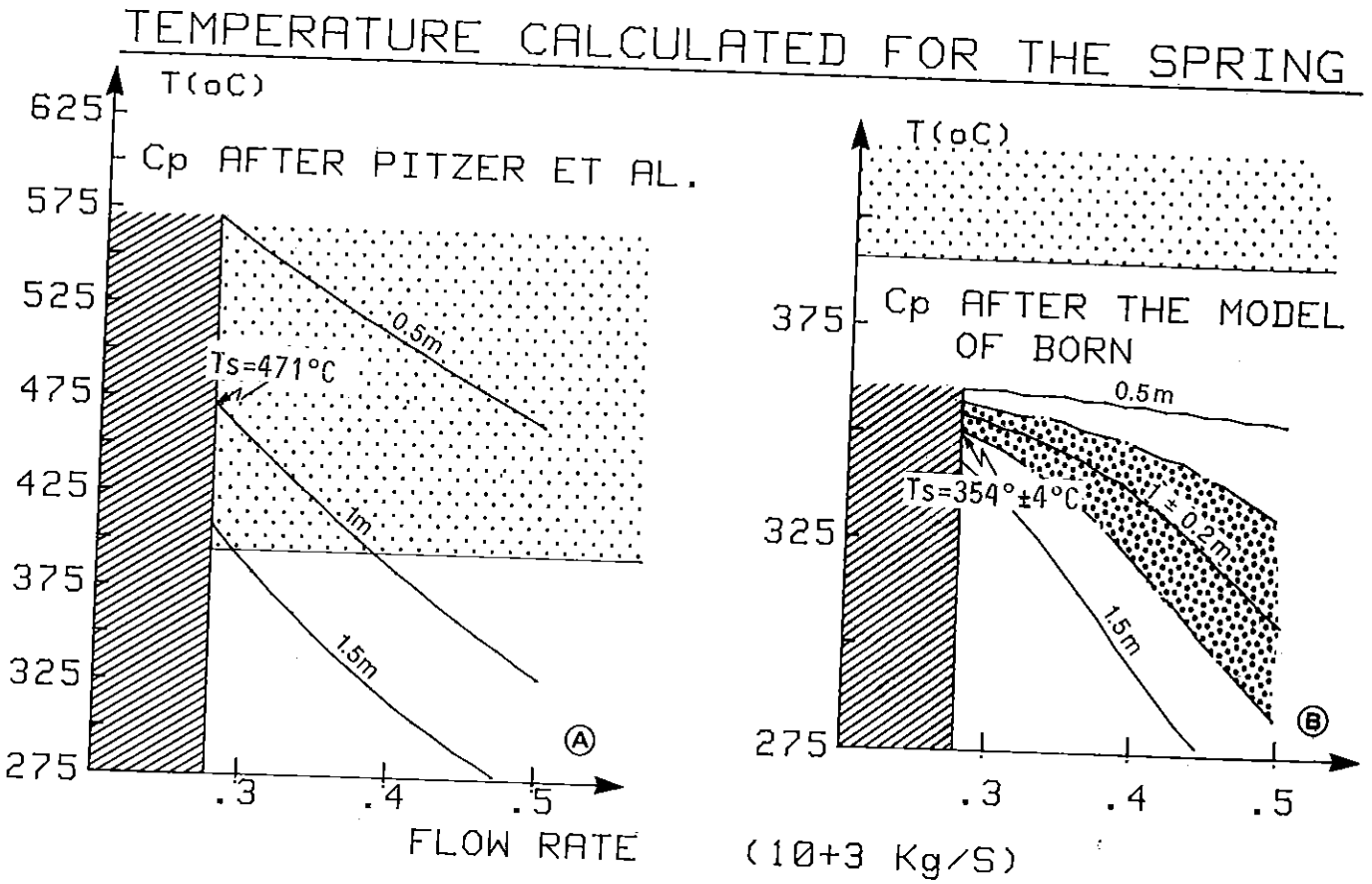

Fig. 7 : Temperatures calculated for the spring as a function of the mass flow rate, using the data summarized in Figure 3 and taking either (A) the equation of Pitzer et al. [54] or (B) the modified equation of Born [56,57] to calculate the cp's (see Fig.6). Numbers above the curves indicate the thickness of the interface chosen in the calculation (0.5, 1, 1.5m). Flow rate values in the hatched area are excluded, given the observed rising rate of the lower interface between 1965 and 1977 (see Fig. 3A). The spring temperatures in the light dotted area are also excluded as they are above the boiling temperature of the hydrothermal brine on the sea floor [21]. The temperature of the spring decreases if the mass of fluid expelled out of the lower brine pool increases (corresponding to increasing flow rates). Fig. 7A shows that the changes in the temperatures and the mass of the lower brine observed from 1965 to 1977 cannot be interpreted in terms of a realistic spring temperature if the cp's calculated below 300°C using the equation of Pitzer et al. [54] are extrapolated to higher temperatures. A spring temperature of 354°± 4°C is calculated using the modified equation of Born [56, 57] which predicts an exponential increase of the cp's above 300°C (x_{li}= 1 ± 0.2 m [23] and M_e=0).

equations have been solved using the data indicated above, including the two possible models for the heat capacities of the hydrothermal brine. The mean temperature of the geyser spring from 1965-1977 calculated for each of the two models for the cp's is shown in Figure 7 as a function of a variable loss of mass out of the system. Figure 8 shows the spring temperatures calculated over shorter periods of time from 1965 to 1980, assuming no loss of mass out of the lower brine.

5. Discussion.

Equations (1) and (11) express the variations of the mass and enthalpy of the system with time, both of which only depend on the initial and final states of the system. The average temperature and flow rate of the spring over a given period can thus be determined, whether the spring has been steady or discontinuous. The precision of the calculated T_S and Q_S depends only on the accuracy of the physical parameters of the Deep, to be discussed below.

5.1. The period 1965-1977.

The homogeneous temperature-depth data set of Preussag provides a unique way to average the temperature and flow rate of brine discharge in Atlantis II Deep from 1965 to 1977. The minimum flow rate of brine discharge, corresponding to no brine overflow towards the near-by Deeps, has been 280 kg/s (Fig. 7). Discharge flow rates are all the greater as more brine has overflowed out of the Deep.

Calculations show that, from 1965-1977, the heat lost from the top of the lower brine ($=\Phi_c^o$) has been about 7.51 W/m^2 ($x_{li}=1$) and the heat flux required to increase the temperature of the lower brine pool from 56° to 61.5°C has been about 3.34 W/m^2. As the conductive input of heat at the

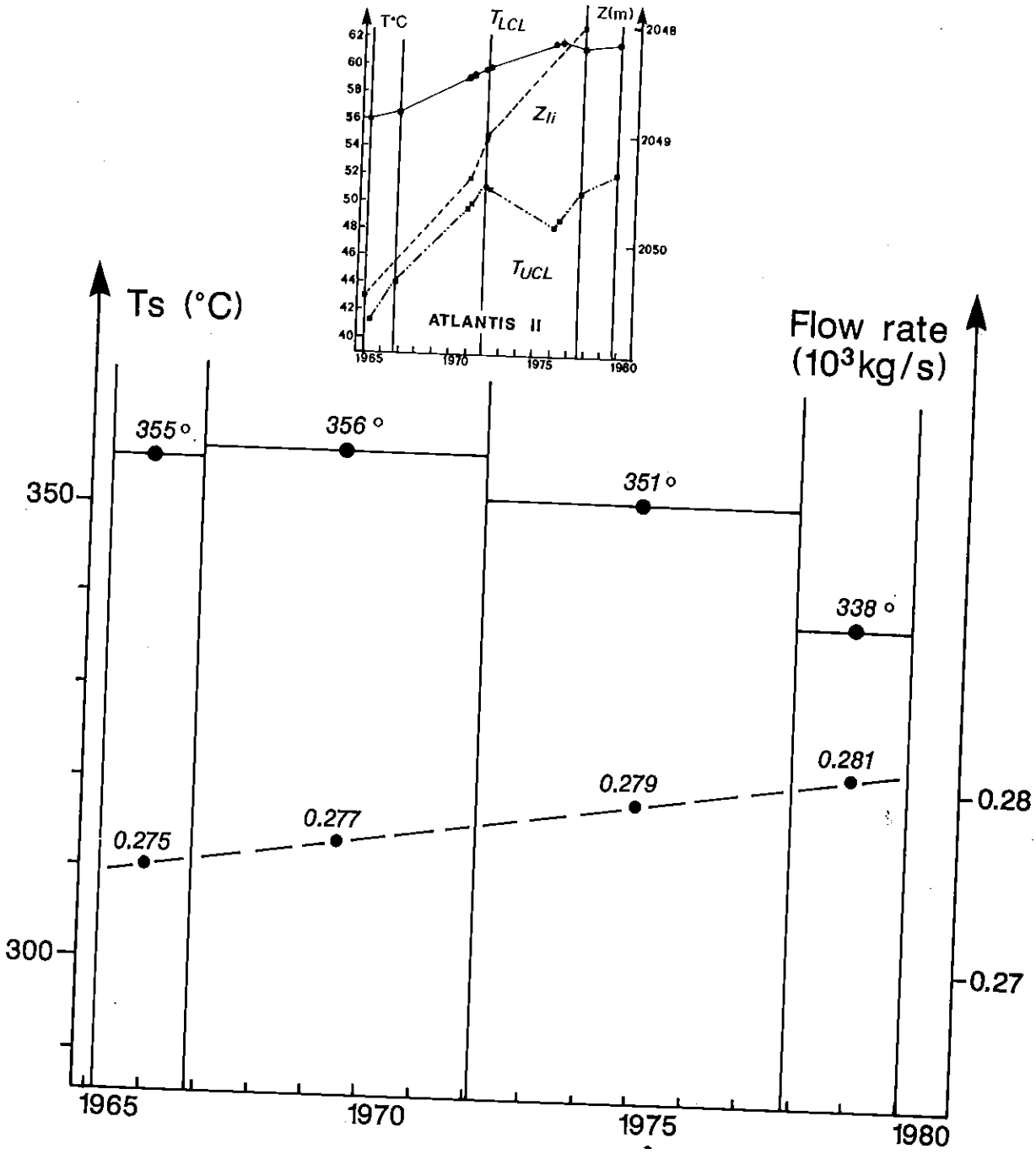

Fig. 8 : Spring temperatures and flow rates calculated in the time ranges 1965-1966, 1966-1971, 1971-1977, 1977-1979 (x_{li}= 1m and M_e= 0), assuming that no mass is lost out of the lower brine, and using the data shown in inset and in Figure 3.

bottom of the Deep has been taken constant and equal to 0.67 W/m^2, Φ_c^o is the major term of the heat-mass balance equations [22]. Previous heat-mass balance calculations have neglected the heat lost by conduction from top of the chosen system. This explains why the temperature of the spring in Atlantis II Deep has been systematically underestimated at values below 215°C (Table 1).

The calculated temperature of the spring strongly depends on the model chosen for calculating the cp's. Using the equation of Pitzer et al. [54] with values of cp(T) between 3240 and 9800 J/ kg/ K in the temperature range 56°-470°C (Fig.6), a maximum spring temperature of 471°C is required to account for the observed changes in the mass and temperature of the lower brine (Fig.7A). Taking into consideration an heat lost from the top of the system of about 6.3 W/m^2, Monin and Plakhin [47] obtained quite a comparable temperature (490°C; Table 1). The temperature of the spring at the bottom of Atlantis II Deep, however, cannot have exceeded 390°C because, at a pressure of 220 bar, this is about the temperature of unmixing at its composition [21]. Hence it is concluded that the heat-mass budget of Atlantis II Deep from 1965 to 1977 cannot be interpreted in terms of a realistic temperature of brine discharge unless the heat capacities of concentrated brines are markedly higher than 4000 J /kg /K over part of the temperature range 56°-390°C. On using the modified model of Born [56, 57] which predicts a near exponential increase of the cp's above 300°C, a temperature of 354°C is obtained for the spring in the time range 1965-1977, assuming that no mass has been lost out of Atlantis II Deep (Fig.7). This mean maximum temperature of brine discharge of 354°C is quite consistent with the mean trapping temperature of the fluid inclusions of 333°C at 220 bars [59] in epigenetic anhydrites containing a 22±1 wt% eq. NaCl solution (Fig.9; [21]). Only

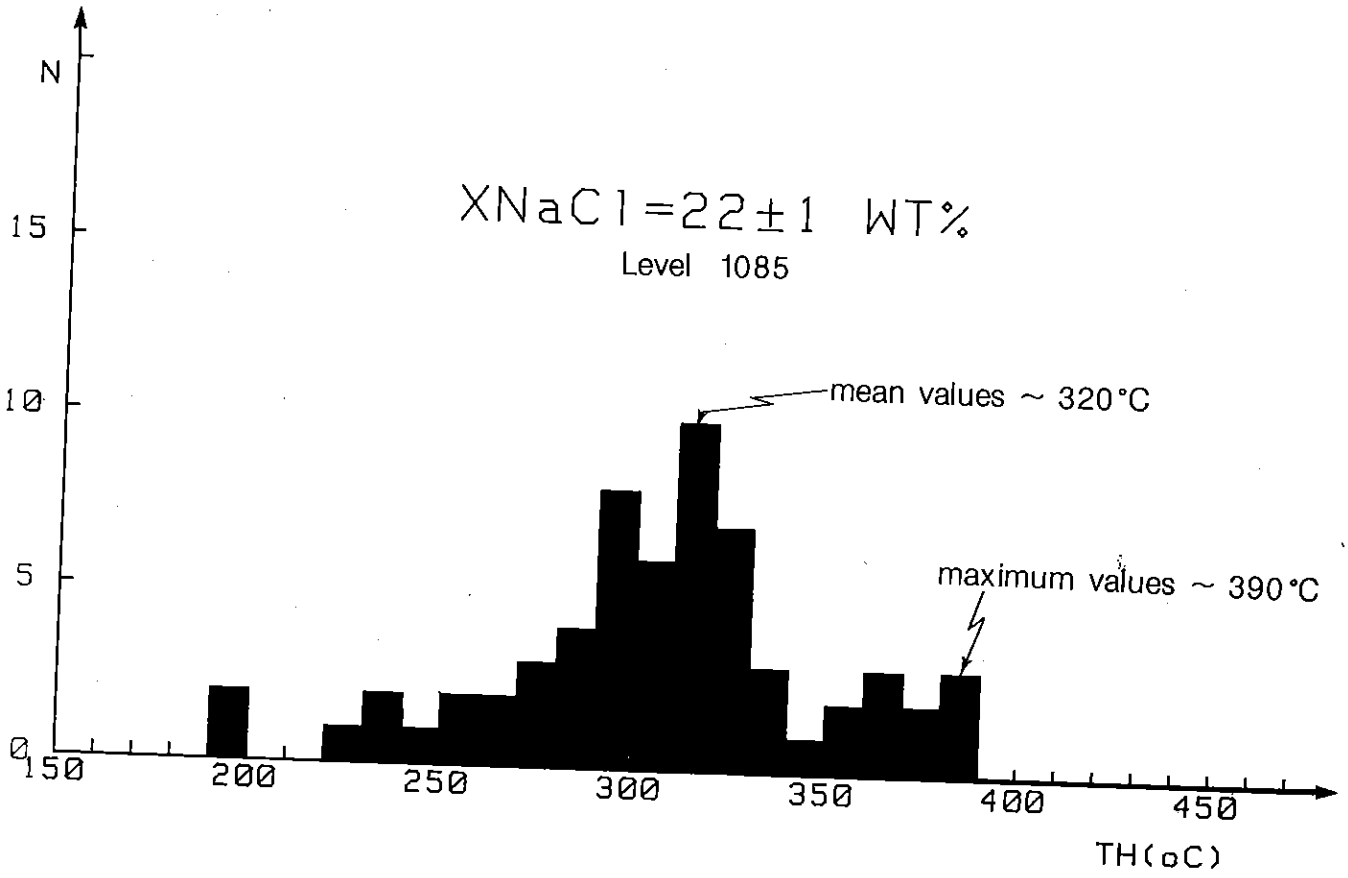

Fig. 9 : Histogram of homogenization temperatures to liquid of the fluid inclusions with a composition in the range 22 ± 1wt.% eq. NaCl in epigenetic anhydrites from the SW Basin [21]. Mean homogenization temperatures around 320°C indicate mean trapping temperatures on the sea floor of 333°C, on account of the pressure correction [59].

the temperatures calculated using the modified model of Born [56, 57] for the cp's will be considered hereafter.

5.2.Precision of the temperature .

x_{li}. Φ_c^o being proportional to $1/x_{li}$, the uncertainty in x_{li} of about ±0.2 m [23] results in an uncertainty in T_S of about ± 4 °C. This uncertainty increases as the temperature decreases to ≈ 300°C and remains at about ± 25°C below 300°C (Fig. 7) because of the exponential form of the cp relation (Fig. 6). Between 1965 and 1977, x_{li} may have varied outside of the range 1±0.2 m. If x_{li} is taken to vary in the range 0.5-1.5 m, the calculated spring temperature varies from 360° to 343°C. It is concluded that such an uncertainty in x_{li} does not result in a large error in T_S, so long as the spring temperature remains around 350°C.

M_{to}, M_{te}. The uncertainty in T_S related to a poor knowledge of the mass of the lower brine is very minor. This is because the calculation involves the changes in the mass of the lower brine with time and this is better known than the mass of the system at a given time t.

T_{LCL}. The temperature of the LCL over the whole Deep at a given time t is difficult to average. The temperature in this layer varies both vertically and horizontally, i.e. from one basin to another. Also, a cooler layer of lower brine, whose temperature has remained unchanged with time [24, 37], exists at the bottom of the N and E basins.The related uncertainty in T_S is however minor because heat-mass balance equations only involve the variations of the temperature in these layers.The temperature of the LCL over the Deep was averaged at a given time using the temperature profiles measured in each basin, taking into account all of the lower brine layers in the separate basins as a function of their specific temperature and volume [24]. The difference between the average value

obtained and the temperature measured in the SW basin was found to be ≈0.8°C, i.e. less than the analytical uncertainty in temperature [23].

5 .3. Precision in the spring flow rate.

The uncertainty in the calculated flow rate, based on planimetry, is around ± 50 kg/s. This is however a minimum value as it does not take into account the uncertainty on the the map itself, which is quite difficult to evaluate.

From the temperature profiles measured in 1971-1972 in the Chain A Deep [24], it is possible to estimate that the amount of brine which has recently overflowed towards that Deep represents a 5 m-thick layer. Given that the area of the top of the lower brine pool in the Chain A Deep is very small, calculations show that the corresponding amounts of brine expelled from Atlantis II Deep from 1965-1977 only results in a negligible underestimation of the calculated flow rate of the spring. There is no indication of any recent significant transfer of mass towards the Discovery Deep (section 3.2). However, calculations show that a one meter increase in the thickness of the lower brine of the Discovery Deep corresponds to an additional mass of around 3.6 10^9 kg brought by the spring in Atlantis II Deep. Over a period of 12 years, this implies an underestimation of around 9 kg/s of the flow rate of the spring. The quantity of brine lost from Atlantis II Deep towards Discovery Deep, if any, must therefore be taken into account in heat-mass balance calculations of Atlantis II Deep. This becomes more important as the time range over which the calculation is made decreases. Otherwise, the flow rate is underestimated and the temperature of the spring overestimated.

The lower interface of Atlantis II Deep may have been recently disrupted for a short period of time. A mm to cm - thick level of limonite enriched in lepidocrocite exits in the amorphous horizon on top of the

sediment [39]. Lepidocrocite is an iron oxyhydroxide, whose formation appears to be related to the rapid oxidation of Fe^{II} [40]. The formation of this mineral in the Atlantis II Deep is probably associated with a transient influx of Fe^{II}-rich lower brine into the upper brine. Lepidocrocite was subsequently sedimented all over the Deep. Hartmann [60] noted that the lower brine contains an excess of dissolved sulfate compared to the theoretical value based on conservative mixing, which has continuously increased from 1966 to 1977. This excess of sulfate originates from the dissolution of particulate anhydrite which was supplied by the lower brine through the lower interface [21, 26]. Turner [22] has shown that molecular diffusion across the lower interface is, by far, more dominant than turbulent mixing. Particulate anhydrite must have been supplied to the upper brine by a transient disruption of the lower interface by the hot brine plume. Preliminary calculations by Urvois and Watremez (in [61]) indeed confirm that such a process is realistic. These considerations show that it is quite probable that losses of lower brine have repeatedly occurred between 1966 and 1977, in addition to that towards the Chain A Deep between 1972 and 1977. There is no way however to estimate precisely the volume of lower brine thus lost.

5.4. Changes in the hydrothermal activity with time.

Heat-mass balance calculations show that the average temperature of the geyser spring has remained essentially constant around 352.5°±2.5°C between 1965 and 1972, if no loss of mass has occurred (Fig. 8). This is for the following reason. Although the amount of heat required to increase the temperature of the lower brine (ΔQ_s^i) and the heat lost through the lower interface (ΔQ_c^o) have both varied independantly by ~15 % during this period, the sum of these two heat flows has remained nearly constant. In contrast, from 1972 to 1977, the spring temperature has dropped by

18°C because both ΔQ_c^o and ΔQ_s^i have decreased. Heat-mass balance calculations therefore show that the hydrothermal activity in Atlantis II Deep has decreased between 1966-1972 compare to that between 1972-1977, in agreement with Hartmann's conclusions [60], based on the changing chemistry of the brines.

The flow rates calculated over short periods of time from 1965 to 1980 continuously increase from 275.2 to 280.6 kg/s (Fig.8), because the area of the lower brine increases as the top of the lower brine rises. On account of an uncertainty of around 50kg/s due to planimetry, the flow rate of the spring can be considered to have remained constant at about 278±3 kg/s from 1965 to 1980. The estimates of temperature and mass flow rate must however be taken with caution, due to the fact that some lower brine was probably added to the upper brine from 1966-1977. This was not taken into account in the calculations (see sections 3.2 and 4.3). It is therefore concluded that the results presented in Figure 8 overestimate T_S over the time range 1966-1972 (and underestimate Q_S) by a larger amount than they do over the time range 1972-1977, thereby making the comparison of the results over the two periods difficult.

The data of Bubnov et al. [35] and Hartmann [23] imply a decrease in the temperature of the lower brine of 0.38 °C from June 1976 to November 1977. Based on heat-mass balance calculations and interpolation of the position of the lower interface in June 1976 between the values given by Hartmann [23], a spring temperature of 308°C is implied. This is 46°C below the one calculated for the previous years. Such a low temperature must be interpreted with caution however, as it may reflect a lack of consistency between the two sets of lower brine temperature data. Also, because of lack of data, the increase in the lower brine volume cannot be precisely estimated for this short time range.

6. Conclusions.

The major term in the heat budget of the lower brine of Atlantis II Deep is the conductive output of heat through the lower interface on top of the system [22]. Most previous heat-mass balance calculations have neglected this term. They therefore have systematically underestimated the temperature of the spring in Atlantis II Deep at values below 215 ° C (Table 1).

The present work shows that the heat-mass balance of Atlantis II Deep cannot be interpreted in terms of a realistic spring temperature if the cp's of the brine are derived from an extrapolation of the Pitzer et al. equation [54] above 300°C. The cp's of the brine have been calculated near the critical point of pure H_2O using the equation of Born [56] modified after Wood et al. [57] (unpublished calculations by Quint, Grolier and Coxham). This model (Fig. 6) predicts a near exponential increase of the cp's above 300°C. From 1965 to 1977, neglecting the loss of matter out of the lower brine of Atlantis II Deep, the calculated spring temperature is 354°±4°C, taking into account a 1±0.2m thickness of the lower interface. These values are comparable to the mean trapping temperatures of the fluids in the epigenetic anhydrites from the SW Basin of about 330°C [21].

Recent hydrographic data on the Discovery, Chain A and Chain B Deeps near Atlantis II Deep [24] show that the transfer of lower brine from Atlantis II to them has been negligible over the past 15 years. In contrast, mineralogical [39] and chemical data [60] suggest that, during the past 15 years and particularly between 1966-1972, the lower interface of Atlantis II Deep has been repeatedly disrupted and that unknown amounts of lower brine were supplied to the upper brine. It is therefore concluded that, unless the transfer of matter out of the lower brine can be precisely estimated over short periods of time, the mean temperature of the spring is

best estimated using heat-mass balance calculations taking into consideration the hydrologic variations of Atlantis II Deep over the longest time range possible, so as to minimize the mass lost on top of the system compare to the mass brought in by the spring.

Acknowlegment:. The authors are grateful to C. Moyne and J.C. Batsale for their help in putting the heat-mass balance equations in a proper thermodynamic form, and to F. Albarède and S.M.F. Sheppard for detailed review. H. Bäcker, P. Guennoc, E. Oudin, J. Post and M. Urvois greatly improved the manuscript by their knowledge of the geology of the Atlantis II Deep area. Many discussions with P. Watremez concerning the physics of the Deep were greatly appreciated. Finally, J.R. Quint, J.-P. E. Grolier and J.Y. Coxham provided a model for the cp's of the hydrothermal brine which was decisive in solving heat-mass balance equations in terms of a realistic spring temperature. This work was fully financed by C.R.P.G. (Nancy, France).

References

1 P.E. RONA, Hydrothermal mineralization at seafloor spreading centers, Earth Science Reviews 20, 1-104, 1984.

2 E. OUDIN, Minéralogie des gisements et indices liés à des zones d'accrétion océaniques actuelles (rive Est-Pacifique et Mer Rouge) et fossile (Chypre), Chron. Rech. Minière 470, 43-56, 1983.

3 F. ALBAREDE, A. MICHARD, J.F. MINSTER and G. MICHARD, $^{87}Sr/^{86}Sr$ ratios in hydrothermal waters and deposits from the East Pacific Rise at 21° N, Earth Planet. Sci. Lett. 55, 229-236, 1981.

4 G. MICHARD, F. ALBAREDE, A. MICHARD, J.F. MINSTER, J.L. CHARLOU and N. TAN, Chemistry of solutions from the 13°N East Pacific Rise hydrothermal site, Earth Planet. Sci. Lett. 67, 297-307, 1984.

5 H. BACKER, Rezente hydrothermal-sedimentäre Lagerstättenbildung, Erzmetall 32, 544-555, 1973.

6 J.L. BISCHOFF and F.W. DICKSON, Seawater-basalt interaction at 200°C and 500 bars; implication for origin of sea-floor heavy metal deposits and regulation of sea-water chemistry, Earth Planet. Sci. Lett. 25, 383-397, 1975.

7 M.J. MOTTL and H.D. HOLLAND, Chemical exchange during hydrothermal alteration of basalt by sea water. I. Experimental results

for major and minor components of seawater, Geochim. Cosmochim. Acta 42, 1103-1115, 1978.

8 M. ARNOLD and S.M.F. SHEPPARD, East Pacific Rise at latitude 21°N : isotopic composition and origin of the hydrothermal sulfur, Earth Planet. Sci. Lett. 56, 148-156, 1981.

9 D.R. CONVERSE , H.D. HOLLAND and J.M. EDMOND, Flow rates in the axial hot springs of the East Pacific Rise (21°N) : implications for the heat budget and the formation of massive sulfide deposits, Earth Planet. Sci. Lett. 69,159-173, 1984.

10 H. CRAIG, Geochemistry and origin of the Red Sea brines, in : Hot brines and recent heavy metal deposits, E.T. DEGENS and R.A. ROSS, eds., Springer Verlag New York, 208-242, 1969.

11 F.T. MANHEIM, Red Sea geochemistry, in : Initial Reports of the Deep Sea Drilling Project 23, R.B. WHITMARSH, O.E. WESER, D.A. ROSS et al., eds., Washington (U.S. Government Printing Office), 975-998, 1974.

12 B. DUPRE, G. BLANC and J. BOULEGUE, Pb isotopes on metalliferous sediments from the Red Sea, Terra Cognita 7, 228, 1987.

13 M.H. DELEVAUX and B.R. DOE, Preliminary report on uranium, thorium, lead contents, and lead-isotopic composition in sediment samples from the Red Sea, in : Initial Reports of the Deep Sea Drilling Project 23, R.B. WHITMARSH, O.E. WESER, D.A. ROSS et al., eds., Washington (U.S. Government Printing Office, 943-946, 1974.

14 W.C. III SHANKS and J.L. BISCHOFF. Ore transport and deposition in the Red Sea geothermal system : a geochemical model, Geochim. Cosmochim. Acta 43, 1507-1519, 1977.

15 I.R. KAPLAN, R.E. SWEENEY and A. NISSEMBAUM, Sulfur isotope studies on Red Sea Geothermal brines and sediments, in : Hot brines and recent heavy metal deposits, E.T. DEGENS and R.A. ROSS, eds., Springer-Verlag New York, 474-498, 1969.

16 R.J. POTTORF and H.L. BARNES, Mineralogy, geochemistry and ore genesis of hydrothermal sediments from the Atlantis II deep, Red Sea, Econ. Geol. Monograph 5, 198-223, 1983.

17 R.J. POTTORF, Hydrothermal sediments of the Red Sea, Atlantis II Deep - a model for massive sulfide-type ore deposits. Unpubl. Ph.D. Thesis, The Pennsylvania State Univ., 192 p, 1980.

18 Y. THISSE, Sédiments métallifères de la fosse d'Atlantis II (Mer Rouge). Contribution à l'étude de leur contexte morpho-structural et de leurs caractéristiques minéralogiques et géochimiques. Unpubl. Thesis Université Orléans et B.R.G.M., Fr., 155 p., 1982.

19 P.A. ZIERENBERG and W.C. SHANKS, Mineralogy and Geochemistry of epigenetic features in metalliferous sediments, Atlantis II Deep, Red Sea, Econ. Geol. 78, 57-72, 1983.

20 E. OUDIN, Y. THISSE and C. RAMBOZ, Fluid inclusion and mineralogical evidence for high-temperature saline hydrothermal

circulation in the Red Sea metalliferous sediments : preliminary results, Marine Mining 5, 3-31, 1984.

21 C. RAMBOZ, E. OUDIN and Y. THISSE, Geyser-type discharge in Atlantis II Deep (Red Sea) : evidence from fluid inclusions in epigenetic anhydrite, accepted for publication in Canad. Mineral.

22 J.S. TURNER, A physical interpretation of the observations of hot brine layers in the Red Sea, in : Hot brines and recent heavy metal deposits, E.T. DEGENS and R.A. ROSS, eds., Springer-Verlag New York, 164-173, 1969.

23 M. HARTMANN, Atlantis II Deep geothermal brine system. Hydrographic situation in 1977 and changes since 1965. Deep-Sea Research, 27A, 161-171, 1980.

24 M. SCHOELL, Valdivia VAO1 Rotes Meer -Golf Von Aden- Hydrography II+III, Daten- Bundesanstalt für Bodenforschung, Hannover, 1063p, 1974.

25 H. BACKER, K. LANGE and H. RICHTER, Morphology of the Red Sea Central graben between Subair Islands and Abul Kizaan, Geol. Jb. 13, 79-123, 1975.

26 P.A. ZIERENBERG AND W.C. SHANKS, Isotopic constraints on the origin of the Atlantis II, Suakin and Valdivia brines, Red Sea, Geochim. Cosmochim. Acta 50, 2205-2214, 1986.

27 J.S. TURNER, Buoyancy effects in fluids, Cambridge University Press, 368 p, 1979.

28 A.D. VOORHIS and D.L. DORSON, Thermal convection in the Atlantis II hot brine pool, Deep-Sea Research 22, 167-175, 1975.

29 M. SCHOELL and M. HARTMANN, Detailed temperature structure of the hot brines in the Atlantis II deep area (Red Sea), Marine Geol.. 14, 1-14, 1973.

30 D.T. PUGH, Origin of hot brines in the Red Sea, Nature 214, 1003-1004, 1967.

31 D.A. ROSS, Temperature structure of the Red Sea brines, in : Hot brines and recent heavy metal deposits, E.T. DEGENS and R.A. ROSS, eds., Springer-Verlag New York, 148-152, 1969.

32 R.G. MUNNS, R.J. STANLEY and C.D. DENSMORE, Hydrographic observations of the Red Sea brines, Nature 214, 1215-1217, 1967.

33 P.G. BREWER, C.D. DENSMORE, R. MUNNS and R.J. STANLEY, Hydrography of the Red Sea brines, in : Hot brines and recent heavy metal deposits, E.T. DEGENS and R.A. ROSS, eds., Springer-Verlag New York, 138-147, 1969.

34 A.J. ERICKSON and G. SIMMONS, Thermal measurements in the Red Sea hot brine pools, in : Hot brines and recent heavy metal deposits, E.T. DEGENS and R.A. ROSS, eds., Springer-Verlag New York, 114-121, 1969.

35 V.A. BUBNOV, V.S. FEDOROVA and A.D. SHCHERBININ, New data on the deep-water brines in the Red Sea, Okeanologia 17, 603-611, 1977.

36 D.T. PUGH, Temperature measurements in the bottom layers of the Red Sea brines, in : Hot brines and recent heavy metal deposits, E.T. DEGENS and R.A. ROSS, eds., Springer-Verlag New York, 158-163, 1969.

37 M. SCHOELL, Heating and convection within the Atlantis II Deep Geothermal system of the Red Sea. Proceedings Second United Nations Symposium on the Development and use of Geothermal resources. San Francisco 20-29 May 1975, 2, 583-590, 1976.

38 D.A. ROSS and J.M. HUNT, Third brine pool in the Red Sea, Nature 213, 687-688, 1969.

39 H. BACKER and H. RICHTER, Die Rezente Hydrothermal-Sedimentäre Lägerstätte Atlantis II-Tief im Roten Meer. Geol. Rundsch. 3, 697-741, 1973.

40 J. W. MURRAY, Iron oxides, in : Marine minerals, R.G. BURNS ed., Mineralogical Society of America short course notes, 47-98, 1979.

41 G. KRAUSE and J. ZIEBENBEIN, Die struktur des heissen salzreichen Tiefenwassers im zentralen Roten Meer - Meteor Forschungsergebnisse 1, 53-58, 1966.

42 M. SCHOELL and M. HARTMANN, Changing hydrothermal activity in the Atlantis II Deep Geothermal system, Nature 274, 784-785, 1978.

43 J.L. BISCHOFF, Red Sea geothermal brines deposits: therir mineralogy, chemistry and genesis, in : Hot brines and recent heavy metal deposits, E.T. DEGENS and R.A. ROSS, eds., Springer-Verlag New York, 368-401, 1969.

44 J.L. BISCHOFF, Goethite-hematite stability relations with relevance to sea water and the Red Sea brine system, in : Hot brines and recent heavy metal deposits, E.T. DEGENS and R.A. ROSS, eds., Springer-Verlag New York, 402-406, 1969.

45 J.P. HACKETT Jr and J.L. BISCHOFF J.L., New data on the stratigraphy, extent and geologic history of the Red Sea geothermal deposits, Econ. Geol. 68, 553-564, 1973.

46 D.A. ROSS, Red Sea hot brine area : revisited, Science 175, 1455-1457, 1972.

47 A.S. MONIN and PLAKHIN, Stratification and space-time variability of Red Sea hot brines, Deep-Sea Research 29,1271-1291, 1982.

48 P.G. BREWER, T.R.S. WILSON, J.W. MURRAY, R.G. MUNNS and C.D. DENSMORE, Hydrographic observations on the Red Sea brines indicate a marked increase in temperature, Nature 231, 37-38, 1971.

49 N. SVAL'NOV, V.P. STRIZHOV, Y.A. BOGDANOFF and A.B. ISAYEVA, Hydrothermal barite crusts on basalts from Atlantis II Deep (Red Sea) : Oceanology 24, p. 716-720, 1984.

50 D.E. WHITE, Hydrology, activity and heat flow of the Steamboat springs thermal system, Washoe County, Nevada, Geol. Surv. Prof. Paper 458-C, 109p., 1968.

51 G. BLANC, 1987, Géochimie de la fosse Atlantis II (Mer Rouge) : évolution spatio-temporelle et rôle de l'hydrothermalisme, Ph. D Thesis, Université P. et M. Curie, Paris, 140 p.

52 R.C. WEAST, Handbook of Chemistry and Physics, 57th edition, CRC Press, 1976.

53 L.-G. DANIELSSON, D. DYRSSEN and A. GRANELI, Chemical investigation of Atlantis II and Discovery brines in the Red Sea, Geochim. Cosmochim. Acta 44, 2051-2065, 1980

54 K.S. PITZER,.J.C. PEIPER and R.H. BUSEY, Thermodynamic properties of aqueous sodium chloride solutions, J. Phys. Chem. Ref. Data 13, 1-102, 1984.

55 H. C. HELGESON, Prediction of the thermodynamic properties of electrolytes at high pressures and temperatures, in : Chemistry and geochemistry of solutions at high temperatures and pressures, D. RICKARD and F.E. WICKHAM eds., Pergamon Press, 133-175, 1982.

56 M BORN, Volumen und hydratationswärme der ionen, Zeitschrift für Physik, 1, 45-49, 1920.

57 R.H. WOOD, J.R. QUINT and J.-P. E. GROLIER, Thermodynamics of a hard sphere in a compressible dielectric fluid. A modification to the Born equation to include the compressibility of the solvent, J. Phys. Chem. 85, 3944-3949, 1981.

58 D.J. BRADLEY and K.S. PITZER, Thermodynamics of electrolytes. 12- Dielectric properties of water and Debye-Hückel parameters to 350°C and 1 kbar, J. Phys. Chem. 83, 1599-1603, 1979.

59 Y.G. ZHANG and J.D. FRANTZ, Determination of the homogenization temperatures and densities of supercritical fluids in the system NaCl-KCl-H_2O using synthetic fluid inclusions, Chem. Geol. 64, in press.

60 M. HARTMANN, Atlantis II geothermal brine system. Chemical processes between hydrothermal brines and Red Sea deep water, Marine Geology, 64, 157-177, 1985.

61 M. URVOY, Apport de l'estimation géostatistique de l'épaisseur des unités métallifères dans la compréhension des mécanismes de mise en place des sédiments de la fosse d'Atlantis II (Mer Rouge), Unpubl. Thesis, Univ. Orléans, 1987.

62 M. HARTMANN, Sound velocity data for the hot brines and corrected depth of interfaces in the Atlantis II Deep, Marine Geol. 12, 1116-1120, 1972.

63 A. R. MILLER, C.D. DENSMORE, E.T. DEGENS, J.C. HATHAWAY, F.T. MANHEIM, P.F. MC FARLIN, R. POCKLINGTON and A. JOKELA, Hot brines and recent iron deposits in deeps of the Red Sea, Geochim. Cosmochim. Acta 30, 341-359, 1966.

64 A. R. MILLER, Highest salinity in the world ocean, Nature 203, 590, 1964.

65 H. CHARNOCK, Anomalous bottom water in the Red Sea, Nature 203, 590, 1964.

66 J.C. SWALLOW and J. CREASE, Hot salty water at the bottom of the Red Sea, Nature 205, 165-166, 1965.

67 P.G. BREWER, J.P. RILEY and F. CULKIN, The chemical composition of hot salty water from the bottom of the Red Sea, Deep-Sea Research 12, 497, 1965.

68 G. DIETRICH and G. KRAUSE, The observations of the vertical structure of hot salty water by R.V. Meteor, in : Hot brines and recent heavy metal deposits, E.T. DEGENS and R.A. ROSS, eds., Springer Verlag New York, 10-14, 1969.

69 M. HARTMANN, Investigation of Atlantis II Deep samples taken by the FS METEOR, in : Hot brines and recent heavy metal deposits, E.T. DEGENS and R.A. ROSS, eds., Springer Verlag New York, 204-208, 1969.

70 D.A. ROSS and J.M. HUNT, Third brine pool in the Red Sea, Nature 213, 687-688, 1967.

71 A.S. MONIN, E.A. PLAKHIN, A.M. PODRAZHANSKY, A.M. SAGALEVICH and O.G. SOROKHTIN, Visual observations of the Red Sea hot brines, Nature 291, 222-225, 1981.

APPENDIX

Chronological list of the oceanographic expeditions which contributed to the knowledge of the temperature-depth -salinity structure of the hot brine pools in Central Red Sea.

R/V	Date	Studied Deeps	References
Atlantis U.S.A.	1963	Atlantis II	[64, 65]
Discovery G.B.	IX-1964	Discovery	[66, 67]
Meteor F.R.G.	X-1964 27-IV-1965	⇒Discovery ⇒Atlantis II	[23, 41, 68, 69]
Atlantis U.S.A.	17,18-II-1965	Atlantis II Discovery	[63]
Chain U.S.A.	30,31-XI-1966 8-XI-1966	Atlantis II Discovery Chain	[30, 32, 33, 34, 70]
Chain U.S.A.	5-II-1971	Atlantis II	[46, 48]
Chain U.S.A.	26-III-1971	Atlantis II	[46]
Valdivia F.R.G.	III-IV-1971	Atlantis II Discovery	[23, 24, 29]
Valdivia F.R.G.	II-III-1972	Atlantis II Chain Valdivia	[23, 24, 37, 42]
Akademic Kurchatov S.S.S.R.	1976 22-III to13-VI 14-VI	⇒Atlantis II ⇒Discovery	[35]
Sonne F.R.G.	15-XI-1977	Atlantis II Discovery	[23, 42]
Akademic Kurchatov S.S.S.R.	winter-1979 II -1980	⇒Atlantis II ⇒Discovery Chain	[47, 71]

R/V= name of the research vessel

CHAPITRE V

LES MECANISMES DES CIRCULATIONS HYDROTHERMALES EN CONTEXTE DE MARGE PASSIVE

Sur les marges de l'Atlantique Nord et de l'Océan Ligure, c'est-à-dire sur la côte Est des Etats-Unis et du Canada, en Europe Occidentale et Centrale et au Maroc, on trouve en bordure du socle hercynien de nombreux filons rubannés, remplis de silice fibreuse et/ou minéralisés en F-Ba-Pb-Zn-U. Les datations par K/Ar ou Rb/Sr des argiles associées à ces filons montrent que ceux-ci témoignent d'une phase de réactivation du socle bordant les plaques européenne et nord-américaine, synchrone du rifting qui a précédé et accompagné l'ouverture des Océans Atlantique et Ligure (Mitchell et Halliday, 1976; Bernard et Skvor, 1980; Bonhomme et al., 1983). Brousse et Bellon (1983) ont établi une synthèse chronologique détaillée des évènements magmatiques et diagénétiques qui ont accompagné, du Trias à nos jours, la mise en place des filons hydrothermaux minéralisés lors du fonctionnement des rifts en Europe Occidentale et Centrale.

Mitchell et Halliday (1976) ont comparé les minéralisations des marges de l'Atlantique Nord mises en place pendant le Mésozoique à celles du fossé de la Mer Rouge, encore en évolution aujourd'hui. Ces auteurs ont proposé que, de façon très générale, il existe une activité hydrothermale génératrice de minéralisations qui est spécifique des zones crustales soumises à l'extension et qui s'étend spatialement au-delà de la zone d'ouverture proprement dite. La synthèse proposée par Pouit et Guennoc (1983) sur les minéralisations associées au fossé de la Mer Rouge confirme bien ce dernier point. L'objet des pages suivantes est d'essayer d'identifier de façon plus précise les mécanismes qui régissent les circulations hydrothermales dans les contextes de dislocation crustale, à partir d'une comparaison détaillée de deux segments minéralisés de la marge occidentale de l'Océan Ligure et du fossé de la Mer Rouge. Il s'agit respectivement de la Bordure Cévenole dans le Massif Central Français, en particulier des minéralisations fissurale et post-fissurale du gisement des

Tableau I : Comparaison des manifestations hydrothermales de la Mer Rouge Centrale et de la Bordure Cévenole (gisement des Malines, minéralisation fissurale)

	Mer Rouge Centrale (Atlantis II)	Bordure Cévenole (Minéralisation F,Les Malines)
Bassin étroit et allongé de type rift continental [1]	oui [2]	oui [3]
Direction de l'extension	NE-SW	E-W
Valeur de l'étirement	$\beta = \infty$ [4]	β=50 [5]
Structuration antérieure du socle	NE-SW [6]	décrochements tardi-hercyniens E-W , NE-SW [7,8]
Drainage des solutions métallifères dans un plan de faille	vertical selon σ_3 [2, 9, 10]	vertical selon σ_3 [11, 12]
Migration des solutions	centripète	centrifuge
Origine des fluides	eau de mer [13, 14] ±eaux météoriques [14]	eaux de formation [15]
Origine des métaux, du Pb	shales miocènes [16, 19]	shales triasiques [17, 18], Pb hercynien des sédiments [20]
Origine S	hydrothermale+bactérienne[21]	sédiments [20]
Présence d'huile, d'hydrocarbures légers	dans les incl. fluides [22] et la saumure inférieure[24]	dans les minerais [18] ou libre [23] dans les stades tardifs[12]
Profondeur de mise en place des mineralisations à proximité d'eaux oxydantes	2200m eau de mer 100 m au-dessus	de 100 à 1500 m eaux météoriques quelques 100m au-dessus
Nature de l'écran protégeant des eaux oxydantes	saumures stratifiées	argiles imperméables [12]
Nature des minéralisations	Zn-Pb-Au	Zn-Pb
Principale signature des inclusions fluides	refroidissement isochimique, évolution isotherme et isochimique; Tmax ≈ 390°-400°C [10]	refroidissement isochimique Tmax ≈ 140°C [15]
Preuve d'ébullition liée au dépôt des minéralisations	oui [10]	non [15]
Mécanisme de la précipitation	saturation brutale due à l'oxydation et l'ébullition	saturation brutale (décompression?)
contemporaine de la transition extension diffuse -extension océanique	selon le modèle de Cochran [25]	[12] [26]

1 : Perrodon, 1983; 2: Bäcker et al., 1975; 3 : Artru, 1968; 4 :Searle and Ross, 1975; 5 : Debrand-Passard, 1984; 6 : Garson et Krs, 1976; 7: Arthaud et Matte, 1975; 8 : Debelmas, 1986; 9 : Pautot, 1983; 10 : Ramboz et al., chapitre III; 11 : Lan, 1854 in Bernard, 1958; 12 : Ramboz et Charef, chapitre II; 13 : Schoell et Faber , 1978; 14 : White, 1974; 15 : Charef et Sheppard, 1988; 16: Manheim, 1974; 17 : Macquar, 1984; 18 : Connan et Orgeval, 1977; 19 : Dupré et al., 1987; 20 : Charef, 1986; 21 : Shanks et Bischoff, 1980; 22 : Oudin, Thisse et Ramboz, non publié; 23 : Verraes, 1983; 24 : Burke et al., 1981; 25: Cochran, 1983; 26 : Marini, 1987.

Malines, et celles de la Mer Rouge Centrale. La comparaison proposée ici est largement justifiée par les nombreuses analogies de structure que présentent les deux segments étudiés.

L'amincissement crustal, dans l'un et l'autre contexte, a été provoqué principalement par le jeu de failles normales, de type listrique, et par les basculements de blocs (Baudrimont et Dubois, 1977; Boillot et al., 1979; Debrand-Passard et al., 1984; de Graciansky et al., 1979; Montenat, 1986; Cochran, 1983). La Marge Cévenole pendant le Bathonien-Oxfordien bordait un bassin constitué de fosses étroites et allongées, séparées par des hauts-fonds, dans lesquels séjournait une eau de mer stratifiée et légèrement sursalée en profondeur. La Mer Rouge présente actuellement une telle structure (Artru, 1968). Il convient cependant de noter qu'un volcanisme réduit a affecté la Marge Cévenole pendant l'extension Mésozoique alors qu'un volcanisme intense a précédé l'ouverture océanique en Mer Rouge.

I- Comparaison des manifestations hydrothermales de la Bordure Cévenole et de la Mer Rouge Centrale.

On a rassemblé dans le Tableau I les éléments de comparaison entre les minéralisations hydrothermales de la fosse d'Atlantis II (Mer Rouge Centrale) et la minéralisation fissurale du gisement des Malines (Bordure Cévenole).

I-1. Contexte géotectonique et structural.

Les contextes structuraux dans lesquels se développent les minéralisations de la Mer Rouge et de la Bordure Cévenole sont représentés de façon simplifiée dans la Figure 1.

(i) Le sud des Cévennes et la Montagne Noire ont été affectés, après le Viséen Supérieur et avant le Stéphanien Moyen, par quatre familles de décrochements sous l'effet d'une compression NW-SE (Arthaud et Matte,

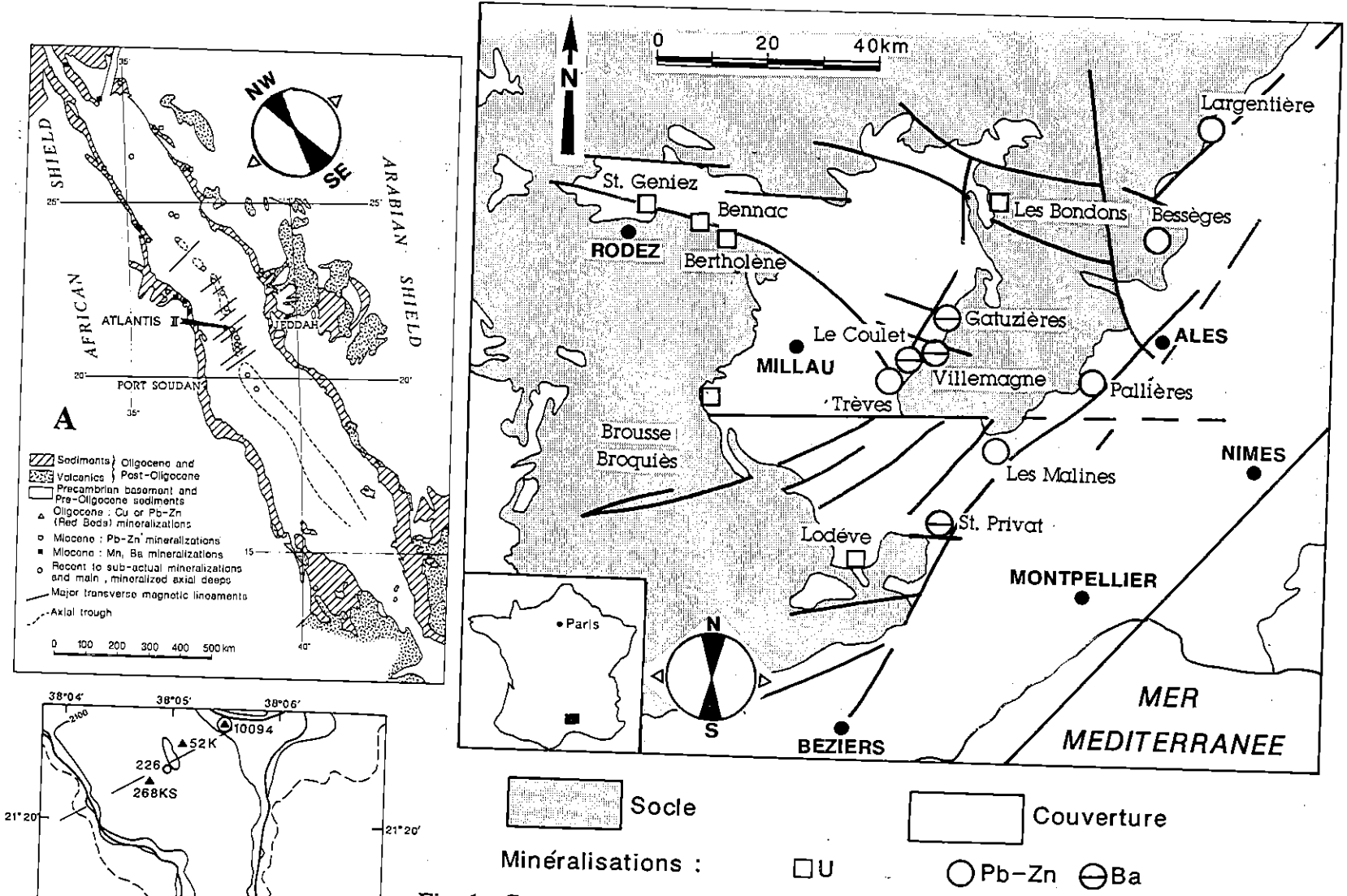

Fig. 1 : Contexte structural des minéralisations de la Mer Rouge Centrale (A, d'après Pouit et Guennoc, in Oudin et al., 1984), du bassin SW de la fosse d'Atlantis II en Mer Rouge Centrale (B, d'après Ramboz et al., chapitre III) et de la Bordure Cévenole, France (C, d'après Baudrimont et Dubois, 1977 et Macquar, 1984). La figure montre que les minéralisations sont localisées le long d'anciennes failles de socle parallèles à la direction de la distension (SW-NE en Mer Rouge, E-W sur la Bordure Cévenole).

1975). Les décrochements E-W à ESE-WNW sont des accidents majeurs dont la longueur dépasse la cinquantaine de kilomètres. Les décrochements NE-SW, NNW-SSE à NW-SE, et NNE-SSW à NE-SW, sont de longueur moindre. Ces accidents tardi-hercyniens, et principalement ceux de direction NE-SW et E-W ont conditionné la subsidence du bassin Sud-Est et les basculements de blocs de la Marge Cévenole pendant le Mésozoique (Debelmas, 1986; Triat et Truc, 1983).

(ii) En Mer Rouge, Garson et Chrs (1976) ont montré que, au nord de 19 °N, les socles arabes et africains sont affectés par d'anciennes failles de direction NE-SW. Ces failles recoupent le fossé sur toute sa largeur (Bäcker et al., 1975; Bertin et al, 1979; Pautot, 1983).

La Figure 1A fait apparaître qu'en Mer Rouge, il n'existe pas de fosses minéralisées au sud de 19°N où les failles de socle transverses n'existent pas. Au nord de cette limite en revanche, les fosses à saumures chaudes et/ou minéralisées se forment là où les failles transverses recoupent la fosse axiale (Bäcker et al. 1975; Bignell, 1975; Shanks, 1983; Fig.1A). Ramboz et al. (chapitreIII) ont confirmé que les évents alimentant actuellement la fosse d'Atlantis II sont alignés précisement sur une faille transverse active (Fig. 1B). La Figure 1C montre que les minéralisations de la Bordure Cévenole se répartissent principalement le long des anciens accidents tardi-hercyniens de direction E-W, NW-SE et NE-SW.

Il existe d'autres exemples illustrant le contrôle que joue la structuration pré-existante du socle sur la mise en place des minéralisations lors des processus d'extension. Le sud et le centre de l'Espagne sont affectés par plusieurs familles de décrochements tardi hercyniens compatibles avec une phase de compression N-S (Arthaud et Matte, 1975). Les minéralisations Pb-Zn-Ag du sud de l'Espagne se répartissent également le long d'une de ces familles d'accidents de direction NW-SE (Gagny et al., 1985).

I-2 Rôle des sédiments comme source des métaux et/ou des solutions hydrothermales.

Les données chimiques et isotopiques sur les fluides inclus dans la dolomie fissurale et la sphalérite qui l'accompagne témoignent que, dans la minéralisation fissurale du gisement des Malines, les fluides hydrothermaux étaient des eaux de formation provenant du Bassin Sud-Est (Charef, 1986; Charef et Sheppard, 1988). Les températures d'homogénéisation maximales voisines de 150°C mesurées dans les dolomies fissurales sont compatibles avec les températures des eaux de formation à ≈ 4km de profondeur (Hanor, 1979). Les données isotopiques sur les saumures hydrothermales de la Mer Rouge indiquent que la source des fluides est pricipalement l'eau de mer (Craig, 1966; Schoell et Faber, 1978), avec une contribution possible d'eaux météoriques provenant d'Arabie (White, 1974). Les données géochimiques et isotopiques suggérent que les métaux et le soufre des deux minéralisations étudiées proviennent des sédiments du Bassin Sud-Est ou du fossé de la Mer Rouge. Dans le Bassin Sud-Est, les shales triasiques sont enrichies en Pb, Zn, Cu et Ba (Besnus et al., 1986) et les shales des Terres Noires sont enrichies en Cu, Pb, Zn et Mo (Artru, 1968). Dans les sédiments de la Mer Rouge, les shales pré-Miocènes sont enrichies en Zn et Cu et les shales interstratifiées dans les évaporites miocènes sont enrichies en Mo et V (Manheim, 1974). On trouvera dans la thèse de Charef (1986) les arguments isotopiques montrant l'origine sédimentaire du Pb et du soufre des minéralisations KII et F du gisement des Malines. De même, Dupré et al.(1987) ont montré que le Pb des sédiments hydrothermaux de la fosse d'Atlantis II avait une composition isotopique similaire à celle du plomb des shales dans les évaporites. Plus précisement, Manheim (1974) notait qu'un niveau de shales bréchifié dans les évaporites d'un forage au sud de la fosse d'Atlantis

II avait fourni des compositions isotopiques du Pb et du S présentant la même dispersion que celle obtenue pour les sédiments hydrothermaux de la fosse d'Atlantis II.

Enfin, la présence d'huile et d'hydrocarbures légers dans les minéralisations des deux contextes étudiés apporte une preuve supplémentaire que les fluides hydrothermaux sont issus au moins en partie des sédiments du bassin. Certaines anhydrites épigénétiques de la carotte 268 KS, dans le bassin SW de la fosse d'Atlantis II, contiennent des huiles non colorées (Oudin, Thisse et Ramboz, non publié). On sait que, dans le golfe de Suez, un niveau de grès du Miocène Moyen constitue la roche magasin pour le pétrole. Ce niveau s'étend tout le long de la côte d'Arabie (Gillmann et al., 1966). Manheim (1974) a suggéré que ce niveau a pu drainer les eaux météoriques depuis la côte d'Arabie jusque vers la fosse d'Atlantis II, selon le modèle proposé par White (1974).

I-3 Signature microthermométrique des circulations hydrothermales.

La Figure 2 résume les données microthermométriques obtenues sur les anhydrites épigénétiques de la fosse d'Atlantis II (Ramboz et al., chapitre III) et sur les dolomies épigénétiques qui accompagnent la mise en place des minéralisations de la phase fissurale des Malines (Charef et Sheppard, 1988). Chacun des diagrammes est constitué principalement de la juxtaposition de groupes d'inclusions de composition constante et de températures d'homogénésation variables. Dans les dolomies de phase I et II des Malines (Charef et Sheppard, 1988; Fig. 2), de même que dans les barytines géodiques postérieures (Ramboz et Charef, chapitre II), on remarquera cependant que les évolutions poikilothermes et isochimiques présentent vers les basses températures des dérives microthermométriques obliques. Ces données suggèrent que les pulsations hydrothermales peuvent subir une dilution tardive dans certains cas. Des données d'inclusions

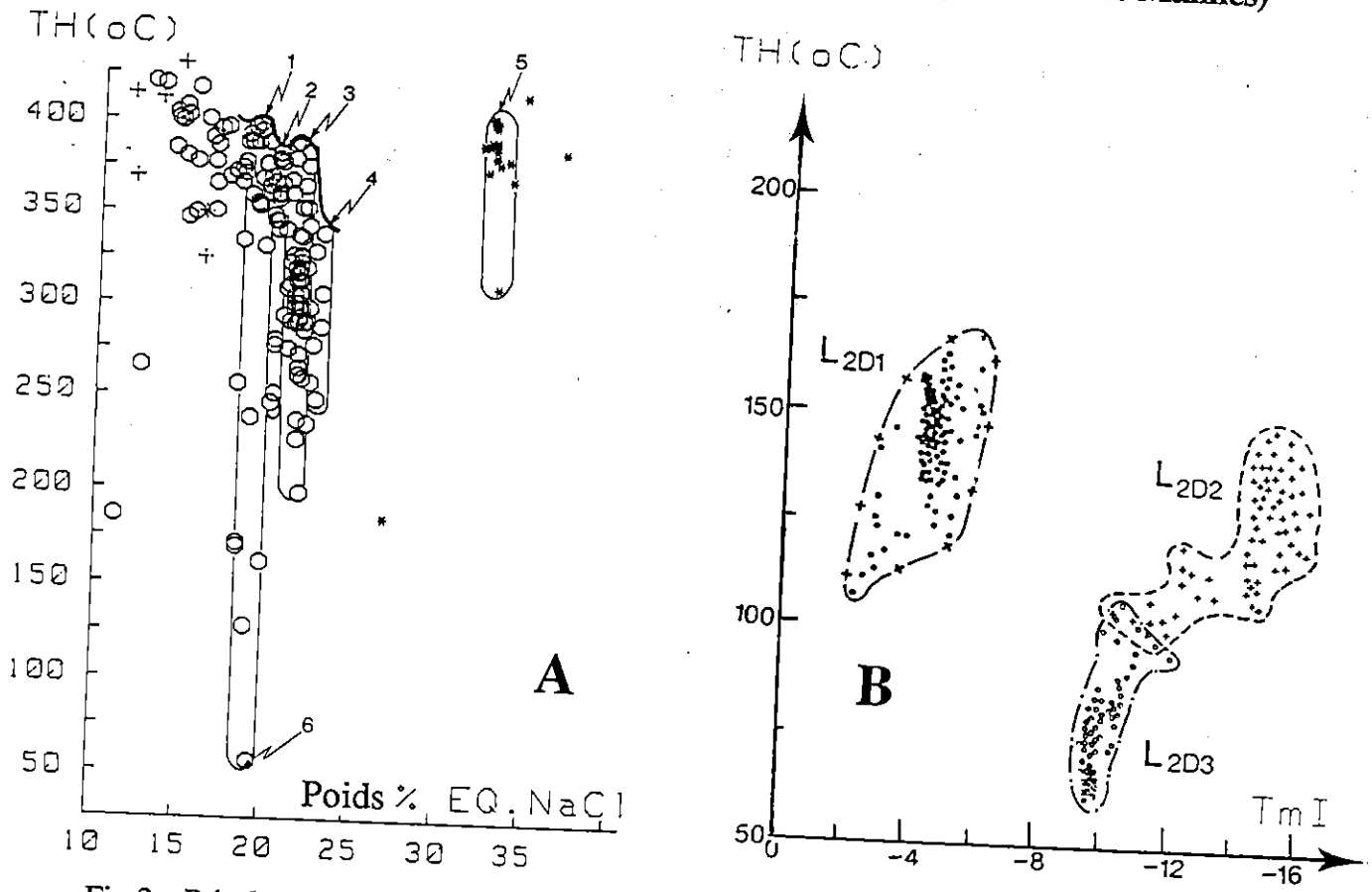

Fig.2 : Résultat de l'étude microthermométrique (A) des inclusions fluides dans 16 cristaux d'anhydrite épigénétique de la fosse d'Atlantis II (Mer Rouge : Ramboz et al., chapitre III) et (B) dans les différentes générations de dolomies associées à la minéralisation fissurale du gisement des Malines (Bordure Cévenole : Charef et Sheppard, chapitre II). TH (°C) : températures d'homogénéïsation; TmI (°C) : températures de fusion de la glace. Figure 3A : rond (croix) = inclusion à liquide (gaz) dominant; étoile = inclusion saturée en NaCl. Ces deux diagrammes, constitués de populations d'inclusions fluides juxtaposées, font apparaître le caractère intermittent de l'activité hydrothermale et montrent par ailleurs le refroidissement isochimique des solutions.

fluides similaires, indiquant principalement le refroidissement isochimique des solutions, ont été obtenues pour nombre de minéralisations de Pb-Zn-F-U-Ba et de dolomitisations associées de la Bordure Cévenole (Sabouraud et al., 1980; Aubague et al., 1982; George, 1985) et, de façon plus large, dans toute la périphérie du domaine hercynien de la plaque européenne affecté par les processus d'extension pendant le Mésozoïque : bordure sud-ouest du fossé rhénan (filons à Pb-Zn-Cu-Si : Gutierrez Lanz, 1985), Nord du Massif Central (filons à Pb-Zn-Sb du district de Brioude - Massiac : Bril, 1983; filons de fluorine du district de Langeac : Bril, 1982); Montagne Noire (filons de fluorine du Burc et de Montroc : Deloule, 1982), Maroc Central (filons de fluorine d'El Hammam : Yajima et Touray, 1970; Jébrak, 1985).... De telles données microthermométriques traduisent une mise en place intermittente, dans un environnement de sub-surface, de pulsations hydrothermales en fort déséquilibre thermique avec l'encaissant. Il convient de noter de plus que dans l'un et l'autre des cas étudiés (fosse d'Atlantis II et gisement des Malines), les données chimiques, isotopiques et géologiques montrent que les fluides proviennent au moins en partie des sédiments imperméables des bassins voisins (cf tableau I et paragraphe I-2 ci-dessus). Compte tenu de ce qui précède, il est permis d'identifier chaque évolution isochimique et poikilotherme marquée par les inclusions fluides de bon nombre de filons Pb-Zn-U-Ba-F-Si à une nouvelle pulsation hydrothermale. Chaque pulsation résulterait de la décompression des eaux de formation en pression anormale dans des niveaux imperméables du bassin. Un modèle semblable a été démontré fiable pour les minéralisations de type Mississipi Valley à la périphérie des grands bassins américains du Middle West (Cathles et Smith, 1983). On remarquera que, dans le gisement des Malines, les températures maximales enregistrées par les inclusions dans la dolomie fissurale (≈150°±10°C) sont compatibles avec l'hypothèse d'une

migration adiabatique des solutions depuis des niveaux profonds du bassin. En Mer Rouge en revanche, les températures maximales enregistrées par les inclusions fluides (≈390°-400°C) impliquent que les solutions ont été chauffées au contact du basalte présent sur le plancher de la fosse.

I-4 Mise en place des solutions sous un écran imperméable.

Le Tableau I souligne que, bien que les minéralisations de la Bordure Cévenole et de la Mer Rouge se soient mises en place à des profondeurs très différentes, celles-ci étaient toutes deux proches d'eaux oxydantes, eau de mer ou eau météorique. Les données d'inclusions fluides présentées dans la Figure 2 et, plus généralement, les données d'inclusions fluides relatives aux mineralisations Pb-Zn-U-Ba-F-Si de la plaque européenne citées plus haut, montrent l'absence de tout mélange important des solutions hydrothermales lors du dépôt des minéralisations et des dolomitisations et silicifications associées. Ce sont les marnes triasiques qui recouvrent le socle cambrien aux Malines, et les saumures stratifiées de la fosse d'Atlantis II en Mer Rouge, qui ont constitué l' écran imperméable ayant empéché la dilution des solutions hydrothermales dans les zones de décharge.

Dans les gisements de type Kuroko cependant, les sulfures se déposent directement au contact de l'eau de mer (Ohmoto et Skinner, 1983). Cathles (1983) a proposé que ces gisements se forment en dessous de 300°C à la suite d'une activité hydrothermale continue pendant environ 5000 ans. Les solutions hydrothermales précipitent leur contenu en sulfures avant tout mélange avec l'eau de mer . Dans ces gisements en effet se produit vers 300°C une phase de dépôt de silice et d'anhydrite sur le plancher océanique, qui est antérieure au dépôt des sulfures. Cette silicification précoce ne se produirait pas si les températures de décharge

hydrothermale étaient plus élevées. Une réduction de la perméabilité s'opère dans les zones de décharge du fait de la silicification. Ceci provoque une augmentation du débit des solutions hydrothermales et, par suite, inhibe tout mélange important des solutions hydrothermales avec l'eau de mer.

On conçoit qu'un écran soit nécessaire au dépôt et à la préservation des concentrations économiques de sulfures associés aux contextes d'extension étudiés. A l'inverse des gisements de type Kuroko, ces dépôts s'éffectuent de façon rythmique par petits incréments et pendant plusieurs dizaines de milliers d'années (Cathles et Smith, 1983). Les gisements situés sur sur les bordures hautes des bassins ne sont jamais recouverts par une sédimentation hydrothermale ou chimique épaisse. Par ailleurs, les températures de décharge des solutions hydrothermales dans la fosse d'Atlantis II sont trop fortes (≈400°C : Ramboz et al., chapitre III) pour provoquer une silicification du plancher de la fosse dans les zones de décharge à une pression de 220bars (Cathles, 1983).

Sur la bordure des bassins, ce sont souvent des dispositifs structuraux ou sédimentaires qui permettent de préserver de l'oxydation précoce les solutions réductrices porteuses de minéralisations sulfurées. Les discordances, qui contrôlent la mise en place de certaines minéralisations à Pb-Zn (Samama, 1980) ou uranifères (Pagel, 1983) sur la Bordure Cévenole, peuvent constituer un écran favorable à la mise en place et / ou à la préservation des minerais primaires sensibles aux conditions d'oxydo-réduction. On notera aussi que certaines concentrations Pb-Zn de la Bordure Cévenole sont encaissées dans des argiles noires imperméables et réductrices (Macquar, 1984).

II - Mécanismes des circulations hydrothermales et des concentrations minérales.

II-1 Fluidogenèse au sein de sédiments imperméables, en particulier dans les piles évaporitiques :

En Mer Rouge comme sur les marges de l'Atlantique Nord et de l'Océan Téthysien, se sont déposées, pendant la phase précédant le rifting et pendant la phase de rifting, d'épaisses séries d'évaporites et / ou de shales. On connait depuis longtemps le rôle que jouent les argiles sous-compactées dans la genèse des pressions fluides anormales dans les bassins sédimentaires (Dickinson, 1953; Magara, 1975 et références dans le chapitre II). Au contraire, les piles d'évaporites contenant des niveaux de shales interstratifiés sont des roches classiquement considérées comme peu affectées par les processus hydrothermaux du fait de leur grande imperméabilité et du fait qu'elles sont la source de fluides carbo-azotés (Roedder, 1972), réputés inertes. Cependant, Dubessy et Ramboz (1986 : publication n°13) ont montré que la production de fluides du système CO_2-CH_4-N_2, au cours de la diagenèse et du métamorphisme des séries porteuses de matières organiques de type I et II, est le résultat de réactions d'oxydo-réduction dont l'importance est primordiale du point de vue mécanique et chimique. En particulier, la production de fluides essentiellement composés de CO_2-N_2 au sein des évaporites marines sulfatées et contenant des intercalations d'argiles noires résulte probablement d'une oxydation de CH_4 et NH_4^+ provenant de la décomposition des matières organiques et des argiles par les sulfates de la roche encaissante :

$$CH_4 + SO_4^{2-} + 2H^+ \rightarrow CO_2 + H_2S + 2H_2O \quad (1)$$

$$8\ NH_4^+ + 3\ SO_4^{2-} \rightarrow 4\ N_2 + 3\ H_2S + 12H_2O + 2H^+ \quad (2)$$

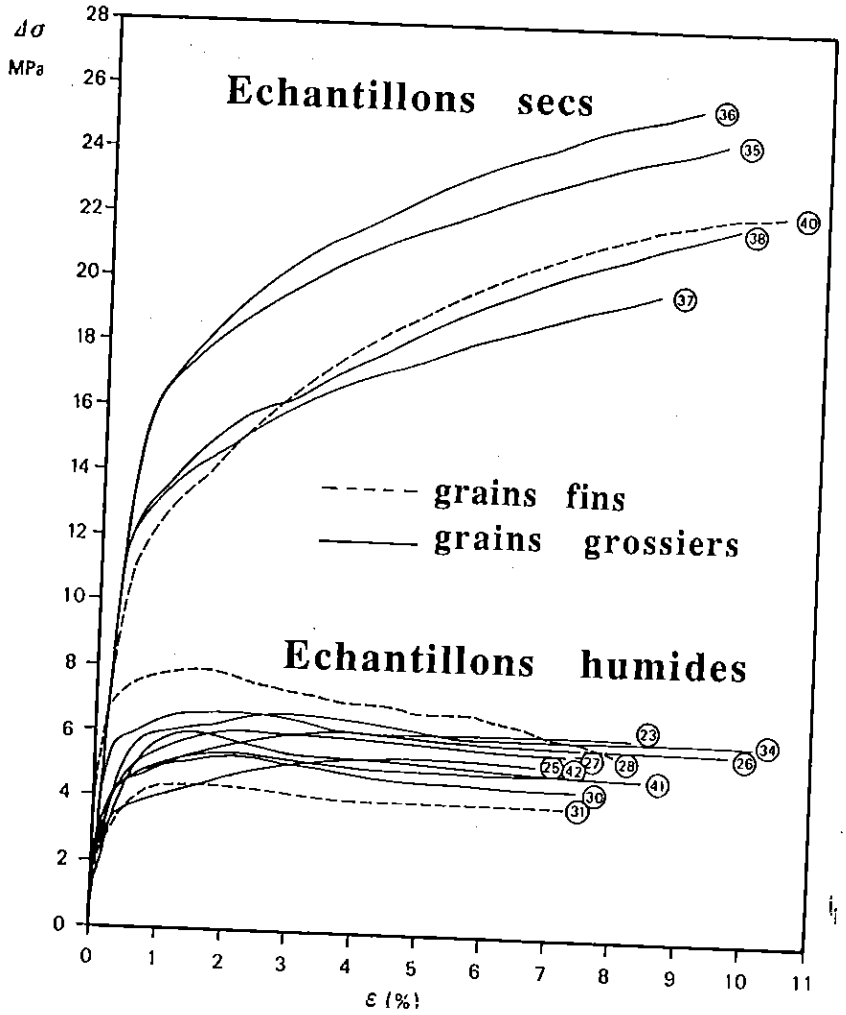

Fig. 3 : Comportement rhéologique de la bischofite ($MgCl_2$-$6H_2O$) : relation entre le déviateur des contraintes ($\Delta\sigma$) et la déformation (ε). Expérience à 60°C, vitesse de déformation $10^{-5}s^{-1}$, pression de confinement 28 Mpa·(Urai, 1983).

De telles réactions impliquent la réduction biogénique ou abiogénique des sulfates et la déshydrogénation des composés organiques. L'étude de l'évolution du contenu en soufre et de la composition isotopique des espèces sulfurées dans les solutions associées aux huiles a confirmé qu'une telle réaction se produit à haute température (T> 80°-120°C; Orr, 1974). Les températures d'homogénéisation mesurées sur les inclusions aqueuses associées aux inclusions à gaz dans les évaporites sont conformes à ces températures ou sont supérieures (Guilhaumou et al., 1981). De même, la présence d'eaux organiques dans les minéralisations Pb-Zn associées aux diapirs de sel de Tunisie est conforme aux réactions proposées ci-dessus (Sheppard et Charef, 1986). Dubessy et Ramboz (1986 : publication n°13) ont en particulier insisté sur les conséquences métallogéniques et isotopiques de la production d'eau et d'hydrogène sulfuré au sein des évaporites associées avec les shales selon les réactions de type (1) et (2). Il convient de souligner ici une autre conséquence importante de la production d'eau sur le comportement rhéologique du sel lui-même. Alors que le sel à l'état sec a une tendance au durcissement quand il est soumis à des contraintes croissantes, le sel en présence d'eau en petite quantité a un comportement ductile (Urai, 1983; Fig. 3). Par ailleurs, la masse salifère a une tendance au gonflement au contact de l'eau (Urai, 1983). Ces deux effets favorisent tous deux le diapirisme. On conçoit que de telles réactions jouent un rôle essentiel dans le contexte de la Mer Rouge Centrale. Un flux thermique particulièrement élevé (Schoell, 1976) y provoque une dégradation accélérée de la matière organique et la création de surpressions fluides, y compris d'eau, sous pression au sein de la masse évaporitique. Ceci entraine finalement la rupture, en particulier le long des directions de faiblesse que constituent les directions "transformantes" actives.

II-2 Rôle des failles parallèles à σ_3 pour le contrôle structural des minéralisations

Alors que les bassins américains du Middle West sont des bassins de plate-forme (Perrodon, 1983), larges (≈200 km de diamètre), en forme de cuvette et avec des pentes relativement fortes sur leur bordure (≈1%), les minéralisations de la fosse d'Atlantis II et des Malines sont situées sur la bordure ou au coeur de bassins de type rift continental, c'est à dire étroits, allongés et limités par des failles normales (Artru, 1968).

Cathles et Smith (1983) ont démontré que, dans les bassins américains du Middle West, les solutions provenant de zones géopressurées ont pu migrer de façon adiabatique sur de grandes distances le long de niveaux aquifères en raison des fortes pentes des bordures du bassin. Ce modèle n'est pas applicable au Bassin Sud-Est au large de la Marge Cévenole. Celui-ci est constitué de fossés limités par des failles de direction cévenoles rejouant en failles normales (Artru, 1968; Triat et Truc, 1983). La pente des couches déposées dans les fossés est très inférieure à 1% (Baudrimont et Dubois, 1977). Par ailleurs, le gisement des Malines se trouve à 15 km à l'est des failles de direction cévenole, celles-ci n'ont donc pas pu constituer un drain pour les solutions hydrothermales. La Figure 1 et les références rassemblées dans le Tableau 1 montrent que, dans les contextes de rift continental étudiés, ce sont des failles de socle réactivées, sub-parallèles à la direction de l'extension qui ont favorisé la plupart du temps la migration adiabatique, centripète (Mer Rouge) ou centrifuge (Les Malines), des solutions.

On sait depuis longtemps qu'en contexte océanique (Le Pichon, 1968), et en particulier actuellement en Mer Rouge Centrale (Fairhead et Girdler, 1970), l'activité sismique est concentrée le long des failles transformantes. Par ailleurs, on a démontré expérimentalement que l'injection de fluides sous fortes pressions dans un bassin sédimentaire

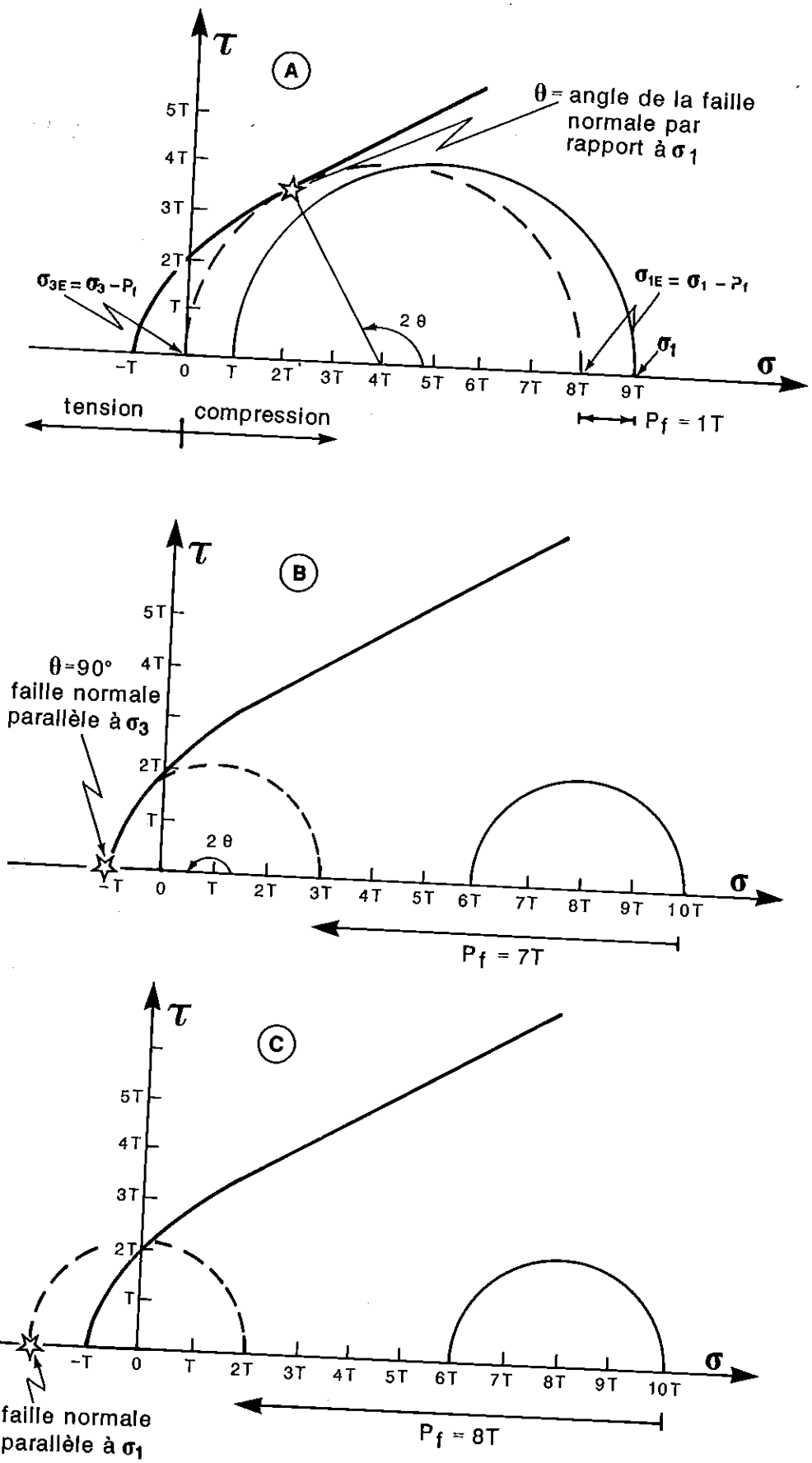

Fig. 4 : Application du cercle de Mohr à la fracturation hydraulique des roches (d'après Phillips, 1972; 1986). (A) Effet de la pression fluide sur la rupture. (B) Fracturation selon σ_3. (C) Fracturation hydraulique selon σ_1. σ_1 (σ_3) =contrainte normale maximale (minimale); σ_E =contrainte effective; τ = contrainte cisaillante

provoquait des tremblements de terre : à Rangely (Colorado), on a observé en particulier que les foyers des séismes ainsi provoqués s'alignaient sur la partie non scellée d'une faille préexistante de direction parallèle à σ_1 (Raleigh et al., 1976). Je propose donc qu'en Mer Rouge Centrale comme sur la Bordure Cévenole, la mise en place des minéralisations ait été liée à décompression des fluides des zones géopressurés, déclenchant une séismicité importante des failles de socle parallèles à σ_3. La Figure 4 résume à l'aide du cercle de Mohr comment, dans un massif rocheux soumis à des contraintes extérieures dont le déviateur reste faible, l'augmentation de la pression fluide favorise la rupture en tension selon des failles faisant avec σ_1 un angle d'autant supérieur à 67° que la pression fluide est plus forte. On trouvera dans l'article de Raleigh et al. (1972) un traitement plus approfondi de la rupture dans le cas d'une roche affectée de fractures préexistantes.

II-4 Mécanismes de précipitation des minéraux rubannés.

Ramboz et al. (chapitre III) ont montré que si les données microthermométriques obtenues sur 16 cristaux d'anhydrite épigénétique de la fosse d'Atlantis II traduisent bien un refroidissement isochimique des solutions hydrothermales, certains cristaux d'anhydrite piègent des fluides de compositions et de températures d'homogénéisation très constantes, c'est-à-dire n'enregistrent pas le refroidissement des solutions (Fig. 5A). Des résultats très semblables ont été obtenus pour certains filons de quartz et de barytine des Vosges (Gutierrez-Lanz, 1985 : Figs. 5B et 5C), pour certains filons à Pb-Zn du district de Brioude - Massiac (Bril, 1983) et pour la fluorine rubannée de Langeac (Haute-Loire; Bril, 1982; Fig.5D). De tels diagrammes sont à priori surprenants car ils ne font apparaître ni déséquilibre thermique ni déséquilibre chimique pouvant être le moteur de la circulation et / ou de la précipitation. Selon Ramboz et al. (chapitre III),

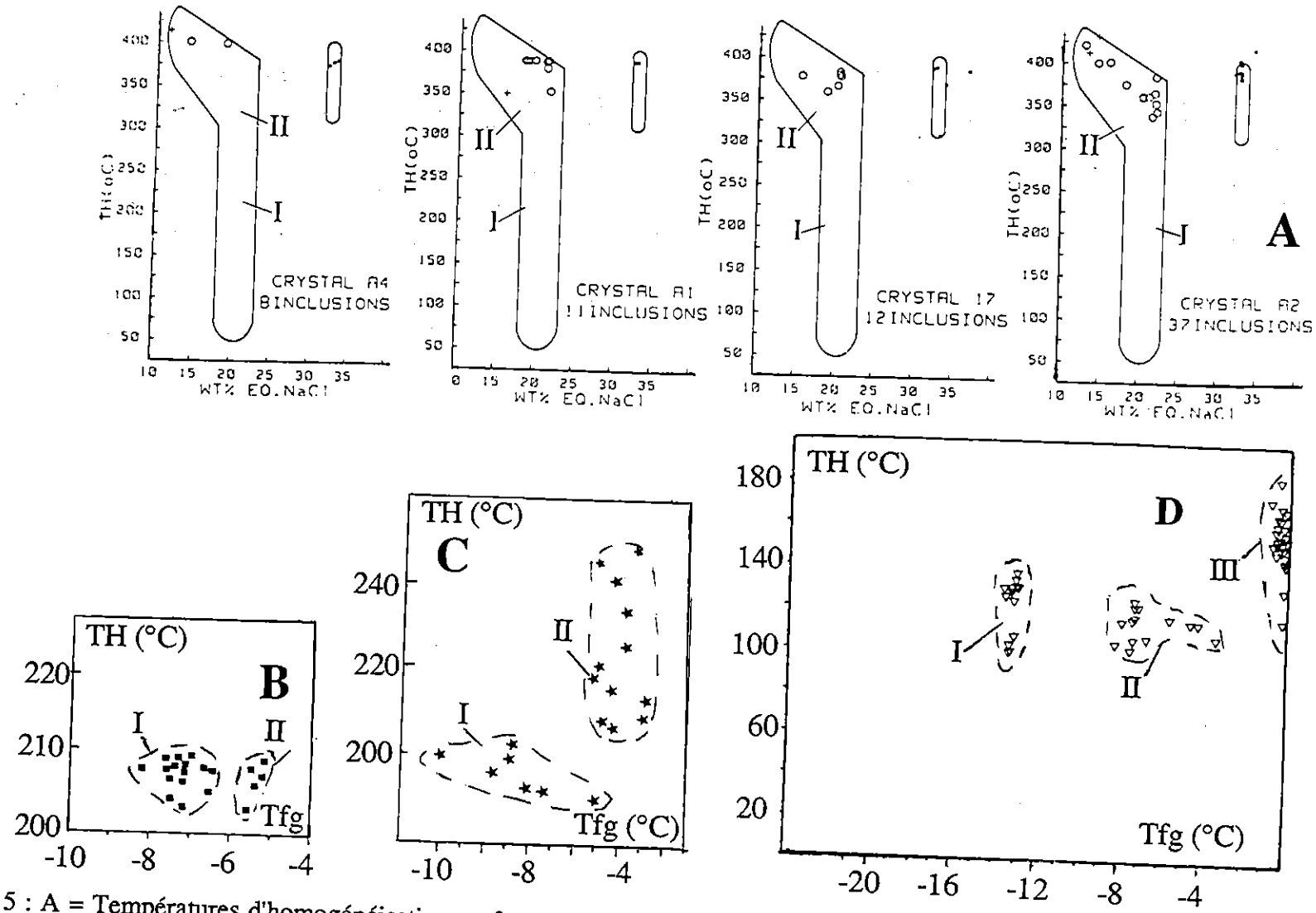

Fig. 5 : A = Températures d'homogénéisation en fonction de la teneur en équivalent NaCl (% poids) pour les inclusions fluides de 4 cristaux d'anhydrite épigénétique de la fosse d'Atlantis II (Mer Rouge : Ramboz et al., chapitre III). Symboles analogues à ceux de la figure 3A. Le contour marque le domaine de projection des mesures obtenues sur 16 cristaux d'anhydrite (partie I = refroidissement isochimique; partie II= piégeage hétérogène); B et C = Diagrammes Tfg-TH pour deux filons de quartz en peigne des Vosges du Sud (Gutierrez-Lanz, 1985); D = Diagramme Tfg-TH pour les fluorines du district de Langeac (Haute-Loire : Bril, 1982). Ces diagrammes montrent que les cristaux n'enregistrent pas toujours un refroidissement marqué des solutions (Fig. 4A, fig. 4B : population I et II, Fig. 4C : population I, Fig. 4D : populations I et II).

les données microthermométriques et l'observation microscopique des cristaux d'anhydrite épigénétique de la fosse d'Atlantis II montrent que le mécanisme à l'origine de la croissance des cristaux n'est pas le refroidissement des solutions mais plutôt une saturation brutale. Le fluide hydrothermal, riche en sulfures et calcium, devient brusquement saturé en anhydrite parce qu'il s'oxyde. Ce processus résulte d'une part de l'ébullition, et d'autre part de réactions chimiques avec le sédiment hématitique. Une croissance discontinue par couches successives des quartz en peigne, de la barytine et de la fluorine rubannée mentionnés plus haut apparait compatible avec les observations microscopiques faites par les auteurs : juxtaposition dans la fluorine, à l'échelle de quelques µm, d'inclusions de salinité différente sans mélange (Bril, 1983), distribution sectorielle des inclusions dans les quartz en peigne (Gutierrez-Lanz, 1985).

L'effet de la décompression du fluide sur la solubilité des éléments qu'il transporte, en particulier des métaux, doit également être considéré (Laffite, 1963). On a vu que les solutions hydrothermales subissent très probablement une décompression lorsqu'elles quittent les zones sources dans le bassin (paragraphe II-2). Il est très vraisemblable qu'elles subissent aussi une décompression lors de leur dépôt sur les marges des bassins. Ramsay (1980) et Phillips (1986) ont interprété que les dépôts rubannés de fluorine, barytine, sphalérite, uraninite et les quartz en peigne associés résultent du remplissage de fractures de tension périodiquement réouvertes par fracturation hydraulique. Dans le gisement des Malines, on a montré à l'aide des inclusions contenant du CO_2 que le socle cambrien où se sont déposées les minéralisations a été mis en pression sous les marnes triasiques. La pression fluide augmentant très rapidement, a excédé de façon transitoire la pression lithostatique (Ramboz et Charef., chapitre II).

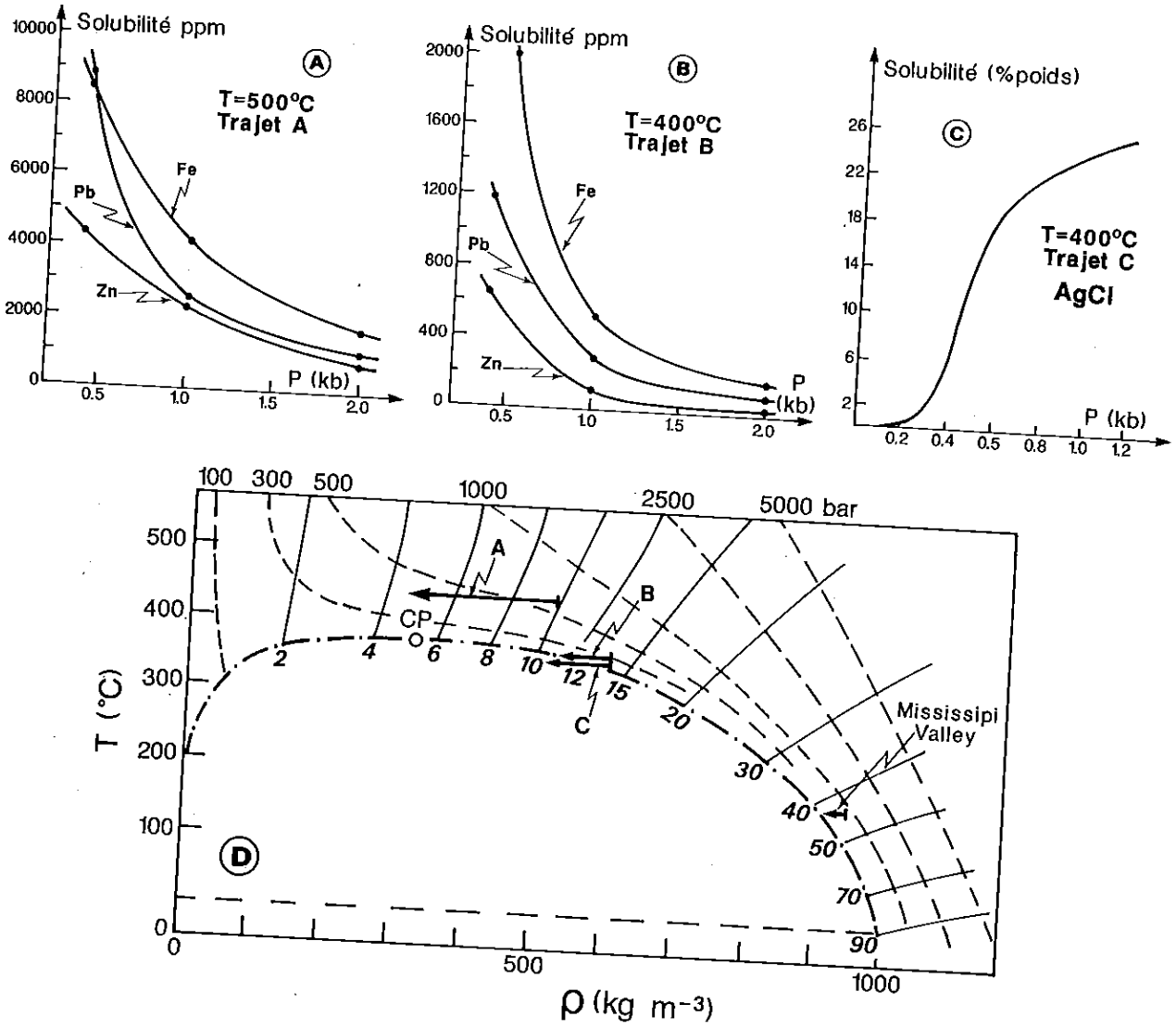

Fig. 6 : Solubilité des sulfures de fer, zinc et plomb à 400° C (A) et à 500°C (B) dans une solution chlorurée 1M, à pression variable. Le pH des solutions est contrôlé par l'assemblage quartz - muscovite - feldspath K (Hemley et al., 1986). C : solublité de AgCl à 400°C dans une solution chlorurée 1.5 M, à pression variable (Gupta, 1978). Le pH des solutions n'est pas contrôlé. D : Variations de la constante diélectrique de l'eau (lignes continues) en fonction de la température et de la densité (d'après Franck, 1982; les lignes pointillées sont isobares). Les trajets marquées A à C rendent compte des variations de la constante diélectrique du fluide dans les expériences polybariques et isothermes de Hemley et al. (1986) et de Gupta (1978), respectivement. L'effet de la fracturation hydraulique sur les variations de la constante dielectrique du fluide lors du dépôt des minerais en environnement carbonaté ('Mississipi Valley') est aussi représenté. Les solutions chlorurées ont été projetées dans le diagramme de l'eau pure en fonction de leurs propriétés réduites ($Tr = T / Tc$, $\rho r = \rho / \rho c$ où Tc et ρc sont les densités et les températures critiques pour les compositions considérées).

Dans la Figure 6, on a rassemblé quelques données expérimentales permettant d'évaluer l'influence d'une décompression sur la solubilité des sulfures dans les solutions chlorurées.

(i) Les Figures 6A et 6B montrent les variations de solubilité des chlorures de Fe, Zn et Pb dans une solution chlorurée 1M, à 400° et 500°C, lorsque la pression varie de 2 et 0.5 kb (Hemley et al., 1986). Dans ces deux expériences, le pH et les conditions fO_2-fS_2 ont été contrôlées par les assemblages quartz-feldspath-muscovite et pyrite - pyrrhotite - magnétite - sphalérite - galène, respectivement. (ii) La Figure 6C montre l'effet d'une décompression entre 1.2 et 0.1 kb à 400°C sur la solubilité du chlorure d'argent dans une solution chlorurée 1.5 M (Gupta, 1978).

Alors que, dans les expériences de Gupta (1978), la décompression a pour effet de diminuer drastiquement la solubilité du chlorure d'argent, ce même processus a un effet strictement opposé dans les expériences de Hemley et al., (1986). L'expérience de Gupta (1978) est en effet conduite à acidité constante, le pH n'étant pas controlé de façon externe. Cette expérience permet d'apprécier le seul effet d'une décroissance de la constante diélectrique de l'eau sur la solubilité de AgCl. Vers 400°C, $AgCl_2^-$ est le complexe d'argent dominant par rapport à $AgCl^\circ$, plus stable à basse température (Seward, 1976). Au cours de la décompression, les complexes d'argent, initialement ioniques, ont tendance à former des complexes neutres. Ceci induit une diminution de la solubilité de AgCl et sa précipitation.

Les résultats très différents des expériences de Hemley et al. (1986) s'expliquent principalement par le fait que, HCl étant un électrolyte plus faible que KCl dans un solvant à faible densité (=à constante dielectrique faible : Fig. 6D), l'équilibre (3) se déplace vers la droite lors de la décompression :

$$\text{muscovite} + 6\ \text{quartz} + 2\ KCl_{(aq)} \rightarrow 2\ HCl_{(aq)} + 3\ \text{Feldspath K} \quad (3)$$

La solubilité des métaux augmente donc au cours de la décompression selon la réaction :

$$8KCl_{(aq)} + 24\ Quartz + 4\ Muscovite + 2\ FeS + Fe_3O_4 \rightarrow$$
$$4\ FeCl_{2(aq)} + FeS_2 + 4\ H_2O + 12\ Feldspath\ K \qquad (4)$$

On peut considérer que, dans les gisements étudiés, les solutions hydrothermales subissent une décompression d'au plus 900 à 400 bars lors de leur expulsion du bassin et une décompression d'au plus 500 à 100 bars lors de mise en place sur la bordure des bassins, la température restant voisine de 150°C. Les expériences présentées plus haut, quoique réalisées à plus haute température, suggèrent que de telles décompression ont des effets importants sur la solubilité des métaux.

La Figure 6D montre qu'à basse température, la constante diélectrique de l'eau est plus élevée qu'à haute température, mais diminue également avec la pression. Dans les zones sources des bassins, le pH des solutions hydrothermales est probablement tamponné par des assemblages de même type que l'assemblage quartz-muscovite-felspath, puisque ces zones sont riches en argiles et en feldspath détritique. Des expériences analogues à celles de Hemley et al. (1986), mais réalisées à plus basse température (vers 150°C), permettraient de vérifier si la décompression des solutions dans ces zones a pour effet d'augmenter leur capacité à transporter les métaux, comme c'est le cas à 400°C. Dans les zones de gisements en revanche, les solutions se mettent en place très vite et ne se ré-équilibrent pas avec leur encaissant, souvent de nature carbonatée. On peut considérer que le pH des solutions n'est plus alors contrôlé par aucun assemblage minéral. Des expériences analogues à celles de Gupta (1978) mais effectuées vers 150°C, permettraient de vérifier si la fracturation hydraulique dans ces zones a bien pour effet instantané, comme à 400°C, de favoriser le dépôt des métaux.

II-5 Chronologie de la mise en place des minéralisations au cours de l'extension.

On ne connait pas l'âge précis de mise en place des différents types de minéralisations qui constituent le gisement des Malines. Marini (1986) a obtenu un âge de 192±10 M.a. en analysant par la méthode K/Ar la fraction argileuse de différents échantillons minéralisés. Cet auteur suggère cependant que l'âge obtenu pourrait être un âge minimum, la dispersion des mesures suggérant la présence de phases détritiques dans la fraction analysée. Ramboz et Charef (chapitre II) ont déduit de la mesure de pressions fluides proches de la pression lithostatique un âge oxfordien probable pour les barytines géodiques qui se déposent après la minéralisation fissurale; ces auteurs ont par suite considéré qu'un âge de ≈170 M.a. était vraisemblable pour la mise en place de la minéralisation fissurale.

Dans le Massif Central et en Forêt Noire, de nombreux âges compris entre 190 et 170 M.a. ont été obtenus par la méthode K/Ar sur des argiles associées à des silicifications et des minéralisations en Ba-Pb-Zn, fluorine ou uranium (Bonhomme et al., 1980; 1983; Lancelot et al., 1984). 170 M.a. est l'âge de la première linéation magnétique identifiée dans l'Océan Atlantique (Jansa et Wade, 1975) et aussi celui de l'apparition des ophiolites dans l'Océan Liguro-Piémontais (Bernouilli et Lemoine, 1980). Dans le Bassin Sud-Est bordant la Marge Cévenole, la structuration en blocs basculés et des efforts de transtension se sont produits vers 170 m.a. (Elmi, 1984). Cet âge marque aussi la culmination de la distension E-W dans le Bassin Subalpin (Debrand-Passard, 1984). On sait que l'océanisation simultanée du bassin piémontais a entraîné la relaxation des tensions sur la marge européenne et le blocage de l'évolution du Bassin Subalpin vers le stade océanique (Debrand-Passard, 1984).

Compte tenu de ce qui a été dit dans le précédent paragraphe, on peut interpréter que les minéralisations formées sur la marge cévenole vers 170 M.a. ont correspondu à une activité sismique intense le long des failles E-W pendant le Dogger. Cette activité a favorisé une migration centrifuge catastrophique des eaux de formation du bassin vers la marge.

Les minéralisations hydrothermales de la fosse d'Atlantis II se sont formées depuis l'Holocène jusqu'à nos jours (Bäcker et Richter, 1973). Le contexte de leur mise en place est cependant moins bien connu. Le fossé de la Mer Rouge est recouvert, sur toute sa largeur au Nord et sur 200 km au Sud, par 3000 à 4000 m de sédiments évaporitiques. Cette épaisse couverture sédimentaire a jusqu'à présent empêché d'accéder au socle par sondage. Il est donc difficile d'identifier précisement la nature du socle à partir des mesures géophysiques seules. La question qui reste posée actuellement est donc la suivante : existe-t-il sous les évaporites une croûte de nature océanique sur tout ou partie de la largeur du fossé (Le Pichon et Gaulier, 1987; Girdler et Southren, 1987) ou bien le socle sous les évaporites est-il constitué au moins en partie d'une croûte continentale de type intermédiaire et injectée de dykes (Cochran, 1983) ?

Selon le modèle de Cochran (1983), la mise en place des saumures hydrothermales en Mer Rouge Centrale serait contemporaine du changement du mécanisme d'extension de cette zone, c'est-à-dire contemporaine du passage d'une extension diffuse à une extension de type océanique. Les minéralisations de la Bordure Cévenole et de la fosse d'Atlantis II présentent de nombreux points communs (source des métaux dans les sédiments, pré-existence de failles de socle selon la direction de la distention...). Le modèle de Cochran (1983) a le mérite de placer ces deux types de minéralisations dans un cadre temporel similaire, celui d'un changement du mécanisme de la distension. L'évolution actuelle de la marge portugaise permet d'étayer l'hypothèse faite ici d'une activité

sismique accrue sur les marges passives selon les directions transformantes lors d'un changement dans le mécanisme de l'extension (Ribeiro et Cabral, 1987). La marge portugaise est actuellement à un stade de transition entre marge passive et marge active : on y a effectivement observé dans les temps historiques une activité sismique intense qui s'est concentrée dans une zone étroite où de nombreuses failles transformantes recoupent la croûte océanique et la croûte continentale.

On peut ajouter pour alimenter le débat sur la structure de la Mer Rouge qu'il existe une dissymétrie de l'activité hydrothermale et séismique en Mer Rouge Centrale et une dissymétrie des données géophysiques sur le nord et le centre du fossé, dont les modèles de Le Pichon et Gaulier (1987), Girdler et Southren (1987) ne rendent pas compte.

(i) Entre 19° et 25°N, l'activité séismique se manifeste seulement sur la partie est des failles transverses (Fairhead et Girdler, 1970). La partie ouest de ces failles serait donc actuellement scellée.

(ii) Les solutions hydrothermales qui alimentent les fosses d'Atlantis II et de Néréus se déchargent dans le Bassin Ouest de ces fosses seulement, le Bassin Est ne présentant pas d'activité hydrothermale (Bäcker et Richter, 1973; Bignell et Ali, 1976).

(iii) Des données récentes de magnétisme sur la fosse d'Atlantis II font apparaître une aimantation positive du plancher de la fosse avec, dans le bassin est, des contrastes d'intensité selon les directions transverses qui n'existent pas dans le bassin SW (Le Quentrec et al., 1987).

(iv) Des données séismiques et gravimétriques ont révélé la structure dissymétrique du fossé vers le nord : sur la bordure ouest , on observe un amincissement crustal et la présence de crôute océanique, tandis que sur la bordure est, la croûte continentale se prolonge au large des côtes (Makris et Rihm, 1987). (v) Finalement, un important volcanisme alcalin se

manifeste sur le bouclier arabe depuis le Tertiaire, qui n'a pas son équivalent sur le bouclier africain.

III-Conclusions

Le modèle proposé pour la mise en place des minéralisations à Pb-Zn de la fosse d'Atlantis II et de la minéralisation F du gisement des Malines, sur la Bordure Cévenole, est une variante du modèle des gisements de type Mississipi Valley adaptée à des contextes de rift continental.

1) Aux premiers stades du rifting se déposent sur les continents d'épaisses séries d'évaporites sulfatées contenant des passées d'argiles riches en matières organiques : on a montré qu'un tel dispositif sédimentaire, parce qu'il favorise la production de gaz et d'eau par volatilisation, constitue une bombe à retardement qui amorcera ultérieurement la relaxation intermittente d'eaux de formation métallifères des zones géopressurées.

2) Dans les environnements de type rift, les niveaux gréseux continus permettant le draînage les solutions du centre du bassin vers les bordures sont rares. De plus, l'approfondissement du bassin se faisant brutalement le long des failles de bordure, les pentes des couches au fond du bassin restent généralement faibles : ceci ne favorise pas la remontée adiabatique des solutions le long d'éventuels niveaux perméables. Le mécanisme privilégié qui permet la migration intermittente des solutions hydrothermales dans les environnements de type rift est probablement celui du "seismic pumping" proposé par Sibson et al. (1975). Il est donc primordial que le socle ait acquis une structuration préalable avant l'amincissement crustal, en particulier qu'il soit faillé selon des directions proches de la future distension. De telles failles seront le siège d'une activité sismique qui permettra l'évacuation intermittente des poches

d'eaux de formation. Elles favoriseront leur migration (centripète ou centrifuge) vers des zones pièges où les minéralisations primaires pourront se déposer : bassins anoxiques, discordances en bordure des socles.

3) On peut identifier la signature microthermométrique du "seismic pumping". Dans des minéraux souvent polygéniques ou à structure rubannée (quartz, fluorine, sulfates, sphalérite...), on trouve des inclusions fluides à distribution zonaire et présentant des formes de cavité hors d'équilibre qui témoignent d'une croissance discontinue et rapide. Ces inclusions indiquent toujours la mise en place strictement isochimique de solutions (sans mélange in situ) en déséquilibre thermique avec l'encaissant. Les cristaux hydrothermaux n'enregistrent cependant pas toujours le refroidissement important que subissent les solutions lors du dépôt.

4) Comme l'a proposé Phillips (1972, 1986), le processus de fracturation hydraulique joue un rôle important dans les environnement de rift : il favorise la relaxation des poches d'eau en pression anormale dans les régions source des solutions métallifères; il permet aux solutions hydrothermales de créer elle-mêmes les vides où pourront se déposer les minerais. Quelques données expérimentales préliminaires suggèrent que les processus de décompression des solutions hydrothermales dans les zones source et dans le zones de décharge peuvent avoir un effet important sur la mise en solution, puis sur le dépôt des métaux, respectivement.

5) Dans les environnements de type rift, les saumures métallifères générées dans les sédiments.imperméables des bassins semblent migrer préférentiellement lors des changements du mécanisme de l'extension ou des changements du régime des contraintes, correspondant à une période de séismicité accrue le long des failles transformantes.

BIBLIOGRAPHIE

Arthaud F., et Matte Ph., 1975, Les décrochements tardi-hercyniens du sud-ouest de l'Europe. Géométrie et essai de reconstitution des conditions de la déformation, Tectonophysics, 25, 139-171.

Artru P., 1968, Répartition du bore et de quelques éléments-traces dans des bassins semi-euxiniques du miogéosynclinal alpin (Terres Noires jurassiques, France Sud-Est), Bull. Centre Rech. Pau S.N.P.A., 2, 83-100.

Aubague M., L'Homer A., et Sureau J.F., 1982, Recherche de guide de prospection pour les gîtes Pb-Zn liés aux strates en environement dolomitique. Exemple des gîtes de Bois-Madame (Hérault), La Croix-de Pallières (Gard) et Figeac (Lot), Bull. B.R.G.M., section 2, n°1, 41-59.

Bäcker H., et Richter H., 1973, Die Rezente Hydrothermal-Sedimentäre Lagerstätte Atlantis II-Tief im Roten Meer, Geol. Rundsch., 3, 697-741.

Bäcker H., Lange K., et Richter H., 1975, Morphology of the Red Sea central graben between Subair Islands and Abul Kizaan, Geol. Jahrb., 13, 79-123.

Baudrimont A.F., et Dubois P., 1977, Un bassin mésogéen du domaine péri-alpin : le sud-est de la France, Bull. Centres Rech. Explor.-Prod. Elf Aquitaine, 1, 261-308.

Bernard A. J., 1958, Contribution à l'étude de la province métallifère sous-cévenole, Thèse d'état, Université Nancy, v.1, 123-403.

Bernard J.M., et Skvor B., 1980, The reactivation of the Ancient Massif and metallogeny : the example of the Bohemian Massif, Econ. Geol., 75, 251-259.

Bernouilli D., et Lemoine M., 1980, Birth and evolution of the Tethys : the overall situation, 26 th Int. Geol. Congress, Paris, C5, 168-179.

Bertin, J., Pedeux, J.P., and Magenham, J.C., 1979, Contribution de la géophysique et de l'océanographie physique à la recherche et à l'exploration des boues métallifères de la Mer Rouge, in Ressources minérales sous-marines : Documents B.R.G.M., Fr., n°7, p. 339-366.

Besnus Y., Marini D., et Macquar J.C., 1986, Lithostratigraphie et distribution de divers éléments traces dans le Trias du district Zn-Pb des Malines (SE du Massif Central), Sciences Géologiques, Strasbourg, v. 39, n° 3, 215-232.

Bignell R.D., 1975, Timing, distribution and origin of submarine mineralization in the Red Sea : Trans. Inst. Min. Metal., sect. B, p.1-6.

Bignell R.D., et Ali S.S., 1976, Geochemistry and stratigraphy of Nereus Deep, Red Sea, Geol. Jahrb., D17, 173-186.

Boillot G., Montadert L., Lemoine M., et Biju-Duval B., 1979, La marge occidentale de la Téthys Ligure, in 'Les marges continentales actuelles et fossiles autour de la France', Masson, 157-248.

Bonhomme M.G., Yerle J.-J., et Thiry M., 1980, Datation K/Ar de fractions fines associées aux minéralisations. Le cas du bassin uranifère permo-houiller de Brousse-Broquiès (Aveyron), C.R. Acad. Sci., Paris, 291, 121-124.

Bonhomme M.G., Bühmann D. et Besnus Y., 1983, Reliability of K-Ar dating of clays and silicifications associated with vein mineralizations in Western Europe, Geol. Rundschau, 72, 105-117.

Bril H., 1982, Nouvelles données thermométriques sur les inclusions fluides dans la fluorine du district de Langeac (Haute-Loire) et place de ces minéralisations dans la métallogénie régionale, C.R. Acad. Sci., Paris, 294, 107-110.

Bril H., 1983, Etude métallogénique des minéralisations à antimoine et associés du district de Brioude-Massiac (Massif Central Français); conditions géochimiques de dépôt; implications génétiques, Annales Scientifiques de l'Université de Clermont-Ferrand, Mém. 77, 340 p..

Brousse R., et Bellon H., 1983, Réflexions chronologiques et pétrologiques sur le volcanisme associé au développement des rifts de France, Bull. Centres Rech. Explor.-Prod. Elf Aquitaine, 7, 409-424.

Burke R.A. Jr., Brooks J.M., et Sackett W.M., 1981, Ligth hydrocarbons in Red Sea brines and sediments, Geochim. Cosmochim. Acta, 45, 627-634.

Cathles L.M., 1983, An analysis of the hydrothermal system responsible for massive sulfide deposition in the Hokoruko basin of Japan, Econ. Geol., Monograph 5, 439-487.

Cathles L.M., et Smith A.T., 1983, Thermal constraints on the formation of Mississipi Valley type lead-zinc deposits and their implications for episodic basin dewatering and deposit genesis, Econ. Geol., 78, 983-1002.

Charef A., 1986, La nature et le rôle des phases fluides associées à la minéralisation Pb-Zn dans les formations carbonatées et leurs conséquences métallogéniques : études des inclusions fluides et des isotopes (H, C, O, S, Pb) des gisements des Malines (France), Jbel Hallouf, Sidi Bou Aouane et Fedj-et-Adoum (Tunisie), Thèse I.N.P.L., Fr., non publié, 291 p..

Charef A., et Sheppard S.M.F., 1988, Les Malines Cambrian shale-hosted Pb-Zn deposit, France : Thermometric and isotopic (H_2O) evidence for pulsating hydrothermal mineralization, Mineral. Deposita., 23, 86-95.

Cochran J.R., 1983, A model for development of Red Sea, Am. Assoc. Petroleum Geologists Bull., 67, 41-69.

Connan J., et Orgeval J.-J., 1977, Un exemple d'application de la géochimie organique en métallogénie : la mine des Malines (Gard, France), Bull. Centre Rech. Pau S.N.P.A., 1, 59-105.

Craig H., 1966, Isotopic composition and origin of the Red Sea and Salton Sea geothermal brines, Science, 154,1544-1547.

Debelmas J., 1986, L'héritage hercynien à l'origine des grands bassins sédimentaires français, Bull. Centres Rech. Explor.-Prod. Elf Aquitaine, 10, 151-161.

Debrand-Passard S., (coordonnateur), 1984, Synthèse géologique du Sud-Est de la France. Mém. B.R.G.M. 125, 615p..

Deloule E., 1982, The genesis of fluorspar hydrothermal deposits at Montroc and Le Burc, The Tarn, as deduced from fluid inclusion analysis, Econ. Geol., 77, 1867-1874.

Dickinson G., 1953, Geological aspects of abnormal reservoir pressures in Gulf Coast Louisiana, A.A.P.Geol. Bull., 37, 410-432.

Dubessy J., et Ramboz C., 1986, The history of organic nitrogen from early diagenesis to amphibolite facies : mineralogical, mechanical and isotopic implications, 5th Congress on Water-rock Interaction, Reykjavik, 171-175 et manuscript n° 13

Dupré B., Blanc G., et Boulègue J., 1987, Pb isotopes on metalliferous sediments from the Red Sea, Terra Cognita, 7, 228.

Elmi S., 1984, (coordonnateur) Le Mésozoique de la Marge Cévenole : nouveaux repères biostratigraphiques, dynamique sédimentaire et diagénèse, Programme Géologie profonde de la France, Documents B.R.G.M., 80, 157-182.

Fairhead J.D., et Girdler R.W., 1970, The seismicity of the Red Sea, Gulf of Aden and Afar triangle, Phil. Trans. Roy. Soc. London, 267, 49-74.

Franck E.U., 1982, Survey of non-thermodynamic properties and chemical phenomena of fluids and fluid mixtures, in : D. Rickard and F.E. Wickam eds., Chemistry and geochemistry of solutions at high temperatures and pressures. Physics and Chemistry of the Earth, Vols. 13 and 14, Pergamon Press.

Gagny C., Gouanvic Y., Ovejero G., Servajean G., et Valverde G., 1985, Eléments nouveaux pour la compréhension de la métallogenèse à Pb-Zn-Ag et Hg dans la partie méridionale de la Péninsule Ibérique : zone de cisaillement crustal et anomalie régionale profonde et permanente, C.R. Acad. Sci., 300, 609-612.

Garson S. M., et Krs M., 1976, Geophysical and geological evidence of the relationship of Red Sea transverse tectonics to ancient fractures, Geol. Soc. America Bull., 87, 169-187.

George E., 1985, Les minéralisations uranifères jurassiques liées spatialement à une discordance hercynienne. Pétrographie, minéralogie et géochimie des gisements du Rouergue (Aveyron-France). Géol. Géochim. Uranium, C.R.E.G.U., Vandoeuvre-lès-Nancy, Mém. 9, 219p..

Gillmann M.A., Letullier A., et Renouard G., 1966, La Mer Rouge : géologie et problème pétrolier, Rev. I.F.P., 21, 1467-1487.

Girdler R.W. et Southren T.C., 1987, Structure and evolution of the Northern Red Sea, Nature, 330, 716-721.

de Graciansky P.C., Bourbon M., de Charpal O., Chenet P.Y., et Lemoine M., 1979, Genèse et évolution comparée de deux marges continentales passives : marge ibérique de l'Océan Atlantique et marge européenne de la Téthys dans les Alpes Occidentales, Bull. Soc. Géol. Fr., 21, 663-674.

Guilhaumou N., Dhamelincourt P., Touray J.C., et Touret J., Etude des inclusions fluides du système N_2-CO_2 de dolomites et de quartz de Tunisie septentrionale. Données de la microcryoscopie et de l'analyse à la microsonde à effet Raman, Geochim. Cosmochim. Acta, 45, 657-673.

Gupta A.K., 1978, Solubility of AgCl in NaCl-bearing solutions at 250°C and 400°C under different pressures, J. Fac. Sci., Hokkaido Univ., 18, 445-448.

Guttierez-Lanz J.R., 1985, Etude des filons à Pb-Zn-Cu comportant une gangue sulfatée silicifiée de la région de Thann-Watwiller (Vosges du Sud), Thèse Doctorat I.N.P.L., 291 p..

Hanor J.S., 1979, The sedimentary genesis of hydrothermal fluids, In : H.L. Barnes Ed., Geochemistry of hydrothermal ore deposits, 2nd ed., 137-172.

Hemley J.J., Cygan G.L., et d'Angelo W.M., 1986, Effect of pressure on ore mineral solubilities under hydrothermal conditions, Geology, 14, 377-379.

Jansa L.F., et Wade J.A., 1975, Geology of the continental margin off Nova Scotia and Newfoundland, Canada Geol. Surv. Prof. Paper 77-21, 17p.

Jebrak M., 1985, Le district de El Hammam, in "Contribution à l'histoire naturelle des filons (F, Ba) du domaine varisque français et marocain", Document B.R.G.M., 99 , 47-228.

Laffite P., 1963, Mécanisme et durée de la formation des dépôts filoniens. Régime thermique- Rôle de la pression- Le coefficient de diffusion thermique en géochronologie. Symposium 'Problems of post-magmatique ore deposition, Prague, vol. 1, 438-445.

Lancelot Y., de Saint-André B., de La Boisse H., 1984, Systématique U/Pb du gisement d'uranium de Lodève, Mineral. Deposita, 19, 44-53.

Le Quentrec M.-F., Sichler B., et Bayer R., 1987, Magnétisme profond au-dessus de la fosse d'Atlantis II (Mer Rouge), Réunion spécialisée de la Société Géologique de France, Paris.

Le Pichon X., 1968, Sea-floor spreading and continental drift, J. Geophys. Research, 73, 3611-3697.

Le Pichon X., et Gaulier J.M., 1987, Oceanic nature of Northern Red Sea crust : implications of seismic measurements made during Minos cruise, Terra Cognita, 7, 201.

Macquar J.C., 1984, Minéralisations triasiques en Pb, Zn, Ba (Cu, Fe) du Bassin Subalpin : typologie, géochronologie, contrôles et modèles, in : Debrand-Passard S., (coordonnateur), Synthèse géologique du Sud-Est de la France, Mém. B.R.G.M., 125, 112-118.

Magara K., 1975, Reevaluation of montmorillonite dehydration as cause of abnormal pressure and hydrocarbon migration, A.A.P.G. Bull., 59 292-302.

Makhris J., et Rihm R., 1987, Crustal structure of the Red Sea region derived from seismic and gravity data, Terra Cognita, 7, 295.

Manheim F.T., 1974, Red Sea geochemitry, in Whimarsh R.B., Weser O.E., Ross D.A., et al., D.S.D.P.Initial Report , 23, Washington, U.S. Government Printing Office), 975-998

Marini D., 1986, Etude des minéralisations Zn, Pb, Ba des conglomérats triasiques de la bordure du district des Malines (Gard, France). Comparaison sédimentologique, minéralogique et géochimique des séries sulfatées et de leurs équivalents latéraux à l'aplomb des sites minéralisés, Laboratoire de géologie du Muséum, Document de l'unité associée 1209, n°9, 448 p..

Mitchell J.G., et Halliday A.N., 1976, Extent of Triassic, Jurassic hydrothermal ore deposits on the North Atlantic margins, Trans. Inst. Min. Metal., 85, 189-161.

Montadert L., de Charpal O., Roberts D.G., Guennoc P., et Sibuet J.C.,1979, Northeast Atlantic passive continental margins : rifting and subsidence processes, in M. Talwani, W. Hay and W.B.F. Ryan, eds., Deep drilling results in the Atlantic Ocean, continental margins and paleoenvironments : Maurice Ewing Symp. Proc. Ser., 3, 154-186.

Montenat C., 1986, (Ed.), Etudes géologiques des rives du golfe de Suez et de la Mer Rouge Nord Occidentale : évolution tectonique et sédimentaire d'un rift néogène, Doc. et Trav. IGAL, Paris, 10, 192p..

Ohmoto H., et Skinner B.J., 1983, The Kuroko and related volcanogenic massive sulfide deposits : introduction and summary of new findings, Econ. Geol., Monograph 5, 1-8.

Oudin E., Thisse Y., et Ramboz C., 1984, Fluid inclusion and mineralogical evidence for high-temperature saline hydrothermal circulation in the Red Sea metalliferous sediments : preliminary results, Marine Mining, 5, 3-31.

Orr W.L., 1974, Changes in sulfur content and isotopic ratios of sulfur during petroleum migration- Study of Big Horn Basin Paleozoic oils, A.A.P.G. Bull., 58, 2295-2318.

Pagel M., 1983, (coordonnateur), Les gisements d'uranium liés spatialement aux discordances, Géol. Géochim. Uranium, Nancy, Mém. 1, C.R.E.G.U., Vandoeuvre-lès-Nancy, 380 p..

Pautot,G., 1983, Les fosses de la Mer Rouge : approche géomorphologique d'un stade initial d'ouverture océanique réalisé à l'aide du seabeam, Oceanologica Acta, 6, 235-244.

Perrodon A., 1983, Géodynamique des bassins sédimentaires et systèmes pétroliers, Bull. Centres Rech. Explor.-Prod. Elf Aquitaine, 7, 645-676.

Phillips W.J., 1972, Hydraulic fracturing and mineralization, J. Geol. Soc., 128, 337-359.

Phillips W.J., 1986, Hydraulic fracturing effects in the formation of mineral deposits, Trans. Instn. Min. Metall., 95, Sect. B, 17-24.

Pouit G., et Guennoc P., 1983, Histoire de l'ouverture de la Mer Rouge et évolution des types de minéralisations associées, Note GMX N° 980, 45p.

Raleigh C.B,. Healy J.H., et Bredehoeft J.D., 1972, Faulting and crustal stress at Rangely, Colorado, Geophys. Monograph Series, 16, in H.C. Heard, I.Y. Borg, N.L. Carter et C.B. Raleigh, eds., Flow and fracture of rocks, American Geophysical Union, Washington, 275-284.

Raleigh C.B,. Healy J.H., et Bredehoeft J.D., 1976, An experiment in earthquake control at Rangely, Colorado, Science, 191, 1230-1237.

Ramboz C., et Charef A., 1988, Temperature, pressure, burial history and paleohydrology of the Les Malines Pb-Zn deposit : reconstruction from aqueous inclusions in barite, accepté pour publication dans Econ. Geol., chapitre II, ce volume.

Ramboz C., Oudin E., et Thisse Y., 1988, A submarine geyser at the bottom of the SW Basin of Atlantis II Deep, Red Sea : the evidence from fluid inclusions in epigenetic anhydrite, chapitre III, ce volume.

Ramsay J.G., 1980, The crack-seal mechanism of rock deformation, Nature, 284, 135-139.

Ribeiro A., et Cabral J., 1987, The neotectonic regime of the West Iberia continental margin : a transition from passive to active ?, Terra Cognita, 7, 120.

Roedder E., 1972, Composition of fluid inclusions, U.S.G.S. Prof. Paper 440 JJ, 164 p.

Sabouraud C., Macquar J.C., et Rouvier H., 1980, Les inclusions fluides, témoins et faux-témoins des conditions de dépôt. Quelques exemples pris dans les minéralisations de Pb, Zn, Ba, F au sud du Massif Central français, Mineral. Deposita, 15, 211-230.

Samama J.C., 1980, (coordonnateur), Les paléosurfaces et leurs métallogenèse, Mém. B.R.G.M., n° 104, 414 p..

Schoell M., 1976, Heating and convection within the Atlantis II Deep geothermal system of the Red Sea : Proceedings second United Nations Symposium on the development and use of geothermal resources, San Francisco 20-29 May 1975, 2, p. 583-590.

Schoell M., et Faber E., 1978, New isotopic evidence for the origin of Red Sea brines, Nature, 275, 436-438.

Searle R.C., et Ross D.A., 1975, A geophysical study of the Red Sea axial through between 20.5° and 22°N, J. Geophys. Royal Astron. Soc., 43, 555-572.

Seward T.M., 1976, The stability of chloride complexes of silver in hydrothermal solutions up to 350°C, Geochim. Cosmochim. Acta, 37, 379-399.

Shanks W.C. II, 1983, Economic and exploration significance of Red Sea metalliferous brine deposits, in Shanks, W.C., ed., Cameron volume on unconventional mineral deposits : A.I.M.E. Monograph, p. 157-171.

Shanks W.C., et Bischoff J.L., 1980, Geochemistry, sulfur isotope composition and accumulation rates of Red Sea geothermal deposits, Econ. Geol., 75, 445-459.

Sheppard S.M.F., et Charef A., 1986, Eau organique : caractérisation isotopique et évidence de son rôle dans le gisement Pb-Zn de Fedj-El-Adoum, Tunisie, C.R.Acad.Sci., 302, 1189-1192.

Sibson R.H., Mc Moore J., et Rankin A. H., 1975, Seismic pumping - a hydrothermal fluid transport mechanism, J. Geol. Soc. London, 131, 653-659.

Triat J.-M., et Truc G., 1983, Le rôle des failles N50 dans la sédimentation des temps méso- et cénozoiques et dans l'évolution tectonique du Bassin Sud-Est, Bull. Centres Rech. Explor.-Prod. Elf Aquitaine, 7, 425-432.

Urai J.L., 1983, Deformation of wet salt rocks, Thèse de l'Université de Utrecht, 221 p.

Verraes, G., 1983, Etude monographique du district minier des Malines et de ses environs (province sous-cévenole, France), Thèse d'Etat, Univ. Montpellier, non publiée, vols. 1 and 2, 591 p.

White D.E., 1974, Diverse origins of hydrothermal ore fluids, Econ. Geol., 69, 954-973.

Yajima J., etTouray J.C., 1970, Analyse thermométrique du gisement de fluorine d'El Hammam (Maroc) (d'après les études d'inclusions fluides), Mineral. Deposita, 5, 23-28.

CONCLUSIONS GENERALES

Vigneresse (1988) a souligné l'importance de la notion d'échelle en géologie, arguant que toute donnée acquise à l'échelle du micron ou du centimètre devait, avant d'être extrapolée à la dimension de la chaîne de montagne ou du continent, être soigneusement confrontée aux observations et mesures faites à des échelles d'ordre supérieur. Les inclusions fluides sont des objets dont la taille n'excède souvent pas quelques dizaines de micromètres. Il convient en effet de confronter les informations quantitatives qu'elles fournissent avec les données minéralogiques, isotopiques... Non pas que les caractéristiques V-X déduites de l'étude des inclusions dépendent de la taille du système fluide étudié, mais parce que toute interprétation quantitative de mesures microthermétriques repose sur un postulat de départ : celui que l'inclusion est un système dont la chimie et le volume sont restés inchangés depuis le moment où le fluide a été piégé dans le cristal jusque et y compris au moment où le fluide a été étudié. Or il est prouvé qu'au voisinage des inclusions fluides, les cristaux peuvent subir des déformations réversibles ou irréversibles lorsqu'ils sont chauffés. L'inclusion peut aussi changer de forme si le minéral hôte est très soluble dans l'eau, que sa solubilité soit prograde ou rétrograde.

Dans les chapitres II à IV de ce mémoire, on s'est efforcé d'obtenir d'abord une information quantitative extensive de l'étude des inclusions fluides, puis de la confronter avec les données et observations acquises à des échelles comparables (données minéralogiques) ou supérieures. A l'inverse, le chapitre I montre comment une étude minéralogique peut être interprétée en terme d'activité de l'eau, de l'oxygène et de mécanismes de croissance des cristaux, à la lumière de données déjà disponibles sur les inclusions fluides.

Les barytines des Malines, comme de nombreuses barytines des stades tardifs des gisements de Pb-Zn (e.g. Hanor, 1979), contiennent des inclusions aqueuses qui fournissent des températures d'homogénéisation élevées et dispersées. Par ailleurs, ces cristaux contiennent, comme la barytine de

Cartersville étudiée par Rife (1971), des inclusions aqueuses et carboniques. Les résultats microthermométriques sur les barytines ont été le plus souvent considérés comme des arte facts témoignant que les sulfates ne sont pas des minéraux fiables pour l'étude des fluides occlus. On a proposé au contraire que les mesures effectuées sur les barytines des Malines traduisaient l'existence de températures et de pressions élevées sur la Marge Cévenole. On a suggéré de plus que c'est l'addition de CO_2 dans les fluides de pore qui a fait que la pression a atteint des valeurs de type lithostatique dans le socle cambrien. De telles conclusions sont tout d'abord étayées par des observations qualitatives simples. Les cristaux contiennent des huiles dont les couleurs variées, allant du blanc laiteux au brun foncé, traduisent une dégradation thermique contemporaine du piégeage dans le cristal. De plus, la présence de fluides carboniques dans les inclusions prouve que les cristaux, loin de fuir, contiennent au contraire des gaz sous pression. Enfin, la présence de CO_2 dissout dans les fluides est en elle-même une indication de température et/ou de pression élevées, du fait de la solubilité limitée de ce gaz dans l'eau. De façon plus générale, on peut interpréter à la lumière des inclusions fluides que les barytines des phases tardives des gisements Pb-Zn se mettent en place lors d'épisodes volcaniques pendant les stades évolutifs terminaux des bassins. Dans les contextes de marge, on sait que ces épisodes volcaniques accompagnent la surrection des marges. Concernant l'hypothèse de pressions fluides proches des valeurs lithostatiques au Malines et les mécanismes proposés pour leur genèse, on peut noter que des pressions fluides équivalentes ou supérieures à la pression lithostatique ont bien été mesurées in situ dans les bassins, quoiqu'elles soient exceptionnelles. Dans la nature, ces pressions élevées concernent, conformément au modèle proposé au Malines, des ceintures volcaniques et des sédiments riches en CO_2 et CH_4 (Matthews et al., 1971).

Dans le contexte de la fosse d'Atlantis II en Mer Rouge Centrale, on a pu contraindre l'interprétation des mesures microthermométriques en terme de

températures maximales de formation de l'anhydrite vers 390° à 400°C et de processus d'immiscibilité, d'une part par une analyse appropriée des fluides du système de référence H_2O-NaCl, et d'autre part par l'étude des variations de l'enthalpie et de la masse de la fosse elle-même, soit d'un système de 2.3 km^3 environ. Les photos présentées en couverture illustrent le fait que les données fournies par le cristal permettent d'étayer l'hypothèse d'une alimentation de type geyser pour la fosse d'Atlantis II. De plus, les résultats du bilan thermique de la fosse, en accord avec les données des inclusions fluides, mettent en évidence une spécificité importante des solutions hydrothermales : des capacités calorifiques qui croissent de façon exponentielle avec la température au dessus de 300°C. Cette dernière propriété permet d'expliquer pourquoi, à 21°N E.P.R., les inclusions fluides dans les anhydrites indiquent des températures moyennes de piégeage d'environ ≈330°C, c'est-à-dire proches de la température du pôle hydrothermal pur(Le Bel and Oudin , 1982), alors que la composition isotopique du strontium du cristal montre que le fluide hydrothermal était déjà mélangé avec 1/3 d'eau de mer pour former l'anhydrite (Albarède et al., 1981).

Les données d'inclusions fluides associées aux minéralisations en contexte d'extension, de type Mer Rouge ou Bordure Cévenole, montrent que le processus de mélange est rarement impliqué dans la formation des minerais. Ce résultat est conforme au fait que, dans les environnements océaniques et de sub-surface, les réservoirs principaux de fluides, eau de mer ou eaux météoriques, sont oxydants et que tout mélange ou contact avec eux est défavorable au dépôt et à la préservation des sulfures (voir Cathles, 1983). Le mélange de fluides a souvent été évoqué pour expliquer le dépôt des sulfates et des sulfures dans les sédiments de la Mer Rouge (Pottorf et Barnes, 1983), à l'encontre des preuves fournies par les inclusions fluides. Cette contradiction résulte du fait que la plupart des auteurs ont négligé toute interaction possible entre le fluide hydrothermal et le sédiment oxydé. Or celui-ci est particulièrement réactif vis à vis des espèces réduites du soufre du fait qu'il est constitué d'argiles et d'oxydes

pulvérulents : des argiles de type nontronite ne sont-elles pas utilisées à basse température dans les pompes à essence pour fixer H_2S?

Finalement, le chapitre I présente une analyse détaillée des mécanismes par lesquels les système fluides et les minéraux parviennent à s'équilibrer en contexte métamorphique. Apparemment, les cinétiques d'équilibrage des fluides du système C-O-H avec le graphite procèdent plus rapidement que les éléments ne diffusent dans le réseau des grenats. On a montré comment les processus de dégazage favorisent l'apparition de grenats à structure de type chiastolite ou de grenats ronds dans les skarns à clinopyroxènes-grenats des Jebilet. Le fait que des grenats à structure similaire soient décrits dans de nombreuses séries métamorphiques témoignent que les processus de dégazage sont importants dans ces contextes mais qu'ils sont souvent méconnus, adu moins à l'échelle minéralogique.

Réferences:

Albarède F., Michard A., Minster J.F., and Michard G., 1981, $^{87}Sr/^{86}Sr$ ratios in hydrothermal waters and deposits from the East Pacific Rise at 21°N, Earth Planet. Sci. Letters 55, 289-236.

Cathles L.M., 1983, An analysis of the hydrothermal system responsible for massive sulfide deposition in the Hokoruko basin of Japan, Econ. Geol., Monograph 5, 439-487.

Hanor J.S., 1979, The sedimentary genesis of hydrothermal fluids, In : H.L. Barnes Ed., Geochemistry of hydrothermal ore deposits, 2nd ed., 137-172.

Le Bel L., and Oudin E., 1982, Fluid inclusion studies of deep-sea hydrothermal sulfide deposits on the East Pacific Rise near 21°N. Chem. Geol.37, 129-136.

Matthews W.R., Rehm W.A., and Louden L. R., 1971, Understanding origin of pressure is a key to better well planning, Oil and Gas Journal November 15, 141-144.

Pottorf R.J. and Barnes, H.L.,1983, Mineralogy, geochemistry and ore genesis of hytrothermal sediments from the Atlantis II deep, Red Sea. Econ. Geol. Mono.5, 198-223.

Rife D.L., 1971, Barite fluid inclusion geothermometry, Cartersville Mining district, Northwest Georgia, Econ. Geol. 66, 1164-1167.

Vigneresse J.L., 1988, Les facteurs d'échelle en Sciences de la Terre, C.R. Acad. Sci. 306, 649-654.

TROISIEME PARTIE

Cette troisième partie rassemble les manuscripts publiés de 1980 à 1987 selon les trois thèmes suivants :

I - CONTRIBUTION A L'INTERPRETATION QUANTITATIVE DES DONNEES MICROTHERMOMETRIQUES EN TERME DE PARAMETRES PHYSIQUES (VOLUME, COMPOSITION) ET DE PROCESSUS (EBULLITION).

PUBLICATION I : Simulation des équilibres de phase dans le système CO_2-CH_4 en dessous de 50° C et de 100 bar. Application aux inclusions fluides.

PUBLICATION II : Simulation des équilibres de phase dans le système CO_2 - CH_4 - C_2H_6 en dessous de 50° C et de 100 bar. Application aux inclusions fluides.

PUBLICATION III : Les fluides moléculaires d'un filon de quartz hydrothermal : comparaison de techniques analytiques ponctuelles et globales, contamination des fluides occlus par des composés carbonés.

PUBLICATION IV : Première détermination expérimentale des relations de phases dans le système haplogranitique en conditions de sous-saturation en H_2O.

PUBLICATION V : Fluid immiscibility in natural processes : use ans misuse of fluid inclusion data. I : Phase equilibria analysis - A theoretical and geometrical approach.

PUBLICATION VI : Fluid immiscibility in natural processes : use and misuse of fluid inclusion data. II : Interpretation of fluid inclusion data in terms of immiscibility.

PUBLICATION VII : Application of V-X projections to the quantitative interpretation of heterogeneous trapping from fluid inclusion study.

II - ETUDES DE CAS :

PUBLICATION VIII : Chemical and isotopic evolution of the fluids in the Sn-W deposit, Panasqueira, Portugal.

PUBLICATION IX : Les concentrations stanno-wolframifères du district de Brioude-Massiac (Cantal) et du sud du Massif Central : analyse comparée de la minéralogie et des phases fluides associées.

PUBLICATION X : The P-V-T-X-fO_2 evolution of H_2O-CO_2-CH_4-bearing fluid in a wolframite vein : Reconstruction from fluid inclusion studies.

PUBLICATION XI : Fluid inclusion and mineralogical evidence for high-temperature saline hydrothermal circulation in the Red Sea metalliferous sediments : preliminary results.

III - ASPECTS DE L'INTERACTION ENTRE ROCHES ET FLUIDES RICHES EN ELEMENTS VOLATILS :

PUBLICATION XII : Oxydation du fer dans les skarns et les schistes à graphite des Jebilet Centrales, Maroc : un indicateur de transfert de matière par les fluides dans une zone de cisaillement ductile.

PUBLICATION XIII : The history of organic nitrogen from early diagenesis to amphibolite facies : mineralogical, chemical, mechanical and isotopic implications.

PUBLICATION XIV : Recherche du tungstène dans le district de la Châtaigneraie. (Cantal, Aveyron - Massif central français) : Géochimie des schistes de la Châtaigneraie.

PUBLICATION XV : Physical and chemical controls (fO2, T, pH) of the opposite behaviour of U and Sn-W as exemplified by hydrothermal deposits in France and Great-Britain, and solubility data.

I

CONTRIBUTION A L'INTERPRETATION QUANTITATIVE DES DONNEES MICROTHERMOMETRIQUES EN TERME DE PARAMETRES PHYSIQUES (VOLUME, COMPOSITION) ET DE PROCESSUS (EBULLITION).

PUBLICATION I : Simulation des équilibres de phase dans le système CO_2-CH_4 en dessous de 50° C et de 100 bar. Application aux inclusions fluides.

GÉOCHIMIE. — *Simulation des équilibres de phases dans le système CO_2-CH_4 en dessous de* 50°C *et de* 100 bar. *Application aux inclusions fluides.* Note (*) de **Georges Heyen, Claire Ramboz** et **Jean Dubessy**, présentée par Jean Wyart.

Une équation d'état est proposée pour le système CO_2-CH_4 en dessous de 50°C et de 100 bar. Cette équation permet de prédire les conditions P-V-T-X des équilibres de phase de ce système. Les données engendrées par le modèle ont été utilisées pour construire un diagramme $\overline{V}$-X adapté à l'interprétation en terme de composition et de densité des mesures microthermométriques obtenues lors de l'étude des inclusions fluides carbonées.

An equation of state is proposed for the CO_2-CH_4 system below 50°C and 100 bar. This equation allows one to predict the P-V-T-X conditions of the phase equilibria in this system. In particular, using the data thus generated, a $\overline{V}$-X diagram has been constructed for the interpretation in terms of composition and density of the microthermometric parameters, measured during the study of carbonaceous fluid inclusions.

INTRODUCTION. — CO_2 et CH_4 sont les constituants majeurs de nombreux fluides géologiques. Dans les inclusions piégeant de tels fluides, la fusion du dernier cristal de CO_2 et l'homogénéisation des phases fluides carbonées sont mesurées pour estimer la composition et la densité de ces mélanges. L'interprétation de ces changements de phase nécessite une connaissance approfondie des propriétés P-V-T-X de ce système dans les domaines à deux et trois phases ($P < 85$ bar et $T < 31{,}1$°C). Les données expérimentales disponibles dans ce domaine sont limitées (*voir* [1] et [2]). C'est pourquoi les diagrammes utilisés pour l'interprétation des mesures microthermométriques ont été tracés par extrapolation des données expérimentales (abaque d'isothermes T_{fCO_2} [1]), ou calculés à l'aide du modèle de mélange idéal (diagramme $\overline{V}$-X [2]). Dans le présent travail une équation d'état pour le système CO_2-CH_4 a été ajustée afin de prédire au mieux les caractéristiques P-V-T-X des équilibres L-V et S-L-V- de ce système. Un diagramme a été construit pour l'interprétation quantitative de tous les paramètres microthermométriques mesurés sur des fluides intraminéraux.

SYMBOLES. — S, CO_2 solide; L, liquide; V, vapeur; f_i^φ, fugacité du constituant i dans la phase φ (atm); n_i^φ, nombre de moles du constituant i dans la phase φ; X_i^φ, fraction molaire du constituant i dans la phase φ; Z_i, fraction molaire du constituant i dans le mélange; P, pression (atm); T, température (°K); R, constante des gaz parfaits $= 82{,}04$ cm^3 . atm . °K^{-1}; V, volume total du mélange; $\overline{V}\,\varphi$, volume spécifique de la phase φ (cm^3/mole); K_c, valeur de la variable K au point critique du corps pur considéré; K_r, « variable K « réduite » $= K/K_c$; T_{fCO_2}, température de fusion du dernier cristal de CO_2 (°C); T_{hCO_2} : température d'homogénéisation de la phase carbonée (°C); D.R.T_{fCO_2} : fraction volumique du liquide dans le système carboné à T_{fCO_2}.

SIMULATION DES ÉQUILIBRES L-V ET S-L-V DANS LE SYSTÈME CO_2-CH_4. — Les conditions thermodynamiques des équilibres L-V dans le système CO_2-CH_4 sont définies par les égalités $f^L_{CO_2} = f^V_{CO_2}$ et $f^L_{CH_4} = f^V_{CH_4}$ [3]. P et T étant fixés, la fugacité du constituant CO_2 dans la phase φ est une fonction du nombre de moles de ce constituant dans cette phase :

$$\ln f^\varphi_{CO_2} = \frac{1}{RT}\int_V^\infty \left(\frac{\partial P}{\partial n^\varphi_{CO_2}}\right) T, V, n^\varphi_{CH_4} - \frac{RT}{V}\,dV - \ln\frac{V}{n^\varphi_{CO_2} RT}.$$

Cette équation peut être utilisée à condition de disposer de la relation $P = F(T, V, n^\varphi_{CO_2}, n^\varphi_{CH_4})$ qui est l'équation d'état du mélange valable en phase liquide ou en

phase vapeur. Un modèle pour le système CO_2-CH_4 a été construit en ajustant une relation de forme analytique identique pour chacun des corps purs CO_2 et CH_4. Les règles de mélange permettent de calculer les paramètres de l'équation d'état du système binaire à partir des paramètres de l'équation du CO_2 et du CH_4 purs. Les équilibres univariants S-L-V du système CO_2-CH_4, décrits par les relations $f^L_{CH_4} = f^V_{CH_4}$ et $f^S_{CO_2} = f^L_{CO_2} = f^V_{CO_2}$ peuvent être calculés à l'aide de l'équation d'état du système binaire. Le calcul du terme $f^S_{CO_2}$ est détaillé plus loin.

ÉQUATIONS D'ÉTAT DU CO_2 ET DU CH_4 PURS. — L'équation d'état de Heyen [4], à trois paramètres dont deux (a et b) sont ajustables avec la température, a été choisie; sa formule analytique est donnée dans le tableau I. Dans les conditions critiques pour un corps pur

TABLEAU I

Expression analytique de l'équation d'état et des règles de mélange de [4]

Équation d'état	Règles de mélange
$P = \frac{RT}{V-b} - \frac{a}{V^2+(b+e)V-be}$	$a_m = \sum_i x_i \times \frac{\sum_j x_j \times \tau_{ij}}{\sum_k x_k \tau_{ik}} \times \sqrt{a_i a_j} \times (1-\delta_{ij})$
$a = a_c \exp k(1-T_r^n)$	(avec $\delta_{ij} = \delta_{ji}$ et $\tau_{ij} \times \tau_{ji} = 1$)
$b = b_c\left(1 - m \tanh\left(\frac{\theta}{2}(T_r - 1)\right)\right)$	$b_m = \sum_i b_i x_i$
$e = e_c$	$e_m = \sum_i x_i e_i$

TABLEAU II

Résultat de l'ajustement paramétrique de l'équation d'état pour le CO_2 pur, le CH_4 pur et leur mélange

Système	Réf.	Paramètres		
CO_2	[8], [9], [10], [11]	$a_c = 0{,}424\,26 \cdot 10^{+7}$	$k = 0{,}581\,94$	$n = 1{,}952\,3$
		$e_c = 59{,}29$	–	–
		$b_c = 23{,}045$	$m = 0{,}244\,17$	$\theta = 9{,}672\,1$
CH_4	[11]	$a_c = 0{,}257\,68 \cdot 10^{+7}$	$k = 0{,}483\,66$	$n = 1{,}648\,11$
		$e_c = 46{,}150$	–	–
		$b_c = 24{,}458$	$m = 0{,}256\,30$	$\theta = 6{,}874\,2$
CO_2-CH_4	[6], [7], [12]	si $i \neq j$	$\delta_{ij} = 0{,}1124$	$\tau = 0{,}9767$
		si $i = j$	$\delta_{ij} = 0$	$\tau_{ij} = 1$

donné ($V = V_c$ et $T = T_c$) l'équation d'état doit vérifier les trois relations : $P = P_c$, $\delta P/\delta V = 0$ et $\delta^2 P/\delta V^2 = 0$. Ce système d'équations définit les valeurs de a, b et e au point critique (a_c, b_c, e_c) pour le corps pur considéré. On admet que seuls a et b dépendent de T, e étant constant. La variation de a et b permet de reproduire de façon optimale deux grandeurs arbitrairement choisies dépendant de T seul : la pression de vapeur et le volume du liquide saturé. Les expressions analytiques de a et b données dans le tableau I, permettent d'ajuster de manière satisfaisante l'information expérimentale disponible pour les substances pures. En particulier, l'expression de $f^S_{CO_2}$ en fonction de T :

$$\left(\ln f^S_{CO_2} = 18{,}46 - \frac{329{,}93}{T} - 0{,}006\,258\,T\right)$$

a été obtenue par simulation de l'équilibre de sublimation du CO_2 pur et ajustement sur les données expérimentales sur ce corps pur (tableau II).

ÉQUATION D'ÉTAT POUR LE SYSTÈME CO_2-CH_4. — Les règles de mélange résumées dans le tableau I [5] définissent l'équation d'état du système CO_2-CH_4. Les paramètres d'interaction binaire δ_{ij} et τ_{ij} ont été choisis de façon à reproduire de façon optimale un fichier de données P-V-T-X dans les domaines à deux et trois phases (*fig.* 1). Cet ajustement a été obtenu à partir des seules données expérimentales de [6].

VALIDITÉ DU MODÈLE. — Le modèle proposé reproduit de façon satisfaisante les données expérimentales disponibles pour le CO_2 et le CH_4 purs, en dessous de 50°C et de 100 bar. Il

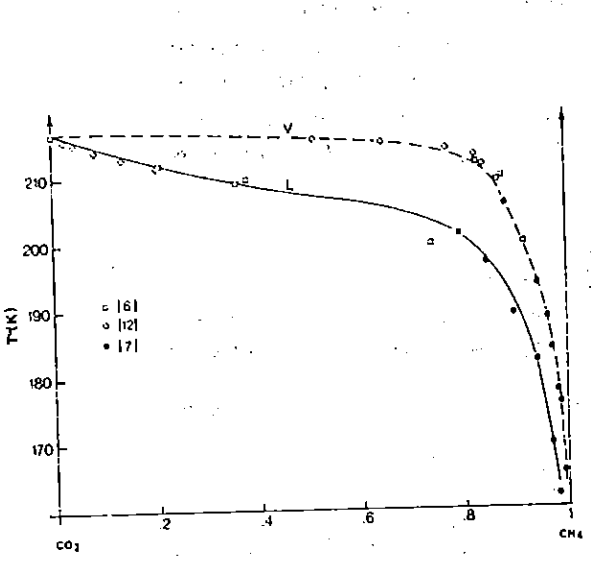

Fig. 1

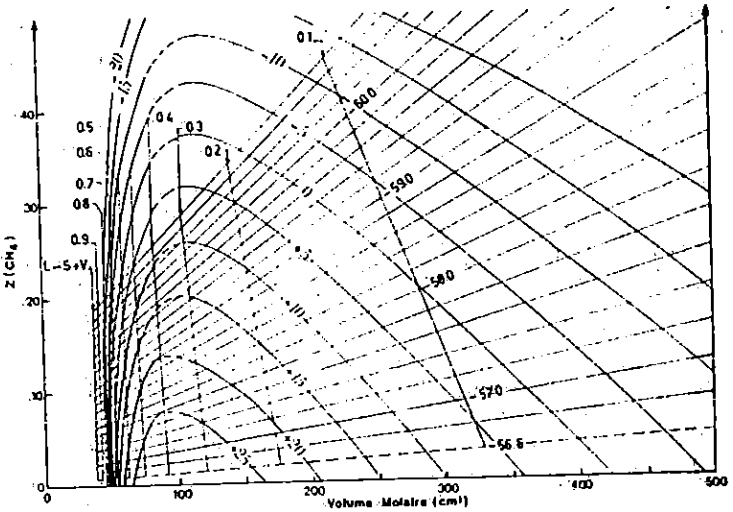

Fig. 2

Fig. 1. — Projection T-X calculée du liquide (L) et de la vapeur (V) en équilibre avec le dernier cristal de CO_2.

Fig. 2. — Projection du système CO_2-CH_4 sur le plan volume-composition, comprenant : 1° les caractéristiques du liquide en équilibre avec CO_2 solide et la vapeur (S+L+V); 2° les conodes L-V à $T = T_{f,CO_2}$ ($-60{,}8 \leqq T_{f,CO_2} \leqq -56.6$°C) graduées en fonction du paramètre « degré de remplissage » ($0{,}1 \leqq D.R.T_{f,CO_2} \leqq 0.9$); 3° les isothermes dans le domaine à deux phases fluides L-V ($-20 \leqq T_{f,CO_2} \leqq +25$°C, nombre en italiques); le trait est discontinu au voisinage des conditions critiques, où le modèle devient moins performant.

peut cependant être amélioré dans ce domaine, notamment pour ce qui concerne la sublimation et la fusion du CO_2 pur : sur la figure 2, la conode reliant le liquide et la vapeur à l'équilibre avec le CO_2 solide à -56.6°C devrait être confondue avec l'axe $Z_{CH_4} = 0$. En revanche, le modèle est inadapté pour prédire les propriétés P-V-T du CO_2 et du CH_4 dans les domaines P-T de la croûte terrestre : on obtient jusqu'à 100 % d'écart entre les pressions calculées par le modèle, et celles expérimentalement mesurées au-dessus de 1 kbar. Ceci limite donc l'utilisation de l'équation d'état du système CO_2-CH_4 à $T < 50$°C et $P < 100$ bar. Dans ce domaine, on peut considérer que l'erreur introduite par le modèle est du même ordre de grandeur que les écarts entre les données expérimentales elles-mêmes (par exemple [7]). Dans ce domaine cependant, comme il est d'usage, le modèle devient moins précis au voisinage des conditions critiques.

APPLICATION AUX INCLUSIONS FLUIDES. — L'équation d'état du système CO_2-CH_4 a été utilisée pour construire un diagramme $\overline{V}$-X adapté à l'interprétation des mesures microthermométriques effectuées sur des fluides carbonés (*fig.* 2). Une inclusion fluide carbonée, système isochimique et isovolumique ([1] et [2]), se projette dans ce diagramme en un point défini par les mesures T_{fCO_2}, T_{hCO_2} et D.F.T_{fCO_2}. La précision du diagramme est d'environ 10 % dans tout le domaine de température. Quelques limitations sont particulières à son utilisation pour les inclusions aqueuses riches en CO_2 et CH_4. La partie non aqueuse de ces inclusions ne constitue pas un système isovolumique entre T_{hCO_2} et T_{fCO_2} du fait de l'expansion volumique de la phase aqueuse lorsqu'elle se solidifie (environ 8 % en volume, [13]).

De plus, le contenu non aqueux de ces inclusions ne peut être considéré comme un système isochimique entre T_{fCO_2} et T_{hCO_2} dès lors qu'un hydrate de gaz est présent dans l'inclusion à l'une de ces températures [14]. Pour de telles inclusions, il convient donc de vérifier l'absence de l'hydrate de gaz lors des mesures de changements de phase, et de tenir compte dans l'interprétation de l'incertitude sur les volumes introduite par l'existence d'une phase aqueuse.

(*) Remise le 9 novembre 1981.

[1] H. SWANENBERG, *Contr. Mineral. Petrol.*, 68, 1979, p. 303.

[2] R. BURRUSS, *Mac Short Course in Fluid Inclusions*, L. HOLLISTER et M. CRAWFORD, ed., Calgary, 1981, p. 39.

[3] J. M. PRAUSNITZ, In *Phase Equilibria and Fluid Properties in the Chemical Industry*, T. S. STORVICK et S. I. SANDLER, éd., Amer. Chem. Soc. (*A.C.S. Symposium*, séries 60, 1977, p. 11).

[4] G. HEYEN, In *Phase Equilibria and Fluid Properties in the Chemical Industry*, E.F.C.E. Publication, séries n° 11, 1980, p. 9, Dechema Frankfurt.

[5] G. HEYEN, In *Actes du Congrès mondial de Génie Chimique*, Montréal, 1981.

[6] H. DONNELLY et D. KATZ, *Ind. Eng. Chem.*, 46, 1954, p. 511.

[7] S. MRAW, S. C. HWANG et R. KOBAYASHI, *J. Chem. Eng. Data*, 23, 1978, p. 135.

[8] L. N. CANJAR et F. S. MANNING, In *Thermodynamic Properties and Reduced Correlations for Gases*, Gulf Publishing Company Houston, Texas, 1967.

[9] S. ANGUS, B. ARMSTRONG et K. M. DE REUCK, In *Carbon Dioxide* (*I.U.P.A.C., International Thermodynamic Tables of the Fluid State*, 3, 1973, Pergamon Press).

[10] D. NEWITT, M. PAI, M. U. KULDOR et J. A. W. HUGGILL, In *Thermodynamic Functions of Gases*, F. DIN, éd. 1, p. 102, Butterworths.

[11] H. E. TESTER, In *Thermodynamic Functions of Gases*, F. DIN, éd., 3, 1956, p. 1, Butterworths.

[12] Y. ARAI, G.-I. KAMINISHI et S. SAITO, *J. Chem. Eng. Japan*, 4, n° 2, p. 113.

[13] P. HOBBS, In *Ice Physics*, Claredon Press, Oxford, p. 346.

[14] C. RAMBOZ et J. M. BENY, soumis à *Contr. Mineral. Petrol.*

G. H. : *Laboratoire d'analyse et synthèse des systèmes chimiques, 2, rue Stévart*, B-4000 *Liège, Belgique*,

C. R. : *C.R.P.G.*, B.P. n° 20, 54501 *Vandœuvre*.

J. D. : *C.R.E.G.U.*, B.P. n° 23, 54501 *Vandœuvre-les-Nancy*.

PUBLICATION II : Simulation des équilibres de phase dans le système CO_2 - CH_4 - C_2H_6 en dessous de 50° C et de 100 bar. Application aux inclusions fluides.

GÉOCHIMIE. — *Simulation des équilibres de phase dans le système CO_2-CH_4-C_2H_6 en dessous de 50°C et de 100 bar. Application aux inclusions fluides.* Note (*) de **Georges Heyen, Jean Dubessy** et **Claire Ramboz,** présentée par Jean Wyart.

Une équation d'état a été construite pour le système ternaire CO_2-CH_4-C_2H_6 en dessous de 50°C et de 100 bar. Ce modèle peut être utilisé pour déterminer la densité des inclusions fluides carbonées de ce système, dont la composition molaire partielle est analysée à l'aide de la microsonde Raman, et pour lesquelles une valeur T_{hCO_2} ou T_{fCO_2} est connue. A quelques réserves près, une interprétation analogue des mesures microthermométriques dans les inclusions aqueuses et carbonées est possible.

An equation of state is proposed for the CO_2-CH_4-C_2H_6 system below 50°C and 100 bar. It can be used to determine the density of carbonaceous fluid inclusions, provided that their relative molar composition is analysed with the Raman microprobe and that T_{hCO_2} or T_{fCO_2} is measured in these mixtures. Within some limitations, a similar interpretation of T_{fCO_2} and T_{hCO_2} in the non-aqueous part of water-rich carbonaceous mixtures is also possible.

INTRODUCTION. — Le gaz carbonique, le méthane et l'éthane sont, avec l'eau, les constituants majeurs des inclusions fluides intraminérales de certaines séries métamorphiques [1]. L'interprétation des températures de fusion du dernier cristal de CO_2 et d'homogénéisation de la partie non aqueuse des inclusions complexes en terme de leur composition et de leur densité nécessite la référence au système CO_2-CH_4-C_2H_6. Les données disponibles sur ce système étant très partielles [2], une équation d'état a été développée afin de prédire les conditions P-V-T-X des équilibres de phases observés dans ce système.

TABLEAU

Systèmes	Références	Paramètres	
CO_2, CH_4, CO_2-CH_4	[5], [6], [7], [14]	*Voir* [10]	
C_2H_6	[8], [9]	$a_c = 0{,}6315.10^{+7}$ $c_c = 75{,}887$ $b_c = 36{,}508$	$k = 0{,}563\,79$ $n = 1{,}782\,84$ $m = 0{,}310\,09$ $\theta = 8{,}766\,2$
CH_4-C_2H_6	[11]		$\delta = 0.569$ $\tau = 0{,}711\,6$
CO_2-C_2H_6	[12], [13]		$\delta = 0.112\,2$ $\tau = 0{,}694\,0$

SYMBOLES. — S, CO_2 solide; L, liquide; V, vapeur; P, pression (atm); T, température (°K); K_c, valeur de la variable K dans les conditions critiques; T_{fCO_2} : température de fusion du dernier cristal de CO_2 (°C); T_{hCO_2} : température d'homogénéisation de la phase carbonée (°C).

LE MODÈLE THERMODYNAMIQUE. — L'équation d'état [3] et les règles de mélange [4] développées par Heyen et résumées dans [10], ont été utilisées comme modèle du système CO_2-CH_4-C_2H_6. Un ajustement préalable des paramètres de l'équation d'état a été réalisé sur les données expérimentales des corps purs CO_2, CH_4 et C_2H_6 (tableau). Les paramètres d'interaction binaire pour les systèmes CO_2-CH_4, CH_4-C_2H_6 et CO_2-C_2H_6, ont été ajustés de même, selon la démarche détaillée dans [10]. Le tableau regroupe les valeurs des paramètres de l'équation d'état pour les trois constituants choisis ainsi que celle des paramètres d'interaction binaire pour leur mélange. Les données expérimentales ayant servi à réaliser l'ajustement des trois couples de paramètres d'interaction binaire sont également indiquées.

L'équation d'état du système CO_2-CH_4-C_2H_6 est définie à l'aide des formules résumées dans [10] et des paramètres de ce tableau.

DOMAINE D'APPLICATION DU MODÈLE. — Les équations d'état des systèmes CO_2-C_2H_6 et CH_4-C_2H_6 ont été éprouvées en dessous de 50°C et de 100 bar, de la même façon que pour le système CO_2-CH_4 [10]. Loin des conditions critiques ($P < P_c$ et $T < T_c$), le modèle reproduit

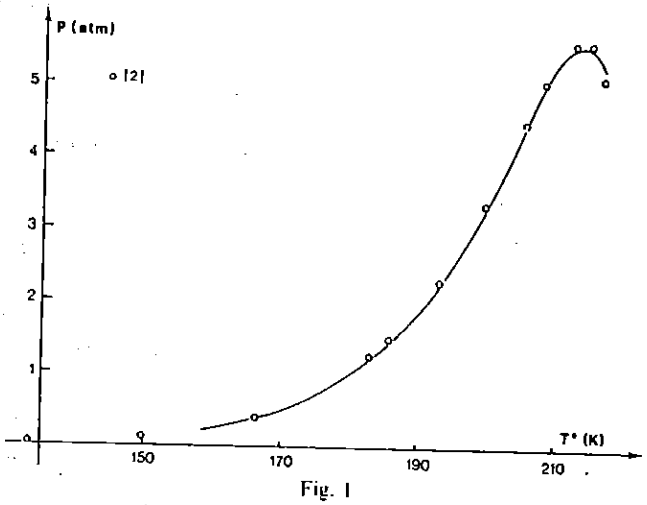

Fig. 1

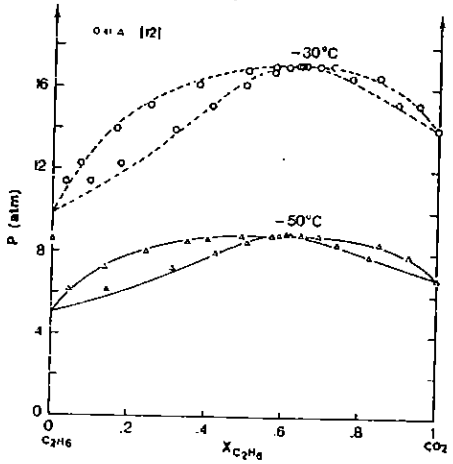

Fig. 2

Fig. 1. — Projection P-T calculée de la courbe de solubilité du système CO_2-C_2H_6.

Fig. 2. — Projection isotherme P-X calculée des courbes de bulle et de rosée dans le système CO_2-C_2H_6.

de façon satisfaisante les propriétés du système CO_2-C_2H_6, en particulier le long de la courbe de solubilité (*fig.* 1). Il reproduit fidèlement l'azéotrope négatif qui caractérise ce système (*fig.* 2). Il prédit convenablement les données volumiques de [13] dans le domaine à deux phases, principalement dans le domaine de composition compris entre 0 et 20 moles % C_2H_6, le plus fréquemment observé en géologie (*fig.* 3). Les prédictions des données P-V-T-X des systèmes CO_2-CH_4 et CH_4-C_2H_6 sont également satisfaisantes (respectivement [10] et *fig.* 4). Ceci est considéré comme un bon critère de validité de l'équation d'état pour le système ternaire CO_2-CH_4-C_2H_6, en dessous de 50°C et 100 bar et hors des domaines critiques.

APPLICATION AUX INCLUSIONS FLUIDES. – Afin de déterminer le trajet isochore P-T le long duquel un fluide du système CO_2-CH_4-C_2H_6 a été piégé dans une inclusion, il est nécessaire de connaître la densité et la composition de ce fluide. Dans les systèmes ternaires contenant du CO_2, les seules mesures microthermométriques T_{fCO_2} et T_{hCO_2} ne peuvent être interprétées directement en terme de composition et de densité des mélanges, contrairement aux mesures relatives aux mélanges binaires contenant du CO_2 [10]. Une donnée supplémentaire est donc

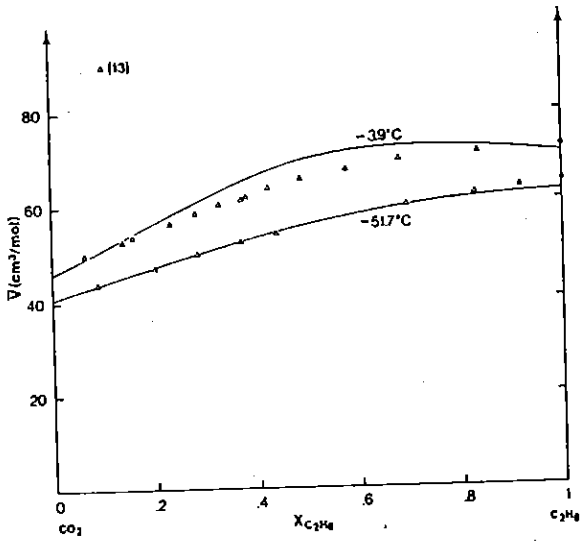

Fig. 3

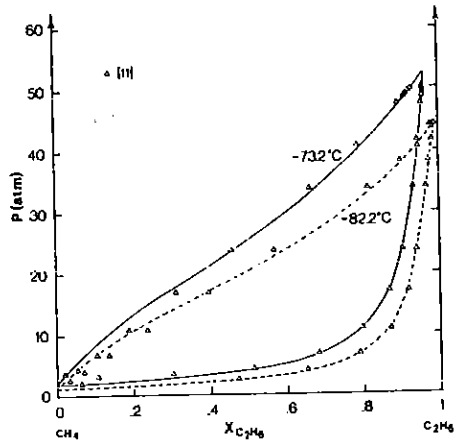

Fig. 4

Fig. 3. – Projection isotherme $\bar{V}$-X calculée des courbes de bulle dans le système CO_2-C_2H_6.

Fig. 4. – Projection isotherme P-X calculée des courbes de bulle et de rosée dans le système CH_4-C_2H_6.

nécessaire à une telle interprétation dans des systèmes carboniques à plus de deux constituants. La microsonde « M.O.L.E. » permet de connaître la fraction molaire de chacun des constituants d'un mélange complexe [14]. Disposant d'une telle analyse, il devient possible d'interpréter les mesures T_{hCO_2} ou T_{fCO_2} d'un mélange composé de CO_2, de CH_4 et de C_2H_6 en terme de sa densité, en utilisant le modèle proposé. A quelques réserves près, détaillées dans [15], cette méthode peut être étendue à la détermination de la densité de la partie non aqueuse des inclusions aqueuses contenant du CO_2, du CH_4 et du C_2H_6. Si la composition et la densité de la partie aqueuse de ces inclusions est également connue, la

composition globale de ces inclusions aqueuses et carbonées peut être calculée [16]. Cette analyse est une étape indispensable pour choisir l'isochore le long duquel il faut envisager les conditions thermobarométriques de piégeage des fluides aqueux et carbonés.

(*) Remise le 23 novembre 1981.

[1] J. MULLIS, *Bull. Minéral.*, 102, 1979, p. 526.

[2] J. DAVALOS, W. ANDERSON, R. PHILIPS et A. KIDNAY, *J. Chem. Eng. Data*, 21, 1976, p. 81.

[3] G. HEYEN, in *Phase Equilibria and Fluid Properties in the Chemical Industry*, E.F.C.E. Publication series n° 11, Dechema Frankfurt, 1980, p. 9.

[4] G. HEYEN, in *Actes du Congrès Mondial de Génie chimique*, Montréal, octobre 1981.

[5] S. ANGUS, B. ARMSTRONG et K. DE REUCK, in *Carbon-Dioxide*, I.U.P.A.C. (*International Thermodynamic Tables of the Fluid State*-3, Pergamon Press, 1973).

[6] D. NEWITT, M. PAI, M. KULOOR et J. HUGGILL, in *Thermodynamic Functions of Gases*, F. DIN, éd., Butterworths, 1, 1956, p. 102.

[7] H. TESTER, in *Thermodynamic Functions of Gases*, F. DIN, éd., Butterworths, 3, 1956, p. 1.

[8] H. TESTER, in *Thermodynamic Functions of Gases*, F. DIN, éd., Butterworths, 3, 1956, p. 162.

[9] L. CANJAR et F. MANNING, in *Thermodynamic Properties and Reduced Correlations for Gases*, Gulf Publishing Company, Houston, Texas, 1967.

[10] G. HEYEN, C. RAMBOZ et J. DUBESSY, *Comptes rendus*, 294, série II, 1982, p. 203.

[11] I. WICHTERLE et R. KOBAYASHI, *J. Chem. Eng. Data*, 17, 1972, p. 9.

[12] A. FREDENSLUND et J. MOLLERUP, *J. Chem. Soc. Faraday Trans.*, 1, 1974, p. 1653.

[13] R. J. GUGNONI, J. W. ELDRIDGE, V. C. OKAY et T. J. LEE, *A.I. Ch. E. J.*, 20, 1974, p. 357.

[14] P. DHAMELINCOURT, J.-M. BENY, J. DUBESSY et B. POTY, *Bull. Minéral.*, 102, 1979, p. 600.

[15] C. RAMBOZ et J.-M. BENY, *Contr. Mineral. Petrol.* (soumis).

[16] C. RAMBOZ, *Thèse 3e cycle*, I.N.P.L., Nancy, 1980.

G. H. : *Laboratoire d'analyse et de synthèse des systèmes chimiques, 2, rue Stévart, B-4000, Liège, Belgique*

C. R. : *C.R.P.G.*, B.P. n° 20, 54501 *Vandœuvre*

J. D. : *C.R.E.G.U.*, B.P. n° 23, 54501 *Vandœuvre*.

PUBLICATION III : Les fluides moléculaires d'un filon de quartz hydrothermal : comparaison de techniques analytiques ponctuelles et globales, contamination des fluides occlus par des composés carbonés.

Bull. Minéral.
(1984), 107, 169-180

Travaux du Centre de Recherches Pétrographiques et Géochimiques

Les fluides moléculaires d'un filon de quartz hydrothermal : comparaison de techniques analytiques ponctuelles et globales, contamination des fluides occlus par des composés carbonés

par ALAIN CHEILLETZ*, JEAN DUBESSY**, CHARLES KOSZTOLANYI**, NICOLE MASSON-PEREZ**, CLAIRE RAMBOZ*, JEAN-LOUIS ZIMMERMANN*

* CRPG, 15, rue Notre-Dame des Pauvres, 54501 Vandœuvre-Lès-Nancy, France.

** CREGU, 3, rue du Bois de la Champelle, 54501 Vandœuvre-Lès-Nancy, France.

Résumé. — Quatre techniques ont été utilisées pour analyser les phases fluides moléculaires dans les cristaux : la Microthermométrie (M.) et la Spectrométrie Raman (S.R.), techniques non destructives ponctuelles utilisables seulement pour les minéraux transparents ; la Spectrométrie de masse (S.M.) et la Chromatographie en phase gazeuse (C.G.) pour l'analyse globale des fluides libérés par écrasement ou chauffage de toutes sortes de minéraux. Une veine de quartz de haute température à scheelite et wolframite provenant du Jbel Aouam (Maroc Central) a été choisie pour cette étude en raison de l'homogénéité de ses fluides inclus. (1) La fraction molaire en H_2O est la même pour les quatre méthodes dans la marge d'erreur des mesures. (2) Le rapport molaire CO_2/CH_4 obtenu par S.R. est conforme à celui trouvé en C.G. ; il est une à deux fois plus grand par S.M. (3) De petites quantités constantes de H_2 n'ont été détectées qu'en S.M. (4) Des espèces carbonées lourdes sont systématiquement identifiées par S.M. et en quantités moindres par C.G. ; elles ne se trouvent pas dans les inclusions fluides où seuls le CO_2 et le CH_4 sont détectés par S.R. (5) Par contre des particules noirâtres sont microscopiquement visibles dans les fissures du quartz ; leur spectre de diffusion Raman montre qu'elles sont du type charbon et peuvent avoir une capacité importante de libération d'hydrocarbures.

Mots-clés : chromatographie phase gazeuse, spectrométrie masse, spectrométrie Raman, microthermométrie, eau - dioxyde de carbone - méthane, composés organiques.

Molecular fluids in an hydrothermal quartz vein : comparison of ponctual and bulk analysis techniques, contamination of inclusion fluids by carbonaceous compounds.

Abstract. — Four techniques have been selected to analyse molecular fluid phases in crystals : microthermometry (M.) and Raman Spectrometry (R.S.), non destructive ponctual techniques available only for transparent minerals ; mass spectrometry (M.S.) and gas chromatography (G.C.) available for the bulk analysis of fluids released by crushing or heating of all kinds of minerals. High temperature vein quartz from the scheelite-wolframite deposit of Jbel Aouam (Central Morocco) has been selected to be analysed by the four techniques because it contains a homogeneous generation of fluids. (1) Within the uncertainty on the measurements, molar fraction of H_2O in the fluids from quartz is consistently measured by the four techniques. (2) The CO_2/CH_4 molar ratio obtained by R.S. is consistent with the analytical data from G.C. ; it is superior by one or two orders of magnitude to that obtained by M.S. (3) Small and constant amount of H_2 is detected only by M.S. (4) Heavy carbonaceous species are systematically identified by M.S. and with less quantities by G.C. ; they are not in fluid inclusions where only CO_2 and CH_4 are detected by R.S. (5) However dark particles are visible under the microscope in fissures of the quartz ; their Raman scattering spectrum is similar to that of coal, therefore they still can yield hydrocarbons on heating.

Key words : gas chromatography, mass spectroscopy, Raman spectroscopy, microthermometry, water-carbon dioxide-methane, organic compounds.

INTRODUCTION

Grâce à la mise en œuvre de techniques instrumentales performantes, de nombreuses recherches sont actuellement effectuées pour permettre un meilleur dosage des espèces ioniques et/ou moléculaires qui constituent les fluides intracristallins, à partir de masses de plus en plus faibles de cristaux, voire d'une inclusion isolée. Un grand nombre de méthodes d'analyse (dites destructives) imposent la destruction par chauffage ou écrasement du cristal ou de l'inclusion analysés. Ces techniques analytiques présentent tout ou partie des inconvénients suivants : 1) Mélange des inclusions de différents types, correspondant le plus souvent à des générations de fluides différents ; 2) Contamination possible du fluide analysé par le cristal hôte ou par les soli-

des contenus dans les inclusions elles-mêmes ; 3) Difficulté d'extraire la totalité des espèces dissoutes dans les fluides occlus ; 4) Pour certaines méthodes d'analyse ponctuelles telles que les microsondes laser couplées à un spectromètre de masse (Deloule et Eloy, 1982), se pose toujours le problème de l'analyse quantitative.

De même, les méthodes d'analyse ponctuelles non destructives présentent elles aussi leurs inconvénients spécifiques : 1) Sensibilité moins grande aux éléments contenus en trace dans les fluides du fait de la petite taille des volumes analysés ; 2) Impossibilité d'analyser les fluides contenus dans les cristaux opaques ou fluorescents.

Le but de la présente étude est de comparer les résultats de l'analyse des espèces moléculaires des fluides riches en eau et en volatils, obtenus par deux sortes de processus analytiques : (1) des méthodes destructives classiques : spectrométrie de masse et chromatographie en phase gazeuse ; (2) des méthodes d'analyses ponctuelles non destructives : microthermométrie et spectrométrie Raman associées.

On sait que la spectrométrie Raman permet de doser de façon relative les espèces moléculaires plus volatiles que l'eau, démixtées à température ambiante dans les inclusions (Dhamelincourt *et al.*, 1979). Des études microthermométriques préalables et conjointes permettent de définir statistiquement les populations d'inclusions géologiquement significatives, et d'estimer avec une précision d'environ 10 % leur composition et leur densité globales dans le système H_2O-CO_2-CH_4-N_2-H_2S (Ramboz, 1983).

Il apparaît d'un grand intérêt méthodologique de vérifier que les espèces moléculaires volatiles extraites lors de l'écrasement ou du chauffage des cristaux sont identiques à celles déterminées ponctuellement dans une famille d'inclusions. De nombreux auteurs ont déjà signalé des processus de contamination des fluides occlus par des phases solides contenues en trace dans les cristaux, ou par le cristal hôte lui-même (Goguel, 1963 ; Behar, 1978). Ces phénomènes ont bien sûr des conséquences catastrophiques pour les interprétations déduites de la composition chimique et isotopique des fluides occlus (Pineau *et al.*, 1981, Charef, 1983). Les méthodes d'analyse globale ont l'avantage de permettre une cartographie des variations chimiques des fluides à l'échelle d'un batholite, d'une pile métamorphique ou d'un district minier. Elles permettent également de caler une séquence paragénétique dans l'évolution physicochimique des fluides définie par ailleurs finement en terme de variations des paramètres P-V-T-X-fO_2-fS_2 par les études combinant microthermométrie et spectrométrie Raman (Ramboz *et al.*, soumis).

II. - LES ÉCHANTILLONS ÉTUDIÉS

Les échantillons étudiés proviennent des minéralisations filoniennes hercyniennes à tungstène du Jbel Aouam dans le Massif Central Marocain (Agard *et al.*, 1958). Ces minéralisations, spatialement associées à de petits stocks de granite (Cheilletz et Zimmermann, 1982) présentent une succession de paragenèses hydrothermales de haute température (400-450 °C) constituées principalement par : quartz, biotite, apatite, feldspath, muscovite, chlorite, calcite, wolframite et scheelite (Cheilletz, 1984).

Une étude des inclusions fluides contenues dans le quartz et la scheelite a été entreprise dans le but de déterminer les conditions physicochimiques du dépôt des minéralisations. Plus de 90 % des inclusions observées sont du type liquide dominant (Figure 1). Ces inclusions ont

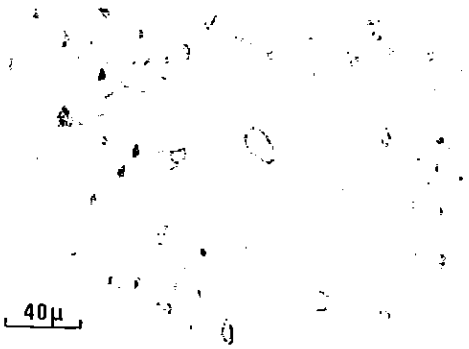

FIG. 1. — *Microphotographie d'un plan d'inclusions fluides de type liquide dominant (type L) montrant le remplissage homogène des différentes cavités.* (liquide/vapeur + liquide ~ 0.6).

Microphotograph of liquid-dominant inclusions in a fracture, with homogeneous degree of filling (liquid/liquid + vapour ~ 0.6).

des caractéristiques chimiques bien définies, comme le montre l'étude microthermométrique (Cheilletz, 1984). De plus, leur densité globale est supérieure à celle des inclusions d'autres types. La prépondérance en volume et en masse des inclusions de type L dans les cristaux étudiés est confirmée par les courbes de libération des espèces CO_2, CH_4 et H_2O, obtenues par analyse au spectromètre de masse après chauffage des cristaux jusqu'à 750 °C. (Figure 2*a*). Les courbes de libération des gaz contenus dans des minéraux contenant un mélange de générations de fluides distincts sont plus complexes (Figure 2*b*).

III. - TECHNIQUES ANALYTIQUES

1. - Méthodes ponctuelles non destructives d'analyse des fluides

Le principe de l'identification des gaz et de la détermination de leur fraction molaire par spectroscopie Raman est décrit par Dhamelincourt *et al.* (1979). Les analyses microspectrométriques ont été réalisées sur une microsonde type MOLE (Jobin Yvon).

Les sections efficaces de diffusion relative des différents constituants ne sont connues qu'à tem-

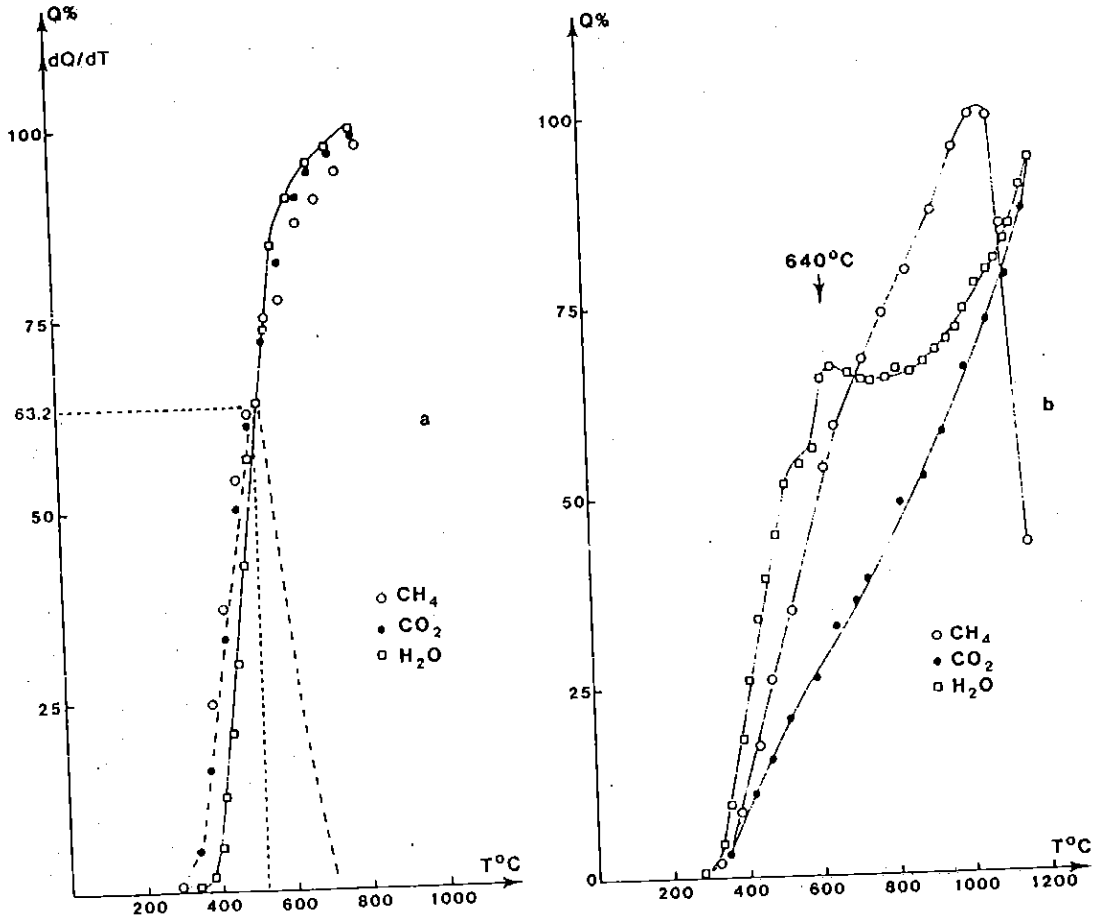

FIG. 2. — *Courbes de dégazage d'H_2O, CO_2 et CH_4 obtenues par chauffage continu et linéaire (400 °C/h) des échantillons. a)* quartz du Jbel Aouam (Maroc). En pointillés, courbe dérivée dQ/dT avec coordonnées du maximum. *b)* quartz de la veine de Serrecourte (France).

Curves of degazing of H_2O, CO_2, CH_4, on continuous heating of the samples at a rate of 400 °C per hour. a) quartz from Jbel Aouam (Morocco). Dashed lines, derivative curve dQ/dT with coordinates of maximum. *b)* quartz from the Serrecourte vein (France).

pérature ambiante sous faible pression. De ce fait, il n'est pas encore possible d'interpréter en terme de la composition globale des inclusions les spectres Raman obtenus sur des inclusions aqueuses homogénéisées par chauffage. Dans cette étude, les spectres ont été enregistrés à température ambiante en focalisant le faisceau laser sur la partie non-aqueuse des inclusions fluides. Les sections efficaces retenues pour le calcul des fractions molaires sont données dans le tableau I. Le seuil de détection de l'azote dans une inclusion fluide de 10 à 15 µm de dimension dans les trois directions de l'espace est de l'ordre de 1 atm à température ambiante. Selon la formule de PLACZEK citée dans Dhamelincourt *et al.* (1979), ce seuil est inversement proportionnel à la section efficace relative de diffusion ce qui implique une meilleure sensibilité pour la détection des hydrocarbures comme l'éthane et le propane.

	N_2	CO_2	H_2S	CH_4	C_2H_6	C_3H_8
$\bar{\nu}$	2330	1388	2610	2917	2955	2965
σ	1	1,21	6,8	9	13	19
Source bibliographique	S-K	S-K	S-K	S-K	L-P	L-P

TABLEAU I. — *Sections efficaces relatives de diffusion Raman (σ) pour une radiation excitatrice de 514,5 nm.* Les espèces gazeuses sont identifiées par leur raie de diffusion Raman correspondant à un nombre d'onde ν (cm^{-1}). S-K : Schrotter et Klockner (1979). L-P : Lapp et Penney (1977).

Relative cross sections of Raman scattering (σ) for the 514.5 nm exciting line. The gaseous species are identified by their Raman line corresponding to a characteristic wave number $\bar{\nu}$ (cm^{-1}).

La surface des raies de diffusion de chaque constituant est mesurée à l'aide d'un planimètre. L'erreur relative sur une telle mesure de même que la reproductibilité des mesures spectrométriques sont de l'ordre du 1 %. La principale source d'erreur dans l'estimation des fractions molaires est due à l'imprécision des mesures de section efficace. D'une part, on constate une variation de ces valeurs entre les différents laboratoires (Schrotter et Klockner, 1979), d'autre part, il semble que le volume molaire de la phase fluide peut également changer sensiblement la valeur des sections efficaces en modifiant le profil des bandes. De ce fait, on considérera que l'erreur relative affectant les fractions molaires des constituants volatils dans la partie non-aqueuse de l'inclusion est de l'ordre de 10 %.

L'étude microthermométrique (Roedder, 1976 ; Weisbrod *et al.*, 1976) des inclusions à liquide dominant a été réalisée avec la platine chauffante et réfrigérante CHAIXMECA (Poty *et al.*, 1976). Les changements de phase suivants ont été mesurés avec une précision d'environ ± 0,2 °C : fusion du CO_2 solide en présence de vapeur ; fusion de la glace et du clathrate complexe ; homogénéisation de la partie non-aqueuse. L'homogénéisation globale de l'inclusion a été mesurée avec une précision d'environ 1 °C. La composition globale des inclusions du type liquide dominant a été calculée dans le système H_2O-CO_2-CH_4-NaCl en utilisant les formules données par Ramboz (1980). Le volume molaire de la partie non-aqueuse des inclusions a été calculé en comparant les compositions relatives obtenues par l'analyse spectrométrique, les températures de fusion du CO_2 et d'homogénéisation du contenu non-aqueux avec la projection $\bar{V}$-X des équilibres solides-liquide-vapeur et liquide-vapeur dans le système CO_2-CH_4 (Heyen *et al.*, 1982). La teneur en sel du contenu aqueux des inclusions a été estimée en interprétant les mesures de TF_C par référence aux données de Bozzo *et al.* (1973) relatives à l'abaissement du point quadruple supérieur dans le système H_2O-CO_2-NaCl, pour des teneurs en sel croissantes. Enfin, on a estimé le contenu en CO_2 dissous de la phase aqueuse au voisinage de la température ambiante à l'aide des données expérimentales de Ellis et Golding (1963).

2. - Analyses globales destructives des fluides occlus

1) Préparation des échantillons

Les échantillons dont la granulométrie est

comprise entre 1 mm et 3 mm sont lavés soit avec de l'acide fluorhydrique (22,5 N), puis avec de l'eau régale (3/4 HCl + 1/4 HNO_3), soit avec de l'eau régale seule. La durée du lavage à l'acide fluorhydrique est de l'ordre de 20 minutes, celle à l'eau régale est au minimum de 3 heures ; le rôle de ces acides est d'une part d'élargir les fissures et de dissoudre les éventuelles impuretés carbonatées, d'autre part d'éliminer par oxydation les matières organiques éventuellement présentes dans l'échantillon ou à sa surface. Ce lavage aux acides est suivi d'un abondant rinçage à l'eau distillée non déminéralisée (pour éviter toute contamination organique sur les colonnes échangeuses d'ions) puis d'un étuvage à 105 °C à l'air pendant environ quinze heures. Avant l'extraction des fluides occlus, un nouvel étuvage est effectué à 115 °C sous pompage secondaire. Il dure environ une heure pour l'analyse par chromatographie et quinze heures pour l'analyse par spectrométrie de masse.

2) Extraction des fluides

Pour l'analyse par chromatographie en phase gazeuse, les gaz sont extraits par chauffage progressif linéaire sous une pression de 10^{-5} mm Hg à 600 °C pendant une heure et demie afin de permettre la décrépitation des inclusions. Le poids de l'échantillon est compris entre 0,5 et 1 gramme.

Pour l'analyse par spectrométrie de masse, les gaz sont libérés par écrasement sous vide sous une charge de 15 tonnes ; l'échantillon (0,5 à 1 g) est placé dans un tube en acier inoxydable, préalablement nettoyé et étuvé sous vide, chauffé à 115 °C pour éviter l'adsorption. En outre, quelques expériences par chauffage continu et linéaire (400 °C/heure) ont également été entreprises afin de suivre le départ des principaux fluides comme l'eau et le gaz carbonique jusqu'à leur extraction totale.

Les gaz peuvent être introduits globalement dans la source du spectromètre de masse ou fractionnés préalablement par piégeage à l'azote liquide (−195,5 °C). Un piégeage complémentaire par de l'alcool réfrigéré à −75 °C n'a pas été effectué pour cette étude.

3) Analyse des gaz

— ***Chromatographie en phase gazeuse*** (Cuney *et al.*, 1976 ; Behar, 1978). Les espèces moléculaires entraînées par un gaz vecteur, l'hélium, sont séparées sur des colonnes de Porapak Q puis analysées séparément par un détecteur du type catharomètre pour les gaz inorganiques et par un détecteur à ionisation de flamme pour les hydrocarbures légers (C_1 à C_4). L'appareillage utilisé est de marque CARLO-ERBA. L'absence d'une colonne spécifique ne permet pas de doser l'hydrogène.

— ***Spectrométrie de masse.*** L'appareil utilisé est du type THN 205 transformé au CRPG (Zimmermann, 1972). Les gaz ionisés par bombardement électronique sont séparés par l'action conjuguée d'un champ électrique et d'un champ magnétique ; les ions captés par le détecteur (Cage de Faraday) forment le spectre de masse ; chaque pic de ce spectre définit, qualitativement par sa position et quantitativement par son amplitude, la composition du faisceau ionique. Un étalonnage préalable a été effectué pour la plupart des gaz courants H_2, H_2O, CO_2, N_2, CO, CH_4, C_2H_2, C_2H_4, C_2H_6.

Pour ces deux méthodes, l'erreur expérimentale, essentiellement conditionnée par le dosage de l'eau (facilement adsorbable), est de l'ordre de 5 %.

IV. - RÉSULTATS ET DISCUSSION

Le tableau II donne la composition molaire de la phase fluide obtenue par les différentes méthodes analytiques (analyse globale des gaz par spectrométrie de masse).

Dans la limite de l'erreur expérimentale (environ 5 %), les teneurs en H_2O sont identiques et se situent autour de 90 %.

En ce qui concerne le gaz carbonique, la spectrométrie Raman associée à la microthermométrie ainsi que la chromatographie en phase gazeuse fournissent des résultats assez voisins ; par contre ils sont sensiblement inférieurs par spectrométrie de masse. Toutefois cette dernière méthode met en évidence des quantités relativement abondantes de composés organiques (1,5 à 7 %), d'hydrogène (1 %) ainsi que des traces notables d'hydrogène sulfuré. Les histogrammes indiquant les rapports CO_2/CH_4 obtenus par les différentes méthodes pour cinq échantillons (Figure 3) schématisent cette abondance relative des composés organiques détectés par spectro-

N° Echantillon	Méthodes analytiques	H_2O%	CO_2%	CH_4%	Σ Composés organiques%	N_2%	H_2%	H_2S%	CO_2/Ec.org. + CH_4
Quartz 496 - a	C.G. S.M. R+μθ	88,4 92,0 89,3	11,5 4,5 9,7	0,04 0,3 0,07	0,13 1,4 -	- 0,9 0,2	- 0,9 -	- ε -	67 2,6 139
Quartz 496 - b	C.G. S.M. R+μθ	89,8 92,2 91,0	10,1 4,8 8,7	0,01 0,4 0,02	0,08 0,9	- 0,6 0,3	- 1,1 -	- 10ε -	112 3,7 98
Scheelite 496	C.G. S.M.	96,9 78,6	3,9 12,3	0,002 0,6	0,17 6,6	- 0,7	- 1,1	- 10ε	16
Quartz 405	C.G. S.M. R+μθ	93,9 91,5 88,1	6,9 3,8 11,6	0,04 1,1 0,09	0,1 1,6 -	- 1,1 0,3	- 0,9 -	- 10ε -	49 1,4 129
Quartz 362	C.G. S.M. R+μθ	87,6 90,1 91,0	12,3 5,4 8,7	0,07 0,3 0,15	- 1,8 -	- 1,1 0,2	- 1,2 -	- 10ε -	175 2,6
Quartz 483	S.M. R+μθ	84,0 92,0	8,6 7,4	2,0 0,3	3,1 -	0,9 0,3	1,4 -	- -	1,7

TABLEAU II. — *Résultats des analyses par chromatographie en phase gazeuse (C.G.) spectrométrie de masse (S.M.), microsonde Raman et microthermométrie (R+μθ) des phases aqueuses et carbonées dans différents quartz du Jbel Aouam (pourcentages molaires)* ; chromatographie gazeuse : extraction des gaz par chauffage sous vide à 600 °C. Spectrométrie de masse : extraction des gaz par écrasement sous vide et analyse globale. Spectrométrie Raman + Microthermométrie : analyses ponctuelles des inclusions. Pour la scheelite l'analyse Raman est impossible à cause de la fluorescence du minéral.

Gas chromatographic (C.G.), mass spectrometric (S.M.), Ramn spectrometric + microthermometric (R+ μθ) analytical data of aqueous and carbonaceous fluids in various quartz crystals from Jbel Aouam (mole percent) ; C.G. : gas extraction by heating under vacuum to 600 °C ; S.M. : gas extraction by crushing under vacuum and bulk analysis. Inclusions in scheelite cannot be investigated with the Raman probe, because this mineral is fluorescent.

métrie de masse. Le méthane est défini dans le spectre par ses masses, 16 : CH_4 (Intensité Relative : 100), 15 : CH_3 (I.R. : 86), 14 : CH_2 (I.R. : 16), 13 : CH (I.R. : 8), 12 : C (I.R. : 3). Comme sa masse principale 16 correspond également à l'ion oxygène (qui peut provenir du cracking des molécules H_2O, CO_2, SO_2, CO,...), on le dose à partir de son deuxième pic (15), celui du radical méthyl, lequel peut, par ailleurs, être engendré par la dissociation dans la source du spectromètre de masse, de composés organiques plus lourds. Cependant le méthane (Point d'ébullition −164 °C) n'est pas condensable par l'azote liquide (Point d'ébullition −195,5 °C), alors que les composés organiques plus lourds le sont. Dans le cas présent, l'analyse des gaz non condensables par l'azote liquide permet de séparer le seul méthane ; ses teneurs sont alors comprises entre 0,02 et 0,1 % de l'ensemble des gaz, et le rapport CO_2/CH_4 devient alors du même ordre de grandeur que celui obtenu par les autres méthodes. L'éthane C_2H_6 n'a pas été détecté. De la même façon l'hydrogène moléculaire peut être distingué de l'hydrogène issu des substances organiques, soit 0,1 à 0,2 % contre environ 1 % pour l'hydrogène total. L'hydrogène des substances organiques provient de leur dissociation dans la source d'ions.

Si l'on fait abstraction des molécules dérivées de composés organiques plus lourds que le méthane, les résultats obtenus par les quatre méthodes, sur l'exemple de l'échantillon n° 362, sont alors tout à fait comparables (Figure 4).

Le pouvoir séparateur du spectromètre THN 205 ne permet d'analyser que les hydrocarbures légers ; la présence de molécules organiques plus lourdes condensables par l'azote liquide, est mise en évidence par leurs masses de cracking dans la source du spectromètre (Figure 5). En particulier les masses 12(C^+), 13(C^+_{13}, CH^+)

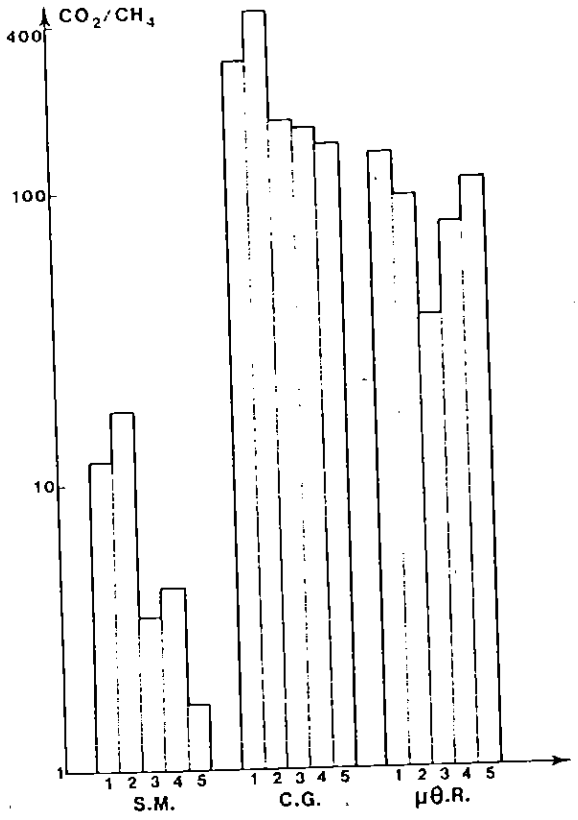

FIG. 3. — *Comparaison des rapports molaires CO_2/CH_4 obtenus par les différentes méthodes sur cinq échantillons.* S.M. (spectrométrie de masse et écrasement) ; C.G. (chromatographie en phase gazeuse). μθ + R : (microthermométrie + spectrométrie Raman).

Comparison of the CO_2/CH_4 molar ratios obtained on analysing five samples by mass spectrometry and crushing (M.S.), gas chromatography (C.G.), microthermometry and Raman spectrometry (μθ + R).

15(CH_3^+), 26(CH_2^+), 28($CH_2CH_2^+$), 30($C_2H_6^+$), 41($C_3H_5^+$), 42($COCH_2^+$, $C_3H_6^+$), 43($COCH_3^+$, $C_3H_7^+$) constituent les plus sûrs indices de présence de composés organiques. L'appareil n'a pas été étalonné pour ces molécules organiques. Les teneurs en ces espèces données dans le tableau sont approximatives et estimées par comparaison avec les courbes d'étalonnage pour les hydrocarbures plus légers (C_1 à C_3) ayant les mêmes masses de cracking (15, 26, 28, 30).

Les composés organiques détectés par chromatographie en phase gazeuse sont environ 10 fois moins abondants. Ceci s'explique par l'appareillage utilisé, non adapté à la détection des molécules organiques plus lourdes que C_4. De plus, un cracking des molécules complexes en cours d'analyse ne peut survenir que lors de l'extraction par chauffage à 600 °C. En effet, les molécules sont ensuite séparées avant d'être ionisées et dosées. La spectrométrie Raman montre que les teneurs en éthane et en propane dans les inclusions fluides sont inférieures à 2.10^{-3} mole %. Il faut donc rechercher l'origine des molécules organiques hors des inclusions fluides.

Des particules opaques, observées sous le microscope dans les fissures du quartz, pourraient être la source des espèces carbonées analysées par spectrométrie de masse. On a donc procédé au dosage du carbone organique présent dans le quartz de l'échantillon 362. L'échantillon a été porphyrisé et préalablement traité avec HCl pour éliminer tous les carbonates éventuellement présents. Puis l'échantillon a été grillé à 1 100 °C sous courant d'oxygène. Le carbone organique est dosé sous forme de CO_2 par coulométrie à impulsions (Analyse CRPG, laboratoire de M. Vernet). Le quartz 362 contient 0,016 ± 0,005 % poids de carbone organique.

Les particules noires ont ensuite été étudiées par micro-spectroscopie Raman. Les plus grosses d'entre elles présentent une fluorescence de 15 000 à 20 000 coups par seconde pour une puissance laser à la sortie du tube de 50 mW et des fentes de 800-900-1 000 μm. Cette fluorescence décroît en quelques minutes d'un facteur cinq. Il a été possible d'enregistrer un spectre Raman interprétable sur les particules de plus petite taille et moins fluorescentes. Nous avons également enregistré un spectre du quartz, minéral hôte de ces particules pour pouvoir attribuer sans ambiguité les raies Raman provenant des particules (Figure 6). Deux bandes caractérisent ces composés noirs : l'une autour de 1 300-1 400 cm^{-1}, mal définie, et une autre autour de 1 600 cm^{-1}. La première est partiellement masquée par le pied des deux bandes plus intenses du quartz (1 160 et 1 235 cm^{-1}). Le spectre enregistré des particules noires est semblable à ceux des couches épaisses de carbone (Rouzaud *et al.*, 1983) et à ceux de charbons naturels (Beny-Bassez *et al.*, 1981). La bande à 1 600 cm^{-1} correspond aux vibrations carbone - carbone de couches aromatiques tandis que le massif centré autour de 1 350 cm^{-1} est dû à différents défauts structuraux (Nakamizo *et al.*,

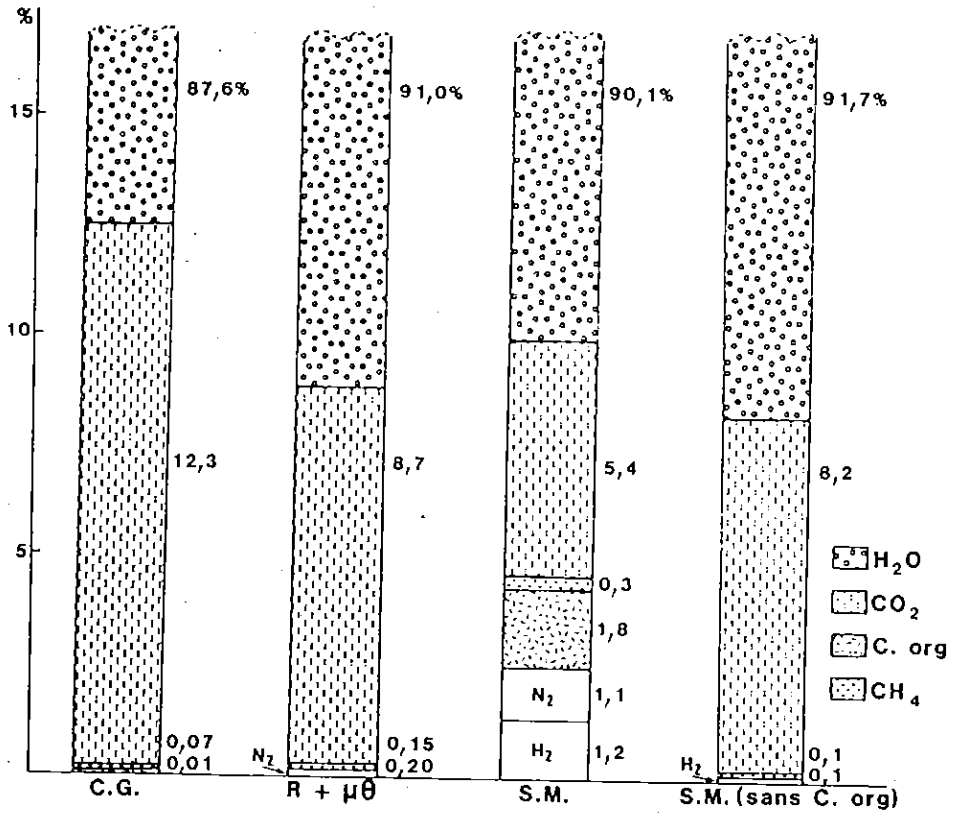

FIG. 4. — *Comparaison des résultats obtenus par les différentes méthodes sur l'échantillon n° 362.* C.G. : chromatographie en phase gazeuse ; R + μθ : spectrométrie Raman et microthermométrie. Deux analyses par spectrométrie de masse (M.S.) : 1) écrasement et analyse globale. 2) écrasement et analyse avec piégeage sélectif et élimination des composés organiques.

Comparison of analytical data obtained by the various techniques. C.G. = Gas chromatography ; R + μθ = Raman spectrometry and microthermometry ; two analyses by Mass spectrometry (M.S.). 1) crushing and bulk analysis ; 2) crushing and use of a liquid N_2 trap for eliminating heavy carbonaceous compounds.

1974 ; Rouzaud *et al.*, 1983). La largeur à mi-hauteur de la bande à 1 600 cm^{-1} est de l'ordre de 100 cm^{-1}. Ces particules noires sont donc des composés carbonés très mal organisés. Ce faible degré d'organisation se rencontre aussi bien dans des films épais de carbone pur que dans les charbons et dans les composés carbonés naturels encore riches en hétéroatomes (Rouzaud *et al.*, 1983). Cependant des conditions très strictes sont nécessaires pour la formation des films de carbone pur : condensation sous vide de vapeurs de carbone. Ceci laisse à penser que les composés organiques naturels analysés dans cette étude sont riches en hétéroatomes (oxygène et hydrogène). Ces hétéroatomes seraient la cause du faible degré d'organisation de la stucture. Certains charbons naturels, donnant des spectres Raman très semblables à celui que nous présentons, ont des rapports atomiques H/C et O/C respectivement de l'ordre de 0,5 et de 0,02 à 0,05 (Beny-Bassez *et al.*, 1981). De tels composés possèdent encore un important pouvoir libérateur d'hydrocarbures lourds comme l'a montré la mise en évidence par microscopie électronique de gouttelettes d'hydrocarbures (Rouzaud et Oberlin, 1983).

Même si les composés carbonés présents dans le quartz ne sont pas identiques à ceux décrits par Beny-Bassez *et al.* (1981) et Rouzaud et Oberlin (1983), il est cependant raisonnable d'admettre qu'ils sont probablement la source

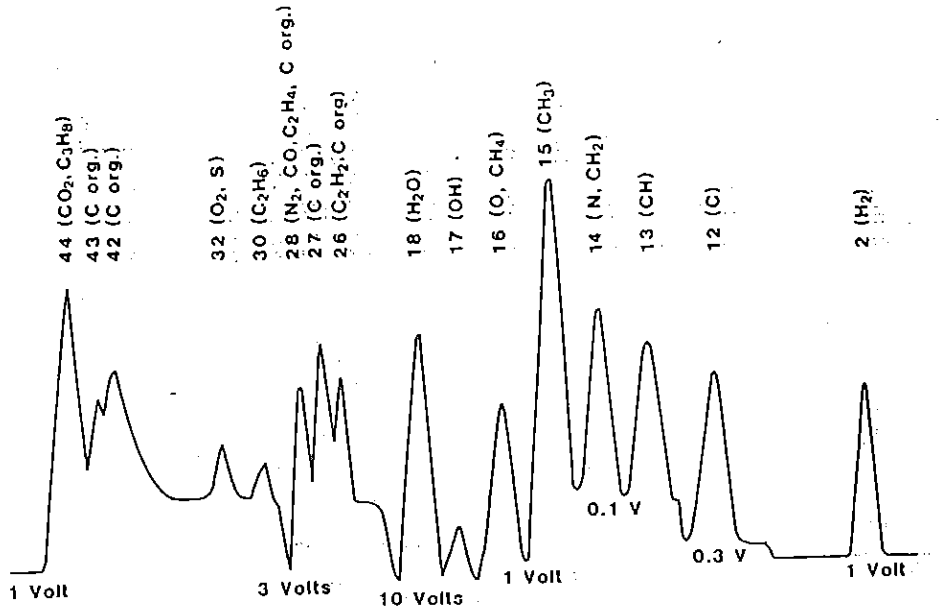

FIG. 5. — *Spectre de masses caractéristique des fluides libérés par écrasement sous vide d'un quartz de Jbel Aouam (n° 362).*

Mass spectrum of fluids degasing out of the crushed quartz (n° 362) from Jbel Aouam.

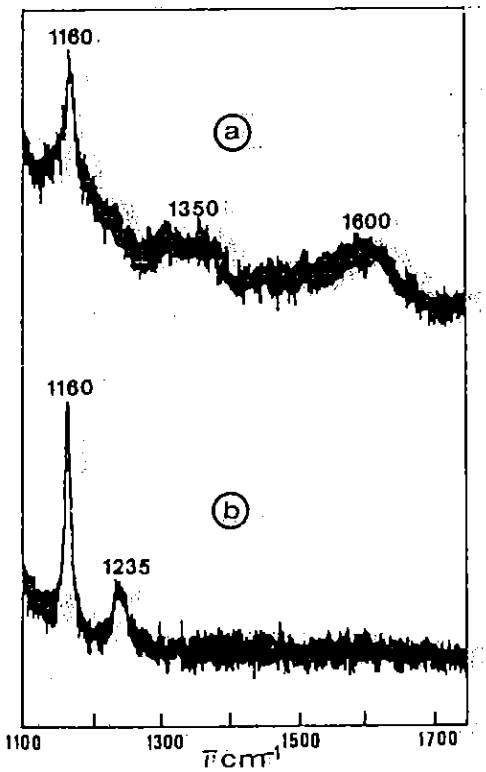

principale des hydrocarbures lourds détectés par spectrométrie de masse.

Afin de conforter cette interprétation, l'analyse par spectrométrie de masse des fluides occlus dans un quartz d'une pegmatite du granite de la Margeride (éch. M. Cuney) caractérisé par sa richesse en inclusions fluides et par sa pauvreté en carbone organique a été réalisée après écrasement sous vide. Les résultats (H_2O : 89 mole %, CO_2 : 9,5 mole %, H_2 : 1,5 mole %) montrent qu'aucune molécule organique n'est détectée par spectrométrie de masse lors de l'analyse des fluides contenus dans un quartz dépourvu de composés organiques.

Enfin, il convient de noter que l'on détecte environ quatre fois plus de composés organiques lourds par spectrométrie de masse lorsque l'ex-

FIG. 6. — *Spectre de diffusion Raman d'une particule solide carbonée incluse dans la matrice du quartz du Jbel Aouam. a)* composé carboné. *b)* quartz.

Raman scattering spectrum of a carbonaceous solid included in the quartz from Jbel Aouam. a) carbonaceous solid inclusion. *b)* quartz.

traction se fait par chauffage sous vide jusqu'à 750 °C que lorsque celle-ci se fait par écrasement (Figure 7). Ceci suggère que les molécules organiques sont peut-être partiellement extraites lors de l'étuvage sous vide à 115 °C, puis libérées et dissociées lors d'un chauffage à plus haute température. De même, on extrait plus de composés organiques lourds du quartz lorsque celui-ci est préalablement traité à HF et à l'eau régale, que lorsqu'il est traité à l'eau régale seule.

Ce résultat suggère que le réseau du quartz est rendu plus fragile par l'attaque à l'acide fluorhydrique et que plus de fissures tapissées de composés carbonés sont ouvertes lors de l'écrasement. En revanche, le traitement ultérieur à l'eau régale s'avère peu efficace pour détruire la matière organique, soit que l'eau régale n'arrive pas à son contact, soit que l'action du chlore et de l'oxygène soit incapable de l'éliminer.

L'hydrogène moléculaire détecté en présence d'un piège à N_2 liquide ne peut provenir de la dissociation de H_2O. De même la contribution du méthane est insuffisante (2 à 3 %). La faible solubilité de H_2 dans le quartz et le mode d'extraction utilisé ne permettent guère d'envisager une importante contribution de la matrice. La température d'étuvage (110°-115 °C) n'est pas non plus suffisante pour produire de H_2 à partir des substances organiques ; par contre leur maturation thermique au cours du temps, non définie dans le cadre de cette étude, pourrait avoir engendré de l'hydrogène.

L'ensemble des résultats présentés indique que les molécules organiques, détectées lors de l'analyse par spectrométrie de masse et chromatographie en phase gazeuse des quartz hydrothermaux du Jbel Aouam, ne constituent pas un artefact analytique. Ces molécules ne sont pas

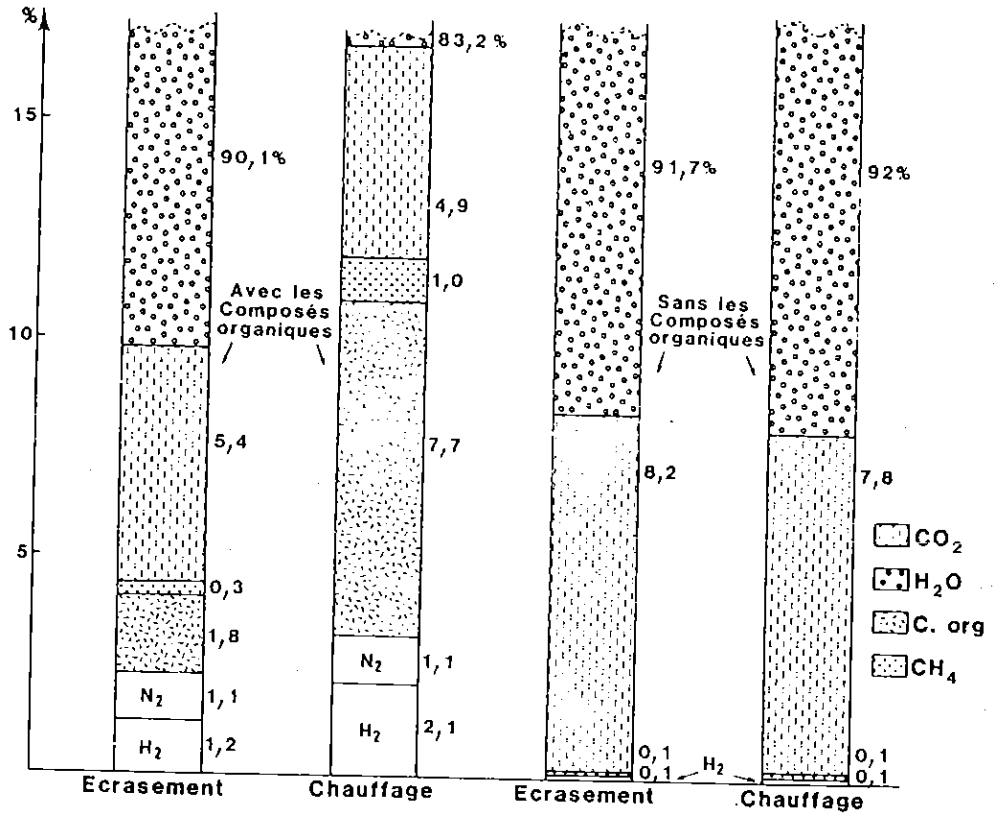

FIG. 7. — *Analyses par spectrométrie de masse*. Comparaison des résultats obtenus par écrasement sous vide et par chauffage sous vide d'un même quartz (n° 362), en tenant compte des composés organiques ou en les éliminant par piégeage dans l'azote liquide.

Mass spectrometric analyses. Comparison of analytical data obtained by crushing and by heating under vacuum of sample 362, taking into account organic compounds or eliminating them with a N_2 trap.

contenues dans les inclusions fluides, car celles-ci ne contiennent ni éthane ni propane détectables par spectroscopie Raman. Elles dérivent très vraisemblablement de particules charbonneuses visibles sous le microscope dans les fissures du quartz et identifiées ponctuellement par spectrométrie Raman. Le spectre Raman de ces particules indique d'ailleurs qu'elles ont encore une importante capacité à produire des hydrocarbures lourds. Par ailleurs, l'analyse par spectrométrie de masse révèle que cette matière organique est relativement riche en soufre et en hydrogène.

Différents auteurs ont mis en évidence des hydrocarbures lourds lors de l'analyse de cristaux par chromatographie en phase gazeuse. Selon Kranz (1968) ces espèces proviennent des inclusions fluides lors de l'écrasement de cristaux de fluorine. Freund *et al.* (1980, 1983) proposent que ces molécules, extraites de cristaux de MgO par chauffage jusqu'à 450 °C, résultent de réactions, jusqu'à des températures ambiantes, entre C, CO_2 et H_2 dissous dans le cristal, et particulièrement concentrés à sa surface. Moh (1982) a, par ailleurs, signalé la présence de carbone dans des minerais de cassitérite.

CONCLUSIONS

Ce travail comparatif a montré qu'il était possible de doser de façon fiable par spectrométrie de masse, par chromatrographie en phase gazeuse et spectrométrie Raman-microthermométrie, les teneurs en H_2O, CO_2, CH_4 et N_2 des fluides contenus dans les cristaux. En effet, une composition globale moyenne de H_2O = 88,7 %, CO_2 = 10,9 % CH_4 = 0,1 % et N_2 = 0,3 % a pu être obtenue avec une marge d'erreur de 5 % dans des quartz provenant de filons hydrothermaux de haute température.

— Lors de l'analyse par spectrométrie de masse, les fluides libérés des inclusions par écrasement sous vide sont contaminés par des composés carbonés contenus dans les fissures du quartz (0,016 ± 0,005 poids % C) et partiellement décomposés au cours de l'étuvage sous vide à 115 °C. L'utilisation d'un piège à azote liquide permet de condenser ces substances, d'analyser le méthane issu des inclusions fluides seulement, et d'obtenir des résultats sur les espèces moléculaires H_2O, CO_2, CH_4 et N_2 des inclusions fluides comparables aux précédents. Toutefois, à l'issue de ce travail, il n'est pas possible de proposer un traitement chimique permettant d'éliminer la matière organique sans détruire les inclusions fluides.

— L'étude par spectrométrie Raman de ces substances piégées dans les fissures du quartz montre que ce sont des composés carbonés contenant des hétéroatomes, qui ont gardé une capacité importante de libération d'hydrocarbures lourds. Cependant, leur analyse détaillée nécessiterait des techniques plus spécifiques (séparation fractionnée, chromatographie en phase liquide de haute précision...).

D'un point de vue général, la présence de composés organiques lourds dans les fissures d'un quartz de haute température pose le problème de l'origine et de l'époque de piégeage de ces composés, de leur participation éventuelle à la formation du CO_2 et du CH_4 présents dans les inclusions fluides, et de leur rôle métallogénique éventuel.

RÉFÉRENCES

AGARD, J., BALCON, J.M. et MORIN, P.H. (1958). — Etude géologique et métallogénique de la région minéralisée du Jbel Aouam (Maroc Central). *Notes et Mém. Serv. Géol. Maroc, 132.*

BEHAR, F. (1978). — Analyse de CO_2, H_2O, hydrocarbures des inclusions fluides par chromatographie en phase gazeuse. Application aux fentes alpines et aux roches métamorphiques. Thèse 3e cycle, Paris, 145 p.

BENY-BASSEZ, C., ROUZAUD, J.N. et OBERLIN, A. (1981). — Premières applications de la microsonde M.O.L.E. à effet Raman à l'étude d'une série de charbons. *C.R. Acad. Sci.*, Paris, *293, série II*, 509-512.

BOZZO, A.T., CHEN, H.S., KASS, J. and BARDUHN, A.J. (1973). — The properties of the hydrates of chlorine and carbon dioxide. International Symposium on Fresh Water from the Sea, *3*, 437-451.

CHAREF, A. (1983). — Les minéralisations cambriennes et karstiques Zn-Pb du district des Malines (Gard, France) : Géochimie isotopique, pétrographie et phases fluides. Thèse 3e cycle, I.N.P.L., Nancy, 285 p.

CHEILLETZ, A. (1984). — Caractéristiques géochimiques et thermobarométriques des fluides associés à la scheelite et au quartz des minéralisations de tungstène du Jbel Aouam (Maroc central). *Bull. Minéral., 107*, 255-272.

CHEILLETZ, A. et ZIMMERMANN, J.L. (1982). — Datations par la méthode K-Ar du complexe intrusif et des minéralisations en tungstène du Jbel Aouam (Maroc Central). *C.R. Acad. Sci.*, Paris, *295, série II*, 255-258.

CUNEY, M., PAGEL, M. et TOURET, J. (1976). — L'analyse des gaz des inclusions fluides par chromatographie en phase gazeuse. *Bull. Soc. fr. Minéral. Cristallogr., 99*, 169-177.

DHAMELINCOURT, P., BENY, J.M., DUBESSY, J. et POTY, B. (1979). — Analyse d'inclusions fluides à la microsonde M.O.L.E. à effet Raman. *Bull. Minéral., 102*, 600-610.

DELOULE, E. and ELOY, J.F. (1982). — Improvement of laser probe mass spectrometry for the chemical analysis of fluid inclusions in ores. *Chem. Geol., 37*, 191-202.

ELLIS, J. and GOLDING, R.M. (1963). — The solubility of carbon dioxide above 100 °C in water and in sodium chloride solutions. *Am. J. Sci., 261*, 47-60.

FREUND, F., KATHREIN, H., WENGELER, H. and KNOBEL, R. (1980). — Carbon in solid solution in forsterite a key to the untractable nature of reduced carbon in terrestrial and cosmogenic rocks. *Geochim. Cosmochim. Acta, 44*, 1319-1333.

FREUND, F., WENGELER, H., KATHREIN, H., KNOBEL, R., OBERHEUSER, G., MAITI, G.C., REIL, D., KNIPPING, U. and KOTZ, J. (1983). — Hydrogen and carbon derived from dissolved H_2O and CO_2 in minerals and melts. *Bull. Minéral., 106*, 185-200.

GOGUEL, R. (1963). — Die chemische zusammensetzung der in den Mineralen einiger Granite und ihrer Pegmatite ein geschlossenen Gase und Flussigkeiten. *Geochim. Cosmochim. Acta, 27*, 155-181.

HEYEN, G., RAMBOZ, C. et DUBESSY, J. (1982). — Simulation des équilibres de phases dans le système CO_2-CH_4 en dessous de 50 °C et de 100 bar. *C.R. Acad. Sci.*, Paris, *294*, 203-206.

KRANZ, R.L. (1968). — Participation of organic compounds in the transport of ore metals in hydrothermal solutions. *Bull. Inst. Ming. Metal. Trans. G.B., 735*.

LAPP, M. and PENNEY, C.M. (1977). — Raman measurements on flames. Advanced in Raman Spectroscopy, Heyden, 3, 242 p.

MOH, G.H. (1982). — The mineralogy and geochemistry of the IV B group elements. *In* "Metallization associated with acid magmatism". Ed. A.M. Evans, Wiley, 221-228.

NAKAMIZO, M., KAMMERECK, R. and WALKER, P.L. (1974). — Laser Raman studies on carbons. *Carbon, 12*, 259-267.

PINEAU, F., JAVOY, M., BEHAR, F. et TOURET, J. (1981). — La géochimie isotopique du faciès granulite du Bamble (Norvège) et l'origine des fluides carbonés dans la croûte profonde. *Bull. Minéral., 104*, 630-641.

POTY, B., LEROY, J. et JACHIMOWICZ, L. (1976). — Un nouvel appareil pour la mesure des températures sous le microscope : l'installation de microthermométrie Chaix-Meca. *Bull. Soc. fr. Minéral. Cristall., 99*, 182-186.

RAMBOZ, C. (1980). — Géochimie et étude des phases fluides de gisements et indices d'étain-tungstène du Sud du Massif Central (France). Thèse 3e cycle, I.N.P.L., Nancy, 278 p.

RAMBOZ, C. (1983). — Reconstitution from fluid inclusion studies of the bulk composition of fossil hydrothermal fluids in the C-O-H-N-S system. Symposium "European Current on Fluid Inclusions", Résumé, Orléans, France, 6-8 avril, p. 51.

RAMBOZ, C., SCHNAPPER, D. and DUBESSY, J. — The P-V-T-X evolution of an H_2O-CO_2-CH_4-bearing fluid in a wolframite vein : reconstruction from fluid inclusion studies. Soumis à *Geochim. Cosmochim. Acta*.

ROEDDER, E. (1976). — Fluid inclusion evidence on the genesis of ores in sedimentary and volcanic rocks. *In* "Ore in sediments. Sedimentary and volcanic rocks" Ed K.H. Wolf, Elsevier, 2, 67-110.

ROUZAUD, J.N. et OBERLIN, A. (1983). — Rôle des résines *b* sur le comportement à la pyrolyse et les propriétés optiques des charbons. *C.R. Acad. Sci.*, Paris, *296*, série II, 757-760.

ROUZAUD, J.N., OBERLIN, A. and BENY-BASSEZ, C. (1983). — Carbon films : structure and microtexture (optical and electron microscopy, Raman spectroscopy). *Thin Solid Films 105*, 75-96.

SCHROTTER, H.W. and KLOCKNER, H.W. (1979). — Raman scattering cross sections in gases and liquids. *In* "Raman spectroscopy of gases and liquids". Ed. A. Weber, Springer-Verlag, 123-166.

WEISBROD, A., POTY, B. et TOURET, J. (1976). — Utilisation des inclusions fluides en géochimie-pétrologie : tendances actuelles. *Bull. Soc. fr. Minéral. Cristallogr., 99*, 140-152.

ZIMMERMANN, J.L. (1972). — L'eau et les gaz dans les principales familles de silicates. Contribution à l'étude de leur mode de répartition. Application aux problèmes de la géochronologie et de la pétrogenèse. *Sci. de la Terre, Mém. 22*, 188 p.

PUBLICATION IV : Première détermination expérimentale des relations de phases dans le système haplogranitique en conditions de sous-saturation en H_2O.

PÉTROLOGIE. — *Première détermination expérimentale des relations de phases dans le système haplogranitique en conditions de sous-saturation en H_2O.* Note de **Michel Pichavant** et **Claire Ramboz,** présentée par Jean Wyart.

On a déterminé expérimentalement les relations de phases dans le système Qz-Ab-Or-B_2O_3-H_2O (B_2O_3=4,5% poids dans le liquide) en conditions de sous-saturation en H_2O à 1 kbar. Les résultats, comparés aux données obtenues antérieurement en conditions de saturation en H_2O dans le même système et à la même pression permettent de préciser l'effet de la teneur en H_2O du bain à pression constante sur les relations de phases dans le système haplogranitique. Les données suggèrent un certain type d'association de H_2O avec les constituants albitiques dans le liquide silicaté.

PETROLOGY. — First experimental determination of the phase relations in the haplogranite system under H_2O-undersaturated conditions.

Phase relations have been determined in the system Qz-Ab-Or-B_2O_3-H_2O (B_2O_3=4.5 wt % in the melt) under H_2O-undersaturated conditions at 1 kbar. The results, compared with the data obtained previously with excess H_2O in the same system and at the same pressure allow to determine the effect of the melt H_2O content at constant pressure on the phase relations in the haplogranite system. The data suggest some type of association between H_2O and the albite-forming components in the melt.

INTRODUCTION. — Les expériences classiques de l'école américaine dans le système haplogranitique Qz-Ab-Or-H_2O [1] ne permettent pas de distinguer l'effet de la pression de celui de la concentration en H_2O du liquide puisqu'elles ont toutes été menées en conditions de saturation en H_2O. En conséquence, dans ces expériences, pression et concentration en H_2O du liquide varient simultanément et les diagrammes de phases obtenus reflètent l'action conjuguée de ces deux paramètres sur la structure du liquide silicaté. Nous présentons les premières déterminations expérimentales des relations de phases dans le système haplogranitique en conditions de sous-saturation en H_2O. Ces données, comparées avec celles obtenues antérieurement en conditions de sursaturation en H_2O dans le même système et *à la même pression* permettent de préciser l'effet de la teneur en H_2O du liquide silicaté sur les relations de phases.

EXPÉRIENCES. — Toutes les expériences ont été réalisées à une pression totale de $1\,000 \pm 20$ bars dans des autoclaves à trempe rapide avec la méthode de la capsule soudée. Les températures sont connues avec une précision meilleure que ± 10°C pour une sensibilité de ± 2°C. Les produits de départ sont quatre verres synthétiques à teneur constante en B_2O_3 de différentes compositions Qz-Ab-Or, utilisés préalablement lors de l'étude en conditions saturées en H_2O, et choisis en raison de leur proximité avec la ligne cotectique déterminée dans ces mêmes conditions [2]. Les verres sont préparés à 1 400°C et à sec à partir de gels à concentration en B_2O_3 légèrement supérieure à la valeur désirée (4,5% poids dans le liquide silicaté) de façon à tenir compte de la légère perte de B_2O_3 dans la phase fluide lors des expériences sous pression [2]. Des conditions de sous-saturation en H_2O du liquide silicaté ont été obtenues en utilisant une phase fluide mixte, de composition de départ H_2O-CO_2 en proportion de 10% poids de la charge (*n. b.* les expériences en conditions de saturation en H_2O sont réalisées avec une proportion identique de 10% en poids de la charge d'H_2O distillée, [2]). Le mélange H_2O-CO_2 est réalisé à partir de quantités appropriées d'H_2O et d'$Ag_2C_2O_4$. Sa composition de départ est constante dans toutes les expériences : $H_2O/(H_2O+CO_2)=60$ mole %. Pour chaque composition, la température liquidus (déterminée par observation au microscope

0249-6305/85/03010607 $2.00

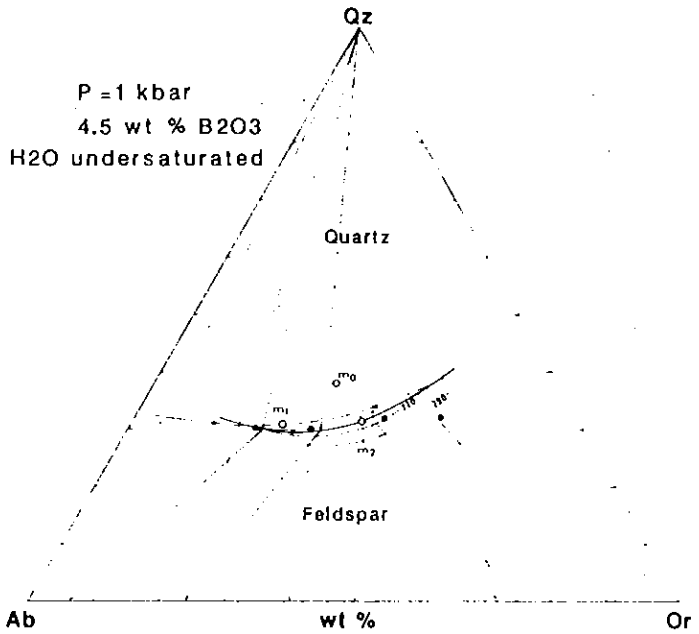

Fig. 1. — Diagramme de phases du système Qz-Ab-Or-B_2O_3-H_2O à 1 kbar (B_2O_3 = 4,5 % poids dans le liquide) en conditions sous-saturées en H_2O. Courbe au trait gras : courbe cotectique de ce système; courbe en pointillés : cotectique du même système en conditions de saturation en H_2O [2]; courbes au trait fin : isothermes (graduées en degrés celsius) de la surface liquidus; cercles pleins : compositions des verres de départ; m_0 : minimum du système Qz-Ab-Or-H_2O à 1 kbar en conditions saturées en H_2O [1]; m_1 : cotectique du système Qz-Ab-Or-B_2O_3-H_2O à 1 kbar (B_2O_3 = 4,5 % poids dans le liquide) en conditions de sursaturation en H_2O [2]; m_2 : minimum du même système en sous-saturation en H_2O (cette étude); droites au trait fin : lignes de conjugaison et triangles à trois phases.

Fig. 1. — Phase diagram of the system Qz-Ab-Or-B_2O_3-H_2O at 1 kbar (B_2O_3 = 4.5 wt % in the melt) under H_2O – undersaturated conditions. Heavy curve: cotectic line of this system; dashed curve: cotectic line of the same system but under H_2O – saturated conditions [2]; light curves: isotherms (labelled in degrees celsius) on the liquidus surface; filled circles: starting compositions; m_0: minimum of the system Qz-Ab-Or-H_2O at 1 kbar with excess H_2O [1]; m_1: eutectic of the system Qz-Ab-Or-B_2O_3-H_2O at 1 kbar (B_2O_3 = 4.5 wt % in the melt) with excess H_2O [2]; m_2: minimum of the same system under H_2O-undersaturated conditions (this work); light lines: tie-lines and three phase-triangles.

pétrographique) est encadrée en cristallisation et en fusion (à partir d'un verre partiellement recristallisé). Le bon accord entre les deux types d'expériences suggère une bonne approche de l'équilibre.

Analyses. — La microsonde électronique a été utilisée pour la détermination des lignes de conjugaison et des triangles à trois phases. Pour certaines expériences, la composition de la phase fluide à l'équilibre avec les phases silicatées au cours de l'expérience a été déterminée à partir des inclusions fluides piégées dans les verres. Les données montrent que la phase fluide est homogène. La détermination de sa composition globale [3] montre qu'elle s'est enrichie en CO_2 par rapport à la composition de départ (dissolution d'une certaine quantité d'H_2O dans le liquide) et qu'elle contient une certaine proportion de CH_4 (réduction partielle du fluide H_2O-CO_2) (composition moyenne : $H_2O = 35 \pm 5$; $CO_2 = 62 \pm 5$; $CH_4 = 3 \pm 1$ mole %). Ceci permet d'estimer par un calcul de bilan de masse une teneur en H_2O du liquide silicaté dans ces expériences sous-saturées en H_2O de 2,4-3,2 % poids H_2O, valeurs nettement inférieures à la teneur de saturation : 6,5 % poids H_2O [2].

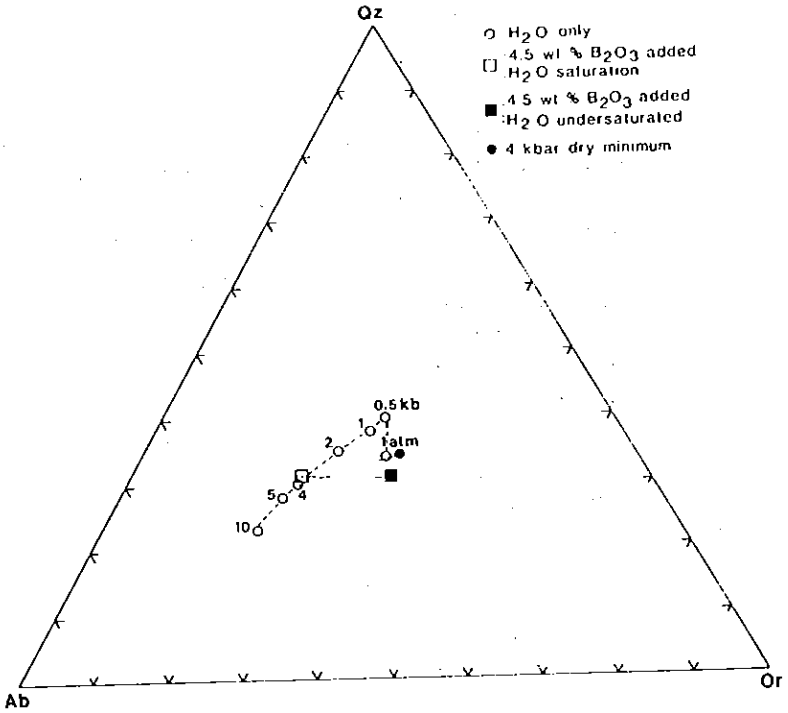

Fig. 2. — Position des minimums et des eutectiques du système Qz-Ab-Or-H_2O à différentes pressions en conditions de saturation H_2O [1] (cercles ouverts). Carré ouvert : m_1 (*fig.* 1); carré plein : m_2 (*fig.* 1); cercle plein : position estimée [4] du minimum du système Qz-Ab-Or à 4 kbar à sec.

Fig. 2. — Position of the minima and eutectics of the system Qz-Ab-Or-H_2O for different pressures under H_2O-saturated conditions [1] *(open circles). Open square: m_1* (Fig. 1); *filled square: m_2* (Fig. 1); *filled circle: estimated position* [4] *of the 4 kbar dry minimum in Qz-Ab-Or.*

Résultats. — Le diagramme de phases partiel obtenu est représenté sur la figure 1. A ce diagramme est surimposée la ligne cotectique obtenue dans le système Qz-Ab-Or-B_2O_3-H_2O ($H_2O = 4.5$ % poids dans le liquide) saturé en H_2O, avec l'eutectique correspondant (m_1, *fig.* 1) qui se situe à $T \sim 630$ C [2]. La position des compositions étudiées et les triangles à trois phases tracés nous permettent de positionner correctement la ligne cotectique du système sous-saturé Qz-Ab-Or-B_2O_3-H_2O ($B_2O_3 = 4.5$ % poids dans le liquide) ainsi que son minimum (m_2, *fig.* 1) pour une $T \sim 760$ C. A teneurs en H_2O du liquide décroissantes, la composition de l'eutectique m_1 ($Qz_{31}Ab_{46}Or_{23}$) se déplace vers le minimum m_2 ($Qz_{31}Ab_{34}Or_{35}$), déplacement qui va de pair avec une augmentation importante de la température liquidus.

Effet de H_2O sur les relations de phases. — Le minimum déterminé dans cette étude dans le système boré en sous-saturation en H_2O est proche de celui *estimé* pour le système Qz-Ab-Or à 4 kbar [4] à sec, lui-même voisin du minimum de ce même système à 1 bar [1] (*fig.* 2). La présente étude expérimentale et les estimations de la littérature [4] s'accordent donc pour définir un déplacement du minimum à teneurs en H_2O croissantes qui s'effectue à Qz normatif approximativement constant et à Ab normatif croissant. Ce déplacement est transverse (particulièrement pour les points à haute pression, > 5 kbar) au déplacement des eutectiques – minimaux à pression croissante en conditions de saturation en H_2O (*fig.* 2), mouvement qui résulte lui-même de la composition des effets de l'H_2O et de la pression. On en déduit donc que la pression contrôle préférentiellement à la teneur en H_2O la position de l'eutectique pour $P \geq 5$ kbar. Ceci peut s'expliquer si

l'on remarque qu'à partir de cette gamme de pression, un accroissement de la teneur en H_2O du liquide (en conditions de saturation) ne produit qu'un abaissement très faible de la température de l'eutectique ce qui suggère une faible interaction à pression élevée entre H_2O et liquide silicaté. Un tel effet peut également résulter d'un changement de la structure de H_2O dissoute dans le liquide silicaté, l'H_2O moléculaire faiblement liée au réseau étant l'espèce dominante à haute pression par rapport à l'eau hydroxylée OH, fortement liée au réseau, espèce dominante à basse pression [5]. De plus les expériences à sec réalisées récemment dans les systèmes binaires Qz-Ab et Qz-Or [6] montrent que l'augmentation de pression a pour effet principal de diminuer l'activité des constituants albite dans le liquide (a^L_{Ab}) ce qui se traduit par un déplacement très important de l'eutectique du binaire Qz-Ab vers l'Ab [6].

Le déplacement des points minimaux à teneur en H_2O variable montre que le mécanisme d'interaction entre le réseau silicaté et H_2O ne se réduit pas à une réaction du type (H_2O moléculaire exclue) :

$$\begin{array}{c} | \quad | \\ -Si-O-Si- \\ | \quad | \end{array} + H_2O \rightleftharpoons 2 \begin{array}{c} | \\ -Si-OH, \\ | \end{array}$$

réaction qui devrait conduire à un déplacement du minimum vers le pôle Qz en réponse à un abaissement de a^L_{Qz}, ce qui n'est pas observé expérimentalement. En revanche le déplacement observé à teneurs en H_2O du bain croissantes suggère un abaissement progressif de a^L_{Ab} qui pourrait résulter d'un certain type d'association entre H_2O et les constituants albitiques du liquide silicaté, comme cela a déjà été proposé sur la base de certaines mesures de solubilité de l'H_2O [7].

APPLICATIONS PÉTROLOGIQUES. — La présente étude fournit les premières données expérimentales permettant de découpler le rôle de l'H_2O et de la pression, paramètres indépendants, sur les équilibres cristaux-liquide qui contrôlent la cristallisation des magmas granitiques. L'augmentation de la teneur en H_2O des liquides silicatés à pression constante conduit à la cristallisation de magmas résiduels enrichis en albite normative.

Remise le 6 mai 1985, acceptée le 22 juillet 1985.

RÉFÉRENCES BIBLIOGRAPHIQUES

[1] O. F. TUTTLE et N. L. BOWEN, *Mem. Geol. Soc. Am.*, 74, 1958, 153 p.; W. C. LUTH, R. H. JAHNS et O. F. TUTTLE, *J. Geophys. Res.*, 69, 1964, p. 759-773.
[2] M. PICHAVANT, *Thèse d'État*, Université de Nancy, 1983, 82 p.; M. PICHAVANT, *E.O.S.*, 65, 1984, p. 298.
[3] C. RAMBOZ, D. SCHNAPPER et J. DUBESSY, *Geochim. Cosmochim. Acta*, 49, 1985, p. 205-219.
[4] J. C. STEINER, R. H. JAHNS et W. C. LUTH, *Geol. Soc. Am. Bull.*, 86, 1975, p. 83-98.
[5] E. STOLPER, *Contrib. Mineral. Petrol.*, 81, 1982, p. 1-17.
[6] A. BOETTCHER, Q. GUO, S. BOHLEN et B. HANSON, *Geology*, 12, 1984, p. 202-204.
[7] S. OXTOBY et D. L. HAMILTON, *Contrib. Mineral. Petrol.*, 66, 1978, p. 185-188.

Centre de Recherches pétrographiques et géochimiques (*C.R.P.G.*),
B.P. n° 20, 54501 *Vandœuvre-lès-Nancy*.

PUBLICATION V : Fluid immiscibility in natural processes : use ans misuse of fluid inclusion data. I : Phase equilibria analysis - A theoretical and geometrical approach.

Chemical Geology, 37 (1982) 1–27
Elsevier Scientific Publishing Company, Amsterdam — Printed in The Netherlands

FLUID IMMISCIBILITY IN NATURAL PROCESSES: USE AND MISUSE OF FLUID INCLUSION DATA
I. Phase Equilibria Analysis — A Theoretical and Geometrical Approach

MICHEL PICHAVANT[1], CLAIRE RAMBOZ[1] and ALAIN WEISBROD[1,2]

[1] *Centre de Recherches Pétrographiques et Géochimiques, 54501 Vandoeuvre-les-Nancy Cedex (France)*
[2] *École Nationale Supérieure de Géologie, 54001 Nancy Cedex (France)*

(Accepted for publication April 14, 1982)

ABSTRACT

Pichavant, M., Ramboz, Cl. and Weisbrod, A., 1982. Fluid immiscibility in natural processes: use and misuse of fluid inclusion data, I. Phase equilibria analysis — a theoretical and geometrical approach. In: R. Kreulen and J. Touret (Guest-Editors), Current Research on Fluid Inclusions. Chem. Geol., 37: 1–27.

Many occurrences of fluid immiscibility in natural geologic systems have been reported recently, most often from fluid inclusion studies. However, the interpretation of fluid inclusion data in terms of immiscibility sometimes suffers from ambiguity of the vocabulary, insufficient knowledge of the immiscibility constraints and insufficient knowledge of the topology (in the *TPX* space) of natural fluid systems. For such reasons some authors have been misled to erroneous interpretations.

The term "chemical immiscibility" is unambiguously redefined as a multiphase multicomponent equilibrium. The consequences of this definition are directly derived from the phase rule and concern the possible equations that relate the various parameters (temperature, pressure, volumes, compositions) to each other. These equations already put constraints on the topology of the phase equilibria in fluid systems.

A particular expression of the phase rule is proposed, which takes into account the multiphase—constant bulk volume—constant bulk composition constraints in fluid inclusions. The consequences of such an expression are of major importance in fluid inclusion studies.

The phase relations of some simple systems that approximate quite efficiently the natural complex fluids are then detailed: H_2O—NaCl, CO_2—CH_4, H_2O—CO_2, H_2O—CO_2—NaCl. The effects of these topologies and of the supplementary constraints (constant bulk composition and constant bulk volume) assumed for fluid inclusions (isopleth—isochoric systems) are discussed.

1. INTRODUCTION

During the last few years, an increasing number of analytical data and experimental results has suggested that immiscibility in the fluid state could be responsible for many spectacular petrological and geochemical phenom-

0009-2541/82/0000—0000/$02.75

ena in sedimentary, metamorphic and magmatic environments: metasomatic changes (Weisbrod and Poty, 1975; Weisbrod et al., 1976; Lagache and Weisbrod, 1977; Weisbrod, 1980) alteration and mineral deposition in porphyry copper deposits (e.g., Nash and Theodore, 1971; Roedder. 1971; Denis, 1974; Moore and Nash, 1974; Poty and Weisbrod, 1976; Chivas and Wilkins, 1977; Etminan, 1977; Eastoe, 1978; Ramboz, 1979; Denis et al., 1980; Le Bel, 1980; Wilson et al., 1980), other types of deposits associated with volcanic activity (e.g., Spooner, 1980) or acid magmatism (Kelly and Turneaure, 1970; Landis and Rye, 1974; Rye and Sawkins, 1974; Leroy, 1978; Bray, 1980; Grant et al., 1980; Ramboz, 1980), ore deposits in sedimentary rocks (Roedder, 1976, 1977) and, of course, in oil deposits.

Moreover, fluid immiscibility is of particular interest in estimating the thermobarometric conditions at specified steps of the evolution of rock systems (Weisbrod and Poty, 1975; Roedder and Bodnar, 1980; Weisbrod, 1981).

In general, fluid immiscibility is expected in H_2O—salts systems at moderate to high temperatures and rather low pressures (for instance, in ore deposits associated with shallow magmatism), or in H_2O—carbonic species systems at low to moderate temperatures.

Proving, or even suggesting immiscibility in the fluid state is practically impossible with the usual petrological, mineralogical and geochemical methods and techniques. On the other hand, it is obvious that studies of fluid inclusions, which are supposed to be the remnants of the fluids that once wet the rocks, are best suited for this purpose. In fact, most of the analytical evidences for "boiling" in natural geologic processes are derived from fluid inclusion studies. Unfortunately, there are many examples in the literature, of fluid inclusion observations and data that have been interpreted in terms of unmixing, although no immiscibility was actually involved. Most often, such interpretations are related to the coexistence in the same sample of inclusion fluids of contrasted compositions or physical properties, or, less frequently, to the simple occurrence of inclusion fluids of "extreme" composition or density (a highly saline brine, or a very low-density fluid, for instance). Still, boiling is not the only process that can generate a brine or a "vapour". For instance, very concentrated inclusion fluids can result from trapping of aqueous solutions enriched in various solutes at late magmatic stages (Roedder and Coombs, 1967; Konnerup-Madsen et al., 1979; Ramboz, 1979; Denis et al., 1980; Weisbrod, 1981; many examples are available in the Soviet literature: see references in Roedder and Bodnar, 1980 and Weisbrod, 1981). Co-occurrences of two chemically and/or physically contrasted types of inclusions in one sample can result of successive trapping of different and non-directly linked fluids (Weisbrod and Poty, 1975; Durisova et al., 1979; Ramboz, 1980; Weisbrod, 1981).

It seems that most of the misinterpretations of fluid inclusion data in terms of immiscibility proceed from: (1) ambiguity of the vocabulary and/

or insufficient knowledge of the immiscibility constraints; and: (2) insufficient knowledge of the geometry (in the *TPX* space) of the fluid systems involved. The purpose of this paper therefore is: (1) to summarize as precisely as possible the peculiarities of some simple representative fluid systems (H_2O–NaCl, H_2O–CO_2, H_2O–CO_2–NaCl) relevant to the topics; (2) to apply these properties together with the immiscibility constraints, to fluid inclusion studies; and finally, (3) to try to define some criteria that should help in estimating the probability of existence of fluid unmixing — *including the impossibility of unmixing*, which is sometimes easier to prove than immiscibility itself.

NOTATION

List of symbols used

"Phase rule":

c	number of independent components (or independent species) in a system; it is reminded that, in a system described by c independent components (whatever they are), any non-degenerate set of c system-forming chemical species also completely describes the system and therefore can be used as a set of independent components
s	total number of chemical species in a system
φ	number of immiscible phases in a system
υ	number of degrees of freedom = variance = number of independent parameters (or variables) in a system

Parameters, or variables:

T	temperature
P	pressure (fluid)
V	molar (or specific) volume
d	density
X_i^j	molar fraction of the component (or species) i in the phase j
X_i°	molar fraction of the component (or species) i in the system (e.g., in a fluid inclusion)
wt.% i	weight fraction of the component (or species) i
x_j	volume fraction of the phase j

Description of fluid systems:

F	fluid
L	liquid
V	vapour
I	ice
H	halite
h	hydrohalite
C	clathrate (gas hydrate)
S	unspecified solid phase
T_i	triple point (solid + liquid + vapour) of the pure substance i (one-component system)
C_i	critical point of the pure substance i
C_X	critical point of a mixture, the composition of which is indicated by the subscript X

NOTATION (*continued*)

BPC	boiling-point curve
DPC	dew-point curve

Fluid inclusions:

DF	"degree of filling" = volume fraction of the specified (generally liquid) phase in an inclusion
T_h	homogenization temperature of the fluid phases: T_{hL} = L + V→L, T_{hV} = L + V→V, $T_{hF} = F_1 + F_2 \rightarrow F$
T_m	melting or dissolution temperature of a solid phase

2. IMMISCIBILITY: DEFINITION AND CONSTRAINTS

The term *immiscibility* has been often used with inaccurate — and therefore different — meanings or, on the contrary, disguised under other names such as boiling, condensation, effervescence, etc. (see, e.g., Roedder and Bodnar, 1980). It is therefore necessary to define this point of vocabulary as precisely as possible.

If a system containing several homogeneous phases is in equilibrium, i.e. if internal equilibrium is realized for every phase *and* if all the phases are in equilibrium with each other, then we shall say that these phases are immiscible. For instance, *two coexisting phases of given compositions are said to be immiscible if their association defines a state of equilibrium at the specified T—P conditions*. The fact that the bulk composition of such a system cannot be realized at the same *T—P* conditions by one single phase (or by two or more other phases, or by the same phases with different compositions) just results from the definition.

With such a definition, "our" immiscibility is synonymous to what is often called *chemical immiscibility* or *stable mechanical mixture (or assemblage)*, and contrasts with the *chemical (or homogeneous) mixture*, or *solution*.

The *constraints on real immiscibility* are directly derived from the definition:

(1) The system must be at (or closely approaches) equilibrium. Therefore, all the various immiscible phases are at the same temperature and pressure.

(2) When the various immiscible phases have different compositions, which is the most common case in multi-component systems, these compositions are related to each other through the principles of chemical equilibrium.

(3) The molar volumes (or the "densities") of the immiscible phases are different, but they are related to each other. This constraint can hardly be taken into account for condensed (solid) phases, but is of primary importance as soon as fluid phases are concerned.

In a system containing c independent components distributed amongst φ immiscible phases, constraint (1), the phase rule, is usually expressed by:

$$v = c - \varphi + 2$$

where 2 stands for T and P.

Assuming that such a system is made of s chemical species (c out of them are independent) and that all the s species are present in every phase, there are (φs + 2) variables: the molar fractions of the s species and the molar volume of each of the φ phases, plus T and P. Only $c - \varphi + 2$ are independent.

So, (c + 1) parameters are needed to characterise each phase individually but only $c - \varphi + 2 \ll (c + 1)$ are adequate to determine the whole system.

For instance, the following species are taken into account in the C—O—H system: H_2O, CO_2, CH_4, O_2, H_2. The first three may be chosen as independent components, thus $s = 5$, $c = 3$.

If the system is made of one phase, only 4 out of the 8 variables (X_{H_2O}, X_{CO_2}, X_{CH_4}, X_{O_2}, X_{H_2}, V, T, P) are independent. For example, if X_{CO_2}, X_{CH_4} and X_{H_2} can be measured at a specified temperature T, then the concentrations of water and oxygen can be calculated, as well as the internal pressure and the molar volume of the phase. When two immiscible phases L and V are present the variables are: $X^L_{H_2O}$, $X^V_{H_2O}$, $X^L_{CO_2}$, $X^V_{CO_2}$, $X^L_{CH_4}$, $X^V_{CH_4}$, $X^L_{H_2}$, $X^V_{H_2}$, $X^L_{O_2}$, $X^V_{O_2}$, V^L, V^V, T, P (14 variables). The knowledge of only three of them permits the calculation of all the others, and therefore the determination of the whole system, once again, if all the necessary data are available. If two fluid phases (L_1 + L_2, or L + V) and a "pure" solid phase (e.g., graphite or ice) are present, there are 14 variables: the 5 molar fractions and the molar volumes of the 2 fluid phases (and not those of the solid phase; of course) plus T and P; only two of them are independent.

The consequences of the principles of chemical equilibrium applied to immiscibility are of primary interest:

(1) There is strong evidence indicating that the φ phases are real immiscible phases, i.e. that they are (or have been) at equilibrium; only ($c - \varphi + 2$) parameters can be measured (or specified). In this case, all the parameters can be calculated, and the whole system determined.

(2) Immiscibility is only suspected, but more than ($c - \varphi + 2$) parameters can be measured (or specified). In that case, $c - \varphi + 2$ are arbitrarily chosen as independent variables, and the others can be calculated. Then, immiscibility (i.e., equilibrium) can be proved or at least more or less strongly supported, if the calculated values agree with the corresponding measured ones. Obviously, the larger the number of such "extra" measured values, the larger the number of checks, and the better the evidence for immiscibility.

3. ANALYSIS OF PHASE EQUILIBRIA IN SOME SIMPLE GEOLOGICALLY RELEVANT FLUID SYSTEMS

3.1. General considerations

3.1.1. Phase equilibrium analysis. Almost all the natural fluids observed in

various geologic environments belong to the C—O—H—N—S—electrolytes system. However, many of them are properly approximated by the system C—O—H—NaCl, or even simpler degenerate ones such as H_2O—NaCl, H_2O—CO_2, CO_2—CH_4, H_2O—CO_2—NaCl. These four systems may be considered as "fundamental", and many data are now available on them; strictly speaking, they are at least ternary systems. However, the first three can be generally properly described as binary systems.

In a binary system containing no solid phase and two fluid phases L and V ("undersaturated boiling system"), the phase rule yields: $v = 2$.

In the *TPX* space, there will be two divariant immiscibility surfaces whose equations relate the compositions of the two fluids ("liquid" and "vapour") to temperature and pressure:

$X_L = f_L(T,P)$ ("boiling" surface, L + V ⇌ L)

$X_V = f_V(T,P)$ ("dew" surface, L + V ⇌ V)

These two surfaces join each other along the phase transition ("boiling" L ⇌ V) curves of the pure end-members, or along a *critical curve*. The volume enclosed between these surfaces and the cylindrical one based on the "saturation" curves defines the domain of immiscibility L + V.

The results remain rigorously true for ternary systems containing a solid buffer and two fluid phases (e.g., the system C—O—H in the presence of graphite or any oxygen buffer) or three immiscible fluid phases (e.g., aqueous liquid, carbonic liquid and carbonic vapour in the system C—O—H).

3.1.2. Applications to fluid inclusion behaviour. In fluid inclusion studies, it is generally assumed that the bulk volume and the bulk composition of an inclusion remain constant between the trapping conditions and the lowest temperatures (~ −200°C) that can be reached with a freezing stage [this point will be briefly discussed in Part II (Ramboz et al., 1982)]. So the changes that occur in a fluid inclusion during natural cooling after trapping or, as indicated in Fig. 4, during heating with a heating stage, are isopleth—isochoric processes. We will say that, during cooling or heating, the inclusion follows an isopleth—isochoric path in the (T,P,X) space.

These supplementary constraints have extremely serious implications on the classical expression of the phase rule, as presented above. Let us consider a system containing φ immiscible phases and c independent components. The following parameters will be taken into account:

X_i^0	= bulk molar fraction of component i in the system	(c values)
X_j^i	= molar fraction of component i in phase j	(c values)
V_0	= bulk molar volume of the system	(1 value)
V_j	= molar volume of phase j	(φ values)
x_j	= volume fraction of phase j in the system	(φ values)
Temperature, pressure, and volume (or mass, or total number of moles, etc.)		(3 values)

The independent equations relating these parameters to one another are:

Equations of chemical equilibrium [$c(\varphi - 1)$ equations]

Relations between the composition of the system and the composition and the amount of the forming phases:

$$X_i^0 = \sum_j x_j X_i^j V_0 / V_j \qquad \text{(c equations)}$$

Equations relating the molar volumes to T, P and X_i ("equations of state"):

$$V_j = f_j(T,P,X_i^j) \qquad \text{and} \qquad V_0 = f_0(T,P,X_i^0) \qquad (\varphi + 1 \text{ equations})$$

Equations of phase stoichiometry:

$$\sum_i X_i^j = 1 \qquad (\varphi \text{ equations})$$

Equations of bulk stoichiometry:

$$\sum_i X_i^0 = 1 \qquad \text{and} \qquad \sum_j x_j = 1 \qquad \text{(2 equations)}$$

The number of degrees of freedom is:

$$v = (\varphi c + c + 2\varphi + 4) - [c(\varphi - 1) + c + 2\varphi + 3] \qquad \text{or} \qquad v = c + 1$$

If the bulk composition and volume of the system are constant (i.e. if c variables are specified: $(c - 1)$ values of X_i^0 and one value of volume, as in any fluid inclusion), *the system must be univariant as regard to the parameters chosen above, but regardless the number of the forming phases* (with, of course, the condition $1 \leqslant \varphi \leqslant c + 1$).

Four major consequences of this result must be mentioned:

(1) When several phases are present, the volume fraction x_j of the phases (minus one) are rather easy to estimate. Although the accuracy of these data is not always very good, they can be of great help in characterizing the system as completely as possible.

(2) On a *TP* section for a given composition, any isopleth—isochoric path is represented by one univariant line, whatever the number of phases (Fig. 1); for an homogeneous fluid ($\varphi = 1$), such a line is named an *isochore*.

(3) For a given bulk composition and a given volume, the *TP* isopleth—isochoric path is naturally unique, in particular in the immiscibility domains. Therefore, such a path intercepts a phase boundary at a unique point. On a constant-composition *TP* section, the location of this point on the boundary depends only on the volume (or the density) of the system. Conversely, and because the set of unknowns and equations given above is linear, *two different points on a phase boundary must correspond to systems with different compositions and/or different densities.*

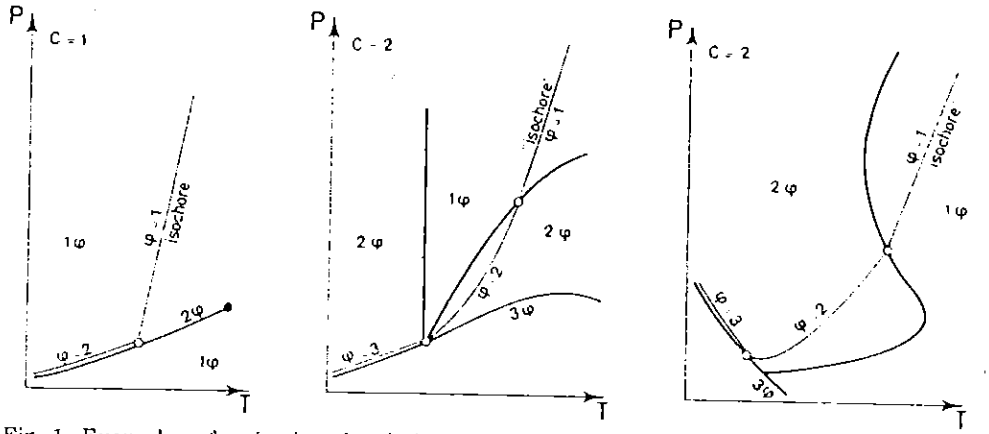

Fig. 1. Examples of univariant isopleth—isochoric paths on constant-composition *TP* sections.
Heavy solid lines: phase boundaries; *light solid lines*: isopleth—isochoric paths; *circles*: phase transitions; c = number of independent components; φ = number of phases.

(4) Another consequence, directly derived from the last point, is that any isochore cannot intercept more than once any phase boundary, including immiscibility surfaces.

3.2. The system H_2O—NaCl

3.2.1. Geometry and phase equilibrium analysis. Like many other binary mixtures, the system H_2O—NaCl admits:

(1) An univariant critical curve joining the critical points of the two pure end-members.

(2) Two pairs of univariant "saturation" curves (halite + L + V and ice + L + V) that originate from the two triple points of the pure end-members and converge towards the invariant eutectic.

In fact, this picture is here slightly complicated by the occurrence of an intermediate compound, hydrohalite ($NaCl \cdot 2H_2O$). This results in the existence of a peritectic invariant point E' (halite + hydrohalite + L + V) and in the fact that the eutectic (ice + halite + L + V) is metastable, and is replaced by another (stable) one, E (ice + hydrohalite + L + V) with the appearance of a third invariant "saturation" curve (hydrohalite + L + V) joining E' and E (Fig. 2).

Unlike the well-known systems H_2O—SiO_2 or H_2O—CO_2, the system H_2O—NaCl is characterized by a saturation curve which does not intercept the critical curve.

Fig. 2 also shows some isopleths (isocomposition sections projected on the *TP* plane) and the corresponding critical points. [It must be remembered that, unlike the critical point of a one-component system or the critical end-points of a multicomponent one, these critical points in a binary system are

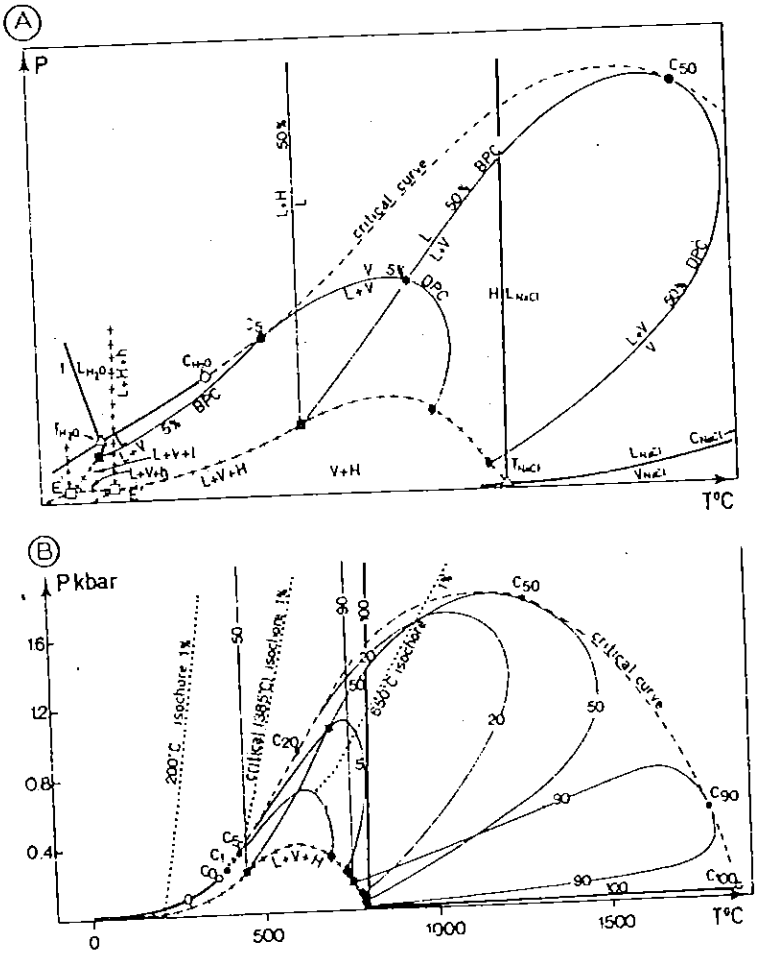

Fig. 2. Geometry of the system H_2O—NaCl.
A. Distorted projection on the *TP* plane. *Heavy solid lines*: phase transition for the pure end-members; *dashed line*: univariant critical curve; C_5 and C_{50} = critical points for 5 wt.% and 50 wt.% NaCl aqueous fluid, respectively; *crosses* = univariant three-phase ("saturation") lines; *open squares* = invariant points; E = eutectic ice + hydrohalite + liquid + vapour (−20.8°C, 10^{-3} bar, 23.2 wt.% NaCl); E' = peritectic hydrohalite + halite + liquid + vapour (0.1°C, $4.5 \cdot 10^{-3}$ bar, 26.3 wt.% NaCl); *solid squares* = saturated liquid; *solid diamonds* = saturated vapour; *thin solid lines* = phase boundaries for the systems with constant compositions of 5 wt.% and 50 wt.% NaCl (isopleths). The *star* indicates the necessary *T*—*P* conditions for a 50 wt.% NaCl liquid to coexist with an immiscible 5 wt.% NaCl vapour.
B. Real-scale projection of the H_2O—NaCl system on the *TP* plane. Five isopleths are given: 1, 5, 20, 50 and 90 wt.% NaCl. The corresponding critical points are C_1, C_5, C_{20}, C_{50}, C_{90}. Critical points for the pure end-members are indicated C_0 (H_2O) and C_{100} (NaCl). Three isochores are also shown in the 1-wt.% NaCl system. Data from Keevil (1942), Sourirajan and Kennedy (1962), Urusova (1975), Potter and Brown (1977). The shape of the immiscibility loops and the location of the critical and saturation points are roughly estimated above 700°C.

not end-points. They just are peculiar points of the immiscibility surface where all the properties of the two coexisting (immiscible) fluids become identical. Their locus is the critical curve.]

On such an isopleth, the "immiscibility loop" is clearly seen; its boundary is made of two branches that join each other at the critical point: the "bubble-point" curve (BPC, L + V = L) and the "dew-point" curve (DPC, L + V = V). When approaching the extreme compositions (pure end-members), the boiling-point and dew-point curves get closer and closer to each other, the loop shrinks and finally mixes into the univariant boiling curves of pure water and pure NaCl.

For any given composition, the isochores originate on the corresponding immiscibility curve, at a temperature that depends on the bulk density of the fluid: on the BPC if the molar volume is lower than the critical one, on the DPC in the other case. Then, the isochores enter the homogeneous fluid (one phase) domain and, as shown in Fig. 2, cannot ever cross again any immiscibility boundary.

In the *TP* domain limited by the critical curve and the "saturation" curve (halite + liquid + vapour) (Fig. 2), every point at a specified temperature and pressure is the intercept (on a *TP* projection) of the BPC of one determined composition and of the DPC of another determined composition.

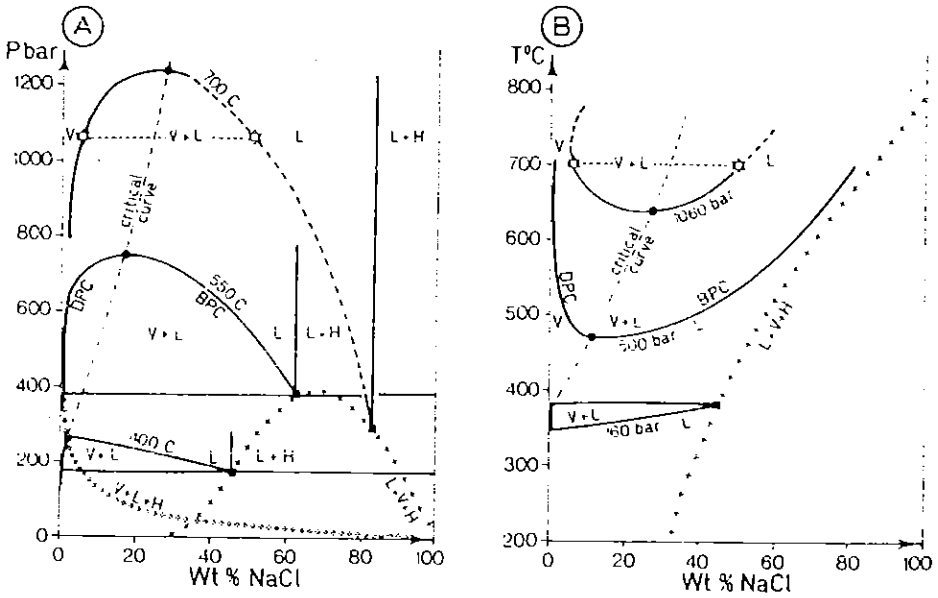

Fig. 3. Isotherms (A) and isobars (B) of the (liquid + vapour) boundaries in the H_2O—NaCl system.
Heavy solid lines: phase boundaries (isotherms and isobars); *light solid lines* = univariant curves, projected on the *PX* and *TX* planes. The *stars* indicate the compositions of two immiscible fluids at 700°C, 1060 bar (5 and 50 wt.% NaCl). Data from Sourirajan and Kennedy (1962), and Urusova (1975). Symbols and abbreviations listed in the Notation.

For instance, the conditions 700°C, 1060 bar correspond to the intercept of the 50 wt.% NaCl BPC and the 5 wt.% NaCl DPC. Conversely, the 50 wt.% NaCl BPC and the 5 wt.% NaCl DPC meet the same temperature and pressure only at 700°C, 1060 bar. This means that a 50 wt.% NaCl "liquid" and a 5 wt.% NaCl "vapour" can coexist at equilibrium only at 700°C and 1060 bar. It is also possible to say that if a fluid with 50 wt.% NaCl is boiling at 700°C, 1060 bar, the corresponding vapour must contain 5 wt.% NaCl. Similarly, if a fluid with 1 wt.% NaCl condenses at 600°C, 700 bar, the corresponding liquid must be a 50 wt.% NaCl solution (Fig. 2).

Other projections that show the *TPX* immiscibility constraints are given in Fig. 3.

3.2.2. Application to fluid inclusions. The behaviour of an inclusion during an isochoric evolution depends on its bulk density and its bulk composition. Such behaviours have been sketched in Fig. 4 for five different fluids of two different salinities (the values 5 and 50 wt.% NaCl are just indicative, since the figure has a very distorted scale for clarity).

If it is assumed that only one homogeneous fluid has been trapped in a given inclusion even if this fluid was at equilibrium with another immiscible one (homogeneous trapping; this point will be discussed later), *each of these five fluids must have been trapped somewhere along the corresponding isochores*. In particular, fluids *1*, *2* and *3* *may* have been trapped at the points H_1 and H_{2-3}, i.e. on the immiscibility surface (or immiscibility curve on the corresponding isopleth). Because the isochoric paths of the fluids 2 and 3 intercept their immiscibility curve (BPC for the 50 wt.% NaCl fluid, DPC for the 5 wt.% NaCl fluid) at the same T and P, these fluids may have been trapped when at equilibrium with each other, and therefore *may* represent the liquid (*3*) and the vapour (*2*) of an unmixed ("boiling") aqueous solution. But this hypothesis is obviously not a certainty, and needs to be supported by other facts related to the general constraints on immiscibility and to the synchronism of trapping.

Fluid *5* *may* have been trapped at point $H_5 = S_5$, and therefore *may* represent the liquid phase of a boiling halite-saturated solution. But, once again, it may have been trapped anywhere else along the isochore, with no unmixing involved. According to its isochoric path, fluid *4* obviously *cannot* have been trapped on the 50 wt.% NaCl immiscibility loop). Therefore, this fluid cannot have been generated by boiling.

3.3. The system CO_2—CH_4 and systems of the same type

The system has been experimentally studied by Donnelly and Katz (1954), and discussed by Hollister and Burruss (1976), Swanenberg (1979), Burruss (1981) and Heyen et al. (1982). It belongs to the same type of system as system H_2O—NaCl, although it is even simpler (no intermediate compound). Many carbonic and/or sulfur-bearing systems also belong to this type: CH_4—C_2H_6, CO_2—SO_2, CO_2—H_2S, etc.

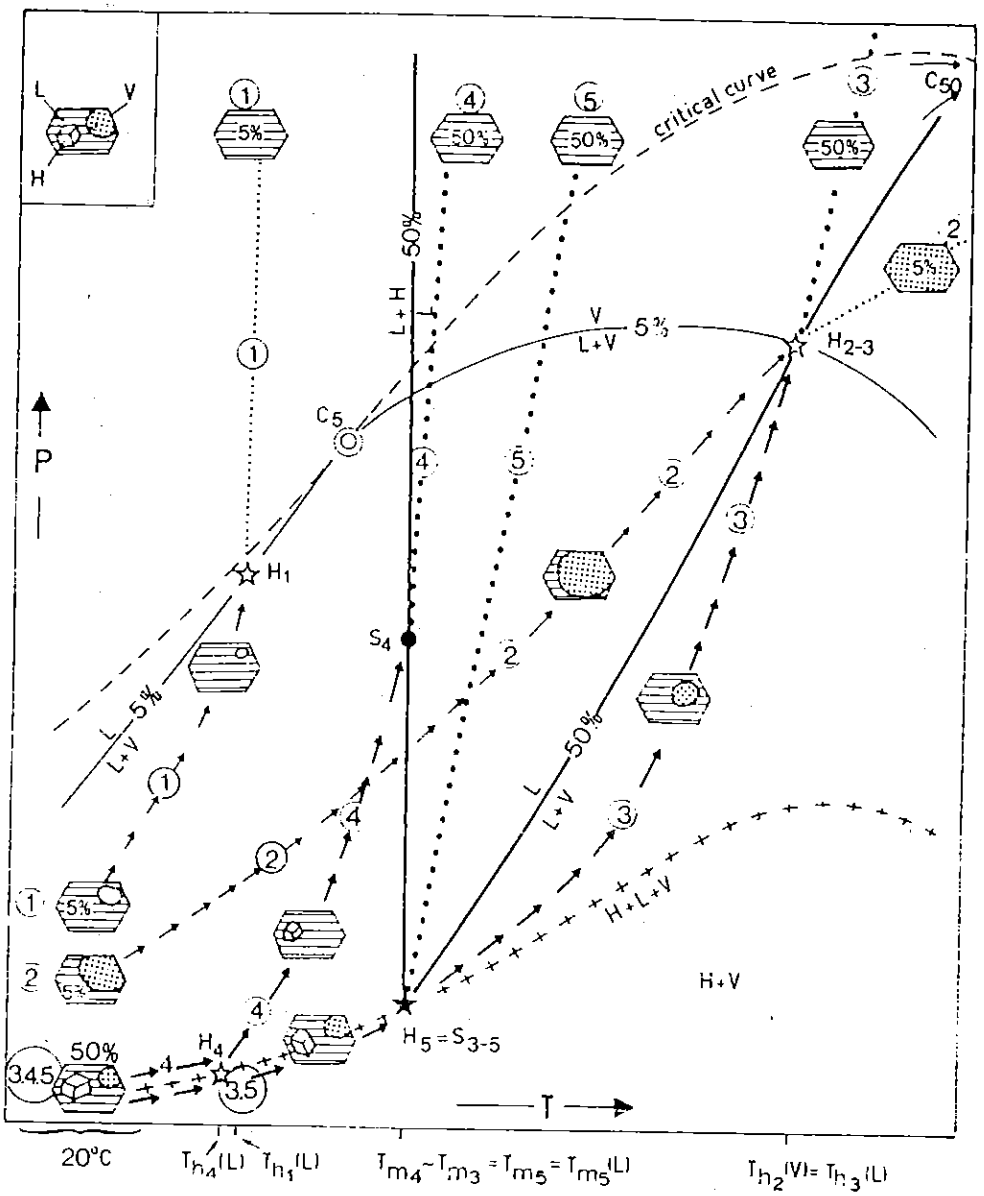

Fig. 4. Trapping conditions and isochoric behaviour of inclusion fluids in the H_2O—NaCl system.

Open stars (*H*) indicate the conditions of homogenization (corresponding temperature T_h into a liquid (L) or a vapour (V). The *solid star* ($H_5 = S_{3-5}$) indicates the conditions of both homogenization and melting of halite. The *solid circle* (S_4) indicates the conditions of dissolution ("melting") of halite (corresponding temperature T_m). *Crosses* (H + L + V) = "saturation" curve; *dashed line* = critical curve.

Two isopleths are projected on the *TP* plane: one for a 5 wt.% NaCl aqueous solution (*light solid lines, arrows, dots*, etc.), the other for a 50-wt.% NaCl aqueous solution (*heavy solid lines, arrows, dots*, etc.); the corresponding critical points are C_5 and C_{50}.

As a consequence, it can be predicted that adding components such as CH_4 and small amounts of SO_2—H_2S, etc., to the "binary" H_2O—CO_2 or the "ternary" H_2O—CO_2—NaCl system will not change significantly the general shape of these systems.

3.4. *The system H_2O—CO_2 and systems of the same type*

Most of the systems containing water and C-bearing compounds (H_2O—C_2H_6, H_2O—C_6H_6, etc.) and many others (H_2O—N_2, H_2O—H_2, etc.) belong to the same type as the H_2O—CO_2 system.

3.4.1. Geometry and phase equilibrium analysis. The system H_2O—CO_2 certainly is the most complicated of the geologically relevant binary ones. As compared with the simple H_2O—NaCl (or the even simpler H_2O—KCl or CO_2—CH_4 systems), it is characterized by:

(1) The existence of an intermediate compound (as in the H_2O—NaCl system), the gas hydrate or clathrate $CO_2 \cdot 5.75H_2O$.

(2) The existence of a liquid—liquid immiscibility domain which intercepts both the clathrate saturation curves and the critical curve.

(3) The fact that the critical curve is intercepted by the two-liquid domain results in splitting the critical curve into two discontinuous branches: the lower critical curve which originates from the critical point of pure CO_2 and ends at a lower critical end-point (LCEP, Fig. 5), where it intercepts the L_1L_2V curve, and the upper critical curve, which originates from the critical point of pure H_2O and probably ends at an upper critical end-point (UCEP, see inset Fig. 5) where it intercepts the L_1L_2C curve.

According to Tödheide and Franck (1963) and Takenouchi and Kennedy (1964) the LCEP is located very close to the critical point of pure CO_2, and the amount of water dissolved in the carbonic fluid along the lower critical curve is exceedingly small. The upper critical curve has a negative slope at low pressures, passes through a minimum temperature ($\partial T/\partial P = 0$) at 266°C, 2450 bar and then exhibits at higher pressures a positive slope up to the highest pressure investigated to date (3500 bar). By comparison with

---

Solid lines: phase boundaries; *arrows* = isochoric *TP* paths in the two-phase domains: *dotted lines*: isochoric *PT* paths in the homogeneous fluid domain ("true isochores"). Five different fluids are considered: the aspect of the corresponding fluid inclusions is shown at room temperature and along the various isochoric paths.

Fluid *1*: 5 wt.% NaCl, high density. Liquid homogenization.

Fluid *2*: 5 wt.% NaCl, low density. Vapour homogenization at H_{2-3}.

Fluid *3*: 50 wt.% NaCl, moderate density. Halite melts at S_{3-5}, liquid homogenization occurs at H_{2-3}. $T_{m3} < T_{h3}$.

Fluid *4*: 50 wt.% NaCl, high density. Vapour disappears at H_4, halite melts at S_4, $T_{h4} < T_{m4}$.

Fluid *5*: 50 wt.% NaCl, density between fluids *3* and *4*. Liquid homogenization and melting of halite occur at the same point $H_5 = S_{3-5}$, $T_{m5} = T_{h5}$.

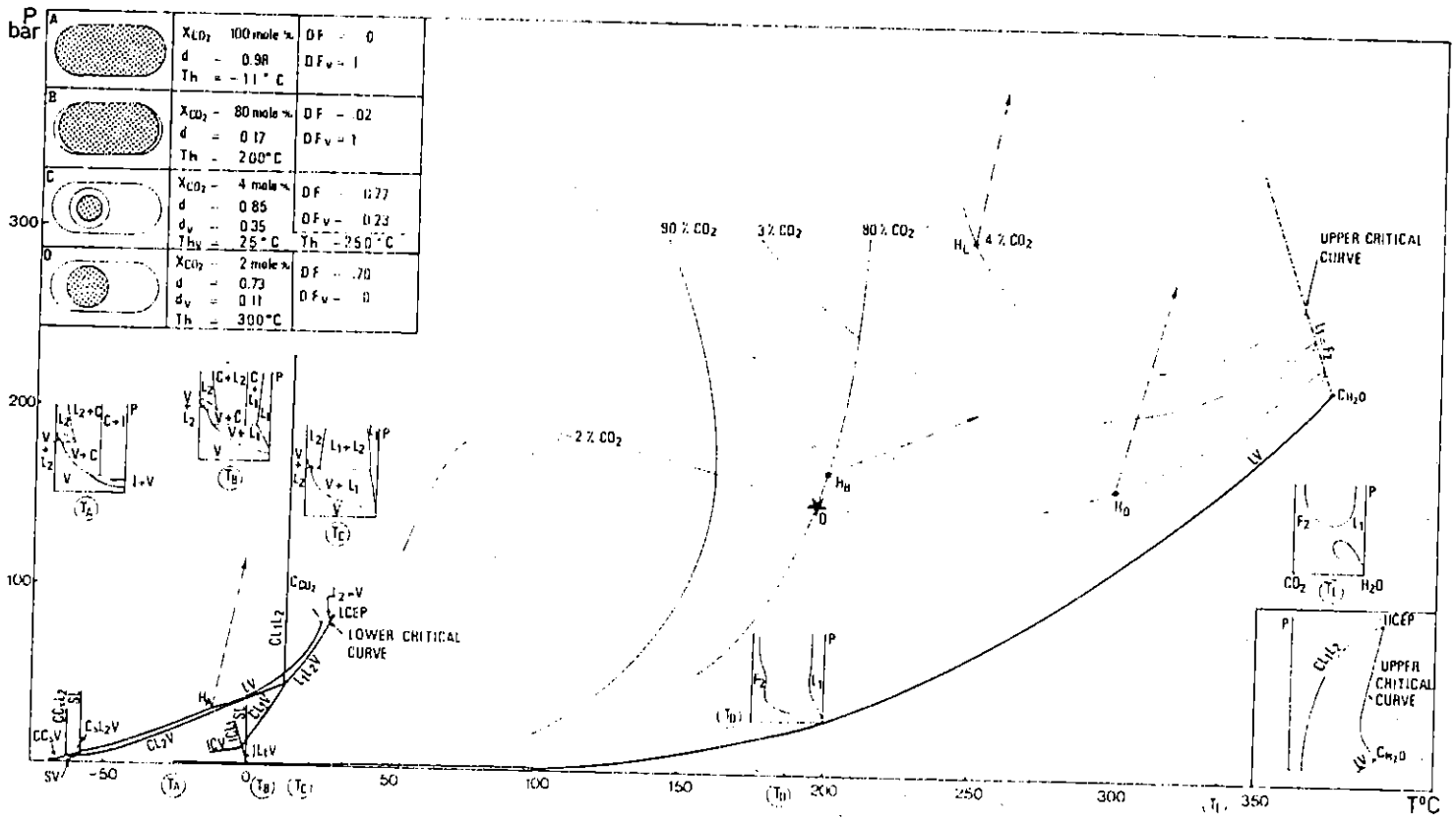
P bar
A
X_{CO_2} 100 mole %
d = 0.98
Th = −11 °C
DF = 0
DF_v = 1
B
X_{CO_2} = 80 mole %
d = 0.17
Th = 200°C
DF = .02
DF_v = 1
C
X_{CO_2} = 4 mole %
d = 0.85
d_v = 0.35
Th = 26 °C
DF = 0.77
DF_v = 0.23
Th = 250 °C
D
X_{CO_2} = 2 mole %
d = 0.73
d_v = 0.11
Th = 300°C
DF = .70
DF_v = 0
300
200
100
90 % CO_2
3 % CO_2
80 % CO_2
4 % CO_2
2 % CO_2
H_L
H_H
H_D
D
UPPER CRITICAL CURVE
C_{H_2O}
LV
ICEP
LOWER CRITICAL CURVE
C_{CO_2}
L_2=V
CL_1L_2
CL_2V
CC_2V
$C_{CO_2}L_2V$
L_1L_2V
L_1V
SV
CO_2
H_2O
UPPER CRITICAL CURVE
−50
50
100
150
200
250
300
350
T°C

other systems of the same type investigated at higher pressures (e.g., NH_3—N_2; Tsiklis, 1952), it is now agreed on the hypothesis that this slope remains positive up to the UCEP, which has been tentatively located by K. Tödheide (in Takenouchi and Kennedy, 1964) above 50 kbar.

In the *TP* projection, the (liquid + vapour) immiscibility domain is therefore limited towards higher temperatures by the upper critical curve.

Some isopleths are also projected on the *TP* plane of Fig. 5. They show some constant-composition sections of the upper immiscibility surface (immiscibility curves and their corresponding critical points on the critical curve). Additional isothermal sections show the changes in phase equilibria at various temperatures between T_A and T_E. In particular, the T_E isotherm seems to indicate that an increase of pressure at constant temperature and for a proper constant composition would result in a first homogenization of two immiscible fluids, followed by a second unmixing. However, this type of process is impossible for systems with constant volume and composition (isochoric paths) and suggestions of that sort just come from projection effects (see also Ypma, 1963, pp. 18—26, for a more detailed discussion of that point). Because of the particular shape of the two-fluid-phase boundary in the system H_2O—CO_2 (due to the temperature minimum on the critical curve), the relative position of the boundary and of isochores must be examined: it seems that some isochores, whose slopes are steep enough, might re-intercept the immiscibility surface. It has been shown above that such a situation is not possible. In fact, the slopes of some isochores, drawn

---

Fig. 5. *TP* projection and selected isothermal sections of the binary system H_2O—CO_2 at low pressures. The inset shows a possible, not to scale, termination of the upper critical curve at high pressures, as discussed in the text. The *heavy lines* are the univariant two or three phase curves for the unary and binary systems, respectively. The *light lines* are isopleths (isocomposition lines) of the two-phase region. The 2%, 3%, 4% CO_2 (mole%) isopleths represent the H_2O-rich liquid phase L_1 in equilibrium with a CO_2-rich fluid. The 90%, 80% CO_2 (mole%) isopleths represent the CO_2-rich fluids F_2 in equilibrium with a H_2O-rich liquid. The point O (*star*), intersection in projection of the 2 and 80 mole% CO_2 isopleths, determines the *PT* coordinates of homogenization of two chemically immiscible fluids of 2 mole% CO_2 and 80 mole% CO_2, respectively. The isothermal sections are not drawn to scale for clarity. The heating behaviour of four fluid inclusions, corresponding to different fluid compositions and densities within the binary H_2O—CO_2 system is illustrated (inclusions represented at room temperature). Inclusion A: homogenization temperature (point H_A) and isochore (*dashed line*) obtained from Kennedy (1954). Inclusions B to D: composition and *PT* coordinates of homogenization (points H_B to H_D) taken from Takenouchi and Kennedy (1964); volumes at the homogenization points and isochores (*dashed lines* originating from these points) obtained by calculation using Kleintjens and Koningsveld (1982) equation of state; degree of filling at room temperature deduced from the calculated volumes. No subscript indicated = pure H_2O or CO_2 phases. Subscripts *1* and *2* refer to H_2O-rich and CO_2-rich phases, respectively, subscript v to the non-aqueous part of the inclusion. C_S: solid CO_2; LCEP = lower critical end-point; UCEP = upper critical end-point; X_{CO_2} = bulk CO_2 content in the inclusion; the other symbols used are listed in the Notation. The figure is based on Tödheide and Franck (1963), Takenouchi and Kennedy (1964), and Hollister and Burruss (1976).

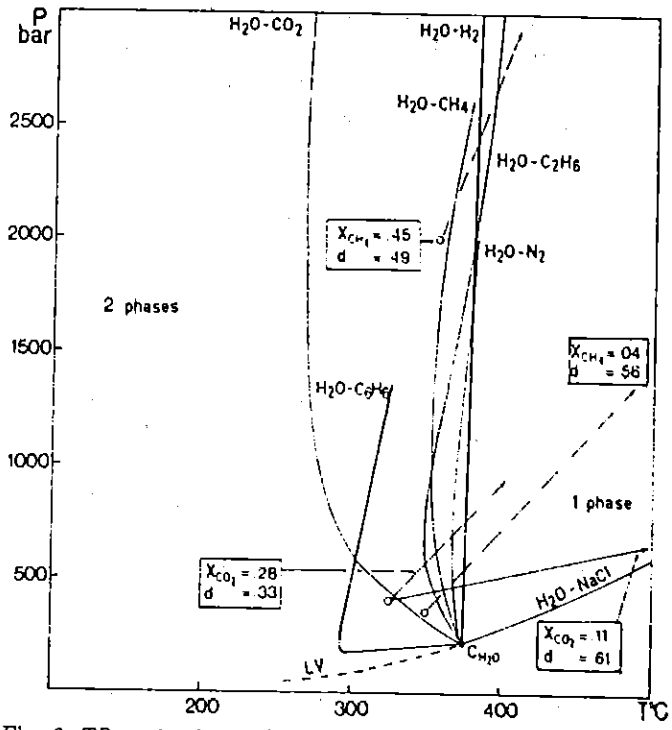

Fig. 6. *TP* projections of the upper critical curves of several geologically relevant binary systems of the H_2O—CO_2 type.
Some isochores were calculated for binary compositions and densities in both the systems H_2O—CO_2 (*full lines*) and H_2O—CH_4 (*dashed lines*) from the equation of state of Kerrick and Jacobs (1981) and Jacobs and Kerrick (1981).
Concentrations are in mole%. Sources of data: H_2O—CO_2 — Tödheide and Franck (1963); H_2O—CH_4 — Welsch (1973); H_2O—C_6H_6 — Alwani and Schneider (1967); H_2O—C_3H_8 — Danneil et al. (1967); H_2O—N_2 — Tsiklis and Maslennikowa (1965); H_2O—H_2 — Seward and Franck (1981); H_2O—NaCl — Sourirajan and Kennedy (1962).

to real scale, in various systems of the same type (Figs. 5 and 6) agree with our general statement. Moreover, large changes of molar volume necessarily occur along an isopleth *TP* path which is steep enough to intercept twice the two-fluid-phase boundary and therefore such a path cannot be isochoric. This is simply due to the values of the compressibility coefficients close to one in most fluid systems as illustrated in Fig. 7.

3.4.2. Application to fluid inclusion behaviour. Four main types of inclusions have been chosen, whose behaviour is shown in Fig. 5:

(1) Type A contains pure CO_2; it homogenizes at a point (H_A) of the pure CO_2 boiling curve. The location of H_A and the type of homogenization (liquid or vapour) depends on the density of the inclusion.

(2) Type B has a bulk composition of 80 mole% CO_2, and exhibits two

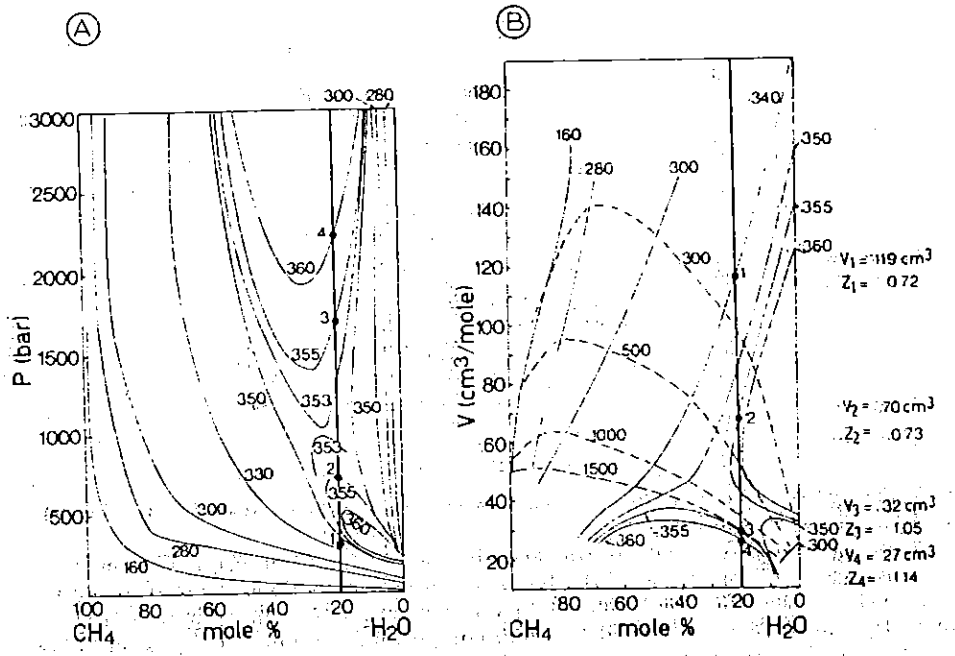

Fig. 7. *PX* (A) and *VX* (B) projections of the two-phase region in the binary system H_2O–CH_4 (data from Welsch, 1973).
The *light lines* and the *light dashed lines* are respectively isotherms and isobars of the two-phase boundary surface. The numbers indicate the values of the pressure and temperature. The *vertical heavy line* corresponds to an isopleth (20 mole% CH_4). The points *1* to *4* are the intersection points of this isopleth with the two-phase surface. Note the sharp increase in volume (*V*) from points *1* to *4* [volumetric data on the two-phase region from Welsch (1973)]. The compressibility factor $Z = PV/RT$ of the mixture from points *1* to *4* along the path is also indicated.

fluid phases (L + V) at room temperature, with a low degree of filling (DF). Upon heating, homogenization occurs by liquid disappearance at point H_B.

(3) Type C contains 4 mole% CO_2 and is made of three fluid phases at room temperature: an aqueous liquid, a CO_2-rich liquid and a CO_2-rich vapour. On heating, a first homogenization occurs which concerns the two CO_2-rich phases.

The homogenization temperature of the carbonic part depends on the density of the fluid, and is lower than the temperature of the LCEP. In the chosen example, the density of the carbonic fluid is close to the critical one, and T_h is very close to the temperature of the LCEP, and therefore to C_{CO_2}.

At higher temperatures, the inclusion is made of a water-rich liquid (L_1) and a CO_2-rich "vapour" (F_2) (Figs. 5 and 8). It follows a unique isopleth–isochoric path until it reaches the immiscibility surface at the point H_C where total homogenization occurs by dissolution of the "vapour" into the liquid.

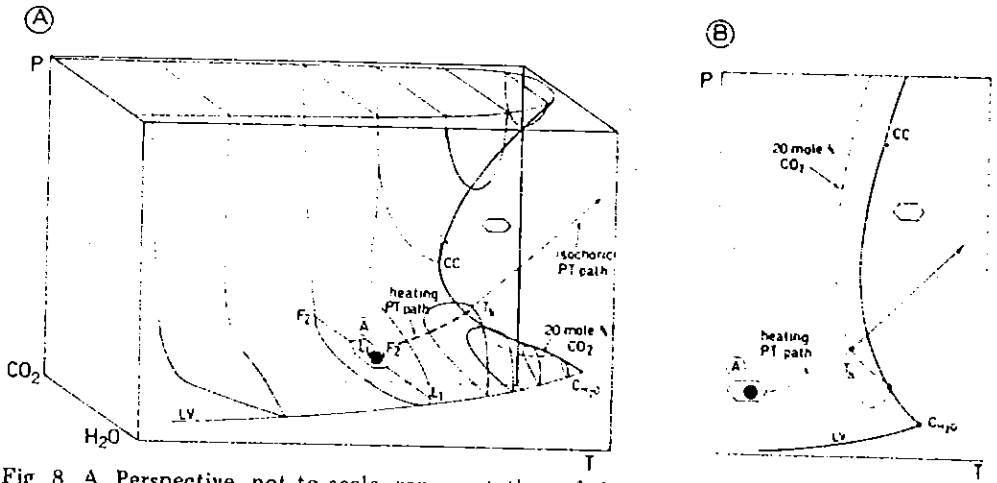

Fig. 8. A. Perspective, not to scale, representation of the two-phase region in the binary system H_2O—CO_2.
The shape of the two-phase region is evidenced by the several isotherms, drawn on the two-phase surface. The magnitude of the temperature minimum along the critical curve has been much exaggerated. The heating *TP* path of inclusion A (consisting of a H_2O-rich liquid L_1 and of a CO_2-rich fluid F_2, bulk composition 20 mole% CO_2) is schematic. The intersection of the heating path with the 20 mole% CO_2 isopleth of the two-phase field defines the point T_h, homogenization point of fluid inclusion A. The isochoric *PT* path followed by the fluid inclusion after homogenization is also schematic.
Symbols as in Fig. 5. CC = H_2O—CO_2 upper critical curve.
B. *TP* projections of (A), showing the critical curve and the particular shape of the 20 mole% CO_2 isopleth.
The curvature of the lines has been significantly enhanced.

(4) Type D (2 mole% CO_2) contains two phases (an H_2O-rich liquid and a CO_2-rich vapour) at room temperature. It homogenizes again by vapour disappearance, at point H_D.

The occurrence at low pressure of thermal maxima on the isopleth dew-point curves of the system H_2O—CO_2 has an interesting consequence, as already noticed by Ypma (1963); for a given inclusion fluid homogenizing into the liquid phase at a given temperature, there can be several inclusion fluids, two of them with the adequate composition, that homogenize into the vapour phase at the same temperature (Fig. 9). Obviously, only one of these may be the vapour at equilibrium with the inclusion liquid at the time of trapping.

A similar situation, due to the same cause, can be expected at high temperatures in the system H_2O—NaCl, although the exact shape of the NaCl-rich isopleths is not known.

3.5. The system H_2O—CO_2—NaCl

Because of the extremely low mutual solubility of CO_2 and NaCl, it can be expected that the miscibility gap(s) in the ternary system H_2O—CO_2—NaCl will be drastically enlarged with regard to those in the systems H_2O—

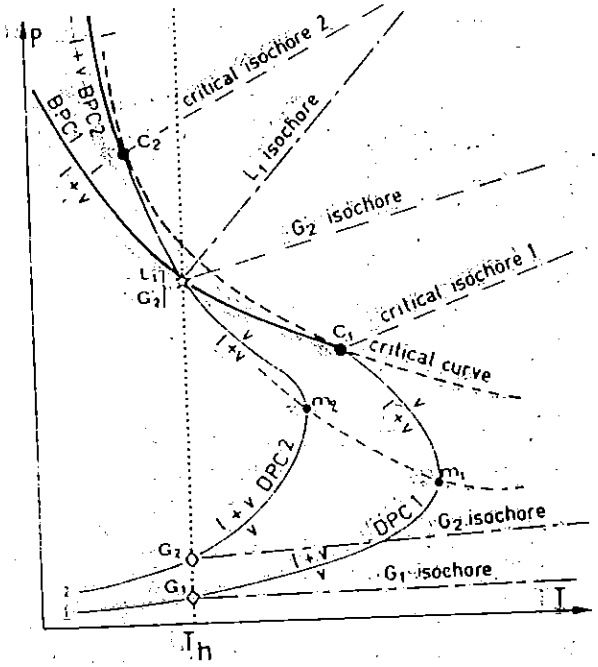

Fig. 9. Enlargement of the high-T–low-P part of Fig. 8B.
Heavy solid lines: boiling-point curves for the two given CO_2–H_2O compositions (isopleths), labelled *1* and *2*; *light solid lines*: dew-point curves for the same compositions. *Heavy dashed line*: critical curve; *light dashed line*: locus of the thermal maxima m of the dew-point curves. C_1, C_2: critical points for the compositions *1* and *2*. G_1, G_2, G'_2: vapour homogenization at $T = T_h$ for inclusion fluids of compositions *1* and *2*. L_1: liquid homogenization at $T = T_h$ for an inclusion fluid of composition *1*. The *dashed*–*dotted* lines are the corresponding isochores.
The liquid L_1 and the vapour G'_2 can have been trapped at the same T and P on the immiscibility boundary (point L_1,G'_2) and therefore may represent the two immiscible phases of an unmixed fluid. Although they also homogenize at the same temperature T_h, neither L_1 and G_2 (correct composition but pressure inadequate) nor L_1 and G_1 (composition and pressure inadequate) can receive the same interpretation.

NaCl and H_2O–CO_2. Preliminary data by Ellis and Golding (1963), and Takenouchi and Kennedy (1965) have confirmed this point.

Most of the data used here are from the extensive work of Gehrig (1980). Fig. 10 shows how adding increasing amounts of NaCl to the system CO_2–H_2O shifts the isopleth immiscibility curves towards higher temperatures, and how adding increasing amounts of CO_2 in the H_2O–NaCl system shifts the same boundaries towards higher pressures.

Some of these isopleth immiscibility curves are characterized by a thermal minimum (as in the H_2O–CO_2 system) and a pressure minimum (for instance, see the 5 mole% CO_2–(H_2O–20 wt.% NaCl) and the 5.1 mole% CO_2–(H_2O–6 wt.% NaCl) curves in Fig. 10). It might be expected that some very steep or, on the contrary, very flat isochore originating at a point of such a curve, could intercept again this curve. As shown above and confirmed by

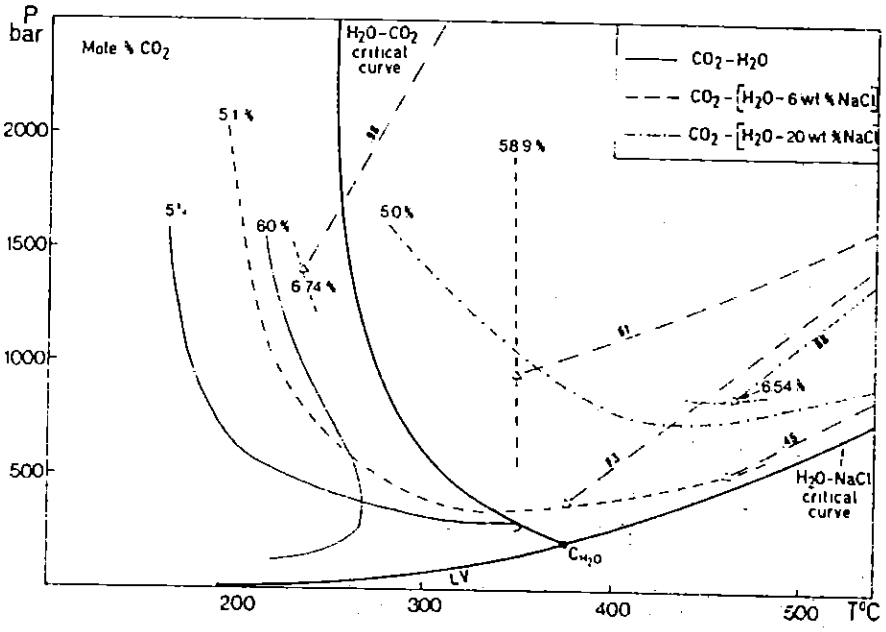

Fig. 10. *TP* projection showing the effect of adding NaCl upon the extension of the two-phase region in the ternary system H_2O–CO_2–NaCl.
Heavy lines: liquid–vapour curve (LV) for the pure H_2O system and critical curves for the binary systems H_2O–CO_2 and H_2O–NaCl. *Light curved lines*: two-phase boundaries: the area of complete miscibility is to the right of the boundaries; the numbers related to each curve refer to the CO_2 concentration (mole%) of the mixture; the binary curves are from Takenouchi and Kennedy (1964); the ternary from Gehrig's (1980) data. *Light "straight" lines*: ternary isochores from Gehrig (1980); they refer either to CO_2–(H_2O–6 wt.% NaCl) mixture (*dashed lines*) or to CO_2–(H_2O–20 wt.% NaCl) mixture (*dashed-dotted* line); the numbers along each isochore are densities of the ternary mixture.

the few isochores indicated in Fig. 10, such an hypothetical isochore does not exist.

In his work, Gehrig (1980) located the L + V (or F_1 + F_2) immiscibility gap for some specified bulk compositions, but did not analyse the compositions of the coexisting fluids. However, it is possible to predict a strong partition of the three components between the immiscible phases (with, of course, the exception of the critical region): the "vapour" must be enriched in CO_2 and very poor in NaCl, and the "liquid" must be enriched in H_2O and NaCl and very poor in CO_2. For this reason, the T–X (or P–X) isobaric (or isothermal)–isosalinity diagrams (X accounts here for mole% CO_2) cannot be true sections and may be fallacious; they should be used with much care in studies of immiscibility in ternary (or higher) systems.

Several ternary isobaric–isothermal sections are given in Fig. 11. They have been constructed using M. Gehrig's data [data from Sourirajan and Kennedy (1962) for the binary H_2O–NaCl system]. The (liquid ⇌ liquid +

halite) boundary has been assumed independent of pressure (Keevil, 1942). The extrapolated tie lines and phase boundaries are indicated for the 500°C isotherm, except for 1 kbar (200° C isotherm). For the reason given above, they are only tentative, although some of the estimates (1 kbar, 200° C section) must be accurate enough.

Three general types of phase relations can be distinguished, depending on the T—P conditions relatively to the H_2O—CO_2 and H_2O—NaCl critical curves:

(1) Type *1* (low-temperature side of the H_2O—CO_2 critical curve) is characterized by a miscibility gap L + V (or F_1 + F_2) which originates on the H_2O—CO_2 side and widens into the ternary (Fig. 11, section 1 kbar, 200°C).

(2) Type *2* (high-temperature side of the H_2O—CO_2 critical curve and high-pressure side of the H_2O—NaCl critical curve) exhibits an immiscibility gap F_1 + F_2 which concerns only the ternary and never reaches the end-member binaries (Fig. 11, section 1.5 kbar, 500°C).

(3) Type *3* (high-temperature and/or low-pressure side of the H_2O—NaCl critical curve) is the reverse of type *1*: the miscibility gap originates on the H_2O—NaCl side, and widens dramatically (particularly for the NaCl-rich liquid) into the ternary (Fig. 11, section 500 bar, 500°C).

Some interesting consequences can be derived from these isobaric—isothermal sections:

(a) The available experimental data do not suggest closing of the ternary fluid miscibility gap at higher temperatures and pressures. Therefore, the co-existence of two immiscible fluids under magmatic conditions is very likely, even in domains where neither the H_2O—NaCl or the H_2O—CO_2 systems exhibit immiscibility. In this respect, experimental data at high-T—P conditions would be particularly pertinent.

(b) In the range of geologically relevant T—P conditions, the ternary system H_2O—CO_2—NaCl never exhibits three *distinct* fluid phases. Therefore, the coexistence, in natural processes, of three immiscible fluids is extremely unlikely, although theoretically possible (of course, like the system H_2O—CO_2, the system H_2O—CO_2—NaCl may contain three fluid phases at low temperatures).

CONCLUSIONS

The analyses of phase equilibria in all types of systems relevant for geological problems result in many consequences that are of primary interest in interpreting the phase transitions and processes observed in fluid inclusions during microthermometric studies, and on modeling the natural hydrothermal processes as well.

(a) In fluid systems, the domains of temperatures, pressures and compositions that can be affected by immiscibility, increase considerably with the number of components. In multi-component natural fluid systems, the fluid

immiscibility gap is so large that immiscibility probably is a common phenomenon in a wide range of geologic processes.

(b) It has been shown and illustrated again several times, that an isochore (constant-composition- constant-volume *TP* univariant line for a homogeneous — one-phase — fluid) originates on a phase boundary and can

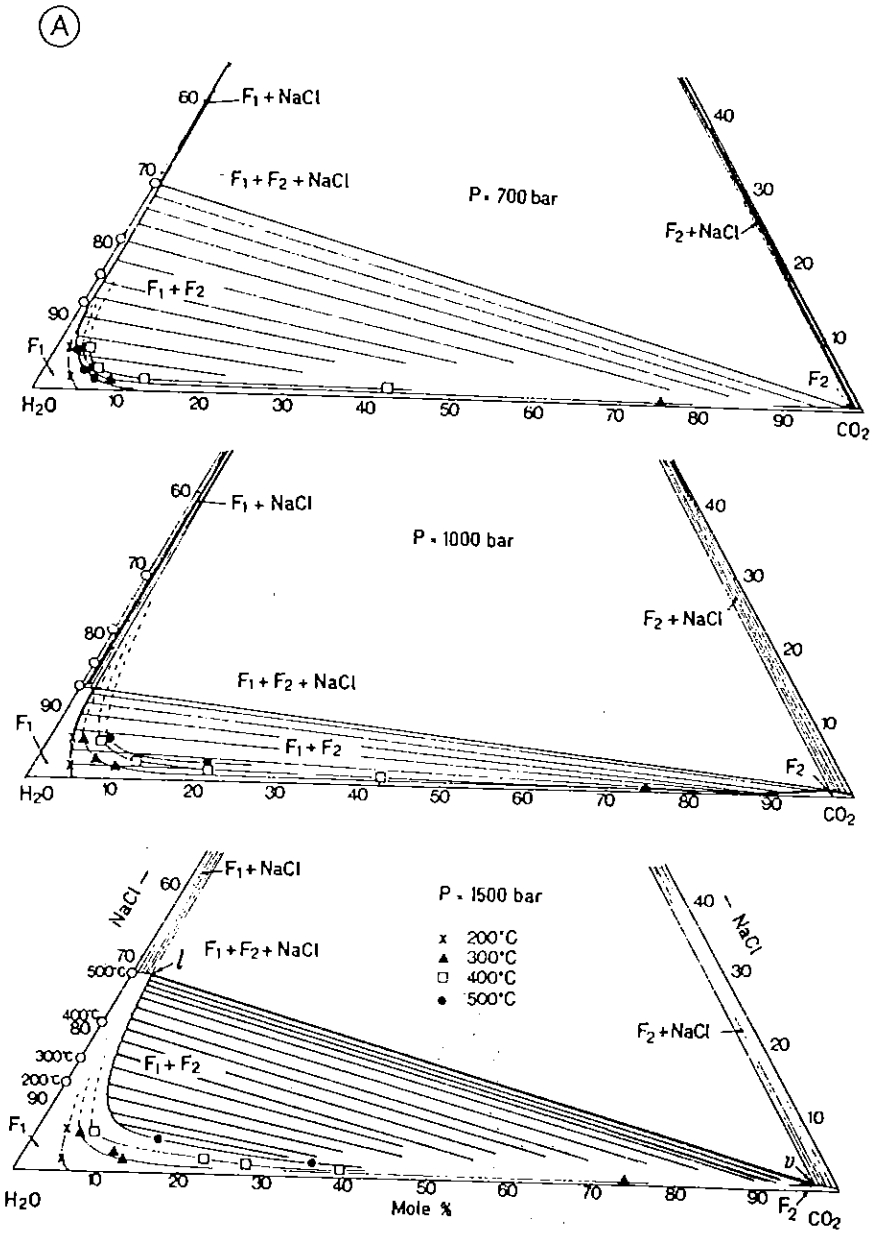

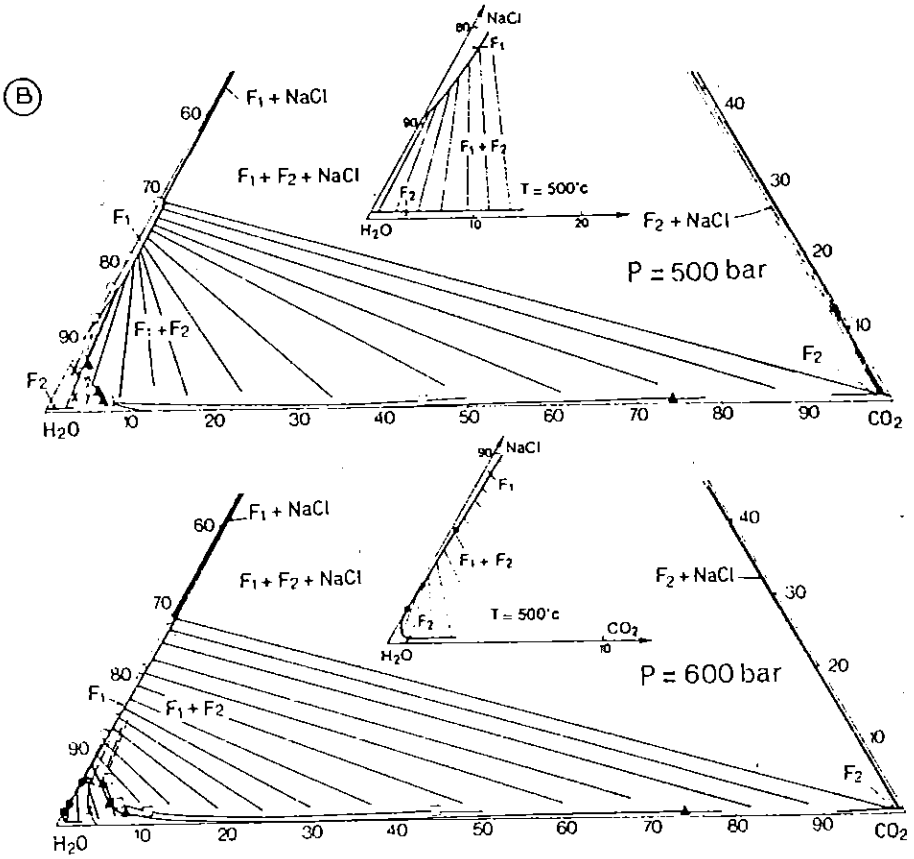

Fig. 11. Isobaric isothermal sections in the system H_2O—CO_2—NaCl: (A) 1500-, 1000- and 700-bar sections; and (B) 600- and 500-bar sections with enlargement of the H_2O corner for the 500°C isotherm. Experimental points for the ternary compositions (symbols on the 1500-bar section) taken from Gehrig (1980). The NaCl saturation points (*open circles*) for the H_2O—NaCl binary are from Keevil (1942) with no pressure correction; they are labelled for temperatures (200°, 300°, 400° and 500°C) on the 1500-bar section only. Points l and v are isobaric isothermal invariant points; they indicate the composition of F_1 ("liquid") and F_2 ("vapour") in the assemblage F_1 + F_2 + halite. Although they are estimated, these points must be very close to the halite saturation in the system H_2O—NaCl and close to the CO_2 corner, respectively, because of: (1) the lowering of the solubility of CO_2 in H_2O with increase of the NaCl concentration; and (2) the very low mutual solubility in the system CO_2—NaCl. Note that an increase of the NaCl content in the ternary system simply results in halite precipitation. The tie lines F_1 + F_2 (= L + V) are not known but their locations are estimated with reasonable accuracy, at least for some of the sections (e.g., 1000 bar, 200°C). The phase boundaries are extrapolated from Gehrig's (1980) data.

never cross again this phase boundary. Some projections or sections (in particular the T—X or P—X diagrams) apparently make possible the reverse statement: this just comes from the fact that "paths" on such diagrams are isobaric or isothermal and therefore do not take into account the constant-volume constraints.

(c) As a simple result of the last point, it must be noticed that, when a fluid inclusion is heated it cannot unmix again, once it has been homogenized (in the same run).

Nevertheless, some particular binary systems (e.g., mixtures of organic compounds with relatively low melting temperature) actually exhibit two distinct fluid immiscibility gaps: besides the "regular" (L + V) immiscibility domain at moderate to high temperatures, another immiscibility domain (L_1 + L_2) exists at lower temperatures although both domains may overlap in a variable extent (Ricci, 1951; Rowlinson, 1969; Schneider, 1970, 1972). Such systems are not known, however, for geologically relevant compositions, and the additional complexities arising from these particular geometries do not need further discussion.

Examples of re-unmixing, upon progressive heating, of previously homogenized fluid inclusions have been published in the Soviet literature. They are reported by Roedder (1981), who states that "under constant volume conditions, such immiscibility is perfectly feasible", and compares it to the "retrograde condensation", and "infracritical and supracritical homogenization" in the system CO_2---H_2O, as described by Ypma (1963). In fact, it has been shown above that these processes cannot be isochoric and therefore cannot apply to fluid inclusion's behaviour during reversible heating. This point had been otherwise noticed by Ypma (1963), who limited their occurrence to isothermal systems.

Amongst several explanations that might account for the facts quoted by Roedder (1981), the following two are most likely:

(1) The rather high viscosity of brines can prevent the inclusions from reaching a state of bulk equilibrium during a significant length of time; the observed re-unmixing could then refer to a metastable local equilibrium or to the disruption of a metastable homogeneous mixture.

(2) A partial leakage of an inclusion quasi-isothermally lowers its density, and therefore its internal pressure, thus yielding unmixing.

ACKNOWLEDGEMENTS

Discussions with M. Cuney, J. Dubessy, J. Holloway, B. Poty, comments and advices from R. Kreulen, S. Sheppard and J. Touret considerably improved earlier versions of the manuscript. Careful reviews by D. Manning, R. Wilkins, S. Sheppard and J. Touret have been greatly appreciated. Expert technical help was provided for typing and drawing by D. Perlangeli, D. Dautel, A. Legros and J. Gorau.

REFERENCES

Alwani, Z. and Schneider, G.M., 1967. Druckeinfluss auf die Entmischung flüssiger Systeme, VI. Phasengleichgewichte und kritische Erscheinungen im System Benzol—H_2O zwischen 250 und 368°C bis 3700 bar. Ber. Bunsenges. Phys. Chem., 71: 633—638.

Bray, C.J., 1980. Mineralisation, greisenisation and kaolinisation at Goonbarrow china clay pit, Cornwall, U.K. Ph.D. Thesis, University of Oxford, Oxford (unpublished).

Burruss, R.C., 1981. Analysis of fluid inclusions: phase equilibria at constant volume. Am. J. Sci., 281: 1104—1126.

Chivas, A.R. and Wilkins, R.W.T., 1977. Fluid inclusion studies in relation to hydrothermal alteration and mineralization at the Koloula porphyry copper prospect, Guadalcanal. Econ. Geol., 72: 153—169.

Danneil, A., Tödheide, K. and Franck, E.U., 1967. Verdampfungsgleichgewichte und kritische Kurven in den Systemen Äthan/Wasser und *n*-Butan/Wasser bei hohen Drücken. Chem.-Ing.-Tech., 39: 816—822.

Denis, M., 1974. Altérations et fluides associés dans le porphyre cuprifère de Sierrita (Arizona, États-Unis). Thesis, University of Nancy I, Nancy, 146 pp.

Denis, M., Pichavant, M., Poty, B. and Weisbrod, A., 1980. Le porphyre cuprifère de Sierrita—Esperanza, Arizona, U.S.A. — Comparaison avec quelques porphyres voisins. Bull. Soc. Fr. Minéral., 103: 613—622,

Donnelly, H.G. and Katz, D.L., 1954. Phase equilibria in the carbon dioxide—methane system. Ind.-Eng.-Chem., 46: 511—517.

Durisova, J., Charoy, B. and Weisbrod, A., 1979. Fluid inclusion studies in minerals from tin and tungsten deposits in the Krušné Hory Mountains (Czechoslovakia). Bull. Soc. Fr. Minéral., 102: 665—675.

Eastoe, C.J., 1978. A fluid inclusion study of the Panguna porphyry copper deposit, Bougainville, Papua New Guinea. Econ. Geol., 73: 721—748.

Ellis, A.J. and Golding, R.M., 1963. The solubility of carbon dioxide above 100°C in water and sodium chloride solutions. Am. J. Sci., 261: 47—60.

Etminan, H., 1977. Le porphyre cuprifère de Sar Cheshmeh (Iran) — Rôle des phases fluides dans les mécanismes d'altération et de minéralisation. Sci. Terre, Mém., Fr., 34: 1—242.

Gehrig, M., 1980. Phasengleichgewichte und *PVT*-Daten ternärer Mischungen aus Wasser, Kohlendioxid und Natriumchlorid bis 3 kbar und 550°C. Thesis, Institute of Physical Chemistry, University of Karlsruhe, Karlsruhe.

Grant, J.N., Halls, C., Sheppard, S.M.F. and Avila, W., 1980. Evolution of the porphyry tin deposits in Bolivia. In: Granitic Magmatism and Related Mineralisations. Min. Geol., Spec. Iss., 8: 151—175.

Heyen, G., Ramboz, C. and Dubessy, J., 1982. Simulation des équilibres de phases dans le système CO_2—CH_4 en dessous de 50°C et de 100 bar — Application aux inclusions fluides. C.R. Acad. Sci., Paris, 294: 203—206.

Hollister, L.S. and Burruss, R.C. 1976. Phase equilibria in fluid inclusions from the Khtada Lake metamorphic complex. Geochim. Cosmochim. Acta, 40: 163—175.

Jacobs, G.K. and Kerrick, D.M., 1981. Methane: an equation of state with application to the ternary system H_2O—CO_2—CH_4. Geochim. Cosmochim. Acta, 45: 607—614.

Keevil, N.B., 1942. Vapor pressures of aqueous solutions at high temperatures. J. Am. Chem. Soc., 64: 841—850.

Kelly, W.C. and Turneaure, F.S., 1970. Mineralogy, paragenesis and geothermometry of the tin and tungsten deposits of the eastern Andes, Bolivia. Econ. Geol., 65: 609—680.

Kennedy, G.C., 1954. Pressure—volume—temperature relations in CO_2 at elevated temperatures and pressures. Am. J. Sci., 252: 225—241.

Kerrick, D.M. and Jacobs, G.K., 1981. A modified Redlich—Kwong equation for H_2O, CO_2 and H_2O—CO_2 mixtures at elevated pressures and temperatures. Am. J. Sci., 281: 735—767.

Kleintjens, L.A. and Koningsveld, R., 1982. Mean-field lattice—gas description of the system CO_2—H_2O. Sep. Sci. Technol., Spec. Iss., 17 (1): 215—233.

Konnerup-Madsen, J., Larsen, E. and Rose-Hansen, J., 1979. Hydrocarbon-rich fluid inclusions in minerals from the alkaline Illimaussaq Intrusion, south Greenland. Bull. Soc. Fr. Minéral., 102: 642—653.

Lagache, M. and Weisbrod, A., 1977. The system: two alkali feldspars—KCl—NaCl—H_2O at moderate to high temperatures and low pressures. Contrib. Mineral. Petrol., 62: 77—101.

Landis, G.P. and Rye, R.O., 1974. Geologic, fluid inclusion, and stable isotope studies of the Pasto Bueno tungsten—base metal ore deposit, northern Peru. Econ. Geol., 69: 1025—1059.

Le Bel, L., 1980. Caractéristiques de la phase fluide associée à la minéralisation de Cerro-Verde, Santa Rosa (Pérou). Mém. Bur. Rech. Géol. Min., 99: 129—139.

Leroy, J., 1978. The Margnac and Fanay uranium deposits of the La Crouzille district (western Massif Central, France): geologic and fluid inclusion studies. Econ. Geol., 73: 1611—1634.

Moore, W.L. and Nash, J.T., 1974. Alteration and fluid inclusion studies of the porphyry copper orebody at Bingham, Utah. Econ. Geol., 69: 631—645.

Nash, J.T. and Theodore, T.G., 1971. Ore fluids in the porphyry copper deposits at Copper Canyon (Nevada). Econ. Geol., 66: 385—399.

Potter II, R,W. and Brown, D.L., 1977. The volumetric properties of aqueous sodium chloride solutions from 0° to 500°C and pressures up to 2000 bars based on a regression of available data in the literature. U.S. Geol. Surv., Bull. 1421-C, 36 pp.

Poty, B. and Weisbrod, A., 1976. Les inclusions fluides comme guide pour la prospection des gites métallifères. Ann. Mines, Feb. 1976, pp. 1—7.

Ramboz, Cl., 1979. A fluid inclusion study of the copper mineralization in the southwest Tintic District (Utah). Bull. Soc. Fr. Minéral., 102: 622—632.

Ramboz, Cl., 1980. Géochimie et étude des inclusions fluides de gisements et indices d'étain—tungstène du Sud du Massif Central (France). Thesis, National Polytechnical Institute of Lorraine (I.N.P.L.), Nancy, 278 pp.

Ramboz, Cl., Pichavant, M. and Weisbrod, A., 1982. Fluid immiscibility in natural processes: use and misuse of fluid inclusion data, II. Interpretation of fluid inclusion data in terms of immiscibility. In: R. Kreulen and J. Touret (Guest-Editors), Current Research on Fluid Inclusions. Chem. Geol., 37: 29—48 (this special issue; in this paper referred to as Part II).

Ricci, J.E., 1951. The Phase Rule and Heterogeneous Equilibrium, Dover, New York, N.Y., 505 pp.

Roedder, E., 1971. Fluid inclusion studies on the porphyry-type ore deposits at Bingham, Utah; Butte, Montana; and Climax, Colorado. Econ. Geol., 66: 98—120.

Roedder, E., 1976. Fluid inclusion evidence on the genesis of ores in sedimentary and volcanic rocks. In: K.H. Wolf (Editor), Handbook of Stratabound and Stratiform Ore Deposits, Vol. 2. Elsevier, Amsterdam, pp. 67—110.

Roedder, E., 1977. Fluid inclusion studies of ore deposits in the Viburnum Trend, southeast Missouri. Econ. Geol., 72: 474—479.

Roedder, E., 1981. Natural occurrence and significance of fluids indicating high P—T conditions. In: D.T. Rickard and F.E. Wickman (Editors), Chemistry and Geochemistry of Solutions at High Temperatures and Pressures. Phys. Chem. Earth, 13/14: 9—40.

Roedder, E. and Bodnar, R.J., 1980. Geologic pressure determinations from fluid inclusion studies. Annu. Rev. Earth Planet. Sci., 8: 263—301.

Roedder, E. and Coombs, D.S., 1967. Immiscibility in granitic melts, indicated by fluid inclusions in ejected granitic blocks from Ascension Island. J. Petrol., 8(3): 417—451.

Rowlinson, J.S., 1969. Liquids and Liquid Mixtures. Butterworth, London, 374 pp.
Rye, R.O. and Sawkins, F.J., 1974. Fluid inclusion and stable isotope studies on the Casapalca Ag—Pb—Zn- Cu deposit, central Andes, Peru. Econ. Geol., 69: 181—205.
Schneider, G.M., 1970. Phase equilibria in fluid mixtures at high pressures. Adv. Chem. Phys., 17: 1—42.
Schneider, G.M., 1972. Phase behaviour and critical phenomena in fluid mixtures under pressure. Ber. Bunsenges. Phys. Chem., 76: 325—331.
Seward, T.M. and Franck, E.U., 1981. The system hydrogen—water up to 440°C and 2500 bar pressure. Ber. Bunsenges. Phys. Chem., 85: 2—7.
Sourirajan, S. and Kennedy, G.C., 1962. The system H_2O—NaCl at elevated temperatures and pressures. Am. J. Sci., 260: 115—141.
Spooner, E.T.C., 1980. Cu-pyrite mineralization and seawater convection in oceanic crust — The ophiolitic ore deposits of Cyprus. In: D.W. Strangway (Editor), The Continental Crust and Its Mineral Deposits. Geol. Assoc. Can., Spec. Pap., 20: 685—704.
Swanenberg, H.E.C., 1979. Phase equilibria in carbonic systems and their application to freezing studies of fluid inclusions. Contrib. Mineral. Petrol., 68: 303—306.
Takenouchi, S. and Kennedy, G.C., 1964. The binary system H_2O—CO_2 at high temperatures and pressures. Am. J. Sci., 262: 1055—1074.
Takenouchi, S. and Kennedy, G.C., 1965. The solubility of carbon dioxide in NaCl solutions at high temperatures and pressures. Am. J. Sci., 263: 445—454.
Tödheide, K. and Franck, E.U., 1963. Das Zweiphasengebiet und die Kritische Kurve im System Kohlendioxid—Wasser bis zu Drücken von 3500 bar. Z. Phys. Chem., Neue Folge, 37: 387—401.
Tsiklis, D.S., 1952. Fluid immiscibility at elevated pressure in the system NH_3—N_2. Dokl. Akad. Nauk S.S.S.R., 86: 993—995 (in Russian).
Tsiklis, D.S. and Maslennikowa, W.J., 1965. Limited mutual solubility of the gases in the H_2O—N_2 system. Dokl. Akad. Nauk S.S.S.R., 161: 645—647.
Urusova, M.A., 1975. Volume properties of aqueous solutions of sodium chloride at elevated temperatures and pressures. Russ. J. Inorg. Chem., 20: 1717—1721.
Weisbrod, A., 1980. Interactions between magmas, rocks and aqueous solutions at the late- to post-magmatic stages in granitoids and associated ore deposits. 26th Int. Geol. Congr., Paris, Abstr. Pap., 1: 103.
Weisbrod, A., 1981. Fluid inclusions in shallow intrusives. In: L.S. Hollister and M.L. Crawford (Editors), Short Course in Fluid Inclusions: Applications to Petrology. Mineralogical Association of Canada, Calgary, Alta., pp. 241—271.
Weisbrod, A. and Poty, B., 1975. Thermodynamics and geochemistry of the hydrothermal evolution of the Mayres Pegmatite. Petrologie, 1: 1—16; 89—102.
Weisbrod, A., Poty, B. and Touret, J., 1976. Les inclusions fluides en pétrologie—géochimie — Tendances actuelles. Bull. Soc. Fr. Minéral. Cristallogr., 99: 140—152.
Welsch, H., 1973. Die Systeme Xenon—Wasser und Methan—Wasser bei höhen Drücken und Temperaturen. Thesis, Institute of Physical Chemistry, University of Karlsruhe, Karlsruhe.
Wilson, J.W.J., Kesler, S.E., Cloke, P.L. and Kelly, W.C., 1980. Fluid inclusion geochemistry of the Granisle and Bell porphyry copper deposits, British Columbia. Econ. Geol., 75: 45—61.
Ypma, P.J.M., 1963. Rejuvenation of ore deposits as exemplified by the Belledone metalliferous province. Ph.D. Thesis, University of Leiden, Leiden (unpublished).

PUBLICATION VI : Fluid immiscibility in natural processes : use and misuse of fluid inclusion data. II : Interpretation of fluid inclusion data in terms of immiscibility.

Chemical Geology, 37 (1982) 29—48
Elsevier Scientific Publishing Company, Amsterdam — Printed in The Netherlands

FLUID IMMISCIBILITY IN NATURAL PROCESSES: USE AND MISUSE OF FLUID INCLUSION DATA
II. Interpretation of Fluid Inclusion Data in Terms of Immiscibility

CLAIRE RAMBOZ[1], MICHEL PICHAVANT[1] and ALAIN WEISBROD[1,2]

[1] *Centre de Recherches Pétrographiques et Géochimiques, 54501 Vandoeuvre-les-Nancy (France)*
[2] *École Nationale Superieure de Géologie, 54001 Nancy Cedex (France)*

(Accepted for publication April 14, 1982)

ABSTRACT

Ramboz, Cl., Pichavant, M. and Weisbrod, A., 1982. Fluid immiscibility in natural processes: use and misuse of fluid inclusion data, II. Interpretation of fluid inclusion data in terms of immiscibility. In: R. Kreulen and J. Touret (Guest-Editors), Current Research on Fluid Inclusions. Chem. Geol., 37: 29—48.

Phase equilibrium analysis of the relevant systems together with the application of the principles of chemical equilibrium put severe constraints on the interpretation of fluid inclusion data in terms of immiscibility (in Part I).

Following from that point, the major limits on the accuracy, and even the validity, of fluid inclusion quantitative data and their interpretation in terms of fluid composition and density are briefly discussed.

The practical implications of the general constraints (temperature, pressure, topology of the fluid systems) are envisaged. Emphasis is laid on some important consequences such as: the use of isochore intercepts (and the possible resulting interpretation of fluid mixing rather than unmixing), the case of highly saline inclusions, the identification and interpretation of heterogeneous trapping.

The composition and density constraints on coexisting fluids are presented, and illustrated by natural examples.

Taking into account all the measurable parameters in fluid inclusions (volume, temperature and nature of phase transitions, more or less complete individual spectroscopic analyses), all the available experimental data, and all the theoretical constraints, may be long and difficult. However, it is most generally very informative and productive although part of these data is often sufficient to deny unmixing. Nevertheless, a final example on metamorphic fluids demonstrates how such an approach can "prove", and also characterize a fluid unmixing during a geologic process.

1. INTRODUCTION

Part I (Pichavant et al., 1982) of these two papers essentially deals with precise definitions and an application of the principles of chemical equilibrium to the topology of fluid systems and to the behaviour of the

0009-2541/82/0000—0000/$02.75

constant-volume—constant-composition systems that fluid inclusions are supposed to be.

First-sight microscopic examination of fluid inclusions is often sufficient to suggest immiscibility. The purpose of this Part II is to show how the results and data obtained in Part I can — and must be — used as severe constraints in interpreting the microthermometric, volumetric and composition data on fluid inclusion, in order to strengthen — or invalidate — the hypothesis of immiscibility.

2. LIMITS ON THE INTERPRETATION OF FLUID INCLUSION DATA

The major purpose of fluid inclusion studies is to estimate, as accurately as possible, the nature and the chemical–physical properties (namely the chemical composition and the molar volume) of the fluids present in the studied rock system at the time these fluids where trapped. Unlike the data collected on experimental solid and/or fluid systems or on natural solid systems (rocks and minerals), the "*PVTX* data" on fossil hydrothermal fluids trapped in inclusions are not directly measured. These data are mostly derived from microthermometric measurements through several interpretative steps which are the base of a good microthermometric procedure. Each step of the procedure defines limits to an extensive interpretation of the phase relations and transitions observed in fluid inclusions.

It is not our purpose to discuss this point in great detail; extensive treatments of the problems have been published elsewhere (see Roedder, 1976, 1979, 1981; Hollister and Crawford, 1981), and they just will be briefly summarized below.

2.1. Limits due to the inclusions themselves

Fluid inclusions are not always faithful witnesses of natural fluids for the following reasons:

(a) Inclusion content can be dramatically changed by necking-down, leaking, or natural decrepitation. These phenomena can often be detected or at least suspected.

(b) Chemical and/or physical changes may occur in the inclusions after trapping by reactions with the host-mineral, with a possible subsequent change of the volume and/or the composition of the inclusion. For the same reason, the assumption of constant-volume—constant-composition (isochoric—isopleth behaviour) may not be valid during the microthermometric study of an inclusion if high temperatures are involved and/or the host-mineral is very soluble.

(c) Heterogeneous trapping consists in trapping more than one phase in the same inclusion. Some interesting consequences of this phenomenon are given below.

In general, mistakes coming from such phenomena can be avoided:

(1) by extensive and precise microscopic observations and statistically significant microthermometric measurements; and (2) on the test of the geological interpretation of these microthermometric results by comparison with the other geochemical, mineralogical and petrological data.

2.2. Limits due to uncertainties about space—time relationships between the various sorts of inclusions

Most often, many types of inclusions coexist in one sample. Determining whether or not some of them were trapped at the same time and/or in the same network of microfractures is obviously quite critical. It must be done by careful examination of the location, shape, etc., of the inclusions, the features of the microfractures intercepts, and also by examining the microthermometric results. This part of the work certainly is the most difficult, the most "naturalistic", and requires much experience.

2.3. Limits due to quantitative informations available from fluid inclusions

The determination of the composition and density of inclusion fluids is based on: (1) the estimation of the volume fraction of the coexisting phases at a specified temperature; (2) the measurements of the temperature of the phase transitions observed in the inclusions; (3) the direct analyses of the composition of the inclusion fluids, when it is possible; and (4) the number and quality of the available experimental data.

(a) The volume estimates are carried out on a two-dimensional projection (surface of a thin section). Their accuracy largely depends on the shape of the cavities.

(b) The temperatures of phase transitions can generally be measured with a very good precision. However, some of these phase transitions are sometimes quite difficult to see under the microscope, and their corresponding temperatures may be erroneous. Some cannot be measured, just because they occur outside the *TP* ranges that can be reached with a microthermometric apparatus. Difficulties of the same sort arise from the fact that a phase may not be seen at all because of its shape and insufficient volume. This is the case, for instance, of the thin film of liquid surrounding a large bubble of gas (<10—15 vol.% liquid): the temperature of the (L + V → V) transition cannot be measured, since the liquid cannot be seen.

(c) During the course of a microthermometric study of an inclusion, some phase transitions can be metastable or, more often, concern stable but local (partial) equilibrium processes. Such a behaviour is common at low temperature but is also possible at higher ones; it must be taken into account when interpreting the corresponding measured values (for further details on that point, see Ramboz, 1980b).

(d) Interpretation of the microthermometric results in terms of fluid composition and density is possible only if quantitative data on the system

dealt with are available. These data must be accurate enough and cover a range of T, P, V, X, etc. conditions large enough to be useful. Presently, the one-component systems are very well known, in a more or less wide range on TP conditions. A few binary systems are well known, but for most of them the data are insufficient or/and inaccurate, or even do not exist in some $TPVX$ ranges of interest. Some partial data are available in limited ranges of $TPVX$ conditions for a very few ternary systems. Recently, a few authors have developed equations of state in the one-phase domain relevant to geologic systems and conditions (e.g., Holloway, 1977, 1981; Touret and Bottinga, 1979). It must be kept in mind that: (1) the precision of an equation of state depends on the accuracy allowed by the system considered and method followed and on the number of the experimental data available (Heyen et al., 1982); and (2) there is no guarantee on the reliability of such an equation when used outside the $TPVX$ domains where the experimental data are available. Semiquantitative estimates can presently be obtained for the liquid—vapour equilibria in systems such as H_2O—CO_2, H_2O—CH_4, etc., using the equations of state of the lattice—gas model (Kleintjens and Koningsveld, 1982).

3. IMMISCIBILITY CONSTRAINTS

3.1. Constraints on the homogenization phenomena

3.1.1. General constraints. Most generally, the number of phases observed in an inclusion at room temperature decreases when temperature increases. Bulk homogenization occurs by fluid homogenization T_h (L + V → L, or V, or F) or melting of a solid T_m [S (+F) → F] at a particular ($TPVX$) point on the corresponding phase boundary. From this point originates a particular isochore which will never intersect again the same phase boundary. Both the coordination point and the isochore are characteristic of the composition and the density of the inclusion fluid. If homogeneous trapping is assumed, the inclusion fluid can have been trapped anywhere on the isochore.

The first consequence of this result is that there is theoretically no way to prove that an individual inclusion fluid was trapped on the originating point of the isochore (i.e. on the phase boundary where several immiscible phases coexist), rather than at any other point (i.e. in the homogeneous fluid one-phase domain) of the isochore. Actually, immiscibility could nevertheless be considered from other constraints such as reasonably accurate temperature and pressure of trapping, estimated for instance from mineralogical studies and consistent with the immiscibility TP domain of the inclusion fluid. As shown below, heterogeneous trapping can also provide good evidence for immiscibility.

Another major consequence is that, if a fluid is suspected to have been trapped on a given phase boundary (e.g., on a fluid immiscibility surface),

the temperature and pressure of entrapment must be the ones measured when crossing the same phase boundary is observed in the corresponding inclusions upon heating; in any case, they can never be higher (the trapping temperature can be lower than the bulk homogenization temperature in case of heterogeneous trapping).

A commonly used criterion for fluid unmixing (L + V, or F_1 + F_2) is the coexistence in the same rock, of two different types of inclusions, that might correspond to two immiscible phases. However, besides some other constraints discussed below, there are three that must be emphasized; they may look trivial, but having not taken them into account led several authors to misinterpretations:

(1) The two types of inclusions must occur in the same regions of the same sample, and there must be good evidence of their contemporaneous trapping.

(2) The two types of inclusions must homogenize at the same temperature, or more realistically within the same range of temperature (because trapping is not an instantaneous and strictly isothermal—isobaric process). One type must homogenize into a liquid (V + L → L), the other must homogenize into a vapour (V + L → V). It must be reminded that this necessary condition is not sufficient.

(3) Upon heating, the pressures in the two types of inclusions before homogenization are different (because of the difference in their compositions and densities). However, and although there may be exceptions, the pressure difference is generally not sufficient to allow the two types to decrepitate at very different temperatures unless their size and shape are very different (Leroy, 1979). Anyway, the pressures reach the same value (trapping pressure) at homogenization temperature. Therefore, if one inclusion type decrepitates before homogenizing, the other type must behave similarly.

3.1.2. About the use of isochore intercepts. Several authors have used the fact that, in some cases, the isochores corresponding to two types of fluid inclusions of contrasted compositions closely associated in a rock (most often a brine and a volatile-rich gas) intercept on a *TP* projection (Crawford et al., 1979; Guha et al., 1979; Cuney, 1980; Guilhamou et al., 1981; and many examples in the Soviet literature). Generally, this situation is interpreted in terms of coexisting ("boiling") immiscible liquid and vapour, trapped separately at the *TP* conditions of the intercept. When the inclusions have homogenized before the temperature of the intercept, it is obvious that such an interpretation is erroneous. Very often the bulk homogenization of the volatile-rich inclusions, usually described by the system H_2O—CO_2 (or H_2O—CH_4), or even by pure CO_2 (or CH_4), cannot be observed. So, it could be argued that this homogenization could occur in the *TP* range inferred for unmixing. However, it must be noticed that, for such inclusions with CO_2 densities between 0.1 and 1 g cm^{-3}, which covers al-

most all the range of geologically relevant situations, the *maximum* homogenization temperature would be around 250—300°C (below 270°C if the inclusions decrepitate before this temperature) in the H_2O—CO_2 system, or around 400—500°C (probably often less) in the H_2O—CO_2—NaCl system with less than 10 wt.% NaCl in the aqueous phase, which is already far beyond the maximum relevant salinity in fluids of this sort. These temperatures are often much lower than many of the temperatures proposed by this "method". Moreover, the recorded homogenization temperatures for the associated brines are clearly measurable, and always lower than the temperatures estimated for the unmixing.

As a conclusion, it is clear that the two types of inclusion cannot represent the liquid and the vapour of an unmixed fluid, at the *TP* conditions of the intercept of their respective isochores — or at any other *TP* conditions. This result can be easily verified everytime the two isochores intercept at a temperature and a pressure that can be reached with a microthermometric apparatus: when heated to these values, the two types of inclusion fluids will remain homogeneous.

Very often, the fact that the isochores crosscut on a *TP* projection has no special significance. However, if there is very good evidence for such pairs of fluids to have been trapped at about the same time, another explanation can be given, which is just the opposite of immiscibility: mixing of fluids of different compositions, and possibly different origin.

Because of high rates of diffusion and usually large physical mobility in liquids (laminar, whirling, etc., flows), metastable immiscibility of coexisting miscible fluids cannot persist very long. Experimental work on (liquid + vapour) boundaries indicates that chemical equilibrium is generally obtained within less than a few days, or even a few hours. Compared to the rates of fluid dynamics, growth of crystals, healing of fractures and therefore of fluid inclusion trapping in natural processes, these values are small. So, the two fluids cannot have been trapped at exactly the same time and the same place. Nevertheless, they can have been trapped in two different networks of fractures and microfractures very close to each other, and/or at two different times also very close to each other. In such cases, the *T*- and *P*-coordinates of the intercept of the isochores are quite good estimates of the *T* and *P* conditions of trapping, although evidence has been given for the co-occurrence of two mechanically separated fluids at the same structural level and still at different fluid pressures (Tissot and Welte, 1978).

Mixing of various amounts of the two different fluids results in fluids of intermediate compositions and densities. The corresponding inclusions should not be confused with inclusions formed by heterogeneous trapping which obviously involves stable immiscibility.

Fluid mixing has been proposed as a common geologic process, mainly from stable-isotope geochemistry, in particular in porphyry-type deposits (Sheppard et al., 1971) but has been seldom suggested from fluid inclusion studies (Denis et al., 1980; Ramboz, 1980a). Generally speaking, fluid mixing is from a geochemical point of view, as interesting as fluid unmixing.

3.1.3. Highly "saline" inclusions. On an isopleth section (system of constant composition) the (L + V) immiscibility domain is limited by the BPC and DPC immiscibility curves that originate on the saturation curves, at two points whose position depends on the composition. As previously shown about the system H_2O—NaCl (see Part I) this results in only two possible situations for a pair of two immiscible fluids:

(1) The liquid phase is not saturated with respect to any solid. In this case, all the solids that might be present in the inclusion at $T < T_h$ must have been dissolved at temperatures $T_m < T_h$. In other words, the inclusion should not contain any solid when it homogenizes.

(2) The liquid phase is saturated with respect to one (or several) solid(s). In this case the final dissolution (or melting) of this (or these) solid(s) and the liquid—vapour homogenization must occur at the same temperature $T_m = T_h$ (the dotted area b in Figs. 1 and 2). In fact, heterogeneous trapping of variable amounts of solid(s) together with the liquid can be expected in a "saturated boiling solution". This would result in scattering and increasing the bulk salinity of the inclusions and therefore the melting temperatures, with no large change in the bulk density (and therefore in the fluid homogenization temperature). The fact that the lowest values of T_m are in the same range as the mean T_h-values is a good indication of such a phenomenon (the dotted area a in Figs. 1 and 2). Most natural fluids are always saturated with respect to some solids, particularly silicates. Tiny grains of such minerals transported in the flowing fluid(s), can be trapped anytime in inclusions. Their melting (or dissolution) temperature is generally very high, often beyond the working temperature range of usual microthermometric apparatus. Although the consequences of such an heterogeneous trapping may be of great interest (saturation of the trapped fluid with respect to a particular mineral, for instance), the T_m-values of those solids must not be taken into account in the condition $T_m \leqslant T_h$ for a boiling fluid. In some cases, the persistence of a mineral after fluid homogenization ($T_m > T_h$) may also be due to its low rate of dissolution, and must not be taken into account either. However, such situations could be checked by repeating low-rated heating experiments.

Arguments have been given and mechanisms proposed that would make the persistence of "soluble" salts (e.g., chlorides) after fluid homogenization to be consistent with fluid unmixing (Chivas and Wilkins, 1977; Eastoe, 1978). None of them is satisfactory. As a matter of fact, and except for the cases mentioned above, any inclusion fluid with real melting temperature(s) of the solid(s) (T_m) significantly higher than the temperature of fluid homogenization (T_h) (the dotted area c in Figs. 1 and 2) cannot have been trapped on the (L + V) boundary, and therefore cannot represent the liquid phase of an unmixed fluid. Among other possible origins for such inclusions, the following two can be mentioned: trapping of vapour-free alkali-chloride(s)-saturated solutions (Cloke and Kessler, 1979), or homogeneous undersaturated very concentrated brines trapped at high temperatures and pressures (Ramboz, 1979; Denis et al., 1980; Weisbrod, 1980, 1981).

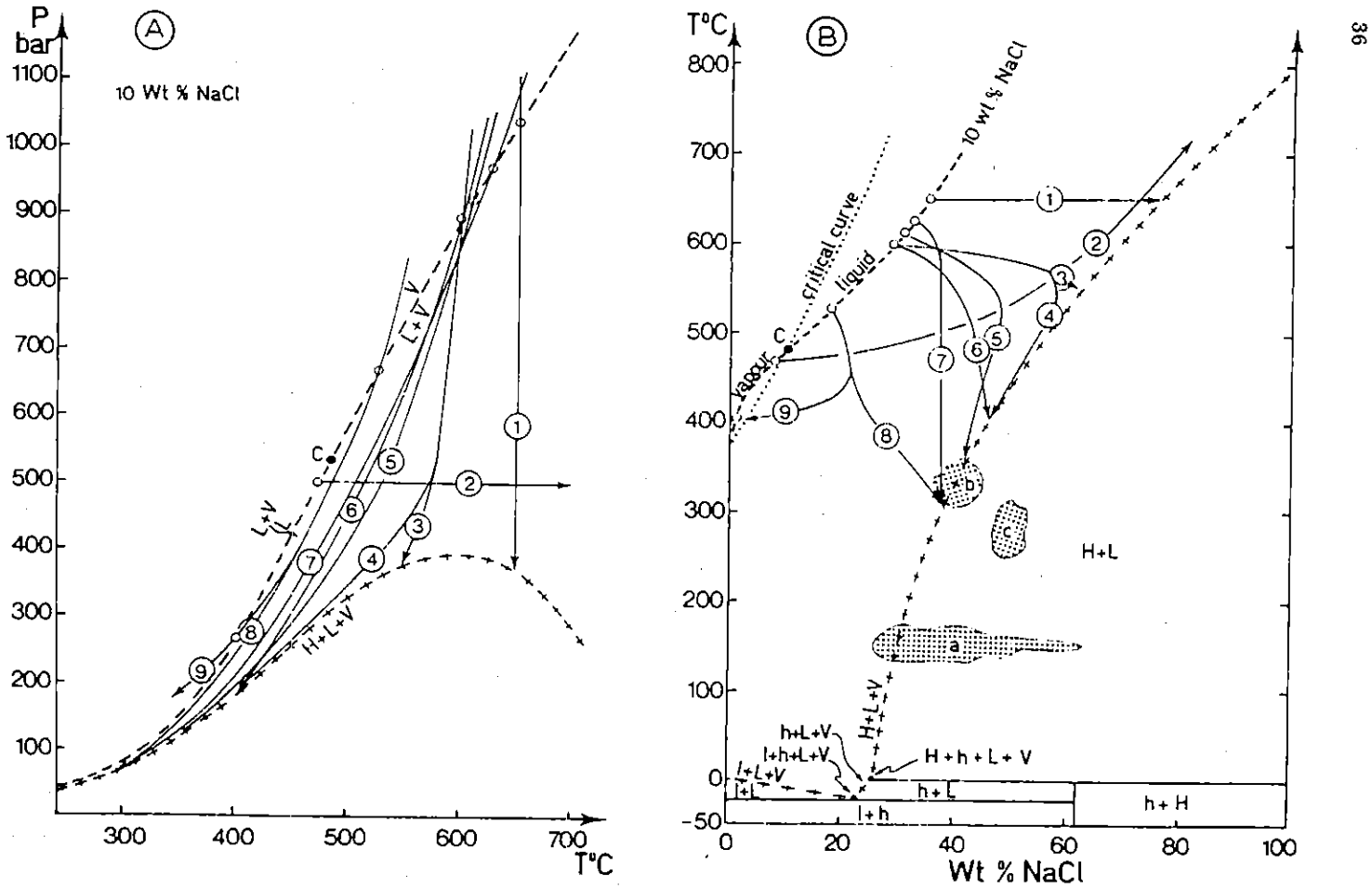
A
P
bar
10 Wt % NaCl
1100
1000
900
800
700
600
500
400
300
200
100
300
400
500
600
700
T°C
C
L+V
L
V
H+L+V
1
2
3
4
5
6
7
8
9
B
T°C
800
700
600
500
400
300
200
100
0
-50
10 wt % NaCl
critical curve
liquid
vapour
C
H+L
a
b
c
H+L+V
h+L+V
l+h+L+V
l+L+V
l+L
h+L
l+h
h+H
H+h+L+V
0
20
40
60
80
100
Wt % NaCl

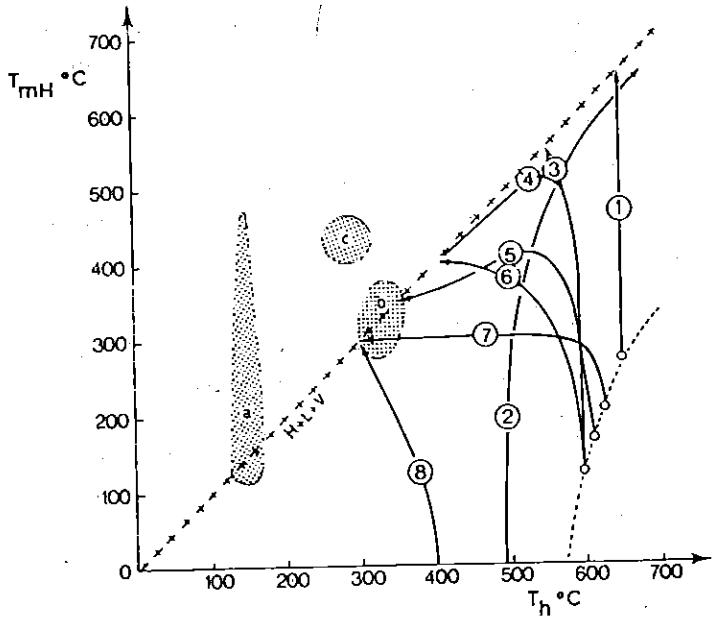

Fig. 2. T_h—T_m trends of liquids during unmixing of a 10 wt.% NaCl aqueous solution along the cooling gradients indicated in Fig. 1A.
Same legend as to Fig. 1. T_h: homogenization temperature; T_{mH}: melting temperature of halite.

3.1.4. Heterogeneous trapping. Heterogeneous trapping has been already mentioned several times in this paper. Entrapment of two fluids in the same inclusion obviously imposes that these fluids were coexisting in tight contact to each other, and therefore were at (or close to) equilibrium at the place and time of trapping: *heterogeneous trapping is a very simple and very good evidence of fluid immiscibility*.

The very variable relative amounts of each phase from an inclusion to another result in scattered densities, degrees of filling at room temperature,

---

Fig. 1. Temperature—pressure—composition paths of unmixed fluids in geologic processes.
A. *TP* paths for fluids in the H_2O—NaCl system. The paths are labelled *1* to *9*. *1* is isothermal, *2* is isobaric; paths *3* to *9* correspond to possible *TP* gradients such as those estimated in hydrothermal processes associated with shallow magmatism (porphyry copper deposits, pegmatites, etc.) Cooling and/or expansion of a 10 wt.% NaCl aqueous fluid along these gradients would result in fluid unmixing, and composition trends such as those indicated in (B) and Fig. 2.
B. Temperature—salinity trends of liquids (or vapours) during unmixing of a 10 wt.% NaCl aqueous solution along the gradients indicated in (A). Some examples, labelled a, b, c, of other frequent types of *TX* plots of fluid inclusions are also shown (see text).
I = ice; H = halite; h = hydrohalite; L = liquid; V = vapour. *Dashed line*: composition of the liquid (or the vapour) at equilibrium with a 10 wt.% NaCl immiscible vapour (or liquid), i.e. along the two-fluid boundary of (A). C = critical point for a 10 wt.% NaCl aqueous solution.

bulk compositions, and therefore homogenization temperatures. The latter will be shifted towards values higher than the actual trapping (unmixing) temperatures for a given grade of heterogeneity of trapping at specified T and P. The magnitude of the possible increases of T_h depends on the considered system.

Trapping an extremely thin film of liquid around a bubble of vapour may be a common mechanism in some cases: it would systematically result in mean values of T_h slightly, and in some cases significantly higher, for the vapour than for the related liquid.

As illustrated in Fig. 3, the criteria for heterogeneous trapping are: (1) simultaneous trapping of all the inclusions of the population of interest; (2) serious evidence, indicating that no leaking and/or necking-down can be suspected; (3) very scattered degree of filling, homogenization temperatures, compositions; and (4) T_h frequency distribution diagrams (T_h histograms) non-symmetrical and flattened, particularly towards high temperatures, but more or less similar for the liquid and the vapour (when both are available).

3.2. Constraints on composition

As a simple consequence of the principles of chemical equilibrium, any component i (or chemical species) is distributed between two immiscible fluid phases L and V, according to:

$$K^{LV}_{D,i} = X^V_i / X^L_i$$

Every distribution coefficient $K^{LV}_{D,i}$ is constant at any specified temperature, pressure and bulk composition. Since T and P are estimated from the homogenization temperature T_h of the two possibly immiscible fluids, and provided that all the necessary data are available, comparing the calculated and measured values of K_D for the largest number of components certainly is one of the best tests for immiscibility. Anyway, the relevance of the measured values of K_D should be systematically checked.

Most commonly, solute species ("salts") are strongly partitioned in favour of the liquid phase, except of course in the close vicinity of the critical conditions where $K_D = 1$. This is so striking at low temperatures and pressures that, in the H_2O–NaCl system below 300°C and 100 bar for example, a pressure drop of only a few bars would result not only in boiling a practically NaCl-free vapour, but also in almost instantly saturating the liquid with respect to halite. On the other hand, the partition is weaker at high temperatures and pressures; under such conditions, significant amounts of alkali chloride can enter the vapour phase.

Some examples of composition trends of the liquid phase at equilibrium with a vapour are given in Figs. 1 and 2. These trends result of unmixing H_2O–NaCl aqueous solutions along a few chosen TP "cooling paths" such as those expected for instance in porphyry-type deposits.

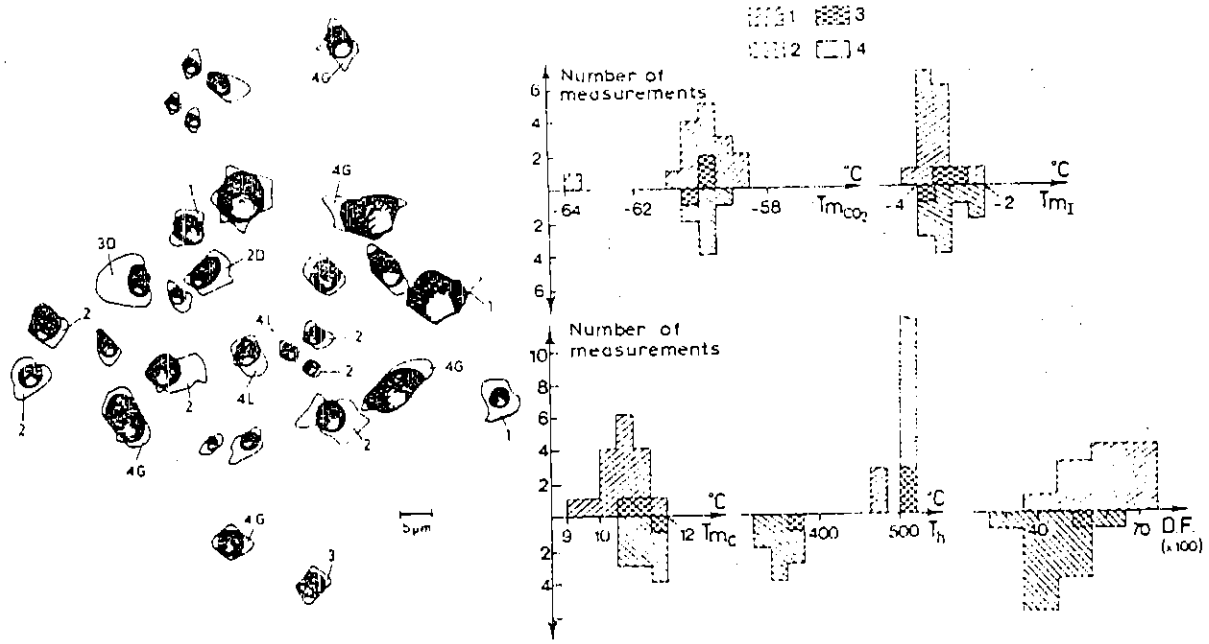

Fig. 3. An example of heterogeneous trapping in a quartz–cassiterite vein from Saint-Cierge, Massif Central, France (Ramboz, 1980a).
Distribution of the inclusions in hyaline quartz and related microthermometric results. *1* = homogenization to the vapour; *2* = homogenization to the liquid; *3* = critical homogenization; *4* = inclusions remaining unhomogenized below 550°C, L = expansion of the liquid phase upon heating (liquid homogenization seen or expected); G = expansion of the vapour phase upon heating (gas homogenization seen or expected); D = inclusion decrepitated below 550°C; T_{mCO_2} = melting temperature of CO_2; T_{mI} = melting temperature of ice; T_{mC} = melting temperature of clathrate; T_h = bulk homogenization temperature; DF: degree of filling of the inclusion at 20°C. Data points above the horizontal axis: bulk homogenization into the vapour; below the horizontal axis: bulk homogenization into the liquid.

All the common volatile species are partitioned in favour of the vapour phase. The distribution coefficient increases with increasing "volatility", according to the following order:

$SO_2 < H_2S < CO_2 < CH_4 < N_2 < H_2$

Unfortunately, there are almost no quantitative data on the partition of components between the coexisting immiscible phases in such complex water—volatiles—salts system. Taking into consideration the general properties mentioned above and the available data on the system H_2O—NaCl—CO_2 yields the following results for this ternary system (these results remain probably valid, at least qualitatively for systems such as H_2O—CO_2—CH_4—N_2—alkali chlorides):

(1) The coexisting fluids generated by unmixing are always ternary mixtures, even under *TP* conditions where the two-phase domain extends to the H_2O—CO_2 and H_2O—NaCl binary end-members. In particular, the presence of CO_2 in a liquid believed to coexist with a CO_2-rich vapour must always

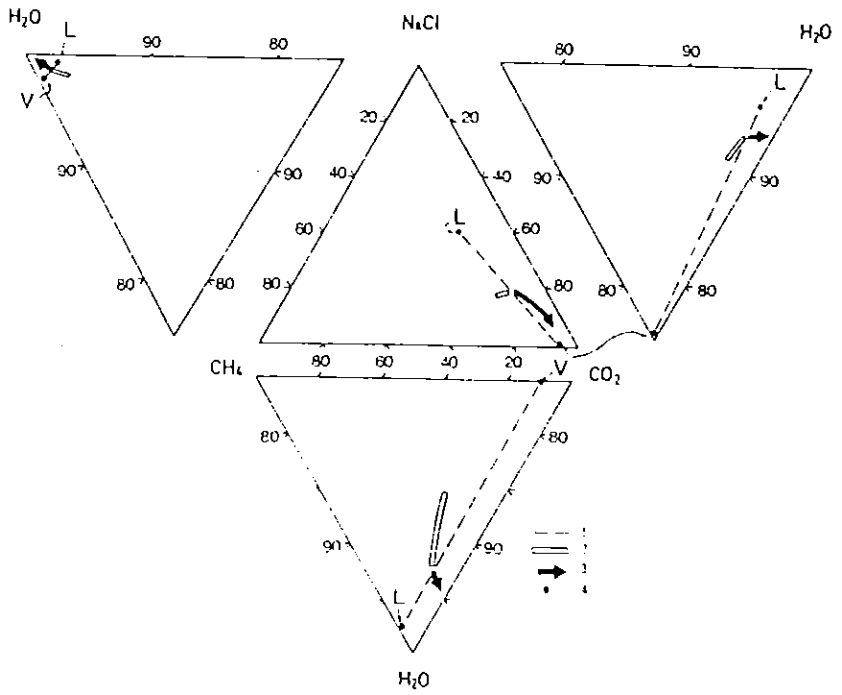

Fig. 4. Reconstitution of the evolution of the chemical composition of the fluid during unmixing in a quartz—cassiterite vein from Saint-Cierge, Massif Central, France (Ramboz, 1980a).
The composition trends are presented on the faces of the H_2O—NaCl—CO_2—CH_4 composition tetrahedron. *1* = tie line, *2* = primary CO_2-bearing vapours; *3* = later CO_2-bearing liquids; *4* = composition of the coexisting fluids. L = liquid; V = vapour. Data are summarized in Table I.

be checked. This can be done easily: (a) by crystallizing a gas-hydrate on cooling, (b) by demonstrating inconsistencies between the density (obtained from T_h and T_{mI} measurements; Potter and Brown, 1977) and the degree of filling of the inclusion (Ramboz, 1980a,b), or (c) by direct analysis, using a Raman microprobe.

(2) The distribution coefficient of NaCl between coexisting liquid and vapour significantly decreases with increasing pressure (see Part I).

A fluid immiscibility in the system H_2O—CO_2—CH_4—NaCl has been predicted and specified, during the hydrothermal evolution of a quartz—cassiterite vein from the southeastern part of the Massif Central, France, using fluid inclusion studies (Ramboz, 1980a). The composition of the coexisting phases has been calculated from microthermometric data and Raman microprobe analysis of the non-aqueous part of the inclusions. The results are indicated in Fig. 4 and Table I; see also Fig. 3.

Most of the inclusions observed in quartz trapped the fluid before and after unmixing. The composition of this fluid (moderate salinity, 1—5 wt.% NaCl and moderate CO_2 content) contrasts with the composition of the liquid (much higher salinity, lower CO_2 content) and of the vapour (much higher CO_2 content, lower salinity) generated by unmixing of this fluid.

TABLE I

Compositions of the homogeneous and unmixed fluids in a quartz—cassiterite vein from Saint-Cierge, Massif Central, France (Ramboz, 1980a, summary of the analytical results)

Average homogeneous fluid before unmixing

$DF \simeq 0.50$
$DF_v \simeq 0.20$
$-60.9°C \leqslant T_{mCO_2} \leqslant -59.2°C$
$-5.4°C \leqslant T_{mI} \leqslant -5°C$
$10.5°C \leqslant T_{mC} \leqslant 11.5°C$
X_{CH_4} (Raman) $\simeq 0.2$

Unmixed fluids

Vapour	Liquid
$DF \simeq 0.1$	$DF \simeq 0.6$
$DF_v \simeq 0.5$	$DF_v \simeq 0.05$
$-63.5°C \leqslant T_{mCO_2} \leqslant -58.5°C$	$-60.6°C \leqslant T_{mCO_2} \leqslant -58.8°C$
T_{mI} ?	$9°C < T_{mC} < 13°C$
X_{CH_4} (Raman) $\simeq 0.05$	X_{CH_4} (Raman) $\simeq 0.4$
	$-10°C < T_{mI} < -4°C$

DF = degree of filling of the inclusion at room temperature; the subscript v refers to the non-aqueous part. T_m = temperature of final melting (°C); CO_2 = solid CO_2; I = ice; C = clathrate; X_{CH_4} = mole fraction of CH_4 in the non-aqueous part, analysed by Raman spectroscopy (Dhamelincourt et al., 1979).

Such a gap between the composition of homogeneous fluids and boiling fluids within a same hydrothermal event is generally characteristic of unmixing and confers on this phenomenon most of its importance in hydrothermal processes. It is generally suggested by striking differences in some of the physical properties of the corresponding inclusions (e.g., low melting temperature of ice on the aqueous "liquid" and large amount of liquid CO_2 at low temperature in the carbonic "vapour" generated by unmixing).

3.3. Constraints on density

A last point that can — and should — be tested everytime immiscibility is

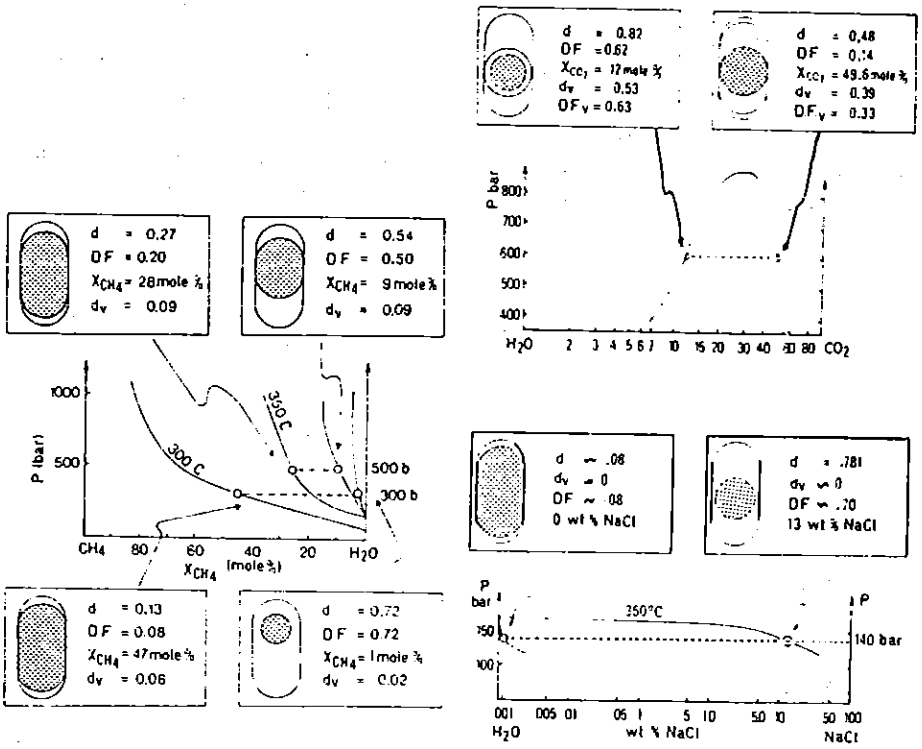

Fig. 5. An illustration of the *TPVX* relations along an immiscibility surface.
The fluid inclusions are supposed to belong to the three most important "binary" systems: H_2O—CH_4 (data from Welsch, 1973), H_2O—CO_2 (data from Takenouchi and Kennedy, 1964; the volumes are calculated with the aid of Kleintjens and Koningsveld's (1982) equation), H_2O—NaCl (data from Sourirajan and Kennedy, 1962; volumes from Hilbert, 1979). Inclusions are shown at room temperature. The carbon-bearing molecules dissolved in water at this temperature have a very little effect on the calculated value of the degree of filling (H_2O—CH_4 and H_2O—CO_2 systems) and have been neglected.
DF = degree of filling of the inclusion at room temperature; d = bulk density (g cm^{-3}); X_{CH_4}, X_{CO_2} are the bulk molar fraction of CH_4, CO_2 in the inclusion, respectively. The subscript v refers to the non-aqueous (carbonic) part of the inclusion.

suspected, is to compare the molar volumes obtained from microthermometric measurements and spectroscopic analyses, on the two types of inclusions that are thought to represent the two immiscible fluids, with those calculated from experimental data. It is reminded that the bulk density of an inclusion can be measured: (1) by combining in appropriate proportions the densities of the two fluids present in the inclusion at any appropriate specified temperature, or (2) from the interpretation of bulk homogenization temperature and composition.

Such an approach is illustrated in Fig. 5 for the H_2O—CO_2, H_2O—CH_4 and H_2O—NaCl systems. The molar volumes predicted for the coexisting phases at specified *TPX* conditions, have been represented in terms of the degrees of filling of the inclusions at room temperature.

4. SUMMARY AND CONCLUSIONS

Because fluid immiscibility may be a common and important phenomenon in many geologic processes, and because it may yield very good estimates of temperature and pressure, its possible occurrence in a rock system must be carefully backed up, if not proved, everytime it is suspected.

Fluid inclusion studies remain the best tool — and often the only one — to achieve this purpose. However, care must be taken in interpreting fluid inclusion data in terms of immiscibility:

(1) The geometry of the phase equilibria in fluid systems obeys some strict rules that should be known. Any interpretation must take this geometry in the *TPX* space into account, not only qualitatively, but also quantitatively.

(2) If one or several solids are present in an inclusion, this inclusion can represent a phase of an unmixed fluid only if the melting temperature of the solid(s) T_m is not higher than the fluid homogenization temperature T_h ($T_m \leqslant T_h$). The case $T_m = T_h$ is characteristic of unmixing of a fluid saturated with respect to the solid(s).

(3) Any isochore originates at a point on an immiscibility boundary, and never intersects again the same boundary. Therefore, any fluid inclusion cannot unmix again once homogenized, and if unmixing is suspected, the temperature of entrapment is necessarily the temperature of homogenization T_h (L + V → L, or V).

(4) As a simple consequence of (3), two contrasted types of inclusions must homogenize (L + V → L *and* L + V → V) at the same temperature if they represent two immiscible fluids.

(5) Further evidence for immiscibility is obtained by comparing all the data that can be obtained by microthermometric, volumetric and chemical analyses with all the experimental and theoretical data available for the system of interest. Generally speaking, unmixing yields fluids of contrasted density and composition: high-density "liquid", enriched in dissolved salts, and poor in (but not free of) volatiles; and low-density vapour, rich in volatiles and poor in dissolved salts.

(6) Much care and experience are needed to evidence the contemporaneous entrapment of two supposed immiscible fluids, and to eliminate the effects of phenomena such as leaking, necking-down and heterogeneous trapping. However, the latter is in itself a very good indication for fluid unmixing.

(7) Mixing of fluids of different composition may result in fluid inclusions whose features should not be confused with those resulting of entrapment of immiscible fluid phases.

It may be thought that using all the informations, taking care of all the constraints and cross-checking all the data, as proposed in these papers and summarized above, often is not very realistic: microthermometric measurements and direct chemical analyses of fluid inclusions can be difficult, and for some of them sometimes impossible to obtain; experimental data and/or equations of state are missing for most of the relevant multicomponent systems at high temperatures and pressures. However, even with some analytical data missing and with approximating the natural fluids by simple ternary (or even binary) systems, it is very often possible to check (at least semiquantitatively) whether or not there are major inconsistencies between all the temperature, density, composition data collected from fluid inclusions and the experimental and theoretical data available on the system of interest.

In order to illustrate this final statement, an example has been chosen, which concerns complex immiscible fluids trapped in very small (5—10 μm) inclusions in concordant veinlets of quartz during the retrograde metamorphism of pelitic schists from Morse Basin, British Columbia, Canada (Hendel and Hollister, 1981). According to the authors, two types of inclusions coexist in the same healed microfracture. They homogenize at the same temperature (272 ± 2°C), one type (H_2O-rich) into a liquid, the other (CO_2-rich) into a vapour. These features, and some other facts (heterogeneous trapping in another microfracture), strongly suggest immiscibility. A pressure of 1—2 kbar is inferred for unmixing on account of the decrepitation of some of the inclusions at temperatures very close to the homogenization temperature.

The average bulk compositions of the two inclusion fluids have been recalculated from the analytical data of Hendel and Hollister, taking into account the salt (considered as pure NaCl) and CO_2 dissolved in water. These compositions and the bulk volumes compare very favourably with the experimental data now available on the H_2O—CO_2—NaCl system (Gehrig, 1980) around the temperature and pressure estimated for the unmixing (Fig. 6; Table II).

In such a case, it is clear that the hypothesis of fluid unmixing is so strongly supported that there can be (almost) no doubt about the actual occurrence of this process.

At the end of a careful study on inclusions, the first-sight features of which strongly suggest boiling, it may also happen that the hypothesis of

TABLE II

Chemical and physical properties of metamorphic fluids in pelitic schists from the Morse Basin, British Columbia, Canada

Microthermometric results interpreted in terms of composition and density of the carbonic phase (X_{CH_4}, d_{CO_2}) and of the aqueous phase (X_{NaCl}, d_{H_2O}) (X = mole fraction, density d in g cm^{-3}), for the two types of inclusions observed by Hendel and Hollister (1981)

Microthermometric results					Interpretation: densities and composition	
DF (× 100)	T_{mCO_2} (°C)	T_{hCO_2} (°C)	T_{mC} (°C)	T_h (°C)	d_{CO_2}	
Vapour:						
10—15	−56.8	+20.6	8.7	274	0.76	$X_{CH_4} = 0$
10—15	−56.9	+21.5	8.7	273	0.75	$X_{NaCl} = 8 \cdot 10^{-3}$
10—15	−56.9	+20.5	8.7	270	0.77	$d_{H_2O} = 1.015$
10—15	−56.8	+20.3	8.6	274	0.77	
Liquid:						
75—80	−56.8	+28.6	8.6	270	0.6	$X_{CH_4} = 0$
75—80	−56.8	+26.8	8.6	271	0.70	$X_{NaCl} = 8 \cdot 10^{-3}$
						$d_{H_2O} = 1.015$

Comparison of the properties of the fluids, calculated from analytical data (*1*) and interpolated from experimental data (*2*) on the H_2O—CO_2—NaCl system (Gehrig, 1980)

		Vapour (*1*)		Liquid (*1*)		Vapour (*2*)		Liquid (*2*)	
P (bar)		1,000—2,000				1,000	1,500	1,000	1,500
T (°C)		272 ± 2				270	300	270	270
V (cm^3 mol^{-1})		47.38	44.45	21.86	21.34	56.5	45	22	22.5
DF		0.10	0.15	0.75	0.80	0.05	0.11	0.76	0.72
X (mole%)	H_2O	26.4	36.25	89.54	91.32	15.0	27.0	90.3	88.4
	NaCl	0.2	0.30	0.73	0.75	0.3	0.5	1.7	1.6
	CO_2	73.4	63.45	9.73	7.93	84.7	72.0	8.0	10.0

T_h = homogenization temperature; T_{hCO_2} = ibidem, for the non-aqueous part; T_m = melting temperature (CO_2 = solid CO_2; C = clathrate); DF = degree of filling; V = molar volume.

unmixing must be dropped. Such a result should never be considered negative and the demonstration of non-unmixing may be of great importance. The obtained data should thus be re-examined and re-interpreted in terms of other particular processes (such as mixing of fluids of different origin) potentially as interesting and productive as fluid immiscibility.

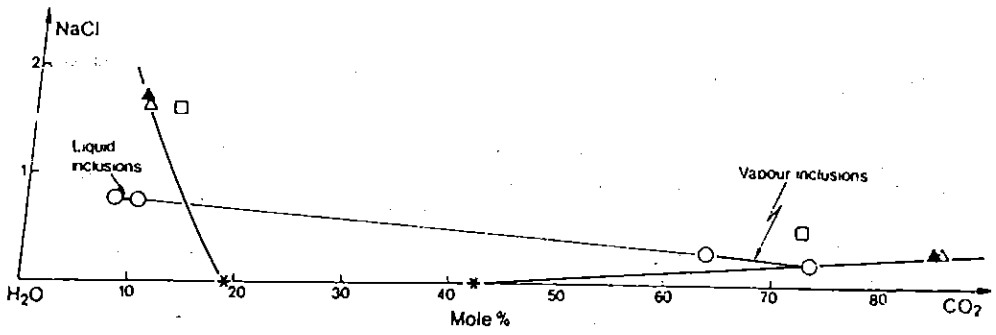

Fig. 6. Composition of unmixed metamorphic fluids from the Morse Basin, British Columbia, Canada, pelitic schists.
The composition is shown in terms of the H_2O—CO_2—NaCl system. Composition calculated from analytical results on fluid inclusions: *open circles* (data in Table II). Compositions interpolated from Gehrig's (1980) experimental data: *solid symbols*, 1 kbar, *open symbols*, 1.5 kbar; *triangles*, 270°C, *squares*, 300°C. *Heavy lines*: limits of the (L + V) domain (Gehrig, 1980); *stars*: experimental points for the same limits in the H_2O—CO_2 system, T = 270°C, P = 1 kbar (Takenouchi and Kennedy, 1964).

ACKNOWLEDGEMENTS

This paper has benefited of discussions, comments and advices from M. Cuney, J. Dubessy, R. Kreulen, J. Touret, R. Wilkins and many others we wish to thank. Careful reviews of D. Manning, S. Sheppard and J. Touret were greatly appreciated. Expert technical help was provided for typing and drawing by D. Perlangeli, D. Dautel, A. Legros and J. Gorau.

REFERENCES

Chivas, A.R. and Wilkins, R.W.T., 1977. Fluid inclusion studies in relation to hydrothermal alteration and mineralization at the Koloula porphyry copper prospect, Guadalcanal. Econ. Geol., 72: 153—169.

Cloke, P.L. and Kesler, S.E., 1979. The halite trend in hydrothermal solutions. Econ. Geol., 74: 1823—1831.

Crawford, M.L., Filer, J. and Wood, C., 1979. Saline fluid inclusions associated with retrograde metamorphism. Bull. Soc. Fr. Minéral., 102: 562—568.

Cuney, M., 1980. Preliminary results on the petrology and fluid inclusions of the Rössing uraniferous alaskites. Trans. Geol., Soc. S. Afr., 83(I): 39—45.

Denis, M., Pichavant, M., Poty, B. and Weisbrod, A., 1980. Le porphyre cuprifère de Sierrita—Esperanza, Arizona, U.S.A — Comparaison avec quelques porphyres voisins. Bull. Soc. Fr. Minéral., 103: 613—622.

Dhamelincourt, P., Bény, J.M., Dubessy, J. and Poty, B., 1979. Analyse d'inclusions fluides à la microsonde M.O.L.E. à effet Raman. Bull. Soc. Fr. Minéral., 102: 600—610.

Eastoe, C.J., 1978. A fluid inclusion study of the Panguna porphyry copper deposit, Bougainville, Papua New Guinea, Econ. Geol., 73: 721—748.

Gehrig, M., 1980. Phasengleichgewichte und *PVT*-Daten ternärer Mischungen aus Wasser, Kohlendioxid und Natriumchlorid bis 3 kbar und 550°C. Thesis Institute of Physical Chemistry, University of Karlsruhe, Karlsruhe.

Guha, J., Leroy, J. and Guha, D., 1979. Significance of fluid phases associated with shear zone Cu—Au mineralizations in the Dore Lake Complex, Quebec. Bull. Soc. Fr. Minéral., 102: 569—576.

Guilhaumou, N., Dhamelincourt, P., Touray, J.C. and Touret, J., 1981. Étude des inclusions fluides du système N_2—CO_2 de dolomites et de quartz de Tunisie septentrionale — Données de la microcryoscopie et de l'analyse à la microsonde à effet Raman. Geochim. Cosmochim. Acta, 45: 657—673.

Hendel, E.M. and Hollister, L.S., 1981. An empirical solvus for CO_2—H_2O—2.6 wt.% salt. Geochim. Cosmochim. Acta, 45: 225—228.

Heyen, G., Ramboz, Cl. and Dubessy, J., 1982. Simulation des équilibres de phases dans le système CO_2—CH_4 en dessous de 50°C et de 100 bar — Application aux inclusions fluides. C.R. Acad. Sci., Paris, 294: 203—206.

Hilbert, R., 1979. *PVT*-Daten von Wasser und von wässerigen NaCl-Lösungen bis 873°K und 25 Gewichtsprozent NaCl. Thesis, Institute of Physical Chemistry, University of Karlsruhe, Karlsruhe.

Hollister, L.S. and Crawford, H.L. (Editors), 1981. Short Course in Fluid Inclusions — Applications to Petrology. Mineralogical Association of Canada, Calgary, Alta., 304 pp.

Holloway, J.R., 1977. Molecular species in supercritical fluids. In: D.G. Fraser (Editor), Thermodynamics in Geology. Nato Advanced Study Institute Series, Series C, D. Reidel, Dordrecht, pp. 161—181.

Holloway, J.R., 1981. Composition and volumes of supercritical fluids in the earth crust. In: L.S. Hollister and M.L. Crawford (Editors), Short Course in Fluid Inclusions — Applications to Petrology. Mineralogical Association of Canada, Calgary, Alta., pp. 13—35.

Kleintjens, L.A. and Koningsveld, R., 1982. Mean-field lattice—gas description of the system CO_2—H_2O. Sep. Sci. Technol., Spec. Iss., 17 (1): 215—233.

Leroy, J., 1979. Contribution à l'étalonnage de la pression interne des inclusions fluides lors de leur décrépitation. Bull. Soc. Fr. Minéral., 102: 584—593.

Pichavant, M., Ramboz, Cl. and Weisbrod, A., 1982. Fluid immiscibility in natural processes: use and misuse of fluid inclusion data, I. Phase equilibria analysis — A theoretical and geometrical approach. In: R. Kreulen and J. Touret (Guest-Editors), Current Research on Fluid Inclusions. Chem. Geol., 37: 1—27 (this special issue; in this paper referred to as Part I).

Potter II, R.W. and Brown, D.L., 1977. The volumetric properties of aqueous sodium chloride solutions from 0° to 500°C and pressures up to 2000 bars based on a regression of available data in the literature. U.S. Geol. Surv., Bull. 1421-C, 36 pp.

Ramboz, Cl., 1979. A fluid inclusion study of the copper mineralization in the Southwest Tintic District (Utah). Bull. Soc. Fr. Minéral., 102: 622—632.

Ramboz, Cl., 1980a. Géochimie et étude des inclusions fluides de gisements et indices d'étain—tungstène du Sud du Massif Central (France). Thesis, National Polytechnical Institute of Lorraine (I.N.P.L.), Nancy, 278 pp.

Ramboz, Cl., 1980b. Problèmes posés par la détermination de la composition des fluides carboniques complexes. C.R. Acad. Sci., Paris, 290: 499—502.

Roedder, E., 1976. Fluid inclusion evidence on the genesis of ores in sedimentary and volcanic rocks. In: K.H. Wolf (Editor), Handbook of Stratabound and Stratiform Ore Deposits, Vol. 2. Elsevier, Amsterdam, pp. 67—110.

Roedder, E., 1979. Fluid inclusions as samples of ore fluids. In: H.L. Barnes (Editor), Geochemistry of Hydrothermal Ore Deposits. Wiley, New York, N.Y., 2nd ed., pp. 684—737.

Roedder, E. and Bodnar, R.J., 1980. Geologic pressure determinations from fluid inclusion studies. Annu. Rev. Earth Planet. Sci., 8: 263—301.

Sheppard, S.M.F., Nielsen, R.L. and Taylor, H.P., 1971. Hydrogen and oxygen isotope ratios in minerals from porphyry copper deposits. Econ. Geol., 66: 515—542.
Sourirajan, S. and Kennedy, G.C., 1962. The system H_2O—NaCl at elevated temperatures and pressures. Am. J. Sci., 260: 115—141.
Takenouchi, S. and Kennedy, G.C., 1964. The binary system H_2O—CO_2 at high temperatures and pressures. Am. J. Sci., 262: 1055—1074.
Tissot, B.P. and Welte, D.H., 1978. Petroleum Formation and Occurrence. Springer, New York, N.Y., 538 pp.
Touret, J. and Bottinga, J., 1979. Équation d'état pour le CO_2: applications aux inclusions carboniques. Bull. Soc. Fr. Minéral., 102: 577—583.
Weisbrod, A., 1980. Interactions between magmas, rocks and aqueous solutions at the late — to post — magmatic stages in granitoids and associated ore deposits. 26th Int. Geol. Congr., Paris, Abstr. Pap., 1: 103.
Weisbrod, A., 1981. Fluid inclusions in shallow intrusives. In: L.S. Hollister and H.L. Crawford (Editors), Short Course in Fluid Inclusions — Applications to Petrology. Mineralogical Association of Canada. Calgary, Alta., pp. 241—271.
Welsch, H., 1973. Die Systeme Xenon—Wasser und Methan—Wasser bei höhen Drücken und Temperaturen. Thesis, Institute of Physical Chemistry, University of Karlsruhe, Karlsruhe.

PUBLICATION VII : Application of V-X projections to the quantitative interpretation of heterogeneous trapping from fluid inclusion study.

TERRA cognita 3, 1983

GD 21

APPLICATION OF V-X PROJECTIONS TO THE QUANTITATIVE INTERPRETATION OF HETEROGENEOUS TRAPPING FROM FLUID INCLUSION STUDY

Claire RAMBOZ
C.R.P.G., B.P. 20, 54501 Vandœuvre Cedex

On a V-X plane, the bulk molar volume (V) and composition (X) of mechanical mixtures of two fluids at equilibrium at given P and T plot on a straight line defined by the bulk V and X of the two pure end-members. This property simply derives from the lever rule, visualised on T-X and P-X projections. This representation applies to the bulk V and X of inclusion fluids resulting from heterogeneous trapping of two immiscible fluids. It imposes a strong correlation on the variations of their homogenization temperature with composition and, therefore, severely constrain the identification of heterogeneous trapping from fluid inclusion study. Besides, the vapour generated because of immiscibility is seldom observed in crystals and/or easily analysed by microthermometry. It bulk V and X can still be calculated provided that the bulk V and X of the pure liquid and of one mixture are known from fluid inclusion study.

II

ETUDE DE CAS

PUBLICATION VIII Chemical and isotopic evolution of the fluids in the Sn-W deposit, Panasqueira, Portugal.

D14

CHEMICAL AND ISOTOPIC EVOLUTION OF THE FLUIDS IN THE Sn-W DEPOSIT, PANASQUEIRA, PORTUGAL

L. TURPIN, C. RAMBOZ, S. M. F. SHEPPARD
Centre de Recherches Pétrographiques et Géochimiques, C.O. n°1, 54500 Vandoeuvre-lès-Nancy, France

Fluid inclusion analyses, $^{18}O/^{16}O$ ratios of quartz, muscovite, cassiterite, whole rock and D/H ratios of both muscovite and fluid inclusions in quartz, cassiterite, arsenopyrite have been determined for two different paragenesis, in the schists($\delta^{18}O \sim +12‰$), at Panasqueira. Fluids associated with the most usual geodic paragenesis (qtz-musc-apat-cass-arspy.) are liquid dominant(~7%wt-equiv.NaCl), two phase fluids containing minor CO_2 and/or hydrocarbons, N_2, etc., which homogenise at 310±10°C and have $\delta D \sim -50$ to $-60‰$(calcul. and/or meas.), $\delta^{18}O \sim +8‰$(calcul.) The CO_2/H_2O ratio decreased whilst the N_2, CH_4, C_2H_6 contents increased with time. The other is a sheared and brecciated qtz-musc-cass-tourm-wolfr-topaz-rutile vein. Fluid inclusions in cassiterite are complex and include saline liquids(~14%wt-equiv.NaCl) with homogenisation temperatures of 270±10°C, low density CO_2 and/or hydrocarbons inclusions and indirect evidence for boiling. Inclusions in quartz are heterogeneous and contain high density CO_2 and hydrocarbons. For quartz and muscovite, δD fluid~ $-45‰$, but for cassiterite δD fluid = $-5‰$. The following results contrast with those of KELLY and RYE(1979): -Evidence for boiling during precipitation of some cassiterite; -At least for some cassiterite, same δD fluid as that for associated quartz, muscovite, arsenopyrite. The interpretation of δD fluid = $-5‰$ at Panasqueira is not certain although Permo-Triassic meteoric waters at some other Hercynian deposits had such values.

PUBLICATION IX :Les concentrations stanno-wolframifères du district de Brioude-Massiac (Cantal) et du sud du Massif Central : analyse comparée de la minéralogie et des phases fluides associées.

MÉTALLOGÉNIE. — *Les concentrations stanno-wolframifères du district de Brioude-Massiac (Cantal) et du sud du Massif Central : analyse comparée de la minéralogie et des phases fluides associées.* Note (*) de **Hubert Bril** et **Claire Ramboz**, présentée par Claude Guillemin.

Les concentrations stanno-wolframifères filoniennes sont analysées de part et d'autre du chevauchement du Haut-Allier. Dans les deux régions, le transport du tungstène et/ou de l'étain commence à des températures supérieures à 400°C, par des circulations de fluides aqueux peu salés, riches en CO_2, CH_4 et N_2. Dans la plupart des cas, le dépôt des métaux résulte de la dilution du fluide carbonique par un fluide aqueux et plus rarement de l'ébullition du fluide carbonique. Les associations de la wolframite avec des minéraux phosphorés, communes aux deux régions, suggèrent que le tungstène est transporté à l'état de complexe phosphoré dans le fluide carbonique.

METALLOGENY. — Tin-Wolfram Bearing Mineralizations from the Brioude-Massiac District and from the South of Central Massif Area (France): A compared Study of Mineralogy and Associated Fluid Phases.

Vein type tin and wolfram deposits are studied on both sides of the Haut-Allier thrust. In both areas, tin and wolfram are found to be transported by a CO_2, CH_4 and N_2-rich low-salinity aqueous fluid, starting to circulate above 400°C. Most metals are precipitated because of the dilution of the CO_2-rich fluid by an aqueous one, less frequently due to the boiling of the CO_2-rich fluid. Because wolframite is commonly associated with phosphorus-bearing minerals in both districts, it is suggested that wolfram was transported in the CO_2-rich fluid as a phosphorus-bearing complex.

INTRODUCTION. — Les concentrations en étain et tungstène situées dans le Massif Central, de part et d'autre du chevauchement du Haut-Allier, ont été analysées de façon indépendante ([1] et [2]) du point de vue de leur minéralogie et des phases fluides associées. Il s'agit, au Nord, des filons de Scoufour, de Bonnac et de Vèze (Cantal), et de diverses concentrations Sn-W du Sud du Massif Central : les indices de Serrecourte et de Saint-Cierge (Ardèche), le gisement de Leucamp (Cantal) et le gisement d'Enguialès (Aveyron) (*fig.* 1). Ces études ont révélé des conditions physico-chimiques, thermobarométriques et minéralogiques similaires dans les deux zones minéralisées.

CADRE GÉOLOGIQUE. — *District de Brioude-Massiac.* — Les filons polymétalliques de ce district affleurent dans un encaissant métamorphique catazonal, parfois migmatitique, plissé en anticlinorium ayant une extension de plusieurs kilomètres [3]. De nombreuses petites intrusions et filons granitiques, ainsi que des filons de microgranite, recoupent les roches métamorphiques. Les trois filons étudiés sont encaissés dans les gneiss à biotite-sillimanite de l'anticlinorium de Massiac [4]. Les filons de Scoufour sont concordants avec l'encaissant gneissique, les filons de Bonnac, nettement sécants sur la foliation, sont fréquemment associés à de petits corps de granite leucocrate, résultant de l'anatexie locale des gneiss encaissants.

Les filons de Vèze enfin, sont associés à de nombreux filons d'aplites, de pegmatite et de microgranite.

Les minéralisations du sud du Massif Central. — Les concentrations essentiellement wolframifères du sud du Massif Central sont pour la plupart encaissées dans les micaschistes épizonaux à mésozonaux de la périphérie du Massif Central, plus particulièrement dans l'auréole du métamorphisme de contact de monzogranites intrusifs tardihercyniens : indice de Serrecourte dans les schistes des Cévennes au contact du granite de Borne ([5], [6]); gisement d'Enguialès et de Leucamp dans les micaschistes de la Chataigneraie, respectivement à la périphérie du batholite d'Entraygues et de son satellite le granite du Veinazès (*fig.* 1) ([1], [8]). L'indice wolframifère de Saint-Cierge est un exemple de minéralisation intragranitique [9] sur la bordure méridionale altérée du granite de Saint-Cierge [10].

PARAGENÈSE. — Les paragenèses essentiellement wolframifères des deux régions sont constituées de wolframite, mispickel et pyrite dans une gangue quartzique. La wolframite est souvent observée en association avec des minéraux phosphorés : apatite dans le sud du Massif Central, strengite dans les filons de Bonnac et Scoufour. Quand elle est bien développée, la paragenèse comprend également dans les deux régions de la scheelite

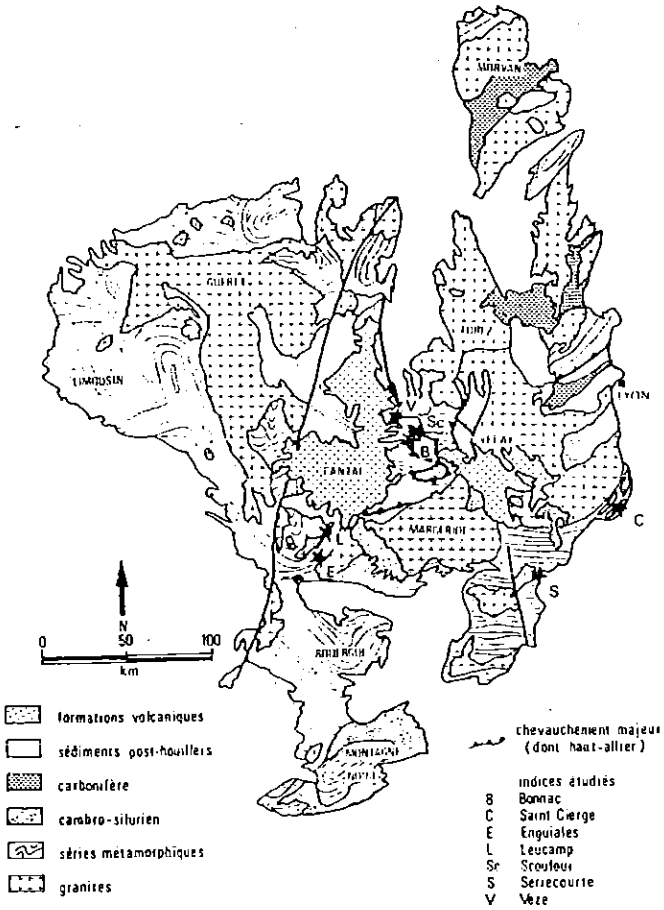

Fig. 1. — Localisation des gîtes stannowolframifères étudiés dans le Massif Central français. Gîtes du district de Brioude-Massiac : B. Bonnac; Sc. Scoufour; V. Vèze. Gîtes du Sud du Massif Central : L. Leucamp; E. Enguialès; S. Serrecourte; C. Saint-Cierge.

Fig. 1. — Localisation of the studied veins in the Central Massif, France. Veins from the Brioude-Massiac district: B, *Bonnac;* Sc, *Scoufour;* V, *Vèze. Veins from the South of Central Massif area:* L, *Leucamp;* E, *Enguiales;* S, *Serrecourte;* C, *Saint-Cierge.*

secondaire, du bismuth, de la bismuthinite, de la pyrrhotite, de la chalcopyrite et de la marcasite. Or, blende et cuivre gris sont spécifiques des filons de Scoufour. La cassitérite et la stannite sont observées seulement dans les filons de Vèze, de même que la tourmaline à leur périphérie [11].

Dans les filons de Leucamp et d'Enguialès, il existe de la scheelite primaire, des muscovites dans les fissures du quartz et de la tourmaline. De plus, une tourmalinisation intense se développe autour de ces filons. Dans le district de Brioude-Massiac en revanche, l'altération

est peu développée à la périphérie des veines minéralisées. la tourmalinisation est observée dans le filon de Vèze seulement.

LES PHASES FLUIDES. — *Types d'inclusions observés.* — Les inclusions fluides ont été analysées dans le quartz (le cas échéant dans la cassitérite) de toutes les concentrations décrites plus haut. Elles peuvent être classées selon deux types principaux : les inclusions à vapeur dominante (type V) contiennent une bulle de vapeur qui occupe plus de 50 % du volume de la cavité; elles s'homogénéisent toujours par expansion de la bulle de vapeur dans l'inclusion. les inclusions à liquide dominant (type L) contiennent une phase liquide qui

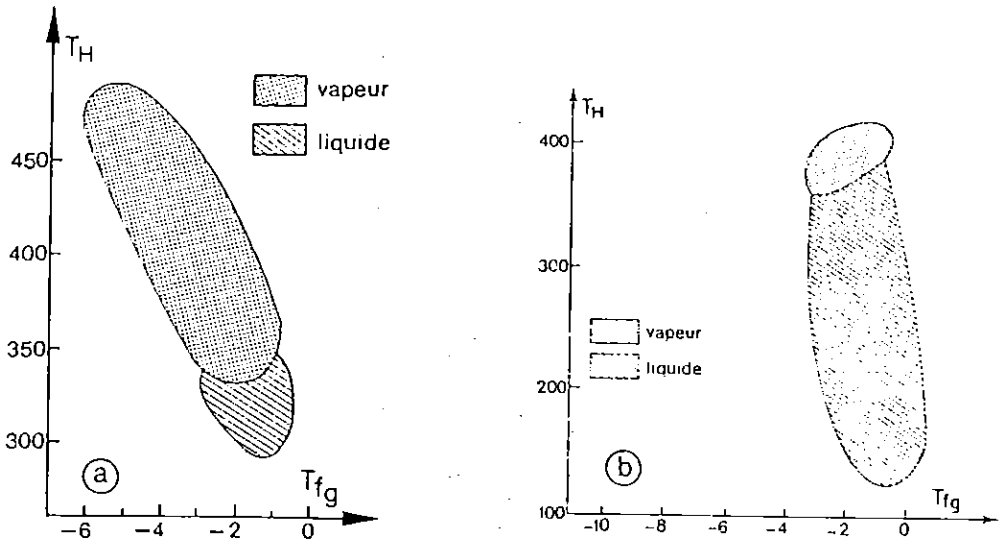

Fig. 2. — Caractéristiques microthermométriques des fluides impliquées dans les minéralisations stannowolframifères du Massif central. *a*, exemple du filon à cassitérite de Saint-Cierge, Ardèche (Sud du Massif Central); *b*, les filons de Bonnac, Scoufour et Vèze (District de Brioude-Massiac); T_H, températures d'homogénéisation; T_{fg}, températures de fusion de la glace.

Fig. 2. — Microthermometric characteristics of the fluids implicated in the tin-wolfram bearing mineralizations: Central Massif, France. a, example of cassiterite vein from Saint-Cierge, Ardèche, South Central Massif; b, Bonnac, Scoufour and Vèze (Brioude-Massiac district); Th, *Homogenization temperatures;* T_{fg}, *Melting temperatures of ice.*

occupe plus de 50 % de la cavité; elles s'homogénéisent toujours par disparition de la bulle de vapeur dans l'inclusion.

Caractéristiques chimiques. — Tous les gisements et indices étudiés sont caractérisés par des fluides de faible salinité (0 à 8 % éq. NaCl).

Dans les inclusions de type V, le CO_2 est toujours mis en évidence par la formation de CO_2 solide ou d'hydrate de gaz au cours du refroidissement. La présence d'autres volatils que CO_2 est indiquée par l'abaissement des points de fusion du CO_2; CH_4 et N_2 sont détectés en quantités variables dans les inclusions de type V à l'aide de la microsonde Raman [12]. Dans les inclusions de type L, les éléments plus volatils que l'eau ont des pressions partielles faibles ou nulles. L'indice stannifère de Saint-Cierge est le seul exemple où CO_2 et CH_4 persistent dans toutes les inclusions de type L.

Évolution thermobarométrique. — Dans tous les gîtes étudiés, les températures d'homogénéisation des inclusions de type V sont supérieures à 350°C. Elles sont comprises

entre 350 et 400°C dans les filons du district de Brioude-Massiac mais peuvent atteindre 470°C dans le sud du Massif Central. Les inclusions de type L s'homogénéisent toutes entre 250 et 360°C. Dans tous les filons étudiés, l'analyse microthermométrique met en évidence une continuité chimique et thermobarométrique entre les inclusions de type V et les inclusions de type L (*fig.* 2). Cette évolution est interprétée comme le résultat de la circulation précoce de vapeurs enrichies en CO_2 au-dessus de 400°C, suivie par le piégeage de liquides essentiellement aqueux à plus basse température. Dans les deux districts étudiés, l'étude microthermométrique, complétée par des études à la microsonde Raman, révèle d'importantes variations de la composition chimique du fluide, lors de sa condensation : variations des rapports molaires CO_2/CH_4 et $(CO_2+CH_4)/(CO_2+CH_4+H_2O)$, principalement. Cette évolution correspond à un processus de dilution du fluide précoce riche en CO_2 et CH_4 par un liquide aqueux. Dans l'indice stannifère de Saint-Cierge seulement, la condensation du fluide carbonique, marquée par l'apparition de liquide enrichi en sels et de vapeur enrichie en volatils, est interprétée comme liée à l'ébullition du fluide.

CONCLUSIONS. – Un épisode minéralisateur en tungstène et étain d'âge tardi-hercynien a été mis en évidence de part et d'autre du chevauchement du Haut-Allier.

Il est caractérisé par la circulation, au-dessus de 400°C, de fluides aqueux peu salés contenant du gaz carbonique et du méthane, et par des associations fréquentes de la wolframite avec des minéraux phosphorés (apatite ou strengite). Les fluides carboniques, piégés dans des inclusions à vapeur dominante sont les fluides qui transportent le tungstène, vraisemblablement sous forme phosphorée, et l'étain.

La dilution du fluide carbonique précoce par un fluide aqueux est le processus majeur qui favorise la précipitation de la wolframite dans les deux districts. L'ébullition du fluide carbonique précoce est impliquée dans le dépôt de la cassitérite d'un seul gîte dans le sud du Massif Central. Les fluides carboniques, moins bien représentés dans les filons du district de Brioude-Massiac (fig. 2) sont également moins riches en volatils, et moins chauds dans ce district que dans le sud du Massif Central. Ces caractères résultent de la mise en place plus superficielle (2 à 3 km de profondeur) des minéralisations stanno-wolframifères du district de Brioude-Massiac, par rapport à celles situées plus au sud du Massif Central (profondeur estimée de mise en place : 4 à 5 km). Ils peuvent expliquer le moins grand développement de l'altération hydrothermale autour des filons du Haut-Allier, ainsi que leur plus pauvre minéralisation en étain et tungstène.

(*) Remise le 4 janvier 1982.

[1] H. BRIL, *Tschermaks Mineralogische und Petrographische Mitteilungen*, 1981 (sous presse).

[2] C. RAMBOZ, *Thèse* 3e *cycle*, I.N.P.L., Nancy, 1980.

[3] J. P. BURG, *Thèse* 3e *cycle*, Montpellier, 1977.

[4] J. TESTARD, *Thèse* 3e *cycle*, Clermont-Ferrand, 1974.

[5] J. MIALHE, *Thèse* 3e *cycle*, Université de Clermont-II, 1980.

[6] A. WEISBROD, M. M. PICHAVANT, C. MARIGNAC, J. MACAUDIÈRE et J. LEROY, *Comptes rendus*, 290, série D, 1980, p. 665.

[7] A. BONNE et J. MOREAU, *Mineral Deposita*, 8, 107, p. 57.

[8] Y. CHEZE, *Thèse* 3e *cycle*, Clermont-Ferrand, 1975.

[9] L. BURNOL, J. GEFFROY et P. SOLER, *Chron. Rech. Min.*, 1978, 441, p. 27 et 443, p. 27.

[10] T. JUTEAU, J. LEROY, J. MACAUDIÈRE, C. MARIGNAC et A. WEISBORD, 2e *R.A.S.T.*, Nancy, 274, p. 232.

[11] J. J. PERICHAUD, *Bull. B.R.G.M.*, Section II, 2, 1970, p. 2.

[12] Les mesures ont été effectuées par C. et J. M. Beny.

H. B. : *Maison des Volcans (Aurillac) et G.I.S. B.R.G.M.-C.N.R.S., 1 A, rue de la Férollerie, 45045 Orléans cedex;*

C. R. : *C.R.P.G., B.P. n° 20, 54501 Vandœuvre-les-Nancy.*

PUBLICATION X : The P-V-T-X-fO_2 evolution of H_2O-CO_2-CH_4-bearing fluid in a wolframite vein : Reconstruction from fluid inclusion studies.

Geochimica et Cosmochimica Acta Vol. 49, pp. 205–219
© Pergamon Press Ltd. 1985. Printed in U.S.A.

0016-7037/85/$3.00 + .00

Travaux du Centre de Recherches Pétrographiques et Géochimiques

The P-$\bar{V}$-T-X-fO_2 evolution of H_2O-CO_2-CH_4-bearing fluid in a wolframite vein: Reconstruction from fluid inclusion studies

C. RAMBOZ[1], D. SCHNAPPER[1] and J. DUBESSY[2]

[1]Centre de Recherches Pétrographiques et Géochimiques, B.P. 20, 54501 Vandoeuvre Les Nancy Cedex, France
[2]Centre de Recherches sur la Géologie de l'Uranium, B.P. 23, 54501 Vandoeuvre Les Nancy Cedex, France

(*Received June* 3, 1983; *accepted in revised form October* 12, 1984)

Abstract—Aqueous-carbonaceous and later pure aqueous fluid inclusions in quartz from a ferberite ($Fe_{95}Mn_{05}$ WO_4) vein within the low-grade metamorphic aureole of the Borne granite (French Massif Central) have been studied by microthermometry and Raman spectrometry. The bulk $\bar{V}$-X properties of the aqueous-carbonaceous inclusions have been derived using the equation of state of HEYEN *et al.* (1982) for the low-temperature CO_2-CH_4 system. A P-T path has been proposed for their trapping using the equations of state of JACOBS and KERRICK (1981a) for the H_2O-CO_2-CH_4 system. Two main episodes were reconstructed for the history of the aqueous-carbonaceous fluid. (1) Primary H_2O-CO_2-CH_4 vapour-rich inclusions in quartz indicated the early circulation of a low-density fluid (65 mole% H_2O-34 mole% CO_2-1 mole% CH_4 and traces of N_2; $d = 0.35$ gcm^{-3}) at around 550° ± 50°C and 700 ± 100 bar. Fluid cooled approximately isobarically to 450°–400°C and was progressively diluted by H_2O with a concomitant increase in density. The fO_2 of the H_2O-CO_2-CH_4 fluid, estimated from the equilibrium $CO_2 + 2H_2O \rightleftharpoons CH_4 + 2O_2$, first ranged from 10^{-32} to 10^{-27} bar, close to the Q-F-M buffer. Within analytical errors, these values were consistent with the presence of graphite in equilibrium with the fluid. (2) A drop in PCO_2, and therefore a drop in fO_2, was recorded by the secondary liquid-rich inclusions in quartz. The inclusions, formed at and below 400°C, were composed of H_2O and CH_4 only, and fO_2 at that stage was below that fixed by the graphite-fluid equilibrium. This second episode in the fluid-rock system could be explained by the drop of temperature below the blocking temperature of the graphite-fluid equilibrium. According to this interpretation, the blocking of the graphite-fluid equilibrium occurred at $T \geq 370$°C and probably at 400°C on account of the pressure correction. Mass spectrometric data show that ferberite contains H_2O, CO_2 and CH_4 in fluid inclusions, which lie in the gap of the $\bar{V}$-X properties of the aqueous-carbonaceous fluid in quartz. Deposition of ferberite probably occurred at around 400°C, the previously inferred blocking temperature, resulting from either the drop in PCO_2, the drop in fO_2 and/or the related pH-increase.

It is concluded that the existence of a blocking-temperature for the graphite-fluid chemical equilibrium may be a critical factor for maintaining a stable fluid pressure gradient in geothermal systems occurring under greenschist facies conditions in graphite-bearing rocks.

INTRODUCTION

ACTUAL AND FOSSIL fluids found in the earth's crust are often composed of aqueous solutions enriched in salts and volatiles. Until now, P-T-X data and in particular oxygen and sulfur fugacities of complex fossil fluids have been generally derived from the study of the mineral assemblages that once equilibrated with such fluids (*e.g.* EUGSTER, 1981; RUMBLE *et al.*, 1982). Very few quantitative P-$\bar{V}$-T-X data have been obtained directly from the study of complex fluid inclusions because of (a) the lack of compositional data on individual fluid inclusions, (b) the lack of sufficient experimental data on multicomponent systems in the low and high P-T range and (c) a poor understanding of the phase equilibria in salt and volatile-rich aqueous inclusions in the low and high P-T range (RAMBOZ, 1980a; PICHAVANT *et al.*, 1982). For complex fluid inclusions, interpretation of microthermometric data in terms of bulk P-$\bar{V}$-T-X properties is now possible using a Raman microprobe to analyze the composition of the non-aqueous part of the inclusion (DHAMELINCOURT *et al.*, 1979) and equations of state to model the multicomponent fluid phase equilibria at low and high pressure and temperature (HEYEN *et al.*, 1982; JACOBS and KERRICK, 1981a). In quartz and wolframite from the Serrecourte vein, Cévennes, France, gaseous species more volatile than H_2O were identified by preliminary crushing tests (as described by ROEDDER, 1970) and by mass spectrometric analyses. This paper reconstructs the P-$\bar{V}$-T-$X H_2O$-$X CO_2$-$X CH_4$-fO_2 evolution of these complex aqueous fluids in quartz, using combined microthermometric and Raman spectrometric analyses of the same fluid inclusions. Chemical equilibria among H_2O, CO_2 and CH_4 in the presence and in the absence of graphite are computed from these data. The variations of fO_2 with changes in fluid composition can thus be determined, despite the absence of a suitable mineral association in equilibrium with these fluids.

GEOLOGY

Two major regional metamorphic events have affected the pelitic series of the Cévennes in the southeastern part of the French Massif Central (MARIGNAC *et al.*, 1980). The first one (pre-Hercynian to early Hercynian in age) was characterized by greenschist facies regional metamorphism, recumbent folding and intense regional shearing resulting in the generation of a flat regional schistosity. The second event (late Hercynian, 320–280 Ma) was characterized by a greenschist to amphibolite facies metamorphism (WEISBROD 1967, 1968, 1970, 1974), isoclinal folding and a new "schis-

tosity" (strain slip cleavage) which was developed only in the upper amphibolite facies. This metamorphism and the related granite magmatism were the consequences of a strong thermal anomaly which in turn might have been related to small but numerous alkaline intrusions (vaugnerite and lamprophyres) (WEISBROD *et al.*, 1980).

During this second episode, large amounts of granitic magma were generated by partial melting of the gneisses and mica schists of the upper amphibolite facies. A part of this magma, with varying degrees of contamination by deeper more basic magmas, intruded the greenschist and upper amphibolite facies as laccoliths (Borne massif, 315 ± 5 Ma: MIALHE, 1980, and Rocles massif). At about the same time, hydrothermal activity took place in and around the intrusions as shown by quartz veins and by pervasive phyllic alteration of the country rocks. The outcrop studied is one of these quartz veins which is found 150 m east of Serrecourte village. It is lens-shaped, one metre long and ten centimetres wide and is located in biotite-muscovite-andalusite-cordierite schists, close to the eastern contact with the Borne granitic massif. Milky quartz, the main vein-forming mineral, shows two facies under the microscope: (1) large zones of clear idiomorphic quartz are rimmed by (2) dark microcrystalline quartz with relics of clearer parts (Fig. 1). Wolframite is mainy located in the clear undeformed quartz. It is almost pure ferberite ($Fe_{0.95}Mn_{0.05}WO_4$) according to the X-ray diffraction method of HSU (1976). Dark microcrystalline quartz formed as a result of plastic deformation and dynamic recrystallization (NICOLAS and POIRIER, 1976). It occurs along a network of fractures with three distinct orientations and mineral associations. From the geometrical relations at intersecting fractures, the relative chronology in decreasing age of the three fracture sets and the related minerals is as follows: 1) arsenopyrite, 2) arsenopyrite + chalcopyrite + pyrite + scheelite, 3) pyrite. Kaolinite outlines fractures in quartz zones which have undergone a later stage of deformation superimposed over the sulfide-enriched deformed parts. Wolframite probably precipitated prior to all deformation, because it is associated with undeformed quartz, it is cut by sulfide-bearing fractures, and it is covered with kaolinite.

ANALYTICAL TECHNIQUES

All symbols used are given in Table 1. Fluid inclusions in doubly polished 200 μm-thick sections in quartz were analyzed using three techniques. Microthermometric measurements (WEISBROD *et al.*, 1976) were performed using a Chaix-Meca stage (POTY *et al.*, 1976). Inclusions that had obviously leaked or necked down were carefully avoided. *Tm*CO_2, *Tm*I, *Tm*C, *Th*CO_2 and *TH* were measured. The temperature of the easily observable phase changes (*Tm*CO_2, *Tm*I in liquid-rich inclusions, *TH L-V*(*L*)) were measured with an accuracy of 0.4°C on letting the temperature increase regularly (1°C per minute). However, *Th*CO_2, *TH L-V*(*V*), *Tm*I and *Tm*C were difficult to observe in vapour-rich inclusions, and their measurement required a multistage ("cycling") procedure. First, the temperature of the phase change was bracketed between two values: *T*min and *T*max. Then, starting from *T*min, the inclusion was cooled a few degrees to allow the melting solid to regrow and become more visible. Once its presence was verified, the temperature was raised to *T*min + 0.2°C and the same procedure was repeated. The temperature at which no crystal growth was observed on cooling was the best estimate of the temperature of the phase transition. Using this procedure, the precision for *Tm*I, *Tm*C and *Th*CO_2 in vapour-rich inclusions was equivalent to that for easily observable phase changes. The precision for *TH L-V*(*V*) was probably about 20°C.

The analysis of the non-aqueous part of the inclusions was performed with a Jobin-Yvon Raman microprobe (type M.O.L.E.) (DELHAYE and DHAMELINCOURT, 1975). The exciting radiation used was the 514.5 nm green line from a 5 W Spectra-Physics ionised argon laser. The photomultiplier was a RCA 31034 type, cooled to −20°C. A Leitz PLX160 objective with a .95 numerical aperture was used. The experimental conditions were as follows: scan speed 20 cm^{-1} mn^{-1}, dwell time 0.7 s, slit width 400 μm determining a spectral resolution of 3 cm^{-1}. The measurements on the three-phase inclusions (*Lw* + *Lc* + *V*) were always made at a temperature slightly higher than *Th*CO_2. Both the point of focus of the laser beam and the polarization were optimized on the Raman scattering of the most abundant component. Thereafter, the spectra of other gases were recorded, then the spectrum of the gas chosen for the optimization was repeated. If the intensity difference between the two spectra of the most abundant gas species was less than 5%, all the spectra were considered good.

Only three gases were identified by their Raman lines: CH_4($\tilde{\nu}CH_4$ = 2917 cm^{-1}), N_2($\tilde{\nu}N_2$ = 2330 cm^{-1}), CO_2($\tilde{\nu}CO_2$ = 1388 cm^{-1}) (HERZBERG, 1951). Because the optical path of the laser beam is in the atmosphere, atmospheric N_2 can give a signal. When this component was detected, we systematically verified whether the N_2 Raman scattering was derived from the fluid inclusion or from the atmosphere by recording a spectrum of the host crystal under the same experimental conditions as those for the fluid in the inclusion. The mole fraction of each gas was calculated from the formulae of PLACZEK (1934) in DHAMELINCOURT *et al.* (1979). We used the relative cross sections of Raman scattering given by SCHRÖTTER and KLÖCKNER (1979) for a 514.5 nm excitation radiation: σCO_2 = 1.21; σCH_4 = 9;

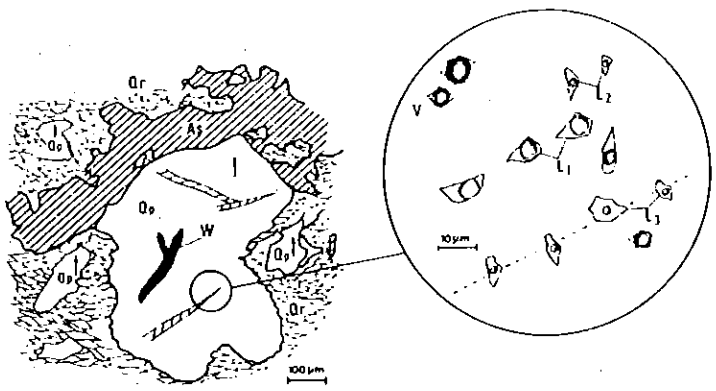

FIG. 1. Schematic representation of the Serrecourte quartz vein and related type V, L1, L2 and L3 fluid inclusions. Qp: quartz porphyroclasts; Qr: recrystallized sheared quartz; As: arsenopyrite; W: ferberite. In Qp, the arrow indicates the c-axis and the hatchured areas mark fracture planes.

TABLE 1. Explanation of the symbols used in the text and figures

C	gas hydrate (= clathrate)
d	bulk density of the inclusion (gcm^{-3})
dl(*dv*)	density of the aqueous part (of the non-aqueous part) (gcm^{-3})
fi	fugacity of the species *i* (bar)
Flc	degree of filling of the non-aqueous part (= volume fraction (carbon-rich liquid)/ volume fraction (carbon-rich liquid + carbon-rich gas)) at *T* slightly > *Tm*CO_2
Flw	degree of filling of the inclusion (= volumetric fraction of the aqueous liquid in the inclusion) at room temperature.
HH	hydrohalite
I	ice
log	logarithm to the base 10
Lc	carbonaceous liquid
Lw	aqueous liquid
ni	number of moles of species *i* in 1 cm^3 of the fluid in the inclusion
P	total pressure (bar)
Pi	partial pressure of the species *i* (bar)
S	solid CO_2
T	temperature (°C)
TH	temperature of total homogenization of the inclusion (°C) (*TH L-V*(*L*): to the liquid; *TH L-V*(*V*): to the vapour; *TH L-V*(crit.): critical)
ThCO_2	homogenization temperature of the non-aqueous part (°C) (*Th*CO_2 *L-V*(*V*): to the vapour)
*Tm*C	melting temperature of clathrate (°C)
TmCO_2	melting temperature of solid CO_2 in the presence of vapour (°C)
*Tm*I	melting temperature of ice (°C)
V	vapour
$\bar{V}$	molar volume (cm^3 $mole^{-1}$)
$\bar{V}l$ ($\bar{V}v$)	molar volume of the aqueous part (of the non-aqueous part) (cm^3 $mole^{-1}$)
Xi	mole fraction of the species *i* in the inclusion
Yi	mole fraction of the gas species *i* in the non-aqueous part
Zeq : CH_4	$ZCH_4 + ZN_2$
Z'CO_2	mole fraction of CO_2 dissolved into the aqueous part at *Th*CO_2 or *Tm*C.
γi	fugacity coefficient of the species *i*
$\tilde{\nu} i$	wave number of the Raman line of the species *i* (cm^{-1})
σi	relative cross-section of Raman scattering of the gaseous species *i* at room temperature for the 514.5 nm exciting line.

σN_2 = 1. The hot band of CO_2 (1414 cm^{-1}) was not considered. The reproducibility of the Raman lines was probably no better than 8%, due to errors on scan speed, transmission of spectrometer, sensitivity to wavelength of detector (BERNSTEIN, 1982). The area of each Raman line was measured with a planimeter with a precision of around 1%. The relative uncertainty on the mole fraction of gases was calculated to be about 10%.

Preliminary mass spectrometric analysis of fluids in quartz and wolframite were performed (J. Zimmermann, analyst). Crystals were crushed to 2 mm-long pieces, cleaned in a hot mixture of ¼HCl + ¼HNO_3 for three hours, washed in double-distilled non-demineralized water, and dried under atmospheric pressure for one night. Then, crystals were heated to 115°C for 15 hours in a high vacuum to eliminate adsorbed gases. Fluids were extracted by continuously heating the crystals to 700°C at a rate of 400°C per hour. Around 15 mg of quartz or wolframite were required for one analysis. The yield of fluid by extraction by heating is higher than that by crushing, and the amount of wolframite available was too small to allow extraction of fluids by crushing. A N_2-trap was used to separate non-condensable gases from condensable gases, in particular organic compounds, prior to the mass spectrometric analysis. A THN 205 spectrometer was used, which allows discrimination of masses 2 to 50. CHEILLETZ *et al.* (1984) give further details of the analytical method and discuss the problem of how to separate gases released out of the inclusions from those derived from the organic compounds in quartz.

ANALYTICAL DATA

Although several thick sections were studied, all the measurements were performed on crystals from one thick section, a few cm-wide. Table 2 presents all the Raman spectrometric data obtained and the microthermometric data on the same inclusions only. *Flw* was estimated by reference to the volumetric chart of ROEDDER (1972).

Four main types of inclusions were identified based on microscopic, microthermometric and Raman spectroscopic characters: types V, L1, L2 and L3. All inclusions in which CO_2 occurred, as evidenced by formation of solid CO_2 on cooling and/or by Raman spectroscopy, were classified as type V. Their non-aqueous part occupied at least 60% of the cavity volume (*Flw* < 0.4). Type V inclusions were systematically found in clear parts of quartz crystals. Their average size was 15 μm, they had negative crystal shape, and they were randomly distributed within the thickness of the section. These characteristics indicate a primary origin of type V inclusions relative to quartz according to the criteria proposed by ROEDDER (1976). Raman spectrometric measurements showed that, together with CO_2, CH_4 was always present in the non-aqueous part of type V inclusions. Some of them contained minor amounts of N_2 (always <5 mole%; Table 2). The measured *Tm*CO_2 were between −58.9° and −63.4°C in type V inclusions (Fig. 2). The distribution of the *Tm*CO_2 is bimodal, with one marked mode at −59.5°C. Because of the volumetric importance of the vapour bubble, only a few *Tm*I could be measured in type V inclusions; these were in the range −3.3° to −1.2°C. The *Tm*C were observed between +9.5° and +14.2°C. In type V inclusions, *Th*CO_2 *L-V*(*V*) occurred between −2.3° and +18.2°C and *TH L-V*(*V*) occurred between +280° and

Table 2 : Analytical data for selected inclusions from the carbonaceous and aqueous stage in quartz.

	MICROTHERMOMETRY							RAMAN SPECTROSCOPY		
N°	Flw	Flc	TmCO$_2$	TmI	TmC	ThCO$_2$ L-V(V)	TH	ZCO$_2$ x10^2	ZCH$_4$ x10^2	ZN$_2$ x10^2
1	.20	.30	-58.9	-3.3	9.7	18.2	324.8^V_V	93.3	4.1	2.6
2	.15	.40	-60.4	-	-	14.9	320.0^V_V	96.2	3.8	n.d.
3	.25	.30	-59.8	-	-	15.4	348.2^V_V	96.6	3.4	n.d.
4	.20	.30	-59.8	-	9.5	11.9	- ^V_V	91.7	3.9	4.4
5	.10	.40	-61.7	-1.2		10.8	235.5^V_V	95.1	4.9	n.d.
6	.25	.20	-61.9	-3	12.1	2	350.5^V_V	90.8	8.4	0.8
7	.20	.10	-59.9	-2.7	-	-	361.3^C_C	95.9	4.1	n.d.
8	.35	.10	-62.2	-	12.5	-	357.7^V_V	88.1	8.4	3.5
9	.30	.25	-60.8	-	10.7	- 2.3	364.5^V_V	87.8	8.6	3.7
10	.20	.25	-61.5	-7.5	10.2	- 0.5	315.4^V_V	83.5	13.1	3.4
11	.35	0	-	-4.4	12.2	-	360.6^L_L	80.6	19.4	n.d.
12	.40	0		-2.8	-		383.0^V_V	n.d.	100	n.d.
13	.50	0		-1.6	-		378.4^V_V	n.d.	100	n.d.
14	.30	0		-	-		375.5^V_V	n.d.	100	n.d.
15	.40	0		-	13.7		373.1^V_V	n.d.	100	n.d.
16	.25	0		-	-		371.7^C_C	n.d.	100	n.d.
17	.55	0		-1.4	13.3		368.7^C_C	n.d.	100	n.d.
18	.55	0		-1.5	-		370.1^C_C	n.d.	100	n.d.
19	.40	0		-1.6	10.0		368.9^L_L	n.d.	100	n.d.
20	.40	0		-0.7	-		356.4^L_L	n.d.	100	n.d.
21	.70	0		-1.2	-		349.5^L_L	n.d.	100	n.d.
22	.60	0		-1.1	-		310.5^L_L	n.d.	100	n.d.
23	.50	0		-1.2	-		285.5^L_L	n.d.	100	n.d.

Symbols as in Table 1. V : homogenization to the vapour. C : critical homogenization. L : homogenization to the liquid. n.d. : not detected.

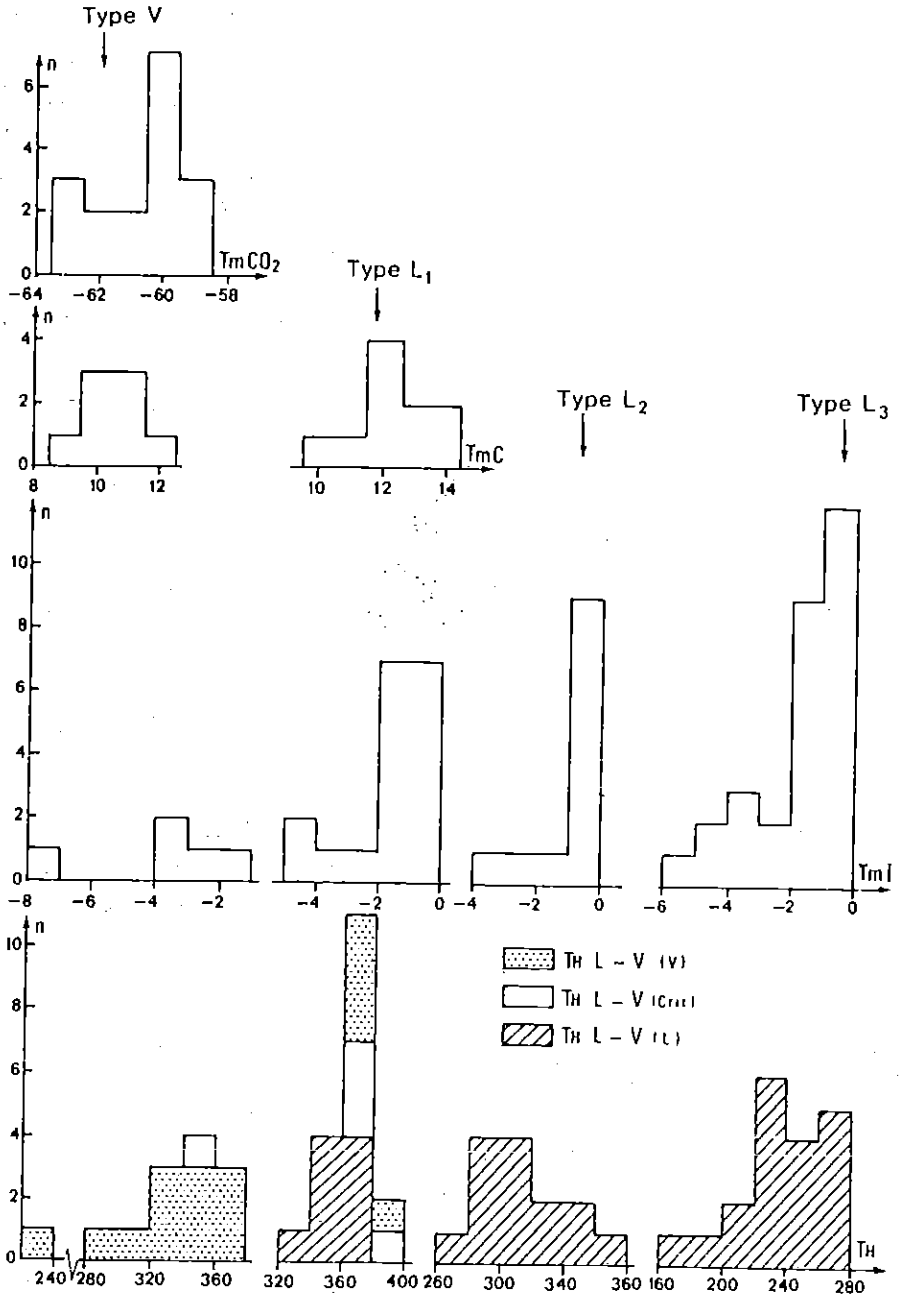

FIG. 2. Histograms of the microthermometric measurements (°C) on the type V, L1, L2 and L3 inclusions in quartz.

+380°C. One inclusion homogenized to the vapour at 235.5°C. Two critical homogenizations were measured at 348.2° and 357.7°C.

In the non-aqueous part of type L1 inclusions, only CH_4 was detected by Raman spectroscopy (Table 2). Their non-aqueous part, which occupied 40 to 80% of the cavity volume ($0.2 \leq Flw \leq 0.6$), was dense enough to form clathrate. Type L1 inclusions were smaller than type V inclusions (5 to 10 μm) and had a more complex shape. They outlined fractures of limited extent in quartz (100 μm to 1 mm). They were therefore thought to be secondary. In type L1 inclusions, the *Tm*I were scattered between −4.9° and 0°C (Fig. 2). *Tm*C always melted above 10°C, mostly between 12° and 14°C. Type L1 inclusions homogenized totally between 334.8° and 383°C, with a marked mode on the *TH* histogram around 365°C. Some type L1 inclusions homogenized to the liquid, some to the vapour, and others were essentially critical (Fig 2).

Type L2 inclusions had $0.60 \leq Flw \leq 0.70$. CH_4 was detected in their non-aqueous part using the Raman microprobe. However, the PCH_4 was too low for clathrate to nucleate on cooling them. Type L2 inclusions were systematically associated with type L1 inclusions in small fractures in quartz. Simple microscopic observation did not allow discrimination between type L1 inclusions and the type L2 inclusions characterized by $Flw \sim 0.60$. Measured *Tm*I were between −3.4° and −0.6°C in type L2 inclusions. *TH L-V(L)* were between 280° and 367.3°C (Fig. 2). It was observed that the intensity of the Raman signal for CH_4 decreased with decreasing *TH* in these inclusions.

Type L3 inclusions were liquid-rich, with $Flw \geq 0.70$. They systematically outlined 10 cm-long fractures in quartz, and therefore they could be distinguished from the type L2 inclusions. Moreover, no species more volatile than H_2O was detected with the Raman probe in type L3 inclusions. Their measured *Tm*I were between −5° and 0°C with a marked mode around −1°C. Measured *TH L-V(L)* were between 152.4° and 252°C (Fig. 2). The distribution of the various inclusion types, of the wolframite and arsenopyrite in the quartz porphyroclasts, and in the recrystallized quartz is schematically shown in Fig. 1.

The results of the mass spectrometric analyses were as follows: (1) fluids extracted from quartz and wolframite were composed of H_2O, CO_2 and CH_4. (2) The release of fluids from quartz started at 280°C. The amount of H_2O, CO_2 and CH_4 released from quartz as a function of temperature is shown in Fig. 2 from the paper by CHEILLETZ *et al.* (1984). A marked step on the curve of release of H_2O at 640°C indicated that two main generations of aqueous fluids were trapped in quartz. Inclusions decrepitating below 640°C were mainly composed of H_2O and CH_4; inclusions decrepitating at and above 640°C contained mainly H_2O and CO_2. (3) H_2O, CO_2, and CH_4 began to be released from wolframite at 320°C. No step was visible in the release curves for wolframite; wolframite therefore contained mainly one generation of fluids. (4) Between 400° and 600°C, the amount of H_2O extracted per gram of quartz was twice that extracted per gram of wolframite. In this temperature range, the XCH_4/XCO_2 ratio of the bulk gases extracted from quartz and wolframite varied from 1.5 to 1 and 5 to 4, respectively. (5) Organic products condensable in liquid N_2 were extracted from quartz only, and identified by their mass spectrum: 12, 13, 15, 26, 28, 30, 41, 43. The Serrecourte vein-quartz contains 0.14 ± 0.005 wt.% organic carbon, analyzed by coulometry (analysis by M. Vernet, C.R.P.G.).

RESULTS AND DISCUSSION

H_2O-CO_2-CH_4 inclusions in quartz

Significance. Figure 3 is a plot of all the inclusions studied in quartz on the *Tm*I-*TH* plane. The H_2O-CO_2-CH_4-bearing inclusions (type V, L1 and L2 inclusions) plot above the line *TH* = 280°C. The type L3 inclusions, bearing only water and dissolved salts, plot below that line. The *Tm*I of some type L3 inclusions are lower than any *Tm*I measured in the H_2O-CO_2-CH_4-bearing inclusions, although type V inclusions contain salts and CO_2 which both lower *Tm*I. Therefore, type V, L1 and L2 inclusions differ from type L3 inclusions by their gas-content, their salt-content and their *TH*. This indicates that two main hydrothermal stages were recorded in quartz: (1) an aqueous-carbonaceous stage represented by type V, L1 and L2 inclusions, and (2) an aqueous stage represented by type L3 inclusions. The type L3 inclusions corresponded to the later input of an aqueous fluid due to vein fracturing. The data on type L3 inclusions will not be considered further. Only the conditions of generation of the earlier H_2O-CO_2-CH_4-bearing V, L1 and L2 inclusions will be characterized. The hypothesis of the coexistence of type V, L1 and L2 fluids can be discounted. Type V inclusions are primary, type L1 and L2 inclusions are secondary. Moreover, in the two-phase field of the H_2O-CO_2-CH_4 system, vapours are always more CH_4-rich than coexisting liquids (RAMBOZ *et al.*, 1982). Hence, it is impossible that CO_2-bearing type V vapours ever coexisted with CH_4-bearing type L1 and L2 liquids. The trapping of each of these types of inclusions occurred in the one-phase stability field. Successive trapping of the type V and type L1 inclusions in that order is suggested by their textural relations to quartz, the decrease in their $TmCO_2$, the increase in their $ThCO_2$ and *Tm*C (Fig. 3), and the increase in their degree of filling. Successive trapping of type L1 and type L2 inclusions can be inferred from their close association in quartz. Moreover, type L1 and L2 inclusions both contain CH_4 and they plot on a continuous surface of the *Tm*I-*TH* plane. Successive trapping of the type V, L1 and L2 inclusions in that order is therefore suggested. In these inclusions, *dv* progressively decreases as shown by the decrease of the $ThCO_2$ in type V inclusions and the decrease of the intensity of the Raman signal for CH_4 in type L1 and L2 inclusions as they homogenize at lower temperature. Secondary type L1 inclusions as a group homogenize at higher temperature than primary type V inclusions (inset, Fig. 3A). This is mainly because type L1 inclusions contain only CH_4 which is less soluble in water than the CO_2 present in type V inclusions. The aqueous-carbonaceous stage represented by type V, L1 and L2 inclusions marked an evolution of the fluid characterized by the transition under supercritical conditions from "vapours" (*i.e.*, fluids with a density lower than the critical density for the composition considered) to "liquids" (*i.e.*, fluids with a density higher than the critical density for the composition considered). Concomitantly, the ratio XCO_2/XCH_4 of the fluid decreased to zero.

Bulk $\bar{V}$-X *evolution.* Fifteen type V, L1 and L2 inclusions were selected for complementary Raman spectrometric analyses. They were representative of the hydrothermal aqueous-carbonaceous fluid at the various stages of its evolution, according to their position in the microthermometric trends. The $\bar{V}$-X properties of both the aqueous and non-aqueous parts of these inclusions have been calculated from the microthermometric and spectrometric data and by reference to the properties of fluids in the CO_2-CH_4-N_2 and H_2O-CO_2-NaCl systems (Table 2). The $\bar{V}$-X properties of the inclusion fluids in the H_2O-CO_2-CH_4-N_2 system are listed in Table 3, and the method of derivation is given in the Appendix. The relative uncertainties in these calculations may be estimated by taking into account an absolute error in *Flw* of $\pm 2.5 \times 10^{-2}$. The absolute uncertainties in *dv* (±10%) and in ZCO_2, ZCH_4, and ZN_2 (±10%) do not significantly affect the bulk $\bar{V}$-X calculation.

Phase equilibria at $TmCO_2$ *and* $ThCO_2$. To make a detailed interpretation of the phase changes observed at low temperature in the aqueous and in the non-aqueous parts of gas-rich inclusions in terms of the $\bar{V}$-X properties of the two parts, it is necessary to know whether clathrate nucleates during cooling or during further heating (RAMBOZ, 1980a; RAMBOZ

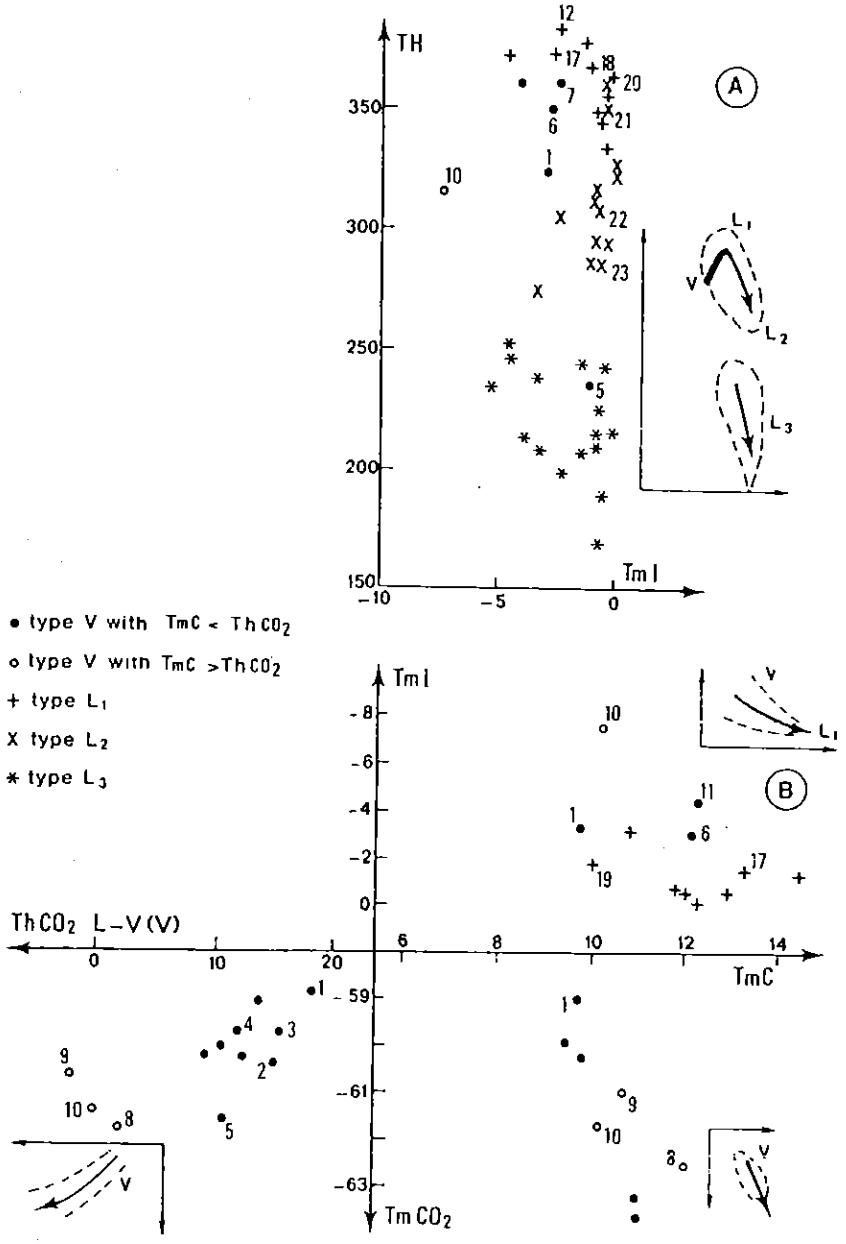

FIG. 3. Correlative variations of the microthermometric data (°C) on inclusions in quartz. 3A: plot of all the inclusions in quartz (types V, L1, L2 and L3) on the *Tm*I-*TH* plane. On the inset, the data are interpreted in terms of two stages, a carbonaceous-aqueous stage comprising type V, L1 and L2 inclusions in that order, and an aqueous stage comprising type L3 inclusions. Fig. 3B is a plot of the low-temperature data on the aqueous part (*Tm*C, *Tm*I) and on the non-aqueous part ($TmCO_2$, $ThCO_2$) of the type V and L1 inclusions. The continuous transition from type V to type L1 inclusions is visible on the *Tm*I-*Tm*C plot (upper right inset). The arrow on the insets from the $TmCO_2$-*Tm*C and $TmCO_2$-$ThCO_2$ plots shows the evolution of type V fluids towards type L1 fluids, not represented in these projections.

and BENY, in prep.). In type V inclusions, the temperatures at which clathrate solidified could not be determined from the observation of inclusions under the microscope during cooling. No visible contraction of the gas bubble accompanied the solidification of the aqueous part to ice, to clathrate or to both ice and clathrate, due to the large size of the gas bubble (*Flw* < 0.4). The comparison between microthermometric and Raman spectroscopic data indicates that clathrate nucleated during cooling of type V inclusions (Fig. 4). $\bar{V}v$ of inclusions containing CO_2, CH_4 and N_2 were estimated by reference to the CO_2-CH_4 system assuming $Zeq.CH_4 = ZCH_4 + ZN_2$. The *P*-$\bar{V}$-*T*-*X* properties of *Lc*-*V* equilibria in the CO_2-CH_4 and CO_2-N_2 systems between −20° and +15°C are very similar (ARAI *et al.*, 1971). For CO_2-CH_4-N_2 mixtures containing less than 5 mole% N_2, the compositions of the coexisting *Lc* and *V* expressed as

Table 3 : Interpreted bulk composition and density of selected fluid inclusions from the carbonaceous and aqueous stage in quartz.

N°	dv		P	$XH_2O \times 10^2$	$XCO_2 \times 10^2$	$XCH_4 \times 10^2$	$XCO_2 \times 10^2$	d
1	0.21	1	60[a]	72.30(3)	25.90(2.7)	1.10(0.10)	0.70(0.07)	0.37(0.02)
2	0.19	1	53[a]	67.70(4)	31.10(4)	1.20(0.15)	0 (-)	0.31(0.02)
3	0.18	1	53[a]	79.55(2)	19.90(1.9)	0.65(0.07)	0 (-)	0.38(0.02)
4	0.17	1	49[a]	76.60(2.50)	21.50(2.5)	0.90(0.10)	1.00(0.01)	0.34(0.02)
5	0.16	1	47[a]	61.70(6.50)	36.90(7.0)	1.40(0.35)	0 (-)	0.24(0.02)
6	0.15	3	60[a]	81.80(2)	16.70(1.6)	1.35(0.15)	0.15(0.02)	0.36(0.02)
8	0.145	3	65[b]	87.50(1)	11.20(0.9)	0.90(0.07)	0.40(0.04)	0.44(0.02)
9	0.145	2	50[b]	85.30(1.5)	13.10(1.10)	1.10(0.10)	0.50(0.05)	0.40(0.02)
10	0.13	2	48[b]	79.35(2.5)	17.50(2.0)	2.5 (0.30)	0.65(0.08)	0.30(0.02)
11	0.12	3	61[b]	88.80(1.0)	9.40(0.75)	1.8 (0.20)	0 (-)	0.43(0.02)
15	0.08		104[b]	88.00(0.9)	0	12.00(0.9)	0	0.45(0.02)
17	0.08		100[b]	93.10(1.0)	0	6.90(0.9)	0	0.58(0.02)
19	0.06		71[b]	90.70(0.90)	0	9.30(0.9)	0	0.43(0.02)
21	n.d.		n.d.	98.00	0	2.00	0	0.56
23	0		0	100.00	0	0	0	0.72

P : internal pressure of the inclusion at some specified temperature (bar). Other symbols as in Table 1. 1 : determined from $ThCO_2$ (see text) ; 2 : determined from TmC (see text) ; 3 : interpolated ; a : P at $ThCO_2$, determined from HEYEN's equation of state ; b : P at TmC determined from experimental data. n.d. : not determined.
The bracketed values are the calculated uncertainties (mole fraction x 10^2) taking into account an uncertainty for Flw of $\pm$ 2.5 x 10^{-2}.

mole% eq.CH_4 are similar to within 5% to the composition of the CO_2-CH_4 *Lc* and *V* coexisting under the same pressure and temperature (SARASHINA *et al.*, 1971). Thus, the *Tm*CO_2, *Th*CO_2 and *Flc* were interpreted using the quantitative $\bar{V}$-*Z*CH_4 projection of the CO_2-CH_4 system of HEYEN *et al.*, 1982 (field B, Fig. 4). The non-aqueous part of type V inclusions is also shown on this projection using *Th*CO_2 and Zeq.CH_4 measured by Raman spectrometry (field A, Fig. 4). The inconsistency between the two sets of data resulted from the presence of a gas hydrate in all type V inclusions at *Tm*CO_2 (RAMBOZ and BENY, in prep.). The gas hydrate was also present in all type V inclusions at *Tm*I and at *Th*CO_2 in inclusions characterized by *Tm*C > *Th*CO_2 (Fig. 3B).

Salt content of the aqueous part. The presence of clathrate and the significant solubility of CO_2 in water prevents the simple derivation of the $\bar{V}$-*X* properties of the aqueous part of the type V inclusions from *Tm*I (COLLINS, 1979; RAMBOZ, 1980a). No experimental data are available in the H_2O-CO_2-NaCl system to interpret the univariant equilibrium $I + C + Lw + V \rightleftarrows C + Lw + V$ in terms of wt% eq.NaCl dissolved in *Lw*. The average salinity of the aqueous part of type V inclusions is estimated to be 4 ± 1 wt% eq.NaCl using a semi-quantitative interpretation of the *Tm*C (Fig. 5). The salinity of the aqueous part of type L1 and L2 inclusions is estimated to vary between 0 and 4 wt% eq.NaCl by interpreting *Tm*I using the data on the H_2O-NaCl system (POTTER *et al.*, 1978). *Tm*I is not affected by the small amount of CH_4 gas, which is rather insoluble in water at the pressure and temperature considered (CULBERSON and MCKETTA, 1951). The salinity of the aqueous part of the inclusions from the aqueous-carbonaceous stage is less than 4 wt% eq.NaCl. NaCl in solution was neglected in the calculation of the bulk composition of these inclusions.

$\bar{V}$v-*Zeq.CH₄ of the non-aqueous part.* The following methods were developed to estimate the $\bar{V}v$ of gas-rich inclusions from the aqueous-carbonaceous stage. Because all *Tm*CO_2 were measured in the presence of a gas hydrate, no quantitative interpretation was derived from this parameter. (a) $\bar{V}v$ of the type V inclusions characterized by *Tm*C < *Th*CO_2 was estimated to range between 185 and 250 cm^3 $mole^{-1}$ by interpreting *Th*CO_2-Zeq.CH_4 (given by Raman spectrometry) on the $\bar{V}$-*Z*CH_4 projection of the CO_2-CH_4 system (Fig. 4). (b) A similar interpretation could not be made for type V inclusions numbers 6, 8, 9, 10 and 11 (Table 2), because they were characterized by *Th*CO_2 measured in the presence of clathrate. $\bar{V}v$ of inclusions 9 and 10 was estimated from *Tm*C to be 280 and 310 cm^3 $mole^{-1}$ respectively. Internal pressure at *Tm*C in these two inclusions was estimated as a function of Zeq.CH_4, using the data of UNRUH and KATZ (1949). $\bar{V}v$ under these *P*-*Tm*C-*Z*CH_4 conditions was approximated using the equation of state of HEYEN *et al.* (1982) for the CO_2-CH_4 system. The approximation PCH_4 = (bulk P) is valid because PH_2O is negligible at the pressure and *Tm*C considered. (c) $\bar{V}v$ of type L1 inclusions was derived from *Tm*C, using the same method as for inclusions 9 and 10. The experimental data for the $C + Lw + V$ curve in the H_2O-CH_4 system (DEATON and FROST, 1946) and the volumetric data for pure CH_4 (TESTER, 1961) were used. (d) $\bar{V}v$ of inclusions 6, 8 and 11 was estimated intermediate between the $\bar{V}v$-Zeq.CH_4 of other type V and L1 inclusions, based on their Zeq.CH_4 derived from Raman spectrometric measurements (Fig. 7). (e) Raman spectrometric data demonstrate that PCH_4 is lower in type L2 inclusions with lower *TH*. The bulk $\bar{V}$ of the type L2 inclusions selected have been estimated to range between 32 and 25 cm^3 $mole^{-1}$ by comparison with isocomposition *Lw*-*V* equilibrium curves in the H_2O-CH_4 system,

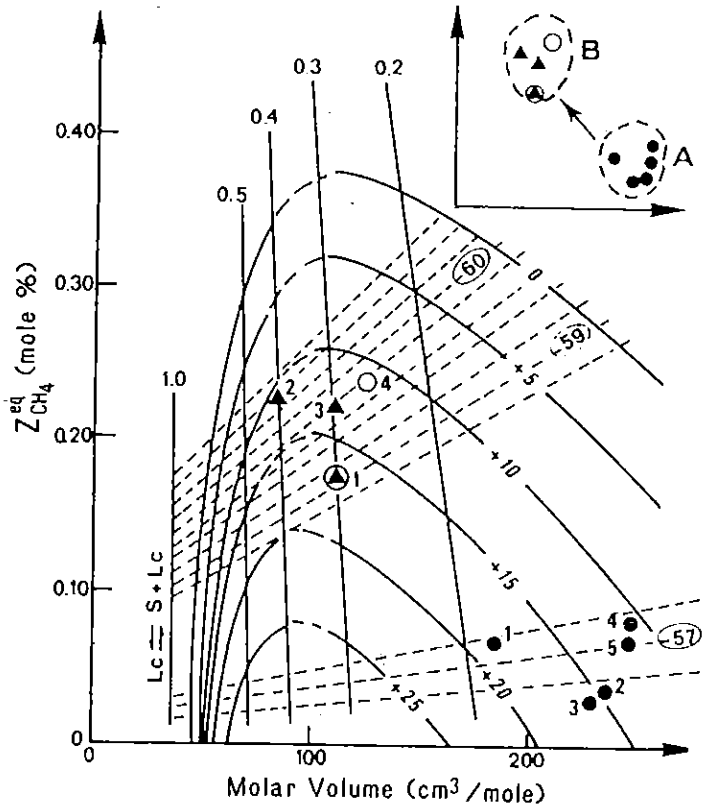

FIG. 4. Comparison of the *Flc*, $TmCO_2$, $ThCO_2$, Zeq.CH_4 of some type V inclusions to a $\bar{V}$-Z projection of the CO_2-CH_4 system (after HEYEN *et al.*, 1982). The isothermal polybaric Lc-V curves are shown from 0° to +25°C, with a dashed part corresponding to the critical region. The dashed lines are the *Lc-V* tie-lines at constant $TmCO_2$ (from −56.8° to −57.2° and −58.8° to −60.6°C). The solid lines indicate constant *Flc* (0.2; 0.3; 0.4; 0.5 and 1.0). The inclusions plot either as a function of $TmCO_2$-*Flc* (triangles), or of $TmCO_2$-$ThCO_2$ (open circles), or of $ThCO_2$-ZCH_4 (full circles). The points obtained from the $TmCO_2$ and/or *Flc* data (field A, inset) do not coincide with those obtained from the $ThCO_2$ and ZCH_4 data (field B, inset). This indicates that *Flc* and $TmCO_2$ cannot be interpreted on a projection of the CO_2-CH_4 system neglecting the aqueous part, because a gas-hydrate is present at $TmCO_2$. In all H_2O-CO_2-CH_4 inclusions characterized by $TmC < ThCO_2$, $\bar{V}$ can be derived from $ThCO_2$-Zeq.CH_4. Inclusion numbers as in Tables 2 and 3.

and with the *Lw-V* equilibrium curve of pure H_2O (Fig. 6). Figure 7 summarizes the evolution of ZCH_4 and *dv* of some inclusions trapped in the course of the aqueous-carbonaceous stage.

Bulk chemical evolution. In the C-O-H system, the bulk $\bar{V}$-X properties of the inclusion fluids determined from measurements obtained below 31°C are representative of the bulk $\bar{V}$-X properties of the fluids under geological P-T conditions of trapping (DUBESSY, 1984). In particular, the species CO and H_2 are negligible in concentration below 600°C under normal conditions of equilibrium in the earth's crust (HOLLOWAY, 1981; DUBESSY, 1984). The bulk X of the fluid inclusions selected are presented in Table 3 and illustrated in Fig. 8 using a projection on the H_2O-CO_2-CH_4 plane.

No accurate chronology can be proposed for the trapping of every inclusion analyzed, because the position of a single inclusion in the trends for *TH*, $ThCO_2$, $TmCO_2$, *TmC*, *TmI* is complex (Figs. 3A and 3B). However, the overall chronology, type V the earliest, then type L1, then type L2 inclusions, implies a bulk chemical evolution with increasing XH_2O and with decreasing XCO_2 and XCH_4. The composition trend on the inset (Fig. 8) outlines this chemical evolution of the fluid with time. The trend is not affected by uncertainties in the inclusion composition (Table 3) because the error bar on the composition of every inclusion is almost parallel to the trend itself (Fig. 8). During the first stage of the hydrothermal evolution, XH_2O increased as dissolved CO_2 decreased and XCH_4 remained nearly constant (around 1.5 ± 1 mole% CH_4, Table 3). Then XCO_2 decreased to near zero. The carbon content of the fluid remained nearly constant and carbon occurred essentially as the species CH_4 only. Finally, XCH_4 also progressively decreased to zero and the fluid became essentially pure water.

P-T *evolution.* The P-$\bar{V}$-T-X properties of every inclusion studied define an isochore in the P-T plane. The fluid in the inclusion was trapped under P-T conditions along the isochore. The isochores of all

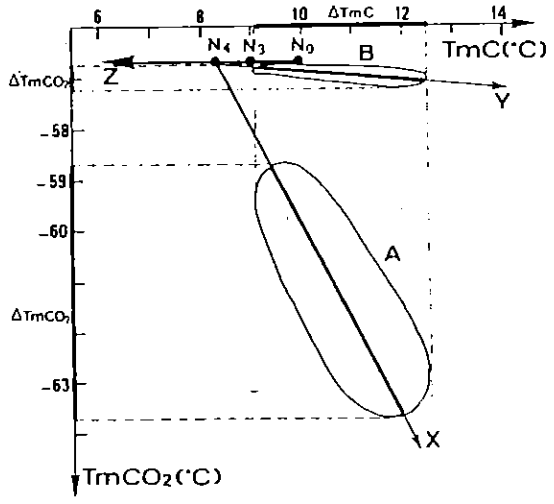

FIG. 5. Estimate of the salt-content of the aqueous part of type V inclusions from TmC-$TmCO_2$, assuming XNaCl does not vary much in these inclusions. Field A: measured TmC and $TmCO_2$ (TmC: $Lc + Lw + C + V \rightleftharpoons Lc + Lw + C$; $TmCO_2$: $S + I + C + Lc + V \rightleftharpoons I + C + Lc + V$). Field B: measured TmC and reconstructed $TmCO_2$ in the absence of C ($TmCO_2$: $S + I + Lc + V \rightleftharpoons I + Lc + V$; see Fig. 4). X and Y axes are the major axes of the ellipses within which plot the $TmCO_2$-TmC and $TmCO_2$-TmC data, respectively. Z-axis is defined by $TmCO_2 = -56.6$°C. N0, N3 and N4 are upper quadruple points in the H_2O-CO_2-NaCl system with 0, 3 and 4 wt.% NaCl respectively (BOZZO *et al.*, 1973). Point N4, at the intersection of X, Y and Z axes is representative of a fictive type V inclusion with pure CO_2 and 4 wt.% eq.NaCl dissolved in its aqueous part.

the inclusions belonging to a specific hydrothermal event provide constraints on its P-T conditions. The P-$\bar{V}$-T-X properties of inclusions 2, 4, 9, 11, 19 and 23 were modeled by the H_2O-CO_2-CH_4 system using the equations of KERRICK and JACOBS (1981) and of JACOBS and KERRICK (1981a) and the $\bar{V}$-X data given in Table 3. In the calculation, dissolved salt was neglected because it was always <1 mole% of the bulk composition, and N_2 was included with CH_4 (Xeq.CH_4 = XCH_4 + XN_2). The isochores are presented in Fig. 9, with some related Lw-V equilibrium curves. The uncertainty on the $\bar{V}$-X properties of each inclusion results in an uncertainty on the slope of the corresponding isochore. The error for each isochore increases with increasing pressure and temperature and is approximately a triangular surface starting from the two-phase field boundary. The surfaces, which are representative of the isochoric behaviour of all the inclusions, overlap one another. A path defining minimum P-T conditions for the trapping of the aqueous-carbonaceous fluid is shown in Fig. 9 (symbol 2). It takes into account the following constraints: (1) the fluid never boiled; the two-phase boundary curves therefore define minimum P-T trapping conditions; (2) the isochores of inclusions 2, 4, 9, 11 and 19 cross around 370°C and 420 bar on the P-T plane. The successive trapping of inclusions 2, 4, 9, 11 and 19 in that order necessarily occurred above these P-T conditions.

Many Sn and W deposits in the Hercynian belt

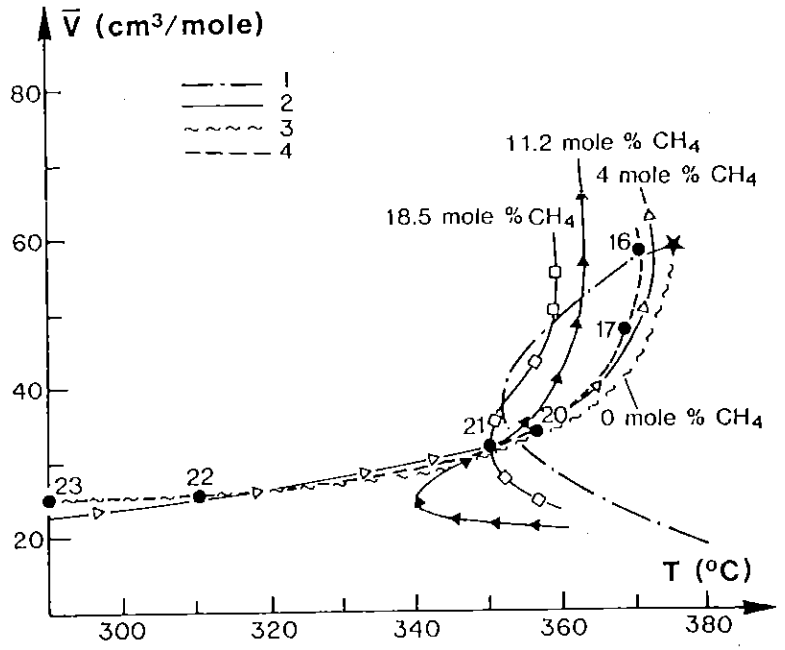

FIG. 6. Estimate of the bulk $\bar{V}$ of type L2 inclusions 21, 22, 23 on a $\bar{V}$-T projection of the H_2O-CH_4 system. 1 = critical curve of the H_2O-CH_4 system starting from the critical point of H_2O (star); 2 (continuous line with superimposed symbols) = isocomposition projections of the two-phase field boundaries of the H_2O-CH_4 system (WELSCH, 1973); 3 = Lw-V equilibrium curve of H_2O (FISCHER, 1976); 4 = $\bar{V}$-TH evolution of the late CH_4-bearing type L1 and the type L2 inclusions (16, 17, 20 and 21, 22, 23 respectively). The solid circles are points representing the inclusions numbered as in Tables 2 and 3.

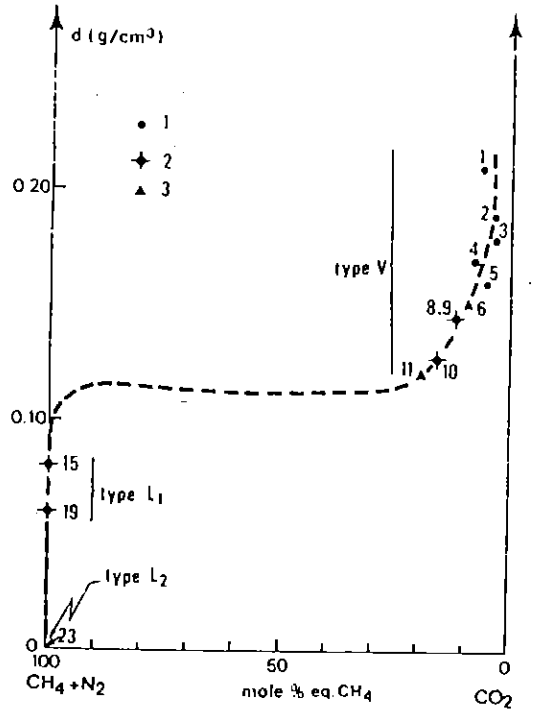

FIG. 7. Summary of the evolution of dv-Zeq.CH_4 of type V, L1 and L2 inclusions. The compositions are those directly derived from the Raman microprobe data. The densities are determined either by interpretation of $Th CO_2$-Zeq.CH_4 in a $\bar{V}$-X projection of the CO_2-CH_4 system (1) or by reference to TmC (2, see text), or are interpolated (3).

occur with thermal anomalies and they are associated with granitic instrusions. Field evidence suggests that tectonic fracturing and vein formation accompanied the emplacement of the Borne granite (WEISBROD *et al.*, 1980). The beginning of circulation of the aqueous-carbonaceous fluid is interpreted as being related in time and temperature to the Borne granite in Fig. 9 (symbol 1). Conditions of 550°C and fluid pressure around 700 bar are consistent with vein emplacement occurring soon after the thermal peak of metamorphism (600°–650°C as indicated by the biotite-muscovite-cordierite-andalusite assemblage, WEISBROD, 1968).

The P-T path proposed for the trapping of type V and L1 inclusions is nearly isobaric. This is because the duration of the aqueous-carbonaceous stage can be estimated at around 10^{+4} years, by analogy with theoretical analysis of convective hydrothermal systems (NORTON and CATHLES, 1979). The depth of emplacement of the vein probably did not vary much during that length of time. The isochores of type V and type L1 fluids have a fan-like distribution above their point of intersection because of decreasing compressibility of the fluids. Large variations of temperature are therefore implied by the proposed nearly isobaric path.

The pressure conditions at the end of the aqueous-carbonaceous stage are uncertain. Two possible paths are presented in Fig. 9. Along path a, it is assumed that the fluid pressure regime essentially remained unchanged during the aqueous-carbonaceous stage. On path b, it is assumed that the fluid pressure increased as a result of the self-sealing of the vein by precipitation of wolframite and minor quartz.

High P-T *chemical equilibria.* The CO_2-rich fluids analyzed in type V inclusions are similar to the fluids from geothermal fields in both their composition and the P-T conditions of their generation (ELLIS, 1970). The T-X data from geothermal systems show that the species H_2O, CO_2 and CH_4 are close to chemical equilibrium under geothermal conditions (GIGGENBACH, 1980). Therefore, it is legitimate to assume that chemical equilibrium between the CO_2, CH_4 and H_2O from type V fluids was maintained *via* the reaction: $CO_2 + 2H_2O \rightleftharpoons CH_4 + 2O_2$. The $\bar{V}$-XCO_2-XCH_4-XH_2O properties reconstructed from the microthermometric and Raman spectrometric data are quite similar to those at the high P-T conditions of trapping and consequently allow calculation of fO_2 using the above equilibrium (DUBESSY, 1984). Temperature and pressure are derived from Fig. 9, the fugacity coefficients γi were obtained from the equation of state of KERRICK and JACOBS (1981), JACOBS and KERRICK (1981a), and the equilibrium constant is that used by OHMOTO and KERRICK (1977). The calculation shows that fO_2 decreased with decreasing temperature from 10^{-22} to 10^{-27} bar along the P-T path proposed for the trapping of the fluids in type V inclusions (Fig. 10). The uncertainties in these values are around half a log unit, given the uncertainties of P, XCO_2, XCH_4 and XH_2O. In addition, the influence of NaCl in solution has been neglected and, even in small amounts (5–10 wt%), it slightly increases the activity of CO_2 in H_2O-rich carbonaceous fluids (JACOBS and KERRICK, 1981b). An estimate of fO_2 during the trapping of type L1 inclusion fluids is difficult because CO_2 is below the detection level of the Raman probe in these inclusions (see below). A maximum fO_2 of 10^{-29} bar can be inferred, assuming a maximum ZCO_2 equal to the detection limit of

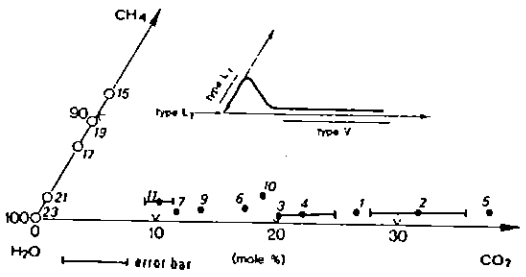

FIG. 8. Bulk composition of some fluid inclusions from the aqueous-carbonaceous stage, projected onto the H_2O-CO_2-CH_4 composition plane. Inclusion numbers as in Tables 2 and 3. Full circles = type V inclusions; empty circles = type L1 and L2 inclusions. The inset shows the bulk fluid evolution and the disappearance of CO_2 in the fluid.

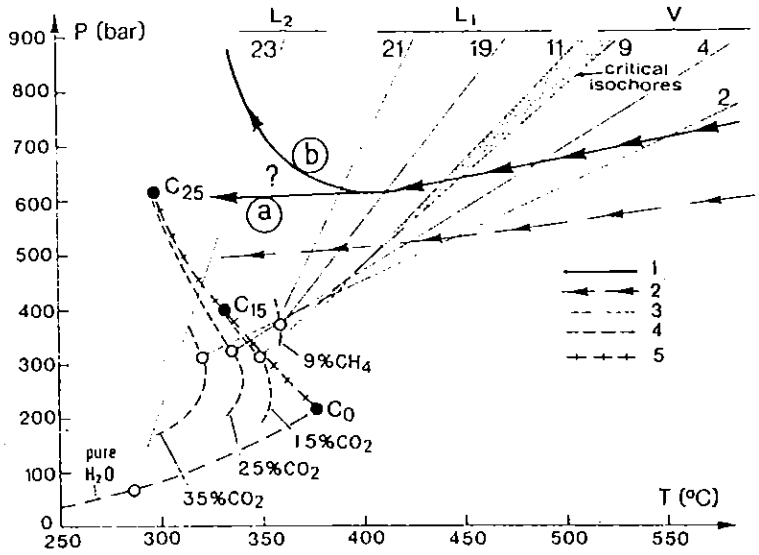

FIG. 9. Reconstruction of the *P-T* conditions during the aqueous-carbonaceous stage. (1) probable *P-T* path. (2) minimum *P-T* trapping conditions. (3) isochores with inclusion numbers as in Tables 2 and 3. (4) isocomposition two-phase field boundaries (mole%). Sources of data: H_2O-CO_2: TAKENOUCHI and KENNEDY, 1964; H_2O-CH_4: WELSCH, 1973; H_2O: FISCHER, 1976. Open circles: starting point of the isochore. (5) critical curve of the H_2O-CO_2 system. C0, C15, C25: critical point of a H_2O-CO_2 mixture with 0, 15, 25 mole% CO_2. The dotted area approximately indicates the isochores of inclusions with critical homogenization.

CO_2 by the Raman probe (0.2 mole% for the inclusion considered, Fig. 10). This suggests that the transition between type V and L1 fluids corresponded to a drop in log fO_2 of at least two units. In addition, pH increased as a result of the formation of CH_4 from CO_2.

It is a debated point whether gases interacted with elemental carbon or not in geothermal fields (D'AMORE and PANICHI, 1980; GIGGENBACH, 1980). It is possible that, during the aqueous-carbonaceous stage, the fluid phase was in equilibrium with graphitic material since graphitic material is observed in both the vein quartz and the metasedimentary rocks. In this case, fO_2 was buffered by the equilibrium $C + O_2 \rightleftharpoons CO_2$, according to the relation $fO_2 = fCO_2/K(P,T)$ where $K(P, T)$ is the equilibrium constant of the reaction at the pressure and temperature considered (HUEBNER, 1971). The *P-T-*fCO_2 of some type V inclusions, computed from the graphite-fluid equilibrium using the equation of state of KERRICK and JACOBS (1981), are the same within the limits of error as the ones calculated from the equilibrium $CO_2 + H_2O \rightleftharpoons CH_4 + 2O_2$. Therefore, the chemical evolution of H_2O-CO_2-CH_4 type V fluids, close to Q-F-M, was possibly controlled by equilibrium with graphitic material from the metamorphic country rocks. At the transition from type V to L1 fluids, dissolved CO_2 essentially disappeared. The chemistry of the fluid must have then no longer been controlled by the presence of graphitic material, since otherwise the fluid would have contained detectable amounts of CO_2 at the *P-T* conditions considered.

Bulk fluid evolution and wolframite deposition

The bulk chemistry of the fluid was controlled by a continuous influx of water into the Serrecourte

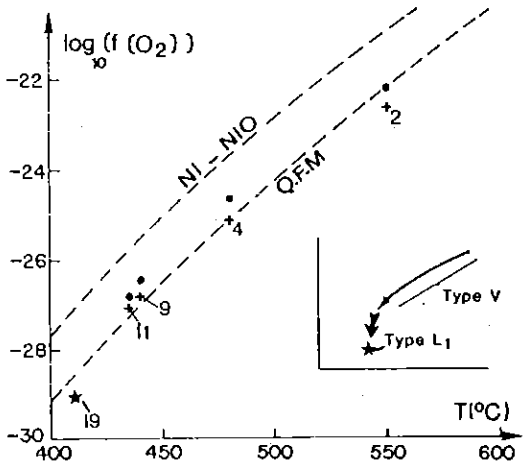

FIG. 10. Log fO_2-T polybaric evolution (= continuous line) along the *P-T* path (symbol 1, Fig. 9). The log fO_2 for type V inclusions 2, 4, 9, 11 and the minimum log fO_2 for type L2 inclusion 19 (star) are shown. Full circles and star = equilibrium $CO_2 + 2H_2O \rightleftharpoons CH_4 + 2O_2$. Crosses = equilibrium $C + O_2 \rightleftharpoons CO_2$. Dotted lines = Ni-NiO and Q-F-M. buffers (ROBIE *et al.*, 1978; HUEBNER, 1971). On the inset, the light arrow indicates the fO_2-T variations during the trapping of type V fluids. The heavy arrow indicates the minimum drop of fO_2 due to the disappearance of CO_2 in the fluid at the transition from type V to type L1 inclusions.

vein. It can be modelled in terms of the mixing of a hot H_2O-CO_2-CH_4 low-density fluid (vapour) with colder high density liquid water. Traces of N_2 were present in the H_2O-CO_2-CH_4-bearing fluid and concentrations of N_2 were erratic (Table 2). This fact suggests that (1) the observed chemical changes did not result from simple two end-member mixing. Several influxes of fluid with different compositions occurred, presumably related to discontinuous periods of fracturing. (2) N_2 was presumably not buffered by any mineral assemblage in the metamorphic rocks (HONMA and ITIHARA, 1981). The N_2-content of the fluid was low and this could indicate that all NH_4-bearing silicates within the thermal aureole around the Borne granite had already released their ammonium (HALLAM and EUGSTER, 1976) during the first pre-Hercynian to early Hercynian metamorphism preceeding granite emplacement (MARIGNAC *et al.*, 1980).

The fO_2 of H_2O-CO_2-CH_4-bearing fluids was maintained close to Q-F-M, although several influxes of fluid entered the system at that stage. This fact suggests that both minerals from the wall-rock (oxides or graphite) and chemical equilibria between CO_2, CH_4 and H_2O within the fluid phase controlled the fluid composition, and specifically fO_2. Calculations show that the fO_2 of type V fluids is compatible with the graphite-fluid equilibrium. In support of that interpretation, graphitic material was observed in the wallrock around the vein.

A later stage of the fluid evolution began with the transition from type V to type L1 fluids. At that stage, no inclusion with a composition intermediate between 90 mole% H_2O-9 mole% CO_2-1 mole% CH_4 (inclusion 11) and 90 mole%-H_2O-10 mole% CH_4 (inclusion 15), was preserved in quartz (Fig. 8). This transition corresponded to a drop in log fO_2 of at least two units. Log fO_2 at this stage was lower than that controlled by the graphite-fluid equilibrium. If fO_2 of the early type V fluids simply resulted from chemical equilibration in a homogeneous phase of H_2O, CO_2, and/or CH_4, the cause of the observed reduction in fO_2 could be the influx of more reduced water in the system. The fO_2 of early H_2O-CO_2-CH_4 fluids however was apparently controlled by the graphite-fluid equilibrium. The observed drop of fO_2 therefore appears to indicate that the temperature of the fluid system had dropped at that time to where rates of chemical exchange between gases and graphite were too slow to maintain equilibrium. A minimum blocking temperature of 370°C for the H_2O-CO_2-CH_4-graphite system is implied (370°C is the minimum trapping temperature of type L1 fluids, see above discussion and Fig. 9). A blocking isotopic temperature of 320° ± 30°C for ^{12}C-^{13}C exchange between CO_2 and CH_4 has been inferred from ^{12}C-^{13}C-isotope data on CO_2 and CH_4 gas from geothermal fields (SHEPPARD, 1981). 320° ± 30°C must be close to the maximum for the blocking temperature of the reaction $CH_4 + 2O_2 \rightleftharpoons CO_2 + 2H_2O$, because the ^{13}C-exchange between CO_2 and CH_4 probably proceeds *via* the reaction $CH_4 + 2O_2 \rightleftharpoons CO_2 + 2H_2O$, and because chemical equilibration between CO_2 and CH_4 proceeds 100 times faster than carbon isotopic equilibration between CO_2 and CH_4 (GIGGENBACH, 1982). A blocking temperature for the chemical equilibrium between H_2O, CO_2, CH_4, and graphite at least 50°C higher than that for the ^{13}C-isotopic equilibrium between CO_2 and CH_4 probably indicates that the kinetics of chemical equilibration of the heterogeneous system graphite-fluid is slower than that of the homogeneous system involving just CO_2, CH_4 and H_2O (*e.g.*, BARTON, 1981).

The density of early type V fluids was lower by 0.2 g cm^{-3} than the density of a H_2O-NaCl solution stable under the same pressure and temperature, whatever its salinity (POTTER and BROWN, 1977). This is because, in the H_2O-CO_2 and H_2O-CH_4 systems, the critical points are shifted towards temperature lower than that of the critical point of H_2O whereas, in the H_2O-NaCl system, the critical points are shifted towards temperature higher than that of the critical point of H_2O (FRANCK, 1981; PICHAVANT *et al.*, 1982). This fact is worth noting because gradients in fluid density are, together with temperature gradients, a driving force for fluid convection around a magmatic intrusion (NORTON and CATHLES, 1979). Type V and type L2 fluids may have been representative, respectively, of the hotter fluid and of the colder fluid that circulated along a streamline of the convective system around the Borne granite at the time of its emplacement. A larger fluid density gradient, compared to that in a convective system involving H_2O-NaCl fluids, could have favoured increased fluid flow around the Borne granite. In all convective systems under greenschist facies conditions in which the fluid chemistry is controlled by the graphite-fluid equilibrium, gradients in fluid density, and hence gradients in fluid pressure, may remain relatively constant in time provided that the maximum temperature of the convective system remains above the blocking temperature of the graphite-fluid equilibrium. In the Hercynian belt where many granites intrude black shales or pelitic rocks (KELLY and RYE, 1979; RAMBOZ, 1980b; CHEILLETZ, 1984; NORONHA, 1974; GIULIANI, 1984), this mechanism could have been the cause for increased fluid flow and ore metal mobilization. In the Panasqueira deposit, in particular, KELLY and RYE (1979) invoked the existence of "an extremely stable fluid pressure gradient", but could not find a mechanism to produce it.

The deposition of ferberite was related to the aqueous-carbonaceous stage because this mineral contains H_2O, CO_2 and CH_4 in fluid inclusions. Based on the results of fluid inclusion studies of quartz, the mass spectrometric data on the fluids extracted from quartz can be summarized and interpreted as follows: (1) type V inclusions in quartz decrepitated mostly above 640°C, whereas type L1,

L2 and L3 inclusions decrepitated mostly below 640°C. (2) Analyses of type L1, L2 and L3 inclusions in quartz were contaminated by some type V inclusions decrepitating below 640°C. The nature of the gases extracted from wolframite, together with the temperature at which gas was released from this mineral gives an indication of the $\bar{V}$-X properties of the fluid trapped in wolframite. This is because (a) wolframite contains mainly one generation of inclusions and (b) because an internal pressure of the same order of magnitude is required to decrepitate fluid inclusions both in quartz and in wolframite (TUGARIMOV and NAUMOV, 1970). The mass spectrometric data suggest that the fluids in wolframite were in the $\bar{V}$-X gap between type V and type L1 fluids from quartz. This suggests that wolframite was formed at a stage when XCO_2 decreased and CH_4 became the dominant carbon species in solution with H_2O. The disappearance of CO_2 from the fluid was possibly the consequence of a drop in temperature below the blocking temperature of the graphite-fluid equilibrium. It might have favoured the destabilization of tungsten complexes and ferberite precipitation either directly in the case of carbonate/bicarbonate complexes (HIGGINS, 1980) or indirectly by pH increase in the case of tungsten heteropolyacids (VON GUNDLACH and THORMANN, 1960).

Tungsten mineralization is frequently associated with CO_2-rich fluids (NORONHA, 1974; LANDIS and RYE, 1974; DURISOVA *et al.*, 1979; KELLY and RYE, 1979; RAMBOZ, 1980b; GIULIANI, 1984; CHEILLETZ, 1984). Although some wolframite mineralization is also associated with H_2O-NaCl fluids (CHAROY, 1979), CO_2-rich fluids are assumed to play an important role in the transport of tungsten (HIGGINS, 1980). In the case studied, there is no evidence to say whether tungsten was transported by the early aqueous-carbonaceous fluid or by the aqueous fluid which diluted it or by both fluids.

CONCLUSIONS

The gangue quartz of the ferberite vein of Serrecourte records two main hydrothermal stages: an early aqueous-carbonaceous stage and a later pure aqueous stage. In order to reconstruct the P-$\bar{V}$-T-X evolution of the earlier H_2O-CO_2-CH_4 stage, it was necessary to combine microthermometric and Raman spectrometric data with the equations of state of HEYEN *et al.*, (1982) and JACOBS and KERRICK (1981a). It was shown that all $Tm CO_2$ in gas-rich inclusions were measured in the presence of gas-hydrate, and were significantly lower than if measured in the absence of gas hydrate.

Based on the distribution of the fluid inclusions in quartz and on the microthermometric and Raman spectrometric data, it was shown that the fluids from the aqueous-carbonaceous stage were (1) trapped in the one-phase stability field, (2) that their compressibility decreased with time, and (3) that they contained progressively less dissolved CO_2 and CH_4 as temperature decreased. An increase of 0.35 g cm^{-3} in the fluid density during the aqueous-carbonaceous stage was the result of both the decrease in temperature and of the decrease in PCO_2 and PCH_4. Above 400°C, the fluid was composed of H_2O, CO_2 and CH_4 and its fO_2 remained close to that of the Q-F-M buffer, compatible with the graphite-fluid equilibrium. A drop in PCO_2 at around 400°C implied a drop in fO_2 and a likely pH-increase. The fluids trapped below 400°C in quartz all contained only H_2O and CH_4 and were characterized by fO_2 below that fixed by the graphite-fluid equilibrium. Control of fO_2 in the fluid by graphitic material in the wall-rock while temperature was above the blocking temperature of the graphite-fluid equilibrium is a possible mechanism to account for the two contrasting parts in the aqueous-carbonaceous stage. According to this interpretation, fluid inclusion data suggest that the blocking temperature of this equilibrium was at least 370°C and probably around 400°C. The fluids in ferberite were in the $\bar{V}$-X gap recorded by the H_2O-CO_2-CH_4 fluid in quartz, and ferberite deposition was probably related to the changes in fluid chemistry at ~400°C.

The fluid inclusion data illustrated an interesting feature of hydrothermal convective systems in graphite-bearing rocks under greenschist facies conditions. As long as temperature in these systems remains above the blocking temperature of the graphite-fluid equilibrium, gradients in fluid composition and hence larger gradients in fluid density and in fluid pressure are maintained. These gradients in turn stimulate more active fluid flow. Ferberite deposition is probably related to the chemical changes caused by the decrease of temperature below the blocking temperature of the graphite-fluid system and fluctuations of temperature around that blocking temperature can cause repeated stages of ferberite deposition.

Finally, with respect to isotope thermometry, it is worth noting that the bulk of quartz precipitated at 550°–500°C, whereas wolframite precipitated at around 400°C. No meaningful thermometry could be derived from the measurement of the fractionation of ^{18}O between quartz and wolframite. Before using isotope thermometry on hydrothermal minerals, it should be verified that they are cogenetic by comparing the nature of the fluids they contain using combined mass spectrometry and fluid inclusion data.

Acknowledgments—The authors are grateful to C. Marignac, A. Weisbrod and to the students from the School of Geology (Nancy) for supplying the samples and their knowledge on the geology of the area studied. The manuscript was improved thanks to the many suggestions from M. Pichavant, S. M. F. Sheppard, A. Weisbrod, C. Harris and J. Ferry and to discussion with A. Boullier, A. Pecher and B. Poty. M. L. Crawford and E. Roedder reviewed the manuscript and contributed to its clarity. This research received financial support from D.G.R.S.T. (n° 78-7-3005) and from A.T.P. "Métallogénie et Géochimie, 1981".

Editorial handling: J. M. Ferry

REFERENCES

ARAI Y., KAMINISHI G. and SAITO S. (1971) The experimental determination of the *P-V-T-X* relations for the carbon dioxide-nitrogen and the carbon dioxide-methane systems. *J. Chem. Eng. Japan* **4**, 113–122.

BARTON P. B. JR. (1981) Physical-chemical conditions for ore deposition. In *Chemistry and Geochemistry of Solutions at High Temperatures and Pressures. Physics and Chemistry of the Earth* (eds. D. RICKARD and F. E. WICKMAN), Vols. 13 and 14, pp. 461–503, Pergamon Press.

BERNSTEIN H. J. (1982) Raman intensities of gases. In *Vibrational Intensities in Infrared and Raman Spectroscopy* (eds. W. B. PERSON and G. ZERBI), Section C, Chap. 3, pp. 258–265, Elsevier.

BOZZO A. T., CHEN H. S., KASS J. and BARDUHN A. J. (1973). The properties of the hydrates of chlorine and carbon dioxide. *Int. Symp. Fresh Water from the Sea*. 3, 437–451.

CHAROY B. (1979) Greisenisation, minéralisation et fluides associés à Cligga Head, Cornwall. *Bull. Minéral.* **102**, 633–641.

CHEILLETZ A. (1984) Caractéristiques géochimiques et thermobarométriques des fluides associés à la scheelite et au quartz des minéralisations tungstifères du Jbel Aouam (Maroc Central). *Bull. Minéral.* **107**, 255–272.

CHEILLETZ A., DUBESSY J., KOSZTOLANYI C., MASSON-PEREZ N., RAMBOZ C. and ZIMMERMANN J. L. (1984) Les fluides moléculaires d'un filon de quartz hydrothermal: comparaison de techniques analytiques ponctuelles et globales, contamination des fluides occlus par des composés carbonés. *Bull. Minéral.* **107**, 169–180.

COLLINS P. L. F. (1979) Gas-hydrates in CO_2-bearing fluid inclusions and the use of freezing data for estimation of salinity. *Econ. Geol.* **74**, 1435–1444.

CULBERSON O. L. and MCKETTA J. J., JR. (1951) Phase equilibria in hydrocarbon-water systems. III. The solubility of methane in water at pressures to 10,000 PSI. *J. Petroleum. Technol.* **4**, 223–226.

D'AMORE F. and PANICHI C. (1980) Evaluation of deep temperatures of hydrothermal systems by a new gas geothermometer. *Geochim. Cosmochim. Acta* **44**, 549–556.

DEATON W. M. and FROST E. M. (1946) Gas hydrates and their relation to the operation of natural gas pipelines. *U.S. Bur. Mines, Monogr.* **8**, 103 p.

DELHAYE M. and DHAMELINCOURT P. (1975) Raman microprobe and microscope laser excitation. *J. Raman Spectrosc.* **3**, 33–43.

DHAMELINCOURT P., BENY J. M., DUBESSY J. and POTY B. (1979) Analyse d'inclusions fluides à la microsonde MOLE à effet Raman. *Bull. Minéral.* **102**, 600–610.

DUBESSY J. (1984) Simulation des équilibres chimiques dans le système C-O-H. Conséquences méthodologiques pour les inclusions fluides. *Bull. Minéral.* **107**, 155–168.

DURISOVA J., CHAROY B. and WEISBROD A. (1979) Fluid inclusion studies in minerals from tin and tungsten deposits in the Krusné Hory Mountains (Czechoslovakia). *Bull. Minéral.* **102**, 665–675.

ELLIS A. J. (1970) Quantitative interpretation of chemical characteristics of hydrothermal systems. *Geothermics Special Issue* **2**, pt. 1, 516–528.

ELLIS A. J. and GOLDING R. M. (1963) The solubility of carbon dioxide above 100°C in water and in sodium chloride solutions. *Amer. J. Sci.* **261**, 47–60.

EUGSTER H. P. (1981) Metamorphic solutions and reactions. In *Chemistry and Geochemistry of Solutions at High Temperatures and Pressures. Physics and Chemistry of the Earth* (eds. D. RICKARD and F. E. WICKMAN), Vols. 13 and 14, pp. 461–503, Pergamon Press.

FISCHER J. R. (1976) The volumetric properties of H_2O. A graphical portrayal. *J. Res. U.S. Geol. Surv.* **4**, 189–193.

FRANCK E. U. (1981) Survey of selected non-thermodynamic properties and chemical phenomena of fluids and fluid mixtures. In *Chemistry and Geochemistry of Solutions at High Temperatures and Pressures. Physics and Chemistry of the Earth* (eds. D. RICKARD and F. E. WICKMAN), Vols. 13 and 14, pp. 65–82, Pergamon Press.

GIGGENBACH W. F. (1980) Geothermal gas equilibria. *Geochim. Cosmochim. Acta* **44**, 2021–2032.

GIGGENBACH W. F. (1982) Carbon-exchange between CO_2 and CH_4 under geothermal conditions. *Geochim. Cosmochim. Acta* **46**, 159–165.

GIULIANI G. (1984) Les concentrations filoniennes à tungstène-étain du massif granitique des Zaër (Maroc Central): mineralisations et phases fluides associées. *Mineral. Deposita* **19**, 193–201.

HALLAM M. and EUGSTER H. P. (1976) Ammonium silicate stability relations. *Contrib. Mineral. Petrol.* **57**, 227–244.

HERZBERG G. (1951) *Molecular Spectra and Molecular Structure. II. Infrared and Raman Spectra.* Van Nostrand Reinhold Company.

HEYEN G., RAMBOZ C. and DUBESSY J. (1982) Simulation des équilibres de phases dans le système CO_2-CH_4 en-dessous de 50°C et de 100 bar. *C.R. Acad. Sci. Paris* **294**, 203–206.

HIGGINS N. C. (1980) Fluid inclusion evidence for the transport of tungsten by carbonate complexes in hydrothermal solutions. *Can. J. Earth Sci.* **17**, 823–830.

HOLLOWAY J. R. (1981) Compositions and volumes of supercritical fluids in the Earth's Crust. In *M.A.C. Short Course in Fluid Inclusions: Applications to Petrology* (eds. L. HOLLISTER and M. L. CRAWFORD), pp. 13–38, Mineral. Assoc. Canada.

HONMA H. and ITIHARA Y. (1981) Distribution of ammonium in minerals of metamorphic and granitic rocks. *Geochim. Cosmochim. Acta* **45**, 983–988.

HSU L. C. (1976) The stability of the wolframite series. *Amer. Mineral.* **61**, 944–955.

HUEBNER J. S. (1971) Buffering techniques of hydrostatic systems at elevated pressures. In *Research Techniques for High Pressure and Temperature.* (ed. G. C. ULMER), pp. 123–177, Springer-Verlag.

JACOBS G. K. and KERRICK D. M. (1981a) Methane: an equation of state with application to the ternary system H_2O-CO_2-CH_4. *Geochim. Cosmochim. Acta* **45**, 607–614.

JACOBS G. K. and KERRICK D. M. (1981b) Devolatilization equilibria in H_2O-CO_2 and H_2O-CO_2-NaCl fluids: an experimental and thermodynamic evaluation at elevated pressures and temperatures. *Amer. Mineral.* **66**, 1135–1153.

KELLY W. C. and RYE R. O. (1979) Geologic, fluid inclusion and stable isotope studies of the tin-tungsten deposits of Panasqueira, Portugal. *Econ. Geol.* **74**, 1721–1822.

KERRICK D. M. and JACOBS G. K. (1981) A modified Redlich-Kwong equation for H_2O, CO_2 and H_2O-CO_2 mixtures at elevated pressures and temperatures. *Amer. J. Sci.* **281**, 735–767.

LANDIS G. P. and RYE R. O. (1974) Geology, fluid inclusion and stable isotope studies of the Pasto Bueno tungsten-base metal ore deposit, Northern Peru. *Econ. Geol.* **69**, 1025–1059.

MARIGNAC C., LEROY J., MACAUDIERE J., PICHAVANT M. and WEISBROD A. (1980). Evolution tectonométamorphique d'un segment de l'orogène hercynien: les Cévennes médianes, Massif Central Français. *C.R. Acad. Sci. Paris.* **291**, 605–608.

MIALHE J. (1980) Le massif granitique de la Borne, Cévennes. Thèse Spéc. Univ. Clermont-Ferrand, 130 p.

NICOLAS A. and POIRIER J. P. (1976) Flow and annealing processes in crystals. In *Crystalline Plasticity and Solid State Flow in Metamorphic Rocks* (ed. M. H. P. BOTT), Chap. 4, pp. 122–170, Wiley.

NORONHA F. (1974) Etude des inclusions fluides dans les quartz des filons du gisement de tungstène de Borralha (Nord du Portugal). *Publicaçoes do Museu e Laboratorio Mineralogico é Geologico da Faculdade de Ciencias do Porto.* LXXXV, 4è série, 1–36.

NORTON D. and CATHLES L. M. (1979) Thermal aspect of ores deposition. In *Geochemistry of Hydrothermal Ore Deposits* (ed. H. L. BARNES), 2nd ed., pp. 611–631. Wiley.

OHMOTO H. and KERRICK D. (1977) Devolatization equilibria in graphitic systems. *Amer. J. Sci.* 277, 1013–1044.

PICHAVANT M., RAMBOZ C. and WEISBROD A. (1982) Fluid immiscibility in natural processes: use and misuse of fluid inclusion data. I. Phase equilibria analysis. A theoretical and geometrical approach. *Chem. Geol.* 37, 1–27.

PLACZEK G. (1934) In *Handbuch der Radiologie* (ed. E. MARX), Vol. 6, Chap. 2, pp. 209–375. Akad. Verlags Gesellschaft.

POTTER R. W. and BROWN D. L. (1977) The volumetric properties of aqueous sodium chloride solutions from 0° to 500°C at pressures up to 2000 bars based on a regression of available data in the literature. *U.S. Geol. Surv. Bull. 1421-C*, C1-C36.

POTTER R. W., CLYNNE M. A. and BROWN D. L. (1978) Freezing point depression of aqueous sodium chloride solutions. *Econ. Geol.* 73, 284–285.

POTY B., LEROY J. and JACHIMOWICZ L. (1976) Un nouvel appareil pour la mesure des températures sous le microscope: l'installation de microthermométrie Chaixmeca. *Bull. Soc. Fr. Minéral. Cristallogr.* 99, 182–186.

RAMBOZ C. (1980a) Problèmes posés par la détermination de la composition des fluides carboniques complexes, à l'aide des techniques microthermométriques. *C.R. Acad. Sci. Paris* 290, 7, 499–502.

RAMBOZ C. (1980b) Fluid phases associated with Sn-W deposits from South of Massif Central, France. *26th Int. Geol. Cong., Paris, Abstr.* 1, 80.

RAMBOZ C., PICHAVANT M. and WEISBROD A. (1982) Fluid immiscibility in natural processes: use and misuse of fluid inclusion data. Part. II: Interpretation of fluid inclusion data in terms of immiscibility. *Chem. Geol.* 37, 29–48.

ROBIE R. A., HEMINGWAY B. S. and FISHER J. R. (1978) Thermodynamic properties of minerals and related substances at 298.15°K and 1 bar (10^5 Pascals) pressure and at higher temperatures. *U.S. Geol. Surv. Bull. 1452*. 456 p.

ROEDDER E. (1970) Application of an improved crushing microscope stage to studies of the gases in fluid inclusions. *Schweiz. Mineral. Petrol. Mitt.* 50, 41–58.

ROEDDER E. (1972) Composition of fluid inclusions. In *Data of Geochemistry* (ed. M. FLEISCHER), *U.S. Geol. Surv. Prof. Paper 440-JJ*, 164 p.

ROEDDER E. (1976) Fluid inclusion evidence on the genesis of ores in sedimentary and volcanic rocks. In *Ores in Sediments. Sedimentary and Volcanic Rocks* (ed. K. H. WOLF), Vol. 2, pp. 67–110, Elsevier.

RUMBLE D. III, FERRY J. M., HOERING T. C. and BOUCOT A. J. (1982) Fluid flow during metamorphism at the Beaver Brook fossil locality, New Hampshire. *Amer. J. Sci.* 282, 886–919.

SARASHINA E., ARAI Y. and SAITO S. (1971) Vapor-liquid equilibria for the nitrogen-methane-carbon dioxide system. *J. Chem. Eng. Japan* 4, 377–378.

SCHROTTER H. W. and KLOCKNER H. W. (1979) Raman scattering cross sections in gases and liquids. In *Raman Spectroscopy of Gases and Liquids* (ed. A. WEBER), Chap. 4, pp. 123–166. Springer Verlag.

SHEPPARD S. M. F. (1981) Stable isotope geochemistry of fluids. In *Chemistry and Geochemistry of Solutions at High Temperatures and Pressures. Physics and Chemistry of the Earth* (eds. D. RICKARD and F. E. WICKMAN), Vols. 13 and 14, pp. 419–443, Pergamon Press.

TAKENOUCHI S. and KENNEDY G. C. (1964) The binary system H_2O-CO_2 at high temperatures and pressures. *Amer. J. Sci.* 263, 445–454.

TESTER H. E. (1961) Methane. In *Thermodynamic Functions of Gases* (ed. F. DIN), Vol. 3, pp. 1–71. Butterworths.

TUGARIMOV A. I. and NAUMOV V. B. (1970) Dependence of the decrepitation temperature of minerals on the composition of their gas-liquid inclusions and hardness. *Akad. Nauk SSSR Doklady* 195, 112–114.

UNRUH C. H. and KATZ D. L. (1949) Gas hydrates of carbon dioxide-methane mixtures. *J. Petrol. Technol.* 1, 83–86.

VON GUNDLACH H. and THORMANN W. (1960) Versuch einer Deundung der Entstehung von Wolfram und Zinnlagerstätte. *Zeitschrift der Deutschen Geologischen Gesellschaft* 112, 1–35.

WEISBROD A. (1967) Explication sommaire de la carte géologique des Cévennes médianes. *Sci. de la Terre* 12, 301–344.

WEISBROD A. (1968) Les conditions du métamorphisme dans les Cévennes médianes *C.R. Acad. Sci. Paris* 266, 755–757.

WEISBROD A. (1970) Pétrologie du socle métamorphique des Cévennes Médianes. Reconstitution sédimentologique et approche thermodynamique du métamorphisme. Thèse Doctorat. Nancy, 4 vol., 530 p.

WEISBROD A. (1974) Carte géologique 1/50 000, feuille Largentière. Service Géologique National.

WEISBROD A., POTY B. and TOURET J. (1976) Utilisation des inclusions fluides en géochimie-pétrologie: tendances actuelles. *Bull. Soc. Fr. Minéral. Cristallogr.* 99, 140–152.

WEISBROD A., LEROY J., MACAUDIERE J., MARIGNAC C. and PICHAVANT M. (1980) Relations structurales et chronologiques entre le magmatisme basique, les granitisations et l'évolution tectonométamorphique tardihercynienne dans les Cévennes Médianes. *C.R. Acad. Sci. Paris.* 291, 665–668.

WELSCH H. (1973) Die systeme Xenon-Wasser und Methan-Wasser bei hohen Drücken und Temperaturen. Ph.D. dissertation, Inst. for Physical Chemistry Karlsruhe.

APPENDIX

Calculation of the bulk composition and bulk density of type V, L1 and L2 inclusions in the H_2O-CO_2-CH_4-N_2 system

The $\bar{V}$-X properties of the fluid inclusions can be calculated, provided that, at a given T, Flw and dl for the aqueous part and Fic, dv, ZCO_2, ZCH_4 and ZN_2 for the non-aqueous part, are known. $Z'CO_2$ can be estimated using the experimental data of ELLIS and GOLDING (1963).

$$n\mathrm{H_2O} = \frac{Flw \cdot dl}{18}$$

$$n\mathrm{CO_2} = \frac{(1 - Flw) \cdot dv \cdot \mathrm{ZCO_2}}{44 - 28\mathrm{ZCH_4} - 16\mathrm{ZN_2}} + Z'\mathrm{CO_2} \cdot n\mathrm{H_2O}$$

$$n\mathrm{CH_4} = \frac{(1 - Flw) \cdot dv \cdot \mathrm{ZCH_4}}{44 - 28\mathrm{ZCH_4} - 16\mathrm{ZN_2}}$$

$$n\mathrm{N_2} = \frac{(1 - Flw) \cdot dv \cdot \mathrm{ZN_2}}{44 - 28\mathrm{ZCH_4} - 16\mathrm{ZN_2}}$$

$$Xi = \frac{ni}{n\mathrm{H_2O} + n\mathrm{CO_2} + n\mathrm{CH_4} + n\mathrm{N_2}}$$

$$d = Flw \cdot dl + (1 - Flw) \cdot dv$$

The data used to estimate Flw, ZCO_2, ZCH_4, ZN_2 and dv are given in the text and in the figure captions. dv is derived from the interpretation of the microthermometric data TmC or $ThCO_2$ and from the spectrometric measurements. In practice, the density derived from ZCO_2, ZCH_4, ZN_2 and TmC can be considered the same as that derived from ZCO_2, ZCH_4, ZN_2 and $ThCO_2$, provided that $TmC < ThCO_2$. If this condition is verified, in the temperature range 0°–31°C, the non-aqueous part of an inclusion behaves as an isochoric and isochemical sub-system due to the low compressibility of H_2O and the low PH_2O over this temperature range. The change in ZCO_2 as a result of a change in $Z'CO_2$ with temperature is neglected. This simplification is all the more valid when $ThCO_2$ is closer to TmC.

PUBLICATION XI : Fluid inclusion and mineralogical evidence for high-temperature saline hydrothermal circulation in the Red Sea metalliferous sediments : preliminary results.

Fluid Inclusion and Mineralogical Evidence for High-Temperature Saline Hydrothermal Circulation in the Red Sea Metalliferous Sediments: Preliminary Results

E. Oudin
Y. Thisse

Bureau de Recherches Géologiques et Minières
Service Géologique National, B.P. 6009,
45060 Orléans Cedex, France

C. Ramboz

Centre de Recherches Pétrographiques et Géochimiques
54501 Vandoeuvre-Les-Nancy, France

Abstract Preliminary mineralogical, geochemical, and fluid inclusion results were obtained on a core sample collected in the hydrothermally active southwest (SW) basin of the Atlantis II Deep (Red Sea). The base-metal content of chemically precipitated oxidic sediments is due to epigenetic circulation, while alternating sulfidic and silicatic layers are probably formed by overlapping base metal–rich chemical and epigenetic precipitation. Epigenetic precipitation forms discordant-to-pseudoconcordant sulfide-sulfate–rich zones, up to 50 cm thick, at the bottom of the core. The mineral association (the presence of anhydrite, pyrrhotite, chalcopyrrhotite, chalcopyrite, or ilvaite), the coarse grain size of the minerals, the

Marine Mining, Volume 5, Number 1
0149-0397/84/020003-00$02.00/0

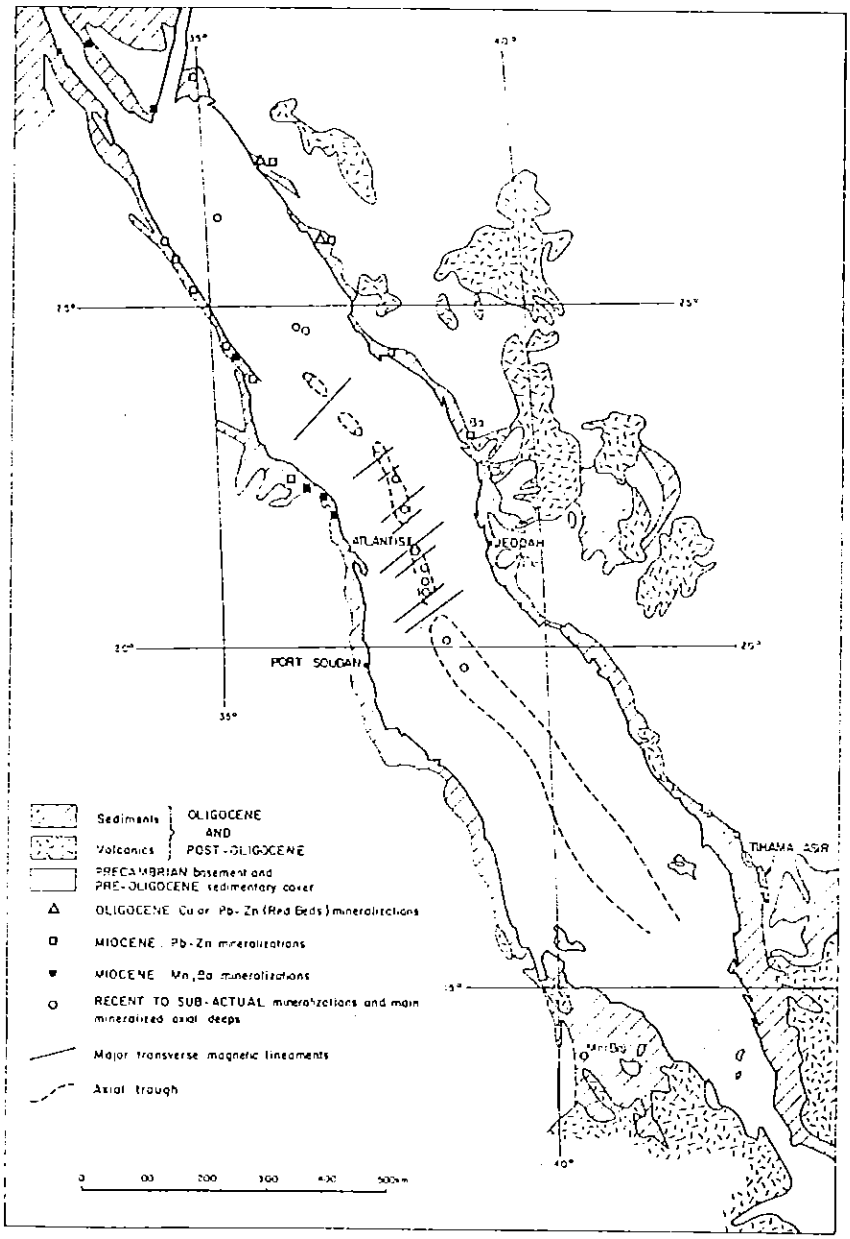

FIGURE 1. Localization of the mineralized deeps in the Red Sea axial trough. Schematic geological map compiled by Coleman (1974). The axial trough has been drawn by P. Guennoc from published geophysical data.

metamorphism of the host sediment at the vein contact, and fluid inclusion studies indicate the high temperature of hydrothermal circulation in the unlithified sediment. The veins are equivalent to high-temperature hydrothermal vents recently discovered near 21°N on the East Pacific Rise. In the veins there are several generations of sulfates (anhydrite or barite) corresponding to the circulation of several fluids whose different temperatures and salinities are in good agreement with the temperature and salinity fluctuation observed over the past twenty years in the hot saline brine pool overlying the sediments.

The Red Sea occupies a 2,000-km-long and 300-km-wide depression created by the separation of the Arabian and Nubian plates. The history of the Red Sea has been reviewed by Guennoc and Thisse (1982) and Cochran (1983). The main stage of rifting started approximately five to six million years ago (Drake and Girdler, 1964; Girdler and Styles, 1974; Roeser, 1975; Izzeldin, 1982). The axial valley (Figure 1) is only well defined on the southern and central part of the Red Sea. The spreading rate increases toward the south (1.5 cm/yr). The central zone (approximately between 20 and 25°N) is characterized by a slower spreading rate (0.5 cm/yr) and the presence of major transform faults (Bäcker, 1973; Bäcker et al., 1975; Bignell et al., 1976; Garson and Krs, 1976). Several deeps containing recent metalliferous sediments, usually overlain by hot brine pools (Miller et al., 1966; Bäcker and Schoell, 1972; Bignell et al., 1976), are situated in the axial trough and tend to concentrate in the central zone (Figure 1).

The Atlantis II deep (Degens and Ross, 1969; Bäcker and Richter, 1973) situated near 21°5N has a maximum depth of 2,200 m. Its flanks are covered by Miocene evaporites, which have flowed from the continental shelf into the main trough. The Atlantis II deep contains 10 to 20 m of metalliferous sediments. The estimated metal content of the sediments varies from 2.5 to 3.5 megatons of zinc, 0.5 to 0.6 megatons of copper, and 4,000 to 9,000 tons of silver, which indicates a sulfide deposit of potential economic importance; indeed, its possible exploitation in the near future is being considered (Mustafa and Amann, 1980;

Lück, 1982; Länge et al., 1981). Consequently, the Atlantis II deep has been studied extensively, and approximately 700 core samples have been recovered from this 60-km^2 area; Bäcker and Richter (1973) have defined five major stratigraphic units in the unlithified sediments. The basal unit that rests on the oceanic basalts (Hackett and Bischoff, 1973) is a biodetrital unit dominated by marls. The hydrothermal sedimentation, which, according to Shanks and Bischoff (1980), started 10–15,000 B.P., consists of two sulfide-rich zones (averaging 2 m in thickness) separated by a 5- to 6-m-thick oxidized unit. The sulfide-rich zones consist of Fe-Cu-Zn sulfides associated with silicates and some sulfates (anhydrite or gypsum). The oxidized unit contains iron and/or manganese oxyhydroxides and silicates. The 2- to 3-m upper part of the cores is semiliquid mud where sulfidic and amorphous phases are predominant. The interstitial saline brines are an important constituent of the sediments, which have an average brine content of 85 wt % (Bischoff, 1969a; Bäcker and Richter, 1973). The mineralogy and geochemistry of the sediments have been described by many authors (Bischoff, 1969a; Bäcker, 1973; Bäcker and Richter, 1973; Hackett and Bischoff, 1973; Bäcker, 1976; Bignell et al., 1976; Weber-Diefenbach, 1977; Bignell, 1978; Weiss, 1979; Nöltner, 1979; Al-Karghuli, 1979; Pottorf, 1980). The Atlantis II deep sediments are overlain by a nearly 200-m-thick hot saline stratified brine pool. According to the data of many authors (Brewer et al., 1965; Miller et al., 1966; Brewer et al., 1966; Munns et al., 1967; Brewer and Spencer, 1969; Brooks et al., 1969; Schoell, 1974; Pushkina et al., 1979; Baturin et al., 1969), the 150-m-thick lower brine is depleted in oxygen, magnesium, and sulfate and enriched in metals (concentration is 1,000 times that of normal Red Sea waters), sodium, and chlorine when compared with normal Red Sea deep waters. The 30-m-thick upper brine represents a transition zone with the overlying seawater.

Lithostratigraphy of Core 268 KS

The core sample 268 KS described in this paper was collected in Atlantis II deep during the R/V Valdivia cruise Va 29 during

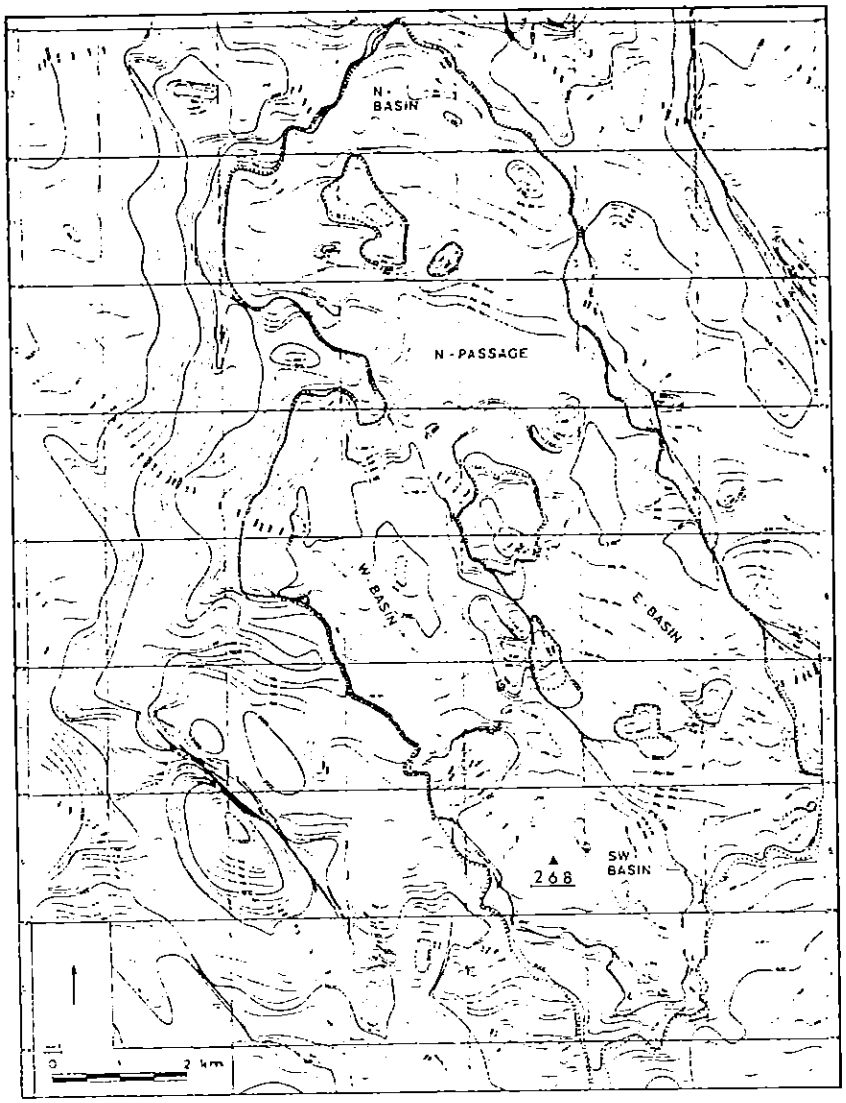

FIGURE 2. Location of core 268 in Atlantis II deep, SW basin. Bathymetric map from Bäcker and Richter (1973).

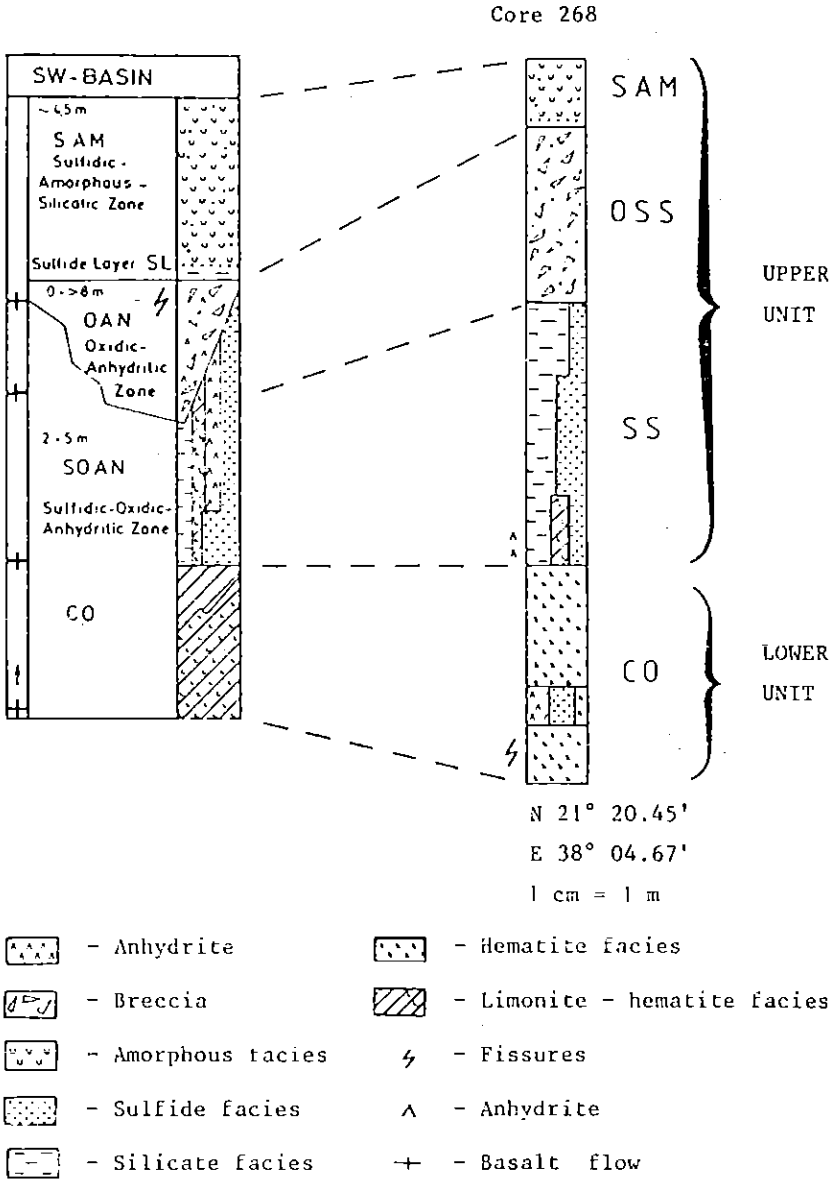

FIGURE 3. Lithostratigraphy of core 268 (after Thisse, 1982) compared with the general SW basin lithostratigraphy defined by Bäcker and Richter (1973).

November and December 1980. The 268 KS core is situated in the SW basin (Figure 2) known to be an active hydrothermal zone (Schoell and Hartmann, 1973). The lithostratigraphy of core samples collected in the discharge zone differs from the preceding general description. It can be characterized, according to Bäcker and Richter (1973), by the predominance of hematite instead of limonite and by frequent epigenetic features (including cross-cutting veins and breccia) due to hydrothermal circulation, which Zierenberg and Shanks (1983) have described extensively. In Figure 3, Thisse (1982) has described core 268 using the SW basin lithostratigraphy established by Bäcker and Richter (1973). The lower unit is approximately 3 m thick and is formed essentially of massive finely crystallized hematite, which has an average grain size of 150 Å (Figure 4). The upper unit is approximately 8 m thick and can be divided into three main zones: (1) a 4.1-m-thick sulfidic silicatic zone (SS) overlying the hematite sediment and overlain by (2) a 2.7-m-thick oxidic silicatic sulfidic zone (OSS) followed by (3) a 1.1-m-thick sulfidic amorphous zone (SAM). The first meter of the SS zone is a transition layer characterized by sulfates (anhydrite and gypsum), especially frequent at the base, and by thin, alternating, somewhat discontinuous layers of hematite grading into goethite. A more homogeneous overlying zone (situated between 610 and 670 cm) has been dated at 8,500 B.P. by microfauna (Bourdillon, 1982). The overlying OSS zone is characterized by its brecciated structure: fragments of hematite sediment are cemented by a sulfidic silicatic material. The upper SAM zone is mostly semiliquid (estimated top loss is approximately 0.8 m).

The upper and lower units differ in their solid particle contents (Figure 5) and crystallinity. The lower unit (CO) contains at least 20% solid particles and well-crystallized sulfide (up to 300 μm) and sulfates (0.5-cm-long crystals are not uncommon). In contrast, the upper unit (comprising SS, OSS, and SAM) has a low particle content (10%): the mineral grain size is usually less than 1 μm, except for a coarser minor fraction and the amount of amorphous material increases toward the top. Weber-Diefenbach (1977) described a similar pattern in a core from the northern passage (Figure 2), which he attributed to early diagenesis of the sediment at the base of the core. However, the discordant

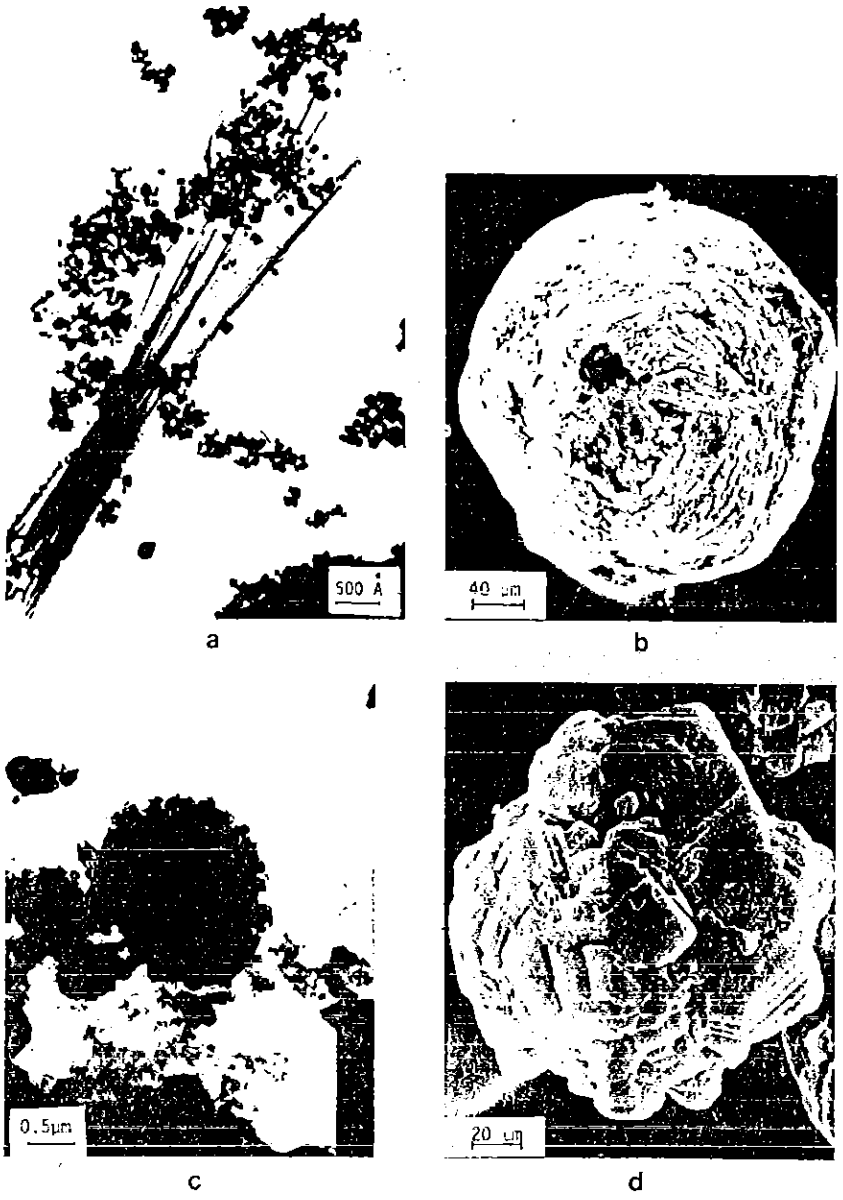

FIGURE 4. *(a)* Fibrous actinolite associated with fine-grained hematite from the lower unit. Photographed with a transmitted light microscope. *(b)* Aggregate of hydrozincite, photographed with a scanning electron microscope. *(c)* Microcrystalline aggregate of sphalerite, photographed with a transmitted light electron microscope. *(d)* Aggregate of sphalerite crystals from zone B in CO (see Figure 7) photographed with a scanning electron microscope.

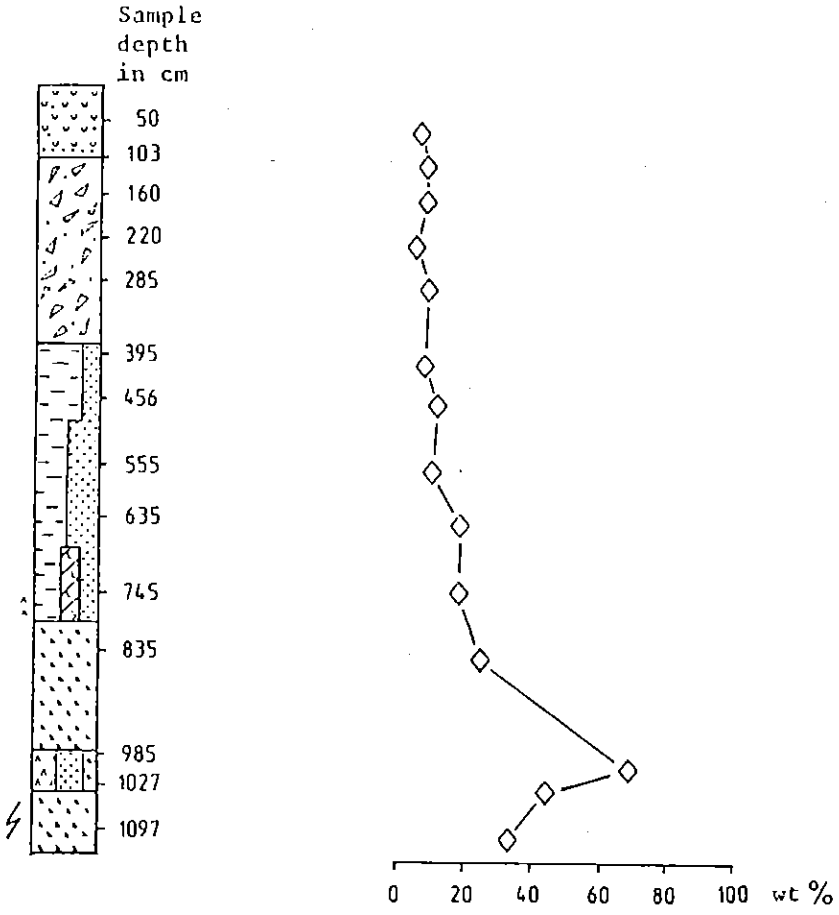

FIGURE 5. Variation of the solid particle content in core 268 (after Thisse, 1982).

nature of the well-crystallized material in core 268 indicates that this epigenetic material probably contributes largely to these observed differences.

Geochemistry and Mineralogy

Fourteen samples selected in various zones of core 268 have been analyzed for SiO_2, Fe_2O_3, Cu, Zn, Pb, Ag, and Cd (Thisse, 1982). The upper zone is generally enriched in SiO_2, Cu, Zn, Pb, Ag, and Cd relative to the lower zone (Figure 6). However, in the

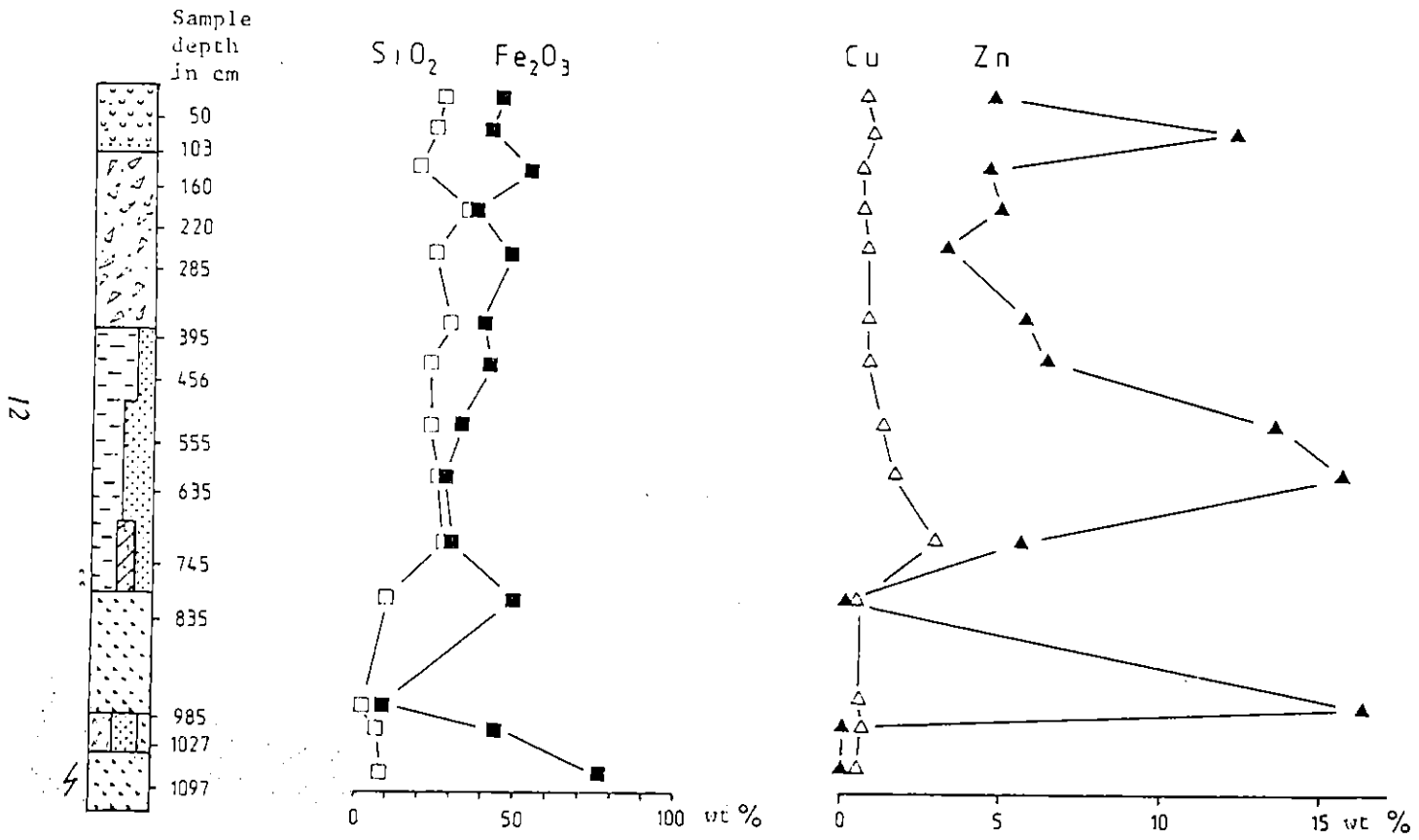
Sample depth in cm
50
103
160
220
285
395
456
555
635
745
835
985
1027
1097
SiO2
Fe2O3
0
50
100
wt %
Cu
Zn
0
5
10
15 wt %

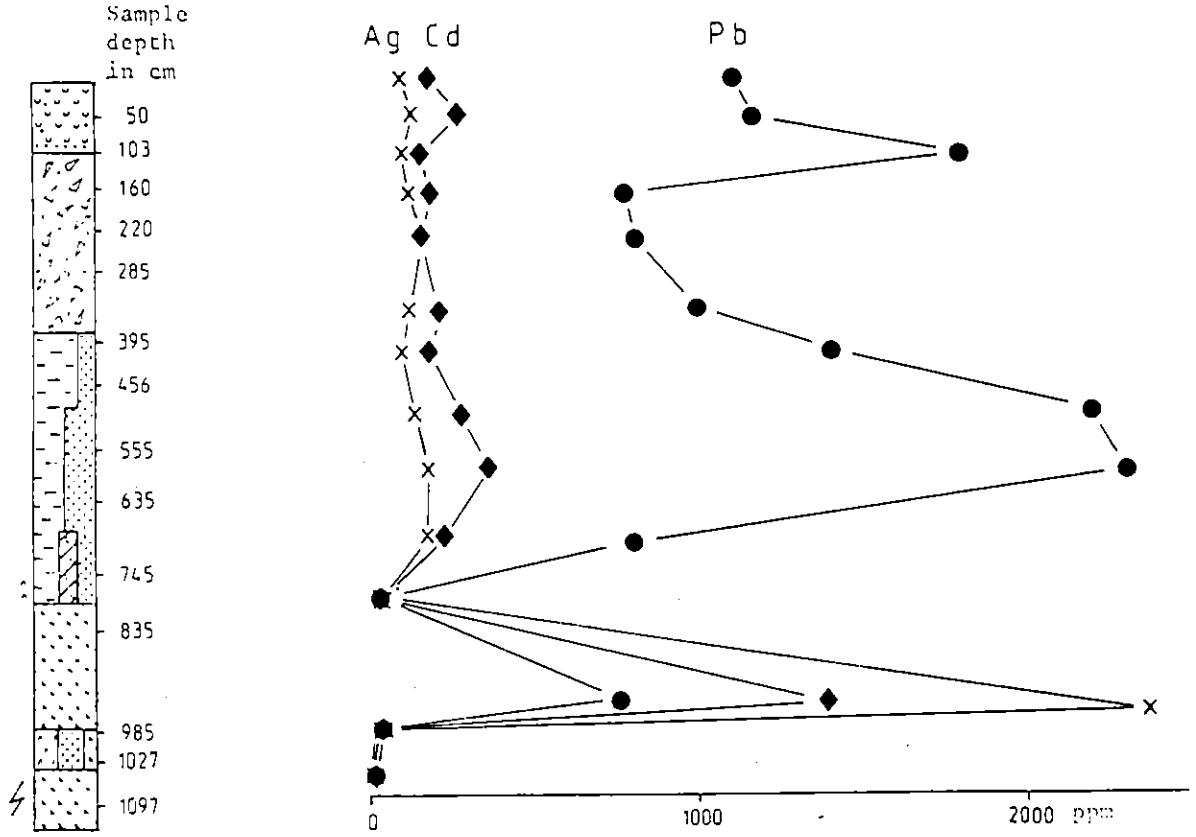

FIGURE 6. Geochemistry of core 268 (after Thisse, 1982).

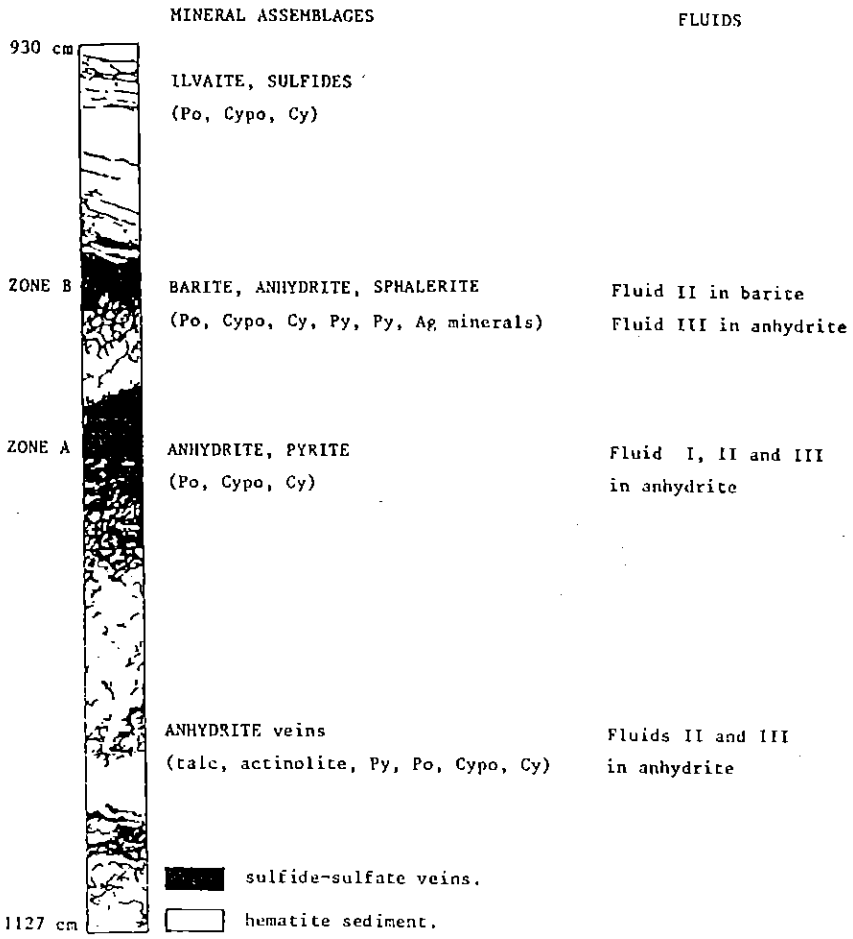

FIGURE 7. Mineral assemblages of sulfide-sulfate–rich veins in the hematite sediment at the base of core 268. Mineral assemblages are Po (pyrrhotite), Cypo (chalcopyrrhotite), Cy (chalcopyrite), and Py (pyrite). Fluids I, II, and III are distinguished by their different salinity determined by fluid inclusion studies (see text).

lower unit one narrow sulfide-rich zone (B, Figure 7) is considerably enriched in Zn, Pb, Ag, and Cd while another underlying sulfide-rich zone (A, Figure 7) is chemically consistent with the lower unit. The maximum silica content in samples from the

lower unit is 9.5%. In the upper unit, silica content varies between 20.3% and 31.9%, forming more abundant clay and amorphous phases. Zinc can reach up to 16.62%, while copper never exceeds 2.5%. In the upper unit, zinc content increases drastically in the two sulfidic zones (SAM and SS in Figure 3), whereas the copper increase in these zones is less obvious. In zone B (Figure 7) from the lower zone, zinc content is also very high (16.33%). In one sample at the base of the sulfidic amorphous silicatic zone (SAM) in the upper unit, zinc is a constituent of hydrozincite (identified by X-ray analysis), a hydrated zinc carbonate forming large fibrous 500-μm aggregates (Figure 4*b*) dispersed in the mud. However, apart from this localized occurrence, sphalerite in polycrystalline aggregates a few microns wide (Figure 4*c*) is the common zinc-bearing mineral. Sphalerite forms well-crystallized (150-μm grains) aggregates in zone B (Figure 7) from the lower unit (Figure 4*d*). Cadmium is more abundant in the zinc-rich zone where it is probably a minor constituent of sphalerite. Copper either forms chalcopyrite or chalcopyrrhotite. Chalcopyrrhotite is cubic and has a composition close to $CuFe_2S_3$. Chalcopyrrhotite forms euhedral (maximum grain size 200 μm) grains in the lower unit of core 268 KS, where it is often associated with chalcopyrite (Figure 8*a*). Lead content is never very high in samples: a maximum of 0.2% is analyzed. Relatively large (100 μm) euhedral grains of galena (Figure 8*b*) are observed in a sample from the sulfidic silicatic zone (SS) at the base of the upper unit. The silver content of upper unit samples varies between 96.4 and 175 ppm. The Ag-Zn correlation diagram in Figure 9 suggests that silver probably is usually a minor constituent of sphalerite. However, a zone B (Figure 7) sample plotted on the same diagram (distinctly enriched in silver—2,335 ppm) does not lie on the correlation line. This and the observation of silver-rich grains by transmitted light electron microscopy lead Thisse (1982) to conclude the presence of distinct silver-bearing minerals. Silver-bearing sulfides and sulfosalts were later identified in the same sample (Oudin, in preparation). Argentite (Ag_2S) has been identified by Weber-Diefenbach (1977) in another core from Atlantis II northern passage (Figure 2).

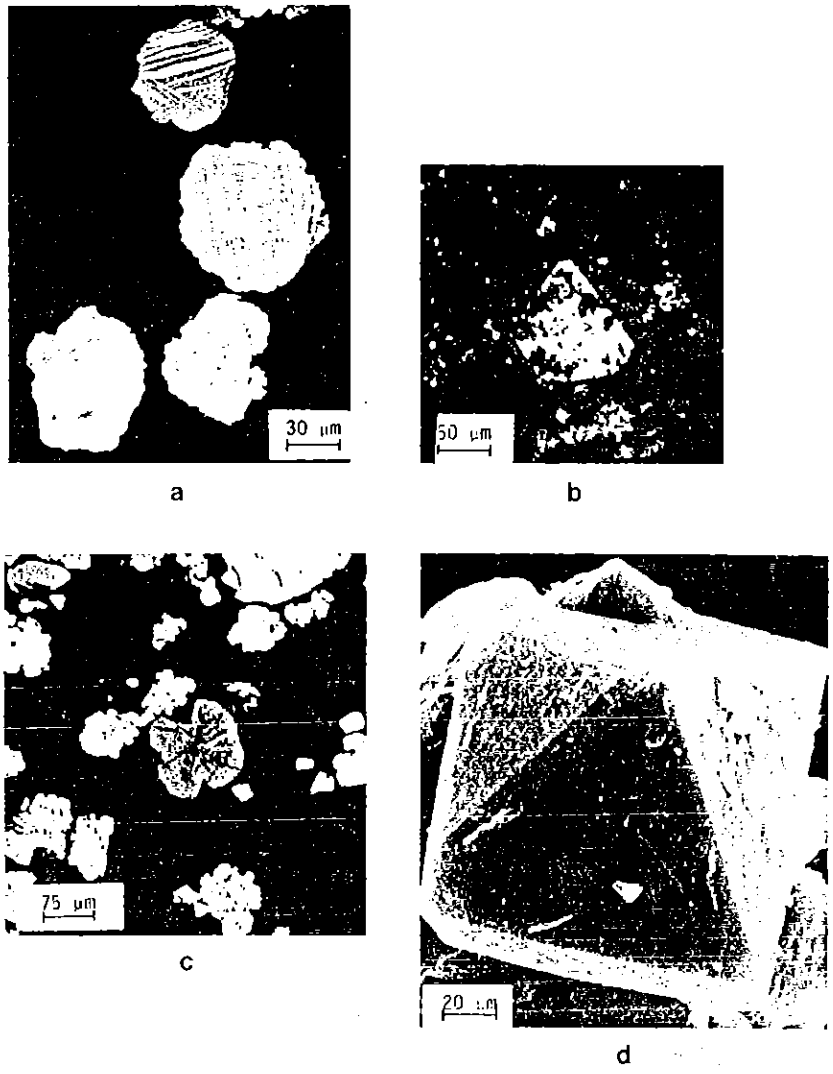

FIGURE 8. *(a)* Chalcopyrrhotite ($CuFe_2S_3$, cubic) euhedral grains associated with chalcopyrite (forming light gray lamellae in the darker chalcopyrrhotite). The grains are included in araldite (black) and photographed in polished section. *(b)* Euhedral galena (white, in the center of photograph) associated with minor pyrite (white in fine grains) sulfates (dark gray). The minerals are included in araldite (black) and photographed in polished section. *(c)* Mushketovite (light gray spherolite in the center) associated with copper and/or iron sulfides (grayish white to white) and anhydrite (dark gray). The minerals are included in araldite and photographed in polished section. *(d)* Euhedral magnetite from the lower unit, photographed with a scanning electron microscope.

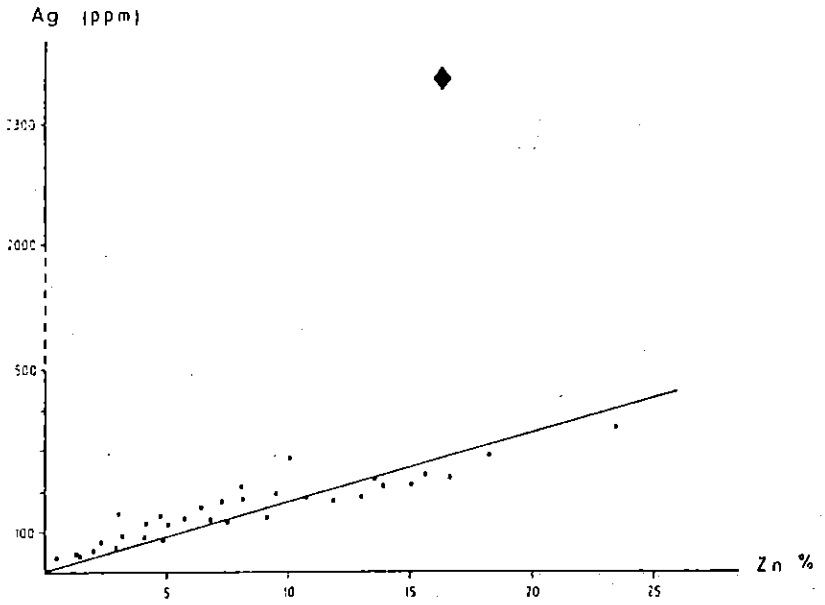

FIGURE 9. Ag-Zn correlation diagram (after Thisse, 1982).

The Lower Unit

In the lower unit, thin (a few millimeters wide), open fissures cut through the hematite sediment. They are coated by anhydrite and variable amounts of talc, actinolite, and sulfides (Figure 4*a*). Two sulfide- and sulfate-rich pseudoconformable zones (A and B, Figure 7) are formed by an intensifying network of veins invading the unlithified sediment. At the contact with the veins created by hydrothermal circulation, the sediment is metamorphosed: magnetite pseudomorphs after hematite (mushketovite facies) are observed (Figure 8*c*), but euhedral magnetite grains are also present (Figure 8*d*). Bischoff (1969b), Hackett and Bischoff (1973), and Zierenberg and Shanks (1983) also have described the transformation of hematite into magnetite in other cores of the Atlantis II deep. Ilvaite, a hydrated iron (manganese) silicate, also is observed in core 268 (Figure 10*a*) and has been described in other cores (Pottorf and Barnes, 1978; Weiss et al., 1980). Mushketovite and ilvaite typically are formed dur-

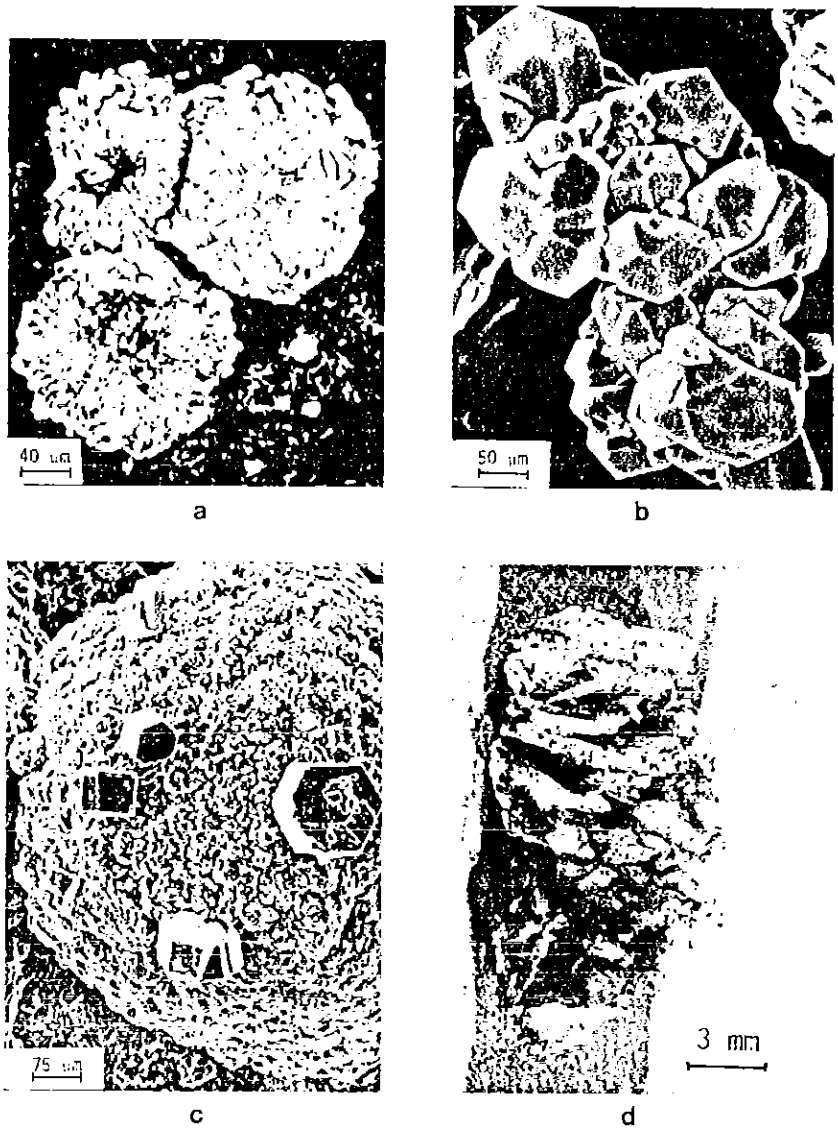

FIGURE 10. *(a)* Polycrystalline ilvaite grains photographed in polished section with a scanning electron microscope. *(b)* Euhedral pyrite grains from zone A (Figure 7) in the hematite sediment at the base of the core. Photographed with a scanning electron microscope. *(c)* Microcrystalline talc coating a concordant veinlet in the hematite sediment. The hexagonal skeletal crystals of pyrrhotite are associated with the talc. Photographed with a scanning electron microscope. *(d)* Open fissure coated by euhedral anhydrite crystals in zone A (Figure 7).

ing contact metamorphism (Ramdohr, 1980). Well-crystallized euhedral pyrite (Figure 10*b*) is the predominant sulfide species associated with anhydrite in the lower sulfide-rich zone (A, Figure 7) while sphalerite associated with barite and anhydrite is predominant in the upper sulfide-rich zone (B, Figure 7). Sulfates (anhydrite and barite) disappear at the top of the second sulfide-rich zone B. Sulfates are present again at the top of the lower unit, but gypsum progressively becomes the predominant phase. Between 980 cm and the base of the upper unit, fine, discontinuous, dark sulfide-rich layers are observed where illvaite (Figure 7) is also a major phase. In the same sulfate-depleted zone, minor concordant veins of talc associated with skeletal pyrrhotite are sometimes observed (Figure 10*c*).

Fluid Inclusion Study

Abundant and large (average size ranges between 20 and 80 μm) fluid inclusions have been observed and are restricted to the lower-unit vein sulfates (Figure 10*d*). Anhydrite growth zones are often marked by fine hematite dust from the sediment or by fine-grained euhedral sulfide inclusions (Figure 11*a*). Anhydrite is present throughout the base of the lower unit, while barite crystals, which are smaller (maximum size is 500 μm) are found only in zone B (Figure 7). The fluid inclusions observed in barite and anhydrite are different, being smaller (from 20 to 50 μm) in the former; they have an irregular shape and never contain opaque phases (Figure 11*b* and *c*). Two types of inclusion can be observed in anhydrite. Inclusions of the first type ($1F_1$) are long and narrow (Figure 11*d*) and may contain one or more fine-grained (10 μm) euhedral (hexagonal or cubic) opaque phases (iron oxide or copper and/or iron sulfide (Figure 12*a*, *b*, and *c*). In these inclusions, the opaque mineral has generated the formation of the fluid inclusion cavity during crystal growth, thus indicating their primary origin (Roedder, 1979). The second type of inclusions observed in anhydrite ($1F_2$) is smaller (from 20 to 50 μm) and more isometric. They very seldom contain an opaque phase, but a halite cube is often present (Figure 11*d*). Several generations of sulfates are usually observed in the veins, which contain different types of inclusions. The fluid inclusions

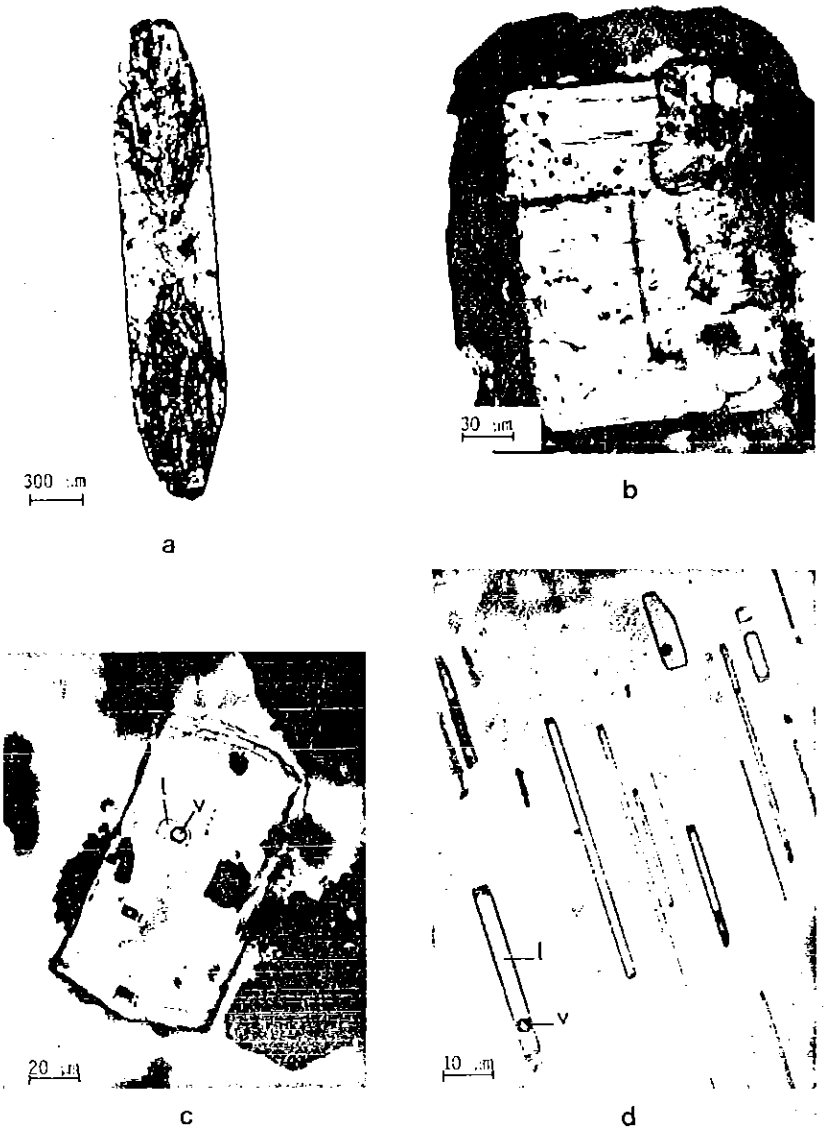

FIGURE 11. *(a)* The growth zones of this euhedral anhydrite crystal, from zone A (Figure 7), are marked by fine-grained sulfide inclusions arranged in a bow-tie structure. *(b)* Microphotograph of a barite crystal from zone B (Figure 7) containing numerous small, two-phased fluid inclusions. *(c)* Fluid inclusion in barite containing a saline liquid phase (L) and a vapor phase (V). The opaque minerals are sphalerite grains. Photographed with a transmitted light microscope. *(d)* Microphotograph of an anhydrite crystal zone containing long and narrow fluid inclusions of the first type (IF_1).

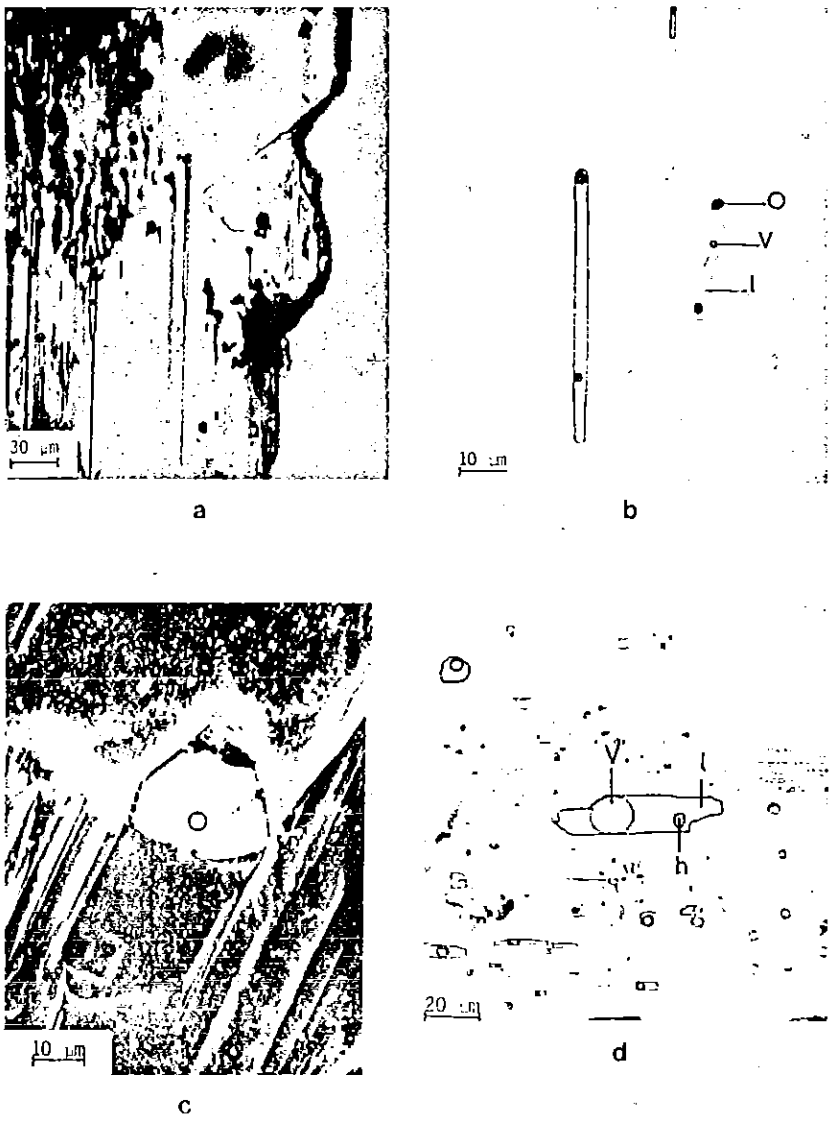

FIGURE 12. *(a)* Microphotograph of an anhydrite crystal containing opaque inclusions (black), which have in some cases generated fluid inclusion growth (see detail in photograph b). *(b)* Fluid inclusions in anhydrite containing a euhedral opaque phase (O), a vapor phase (V), and a liquid phase (L). *(c)* Fluid inclusion cavity in anhydrite containing an opaque copper iron sulfide (white). Photographed with a scanning electron microscope. *(d)* Fluid inclusion of the second type (IF_2) included in anhydrite and containing a halite cube (H), a saline liquid (L), and a vapor phase (V).

were studied on a standard Chaixmeca heating and freezing stage (Poty et al., 1976). Detailed analytical data of the measured inclusions are being compiled by Thisse et al. (in preparation).

The inclusion cavities contain saline liquid and vapor phases at room temperature. The salinity of the fluid was estimated by measuring either the melting point of the ice during freezing experiments or that of the halite cube during heating experiments. Three types of fluids can be distinguished in the inclusions according to their respective approximate salinity: (1) a 15 wt % equivalent NaCl fluid I, (2) a 22 wt % equivalent NaCl fluid II, and (3) a 32 wt % equivalent NaCl fluid III. Anhydrite first type of inclusions (IF_1) may contain fluid I or II, while fluid III is only found in the second type of inclusion (IF_2). Barite inclusions usually contain fluid II. Distribution of the three fluids in the veins and the sulfide-sulfate–rich zones is shown in Figure 7. Different high-temperature ranges (approximately 250–420°C) are measured in the different types of inclusion fluids during heating experiments.

Discussion and Concluding Remarks

The Red Sea metalliferous sediments are formed by three different processes (Bäcker and Richter, 1973): (1) a detrital sedimentation, (2) a predominant chemical precipitation occurring in the lower brine and/or at the lower-upper brine interface, and (3) an epigenetic mineral precipitation in the unlithified sediment during hydrothermal circulation. The chemical precipitation rate is much higher than that of normal detrital sedimentation (Bäcker and Richter, 1973; Shanks and Bischoff, 1980). The former forms thinly bedded to massive poorly crystallized fine-grained sediments that are predominant in the core previously described. However, the discordant to pseudoconcordant sulfate-sulfide–dominated veins zone, up to 50 cm thick, the higher solid-particle content and coarser grain size, and the minor recrystallization of the sediment at the vein contact are caused by high-temperature fluid circulation in the sediment at the base of the core. In the upper part of core 268, the epigenetic features are essentially recognized in the brecciated zone (OSS). Al-

though this zone has not been studied extensively, the finer grain size of the sulfides, as well as the presence of fine-grained gypsum instead of coarse-grained anhydrite, suggests the circulation of a cooler fluid. This coincides with the observations of Zierenberg and Shanks (1983). The two sulfidic layers from the upper part of the core are characterized by low solid-particle content, fine grain size, and abundant clay and amorphous material; the last could result from predominant metal-rich chemical precipitation with a certain amount of epigenetic material, as suggested by the presence of an accessory coarser grain fraction. This alternation of oxidic and sulfidic layers in the metalliferous sediments could be related to variations in the chemical composition and temperature of the lower brine over the past 11,000 years due to episodic hydrothermal activity (Shanks and Bischoff, 1980).

Abundant fluid inclusions have been discovered in the sulfates from the base of core 268. Their presence, although not clearly understood, may correspond to present-day circulation and/or recently recovered core samples. Most samples described in literature were collected during early campaigns in 1969 and 1971–72, as opposed to 1980 for core 268. Neoformations of mineral during core storage have been recognized by Shanks and Bischoff (1980). The clear, platy euhedral inclusion-bearing anhydrite from core 268 contrasts with the fibrous facies of anhydrite observed in epigenetic veins from Zierenberg and Shanks' (1983) samples, and with the very fine-grained anhydrite observed elsewhere in core 268. These observations suggest that recrystallization of anhydrite could be caused by reequilibration due to postdepositional conditions or during core storage. Prior fluid-inclusion work in Red Sea sediments consisted of temperature measurements of three inclusions from another SW basin core by Pottorf (1980). The temperature and salinity fluctuations observed in the lower brine over the past twenty years (Hartmann, 1980) are consistent with the circulation of several generations of fluid of variable temperatures and salinities as deduced from fluid inclusion studies. In contrast with the high-temperature hydrothermal circulation at the base of core 268, the present-day lower brine has a temperature of 62.3°C (Monin and Plakhin,

1982). The lower brine, according to fluid inclusion data, results from a mixture of several fluids (which may have cooled down during percolation) as well as seawater (through the upper brine). The estimated temperature of the incoming fluid—based on chemical geothermometry, isotopic data, or volumetric change in the lower brine (as summarized by Shanks and Bischoff, 1977), which varies between 110° and 260°C—is distinctly lower than the temperature range measured in the fluid inclusion trapped in the sulfates at the base of the sediments. However, fluid inclusions have recorded the complex behavior of the fluids, including adiabatic expansion, mixing, and boiling (Thisse et al., in preparation). Qualitative and quantitative evidence of boiling (Ramboz et al., 1982; Ramboz, 1983) is locally observed in fluid II (salinity of 22 wt % equivalent NaCl) at a temperature of 390°C and an approximate pressure of 220 bars (corresponding to the sediments, brines, and seawater column), which corresponds with experimental data on the H_2O-NaCl system from Parisot and Plattner (1981). The temperature of the fluid might have been higher than 390°C prior to expansion and boiling. The role of adiabatic expansion has been discussed by Bischoff (1980), who wrote of recently discovered submarine sulfide deposits near 21°N on the East Pacific Rise (Francheteau et al., 1979; Spiess et al., 1980). Boiling from a present-day submarine sulfide deposit has never been reported. Fluid II trapped in some inclusions has the approximate salinity of the present-day lower brine (25.7 wt % equivalent NaCl measured by gravimetric titration, Danielsson et al., 1980), while fluids I and III have respectively a lower and higher salinity. Fluid II has the average salinity of fluids I and III and could result from their mixing, but preliminary fluid inclusion data do not support this hypothesis. The interpretation is complicated by a superimposed salinity shift due to boiling. Further investigations are needed to interpret the temperatures and salinities of the inclusion fluids, as well as the mechanism of precipitation of the sulfates and sulfides. The extension of the high-temperature fluid circulation is not known; however, observations of high-temperature minerals, such as chalcopyrrhotite or ilvaite, in five other cores from

the SW basin (Nöltner, 1979; Pottorf, 1980; Schumann, 1978) indicate that it could be a widespread phenomenon in this zone.

The epigenetic sulfide-sulfate veins in core 268 can, to some extent, be directly compared to the high-temperature (350°C measured in situ, MacDonald et al., 1980) hydrothermal vents near 21°N on the East Pacific Rise. Similarities include the high temperature of hydrothermal fluids and the resultant specific mineral association found in both deposits, which consists of anhydrite, pyrrhotite, chalcopyrrhotite, chalcopyrite, and zinc sulfide (wurtzite in 21°N and a small amount of sphalerite in the Red Sea) (Oudin, 1981; Haymon and Kastner, 1981; Styrt et al., 1981). Chalcopyrrhotite ($CuFe_2S_3$, cubic), also called cubic cubanite, isocubanite, or intermediate solid solution (ISS), is an unstable phase characteristic of present-day, high-temperature submarine sulfide deposits (Oudin, 1983). The fluid temperature estimated by inclusion studies in the anhydrite from 21°N (Le Bel and Oudin, 1982; Kusakabe et al., 1982) are in good agreement with temperature measured in situ. In both deposits, a convective circulation of seawater heated at the proximity of the magma chamber at the spreading axis has been proposed for the origin of the hydrothermal fluid. In the East Pacific Rise, the 350°C hydrothermal fluid has a salinity equivalent to that of seawater and is depleted in magnesium, sulfate, and oxygen and enriched in calcium and metals (Albarede et al., 1981; MacDuff and Edmond, 1982) due to interaction with the basalt of the young oceanic crust, which corresponds with other experimental data (Bischoff and Dickson, 1975; Mottl and Holland, 1978; Seyfried and Bischoff, 1981). The Atlantis II lower brine is also depleted in magnesium, sulfate, and oxygen and enriched in calcium and metals, indicating seawater-basalt interaction. The high salinity observed in fluid inclusions and in the lower brine probably corresponds to the fluid circulation in the thick Miocene evaporite sequence bordering the deep. Oxygen isotope data support the seawater origin of the brine, although other sources also have been discussed (Craig, 1969; Schoell, 1975; Schoell and Faber, 1978; White, 1981). The high-temperature epigenetic veins in unlithified sediments at the base of a

metalliferous sediment core collected in the Atlantis II deep SW basin in the Red Sea, and some high-temperature active chimneys from the East Pacific Rise, are both the result of convective circulation near a spreading axis. The differences can be explained by the specific geological settings during circulation and discharge.

Acknowledgments

We wish to thank H. E. Z. Mustafa and Z. A. Nawab, respectively Secretary General and Deputy of the Saudi Sudanese Red Sea Joint Commission, for allowing us to study the core sample described in this paper and for their technical and scientific assistance. We also wish to thank F. Le Lann for his helpful support. Electron microscope photographs were provided by C. Vilbert, J. Breton, and J. L. Boulmier. The photograph of Figure 10*d* was taken by J. J. Poulin. Special thanks to Hugh Dunlop, who kindly helped with the translation.

References

Albarede, F., Michard, A., Minster, J. F., Michard, G. 1981. $^{87}S_R/^{86}S_R$ ratios in hydrothermal waters and deposits from the East Pacific Rise at 21°N. *Earth Planet. Sci. Lett.* 55:229–236.

Al-Karghuli, A. 1979. Röntgenographische Untersuchungen an Erzschlämmen aus dem Atlantis II—Tief, Rotes Meer. Diplom-Arbeit, Heidelberg University (FRG) (unpublished).

Bäcker, H., and Schoell, M. 1972. New deeps with brines and metalliferous sediments in the Red Sea. *Nat. Phys. Sci.* 240 (103):153–158.

Bäcker, H. 1973. Rezente Hydrothermal-Sedimentäre Lagerstättenbildung. *Erzmetall* 32 (11):544–555.

Bäcker, H., and Richter, H. 1973. Die Rezente Hydrothermal-Sedimentäre Lägerstätte Atlantis II—Tief im Roten Meer. *Geol. Rundsch.* 3:697–741.

Bäcker, H., Länge, K., and Richter, H. 1975. Morphology of the Red Sea Central Graben between Subair Islands and Abul Kizaan. *Geol. Jahr.* D13:79–123.

Bäcker, H. 1976. Fazies und Chemische zusammensetzung rezenter Ausfällungen aus Mineralquellen im Roten Meer. *Geol. Jahr.* D17:151–172.

Baturin, G. N., Kochenov, A. V., and Trimonis, Y. S. 1969. Composition and origin of iron-ore sediments and hot brines in the Red Sea. *Oceanology* 9 (3):360–378.

Bignell, R. D., Cronan, D. S., and Tooms, J. S. 1976. Red Sea metalliferous brine precipitates. *Geol. Assoc. Can., Spec. Pap.* 14:147–179.

Bignell, R. D. 1978. Genesis of the Red Sea metalliferous sediments. *Mar. Min.* 1 (3):209–235.

Bischoff, J. L. 1969a. Red Sea geothermal brine deposits: their mineralogy, chemistry, and genesis. In *Hot Brines and Recent Heavy Metal Deposits in the Red Sea*, edited by E. T. Degens and D. A. Ross. Berlin, Heidelberg, New York: Springer Verlag, pp. 368–401.

Bischoff, J. L. 1969b. Goethite-hematite stability relations with relevance to seawater and the Red Sea brine system. In *Hot Brines and Recent Heavy Metal Deposits in the Red Sea*, edited by E. T. Degens and D. A. Ross. Berlin, Heidelberg, New York: Springer Verlag, pp. 402–406.

Bischoff, J. L., and Dickson, F. W. 1975. Seawater-basalt interaction at 200°C and 500 bars: implications for origin of sea-floor heavy metal deposits and regulation of seawater chemistry. *Earth Planet. Sci. Lett.* 25:385–397.

Bischoff, J. L. 1980. Geothermal system at 21°N, East Pacific Rise: physical limits on geothermal fluid and role of adiabatic expansion. *Science* 207:1465–1469.

Bourdillon, C. 1982. Etude micropaléontologique de la carotte 268 KS (Fosse Atlantis II, mer Rouge). Corrélations avec les carottes 198 KS et 264 KS. Rapport B.R.G.M. n° 82 SGN 891 GEO (unpublished).

Brewer, P. G., Riley, J. P., and Culkin, F. 1965. Chemical composition of the hot salty water from the bottom of the Red Sea. *Nature* 206:1345.

Brewer, P. G., Riley, J. P., and Culkin, F. 1966. The chemical composition of the hot salty water from the bottom of the Red Sea. *Deep-Sea Res.* 12:497.

Brewer, P. G., and Spencer, D. W. 1969. A note on the chemical composition of the Red Sea brines. In *Hot Brines and Recent Heavy Metal Deposits in the Red Sea*, edited by E. T. Degens and D. A. Ross. Berlin, Heidelberg, New York: Springer Verlag, pp. 174–179.

Brooks, R. R., Kaplan, I. R., and Peterson, M. N. A. 1969. Trace element composition of Red Sea geothermal brine and interstitial water. In *Hot Brines and Recent Heavy Metal Deposits in the Red Sea*, edited by E. T. Degens and D. A. Ross. Berlin, Heidelberg, New York: Springer Verlag, pp. 180–203.

Cochran, J. R. 1983. A model for development of Red Sea. *Am. Assoc. Pet. Geol. Bull.* 67 (1):41–69.

Coleman, R. G. 1979. Geological background of the Red Sea. Initial Reports of the Deep Sea Drilling Project, Volume XXIII, Washington, D.C., pp. 813–820.

Craig, H. 1969. Geochemistry and origin of the Red Sea brines. In *Hot Brines and Recent Heavy Metal Deposits in the Red Sea*, edited by E. T. Degens and D. A. Ross. Berlin, Heidelberg, New York: Springer Verlag, pp. 208–250.

Danielsson, L. G., Dyrssen, D., and Graneli, A. 1980. Chemical investigations of Atlantis II and Discovery brines in the Red Sea. *Geochim. Cosmochim. Acta* 44:2051–2065.

Degens, E. T., and Ross, D. A. 1969. *Hot Brines and Recent Heavy Metal*

Deposits in the Red Sea. Berlin, Heidelberg, New York: Springer Verlag, 600 pp.

Drake, C. B., and Girdler, R. W. 1964. A geophysical study of the Red Sea. *Geophys. J. R. Astron. Soc.* 8:473–495.

Francheteau, J., Needham, H. D., Choukroune, P., Juteau, T., Seguret, M., Ballard, R. D., Fox, P. J., Normark, W., Carranza, A., Cordoba, A., Guerrero, J., Rangin, C., Bougault, H., Cambon, P., and Hekinian, R. 1979. Massive deep sea sulphide ore deposits discovered on the East Pacific Rise. *Nature* 277:523–528.

Garson, M. S., and Krs, M. 1976. Geophysical and geological evidence of the relationship of Red Sea transverse tectonics to ancient fractures. *Geol. Soc. Am. Bull.* 87:169–181.

Girdler, R. W., and Styles, P. 1974. Two stages of Red Sea floor spreading. *Nature* 247:1–11.

Guennoc, P., and Thisse, Y. 1982. Genèse de l'ouverture de la mer Rouge et des minéralisations des fosses axiales. Synthèse bibliographique. Documents du B.R.G.M., n° 51, 112 pp.

Hackett, J. P., and Bischoff, J. L. 1973. New data on the stratigraphy, extent, and geologic history of the Red Sea geothermal deposits. *Econ. Geol.* 68:553–564.

Hartmann, M. 1980. Atlantis II geothermal brine system. Hydrographic situation in 1977 and changes since 1965. *Deep-Sea Res.* 27 (2A):161–171.

Haymon, R., and Kastner, M. 1981. Hot springs deposits on the East Pacific Rise at 21°N: preliminary description of mineralogy and genesis. *Earth Planet Sci. Lett.* 53: 363–381.

Izzeldin, A. Y. 1982. On the structure and evolution of the Red Sea based on geophysical data from the central and northern parts. Thesis, Strasbourg, 165 pp. (unpublished).

Kusakabe, M., Chiba, H., and Ohmoto, H. 1982. Stable isotopes and fluid inclusion study of anhydrite from the East Pacific Rise—21°N. *Geochem. J.* 16:89–95.

Länge, J., Bäcker, M., and Karbe, L. 1981. Metalliferous sediments in the Atlantis II Deep deposit and environmental investigations. *Inter-Ocean* 81:91–102.

Le Bel, L., and Oudin, E. 1981. Temperature evolution of deep-sea hydrothermal vents at 21°N (East Pacific Rise) recorded by fluid inclusions. *Chem. Geol.* 37:129–136.

Lück, K. 1982. Deep sea mining: practical technological developments in ocean mining. Conference of "Technical-legal Aspects of Seabed Mining," 15 pp.

Macdonald, K. C., Becker, K., Spiess, F. N., and Ballard, R. D. 1980. Hydrothermal heat flux of the "black smoker" vents on the East Pacific Rise. *Earth Planet. Sci. Lett.* 48:1–7.

Macduff, R. E., and Edmond, J. M. 1982. On the fate of sulfate during hy-

drothermal circulation at mid-ocean ridges. *Earth Planet. Sci. Lett.* 57:117–132.

Miller, A. R., Densmore, C. D., Degens, E. T., Hathaway, J. C., Manheim, F. T., McFarlin, P. F., Pocklington, R., and Jokela, A. 1966. Hot brines and recent iron deposits in deeps of the Red Sea. *Geochim. Cosmochim. Acta* 30:341–359.

Monin, A. S., and Plakhin, E. A. 1982. Stratification and space-time variability of Red Sea hot brines. *Deep-Sea Res.* 29(11):1271–1291.

Mottl, M. J., and Holland, H. D. 1978. Chemical exchange during hydrothermal alteration of basalts by seawater. I. Experimental results for major and minor components of seawater. *Geochim. Cosmochim. Acta* 42:1103–1115.

Munns, R. G., Stanley, R. J., and Densmore, C. D. 1967. Hydrographic observations of the Red Sea brines. *Nature* 214:1215.

Mustafa, Z., and Amann, H. 1980. The Red Sea pre-pilot mining test 1979. Offshore Technology Conference, Houston, 12th Annual, 3874.

Nöltner, T. 1979. Erzmikroskopische Untersuchungen an Erzschlämmen aus dem Atlantis II—Tief, Rotes Meer. Diplom-Arbeit, Heidelberg University (FRG) (unpublished).

Oudin, E. 1981. Etude minéralogique et géochimique des dépôts sulfurés sous-marins actuels de la Ride Est Pacifique (21°N). Documents du B.R.G.M., n° 25, Edit. B.R.G.M., 241 pp.

Oudin, E. 1983. Minéralogie de gisements et indices liés à des zones d'accrétion océaniques actuelles (ride Est-Pacifique et mer Rouge) et fossile (Chypre). *Chron. Rech. Minière* 470:43–56.

Oudin, E. In preparation. Silver bearing veins in the Red Sea metalliferous sediments from Atlantis II Deep.

Parisot, C. T., Plattner, E. 1981. Vapor-liquid equilibria of the H_2O-NaCl system in the temperature range 300–400°C. *J. Chem. Eng. Data* 26:16–20.

Pottorf, R. J., and Barnes, H. L. 1978. The nature of hydrothermal sediments in the Atlantis II deep of the Red Sea. *Geol. Assoc. Can. Geol. Soc. Am. Abstr.* 3:473.

Pottorf, R. J. 1980. Hydrothermal sediments of the Red Sea, Atlantis II deep. A model for massive sulfide-type ore deposits. Ph.D. dissertation, Pennsylvania State University, 193 pp. (unpublished).

Poty, B., Leroy, J., and Jachimowicz, L. 1976. Un nouvel appareil pour la mesure des températures sous le microscope: l'installation de microthermométrie Chaixmeca. *Bull. Soc. Fr. Minéral. Cristallogr.* 99:182–186.

Pushkina, Z. V., Stepanets, M. I., and Yashkichev, U. I. 1979. Basic chemical composition of mud waters from sediments in brine-bearing depressions in the Red Sea. *Lithol. Miner. Resour.* (USSR) 144:479–488.

Ramboz, C., Pichavant, M., and Weisbrod, A. 1982. Fluid immiscibility in natural processes: use and misuse of fluid inclusion data. II. Interpretation of fluid inclusion data in terms of immiscibility. *Chem. Geol.* 37:29–48.

Ramboz, C. 1983. Application of V-X projections to the quantitative interpretation of heterogeneous trapping from fluid inclusion study. *Terra Cognita* 3(2–3):164.

Ramdohr, P. 1980. *The Ore Minerals and Their Intergrowths*, 2d ed., edited by Pergamon, New York: Oxford.

Roedder, E. 1979. Fluid inclusions as samples of ore fluids. In *Geochemistry of Hydrothermal Ore Deposits*, 2d ed., edited by H. L. Barnes. New York: Wiley.

Roeser, H. A. 1975. A detailed magnetic survey of the southern Red Sea. *Geol. Jahrb.*, D13:131–153.

Schoell, M., and Hartmann, M. 1973. Detailed temperature structure of the hot brines in the Atlantis II deep area (Red Sea). *Mar. Geol.*, 14:1–14.

Schoell, M. 1974. Valdivia VA 01/03 Rotes Meergolf von Aden. Hydrographie II & III. Daten. Bundesanstalt für Bodenforschung, Hannover, 1063 pp.

Schoell, M. 1975. Previous and current ideas on the origin of the Red Sea brines. *Oceanology Int.* (Brighton).

Schoell, M., and Faber, E. 1978. New isotopic evidence for the origin of Red Sea brines. *Nature* 275:436–438.

Schumann, D. 1978. Mineralbestimmungen mit röntgendiffraktometerie an sedimenten der Erzschlämm Kampagnen VA-01 und VA-03 der Valdivia. *Thesis*, University of Mainz, 326 pp. (unpublished).

Seyfried, W. E., and Bischoff, J. L. 1981. Experimental seawater-basalt interaction at 300°C, 500 bars, chemical exchange, secondary mineral formation and implication for the transport of heavy metals: *Geochim. Cosmochim. Acta* 45:135–148.

Shanks, W. C., and Bischoff, J. L. 1977. Ore transport and deposition in the Red Sea geothermal system: a geochemical model. *Geochim. Cosmochim. Acta* 41:1507–1519.

Shanks, W. C., and Bischoff, J. L. 1980. Geochemistry, sulfur isotope composition and accumulation rates of Red Sea Geothermal Deposits. *Econ. Geol.* 75:445–459.

Sourirajan, S., and Kennedy, G. C. 1962. The system H_2O-NaCl at elevated temperatures and pressures. *Am. J. Sci.* 260:115–141.

Spiess, F. N., MacDonald, K., Atwater, T., Ballard, R., Carranza, A., Cordoba, D., Fox, C., Diaz Garcia, V. M., Francheteau, J., Guerrero, J. T., Hawking, J., Haymon, R., Hessler, R., Juteau, T., Kastner, M., Larson, R., Luydendyk, B., Macdougall, J. D., Miller, S., Normark, W., Orcutt, J., and Rangin, C. 1980. Hot springs and geophysical experiments. *Science* 207:1421–1432.

Styrt, M. M., Brackmann, A. J., Holland, H. D., Clark, B. C., Pisutha-Arnaud, V., Elridge, C. S., Ohmoto, H. 1981. The mineralogy and the isotopic composition of sulfur in hydrothermal sulfide/sulfate deposits on the East Pacific Rise, 21°N latitude. *Earth Planet. Sci. Lett.* 53:382–390.

Thisse, Y. 1982. Sédiments métallifères de la fosse Atlantis II (mer Rouge). Contribution à l'étude de leur contexte morpho-structural et de leurs caractéristiques minéralogiques et géochimiques. *Thesis*, Université Orléans et B.R.G.M., 155 pp. (unpublished).

Thisse, Y., Oudin, E., and Ramboz, C. In preparation. Throttling and boiling fluids in the Red Sea metalliferous sediments from Atlantis II deep.

Weber-Diefenbach, K. 1977. Geochemistry and diagenesis of recent heavy metal deposits at the Atlantis II Deep (Red Sea). In *Time and Stratabound Deposits Ore*, edited by D. D. Klemm and H. J. Schneider. Berlin, Heidelberg, New York: Springer-Verlag, pp. 419–436.

Weiss, H. M. 1979. Rasterelektronenmikroskopische Untersuchungen an Erzschlämmen des Atlantis II—Tief, Rotes Meer. Diplom-Arbeit Heidelberg University (FRG) (unpublished).

Weiss, H. M., Nöltner, T., and Stoffers, P. 1980. Occurrence of ilvaite in metalliferous brine muds from the Red Sea. *Neues Jahrb. Mineral. Abh.* 139 (3):239–253.

White, D. E. 1981. Active geothermal systems and hydrothermal ore deposits. *Econ. Geol.* (75th Anniversary Volume): 392–423.

Zierenberg, P. A., and Shanks, W. C. 1983. Mineralogy and geochemistry of epigenetic features in metalliferous sediments, Atlantis II deep, Red Sea. *Econ. Geol.* 78:57–72.

III

ASPECTS DE L'INTERACTION ENTRE ROCHES ET FLUIDES RICHES EN ELEMENTS VOLATILS

PUBLICATION XII : Oxydation du fer dans les skarns et les schistes à graphite des Jebilet Centrales, Maroc : un indicateur de transfert de matière par les fluides dans une zone de cisaillement ductile.

GÉOCHIMIE. — *Oxydation du fer dans les skarns et les schistes à graphite des Jebilet Centrales, Maroc : un indicateur de transfert de matière par les fluides dans une zone de cisaillement ductile.* Note de Claire Ramboz et Abdelmajid Bastoul, présentée par Georges Millot.

A l'aide des mesures du taux d'oxydation du fer des roches ($7 < O.R. < 74$ mole%), on montre que des fluides oxydants ont circulé dans le cisaillement ductile des Jebilet Centrales lors du métamorphisme prograde. Puis, le fer a été réduit sur 100 m autour de la granodiorite de Ouled Ouaslam. Les roches les plus oxydées sont associées aux mines de graphite, suggérant que du graphite a pu précipiter à partir du fluide par oxydoréduction.

GEOCHEMISTRY. — Oxidation of iron in graphite-bearing skarns and schists in Central Jebilet, Morocco: an evidence for mass transfer by fluid flow in a ductile shear zone.

Based on measured oxidation ratios of iron in the rocks ($7 < O.R. < 74$ mole%), it is shown that a flux of oxidizing fluids took place during prograde metamorphism in the shear zone of Central Jebilet. Reduction of iron occurred later 100 m around the Ouled Ouaslam granodiorite. The rocks the most oxidized are associated with the graphite concentrations, suggesting that graphite may partly have precipitated from the fluid by oxidoreduction.

INTRODUCTION ET CADRE GÉOLOGIQUE. — Dans l'écorce terrestre, les pressions partielles d'oxygène sont en général maintenues à des valeurs très faibles du fait des assemblages minéraux, oxydes ou composés carbonés qui tamponnent ces espèces [1]. Pour cette raison, le rapport Fe^{2+}/Fe^{3+} des roches n'est susceptible d'être modifié à une échelle régionale que lors de processus métasomatiques impliquant des rapports eau/roche élevés ([2], [3]). Les exemples géologiques où a été démontrée soit l'oxydation, soit la réduction du fer concernent des zones à perméabilité élevée : par exemple des roches de degré de métamorphisme faible à moyen en contexte océanique [2], ayant subi une fracturation importante [4]; ou bien des roches de haut degré de métamorphisme engagées dans un cisaillement ductile ([3], [5]).

Le chaînon des Jebilet (Sud de la Meseta Marocaine, *fig.* 1) est constitué à l'Ouest d'un socle cambro-ordovicien surmonté en discordance vers l'Est par des terrains d'âge Viséen supérieur-Namurien, peu métamorphiques dans leur ensemble : les Jebilet Centrales et Orientales ([6], [7]). Dans un couloir de 10 km autour de l'axe N-S Sidi Bou Othmane-Marrakech, les Jebilet Centrales sont engagées dans un cisaillement ductile et sont recoupées par des granites syntectoniques post-viséens ([6], [8]). De façon quasi synchrone se développe un métamorphisme thermique marqué par des associations à cordiérite - andalousite - sillimanite - muscovite - biotite - clinopyroxène - grenat - wollastonite-idocrase ([9], [10]). Des concentrations économiques de graphite sont localisées autour de Sidi Bou Othmane ([6], [10], [11]).

L'objet de cette Note est de présenter une étude de l'état d'oxydation du fer des schistes, des calcaires et des skarns graphiteux de cette zone. Une étude minéralogique incluant des mesures à la microsonde électronique a révélé que les grenats et les pyroxènes dans l'encaissant et dans les veines des zones minéralisées en graphite contenaient du Fe_2O_3 en quantité $> 2\%$ poids [12]. Il importait donc de vérifier si le développement de ces minéraux ferriques impliquait un enrichissement en oxygène de la série dans sa masse.

MÉTHODOLOGIE. — 32 échantillons ont été prélevés dans les Jebilet Centrales (29) et dans les Jebilet Orientales (3) (*fig.* 1). Dans les Jebilet Centrales, l'échantillonnage concerne principalement les alentours des concentrations de graphite (17 échantillons) et l'encaissant immédiat de la granodiorite de Ouled Ouaslam (9 échantillons). Les éléments

0249-6305/85/03010931 $2.00

majeurs des roches de cet échantillonnage ont été dosés par spectrométrie d'émission avec torche à plasma [13]. Certaines roches riches en grenat ont dû être analysées par voie humide, par absorption atomique ou par colorimétrie [14]. Pour le fer total, en particulier, les deux méthodes donnent des résultats comparables à 4% près pour les argilites et à 8% près pour les calcaires. Le fer divalent a été dosé par titrage volumétrique avec $K_2Cr_2O_7$ avec une précision relative de 0,5% poids [14]. Dans l'ensemble des échantillons, le carbone organique (C_{org} = carbone total − carbone des carbonates) a été dosé par coulométrie à impulsion avec une précision relative de 5.10^{-3}% poids.

RÉSULTATS. — Les figures 2 à 4 illustrent les variations de certains pourcentages en poids d'oxydes des roches (FeO, Fe_2O_3, MnO, C_{org}, ...) en fonction du taux d'oxydation du fer :

$$\left(\text{O.R.} = \text{mole}\frac{Fe_2O_3 \times 2 \times 100}{2 \times Fe_2O_3 + FeO}, \text{[15]}\right).$$

Les taux d'oxydation du fer de l'ensemble des échantillons varient largement et de façon continue : 12 à 56 pour les cornéennes autour de la granodiorite, 10 à 75 pour les argilites, 7 à 72 pour les calcaires de la région de Sidi Bou Othmane (*fig.* 2 et 3). Par ailleurs, tous les échantillons contiennent du graphite (>0,07% poids C_{org}), le plus souvent à des teneurs élevées (M = 0,61% poids C_{org}, σ = 0,92 pour 29 échantillons loin des zones minéralisées, *fig.* 4). Chinner [15] a montré que les séries pélitiques graphiteuses

EXPLICATIONS DE LA PLANCHE

Fig. 1. — A, carte géologique des Jebilet et localisation des échantillons étudiés (d'après [6], [8]). La série volcano-sédimentaire des Jebilet Occidentales et le flysch des Jebilet Orientales ne sont que partiellement représentés. B, détail de la région autour de Sidi Bou Othmane : 1, recouvrement plio-quaternaire; 2, formation d'âge Viséen supérieur-Namurien; 3, calcaires d'âge Viséen supérieur; 4, granodiorite. Échantillons analysés : 5, argilites et 6, calcaires; 7, mine (Gph = graphite); 8, zone d'échantillonnage autour de la granodiorite. Le taux d'oxydation du fer est indiqué entre parenthèses, après le numéro d'échantillon.

Fig. 1. — A. Location of the studied samples on the geological map of the Jebilet (after [6], [8]). The volcano-sedimentary unit of Western Jebilet and the flysch of Eastern Jebilet are partly shown. B, detailed map of the area around Sidi Bou Othmane: 1, Plio-Quaternary alluvium; 2, upper Visean-Namurian terranes; 3, upper Visean limestones; 4, granodiorite. Samples analyzed: 5, shales and 6, carbonates; 7, mine (Gph = graphite); 8, sampling area around the granodiorite. The oxidation ratio of iron is indicated between brackets after the sample number.

Fig. 2. — Argilites (=cercles) et calcaires (=étoiles). 2*a* à 2*e*, variations de FeO, Fe_2O_3, Fe_2O_3 total en fonction du taux d'oxydation du fer. 2 *f*, variations du taux d'oxydation du fer en fonction de la distance à l'axe de déformation maximale (d'Ouest en Est, échantillons 88, 83-84, 69-70-71).

Fig. 2. — Shales (=circles) and limestones (=stars). Variations of the oxidation ratio of iron as a function of FeO, Fe_2O_3, Fe total as Fe_2O_3 (2 a to 2 e) and as a function of the distance to the axis of major deformation (2 f; from West to East, samples 88, 83-84, 69-70-71).

Fig. 3. — Échantillons proches de la granodiorite = variations de FeO, Fe_2O_3, Fe_2O_3 total, CaO, MnO en fonction du taux d'oxydation du fer. 3 *e*, variation du taux d'oxydation du fer en fonction de la distance à la granodiorite.

Fig. 3. — Samples close to the granodiorite = correlation between FeO, Fe_2O_3, Fe total as Fe_2O_3, CaO, MnO and the oxidation ratio of iron. 3 e, Correlation between the oxidation ratio of iron and the distance to the granodiorite.

Fig. 4. — Variations de la teneur en carbone organique en fonction du taux d'oxydation du fer (symboles, cf. *fig.* 2). Zone hachurée = schistes noirs ayant évolué en système fermé pour l'oxygène (d'après [15]).

Fig. 4. — Variations of the content in organic carbon as a function of the oxidation ratio of iron (symbols as in Figure 2). Hatched area = graphite-bearing schists having evolved as systems closed to oxygen (after [15]).

Fig. 5. — Composition chimique de calcaires et d'argilites de la série des Jebilet (fer total comme Fe_2O_3, P.F. perte au feu). Les échantillons choisis, bien que de composition chimique très voisine, ont un taux d'oxydation du fer très différent en fonction de leur localisation.

Fig. 5. — Chemical composition of shales and limestones from the Jebilet series (Fe total as Fe_2O_3, P.F. ignition loss). The samples selected have very contrasted oxidation ratios of iron, depending on their location, although they are chemically similar.

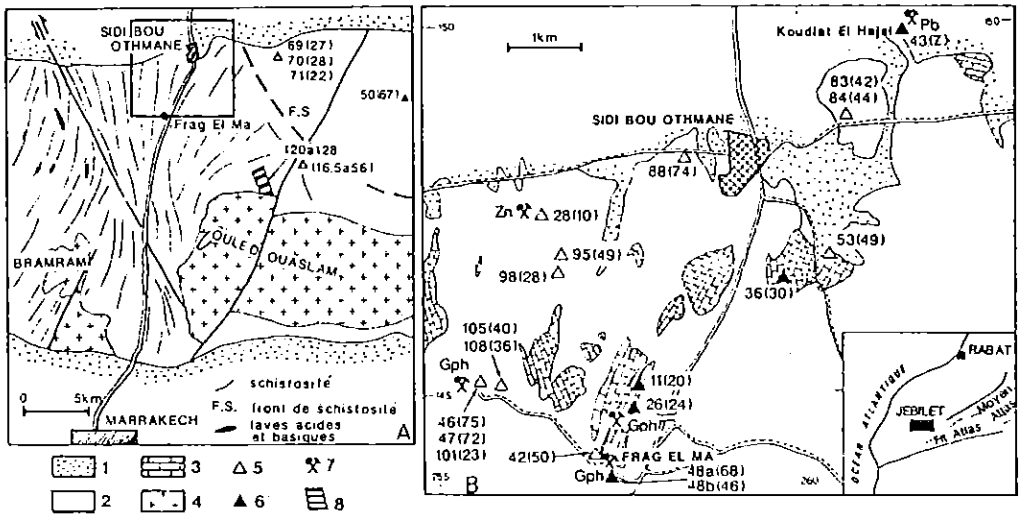

Fig. 1

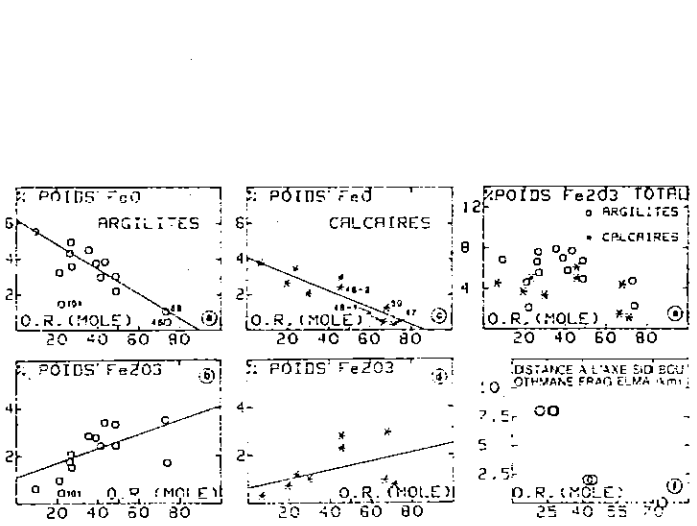

Fig. 2

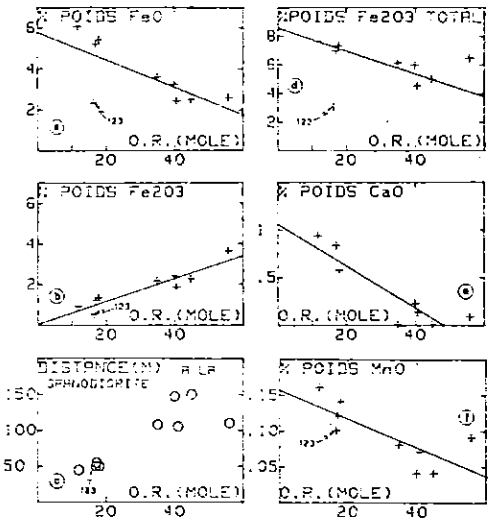

Fig. 3

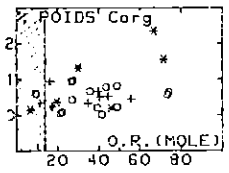

Fig. 4

	ARGILITES		CALCAIRES	
	104	95	4J26	E46b
SiO2	50.37	61.82	37.79	38.55
Al2O3	21.58	19.18	13.29	16.16
Fe2O3t	6.09	6.83	4.95	4.94
MgO	1.39	1.36	2.56	1.46
CaO	0.00	.50	22.40	30.22
Na2O	.52	.78	.12	.03
K2O	3.71	3.75	1.68	.01
TiO2	1.09	1.13	.59	.50
P.F.	4.34	3.76	15.38	7.69
O.R.	35.00	49.40	23.90	46.00

Fig. 5

qui ont évolué en système clos dans le métamorphisme régional conservent un caractère réducteur marqué, avec un taux d'oxydation du fer <14 compatible avec la présence d'ilménite, de magnétite et l'absence d'hématite. Il apparaît donc (*fig.* 4) que le contenu en oxygène des échantillons étudiés n'est pas représentatif du contenu en oxygène originel, diagénétique, mais résulte plutôt de processus métasomatiques surimposés et qui ont transféré de l'oxygène à toute la série. Les pourcentages en poids de Fe_2O_3 et FeO de tous les échantillons sont respectivement corrélés positivement et négativement avec le taux d'oxydation du fer de la roche, en bon accord avec l'interprétation d'une oxydation massive de la série. Alors qu'apparaît une corrélation négative entre le fer total et le taux d'oxydation du fer des échantillons prélevés autour de la granodiorite (*fig.* 3*d*), ces paramètres varient de façon aléatoire dans tous les autres échantillons (*fig.* 2*e*).

Schistes et calcaires autour de Sidi Bou Othmane. — Dans ces échantillons prélevés loin de la granodiorite, on n'a observé aucune corrélation entre le taux d'oxydation du fer et l'un quelconque des éléments majeurs dosés (cf. *fig.* 2*e*), y compris le carbone (*fig.* 4). Le taux d'oxydation du fer de ces roches est donc bien indépendant de l'histoire sédimentologique précoce de la série, telle qu'elle se marque dans la composition en éléments majeurs (*voir* par exemple [15]). En revanche, le taux d'oxydation du fer est dépendant de la localisation géographique (*fig.* 1) : (1) Les échantillons anormalement oxydés sont tous situés dans la zone déformée. Ceci prouve que le cisaillement ductile a constitué un drain privilégié pour les fluides ([3], [5]). Les échantillons 101 et 123 sont éloignés des droites de corrélation entre FeO et O.R. et Fe_2O_3 et O.R., parce qu'ils sont moins oxydés que les autres échantillons. Ce sont des quartzites qui ont été probablement moins affectés par les circulations hydrothermales, parce qu'ils sont devenus imperméables lors de la recristallisation dynamique. (2) Les échantillons prélevés en un même endroit ont un taux d'oxydation voisin, quelle que soit leur composition chimique (*fig.* 1). Les échantillons chimiquement voisins sont différemment oxydés selon leur origine géographique (*fig.* 5). (3) Le taux d'oxydation du fer des roches décroît lorsque l'on s'éloigne de la zone déformée (*fig.* 2*f*). (4) On remarque enfin que les droites de corrélation entre Fe_2O_3 et O.R. et entre FeO et O.R. ont des pentes distinctes pour les argilites et pour les calcaires seulement du fait de la moindre teneur en fer des calcaires (*fig.* 2*a* à 2*d*). Les droites de corrélation entre FeO et O.R. pour les argilites et pour les calcaires convergent pour les échantillons dont le fer a subi l'oxydation la plus forte, c'est-à-dire pour les schistes et les calcaires directement en contact dans les zones riches en graphite.

Les cornéennes autour de la granodiorite. — On observe des corrélations négatives entre le taux d'oxydation du fer et certains éléments majeurs de ces roches : Fe_2O_3 total, MnO, CaO (*fig.* 3*d* à 3*f*), Na_2O (non représenté). Ces données ne sauraient traduire que l'état d'oxydation du fer de ces roches est directement hérité de l'histoire sédimentaire : les cornéennes à graphite ont un taux d'oxydation du fer anormalement haut ($12<$O.R.<55; *fig.* 4) et ont donc, elles aussi, subi une métasomatose importante. Au reste, en raison du comportement de Mn^{3+} et Fe^{3+} lors de la sédimentation, les corrélations entre Fe_2O_3 total et O.R. et MnO et O.R., quand elles sont héritées de l'histoire sédimentaire précoce, sont positives [15] à l'inverse de ce qui est observé ici (*fig.* 3*d*, 3*f*). La figure 3*c* montre qu'à l'échelle de la centaine de mètres, les échantillons sont d'autant plus réduits qu'ils sont proches de la granodiorite. Ces données illustrent une réduction du fer qui est classique dans les auréoles thermiques [15]. Il faut conclure que les cornéennes ont subi à l'instar des autres échantillons, une métasomatose ayant oxydé le fer avant la mise en place de l'intrusion, c'est-à-dire au cours du métamorphisme prograde. Puis elles ont été

réduites de façon inversement proportionnelle à leur distance à l'intrusion. Les corrélations observées résultent simplement du fait que les échantillons ont été prélevés en deux points, et qu'en chacun des points, ils étaient géochimiquement voisins.

CONCLUSIONS. — (1) Dans les Jebilet Centrales, les calcaires et les schistes graphiteux dans la zone de cisaillement ductile n'ont pu évoluer en système clos pour l'oxygène, en raison de leurs taux d'oxydation du fer anormalement élevés. (2) Un flux de fluides oxydants s'est donc produit dans cette zone à la faveur du gradient thermique important et de la forte perméabilité créée par la déformation ductile. (3) La circulation hydrothermale est contemporaine de la phase prograde du métamorphisme qui accompagne la mise en place des granites post-viséens, conclusion que confirme l'étude de la zonation chimique des grenats des skarns de Sidi Bou Othmane [12]. (4) Les roches les plus oxydées sont de part et d'autre du contact entre schistes et calcaires, loin des zones de déformation maximale. Cette discontinuité lithologique a donc joué un rôle prépondérant pour favoriser les réactions chimiques libérant l'oxygène fixé par la roche : elle a pu constituer un drain naturel pour les fluides [10] et surtout elle a permis de générer localement des gradients de potentiel chimique élevés [16]. (5) Les zones les plus riches en graphite sont aussi les plus oxydées. Ceci pourrait suggérer qu'une partie du graphite des roches a pu précipiter directement à partir d'un fluide par réaction entre espèces moléculaires CO, CO_2, CH_4 impliquant la libération d'oxygène (*cf.* [17]). Dans l'encaissant des mines de graphite, Fe^{3+} se trouve dans les grenats titanifères et dans les clinopyronènes [12]. En se basant sur l'étude des inclusions fluides dans les quartz sécants [10] et sur les conditions de stabilité des titandradites [18], on peut préciser que, dans le cas étudié, les roches oxydées et riches en graphite se sont formées à des fugacités d'oxygène globalement très faibles ($f_{O_2} = 10^{-30}$ bar, T = 500°C).

Remise le 16 septembre 1985.

RÉFÉRENCES BIBLIOGRAPHIQUES

[1] H. P. EUGSTER et D. R. WONES, *J. Petrol.*, 3, 1962, p. 82-125; A. F. BUDDINGTON et D. H. LINSLEY, *J. Petrol.*, 5, 1964, p. 310-357; B. M. FRENCH, *Rev. Geophysics*, 2, 1966, p. 223-253.
[2] E. T. C. SPOONER, The Geological Society of London, Spec. Publ., 7, 1977, p. 58-71.
[3] A. BEACH et W. S. FYFE, *Contrib. Mineral. Petrol.*, 36, 1972, p. 175-180.
[4] C. R. B. LISTER, *Geophys. J. R. Astron. Soc.*, 39, 1974, p. 465-509.
[5] R. KERRICH et W. S. FYFE et I. ALLISON, *Econ. Geol.*, 72, 1977, p. 657-663.
[6] P. HUVELIN, *Notes Mém. Serv. Géol. Maroc*, 232 *bis*, 1977, 308 p.
[7] A. PIQUE, *Thèse Sc.*, Univ. Strasbourg, 1979, 253 p.
[8] J. L. LAGARDE et P. CHOUKROUNE, *Bull. Soc. géol. Fr.*, XXIV, n° 2, 1982, p. 299-307.
[9] A. EL HASSANI, *Thèse 3e cycle*, Univ. Aix-Marseille, 1980, 110 p.
[10] A. BASTOUL, *Thèse 3e cycle*, Univ. Nancy-I, 1983, 190 p.
[11] P. HUVELIN et F. PERMINGEAT, *Notes Mém. Soc. géol. Maroc*, 276, 1980, p. 245-256.
[12] C. RAMBOZ, en préparation.
[13] K. GOVINDARAJU, G. MEVELLE et C. CHOUARD, *Anal. Chem.*, 48, 1976, p. 1325-1331.
[14] M. VERNET, Rapport annuel C.R.P.G., 1984-1985.
[15] G. A. CHINNER, *J. Petrol.*, 1, 1960, p. 178-217.
[16] D. RUMBLE III, Carnegie Inst. Washington, Ann. Report Dir. Geophys. Lab., 1973-1974, p. 371-380; M. CUNEY, *Thèse Sc.*, Univ. Nancy-I, 1981, 520 p.
[17] W. I. GUSTAFSON, *J. Petrol.*, 15, 1974, p. 455-496; H. HUCKENHOLZ, E. HOLZL, F. E. HUGGINS et D. VIRGO, Carnegie Inst. Washington, Ann. Report Dir. Geophys. Lab., 1975-1976, p. 711-720.
[18] C. A. SALOTTI, E. W. HEINRICH et A. A. GIARDINI, *Econ. Geol.*, 66, 1971, p. 929-932; P. L. WEIS, I. FRIEDMAN et J. P. GLEASON, *Geochim. Cosmochim. Acta*, 45, 1981, p. 2325-2332; W. GLASSLEY, *Nature*, 295, 1982, p. 229-231.

C. R. : *Centre de Recherches pétrographiques et géochimiques (C.R.P.G.)*, B.P. n° 20, 54501 *Vandœuvre-lès-Nancy Cedex*;
A. B. : *Département de Géologie, Faculté des Sciences de Marrakech, boulevard de Safi, Marrakech, Maroc.*

PUBLICATION XIII : The history of organic nitrogen from early diagenesis to amphibolite facies : mineralogical, chemical, mechanical and isotopic implications.

5th Internat. Symposium, Water-Rock Interaction, Reykjavik, Iceland, August 8-17 1986, Extended Abstracts, 170-174.

THE HISTORY OF ORGANIC NITROGEN FROM EARLY DIAGENESIS TO AMPHIBOLITE FACIES : MINERALOGICAL, CHEMICAL, MECHANICAL AND ISOTOPIC IMPLICATIONS

Jean Dubessy[1] and Claire Ramboz[2]
(1) CREGU, GS-CNRS-CREGU, BP 23, 54501 VANDOEUVRE LES NANCY CEDEX FRANCE
(2) CRPG, BP 20, 54501 VANDOEUVRE LES NANCY CEDEX FRANCE

Gas chromatography and Raman spectrometry have provided strong evidence that N_2 is a common fluid component in the continental crust. Despite this evidence, the influence of nitrogen on geological processes has seldom been considered. The purpose of this paper is to show that, far from being inert, nitrogen is involved in major mineralogical, chemical and mechanical processes.

N_2 IN DIAGENESIS (S.L.)

Sources of organic nitrogen. The classification of organic matter (O.M.) based on its elemental composition reflects the different types of living matter and also allows discrimination of the amount and chemical type of nitrogen associated. Nitrogen is involved either in proteins or in heterocyclic bonds. Proteins account for most of the organic nitrogen. O.M. of type I and II (algae, bacteria, plankton) is composed of proteins (up to 80 %) whereas type III O.M. (higher terrestrial plants) is protein-poor and contains mainly heterocyclic nitrogen (Tissot and Welte, 1978). The amount and nature of the nitrogen-bearing species released from O.M. during diagenesis is essentially controlled by the O.M. type.

The evolution of organic nitrogen. The two stage release of nitrogen from O.M. during diagenesis (s.l.) is summarized in Fig. 1 after Tissot and Welte (1978).

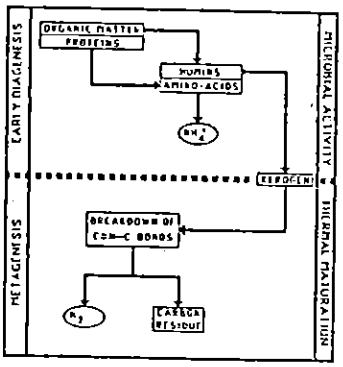

Fig. 1 : General scheme of loss of nitrogen from organic matter during diagenesis.

NH_4^+ is released during early diagenesis at near surface temperatures mainly from O.M. of types I and II. By contrast, at 150°-250°C, N_2 is probably produced from O.M., whatever its type, as a result of the breakdown of heterocyclic bonds. During early diagenesis, the nature of the nitrogen-bearing species in the fluid is mainly controlled by the equilibria :

$$(1)\ NH_4^+ = NH_3 + H^+ \qquad (2)\ 2NH_3 = N_2 + 3H_2$$

At pH < 9, NH_4^+ is dominant over NH_3 (Stumm and Morgan, 1981). In fluids containing either dissolved O_2 or SO_4^{--}, NH_4^+ is oxidized to N_2 (see $p\varepsilon^\circ$ values in Stumm and Morgan, 1981, p. 449). During diagenesis, nitrogen is incorporated into minerals in the form of NH_4^+ only : into the interlayer space of clay minerals (Mortland, 1958), in the lattice of feldspars (Loughnan et al., 1983), sylvites and carnallites (Kühn, 1968). This points out that nitrogen can be stored in minerals only under permanently reducing conditions (at pH = 7 and 25°C, Eh < -250 mV, Stumm and Morgan, 1981 ; see also Loughnan et al., 1983). Hydrogen, partly of organic

origin, is necessarily stored with the nitrogen in the minerals. If NH_4^+ is oxidized to N_2, it becomes an inert component which easily migrates because of its small size (Tissot and Bessereau, 1982).

N_2 in salt diapirs : a case study. The presence of N_2 together with CH_4 or CO_2 in salt domes has long been known (references in Roedder, 1972). However, two kinds of fluid chemistry, strictly related to the wall-rock minerals, can be distinguished : 1) CH_4-N_2-bearing fluids with little or no CO_2 characterize potash mines (Hoy et al., 1962). 2) By contrast, the gases associated with marine halites mainly contain CO_2 and N_2 with minor CH_4 (Hoy et al., 1962 ; Guilhaumou et al., 1982). These data suggest that in marine halite deposits, rich in anhydrite, organic NH_4^+ and CH_4 are oxidized as follows :

$$(3)\ CH_4+SO_4^{--}+2H^+ \rightarrow CO_2+H_2S+2H_2O \quad (4)\ 8NH_4^+ + 3SO_4^{--} \rightarrow 4N_2+3H_2S+12\ H_2O+2H^+$$

These reactions occur either within the salt mass or at the contact between the salt dome and the O.M.-bearing environment. CO_2 in gas and oil fields has been suggested to result from the oxidation of petroleum by SO_4^{--}-bearing waters (Farmer, 1965). This reaction has also been proposed as a source of sulphur in cap-rock deposits. In potash and lacustrine halite mines where anhydrite is rare, NH_4^+ is oxidized to N_2 whereas CH_4 remains stable. In some potash mines, NH_4^+ bearing waters and carnallites (Kühn, 1968) and NH_4Cl crystals have been found.

Finally, reaction (4) has a large $\Delta V(R)$. This induces an increase of fluid pressure in the impermeable water-poor halite and shale environment which in turn can favour hydraulic fracturing (Watts, 1983). This process can account for some aspects of salt tectonics (fracture-induced diapirism ; slicing).

N_2 IN METAMORPHIC AND GEOTHERMAL ENVIRONMENTS

The occurrence of N_2-rich paleo-fluids in metamorphic and geothermal environments is now well established (Turpin et al., 1981 ; Kreulen and Schuiling, 1982 ; Bastoul, 1983 ; Bussink et al., 1984 ; Cheilletz, 1984). NH_4^+-bearing micas and feldspars are stable in metamorphic rocks (Honma and Itihara, 1981). N_2-bearing fluids associated with NH_4^+-silicates has been established only in the Dome de l'Agout, (Kreulen and Schuiling, 1982) and in the Jebilet Mountains, (unpub. data by Dubessy, Kreulen and Ramboz). The release of ammonium from micas to the fluid has also been shown to occur experimentally at 550°-600°C (Hallam and Eugster, 1976). Calculation shows that N_2 is dominant as soon as $\Sigma N_2 + NH_3$ mole fraction > 10^{-4} and/or if fO_2 is > QFM (Dubessy, 1985 ; Fig. 2).

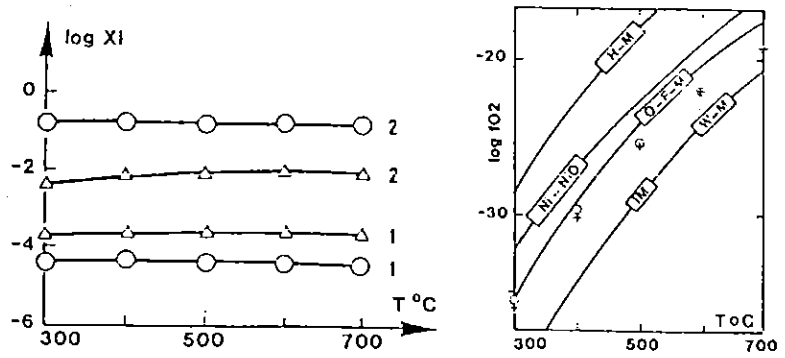

Fig. 2 : a) Molar fraction of N_2(O) and NH_3(Δ) in the two following mixtures at molecular equilibrium :
1 : $X(CH_4)=0.5; X(H_2O)=0.5; X(N_2)+X(NH_3)=.2\ 10^{-3}$
2 : $X(CH_4)=0.4; X(H_2O)=0.4;\ X(N_2)+X(NH_3)=.2$
b) Oxygen fugacity of the fluids defined in 2a : + = 1 ; O = 2.

These results explain why NH_3 has never been detected in inclusions by Raman spectrometry. These facts have the following geochemical consequences :

a) in thermal domes, contact metamorphic aureoles or high grade amphibolite facies, N_2 must be considered to have been primarily of organic origin ;

b) the release of NH_4^+ also provides H^+ or HCl° and H_2 to the fluid. Therefore, the inert character of nitrogen in metamorphic systems is not primary but results from redox reactions.

c) a consequence of metamorphic N_2 being derived from type I and II O.M. is that graphitic material is found in N_2-producing rocks. In the Jebilet, N_2 and CH_4-rich fluids occur in graphite-bearing rocks : in skarns located within graphite mines, fO_2 close to I-W is implied by the presence of Ti-bearing garnets (Ramboz and Bastoul, 1985). This fO_2 is compatible with the CH_4-N_2-bearing fluids which have a low H_2O-content at equilibrium with graphite ;

d) such low H_2O and CO_2 activities in nitrogen and carbon rich fluids may enhance the devolatilization of carbonates and hydroxyl minerals to lower T.

3) Finally, N_2 release in metamorphic fluids probably produces the following consequences :

a) in open systems, the fluid pressure will remain constant. The fluid density is expected to be lowered because of the N_2 added in the hotter parts of the system where silicates release their NH_4^+. This enhances convection.

b) in closed systems, the release of N_2 will increase the fluid pressure, favouring ductile fracturing.

HYDROGEN ISOTOPIC SIGNATURE

Hydrogen of the biogenic CH_4 produced throughout diagenesis is characterized by $\delta D < -100$ (Schoell, 1980). In the above mentioned environments, fluids with low δD, in particular waters (see reaction (4)), are expected to be found with N_2. Indeed, waters with $\delta D < -100$ have been reported in several N_2 producing diagenetic, metamorphic-hydrothermal environments (e.g. cap-rock deposits from Tunisia : Sheppard and Charef, 1986 ; Sn-W deposit of Panasqueira : Turpin et al., 1981 ; Bussink et al., 1984 ; Kelly and Rye, 1979,).

REFERENCES

Bastoul, A. (1983). Etude des fluides carbo-azotés associés au métamorphisme de contact des schistes noirs sur l'exemple des Jebilet Centrales (Maroc). Comparaison avec la région des Bondons et de Pen Ar Ran (France). Thesis, INPL, Nancy, 191 p.

Bussink, R.W., Kreulen, R. and De Jong, A.F.M. (1984). Gas analyses, fluid inclusions and stable isotopes of the Panasqueira W-Sn deposits, Portugal. Bull. Minéral., 107, 703-714.

Cheilletz, A. (1984). Caractéristiques géochimiques et thermo-barométriques des fluides associés à la scheelite et au quartz des minéralisations de tungstène du Jbel Aouam (Maroc central). Bull. Minéral., 107, 255-272.

Dubessy, J. (1985). Contribution à l'étude des interactions entre paléo-fluides et minéraux à partir de l'étude des inclusions fluides par microspectrométrie Raman. Conséquences métallogéniques. Unpub. Thesis, INPL Nancy, 198 p.

Farmer, R.E. (1965). Genesis of subsurface carbon dioxide, in Fluids in subsurface environments- A Symposium, A.A.P.G. Mem., 4, 378-385.

Guilhaumou, N., Dhamelincourt, P. and Touret, J. (1981). Etude des inclusions fluide du systeme N_2-CO_2 de dolomites et de quartz de Tunisie septentrionale. Données de la microcryoscopie et de l'analyse à la microsonde à effet Raman. Geochim. Cosmochim. Acta, 45, 657-673.

Hallam, M. and Eugster, H.P. (1976). Ammonium silicate stability relations. Contrib. Mineral. Petrol., 57, 227-244.

Honma, H. and Itihara, Y. (1981). Distribution of ammonium in minerals of metamorphic and granitic rocks. Geochim. Cosmochim. Acta, 45, 938-988.

Hoy, R.B., Foose, R.M. and O'Neill, B.J.Jr (1962). Structure of Winnfield salt dome, Winn Parish, Louisiana. A.A.P.G. Bull., 46, 1444-1459.

Kelly, W.C. and Rye R.O. (1979). Geologic, fluid inclusion, and stable isotope studies of the tin-tungsten deposits of Panasqueira, Portugal. Econ. Geol., 74, 1721-1819.

Kreulen, R. and Schuiling, R.D. (1982). N_2-CH_4-CO_2 fluids during formation of the Dome de l'Agout France. Geochim. Cosmochim. Acta, 46, 193-203.

Kühn, R. (1968). Geochemistry of the German potash mines. G.S.A. Special Papers, 88, 427-504.

Loughnan, F.C., Roberts F.I.and Lindner A.W. (1983). Buddingtonite (NH_4^+-feldspar) in the Condor Oilshale deposit, Queensland, Australia. Min. Mag., 47, 327-334.

Mortland, M.M. (1958). Reactions of ammonia in soils. Advan. Agron. 10, 325.

Ramboz, C. et Bastoul, A. (1985). Oxydation du fer dans les skarns et les schistes à graphite des Jebilet Centrales, Maroc : un indicateur de transfert de matière par les fluides dans une zone de cisaillement ductile. C.R. Acad. Sci., Paris, t. 301, Série II, 13, 931-936.

Roedder, E. (1972). Composition of fluid inclusions. U.S. G.S., Prof. Paper 440 JJ, 164 p.

Schoell, M. (1980). The hydrogen and carbon isotopic composition of methane from natural gases of various origins. Geochim. Cosmochim. Acta, 44, 649-661.

Sheppard, S.M.F. and Charef, A. (1986). Eau organique : caractérisation isotopique et évidence de son rôle dans le gisement Pb-Zn de Fedj-el-Adoun. C.R. Acad. Sci., Paris, 302, Série II, 1189-1192.

Stumm, W. and Morgan, J.J. (1981). Aquatic chemistry. An introduction emphasizing chemical equilibria in natural waters. 2nd edition. Wiley 780 p.

Tissot, B. and Bessereau, G. (1982). Géochimie des gaz naturels et origine des gisements de gaz en Europe occidentale. Rev. I.F. P., 37, 63-77.

Tissot, B.P. and Welte, D.W. (1978). Petroleum Formation and Occurrence. A new approach to Oil and Gas Exploration. Springer-Verlag, 538 p.

Turpin, L., Ramboz, C. and Sheppard S.M.F. (1981). Chemical and isotopic evolution of the fluids in the Sn-W deposit of Panasqueira, Portugal. Terra Cognita, Spec. Iss., 1st EUG Meeting, 42.

Watts, N.L. (1983). Microfractures in chalks of Albuskjell Field, Norwegian Sector, North Sea : Possible origin and distribution. A.A.P.G. Bull., 67, 201-234.

PUBLICATION XIV : Recherche du tungstène dans le district de la Châtaigneraie. (Cantal, Aveyron - Massif central français) : Géochimie des schistes de la Châtaigneraie.

Chron. rech. min., n° 487, pp. 11-30, 9 fig., 2 tabl.

Travaux du Centre de Recherches Pétrographiques et Géochimiques

Recherche du tungstène dans le district de la Châtaigneraie

(Cantal, Aveyron - Massif central français)

Géochimie des schistes de la Châtaigneraie

S. BOGDANOFF[1], J.L. CIRODDE[1], A. PLOQUIN[2], C. RAMBOZ[2]

Une décennie de recherche minière dans la Châtaigneraie

J.R. LE CHAPELAIN[3], R. MIGNON[3]

Exploration for tungsten in the Châtaigneraie district

Mots-clés : Micaschiste, Métapélite, Faciès schiste vert, Faciès amphibolite, Leptynite, Tungstène substance, Filon champ, Stream sediment, Roche totale, Granite, Cornéenne, Prospection géochimique région, Reserve
Cantal, Aveyron (District la Châtaigneraie, Leucamp, Enguialès).

Avertissement

Cet article réunit deux communications du Colloque sur les gisements de tungstène. Les travaux et les résultats présentés procèdent de disciplines d'investigation différentes mais concernent tous la recherche du tungstène dans une même région : la Châtaigneraie. Pour éviter des répétitions inutiles (localisation, descriptions géologiques ou gîtologiques et références bibliographiques), les auteurs ont accepté de fondre leurs deux manuscrits en un seul article dans lequel, après une première partie de présentation de la Châtaigneraie due aux divers auteurs, la seconde partie : "Géochimie des schistes de la Châtaigneraie" est l'oeuvre de S. Bogdanoff, J.L. Cirodde, A. Ploquin et C. Ramboz (Université d'Orsay et CNRS de Nancy). La troisième partie : "Une décennie de recherche minière dans la Châtaigneraie" est due à J.R. Le Chapelain et R. Mignon (Direction des Activités Minières, BRGM).

Abstract

This paper gives an account of the exploration for tungsten conducted the last ten years in the Châtaigneraie district.

From 1916 to 1979, tungsten was mined intermittently in the district, in particular at the Leucamp, Teissières, Murols and Enguialès mines with a total production of 3,900 t contained WO_3. The Châtaigneraie district, which is centred on the Veinazès granite, is a homogeneous structural and metallogenic unit dominated by a gitological feature: peribatholithic wolframite-bearing quartz-vein systems.

Since 1975 a number of general exploration methods (multi-element and stream-sediment geochemistry) and detailed exploration methods (surveying of occurrences by direct outcrop observation, geochemistry, trenching, percussion drilling, geophysics and remote sensing) has been developed. From 1981 exploration has been backed up by studies made by specialists, involving geochemists, gitologists and structural geologists from the BRGM and various university research laboratories.

• The geochemical study made by S. Bodganoff's team bears on the Châtaigneraie schists, host to the tungsten deposits. This series consists of a pile of nappes comprising schists and pelitic-arenaceous rocks the grade of metamorphism increasing upwards. This pile is cut by Hercynian granites and tungsten-bearing quartz veins with associated tourmalinisation

Two sedimentologically distinct groups have been distinguished on the basis of the geochemical characterisation that is the principal subject of this paper. *The lower, pelitic group* is the most mature and is mainly of quartz-illitic origin. Pelitic rocks are far more abundant than quartzites. *The arenaceous upper pelitic group*, with more variable quartz content is distinctly marked by significant albite content, most probably of volcanic origin. This volcanic heritage appears to be related to the siliceous-sodic leptynites occuring in this group. Apart from the mineralizations, the W contents of these rocks are not anomalous.

The location of the economic concentrations and of the main tungsten occurrences appears to be unrelated to the sedimentological and geochemical nature of the host rocks. It seems to be controlled by oxidation related to tectono-metamorphic events which took place prior to the intrusion of the Hercynian granites.

• The various mineral exploration phases and the results obtained in the course of ten years of activity are presented by the BRGM team (J.R. Le Chapelain and R. Mignon).

During the preliminary prospecting phase, the application of various techniques resulted in the discovery of numerous wolframite and/or scheelite occurrences, none of which, in the present state of knowledge, appear to contain economically interesting concentrations.

Given these rather discouraging results, the BRGM has progressively focussed its exploration efforts on the mineralised sectors of the Leucamp and Enguialès concessions in order to find lateral and deeper extensions to the known deposits.

During the second phase of "oriented" investigation in addition to core drilling, the work included development aiming at qualitative and quantitative evaluation of a potential which could warrant resumption of mining activity.

The work conducted at Enguialès from 1980 to 1983 showed a tonnage of about 1,400 t of contained WO_3, in a block 300 m along strike and down dip with thin (0,4 m at most) ramifying veins welded to the walls by tourmalinite.

At Leucamp, a possible potential of 7,000 t of contained WO_3, was revealed in a vein system forming down dip or lateral extensions of veins similar to those mined in former times, 0.3 to 0.7 m in thickness with tourmalinized walls independent of the host rock. This characteristic was utilized for a selective stoping test which resulted in the conclusion that it would be possible to extract undiluted ore.

In addition to these positive results, exploration in the Châtaigneraie area, especially mapping at various scale, has considerably contribued to the gitological understanding of the district. It has provided important detailed information on the structural control of the deposits, their lithogeochemical setting and the mineral paragenesis.

(1) Université d'Orsay, Laboratoire de Géologie historique et structurale. Bât. 504. 91405 Orsay cedex.
(2) CNRS, CRPG, BP 20. 54501 Vandoeuvre-lès-Nancy cedex.
(3) BRGM, DAM/DEX, BP 6009. 45060 Orléans cedex.

Résumé

Cet article fait le point sur les recherches relatives au tungstène développées depuis une dizaine d'années dans le district de la Châtaigneraie.

Ce district a été le siège d'une activité extractive discontinue pour le tungstène entre 1916 et 1979, avec les exploitations de Leucamp, Teissières, Murols et Enguialès (production globale cumulée : 3900 t de WO_3 contenu). Centré sur le granite de Veinazès, il représente une unité structurale et métallogénique homogène, avec une expression gîtologique prépondérante : des faisceaux filoniens péribatholithiques à quartz-wolframite.

Depuis 1975, l'exploration a mis en oeuvre un ensemble de prospections stratégiques (géochimie multiélémentaire, alluvionnaire) et tactiques (relevés d'indices en prospection au marteau, géochimie, tranchées et sondages percutants, géophysique, télédétection,...). A partir de 1981, cette reconnaissance a été appuyée par des études de spécialistes (géochimistes, gîtologues, structuralistes,...) du BRGM et de divers laboratoires de recherches universitaires.

• L'étude géochimique (conduite par l'équipe de S. Bogdanoff) porte sur les schistes de la Châtaigneraie qui encaissent les gisements du tungstène. Cette série est très probablement constituée de nappes qui s'empilent, à métamorphisme croissant vers le haut, des formations schisteuses et gréso-pélitiques. Cet empilement est recoupé par des granites hercyniens, puis par des filons de quartz tungstifères avec tourmalinisations associées.

La caractérisation géochimique (éléments majeurs) conduit à proposer deux groupes sédimentologiquement distincts :

- *Le groupe pélitique*, structuralement inférieur, est le plus mature, essentiellement d'origine quartzo-illitique, les roches pélitiques y dominent largement sur les quartzites.

- *Le groupe gréso-pélitique*, structuralement supérieur, avec ses teneurs en quartz plus variables, est caractérisé en outre par des leptynites silico-sodiques qui sont probablement d'anciens tufs.

Les teneurs en W de ces formations, hors minéralisation, ne sont pas anormales.

La localisation des concentrations économiques et des principaux indices en W paraît indépendante de la nature sédimentologique/géochimique en grand de la formation encaissante, mais serait contrôlée par une oxydation liée aux évènements tectono-métamorphiques antérieurs aux intrusions granitiques hercyniennes et aux filons de wolframite.

• L'équipe du BRGM (J.R. Le Chapelain et R. Mignon) présente les diverses phases d'exploration minière et les résultats obtenus au cours de ces dix années d'activité.

Lors d'une première période de prospection régionale, l'application des diverses techniques a abouti à la découverte d'indices nombreux à wolframite et/ou scheelite dont aucun ne semble, dans l'état actuel des connaissances, être une concentration de taille économique.

Les résultats peu encourageants de l'exploration régionale ont progressivement conduit le BRGM à concentrer les efforts de la recherche sur les secteurs minéralisés connus antérieurement, c'est-à-dire les concessions de Leucamp et d'Enguialès, pour y mettre en évidence des extensions (latérales et profondes) aux gisements connus.

Lors de cette deuxième période de reconnaissance "ciblée", les recherches ont comporté (outre des sondages carottés), des travaux miniers visant à apprécier qualitativement et quantitativement un potentiel susceptible de justifier une reprise d'exploitation.

Les travaux d'Enguialès (1980-1983) montrent un tonnage de l'ordre de 1400 t de WO_3 contenu, dans un panneau de 300 m d'allongement et d'aval pendage avec des filons minces (au plus 0,4 m), ramifiés et soudés aux épontes par des tourmalinites.

Les opérations menées à Leucamp ouvrent une possibilité de 7 000 t de WO_3 contenu, dans un système de filons représentant soit l'aval pendage, soit des extensions latérales de filons similaires à ceux anciennement exploités : 0,3 à 0,7 m de puissance, à épontes tourmalinisées non solidaires de l'encaissant. Cette propriété a été mise à profit lors d'un test d'abattage sélectif concluant quant à la possibilité d'extraire un minerai non dilué.

Outre ces résultats positifs sur le plan minier, cette exploration de la Châtaigneraie apporte une importante contribution à la connaissance gîtologique du district qui se traduit par des acquisitions cartographiques à différentes échelles, des précisions importantes sur le contrôle structural des gîtes, sur leur contexte litho-géochimique et l'étude des paragenèses minérales.

I. LA CHÂTAIGNERAIE, CADRE GEOLOGIQUE ET MINERALISATIONS

Introduction

Située une quarantaine de kilomètres au sud d'Aurillac, à cheval sur les départements du Cantal et de l'Aveyron, la Châtaigneraie est le coeur d'un district minéralisé en tungstène qui regroupe d'anciennes exploitations : Leucamp, Murols, Teissières, Enguialès (production cumulée de l'ordre de 3900 t de WO_3) ; et des indices anciennement connus : Le Viala, Lafeuillade, ou récemment découverts dans le cadre de l'inventaire des ressources minières. Cette région correspond à un ensemble structural et lithologique cohérent, représenté par une série métamorphique relativement monotone (la série de la Châtaigneraie) recoupée par les granites d'Entraygues, de Veinazès, de Marcolès, de Boisset et d'Omps. Ce domaine disparaît au nord sous les dépôts sédimentaires cénozoïques du Bassin d'Aurillac, recouverts à leur tour par les épanchements volcaniques tertiaires des Monts du Cantal. Il est limité à l'ouest par les accidents méridiens du Sillon Houiller, au sud par le bassin houiller de Decazeville, par le Permien du graben du détroit de Rodez et à l'est par le massif granitique d'Entraygues (extrémité ouest du massif de la Margeride). Il s'étend sur les feuilles au 1/50 000 d'Aurillac, Vic-sur-Cère, Maurs, Entraygues, et pro parte, Decazeville.

1. La série cristallophyllienne

(S. Bogdanoff, J.L. Cirodde, A. Ploquin).

Cette série appartient à l'ensemble micaschisteux épi- à mésozonal situé à l'est du Sillon Houiller (vallée du Lot, Cévennes, Albigeois, où la part respective des influences éohercyniennes et hercyniennes n'est pas clairement établie (A. Autran *et al.*, 1980).

Des schistes, micaschistes, grès et quartzites métamorphisés, associés en toutes proportions sont les constituants essentiels. Les pendages de la stratification et de la schistosité principale plongent, le plus souvent modérément, parfois fortement, vers le nord ou le nord-est. La comparaison avec les séries paléozoïques de la Montagne Noire et l'analyse structurale à toutes les échelles ont amené à penser que la Série de la Châtaigneraie serait constituée par du matériel d'âge paléozoïque inférieur impliqué dans des nappes déversées vers le sud-ouest (S. Bogdanoff *et al.*, 1984, et note en cours). Ce matériel a subi un métamorphisme des faciès amphibolite puis schiste vert que les nappes ont empilé en ordre inverse (M. Boule, 1899-1900 ; M. Roques, 1941). Cette structuration tectonique est antérieure aux intrusions des granites hercyniens d'âge namurien (G. Vivier et M. Lasserre, 1973 ; J.P. Couturié *et al.*, 1979). Selon les interprétations présentées par

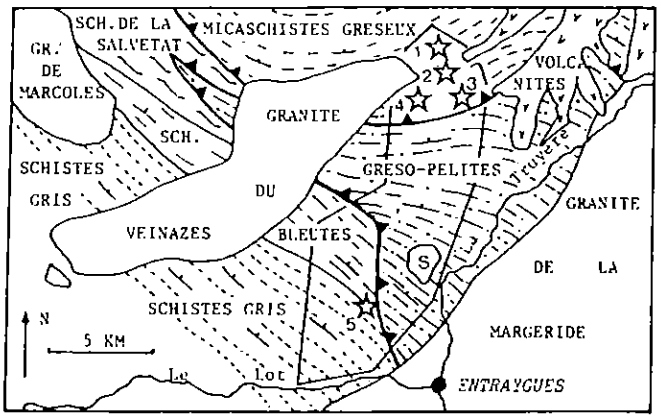

Fig. 1.- Schéma structural de la Châtaigneraie.

S : Granodiorite de Soulaque. : Contacts tangentiels. : Pendages. L'encadré entoure la zone de prélèvement des échantillons.
Mines de wolframite :
1 : Tessières-lès-Bouliés. 2 : Caylus ; 3 : Murols-Lantuéjouls ; 4 : Leucamp-Bancarel ; 5 : Enguialès.

A. Autran et J. Cogné (1980), puis par C. Pin (1980), cette tectonique tangentielle se placerait au Carbonifère inférieur.

Les minéralisations, essentiellement à wolframite, sont liées à des filons de quartz qui recoupent les unités structurales, et à l'auréole de métamorphisme des granites de Veinazès et d'Entraigues. L'étude des fluides des veines minéralisées (C. Ramboz, 1980) oblige à lier minéralisation et évolution thermique syn- à tardi-granitique. Pour une étude localisée autour du gîte de Leucamp voir M. Demange et V.A. Nicolas (1983) et M. Demange *et al.* (ce colloque, 1986), ou autour du gîte d'Enguialès voir M. Laval *et al.* (ce colloque, 1986). Les travaux récents (Y. Chèze, 1975 ; M. Joubert, 1978 ; S. Bogdanoff *et al.*, 1980 et 1985 ; J.M. Boessé, 1980 ; V.A Nicolas, 1985 ; J.L. Cirodde, thèse en cours) ont permis de diviser la série de la Châtaigneraie en cinq unités, de bas en haut et du sud-ouest vers le nord-est (fig. 1) :1 - La Formation des schistes gris, à muscovite et chlorite ; 2 - La Formation des schistes bleutés, à muscovite et chlorite ; 3 - La Formation des micaschistes de La Salvetat, à muscovite et chlorite au sud, à grenat et cordiérite plus au nord ; 4 - La Formation des gréso-pélites, à biotite, grenat, staurotide, et à chlorite, muscovite secondaires ; 5 - La Formation des micaschistes gréseux, à biotite, grenat, et à chlorite, muscovite secondaires.

Les unités 4 et 5 contiennent des leptynites en bancs décimétriques à plurimétriques, parallèles à la stratification (unité 4) ou à la schistosité régionale (unité 5). Les amphibolites et les roches carbonatées sont apparemment absentes ou rares ; Y. Chèze (1975) a néanmoins signalé, dans les gréso-pélites, une amphibolite (m) maintenant détruite par des travaux routiers. Enfin, on connaît quelques conglomérats polygéniques, au nord-est de la zone étudiée ici, dans les schistes gris (J.M. Boessé, 1980). Les cartes géologiques à 1/50 000 Entraygues et Maurs, où est figuré l'agencement des métamorphites et des granites, sont en cours de publication (S. Bogdanoff *et al.*, 1980 et 1985). Dans cet article, nous avons conservé la nomenclature proposée par ces auteurs.

2. Les intrusions plutoniques (R. Mignon).

2.1. Le granite d'Entraygues, d'allongement hercynien (N60°) comme la bordure nord du granite de la Margeride s.s. est probablement en continuité avec celui-ci dont il n'est séparé que par un grand accident NW-SE (P. Lapadu-Hargues, 1951) sur lequel s'est installé l'épanchement volcanique de l'Aubrac. L'ensemble Margeride *s.l.* grand massif monzogranitique et granodioritique, présente une remarquable stratification verticale avec concentration de ferromagnésiens, de plagioclases et de phénocristaux de feldspaths potassiques à la base (J.P. Couturié, 1977). Cette évolution régulière vers un type granitique leucocrate, alcalin et siliceux, dont la structure porphyroïde tend à disparaître dans la partie haute du pluton, est confirmée par l'étude géochimique des éléments majeurs et mineurs. Le massif d'Entraygues est recoupé par une quantité de stocks de leucogranites à tourmaline et d'aplites de direction moyenne N45°, eux-mêmes recoupés par des petits massifs et des filons plus ou moins réguliers de microgranites, microdiorites et lamprophyres d'orientation générale N135° (C. Derré, 1977). Ce cortège filonien sort du granite et larde littéralement la Châtaigneraie méridionale. Le massif de la Margeride-Entraygues a été daté 323 Ma ± 10 Ma (J.P. Couturié *et al.*, 1979).

2.2. Les petits massifs de granite monzonitique. Ce sont :

– Le granite de Veinazès. Affleurant sur 19 km selon un axe NE-SW, il se situe 4 km au NW du massif d'Entraygues. C'est sur la frange externe de son extrémité NE que se localisent les gisements de tungstène de Leucamp, Tessières et Murols. C'est un granite à tendance porphyroïde dont un compartiment (compris entre les grandes failles NW-SE de Pons et du Langairoux) présente un faciès plus leucocrate. Age possible : ± 320 Ma (J.L. Duthou, S. Bogdanoff, J.L. Cirodde, V. Nicolas, 1986).

– Le granite porphyroïde de Marcolès. Il affleure 2 à 3 km au NW du précédent, en un petit massif ovoïde d'axe NW. C'est un granite hololeucocrate à biotite et muscovite plus abondante que dans les faciès clairs du Veinazès, qui présente une apophyse leucogranitique sur sa bordure sud (M. Joubert, 1978). Cette apophyse leucogranitique borde au sud le couloir tectonique qui suit approximativement la haute vallée de la Rance de direction N130° à N140° (Marcolès-Costeveyre). Cet axe correspond à un linéament régional, l'accident de Pons, au sud duquel, au niveau de la granodiorite de Soulaque existent également des leucogranites au Viala.

Ces petits massifs de granite monzonitique qui recoupent la série de la Châtaigneraie ont été considérés comme des apophyses du granite d'Entraygues, sans que la preuve d'une liaison en profondeur de tous ces massifs ait été apportée. Les données gravimétriques et géochimiques acquises récemment tendent plutôt à infirmer, ou tout au moins à nuancer cette interprétation.

En effet, sur le plan de la géochimie (stream), le Be différencie très nettement l'intrusif de Veinazès de celui de Marcolès et du massif d'Entraygues ; ces

deux derniers massifs sont très beryllifères, surtout le Marcolès (7 valeurs > 20 ppm pour le Marcolès, 1 seule pour Entraygues), alors que le Veinazès l'est nettement moins ; de plus, à l'intérieur du monzogranite de Veinazès, la répartition du béryllium est tout à fait hétérogène (J.C. Delille, Y. Peronne 1982). Cette répartition, en corrélation inverse du Ba-Sr, est corrélée avec le critère de couleur déterminé par M. Joubert, les secteurs les plus riches en Be correspondent, grosso-modo aux faciès clairs (< 10 % biot.). On note une trainée à Be > 5 ppm qui trace curieusement le cours inférieur de l'Auze, rectiligne et NE-SW, en dehors du granite de Veinazès.

Le W différencie encore mieux les trois massifs : les valeurs supérieures à 25 ppm sont très nombreuses et régulièrement réparties dans le massif d'Entraygues et à sa périphérie immédiate (dont 7 valeurs supérieures à 75 ppm). Elles sont pratiquement absentes du Veinazès (hors du périmètre entourant Leucamp-Teissières-Murols) et totalement absentes du Marcolès. Notons une valeur supérieure à 75 ppm au sud d'Aubespeyre (un peu au sud d'une tache en Be de 8 valeurs supérieures à 5 ppm) à la limite d'une plage légère en gravimétrie.

2.3. Les leucogranites. Ils se sont mis en place à 300 ± 5 Ma. pour J.P. Couturié, M. Vachette (1980) ou entre 338 et 265 Ma pour H. Bellon et J.P. Gibert (1981). Ils recoupent les différents éléments du bâti et en particulier :

a) Le massif d'Entraygues, au SW et au NE de cette localité, où ils forment des stocks et dykes d'orientation générale N à N135° à N145° (Toyer 1963, C. Derré 1980). Au SW d'Entraygues (Valysac, la Castanié), le leucogranite renferme de la wolframite disséminée (de type ferbérite), la microsonde a permis de déterminer des oxydes de titane colombifères et tantalifères qui correspondraient à la struvérite (P. Picot). Des leucogranites existent également sur la bordure SE du massif d'Entraygues, où ils sont localement parcourus par des filonnets de quartz à wolframite de puissance millimétrique à pluricentimétrique ; *cf.* l'indice du Bousquet, sondé par le BRGM. Il s'agit ici de leucogranites à cordiérite, en stocks lenticulaires plus ou moins horizontaux.

b) Les zones de contact entre la série cristallophyllienne et les granitoïdes sur la bordure nord du Veinazès où le filon d'Auberoque (à cordiérite) présente une composition chimique comparable aux leucogranites de l'apophyse de Marcolès.

c) Au contact du massif de Soulaque, dans le secteur du Viala, un stock leucogranitique est lardé de filonnets et de stockwerks de quartz à wolframite et scheelite (avec molybdénite et bismuthinite). Cette roche est affectée d'une altération hydrothermale plus ou moins intense (*cf.* l'indice du Viala).

d) Le massif du Marcolès est recoupé par le filon de Vitrac qui, comme le filon d'Auberoque, est caractérisé par une teneur très forte en Ba. Ils soulignent l'un et l'autre, des couloirs d'accidents NW-SE (accidents de Pons et de la Rance - accident du Langairoux).

2.4. La granodiorite de Soulaque (Y. Chèze 1975). Ce petit massif affleure sur 4 km² environ aux abords du village de Couesques. Il est séparé du massif d'Entraygues par une bande de gréso-pélites cornéifiées de plusieurs centaines de mètres. Il apparaît, au sein d'une virgation de la schistosité, dans un compartiment délimité par des accidents N125° (accidents de Pons). La schistosité de l'encaissant est, en général, redressé à son contact. Sa composition chimique riche en Ca et Al, le rapproche du granite de Glénat situé à l'ouest du sillon houiller. Tous deux sont à grain moyen, non porphyroïdes. Les diagrammes chimiques permettent de visualiser leur ressemblance, ils se placent dans un domaine de granodiorite moyennement quartzique. Mise en place : 275 Ma (H. Bellon et J.P. Gibert 1981), soit contemporaine du granite de Glénat : 272 ± 4 Ma (G. Vivier et M. Lasserre, 1973).

2.5. Le métamorphisme de contact. Les granites de la Châtaigneraie développent une auréole de contact importante, qui prend en écharpe les différents faciès de la série.

Autour du massif d'Entraygues, P. Becarie (1958) définit deux zones dans cette auréole :

- une zone de cornéennes à biotite-cordiérite au contact du granite,
- une zone de schistes tachetés, plus externe.

La zone de cornéennes enveloppe régulièrement le massif d'Entraygues d'une auréole de 200 à 1 000 m de largeur.

La zone des schistes tachetés débute par l'apparition progressive de taches ovoïdes centimétriques, dont la constitution minéralogique est variable : association de cordiérite-séricite, ou d'andalousite-quartz-cordiérite pinitisée, ou encore de chlorite. Cette auréole de schistes tachetés atteint 500 à 1 000 m de large, et sa cartographie par C. Derré (1977) suggérait l'existence d'une voussure du toit du granite selon un axe N-S allant en direction du champ filonien d'Enguialès. Cette cartographie a été nuancée par celle de G. Croisé (1982), cependant il existe bien une remontée du toit des cornéennes. Celles-ci ont été retrouvées au niveau 465 dans les travaux miniers d'Enguialès, accompagnées de filonnets de matériel feldspathique fin (épisyénite ?) associé aux filons de quartz minéralisés (B. Foissy, R. Mignon 1983). C. Derré distingue de plus, à l'extérieur de la zone des schistes tachetés, une zone à biotite et une zone à albite d'extension plurikilométrique.

Indépendamment de cette zonalité, il existe des domaines à tourmaline dont l'un deux se superpose largement au champ filonien d'Enguialès et se prolonge vers le nord en direction de l'indice du Viala (granodiorite de Soulaque).

Autour des granites de Veinazès et de Marcolès, l'auréole de contact est d'extension très variable (Y. Chèze, 1975) ; les véritables cornéennes sont bien développées mais irrégulièrement réparties. Elles affleurent sur une bande de 750 m de large seulement sur la bordure NE du Veinazès (M. Joubert, 1978), alors que la tourmaline est régu-

lièrement présente sur toute la périphérie du massif (J.R. Le Chapelain 1976-1978). Les schistes tachetés affleurent très irrégulièrement (zone à andalousite de Joubert). Au delà se rencontre une zone à cordiérite seule, puis une zone à biotite qui s'étend pratiquement sur l'ensemble du domaine compris entre les massifs de Veinazès et de Marcolès (ce qui corrobore les indications de la gravimétrie plaçant le toit des granites à une profondeur moyenne dans cette zone, sauf sur une césure NS entre Lafeuillade et Lacapelle).

3. Evolution tectonique

3.1. Déformations souples (V. Nicolas, 1982-1985)

L'analyse structurale la plus récente a été réalisée à partir de données obtenues principalement dans le périmètre de Leucamp, ; dans ce domaine, l'évolution tectonique peut être schématisée en trois étapes :

– P1 phase précoce ; la foliation liée à cette phase, plan axial des plis, est plus souvent indistincte de la stratification ; elle n'est bien reconnue que par des lentilles de quartz déformées en plis isoclinaux à charnières bien conservées dont S1 est plan axial.

– P2 phase rarement observable, plis isoclinaux métriques en chevrons sans schistosité décelable, déformés par la phase suivante.

– P3 phase majeure (flexure) à effet prépondérant dans la partie est de la Châtaigneraie, bien caractérisée par son style et ses éléments structuraux, elle engendre des plis dissymétriques, centimétriques à plurimétriques, de vergence sud, à plan axial peu incliné, présentant en dehors des zones de charnières majeures, un flanc long peu penté suivi par une série de petits plis verticalisant localement les couches.

– P4-5 phases tardives, engendrant des plis mous, décamétriques à kilométriques, et des kinks, accompagnés d'une schistosité de fractures, exprimée principalement par des diaclases subverticales.

La phase P1 est sans doute responsable des plis couchés déterminant la répartition régionale des séries (V. Nicolas).

Les effets de la phase majeure P3, prépondérante dans la région de Leucamp comme celle d'Enguialès, est bien caractérisée par son style : dans des domaines où, dans l'ensemble, la schistosité reste peu pentée, il apparaît des couloirs décamétriques à hectométriques ou la série se verticalise et où la schistosité s'exprime vigoureusement (V. Nicolas). L'action des phases tardives sur P3 a pour résultat de mettre en place une structure en dômes et bassins qui se traduit par la dispersion des plans axiaux de P3.

3.2. Fracturation (autour du chantier de Roquefeuil, mine de Leucamp) (Y. Gros, B. Guérangé, P. Martin, 1981)

Après la mise en place du granite d'Entraygues (323 ± 10 Ma), on observe une série de couples compression-distension, responsables de familles d'accidents cassants dont certains sont repris par différentes phases qui sont (des plus anciennes aux plus récentes) :
– Compression NE-SW (plus ou moins contemporaine de P4 selon Nicolas).
– Compression NW-SE.
– Distention NNE-SSW.

Il faut noter que les grandes fractures N50 (cours inférieur de la Rance entre le granite de Marcolès et Maurs, dans le prolongement du cours de la Jordanne ; vallée de la Ressegue et de l'Auze ; vallée de la Truyère en amont de Couesque), se parallélisent avec les axes des granites du Veinazès et d'Entraygues et jalonnent peut-être des directions de faiblesse précoce. (Le cours inférieur de la Rance est le seul linéament aurifère sur la partie ouest de la feuille Maurs - *cf.* stratégique alluvionnaire).

4. Les minéralisations tungstifères de la Châtaigneraie

4.1. Rappel des activités minières régionales.

Le gisement de Leucamp fut le premier découvert en 1910. A la suite de sa très rapide mise en exploitation, la Châtaigneraie fit l'objet de nombreuses recherches minières dont les principales étapes furent les suivantes :

- 1910-1925 : Leucamp : Exploitation à Bancarel et très partiellement à Roquefeuil.
- 1921 : Découverte des indices de Manhaval-Lantuéjouls (Murols) ; mais il faut attendre 1940 pour que soient effectués les premiers travaux de recherche, et 1952 pour que soit déposée une demande de permis d'exploitation par la Compagnie Minière du Massif central.
- 1942 : Découverte des filons de Teissières-les-Bouliès.
- 1942-1943 : Prospection de la partie NE du Veinazès par J. Jung. A la même époque, quelques indices de wolframite sont trouvés et un peu de minerai récupéré dans le ravin de Cancelade.
- 1943 : Reprise de l'exploitation de Leucamp : Roquefeuil fournit l'essentiel de la production. L'exploitation cesse en 1959.
- 1944-1945 : Début de l'exploitation de Teissières.
- 1958 : Découverte des premiers indices d'Enguialès par un prospecteur privé. Le permis d'Enguialès est attribué en 1962 à la Société Minière et Métallurgique du Châtelet (SMMC) et la concession de Mirabel en 1969. L'exploitation fut suspendue en 1979.
- 1971-1972 : Prospection géochimique stream régionale par la SMMC. Découverte des indices de Lafeuillade et du Viala (PER de Lafeuillade 1968-1974).
- A partir de 1973, débute la prospection générale de la Châtaigneraie effectuée par le BRGM (voir 3ème partie de cet article).

4.2. Le gisement de tungstène de Leucamp.

La concession minière de Leucamp est située à une vingtaine de kilomètres au SSE d'Aurillac, sur la rive ouest de la vallée du Goul qui forme une limite départementale entre le Cantal et l'Aveyron ; elle comprenait plusieurs gisements exploités durant la première moitié de ce siècle par des méthodes tout à fait artisanales (forage à sec sans ventilation forcée, scheidage). Il s'agit des anciennes mines des communes de Teissières-les-Bouliès (Falguière et Cauvignat), Murols-Soubeyre (Lantuéjouls), Leucamp (Bancarel et Roquefeuil), et quelques travaux de moindre ampleur comme ceux de Caylus, Gramont, etc.

Le gisement de Leucamp eut sa période d'activité principale entre 1916 et 1959 au cours de laquelle il produisit 2200 t de concentrés à 77,3 M de WO_3 (1700 t métal) pour des teneurs maximales du minerai extrait inférieures à 2,5 % WO_3. L'exploitation a porté d'abord sur la colline de Bancarel (filons de direction N130) puis sur le quartier de Roquefeuil (filons N-S et E-W) à partir des années 1950. La surface intéressée par l'exploitation est de l'ordre de 10 km^2 vers 1951.

Parallèlement, durant la seconde guerre mondiale, les gisements de Teissières-les-Bouliès et Murols produisent 300 à 400 t de WO_3 pour une teneur de tout-venant d'environ 1 %.

L'exploitation portait sur des filons de quartz à wolframite d'orientations diverses, de pendage généralement très fort. Leurs épontes sont caractérisées par la présence d'une tourmalinisation pénétrant la roche encaissante sur plusieurs dizaines de centimètres. Cependant, l'abattage du filon était largement facilité par la présence de ce feutrage de tourmaline qui favorisait le décollement de la caisse.

La paragenèse est la suivante (J.P. Candoret) par ordre de fréquence : mispickel, löllingite, pyrite, wolframite, scheelite, pyrrhotite, chalcopyrite, bornite, bismuth, bismuthinite, wittichenite, tétradymite, casolite, kobellite.

Certains filons contiennent en outre de la sidérite, de l'uranothorianite, de la molybdénite ; et ceux, proches du granite, à défaut de wolframite, contiennent de la blende noire et de la galène.

Du point de vue contrôle structural et orientation des filons, V. Nicolas (1982-1985) distingue quatre types :

Type 1 - filon E-W à pendage sud fort :
Ce sont les plus importants du point de vue minier en raison de leur puissance (20 cm à plus d'un mètre), leur longueur reconnue atteint plus d'une centaine de mètres (traçage 158 W). Ils se localisent dans les zones verticalisées par P3. Les épontes de ces filons sont relativement peu tourmalinisées. Ils pourraient s'être mis en place à l'occasion d'une distension horizontale N-S.

Type 2 - filon E-W à pendage N45° à N65° :
De puissance très régulière (10 à 20 cm), ils présentent une tourmalinisation très développée. Ils occupent des champs de joints de tension indépendants des structures préexistantes.

Type 3 - filon N-S et NW-SE subverticaux :
Ils sont contrôlés par des kinks et diaclases associés à la phase P4 ou P5. Les filons N-S de ce type ont fourni une notable partie de la production du secteur de Bancarel.

Type 4 - Veines à carbonates et sulfures :
Elles se groupent en faisceaux grossièrement méridiens, larges de quelques mètres, qui recoupent l'ensemble des filons précédents, et imprègnent les brèches de faille.

Il est impossible d'établir une chronologie entre les trois premiers types de filons, seules les veines à carbonates leur sont nettement postérieures.

4.3. Le gisement de tungstène d'Enguialès

Le gîte à wolframite d'Enguialès (Aveyron) est situé 3,7 km au NW d'Entraygues-sur-Truyère. Il a fait l'objet de travaux miniers souterrains entre les cotes 460 et 640. Sa production commerciale a été d'environ 1300 t de WO_3 contenu.

Le champ filonien d'Enguialès est situé principalement dans les schistes gris, entre le granite à tendance porphyroïde à biotite de Veinazès au NW, le granite porphyroïde d'Entraygues au SW, et la granodiorite de Soulaque au nord. La gravimétrie n'indique aucune extension possible à faible profondeur du granite d'Entraygues à son aplomb, nonobstant les cornéennes connues au niveau 465 de la mine d'Enguialès.

Le champ est constitué par un ensemble de filons de quartz présentant deux directions moyennes :

– La direction NW-SE, concordante avec la schistosité, à pendage moyen 45° au NE. Ces filons, dits "mâles", ont une puissance maximum de 50 cm.

– La direction NE-SW, recoupant la schistosité, à pendage variant de 35° à 65° vers le NW. Ces filons, dits "femelles", ont une puissance maximum de 80 cm.

Les filons les plus intéressants, particulièrement les "femelles", se groupent en faisceaux plus ou moins continus, reconnus et exploités en travaux miniers sur environ 300 m d'allongement et 200 m d'aval pendage. L'ensemble est affecté par un système de failles normales de direction moyenne N135°, à pendage 45° au NE, qui décale donc les filons femelles vers le SE quand on avance vers le NE (pour une cote donnée).

Les deux groupes de filons se sont mis en place simultanément : on n'observe, en effet, aucun décalage systématique de l'un par rapport à l'autre. Ce système filonien se poursuit au moins jusqu'à 800 m au NE des anciens travaux, où il a été reconnu par sondage, et la fermeture du gisement n'est pas connue dans cette direction. Vers le SW, par contre, la zone exploitée est limitée par un accident méridien très redressé, au-delà duquel les filons s'amenuisent rapidement.

La minéralisation de ces filons est constituée de wolframite, scheelite, pyrite et mispickel comme minéraux principaux. On y rencontre en outre : molybdénite, chalcopyrite, bismuthinite et electrum

comme minéraux accessoires. Les épontes sont très fréquemment tourmalinisées ; de plus, la tourmaline est fréquemment présente dans le remplissage.

La tourmalinisation des épontes provoque la soudure du filon avec son encaissant. En effet, les zones tourmalinisées pénètrent à la fois dans le quartz et dans les schistes encaissants, ce qui, lors de l'abattage du filon, entraine une forte pollution du minerai par des blocs provenant des épontes.

II. ETUDE GEOCHIMIQUE DES SCHISTES DE LA CHÂTAIGNERAIE

(S. Bogdanoff, J.L. Cirodde, A. Ploquin, C. Ramboz).

1. But et méthodes

Le but de cette étude géochimique est de :
- caractériser les formations cartographiées,
- cerner les types d'héritages et de dépôts, donc :
- apporter des éléments de corrélations régionales,
- apporter des éléments à la discussion sur la genèse des gîtes de tungstène de la région en testant les liens possibles avec la série encaissante régionale.

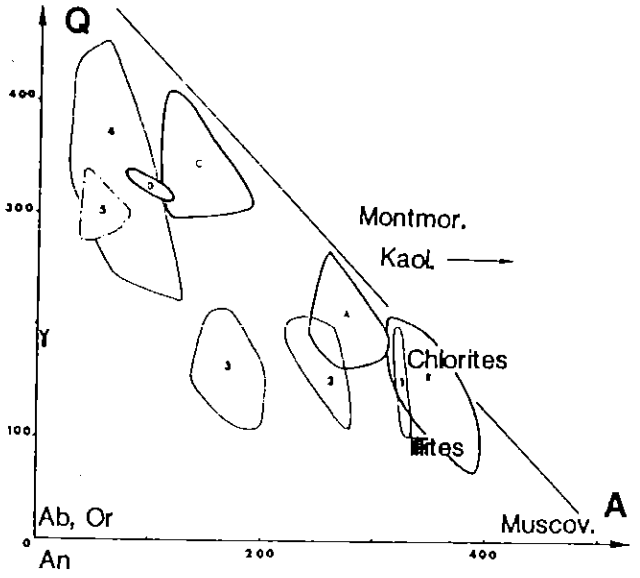

Fig. 2. - Diagramme Q, A.
Le paramètre Q = Si/3 - (Na + K - 2 Ca/3) est comparable à un quartz normatif (quartz Q × 1/5,55).
Le paramètre A = Al - (Na + K + 2Ca) est un indicateur de l'éxcédent d'Al par rapport aux structures de feldspaths, sous réserve de la calcite.
Groupe pélitique : *trait fort*. A et B les 2 sous-ensembles "pélitiques" ; C "quartzites phylliteux" ; D "quartzites sodiques".
Groupe gréso-pélitique : *trait fin* : 1 "Shales" ; 2 "pélites" ; 3 "grès intermédiaires" ; 4 "grès et quartzites".
Trait alterné : 5 leptynites.
Ce diagramme est adapté à la mise en évidence des contrastes entre quartz et phyllites (tri), de la destruction des feldspaths en phyllites. Les alcalins sont confondus.

La zone de prélèvement se situe entre les granites du Veinazès et de la Margeride (fig. 1). Cette zone a été choisie pour la qualité relativement bonne de ses affleurements, cependant l'unité 3 (micaschistes de La Salvetat) n'a pas pu être prise en compte. La plupart des 83 échantillons choisis l'ont été pour leur caractère banal dans la série et ils représentent l'essentiel des faciès observés. Nous nous sommes tenus à l'écart des minéralisations. Cette étude est donc régionale. Son but est de servir de cadre aux études centrées sur un ou plusieurs gîtes (voir les travaux de M. Demange, V. Nicolas *et al.* 1983-1984). Le tableau 1 résume la répartition des échantillons et le tableau 2 donne quelques exemples d'analyses.

Toutes les analyses ont été faites au CRPG par quantométrie (Govindaraju, 1976) après porphyrisation au mortier d'agate afin d'éviter les pollutions en W. Elles seront disponibles avec des renseignements tels que les coordonnées, auprès de la Banque de données Artémise (J. Leterrier *et al.*, 1983) sous les références Ploquin-Bogdanoff - 1982 - WCE, 1 à 97 - Schistes de la Châtaigneraie.

Leur traitement a fait appel à la méthode des diagrammes chimico-minéralogiques développée au CRPG (H. de la Roche, 1978, 1986 ; B. Moine et A. Ploquin, 1972, B. Moine *et al.*, 1974 ; Y. Deschamp, 1980 ; A. Ploquin, 1980, etc.).

Le principe de cette méthode d'interprétation consiste à structurer les analyses à l'aide de paramètres, calculés en milliatomes-grammes pour 100 g de roche, élaborés de manière à disposer les composants selon un réseau adapté au problème posé ; le point représentant l'échantillon sera le barycentre des points représentant ses composants minéraux. Dans le cas d'une roche métamorphique, ces composants sont ceux de la paragenèse néoformée, mais l'on peut considérer également les composants virtuels de la roche antérieure. Dans le cas d'une évolution en système ouvert, le point représentatif se rapproche ou s'éloigne du (de (s) composant (s) néoformé (s) ou détruit (s). De fait, il est indispensable d'utiliser une batterie de diagrammes ; chacun d'entre eux étant une projection particulière de l'espace géochimique, il est nécessaire de varier ces points de vue afin d'éviter des ambiguïtés. Dans cet article, nous n'en présenterons que trois (fig. 2, 3 et 4). Une présentation plus complète sera disponible dans le mémoire de thèse de J.L. Cirodde.

2. Caractères géochimiques de la série

2.1. Caractères globaux

Les diagrammes ont immédiatement montré que les formations des schistes gris et des schistes bleutés d'une part et celles des gréso-pélites et des micaschistes gréseux d'autre part, forment respectivement deux ensembles géochimiques. Il apparaît que les distinctions "sur le terrain" entre formations, au sein de chacun de ces deux ensembles, sont pétrographiques et liées à des textures acquises lors de l'histoire tectono-métamorphique (pour la discussion *cf.* le mémoire de thèse J.L. Cirodde, à paraître).

Nous regroupons donc les quatre formations étudiées en deux groupes :

1. Le groupe pélitique structuralement inférieur : la formation des schistes gris et la formation des schistes bleutés ;

2. Le groupe gréso-pélitique structuralement supérieur : la formation des gréso-pélites et la formation des micaschistes gréseux.

Les leptynites sont limitées au groupe gréso-pélitique.

Globalement (fig. 2), les deux groupes présentent des associations ou tendances différentes, avec une convergence réduite de leurs pôles "shales". Les points représentatifs du *groupe pélitique* sont can-

FORMATION (Nbre d'échant.)	N°	LOCALISATION
Schistes Gris (21)	n° 1 à 12 n° 89 à 97	de Vieillevie à Montsalvy de Montsalvy au Granite de La Margeride
Schistes Bleutés (26)	n° 13 à 17 n° 18 à 24 n° 83 à 85 n° 86 à 88 n° 20, 21 et 25 à 30	à l'W de Montsalvy au SE de Montsalvy à l'W du granite du Veinazès au S de Montsalvy au N de Pons
Gréso-Pélites (25 dont 4 leptynites)	n° 31 à 36 n° 38 à 43 n° 44 à 56	près de Izaguette rive droite Truyère Plainecoste
Micaschis. gréseux (13 dont 3 leptynites)	n° 70 à 72 n° 73 à 82	Caylus-Bancarel La Raygasse-Manhaval

Tabl. 1.- Répartition de l'échantillonnage.

Tabl. 2.- Exemples d'analyses, roches totales.

Groupe pélitique :
- Formation des schistes gris : 2 pélite A, 12 pélite B, 3 grès C,
- Formation des schistes bleutés : 22 pélite A, 18 pélite B, 84 grès sodique.

Groupe gréso-pélitique :
- Formation des gréso-pélites : 34 shale, 31 pélite, 43 grès intermédiaires, 49 grès, 45 leptynite,
- Formation des micaschistes gréseux : 72 shale, 82 schiste noir, 73 grès intermédiaire, 71 quartzite, 78 leptynite gneissique.

M, E : = moyenne, écart type des 83 échantillons.

tonnés au voisinage de la ligne quartz-phyllites avec une nette prédominance des compositions illitiques (A et B) et quelques compositions quartzo-phylliteuses (C), un espace vide séparant ces regroupements de points. Sur le terrain, ces trois types A, B et C sont interstratifiés à l'échelle de l'affleurement. Les points représentatifs du *groupe gréso-pelitique* sont répartis selon une tendance courbe quartz-illite nettement plus déviée vers les feldspaths ; mais là aussi, les coupures établies au long de cette tendance ne correspondent pas à des unités cartographiables. Notons une certaine convergence entre les leptynites et certains des faciès gréseux de la formation les contenant.

Les points communs sont la charge Fe, Mg, Ti semblable pour les faciès argileux (diagramme non présenté ici), l'absence d'arkoses ou de grauwackes vraies, de marnes ou calcaires dans notre échantillonnage. La pauvreté en Ca est un trait dominant de la série. En résumé, il est donc justifié de considérer deux groupes.

La présentation géochimique suivante de chacun des deux groupes fait appel aux figures 2, 3 et 4 simultanément.

2.2. Le groupe pélitique (A à D, fig. 2, 3 et 4)

Sa disposition dans le diagramme Q, A (fig. 2) est la marque d'une formation très mature, pauvre en feldspaths, et fortement triée. Le diagramme Na/Al, K/Al (fig. 3) montre une tendance sodique très limitée (sauf 2 points, les n° 27 et 84, en D, qui représentent des grès albitiques et chloriteux). Les faciès pélitiques de ce groupe se partagent selon deux nuages de points A et B : ces sous-ensembles sont tous les deux essentiellement illitiques avec une légère composante chloriteuse. L'observation en lame mince n'ayant pas révélé de feldspath potassique (détritique ou néoformé), l'examen des divers diagrammes suggère en outre que :

N°	2	12	3	22	18	84	14	31	43	49	45	72	82	73	71	78	M	E
SiO_2	58,13	57,34	72,51	60,26	55,00	75,54	46,79	55,00	62,91	66,10	69,22	56,09	62,10	64,41	42,12	75,46	63,42	(10,3)
Al_2O_3	21,44	23,08	12,12	21,24	23,01	10,95	25,79	21,19	17,13	14,34	11,01	23,70	20,24	17,53	9,32	14,73	18,28	(5,7)
Fe_2O_3t	7,96	6,82	4,60	6,53	8,18	5,42	11,48	9,22	6,43	5,70	2,24	7,92	4,67	5,06	2,64	2,87	6,19	(2,2)
MnO	0,09	0,11	0,10	0,07	0,10	0,08	0,12	0,07	0,06	0,06	0,03	0,12	0,02	0,05	0,04	0,03	0,08	(0,04)
MgO	2,16	1,69	1,20	1,76	2,09	1,33	3,12	2,25	2,35	2,22	0,82	1,73	0,32	2,09	0,51	0,78	1,61	(0,7)
CaO	0,13	tr	0,35	tr	tr	tr	0,36	0,17	0,40	0,29	tr	tr	tr	0,68	0,91	tr	0,18	(0,3)
Na_2O	1,02	1,11	1,32	0,82	0,86	2,51	0,67	1,15	2,07	2,75	3,29	0,78	0,75	2,52	1,63	3,63	1,61	(0,86)
K_2O	4,45	4,13	2,33	4,39	4,26	1,06	5,77	5,43	4,01	3,10	1,36	5,52	5,50	3,95	1,30	1,00	3,72	(1,4)
TiO_2	1,08	0,89	0,64	0,94	0,96	0,73	1,01	0,82	0,78	0,76	0,32	1,16	0,91	0,84	0,52	0,64	0,83	(0,23)
P_2O_5	0,10	0,09	0,13	0,10	0,06	0,02	0,22	0,08	0,13	0,15	0,11	0,09	0,08	0,12	0,09	0,05	0,09	(0,05)
PF	3,61	4,97	3,10	4,24	4,90	2,02	4,98	3,36	2,66	2,33	1,62	4,34	4,54	2,92	1,58	1,39	3,42	(1,4)
Total	100,17	100,23	98,90	100,35	99,42	99,66	99,31	99,31	100,15	99,86	100,29	99,50	99,37	100,07	100,26	99,38	-	-
Ba ppm	773	617	374	663	710	190	1105	873	632	537	322	1008	1031	834	273	306	623	(260)
Cr	126	117	<10	88	126	33	143	116	91	61	<10	123	106	124	12	25	85	(37)
Cu	46	<10	10	<10	<10	15	106	11	17	28	<10	13	21	10	<10	<10	19	(19)
Ni	76	44	44	44	55	44	62	71	50	46	21	42	21	29	27	29	59	(89)
Sr	132	127	96	106	148	63	139	136	127	119	83	122	70	104	88	83	118	(48)
V	162	143	<10	134	157	56	224	121	115	122	29	144	186	131	22	50	120	(51)
Rb	217	207	94	230	210	28	304	261	161	216	66	298	192	191	68	83	176	(80)
W ppm	4,1	2,8	-	3,3	3,7	1,8	-	2,8	2,5	1,9	1,3	-	8,0	5,7	5,4	4,1	3,4	
CO_2 %	0,39	0,09	-	-	-	0,15	-	0,18	0,23	0,10	0,15	0,16	1,99	0,11	0,13	0,16		
FeO%	6,16	4,90	-	-	-	4,31	-	7,35	4,61	4,33	1,54	5,87	0,65	3,37	1,66	1,73		
OR	13,99	20,18	-	-	-	11,63	-	11,40	20,31	15,57	23,62	17,64	84,90	26,01	30,10	32,96		

A. est un peu plus variable sur la chlorite et l'albite, un peu plus riche en quartz, et un peu plus potassique.

B. est un peu plus alumineux, cependant il serait hasardeux de préciser s'il s'agit d'une participation de kaolinite (+/- chlorite) ou de montmorillonite.

Ajoutons que les faciès gréseux (C) possèdent une phase argileuse qui paraît proche de celle des faciès de type A.

2.3. Le groupe gréso-pélitique (1 à 5, fig. 2, 3 et 4)

Le caractère moins mature de ce groupe est révélé par une participation plus nette des feldspaths mais sans aller jusqu'aux arkoses vraies. Une tendance sodique marque les faciès gréseux et quartzitiques, d'où une intersection avec les leptynites.

Les points se répartissent tout au long de la tendance "illites, quartz + albite, quartz", mais l'on peut noter une prédominance dans la zone gréseuse intermédiaire. En comparant les modes de regroupement dans les divers diagrammes, il a été possible d'établir quelques coupures entre des types, mais elles sont quelque peu arbitraires. Ces types n'ont pas de signification cartographique (stratigraphique ou locale) ; c'est pourquoi les sous-tendances internes, obliques sur la tendance principale n'ont pas de signification prouvée : un échantillonnage plus fin et plus abondant aurait été nécessaire pour cela ; retenons simplement des variations de la teneur en quartz et du rapport Na/K non négligeables au sein d'un même type.

Les "shales" et "pélites" sont nettement illitiques avec probablement une légère composante kaolinique dans les "shales" (fig. 4). Le shale n° 34 est particulièrement marqué par des oxydes de fer. Les "pelites" sont plus feldspathiques que les "shales".

Les "grès" et "quartzites" ont une phase phylliteuse illitique avec une composante biotitique assez nette (pétrographiquement confirmée) : la phase feldspathique est albitique, seul l'échantillon n° 33 est déporté vers le feldspath K et se rapproche ainsi des arkoses. La comparaison de l'ordre des points dans les diagrammes Q, A (fig. 2) et Na/Al, K/Al (fig. 3) révèle une corrélation assez nette entre les "teneurs" en quartz paramétrique (*cf.* une "norme") et le rapport Na/K. Ce caractère sodique paraît plutôt inhabituel dans les roches détritiques quartzitiques et peut être la marque d'un héritage volcanique sodique-acide plutôt que d'une authigenèse diagénétique d'albite.

Les leptynites dessinent une tendance "albite-orthose +/- quartz" oblique sur celle des "quartzites" du groupe hôte, tout en étant moins dispersées selon le paramètre Q. Les échantillons dits "oeillés" sont plutôt hyposodiques siliceux. La teneur en Ca reste à un niveau très faible (sauf le n° 79 qui contient des carbonates tardifs, CaO = 1.36 %). Un caractère alumineux non négligeable doit être relevé mais délicat à caractériser, il est probablement dû à la kaolinite. Cette tendance "Na-K", avec Na > K, associée à une relative constance du quartz oblige à proposer une origine ignée ; cependant une altération sédimentaire (ou hydrothermale) doit aussi être envisagée pour expliquer l'excès de silice et d'alumine par rapport aux alcalins.

Nous avons vu que le caractère sodique se retrouve dans les sédiments associés et il est d'autant mieux marqué que le sédiment est siliceux ; c'est pourquoi nous confirmons un apport volcanique silico-sodique synsédimentaire, dû soit à une érosion mécanique avec faible dégradation chimique, soit à un apport de cinérites, une part importante de la silice étant liée à cet apport. Ceci nous semble plus cohérent que de proposer une forte albitisation diagénétique ou métamorphique car les diagrammes tels que Q, A ne montrent pas une tendance vers l'albite seule (fig. 2).

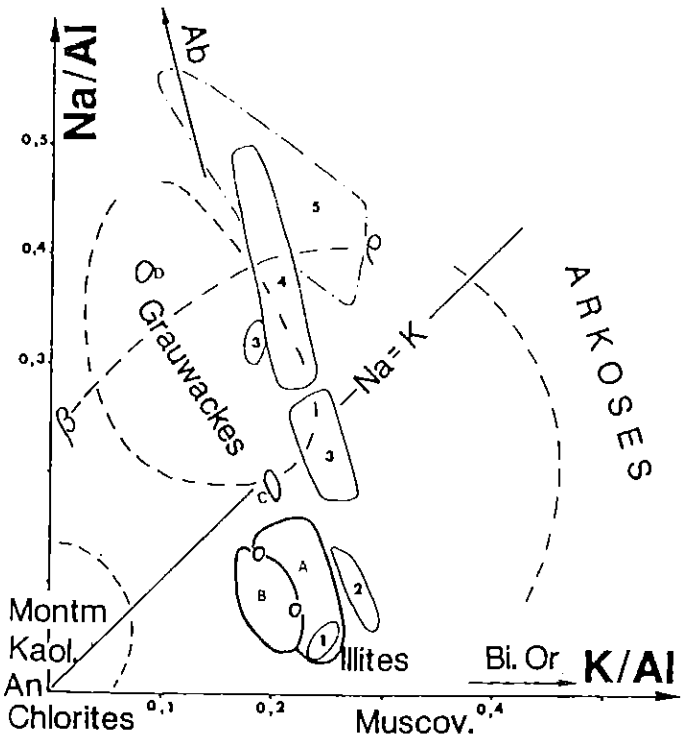

Fig. 3.- Diagramme Na/Al, K/Al.
(légende cf. fig. 2). Ce diagramme est adapté à la mise en évidence du jeu des alcalins et/ou des feldspaths. Les charges siliceuses, carbonatées ou minerais n'ont pas d'influence.

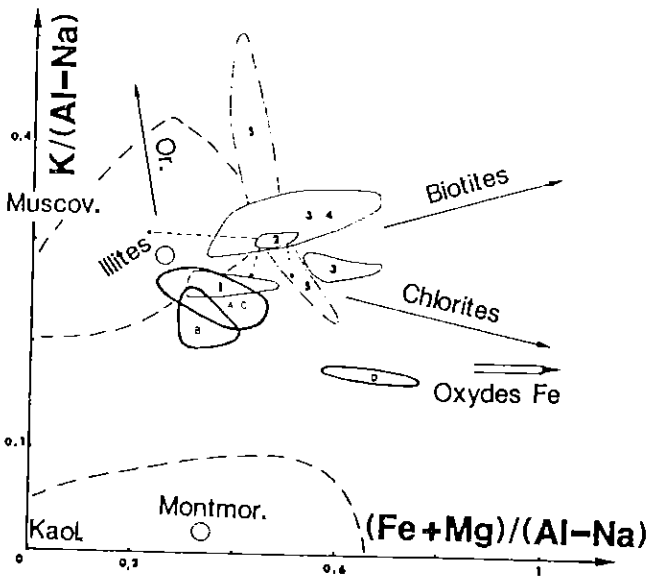

Fig. 4.- Diagramme K (Al-Na), (Fe + Mg) / (Al-Na)
(légende cf. fig. 2). Ce diagramme est adapté à l'analyse du jeu des principaux minéraux phylliteux.

Le groupe pélitique ne présente cette tendance silico-sodique que d'une manière réduite et seuls deux de ses "quartzites" sont franchement sodiques (D, n° 27 et 84), tout en restant plus alumineux que les "quartzites" du groupe gréso-pélitique ; ceci évoquerait une certaine parenté entre les deux groupes.

2.4. Conclusion - prolongements éventuels

Les caractères "sédimentaires" ainsi reconstitués sont de types plate-forme non carbonatée. Le groupe pélitique, structuralement inférieur, paraît plus trié, plus mature et moins contaminé par un volcanisme (cinéritique ?), donc apparemment plus distal que le groupe gréso-pélitique, structuralement supérieur.

Les gréso-pélites de la Châtaigneraie ont été comparées lithologiquement aux grès de Marcory, d'âge cambrien inférieur présumé, affleurant en Montagne Noire (S. Bogdanoff *et al.*, 1984). Une étude géochimique de ces derniers est en cours (bibliographie et données nouvelles, B. Moine *et al.*) ; il est déjà acquis que le style des tendances "Marcory" est assez différent de celui de la Série de la Châtaigneraie prise dans son ensemble. Mais si l'on restreint la comparaison au groupe gréso-pélitique, une similitude apparaît dans la répartition en deux branches dans le diagramme Q, A. Cependant, le "Marcory" est moins phylliteux et la branche quartzitique ne montre pas la grossière corrélation silico-sodique ; le bel alignement dessiné dans le diagramme Na/Al, K/Al (fig. 3) par le groupe gréso-pélitique (*cf.* une corrélation négative) ne s'exprime pas dans le "Marcory" qui montre une dispersion vers les arkoses et les grauwackes ; les leptynites de la Châtaigneraie et les blaviérites (tufs rhyolitiques) qui surmontent parfois les grès de Marcory, sont dissemblables. Certes, ces différences n'excluent pas toute possibilité de "corrélation stratigraphique" mais elle exigera une argumentation.

3. Le tungstène et la série de la Châtaigneraie

La carte des indices W (prospection en "stream sediments") fournie par le BRGM montre une large dispersion sans lien apparent avec la géologie. Par contre, les gisements et indices importants (fig. 1) sont localisés principalement dans la formation des micaschistes gréseux, ou dans les schistes gris, sous un contact anormal, c'est-à-dire dans les formations ou parties de formations a priori les plus déformées.

Nos 20 dosages W en roches totales effectuées sur les deux groupes, indiquent un fond géochimique non anomalique quelle que soit la formation (1 à 6 ppm, mode à 3 ppm, moyenne à 3, 4 ppm ; seul l'échantillon de schiste noir n° 82 atteint 8 ppm).

Nous avons effectué des dosages complémentaires sur 25 échantillons : le carbone et le partage du fer selon son état d'oxydation. En effet, dans les séries à graphite et/ou ilménite, seules les zones ayant subi une forte circulation de fluides sont susceptibles de voir leurs rapports Fe^{2+}/Fe^{3+} modifiés ; (E.A. Chinner, 1960, C. Ramboze *et al.*, 1985). La figure 5 montre qu'il n'y a pas de corrélation entre le caractère oxydé et la teneur en C, sauf peut-être en ce qui concerne des "shales" du groupe pélitique. Les échantillons à net héritage volcanique sont dans la dispersion générale. Les teneurs en C sont faibles à très faibles mais supérieures au seuil de détection (5.10^{-3} % poids). Notons que les zones les moins tectonisées apparaissent d'après notre échantillonnage restreint comme présentant du fer essentiellement réduit ; ce peut être la marque d'une évolution métamorphique en système clos. Par contre, les zones ou formations les plus déformées (micaschistes gréseux, schistes bleutés), présentent un fer plus variablement oxydé. On peut penser qu'il en est de même pour les schistes gris encaissant les filons d'Enguialès et qui sont situés sous les gréso-pélites charriées.

Si l'on prend comme valeur limite du taux molaire d'oxydation, arbitraire, la borne supérieure des points représentant les formations inférieures (soit O.R. = 25, fig. 5), on constate que les teneurs en W de 75 % des échantillons "oxydés" contre 33 % des échantillons "non oxydés" sont supérieures au mode ou à la moyenne des teneurs en W.

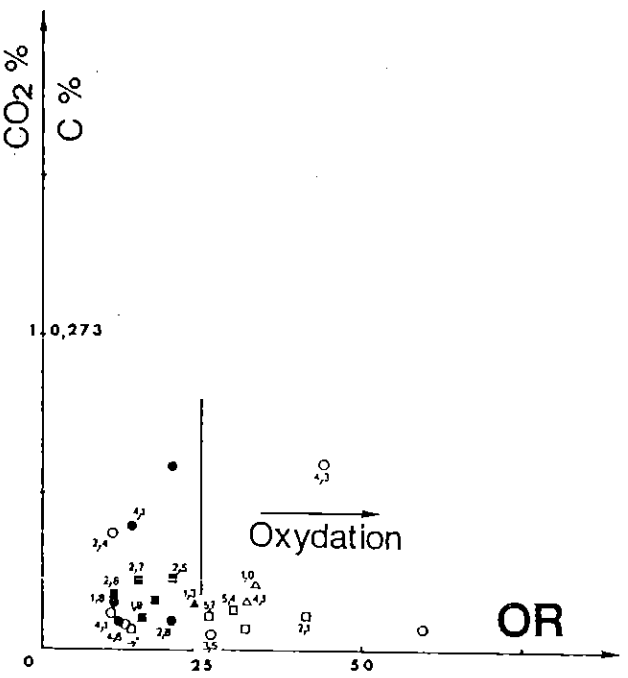

Fig. 5. - Diagramme CO_2, OR, W.
Les carbonates étant pratiquement absents, l'approximation 1 % CO_2 total = 0,273 C est justifiée
Le taux modulaire d'oxydation :

$$OR = \text{mole}\ \frac{Fe_2O_3 \times 2 \times 100}{2 \times Fe_2O_3 + FeO} = \frac{100}{1 + 1{,}1113 \dfrac{FeO}{Fe_2O_3}\ \text{ox\%}}$$

Les nombres adjacents aux points figuratifs expriment les teneurs en W en ppm.

Groupe pélitique :
- ronds pleins : Formation des schistes gris
- ronds vides : Formation des schistes bleutés

Groupe gréso-pélitique :
- carrés pleins : Formation des gréso-pélites
- carrés vides : Formation des micaschistes gréseux
- triangles : Leptynites dans la formation des gréso-pelites
- triangles vides : Leptynites dans la formation des micaschistes gréseux.

Rappelons que le granite du Veinazès est antérieur aux minéralisations mais postérieur au métamorphisme régional et à la tectonique ; de même la distinction entre unités "oxydées et "non oxydées" paraît acquise antérieurement à l'intrusion du granite donc indépendante de lui. Par contre, il semble y avoir coïncidence entre unité "oxydée" et localisation des gisements et indices importants (fig. 1), malgré le diachronisme.

D'après l'état de non-altération des échantillons, d'après l'indépendance du rapport Fe^{2+}/Fe^{3+} vis-à-vis de la position stratigraphique et topographique, il nous paraît exclu qu'il puisse s'agir de l'influence de la paléo-surface tertiaire. La validité de cette répartition de l'état d'oxydation est limitée par la représentativité de l'échantillonnage testé ; remarquons que le domaine de la formation des grésopélites situé entre le gîte d'Enguialès et l'intrusion de Soulaque (fig. 1) n'est pas représenté (*cf.* supra).

En conclusion, ni la composition des sédiments, ni l'apport volcanique silico-sodique ne paraissent être des facteurs déterminants du fond régional en W ou des anomalies. Par contre, le caractère "oxydé" pourrait être un métallotecte intéressant, même si ce caractère, lié aux évènements tectono-métamorphiques régionaux, est antérieur à la minéralisation effective, liée à l'évolution des domaines affectés par le métamorphisme de contact des granites hercyniens *sensu stricto*.

III. UNE DECENNIE DE RECHERCHE MINIERE DANS LA CHÂTAIGNERAIE

(J.R. Le Chapelain, R. Mignon)

Jusqu'en 1975, l'essentiel des études géologiques avait été réalisé par G. Fisher (1943), M. Weppe (1951). A partir de 1973 par le BRGM, notamment J.R. Le Chapelain, et des chercheurs travaillant en coordination avec le BRGM : Y. Chèze (1975), V. Nicolas (1982-1985), S. Bogdanoff *et al.* (1980-1985), M. Demange (1983-1986).

• Durant la période 1973-1977, le BRGM commence par effectuer une large prospection régionale couvrant l'ensemble de la Châtaigneraie. Pour ce faire sont réalisées :
- une cartographie géologique détaillée,
- une prospection marteau,
- une prospection stratégique alluvionnaire et géochimique multiélémentaire couvrant l'ensemble des feuilles 1/50 000 de Maurs, Entraygues et Vic-sur-Cère,
- une prospection gravimétrique,
- des campagnes de tranchées,
- des campagnes de sondages wagon-drill.

Cette vaste exploration régionale a conduit à une meilleure connaissance géochimique de la Châtaigneraie et à la découverte de quelques gîtes nouveaux (voir ci-après). Mais les potentialités en tungstène de ces nouveaux sites s'avèrent assez décevants et, progressivement, l'intérêt des chercheurs se focalise sur les secteurs couverts par les concessions de Leucamp et d'Enguialès.

• C'est alors que commence la deuxième phase de l'exploration avec un programme de travaux qui vise à reconnaître les extensions (latérales et profondes) de ces gisements. Entrepris, dès 1975, sur Leucamp et en 1979 sur Enguialès, ces travaux comportent des sondages wagon-drill, des sondages carottés (du jour et du fond), des travaux miniers souterrains.

1. Première période : la prospection régionale

1.1. Les moyens mis en oeuvre

– **Cartographie géologique** (J.R. Le Chapelain). Elle met l'accent principalement sur les zones de contacts, les zones tourmalinisées, l'étude et l'analyse des éléments de la tectonique cassante, la recherche des leucogranites (synthèse 1976).

Elle oriente la prospection au marteau sur les zones à tourmaline et conduit très vite à la découverte des filons à wolframite de la Granière dans l'exocontact greisénisé et tourmalinisé du Veinazès, et des indices de Jurlhes. Y. Chèze signale, d'autre part, dès 1975 les indices de quartz à wolframite et mispickel de Pons-Couesque, et les niveaux carbonatés à scheelite de la vallée du Goul.

– **Prospection alluvionnaire stratégique** (1973-1975). Elle amène à la découverte d'un certain nombre d'indices à wolframite ou scheelite : Puech de Saint-Mary (scheelite) Gimax (wolframite), Jurlhes-Cancelade (wolframite), Lafeuillade (wolframite, cassitérite).

La cassitérite, quant à elle, se distribue, en dehors des linéaments N135° sur tous les granites à l'Ouest du sillon houiller, et sur l'ensemble des massifs du Veinazès et d'Entraygues. Dans la région de Laguiole, elle atteint des teneurs sub-économiques dans certains flats (Guillemasse) en liaison avec des filonnets de quartz associés à des leucogranites.

Il faut noter que les seuls indices à cassitérite étudiés du Veinazès, ceux de Lafeuillade, sont liés à des greisens et à des zones complexes bréchifiées à épisyénite de direction N130° à N160°.

– **Prospection géochimique** stream sédiment (maille 2,5 éch./km^2), elle donne d'une part des informations à l'échelle régionale grâce à la visualisation des résultats pour un certain nombre d'éléments ou facteurs, et révèle d'autre part des anomalies locales. Dès 1977, J. Barbier et H. Boudet signalent notamment les points suivants :

• *A l'échelle régionale :*

As - Les teneurs en arsenic varient beaucoup (30 ppm à plus de 1 000 ppm). Elles sont très élevées dans toute la partie NE de la feuille de Maurs entre les granites de Veinazès et de Marcolès et culminent dans la zone de Prunet-Cancelade-Lafeuillade. J. Barbier et H. Boudet soulignent l'analogie entre cette auréole "périgranitique" et celle connue à

Echassières, en précisant qu'ici les teneurs en Sn et W ne sont pas vraiment élevées.

C'est toutefois dans cette zone que se trouvent les indices de cassitérite de Lafeuillade, et ceux de tungstène (wolframite de Gimax et de la Granière ; scheelite de Puech de Saint-Mary). Cette zone correspond également à la localisation de l'or alluvionnaire.

B - La carte du Bore montre trois zones à fortes teneurs :

- L'angle SW de la feuille de Maurs correspondant au bassin de sédimentation de Saint-Santin-Maurs.
- La partie SW du granite de Veinazès et son auréole de contact.
- La partie NE du granite de Veinazès et son auréole de contact. Il s'agit là du faciès clair du granite de Veinazès ; la tourmaline y est fréquente dans la roche ou dans les "bouffées" pegmatitiques et les aplites. Dans les micaschistes, l'auréole de contact et la tourmalinisation sont bien développées. C'est dans cette zone que la gravimétrie a mis en évidence l'extension du granite sous une faible épaisseur de micaschiste.

• *A l'échelle des anomalies :*

W - Pour le tungstène, les anomalies (supérieures à 40 ppm) correspondent aux zones déjà connues par la prospection alluvionnaire.

– secteur de Lafeuillade.

– secteur de Puech de Saint-Mary et de Gimax (entre Marcolès et Lafeuillade).

En conclusion, la géochimie "stream-sédiment" confirme les indices minéralisés en tungstène, connus ou trouvés lors de la prospection alluvionnaire.

Une analyse plus complète des informations disponibles en géochimie est donnée en 1982 par J.C. Delille et Y. Peronne, étayée par la confrontation avec les résultats de la prospection alluvionnaire, des tactiques développées sur les anomalies stratégiques et des données des études gravimétriques (B. Madelaine et M. Ogier, 1977 - N. Débéglia, 1981) ou aéromagnétiques (M. Pétrequin, 1979) réalisées entre-temps. Elle comporte notamment une analyse des données géochimiques par traitement mutlivariable de 483 échantillons des feuilles Maurs, Entraygues, Aurillac, Vic-sur-Cère, Espalion et Chaudes-Aigues, sélectionnées pour leur teneur en W supérieure à 10 ppm. Cette analyse fait ressortir le fait que les secteurs d'indices tungstifères sont liés de manière assez précise aux zones béryllifères. Ce lien déjà connu (et évident sur la superficie considérée) n'a pas de réciproque ; aucun indice n'est connu dans la zone très béryllifère (à titre d'exemple : granite de Boisset, ou partie centrale du granite de Marcolès).

En conséquence, il devient assez clair que les indices occupent une position intermédiaire entre certaines zones fortement béryllifères et les zones non béryllifères des micaschistes encaissant les granites.

A partir de 1976, les résultats des prospections stratégiques sont exploités à l'échelle tactique, tandis que sont mises en oeuvre des méthodes géophysiques (principalement gravimétrie et magnétisme) destinées à préciser les caractéristiques des extensions des massifs granitiques en profondeur, afin de trouver des guides de sélection et de recherche pour les indices de minéralisations de départ acide. Le modèle des gîtes recherchés est fourni par les gisements voisins de Leucamp et Enguialès : faisceaux filoniens extragranitiques, se développant entre 200 et 1 000 m au toit d'un granite porphyrique, sans liaison apparente avec des leucogranites. Mais il ne peut être exclu a priori la possibilité d'existence de gîtes filoniens péri ou intragranitiques associés à des zones greisenisées ou à des leucogranites, du type de certains gîtes portugais ou chinois. C'est ainsi que sur le massif d'Entraygues voisin sont testées des anomalies géochimiques ou des indices de surface intragranitiques : Benaven, le Laussier, le Bousquet, les Bessades.

– **Gravimétrie**. En 1976-77 est réalisée une étude gravimétrique sur le périmètre du permis de la Châtaigneraie, afin de fournir de nouveaux éléments prévisionnels (B. Madelaine, M. Ogier 1977). Les résultats mettent en évidence :

- Une extension possible du granite de Marcolès en direction du granite de Veinazès, avec toutefois une importante discontinuité entre les deux.

- Une structure complexe du Veinazès correspond à des différences lithologiques notées sur le terrain.

- Un réseau important de discontinuités gravimétriques, avec prédominance des directions N-S et NW-SE, confirme les données de la photo-fracturation (J.Y. Scanvic, 1976). Les discontinuités gravimétriques principales n'apparaissent pas sur la carte des linéaments, ce qui amène à supposer qu'elles ont une origine profonde.

- L'existence de structures circulaires (à Jurlhes en particulier).

Ces données sont réinterprétées en 1981 par N. Débéglia à la lumière de nouvelles informations : aéromagnétisme et magnétisme au sol (M. Pétrequin). Cette étude fait apparaître les points suivants :

- Bonne corrélation générale entre les indices minéralisés et les structures légères périgranitiques.

- Il existe une structure légère superficielle à l'aplomb de Murols, sur la bordure nord de laquelle se situent les gîtes de Manhaval et Lantuéjouls.

- Les éléments structuraux de direction N-S apparaissent moins importants que dans l'interprétation précédente. Les indices de la Granière, Gimax et Puech de Saint-Mary se trouvent bien localisés sur la bordure de structures légères alignées N-S. Mais l'alignement N-S des gîtes de Teissières-Leucamp-Le Viala-Enguialès ne correspond à aucune donnée gravimétrique.

En 1984, des mesures gravimétriques complémentaires sont effectuées avec l'objectif de couvrir particulièrement la zone située entre les massifs du Veinazès et d'Entraygues, et entre ceux de Veinazès

et de Marcolès, ainsi qu'une zone périphérique d'environ 105 km² pour déterminer le gradient régional. L'interprétation de l'ensemble des données disponibles aboutit à préciser la forme de la jonction probable en profondeur entre ces massifs (N. Débéglia, Nov. 1984).

1.2. Les indices découverts lors de la prospection régionale (fig. 6)

– **La Granière.** (Indices : la Granière, Chaubert, Puy Majou, Combe del Bos, Prentegarde), (communes de Sénezergues et Calvinet, Cantal).

Le filon de la Granière a été trouvé en 1976 par prospection au marteau dans la zone de contact greisenifiée et tourmalinisée de la bordure nord du massif de Veinazès, à environ 400 m de celui-ci. De 40 à 60 cm de puissance, orienté N50 à 70, et reconnu sur une cinquantaine de mètres d'allongement, il est sécant sur la foliation des micaschistes à biotite, andalousite et cordiérite à bouffées métriques greisenisées. Ces greisens renferment : tourmaline, pyrite et mispickel. Les épontes sont elles-mêmes greisenisées, la tourmaline y est abondante et pénètre dans les parties marginales de la caisse filonienne constituée de quartz blanc laiteux à wolframite (5 cm max.), scheelite, pyrite et mispickel. On note comme minéraux accessoires le bismuth natif et la bismuthinite en alignements de goutelettes arrondies dans le quartz. Un deuxième filon identique en puissance et direction a été mis à jour par tranchée ultérieurement, sans wolframite ni scheelite, mais avec la kobellite Pb_2 (Bi-Sb) 2 S5. Il fut trouvé un autre affleurement filonien et des volantes à wolframite-scheelite sur une zone de 3 km d'allongement de direction N70° : Puy Majou, Combe del Bos, Prentegarde la Granière, Chaubert. Une prospection géochimique tactique en couvrit par la suite certains secteurs, l'anomalie obtenue, de faible niveau (contour à 32 ppm W) mais bien directionnelle (70°), est testée par tranchées, qui révèlent d'autres filons à pyrite, mispickel et trace de wolframite (teneur moyenne 7 g/t). Le prospect est abandonné.

– **Gimax et Puech de Saint-Mary** (commune de Marcolès - Cantal).

Ces indices, situés entre le granite de Veinazès et celui de Marcolès, sont alignés sur un axe N-S passant aussi par la Granière. Ils sont localisés sur une zone d'extension à moyenne profondeur du granite de Marcolès, en bordure d'une structure légère (leucogranite ?).

Ils ont été découverts par la prospection stratégique alluvionnaire, et confirmés par la géochimie stratégique (6 valeurs supérieures à 30 ppm à Gimax) et la présence de volantes à mispickel wolframite (Gimax) et à scheelite (Puech). Par la suite, ils sont quadrillés par une maille géochimique tactique en sol accompagnée de batées alluvionnaires, qui donnent des anomalies directionnelles de plusieurs centaines de mètres, bien cernées par les contours à 40 ppm au Puech ou à 100 ppm à Gimax Nord. Ces axes respectivement N70° et N170°, sont reconnus par tranchées. Ils révèlent des réseaux filoniens peu denses, de 5 cm de puissance maximale, à wolframite dominante, à Gimax, et de 30 cm avec scheelite au Puech. Ils sont explorés par la suite en sondages percutants. La meilleure teneur obtenue est de 1 % WO_3 sur 2,40 m au Puech.

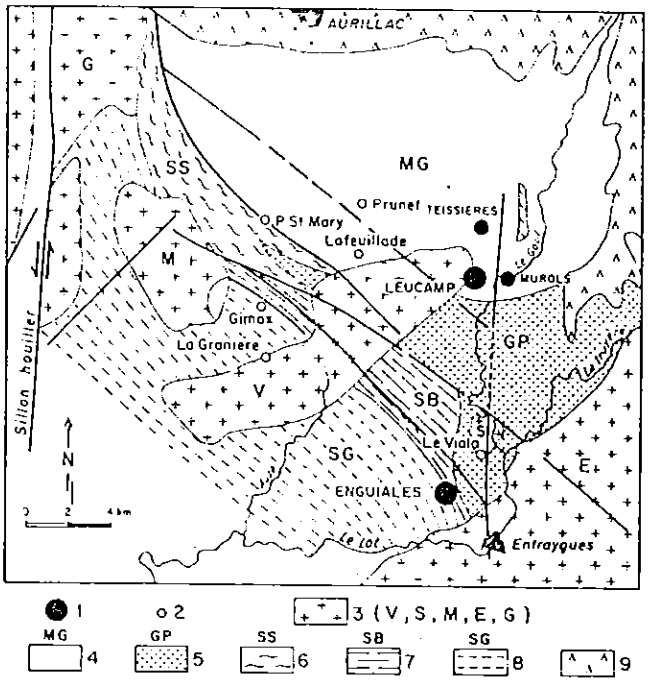

Fig. 6.- Localisation des gisements et prospects de tungstène dans leur cadre géologique

1 : gisement de W ; 2 : prospects de W ; 3 : granite (V : de Veinazès ; S : de Soulaque, M : de Marcolès, E : d'Entraigues, G : de Glénat) ; 4 : micaschistes gréseux ; 5 : gréso-pélites ; 6 : schistes de La Salvetat ; 7 : schistes bleutés ; 8 : schistes gris ; 9 : volcanites.

Au total, la présentation de ces indices est peu encourageante, mais les prospects se trouvent dans une zone prévisionnelle favorable : bonne distance du toit du granite, possibilité d'un leucogranite à l'aplomb. Ils pourraient constituer le chevelu sommital d'un réseau filonien avec des possibiiités de développement de plusieurs centaines de mètres en aval pendage.

– **Prunet, Jurlhes, Cancelade** (commune de Prunet - Cantal)

Ce groupe de prospects voisins est issu de l'exploitation d'occurences alluvionnaires à wolframite, scheelite, cassitérite et or découvertes par la prospection stratégique en 1975. Ils correspondent en outre à une plage fortement anomale en As, Cu, Sb, Bi de la stratégique géochimique. Ils se situent à l'aplomb d'une extension à "faible profondeur" du granite du Veinazès, sur sa périphérie nord. Ils jalonnent, du NW vers le SE, un couloir d'accident N135° souligné par des brèches tourmalinisées à mispickel. Les trois prospects ont été découverts en géochimie à maille tactique qui confirme les anomalies en tungstène (maximum 200 ppm) sans que les supports de la minéralisation aient pu être reconnus. Les brèches tourmalinisées sont responsables des occurences en cassitérite, et pour partie des occurences en or. Ces prospects, abandonnés pour la wolframite, sont en cours d'examen pour l'or.

– **Lafeuillade** (commune de Lafeuillade en Vézie - Cantal)

Cet indice a été trouvé en 1971 à partir de la prospection géochimique stream réalisée par la SMMC de 1968 à 1971. Il se situe sur la bordure nord du granite de Veinazès, au contact de ce dernier avec des lambeaux de schistes cornéifiés flottant au toit du granite. Après réalisation d'une géochimie tactique, il a été étudié en tranchées et sondages percutants et carottés. Il a fait l'objet d'un rapport de A. Bernard et de C. Mérignac (1972) ; la géochimie a mis en évidence :

- Des anomalies stannifères en auréole autour et partiellement sur des anomalies tungstifères.

- Des structures orientées N355 à N365 dans le granite, N335 à N345 dans les schistes.

Les tranchées et les sondages démontrent l'existence d'un champ filonien comprenant :

- Dans les schistes : des filons et brèches quartzeuses où la concentration de la cassitérite s'effectue dans des zones de coupoles greisenifiées, et dans des fractures à quartz, tourmaline, mispickel, les teneurs maximales étant dans les brèches.

- Dans les schistes épisyénitisés, ou dans le granite (avec ou sans épisyénite) : des fractures à quartz, fluorine, adulaire, scheelite. Les zones de broyage épisyénitisées ayant seules une importance significative, les teneurs moyennes sont de 0,1 à 0,4 % Sn et 0,3 à 0,85 % W, sur des structures de plusieurs dizaines de mètres de long, et de 1 à 8 m de puissance.

Le potentiel économique reste à démontrer.

– **Le Viala** (commune d'Enguialès - Aveyron)

Cet indice se situe à environ 3 km au nord du gisement d'Enguialès, sur l'exocontact SW de la granodiorite de Soulaques. Il a été découvert lors d'une prospection marteau de la SMMC, qui y effectua de petits travaux de décapage sur des affleurements de quartz à wolframite. Il donne un groupement de points anomaux sur la stratégique géochimique (1976) et sur la tactique sol (1980) prolongeant au Nord la zone d'Enguialès (anomalie à contour 70 ppm). En 1980-1981, l'indice est exploré par le BRGM par trois sondages carottés totalisant 726 m. Ces sondages traversent principalement des leucogranites et des granodiorites. Les filonnets de quartz, minéralisés en wolframite et (ou) scheelite, se localisent de façon presque exclusive dans le leucogranite, avec mispickel et pyrite fréquente, blende, molybdénite et chalcopyrite accessoire. La tourmaline est rare. Les teneurs les plus élevées atteignent 12,50 % WO_3 sur 45 cm de traversée de quartz. Mais on ne connaît pas la géométrie des filons de quartz.

Ces résultats justifient néanmoins un programme de reconnaissance en travaux miniers souterrains, qui pourrait être réalisé ultérieurement.

2. Deuxième période : la recherche d'extensions aux gisements connus

2.1. Sur le gisement d'Enguialès

Rappel des travaux antérieurs à 1981

Les premiers indices de wolframite sont découverts en 1958 par un prospecteur privé, M. Lenormand, qui cède ses droits à la Société Minière et Métallurgique du Châtelet (SMMC). Celle-ci obtient un PER de 1576 ha le 5 mai 1962, et après avoir reconnu en surface et en travaux souterrains un certain nombre de faisceaux mâles, met en évidence des réserves de 3 200 tonnes à 70 % WO_3.

Une concession est octroyée en 1969 et la production se situe dans une fourchette de 170 à 210 t/an de concentrés à 70 % WO_3, à partir de tout-venant à 0,6 % WO_3, jusqu'en 1973. Mais le rendement de la laverie est déplorable, et l'effondrement des cours à partir de 1971 provoque la mise en règlement judiciaire. La poursuite de l'exploitation est assurée grâce à un prêt du FDES jusqu'en 1979, après l'adoption en 1977 d'un programme de redressement inspiré par une expertise du BRGM. Le tonnage de tout-venant traité passe de 3 500 t/mois en 1976 à 7 300 t/mois en 1978, mais s'accompagne d'une baisse des teneurs provoquée par le salissage du minerai. Pour la meilleure période, la teneur récupérée est montée à 7,3 kg à 70 % par tonne de TV (23 kg/m^2). La mine est fermée en avril 1979. La production commerciale a été, pour toute la durée de l'exploitation, d'environ 1 300 tonnes de WO_3 contenu. (Bedouret-Prouhet, 1976).

En dépouillant les documents d'exploitation de la SMMC, on constate :
– Les puissances et surtout les teneurs exploitées (ou ayant donné lieu à des essais d'exploitation) varient dans les fourchettes très larges si l'on considère le contenu métal par m^2 de panneau. Le panneau le plus riche (Béatrice entre 527 et 588 sur 144 m d'allongement) présente une valeur moyenne de 31,4 kg/m^2 de WO_3 (puissance moyenne : 71 cm ; teneur moyenne du quartz : 1,14 % WO_3) et renferme des zones à très forte teneur (plus de 110 kg/m^2 sur 60 m^2). Les panneaux les plus pauvres (Berthe 623/637 et Jules 558/surface) ont seulement fourni 1 kg/m^2. La distribution des zones riches est donc parfaitement aléatoire, il n'y a pas de variation systématique en fonction d'un axe quelconque ou une corrélation avec la puissance des filons (fig. 7).
– Les filons femelles ont constitué la source presque exclusive de minerai exploitable, seuls, quelques panneaux de surface très modestes de filons mâles ont été estimés exploitables (et souvent s'agissait-il de tentatives très vite abandonnées) ; certaines zones très limitées de ces panneaux ont cependant présenté des contenus métal relativement élevés : Jacques 470/476 sur 20 m autour de l'intersection avec Barbara (17 kg/m2). Les filons femelles représentent donc un objectif de recherche prioritaire.
– Les teneurs moyennes réelles d'entrée en laverie du tout-venant baissent constamment avec l'approfondissement de la mine, mais cet appauvris-

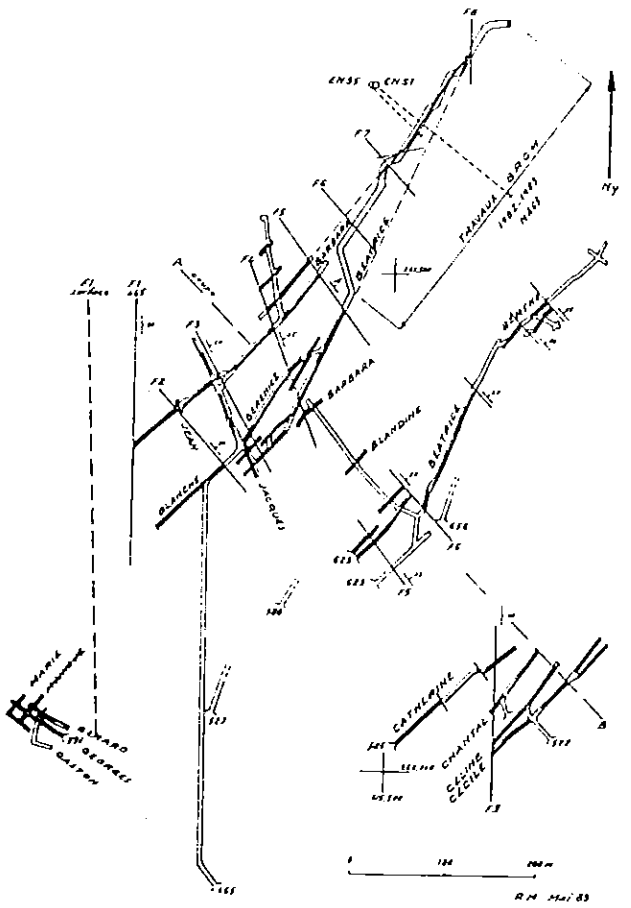

Fig. 7. - Mine d'Enguialès, schéma des travaux miniers (niveau : 465, 577, 585, 591, 623) montrant les deux familles de filons minéralisés en W (femelles : NE-SW, mâles : NW-SE).

sement est lié uniquement à la mécanisation du chantier et à la dilution du quartz par le stérile des épontes. Les teneurs moyennes du quartz s'établissent entre 1,00 et 1,10 % sur l'ensemble de l'exploitation.

En octobre 1979, un groupement est formé pour la prospection de la concession, il comprend : Charter France Service, BRGM, SM Anglade et Pétrofina, avec une option de 24 mois. L'objectif était de trouver, près de la surface, des réserves suffisantes pour justifier une exploitation à ciel ouvert (de l'ordre de 2 000 t/jour à une teneur récupérée de 0,15 % WO3, pendant 10 ans). Une campagne de 4 000 m de sondages percutants verticaux de 80 m est effectuée à la maille 40 x 40 m sur deux blocs, à l'est et à l'ouest du gisement. Les résultats sont décevants et aboutissent à l'abandon du projet.

Les travaux BRGM à partir de 1981

Début 1981, une option de 2 ans est formulée par le BRGM ; un programme de recherche est établi, avec, comme objectif, la recherche des extensions NE et SW du gisement, et la reconnaissance plus détaillée des faisceaux minéralisés. Ce programme comportait les opérations suivantes :

- reconnaissance par sondages carottés courts des faisceaux Barbara et Blanche-Bérénice au niveau 465, le plus profond ;
- étude géologique destinée à préciser le comportement de la faille NS sur laquelle butent, à l'ouest, les faisceaux minéralisés, l'objectif étant de retrouver ces faisceaux à l'ouest de cette faille ;
- recherche des extensions vers le NE des faisceaux minéralisés par prospection géochimique et alluvionnaire ;
- sondages jour d'environ 300 m destinés à vérifier les extensions NE et SW des faisceaux minéralisés et préciser leurs caractéristiques.

Première phase - *recherche des extensions du système filonien.*

a - Les sondages fond au niveau 465 - 21 sondages horizontaux courts ont été réalisés (métrage total = 480,50 m).

Les résultats d'ensemble sont décevants en ce qui concerne la possibilité de trouver un appoint au potentiel des filons principaux dans l'existence de filonnets situés à proximité immédiate et fournissant une puissance cumulée insuffisante pour justifier une exploitation sur un front de taille élargi.

Le programme de sondages fond a cependant permis de vérifier les caractéristiques des filons vers l'aval pendage et de les retrouver dans leur extension NE.

b - Les sondages jour - 6 sondages longs carottés ont été réalisés (métrage total = 2262,45 m) - 5 sondages ont exploré l'extension NE, le sixième a été placé sur l'extension SW.

Le sondage S5, de 483,30 m de longueur (fig. 8), a atteint la cote 250 m sans rencontrer ni granite ni cornéennes. En raison de la bonne tenue des terrains, le carottage a été excellent. Ce programme de

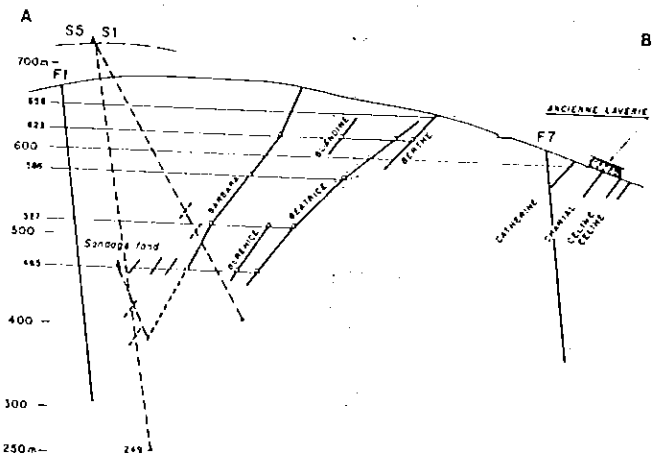

Fig. 8.- Coupe schématique AB de la mine d'Enguialès.

sondages a démontré l'extension NE des filons minéralisés sur environ 800 m, avec des caractéristiques comparables à celles des filons exploités. L'aval pendage de la zone minéralisée a été reconnu jusqu'à la cote 350, soit une dénivelée de près de 300 mètres (le sondage S5 a atteint la cote 250).

On dispose alors théoriquement d'un potentiel métal de l'ordre de 5 000 à 10 000 t de WO_3 contenu justifiant la poursuite des recherches au stade de l'évaluation des réserves exploitables. Cet enjeu est conditionné par la possibilité économique d'exploitation des filons minces.

Il était donc logique de se fixer comme objectif de la nouvelle étape de recherche de reconnaître en détail les caractéristiques (géométrie et contenu métal) d'au moins l'un des faisceaux femelles majeurs (Barbara) sur une distance suffisante pour être représentative. Compte tenu de la nécessité d'effectuer pour cela un échantillonnage massif, cette reconnaissance ne pouvait être réalisée qu'en travaux miniers souterrains. Le second faisceau majeur devait être exploré par sondages fond carottés à partir du traçage du premier.

Deuxième phase - *travaux miniers et sondages souterrains (1982-1983).*

- Recarrage des galeries anciennes = 692,5 m + 9 m de recoupe.
- Travers-bancs Béatrice-Barbara = 42 m.
- Traçage de la galerie de recherche Barbara 326 m + 11 m de recoupe.
- Sondages carottés = 631,23 m en 22 sondages.

Au cours de l'avancement, 61 échantillons miniers ont été réalisés, ils représentent une longueur échantillonnée de 105,95 m et un tonnage total d'échantillons de 432,690 t. En outre, 71 échantillons par rainurage, représentant 136 m de longueur, ont été collectés, ils représentent un tonnage de quartz pur de 6 854 kg.

Ces travaux ont permis de compléter la connaissance d'un panneau déjà testé par des sondages jour.

– Les informations acquises concernant la géométrie et le contenu métal des filons : ceux-ci se subdivisent fréquemment, se relaient latéralement et sont de plus affectés de nombreuses failles normales donnant un rejet apparent dextre pouvant atteindre 5 m.

– Le faisceau Barbara présente un groupe de filons, reconnus par sondages et galeries, d'environ 234 m de longueur avec une puissance moyenne d'environ 24 cm, pour un contenu de 6,46 kg WO_3/m^2. Cette valeur paraît trop faible pour pouvoir garantir actuellement une exploitation bénéficiaire. La fraction la meilleure de ce faisceau est de 50 m à 9,13 kg/m² (de 150 à 200 m).

– Le faisceau Béatrice présente un segment de 200 m de long reconnu par sondage, avec une puissance de 58,8 cm et un contenu de près de 10 kg WO_3/m^2. Il correspond, en outre, probablement à un segment de 15 m reconnu en galerie, avec une puissance voisine de 23,17 cm et un contenu de 15,74 kg WO_3/m^2.

Résultats de ces investigations

Les filons reconnus paraissent, dans l'ensemble, de caractéristiques moins bonnes que la moyenne des filons exploités.

Pour fixer les idées en faisant l'hypothèse très optimiste que le contenu métal au m² reconnu en galerie sur les 15 m correspondant à Béatrice représente la moyenne du panneau de 300 m d'allongement (et sur 300 m d'aval pendage), on aurait un stock WO_3 contenu de 1 420 t. Si l'on veut franchir la barre des 5 000 t de WO_3, on voit que pour un même aval pendage, il faudrait encore reconnaître trois fois l'allongement ci-dessus.

On a reconnu, d'autre part, que des faisceaux majeurs comme Barbara peuvent pratiquement disparaître. Peut-on s'attendre à les voir relayés, et à quelle distance latérale ou longitudinale, par d'autres faisceaux économiques ? La présence dans le S6 de 70 cm de quartz cumulé sur 3 m de tranche horizontale, avec wolfram et scheelite bien exprimés (5 intersections entre 340 et 346 m de profondeur) est cependant un élément positif. Mais les sondages S3 et S6 sont-ils bien placés pour recouper les faisceaux existant à cet endroit là à une cote convenable ?

– De toute façon, le gîte d'Enguialès ne semble pas pouvoir atteindre la dimension économique avec les caractéristiques fournies par les travaux de recherches réalisées en 1982-1983, tant sur le plan tonnage que sur celui des teneurs.

– Si l'on veut s'en tenir aux objectifs définis initialement, il faut donc élargir le champ d'investigation et éventuellement le déplacer pour atteindre une dimension économique.

2.2. Sur le gisement de Leucamp

Première phase - Recherche des extensions au jour - Géochimie - Tranchées - Sondages jour (1975-1980).

Dès 1975, une campagne de prospection : marteau, géochimie, sondages wagon-drill est entreprise sur la zone de Bancarel et son prolongement au sud-ouest. Elle démontre une possibilité d'extension des zones minéralisées dans deux secteurs : au nord du village de Bancarel, à l'ouest : dans le ravin de la Souque. Hors de la concession de Leucamp, une prospection stratégique dans la commune de Murols focalise l'intérêt sur l'alignement Teissières, Gramont, Caylus.

Les travaux suivants (1977-1978) comportent :

– Une recherche des filons non affleurants dans les zones riches en volantes minéralisées. Les tranchées réalisées montrent que le gisement n'est pas limité à l'éperon de Bancarel ; cependant l'importance du recouvrement rend illusoire l'investigation de surface.
– Un test sur la possibilité d'existence d'un stockwerk et la recherche des extensions vers l'ouest des filons exploités. Sur la crête de Trapouet, 44 sondages percutants sur 3 profils recoupent le prolongement du faisceau de Roquefeuil et du faisceau de Bancarel. Résultat : le repérage des filons est aisé mais les corrélations sont difficiles.

Une prospection sur Teissières, Caylus et Cabrespine donne des anomalies alluvionnaires et géochimiques qui confirment l'intérêt de Caylus mais les filons minéralisés ne franchissent pas le ruisseau principal.

Les résultats apportés par les géochimies sol et les sondages destructifs apparaissent peu précis et peu fiables ; mais dans le même temps (1979) des travaux d'élargissement de chemins ruraux amènent la découverte fortuite d'un certain nombre de filons bien minéralisés. Une campagne extensive de décapage au bull est donc réalisée par le BRGM. Elle aboutit à la découverte de plus de 100 affleurements de filons minéralisés se répartissant en quatre faisceaux :

- faisceau de la Caze, prolongement occidental des faisceaux exploités de Roquefeuil et du Ravin de la Mine ;
- faisceau du Ravin de la Mine, prolongement oriental ;
- faisceau du Moulin, en aval du hameau de Bancarel ;
- faisceau du Bos, prolongement du faisceau de Teissières, se raccordant peut-être aux anciennes exploitations de Gramont et de Caylus.

Un échantillonage sur coupes donne en moyenne 1,31 % W (soit 1,65 % WO_3) et montre que, comme dans les anciennes exploitations, les filons les plus riches sont NW-SE.

A la suite des résultats, 7 sondages carottés (1 357,55 m) sont réalisés pour explorer les extensions ainsi pressenties et l'aval pendage du gisement connu. Les résultats sont très décevants, pratiquement aucun filon connu en surface n'est retrouvé.

En novembre 1980, J-R. Le Chapelain (DL Clermont 324, 1981) fait le bilan suivant : l'ancienne exploitation n'intéressait qu'une tranche de 150 m d'épaisseur entre la crête de Trapouet et les niveaux inférieurs. Au dessous, le gisement était réputé inexistant ou inexploitable. On admettait qu'il s'arrêtait sur une sorte de plancher passant, dans le Ravin de la Mine, vers l'altitude de 500 m. Les théories divergeaient quant à sa nature et sa géométrie : grande faille plus ou moins plate (glissement concordant avec la schistosité ou même rejeu d'une ancienne surface de charriage ?) ; fond de calotte érodée, simple diminution progressive de la minéralisation devenant difficilement récupérable en laverie, etc... Aucune preuve irréfutable n'était avancée, l'idée n'étant basée que sur l'absence d'affleurements filoniens au dessous de cette altitude. Les résultats carottés tendaient à confirmer, sans toutefois la prouver l'existence de ce plancher. Or les prospections BRGM au bulldozer avaient mis à jour des filons bien minéralisés, jusqu'alors inconnus, en dehors de la zone exploitée, et au dessous même de l'altitude 400 m. L'existence aval des filons exploités et les extensions latérales retenues (faisceau de la Caze, du Moulin, zone méridionale du Ravin de la Mine) représentent alors un potentiel théorique de 7 300 tonnes de WO_3 contenu.

Ce potentiel restait à démontrer par la confirmation des extensions minéralisées dans une présentation et avec une fréquence analogue à celles observées dans la tranche exploitée, et cette démonstration ne pouvait être faite qu'en travaux miniers souterrains. Ces travaux miniers permettraient, en outre, de procéder à un test minier sur un ou plusieurs filons choisis pour connaître : la tenue des terrains et des épontes, les conditions d'abattage sélectif, la continuité des filons, les effets de la tectonique tardive, et effectuer une première étude de faisabilité. Ces sondages quant à eux, devaient grossièrement définir les limites du gisement en extension et en profondeur.

Deuxième phase - *Travaux miniers souterrains* (1980-1983) : confirmation des extensions et continuité des filons vers l'aval pendage.

Ces travaux miniers (fig. 9) ont comporté :

– Un travers-bancs à plat (environ 25 mètres sous le niveau inférieur de l'ancienne exploitation). Ce travers-banc de direction N230° puis N260°, de 290 m de long, permet l'échantillonnage de 5 tronçons filoniens de quartz traversés, teneur moyenne pondérée : 1,62 % WO_3.

– Une descenderie de direction N210°, de 360 m de long, pente moyenne 18 %, qui recoupe 4 filons principaux (à 23 m, 158 m, 200 m et 286 m de la tête de la descenderie).

– Des traçages dans les filons recoupés (478 m au total), complétés par des sondages fond d'exploration (964 m de sondages percutants, 1 162 m de sondages carottés). L'échantillonnage minier (445 tonnes au total) est réalisé par tranches de 1 m à 1,50 m sur certains secteurs seulement pour des raisons techniques. Les teneurs s'établissent entre 0,18 et 2,65 % WO_3 et représentent un contenu métal variant de 5,4 à 41,0 kg/m^2.

– Un test d'abattage sur le filon 23 m entre les cotes 500 et 515 :

- abattage sélectif (500-508), réalisé avec un matériel expérimental (brise roche hydraulique monté sur chassis Montabert) se révèle satisfaisant,
- essai par chambres vides entre les cotes 508 et 515. Le contenu métal s'établit sur ce chantier à 38,3 kg/m^2.

La seconde phase des travaux BRGM s'achève donc sur des observations favorables :

– Extension des filons en aval pendage et découverte de nouveaux filons dans l'extension ouest (un filon inconnu a été découvert à 50 m à l'extrémité Sud de la descenderie. Sondage F1).

– Teneurs pondérées satisfaisantes : la moyenne générale s'établit à 14,4 kg/m^2.

– Test d'abattage positif.

3. Bilan et perspectives

Dans ce district ayant produit de 1910 à 1979 environ 3 600 t de WO_3 contenu, le BRGM a réalisé, à partir de 1973, une exploration régionale qui a progressivement recentré ses recherches sur la zone des gisements extragranitiques de Leucamp et d'Enguialès-le Viala. Les opérations menées à

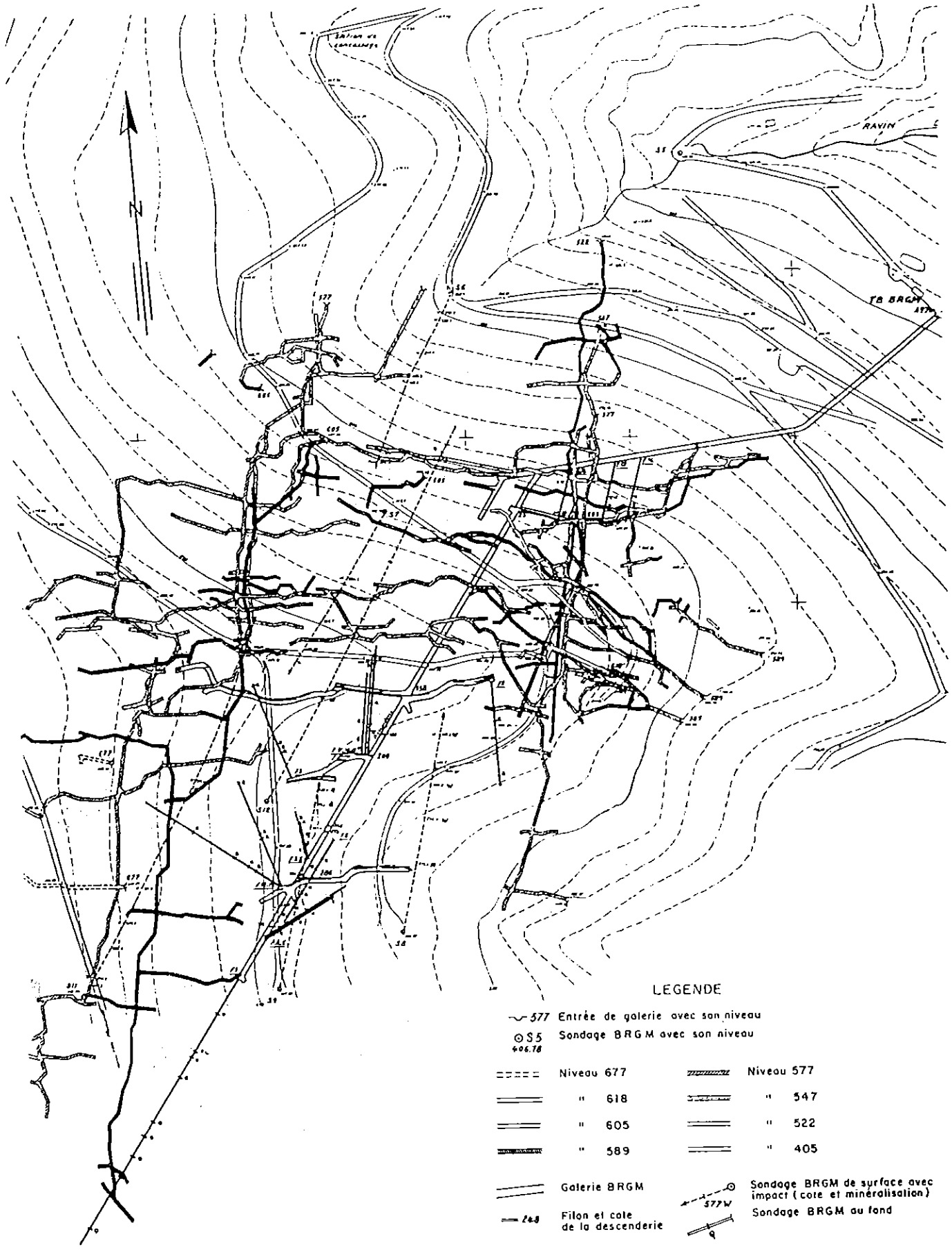

Fig. 9.- Mine de Leucamp, quartier de Roquefeuil, plan des travaux miniers (exploitation de Creusot-Loire et recherches BRGM). Le tracé des galeries montre bien l'existence de 3 familles de filons minéralisés en W (N-S, E-W et N130 gr).

Leucamp (1975-1983) ouvrent une possibilité de 7 000 t de WO_3 contenu, dans un système filonien représentant soit l'aval pendage, soit des extensions latérales des filons anciennement exploités sur les quartiers Roquefeuil et Bancarel. D'autre part, les gîtes voisins de Teissières et de Murols restent vierges de toute exploration en aval pendage des zones exploitées. Teissières notamment (faisceau de Cauvignat et son extension vers Gramont) se situe dans une position tout à fait comparable à celle de Roquefeuil et Bancarel, en bordure d'une extension du granite à moyenne profondeur, limitée par un accident gravimétrique majeur. Par ailleurs, si l'extension nord d'Enguialès se révèle décevante sur la zone de 300 m reconnue en exploration minière (1980-1983), en raison des caractéristiques des filons, l'axe Enguialès-le Viala, jalonné par des anomalies géochimiques en sol, reste une zone de recherche favorable à moyenne profondeur.

Contribution GRPG n° 703.

Références bibliographiques

AUTRAN A., BRETON J.P., CHANTRAINE J., CHIRON J.C., GROS Y., ROGER P. (1980).- Introduction à la carte tectonique de la France. *Mémoire du BRGM*, n° 110, 52 p. carte.

AUTRAN A., COGNÉ J. (1980).- La zone interne de l'orogenèse varisque dans l'ouest de la France et sa place dans le développement de la chaine hercynienne. *In* "Colloque C7 : Géologie de l'Europe", 26e C.G.I., 90-111.

BECARIE P. (1958).- Le métamorphisme de contact du granite d'Entraigues dans la vallée du Lot. D.E.S., Fac. Sci. Clermont-Fd., 1 vol.

BELLON H., GIBERT J.P. (1981).- Analyses radiométriques (K-Ar) des associations plutoniques et hypovolcaniques hercyniennes de la région Nord-Margeride (Massif central, France). *Bull. Soc. géol. Fr.*, 23, n° 5, pp. 929-937.

BOESSÉ J.M. (1980).- Lithologie, structure et métamorphisme de la Châtaigneraie septentrionale (Cantal, Massif central français). Thèse 3ème Cycle, Orsay, 129 p.

BOGDANOFF S., CIRODDE J.L., COLIN J. (1980).- La carte géologique à 1/50 000. Entraygues et notice BRGM (à paraître).

BOGDANOFF S., CIRRODDE J.L., DONNOT M. (1984).- Présence de grès à faciès Marcory dans la partie orientale de la Châtaigneraie (Massif central français). Résumés des comm. orales, 10ème Réunion ann. Sci Terre, Bordeaux.

BONNE A. (1970).- Note préliminaire sur le gisement de wolframite d'Enguialès (Aveyron). *CR Acad. Sci. Fr.*, 271, série D, pp. 12-15.

BONNE A., MOREAU J. (1973).- Etude structurale du gisement de wolframite d'Enguialès, *Mineral Deposita*, vol. 8, pp. 57-63.

BOULE M. (1899-1900).- Géologie des environs d'Aurillac. *Bull. Serv. Carte géol. Fr.*, 11, pp. 279-290.

CHEZE Y. (1975).- Etude géologique de la Châtaigneraie au nord d'Entraygues (Aveyron). Pétrographie, structure et minéralogie. Thèse 3ème Cycle. Clermont-Fd, 158 p.

CHINNER E.A. (1960).- Pelitic gneisses with varying ferric-ferrous ratios from Glen Glova Angus, Scotland. *J. Petrol., G.B.*, n° 1, pp. 178-217.

CROISE G. (1982). - Etude géologique et gîtologique autour de l'ancienne mine de wolframite d'Enguialès (Aveyron). Rapport de stage (Nancy, E.N.S.G.).

COUTURIÉ J.P., VACHETTE-CAEN M., VIALETTE Y. (1979).- Age namurien d'un laccolite différencié par gravité : le granite de la Margeride (Massif central français). *CR Acad. Sci. Fr.*, (D), 289, pp. 449-452.

COUTURIÉ J.P., VACHETTE-CAEN M., (1980).- Age westphalien des leucogranites recoupant le granite de la Margeride. *CR Acad. Sci. Fr.*, série D, 291, pp. 43-45.

DÉBÉGLIA N. (1984).- Réinterprétation et Modélisation des données gravimétriques disponibles dans le secteur de la Châtaigneraie. Rapport BRGM, 84 SGN 329 GPH - Novembre 1984. Inédit.

DELILLE J.C., PERONNE Y. (1982).- Minéralisations liées aux granitoïdes de l'Ouest du Massif central. Rapport BRGM, 82 SGN 176 GMX. Inédit.

DEMANGE M., NICOLAS V.A. (1983).- La tectonique en Châtaigneraie aux abords du district wolframifère de Leucamp (Massif central français). Contrôle structural des minéralisations filoniennes. *CR Acad. Sci. Fr.*, (II), 297, pp. 807-809.

DEMANGE M., NICOLAS V.A., SOLER P., GLOUSE H. (1986).- Le gisement tungstifère de Leucamp (Cantal, France) dans son cadre géologique. Résumé p. 97, gisements de tungstène, colloque européen, 12-14 mai 1986, Toulouse, France.

DESCHAMPS Y. (1980).- Contribution à l'étude des gisements à pyrite-hématite de Rio Marina (Ile d'Elbe, Italie). Approche pétrographique, géochimique et structurale. Thèse Univ. Lyon et CRPG.

DERRE C. (1982).- La province Sn-W ouest européenne. Histoire de divers types de gisements du Massif central, des Pyrénées et du Portugal. Thèse de doctorat ès sciences. Université de Paris VI.

DUTHOU J.L., BOGDANOFF S., CIRODDE J.L., NICOLAS V. (1986).- Chronologie Rb-Sr du granite du Veinazès environnant le gisement wolframifère de Leucamp. 11e R.S.T. Clermont-Fd.

FOISSY B, MIGNON R. (1983).- Travaux miniers d'Enguialès 1982-1983. Rapport BRGM RDM/FE/DSO. Inédit.

GROS Y., GUERANGÉ B., MARTIN P. (1981).- Etude structurale du champ filonien WO_3 de Leucamp (Cantal). Déformation souple et fracturation dans les travaux BRGM et leur environnement. Rapport BRGM 81 SGR 734 GE. Inédit.

JOUBERT M. (1978).- Etude pétrographique, structurale et métallogénique de la Châtaigneraie (secteur de Veinazès, Cantal). Thèse 3ème Cycle, Clermont-Fd, 206 p.

LABOUE M. (1982).- Etude structurale du massif granitique de la Margeride, thèse 3ème Cycle, Clermont-Fd.

LA ROCHE H. DE (1978).- La chimie des roches présentée et interprétée d'après la structure de leur faciès minéral dans l'espace des variables chimiques : fonctions spécifiques et diagrammes qui s'en déduisent - Applications aux roches ignées. *Chemical geology*, n° 21, pp. 63-87.

LA ROCHE H. DE (1986).- Classification et nomenclature des roches ignées : un essai de restauration de la convergence entre systématique quantitative, typologie d'usage et modélisation génétique. *Bull. Soc. géol. Fr.*, II, n° 2, pp. 337-353.

LAVAL M., VIALLEFOND L., CAIA G. (1986).- Le gîte à wolframite d'Enguialès : géochimie du plutonisme et signatures de la géochimie sol. résumé p. 100, gisements de tungstène, colloque européen, 12-14 mai 1986, Toulouse, Fr.

LE CHAPELAIN J.R. (1978).- Etat des travaux réalisés par le BRGM dans la zone de Leucamp. rapport BRGM/DL Clermont n° 281. Inédit.

LE CHAPELAIN J.R. (1980).- Leucamp - Travaux BRGM 1978-1980 - Rapport BRGM/DL Clermont n° 320. Inédit.

LE CHAPELAIN J.R. (1981).- Travaux réalisés sur le gisement de tungstène de Leucamp dans le cadre du Plan Métaux. Novembre 80 - Juillet 1981. Rapport BRGM/DL/Clermont n° 324. Inédit.

LETERRIER J., MARCHAL M., DUBUIT M., DREUX G. (1983).- La Banque de données géochimiques ARTEMISE (analyses roches totales, minéraux, sols et eaux), exemples de valorisation scientifique. *Bull. Soc. géol. Fr.*, 25, n° 5, pp. 697-704.

MADELAINE B., OGIER M. (1977).- Etude gravimétrique dans la région de la Châtaigneraie - Rapport confidentiel BRGM 77 GPH 039 - Novembre 1977. Inédit.

MIGNON R. (1982).- Enguialès, sondages jour et fond 1981-1982. Rapport BRGM 82 DSO 002. Inédit.

MOINE B., PLOQUIN A. (1972).- Etude chimique des Séries de Roches Supracrustales du Telemark (Précambrien du Sud de la Norvège). *Sci. de la Terre Fr.*, 17, n° 1-2, pp. 49-79.

MOINE B., PROST A., ENGLUND J.O. (1974).- Etude chimique d'une série détritique : les Sparagmites de Norvège du Sud, région du Lac Mjösa. CR 2ème R.A.S.T., Point-à-Mousson, 291 p.

NICOLAS V. (1985).- Le gisement wolframifère de Leucamp dans son environnement géologique (Châtaigneraie du Cantal, France). Thèse 3ème Cycle, Paris, 384 p.

PIN Ch. (1980).- Données microstructurales sur les terrains métamorphiques de la vallée du Lot. *Bull. BRGM*, (2), I, 4, pp. 293-313.

PLOQUIN A. (1980).- Etude géochimique et pétrographique du Complexe de gneiss, migmatites et granites du Telemark-Aust Agder (Précambrien de Norvège du Sud). Sa place dans l'ensemble épizonal à catazonal profond du Haut Telemark au Bamble. *Sci. de la Terre*, Mém. 38, 389 p., 8 pl. h.t., 1 carte h.t., Thèse d'Etat, Nancy 1975.

RAMBOZ C. (1980).- Géochimie et étude des phases fluides de gisements et indices d'étain et de tungstène du Sud du Massif central (France). Thèse 3ème Cycle, Nancy, 278 p.

RAMBOZ C., BASTOUL A. (1985).- Oxydation du fer dans les skarns et les schistes des Jebilet centrales, Maroc : un indicateur du transfert de matière par les fluides dans une zone de cisaillement ductile. *CR Acad. Sci. Fr.*, 301 (II), n° 13, pp. 931-936.

RECHOCHE G. (1983).- Etude minéralogique des filons de tungstène et de leur encaissant dans les nouveaux travaux du niveau 465. Mine d'Enguialès (Aveyron). DEA Université Toulouse, 1983.

VIVIER G. (1970).- Etude pétrographique et géochronologique de la Châtaigneraie (Sud-Ouest du Massif central français). Thèse 3ème Cycle, Clermont-Fd., 214 p.

VIVIER G., LASSERRE M. (1973).- Age hercynien des granites de la Châtaigneraie (Sud-Ouest du Massif central français). *Bull. Soc. géol. Fr.*, (7), 15, pp. 283-287.

WEPPE M. (1958).- Les gisements de wolfram de Leucamp, Puy-les-Vignes, Montbelleux. Nancy. Doct.Sci. Nat. 196 p.

PUBLICATION XV : Physical and chemical controls (fO_2, T, pH) of the opposite behaviour of U and Sn-W as exemplified by hydrothermal deposits in France and Great-Britain, and solubility data.

Bull. Minéral.
(1987), 110, 261-281

Physical and chemical controls (fO_2,T,pH) of the opposite behaviour of U and Sn-W as examplified by hydrothermal deposits in France and Great-Britain, and solubility data

by JEAN DUBESSY*, CLAIRE RAMBOZ**, CHINH NGUYEN-TRUNG*, MICHEL CATHELINEAU*, BERNARD CHAROY**, MICHEL CUNEY*, JACQUES LEROY*, BERNARD POTY* and ALAIN WEISBROD**

* CREGU and GS C.N.R.S.-CREGU, B.P. 23, 54501 Vandœuvre-les-Nancy Cedex, France.

** C.R.P.G., B.P. 20, 54501 Vandœuvre-les-Nancy Cedex, France.

Abstract. — The aim of this paper is to determine the physical and chemical parameters which control the opposite behaviour of uranium and tin-tungsten between 300° and 500 °C. In uranium deposits, fO_2 and fS_2 of mineralizing fluids are higher than values fixed by the pyrite-hematite-magnetite triple point, as shown by uraninite-hematite and/or pyrite mineral association. The stability of quartz-K feldspar-muscovite paragenesis in the wall-rocks of hydrothermal U deposits indicates weakly acid pH. By contrast, in the Sn-W occurrences from the French Southern Massif Central, the fO_2 of mineralizing fluids is between Ni-NiO and Q-F-M buffers as shown by CO_2-CH_4-H_2O-NaCl bearing fluid inclusions. The pH of these fluids is weakly acid to weakly basic as shown by the stability of muscovite in presence or absence of quartz and/or feldspar. Sn-W mineralizing fluids from Cornwall are by contrast purely aqueous and acid, as indicated by the mineral assemblage muscovite-quartz which is typical of greisens.

Experimental data on UO_2, SnO_2, $FeWO_4$, $CaWO_4$ solubility and metal species in fluids show that $fO_2 >$ H-M are required for uranium transport whereas $fO_2 \leq$ Ni-NiO favours Sn transport. The fluid oxidation state has no direct influence on the transport and deposition of tungsten. The fO_2 control on the hydrothermal transport properties of these three metals is related on the one hand to the fluid and rock composition, and on the other hand to the minimal 320 °C temperature required for homogeneous equilibria in the C-O-H system to control the oxidation state at low values.

At high temperatures, Sn, Fe and Ca chloride complexes are more stable than carbonate and phosphate uranium complexes ; this is attributable to their structure and to the dielectric content of the fluid. The presence of dissolved gases at high concentration, which are produced by devolatilization reactions at high temperatures, is emphasized since they lower the dielectric constant of the fluid which enhances the stability of chloride complexes.

All these results show that temperature and fO_2 account for the opposite behaviour of uranium and tin-tungsten in hydrothermal systems between 300° to 500 °C.

Key-words : U, Sn, W, hydrothermal stage, fO_2, temperature, pH, solubility, speciation.

Contrôles physico-chimiques (fO_2, T, pH) du comportement antagonique de U et Sn-W mis en évidence à partir des gisements hydrothermaux de France et de Grande-Bretagne, et des données de solubilité.

Résumé. — Le but de ce travail est de déterminer les paramètres physico-chimiques qui contrôlent le comportement antagonique de l'uranium et de l'étain-tungstène entre 300° et 500 °C. Dans les gisements d'uranium, les fO_2 et fS_2 des fluides minéralisateurs sont supérieures à celles fixées par le point triple pyrite - hématite - magnétite comme le montre l'association uraninite - hématite - et/ou pyrite. La stabilité de la paragenèse quartz - feldspath potassique - muscovite dans les roches encaissantes des minéralisations uranifères considérées témoignent de pH faiblement acides. En revanche, pour les minéralisations à Sn-W du sud du Massif Central français, la fO_2 des fluides minéralisateurs est comprise entre les tampons Ni-NiO et Q-F-M comme l'indiquent les inclusions fluides à CO_2-CH_4-H_2O-NaCl. Le pH de ces fluides est faiblement acide à faiblement basique comme le montre la stabilité de la muscovite en présence ou en absence de quartz et/ou de feldspath. Les fluides minéralisateurs en Sn-W de Cornouailles sont, au contraire, purement aqueux et acides, comme l'indique l'assemblage muscovite - quartz typique des greisens.

L'analyse des données expérimentales de solubilité de UO_2, SnO_2, $FeWO_4$, $CaWO_4$ et de spéciation des métaux montrent que des $fO_2 \leq$ Ni-NiO favorisent le transport de l'étain. L'état d'oxydation du fluide n'a aucune influence directe sur le transport et le dépôt du tungstène. Le contrôle de la fO_2 sur les capacités de transport hydrothermal de ces trois métaux est mis en relation d'une part avec la composition des fluides et des roches,

d'autre part avec la température minimum de 320 °C requise pour que les équilibres homogènes du système C-O-H fixent l'état d'oxydation à des valeurs basses.

A haute température, la stabilité accrue des complexes chlorurés de Sn, Fe, Ca comparée à celle des complexes carbonatés et phosphatés d'uranium est discutée en fonction de la structure des complexes, et de la constante diélectrique du fluide. On souligne également que la présence de gaz dissous (concentration élevée), produits à haute température par les réactions de dévolatilisation, diminue la constante diélectrique du fluide et stabilise corrélativement les complexes chlorurés.

L'ensemble de ces résultats montre que la température et la fugacité d'oxygène rendent compte du comportement antagonique de l'uranium et de l'étain - tungstène au stade hydrothermal entre 300° et 500 °C.

Mots-clés : U, Sn, W, stade hydrothermal, fO_2, température, pH, solubilité, spéciation.

INTRODUCTION

The Hercynian belt in Europe and NE America is an important metallogenic province for uranium, tin and tungsten. Mineralizations were discovered both inside granitic rocks and in the surrounding metamorphic series. A main tool for U and Sn-W exploration in the Hercynian belt is the clear spatial relationship between mineralizations and peraluminous felsic magmatism (Chauris, 1965 ; Tischendorf, 1973 ; Burnol, 1974 ; La Roche *et al.*, 1980 ; Chatterjee *et al.*, 1983 ; Poty *et al.*, 1986). It has long been noted however that major U-producing districts in Europe do not include significant Sn and/or W deposits and vice versa. For instance, Cornwall is by far the most important district for Sn but presents very subordinate U showings, whereas in Limousin (French Massif Central), U is the main mined ore and Sn occurs only in minor amounts. It is also worth pointing out that U mineralizations in France are usually associated with large granitic massifs and they do not appear to be linked to any specific granitic facies. In contrast, most Sn and, to a lesser extent, W mineralizations are preferentially related to smaller stocks or cupolas (La Roche *et al.*, 1980) particularly enriched in incompatible elements, whether they result from magmatic differentiation or represent primary melts.

At the magmatic stage, U, W and Sn have the same incompatible behaviour although there is less information about W. This has been observed in many volcanic suites (Treuil *et al.*, 1979) and in peraluminous leucogranites (Friedrich, 1984 ; Friedrich *et al.*, in press). U, W and Sn have been shown to be simultaneously enriched in peraluminous rhyolites resulting from partial melting (Valencia Herrera *et al.*, 1984).

Some authors have tried to explain the specific metallogenic potential of Hercynian granitic provinces by the early specialization of the continental crust (Derré, 1982). Whole rock geochemistry has also been used to discriminate U and Sn-W specialized granites (La Roche *et al.*, 1980 ; Chatterjee *et al.*, 1983). But this approach has not provided definite conclusions so far. For the hydrothermal stage, attempts have been made to compare the behaviour of U and Sn-W only during greisenization. Sn and W are typically concentrated during this process. Uranium is also probably mobilized at that stage as shown by the uranium-bearing wolframite and cassiterite from Cornish greisens (Swart and Moore, 1982). Studying greisens from Lervir-Kervenguy, Pen-feunten (Brittanny), and Cligga-Head (Cornwall), Pagel (1981) concluded that greisenization is an uranium- conservative process. In contrast, Simpson *et al.* (1979), concluded that uranium is lost during greisenization at Cligga-Head. Despite these contradictory results concerning the behaviour of U and Sn-W during greisenization, the hydrothermal stage is certainly a key in understanding the contrasting behaviour of U and Sn-W simply because most U and Sn and W deposits in the Hercynian belt are hydrothermal.

The purpose of this paper is to investigate the rôle of fO_2, fS_2, pH and complexing agents as factors controlling the ability of hydrothermal fluids for transport and deposition of U, Sn and W in the range 500°-300 °C. From occurrences of these metals in Cornwall, Brittany, Vendée and French Central Massif (Figure 1), fO_2, fS_2, pH and complexing agents have been constrained by mineral paragenesis. In addition, fO_2 and fS_2 were also derived, when possible by P-V-T-X properties of individual fluid inclusions in the C-O-H-S system (see Appendix). The contrasting behaviour of U and Sn-W in hydrothermal systems is here addressed in terms of mineralogical and geochemical data, experimental or calculated solubility of U, Sn and W, including

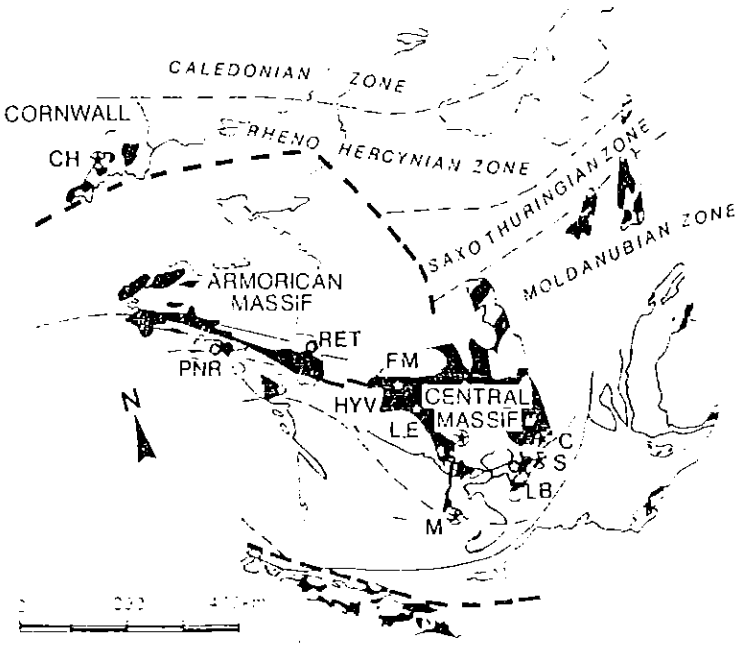

FIG. 1. — *Map of the U, Sn and W occurrences or deposits (stars) in the Hercynian belt from France and England.* In dark : leucogranites.
U : PNR = Pen Ar Ran and Metairie Neuve ; LB = Les Bombes ; RET = Retail ; FM = Fanay-Margnac ; H = Hyvemeresse.
Sn-W : CH = Cligga Head ; C = Saint-Cierge ; S = Serrecourte ; L = Leucamp ; E = Enguiales ; M = Montredon.

Localisation des indices ou gisements d'U, Sn et W (étoiles) dans la chaîne Hercynienne française et anglaise. En noir : les leucogranites.

new measurements on uraninite solubility by Nguyen-Trung (1985), and available information on the speciation of U, Sn and W.

P-T-fO_2-fS_2-pH CONDITIONS OF U, Sn AND W TRANSPORT AND DEPOSITION : EVIDENCE FROM MINERALOGY AND FLUID INCLUSIONS

Uranium deposits or occurrences

Mineralogy

According to Geffroy (1971), the most common paragenetic sequence in Hercynian intragranitic uranium deposits from France (*Margnac-Fanay, Hyvernieresse* successively) is : minor quartz (Q1), pitchblende + pyrite, quartz (Q2) + hematite + pyrite (Table I, figure 2), followed by an axial vein filling. This general sequence may vary in detail, especially in deposits located in metamorphic formations close to granitic massifs (*Retail, Métairie Neuve* ; Cathelineau, 1981, 1984). In most veins, pyrite is cogenetic with pitchblende, but various occurrences are characterized by the lack of sulphides during ore stage (*Pen Ar Ran, Métairie Neuve, Retail* at the second ore-stage). Hematite is almost systematically observed as inclusions in quartz combs Q1 (*Pen Ar Ran*) or Q2 (*Margnac-Fanay*).

In *Les Bombes*, the mineralogical form of uranium is urano-phosphothorite which crystallized together with apatite, secondary quartz and hematite (Cathelineau, 1987).

Wall-rocks in the vicinity of uranium veins

METAL	OCCURRENCE	WALL-ROCK	VEIN MINERALOGY	WALL ROCK ALTERATION DURING ORE DEPOSITON
U	Les Bombes	Peraluminous granite	Ap-Zr(U)/Q_1-Ap-UPTh	No alteration Ab and Hm stable
	Penaran Metairie Neuve	Blastomylonites Graphitic quartzites	Q_1/Pitch	No alteration, Hm stable No alteration Q, Fk, Ab, Mu stable
	Retail (second ore stage)	Retromorphosed two micas gneisses and amphibolites	Q_1/Pitch/Q_2	Unspecified alteration at this stage
	Margnac Fanay	Peraluminous granite, episyenite, lamprophyres	Q_1/Pitch-py/Q_2-Mm	Phengite crystallization Q, Ab, Fk, Mu stable
	Hyverneresse	Peraluminous granite, episyenite	Q_1/Pitch-Py	Phengite crystallization Q, Ab, Fk, Mu stable
Sn	Cligga Head I	Peraluminous granite	Q/Q-Mu-Cas-Wo_1/ blue To-Wo_2(?)	Greisenization (1) + tourmalinization (1)+(2)
	Cligga Head II		Q-Mu-Cas-Chl-green To Fl-Ap-Apy-Py-Cpy	Greisenization (1)
	Saint Cierge	Metamorphic rocks	Q/Q-To/Cas-To-Q/ Mi-Ad-Chl/Cpy-Py	
W	Saint Cierge	Saint Cierge granite	Mu/Mu-Q/Wo-Sch-Ap/To	Muscovitization + silicification (2)
	Serrecourte	contact aureole Pelitic schists	Q/Q-Wo/ Apy-Py-Cpy/Py	
	Leucamp	contact aureole Pelitic schists	Q/Q-Wo-Ap-(Sch)/ Sch]Wo[-Bi Apy-Py]Wo[-]Q[/ To]Wo[-]Q[/Mu-]Q[	Tourmalinization (2)
	Enguiales	Pelitic schists (contact aureole)	Q/Q-Wo-Ap/ Apy-py]Wo[-]Q[/ Sch]Wo[/To]Wo[-]Q[/ Mu-]Q[/Fl	Tourmalinization (2)
	Montredon pegmatoïds	Contact between black shales and micaschists	Mi-Ad/Q-Sch-Fl/To	
	Montredon stockwerk	Micaschists	Fk-Wo-(Cas)/Sch/ Mu/Fl	Tourmalinization (2)

TABLE I. — *Synthetic vein and wall rock mineralogy of the studied U, Sn and W occurrences.*
To]Wo[= tourmaline growing at the expense of wolframite ;]Q[= quartz dissolution ; (1) = alteration developed at the expense of the wall rock aluminous minerals ; (2) = minerals precipitated from the fluid.
Ab : Albite ; Ap : Apatite ; Apy : Arsenopyrite ; Bi : Bismuthinite ; Cal : Calcite ; Cas : Cassiterite ; Chl : Chlorite ; Fk : K-feldspar ; Fl : Fluorite ; Hm : Hematite ; Mt : Magnetite ; Mi : Microcline ; Mu : Muscovite ; Ph : Phengite ; Pitch : Pitchblende ; Py : Pyrite ; Q : Quartz ; Sch : Scheelite ; To : Tourmaline ; UPTh : Uranophosphothorite ; Wo : Wolframite ; Zr (U) : Uraniferous zircon-silicate.

Synthèse minéralogique sur les filons et leurs épontes pour les minéralisations d'U, Sn et W étudiées.
To]Wo[= tourmaline se développant aux dépens de la wolframite ;]Q[= dissolution du quartz ; (1) = altération développée aux dépens des minéraux alumineux ; (2) = minéraux précipités à partir du fluide.

show various iron mineralogy. Hematite, if present in the pre-ore stage, may remain stable during uranium deposition (*Pen Ar Ran and Les Bombes*, figure 2*b*). In other cases, iron is leached from surrounding silicates (biotite, pyroxene,...) and precipitates as pyrite. Finally, magnetite coexists with pitchblende and pyrite in the altered lamprophyres from *Margnac-Fanay* (Figure 2*a*).

In all the uranium deposits, the initial association quartz-K feldspar-muscovite of either granitic or metamorphic wall rocks remains stable during the ore stage. A discrete crystallization of

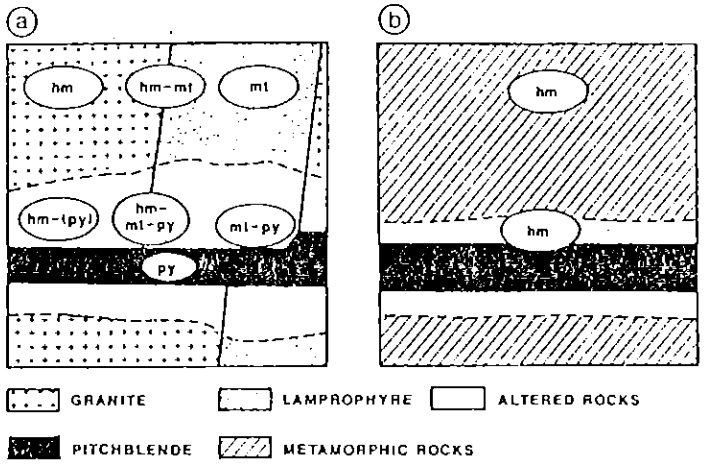

FIG. 2. — *Iron minerals in uranium vein and in their altered and fresh surrounding rocks.* a) *Margnac-Fanay ;* b) *Pen Ar Ran.*

Les minéraux du fer dans les veines d'uranium et les roches encaissantes. a) *Margnac-Fanay ;* b) *Pen Ar Ran.*

authigenic phengite and/or illite can occur before and/or during pitchblende deposition (Leroy, 1978 ; Leroy and Cathelineau, 1982).

Geothermometry and fluid inclusion chemistry (Table II)

The fluid inclusion from *Les Bombes* are primary and are located at the base of euhedral quartz growing at the end of the uranophosphothorite deposition. These aqueous fluids with medium salinity have no molecular species of the C-O-H-N-S system detectable by microthermometry and micro-Raman spectrometry. They

METAL	OCCURRENCES	TH(°C)		NaCl eq.-------- (mole) NaCl+H_2O	d ($g.cm^{-3}$)	mole % H_2O	CO_2	CH_4	N_2	H_2S
U	Les Bombes	L-V(L)	360-420	3.1 - 5.5	.70 - .80	100	0	0	0	0
	Penarun	L-V(L,V,C)	340-430	1 - 1.6	.60 - .80	100	0	0	0	0
	Rezail	L-V(V)	320-400	1 - 1.6	.65 - .80	100	0	0	0	0
	Margnac	L-V(L,V,C)	320-360	1.6 - 3.3	.25 - .75	64-80	19-35	.03-.05	.3-.7	.019-.020
	Hyvernesse	L-V(L)	260-385	1-3	.70 - .80	85-95	5-15	*	*	*
Sn	Cligga Head1 I-IIQ	L-V(L)	450-350	1 - 3.3	.60 - .75	100	0	0	0	0
	Cligga Head2 I-IIQ	L-V(L)	350-300	2.6 - 1.9	.74 - .80	100	0	0	0	0
	Saint Clerge IQ	L-V(V)	450-350	2.2 - 2.0	.52 - .57	90-92	9-7	1.7-1	0	0
	IIeas	L-V(L)	310-290	2.5 - 3	.68	95	3.5	1.5	0	0
W	Saint Clerge IQ	L-V(V)	427-348	1.8 - 2.2	.50 - .57	85-92	14.0-7.0	1.5-1.0	0	0
	IQ	L-V(L,C)	360-369	1.9	.64	93-96	4	.5	0	0
	Serrecourte IQ	L-V(V)	380-280	1.2	.31 - .44	62-89	37-9	1-2	Tr.	0
	IQ	L-V(L,C)	383-335	1.2	.45 - .58	88-93	0	12-7	0	0
	Leucamp IQ	L-V(V)	>00	2	.61	84.5	13.5	2	Tr.	0
	Enguialès*(Sch(W)	L-V(L)	350	1	.65	93	7	<7	0	0
	II Q	L-V(L)	320	.5	.8	87	13	0.2	0	0
	Montredon I-IIQ regatoid + Q rod	L-V(V,C)		1.9 - .5	.5 - .57	90-93	8.5-6	1.5	Tr.	0

* CH_4 is detected with the Raman probe but the Raman line for CO_2 is obliterated by a line derived from scheelite.

TABLE II. — *Microthermometric, composition and density of fluid inclusions associated with the ore stage from the U, Sn and W occurrences.* TH (°C) : bulk homogenization temperature ; L-V (L,V,C) : liquid - vapour equilibrium with homogenization to the liquid (L), vapour (V) or critical (C) phase ; eq. : equivalent.

Données microthermométriques, composition et densité des inclusions fluides associées au stade de minéralisation des occurrences de U, Sn et W.

TH (°C) : température d'homogénéisation globale ; L-V (L,V,C) : équilibre liquide - vapeur avec homogénéisation en phase liquide (L), vapeur (V) ou critique (C) ; éq. : équivalent.

homogenize to liquid at around 380° ± 20 °C (Cathelineau, 1987). These temperatures correspond to minimal trapping temperatures. On the other hand, oxygen isotope studies on quartz and feldspar give an equilibrium temperature of 400°-500 °C (Turpin, 1984). This indicates a fluid pressure around 500-700 bars.

In the *Pen Ar Ran and Retail* deposits, the fluid inclusions are also primary with respect to the quartz Q1. These inclusions, therefore, are expected to have trapped the uranium transporting fluid. Their salinity is low and no gas has been identified. Their temperature and pressure of trapping, indicated by boiling phenomena is around 380°-400 °C and 300-400 bars (Cathelineau, 1981, 1984).

In contrast, the fluids associated in space and time with pitchblende deposition in *Margnac and Fanay* are CO_2-rich and their trapping occurred at around 340°-350 °C, as indicated by boiling (Leroy, 1978). The corresponding fluid-pressure does not exceed 1 000 bars. Unpublished micro-Raman analyses indicate the presence of N_2, CH_4 and H_2S besides CO_2 (Table II), which confirms previous gas chromatography results (Lecerf, 1973). The fluids in hematitic quartz Q2, which post-dates pitchblende deposition, become progressively more aqueous and the temperature regularly decreases from 350° to 150 °C. Based on the microthermometric data by Martin (1981), summarized in table II, the conditions of U-mineralizations at *Hyvernresse* are expected to have been similar to those in the *Margnac-Fanay* deposits.

Implications for pH and fO_2-fS_2 conditions of U mineralizations

pH can be calculated from the following equilibrium ($3KAlSi_3O_8 + 2H^+ = KAl_3Si_3O_{10}(OH)_2 + 6SiO_2 + 2K^+$) and an estimation of the potassium content of the fluid since quartz, K feldspar and muscovite are stable in most of uranium deposits wall-rocks (Montoya and Hemley, 1975). The potassium content is calculated from the data of Lagache and Weisbrod (1977) assuming that the K/Na ratio is buffered by the two feldspars at 400 °C and a total salt concentration close to 3 mole % (Table II). The calculated pH is around 5 for the CO_2 depleted fluids. If CO_2 is present in the fluid, the formation of potassium carbonate or bicarbonate ion-pairs is expected to decrease the activity of K^+ and consequently to increase the pH.

The mineralogy of oxides and sulphides at the uranium ore stage (Table I) shows that the fS_2 was rather high, compatible with pyrite formation and that the fO_2 was either close to the hematite-pyrite boundary or within the hematite stability field or around the pyrite-hematite-magnetite triple point (Figure 3).

At *Margnac-Fanay*, calculations based on the composition of the CO_2-CH_4-H_2S bearing fluid inclusions indicate log $fO_2 = -30.4$ and log

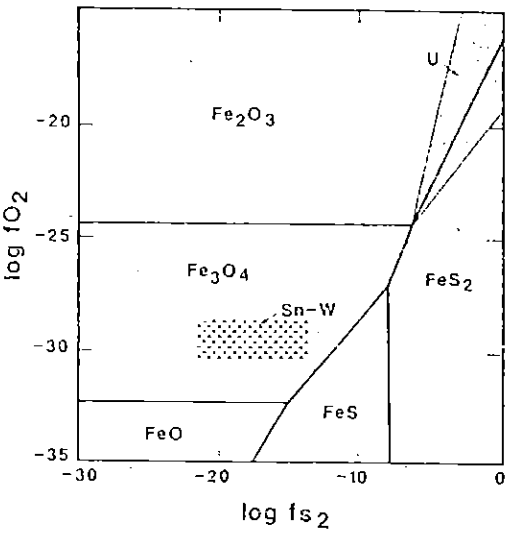

FIG. 3. — *Projection of the fluids associated with U, Sn, W showings in the log fO_2-log fS_2 plane at 400 °C and 1 kbar* (from Bowers *et al.*, 1984).

Projection des fluides associés aux indices ou gisements d'U, Sn, W dans le plan log fO_2-log fS_2 à 400 °C et 1 kbar (diagramme construit à partir de celui de Bowers *et al.*, 1984).

$fS_2 = -10.4$ at 350 °C. These values are close to the Ni-NiO buffer (log $fO_2 = -30.6$) and to the equilibrium between pyrite and pyrrhotite (log $fS_2 = -9$; Barton and Skinner, 1979) at 350 °C. The fluid composition is along the boundary between magnetite and pyrrhotite. Magnetite has been found in the lamprophyre, whereas hematite is present in small amounts in the muscovitic pipes of dequartzified granite or in the crushed granite, all these rocks being in contact with the uranium mineralization (Figure 2*a*). The stability of hematite is contradictory

with the reduced characters of the CO_2-CH_4 fluids. It is concluded that the C-bearing fluids were the reducing agent which allowed pitchblende to precipitate from the uraniferous and oxidized aqueous fluids. C-O-H isotope studies support the hypothesis of fluid mixing (Turpin, 1984).

Sn-W deposits and occurrences

Mineralogy (Figure 4 and table I)

Quartz is usually the most abundant and the earliest mineral of the paragenesis. It can form veins up to 1 m thick. However vein quartz may be dissolved at the later muscovite stage (see below). In addition, in the intragranitic wolframite-scheelite- bearing veins of *Saint-Cierge*, only a few euhedral quartz crystals ($\leq$ 5 mm) coexist with the ores in a gangue of muscovite.

Cassiterite and wolframite are the main ore forming minerals of the studied Sn-W districts. It can be noted that wolframite is rare or minor in Sn-producing districts and vice-versa. Scheelite is the only W-bearing phase in pegmatitic pods from *Montredon* but it more often replaces primary wolframite in other deposits. Stannite is present in rare occurrences from Cornwall.

K-feldspars (microcline and adularia overgrowth) are present in the pegmatitic pods from *Montredon* and in the quartz-cassiterite veins from *Saint-Cierge*.

Muscovite is present in all the Sn-W deposits where K feldspar is absent or unstable. Muscovite occurs in three types of mineral association (Figure 4). (a) In greisens, muscovite essentially grows at the expense of granitic feldspar and always coexists with quartz. At *Cligga Head*, Charoy (1979*a*, and *b*) has described muscovite trapped in fluid inclusions contemporary with early greisenization and with cassiterite precipi-

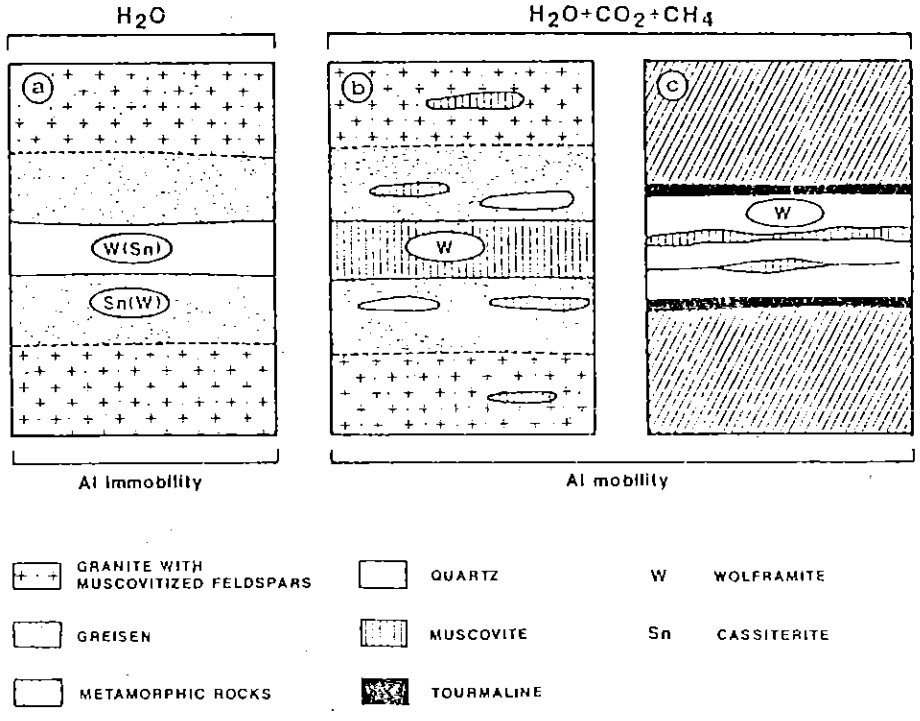

FIG. 4. — *Variations in wall-rock alterations and fluid chemistry in Sn and W occurrences.* a) *Cligga Head* ; b) *Saint-Cierge* ; c) *Leucamp, Enguiales, Montredon, Serrecourte.*

Les différentes altérations et chimies des fluides associées aux gisements ou indices de Sn-W. a) *Cligga Head* ; b) *Saint-Cierge* ; c) *Leucamp, Enguiales, Montredon, Serrecourte*

tation. (b) In intragranitic wolframite-scheelite veins from *Saint-Cierge*, muscovite precipitates directly from the fluid, first alone, later on at equilibrium with quartz. Wolframite + scheelite + apatite precipitate afterwards and coexist with earlier muscovite and quartz. (c) In intrametamorphic veins from *Leucamp, Enguiales* and *Montredon*, muscovite clearly postdates wolframite. It forms monomineral centimetric veins in quartz, which locally widen to vugs as a result of quartz dissolution.

We may conclude that the conditions of precipitation of muscovite were quite different in Cornwall and in South Massif Central. In Cornish greisens, aluminium was immobile and the solution was saturated with respect to quartz. In South Massif Central, the fluids transported significant amounts of aluminium and were now and then undersaturated with respect to quartz.

Iron sulphides and oxides are not present in the ore stages of the studied Sn-W deposits from France and Cornwall, except in the second stage mineralizations from Cornish lodes where cassiterite II + pyrite + arsenopyrite + chalcopyrite associations can be observed. Arsenopyrite, pyrite and sometimes bismuthinite precipitate later than primary Sn-W ores. In *Leucamp* and *Enguiales*, pyrite may develop at the expense of wolframite.

Tourmaline is always present prior, during and after the ore stage in the studied districts. In *Leucamp, Enguiales* and *Saint-Cierge*, tourmaline always precipitates directly from the fluid either in the quartz gangue, sometimes at the expense of wolframite, or in the vein periphery. In the two ore stages from Cornwall, tourmaline may precipitate directly from the fluid or may develop at the expense of feldspars or biotites.

Apatite quite systematically occurs together with wolframite in veins from Massif Central, which suggests coprecipitation of the two minerals (Ramboz, 1980*a* ; Brii and Ramboz, 1982). Apatite coexists with secondary cassiterite in Cornish lodes.

Geothermometry and fluid chemistry derived from fluid inclusions (Table II)

The Sn-W transporting and depositing fluids in the French South Massif Central have a low salinity and contain H_2O, CO_2, CH_4 and N_2 (Ramboz 1980*a* and *b* ; Ramboz *et al.*, 1985). By contrast, the fluids in Sn-W deposits from Cornwall are essentially dilute aqueous solutions (Charoy, 1979*b*) (Table II).

In both Cornwall and South Massif Central, inclusions have homogenization temperatures in the range 450°-250 °C. The fluids are interpreted as having been trapped in the one phase stability field under $\simeq$ 1 kbar fluid-pressure and in the T range 550°-300 °C. In both cases, the bulk fluid evolution corresponds to a progressive dilution of the fluids during isobaric cooling, resulting in ore deposition at $\simeq$ 400°-450 °C (Charoy, 1979*b* ; Ramboz, 1980*a* ; Ramboz *et al.*, 1985). The fluid density gradients are larger in South Massif Central than in Cornwall, due to a higher volatile content (Table II). The bulk P-$\overline{V}$-T-X properties of the fluids in quartz from the *Saint Cierge* cassiterite veins are similar to the ones in wolframite veins from South Massif Central. However, unmixing in the H_2O-CO_2-CH_4-NaCl system occurs at 310 °C during cassiterite deposition (Ramboz, 1980*a*), as demonstrated by the high salinity of the liquids trapped in cassiterite and by the heterogeneous trapping (Ramboz *et al.*, 1982). Fluid unmixing cannot be excluded in *Leucamp, Enguiales* and *Montredon*, because the data on these deposits are only at a preliminary stage.

Implication for pH-fO_2-fS_2 conditions of Sn-W mineralizations

The assemblage muscovite + quartz in the presence of unstable K-feldspar buffers the pH to acid values during the two ore stages from Cornwall (Montoya and Hemley, 1975). More precisely, Charoy (1979*a* and *b*) has established that the pH of Sn-W mineralizing fluids in Cornwall was comprised between 3 and 4.8 at 400 °C using both mineralogy and fluid inclusion chemistry. The formation of quartz at all stages of the deuteric alteration in Cornwall also implies acid pH conditions (Pascal, 1984).

In contrast, the Sn-W mineralizations from South Massif Central were formed under slightly acid, near neutral or weakly basic conditions. In the pegmatitic pods from *Montredon* and in the quartz cassiterite veins from *Saint Cierge*, neutral to slightly basic mineralization conditions are inferred from the presence of K-feldspar and the absence of muscovite from the ores (Mon-

toya and Hemley, 1975). In the other Sn-W deposits from South Massif Central, where muscovite is present, the fact that aluminium was soluble in the mineralizing fluids and that the solutions were occasionnally quartz deficient (during the tourmaline stage) or quartz destructive (e.g. at the muscovite stage) implies near neutral to basic pH conditions (Pascal, 1984).

The fO_2 conditions close to Q-F-M during transport and deposition of Sn-W ores in South Massif Central are inferred from the P-V-T-X properties of the H_2O-CO_2-CH_4-bearing fluids in quartz and in the ores (Dubessy, 1984 ; Ramboz *et al.*, 1985 ; table II).

The absence of pyrite at equilibrium with wolframite or cassiterite near neutral pH conditions indicates that the fS_2 of the Sn-W ore stage in Massif Central was lower than the fS_2 of the intragranitic U-stage. In the Sn-W-Sb veins from North Massif Central, Bril (1985) shows a fS_2 of 10^{-11} bar at 400 °C during SnO_2 precipitation. It is probably relevant to the fS_2 conditions of mineralizations in South Massif Central, because the Sn-W veins present very similar mineralogy and fluid inclusion chemistry in the North and South French Massif Central (Bril and Ramboz, 1982).

From fluid pH, it is possible to discriminate the Sn-W mineralizations from Cornwall on the one hand, and the U, Sn-W mineralizations from the French Massif Central on the other hand. But the pH of fluids of U and Sn-W mineralizations in South Massif Central seems rather similar (weakly acid, neutral or weakly basic). In contrast, fO_2 and fS_2 clearly discriminate U and Sn-W deposits (Figures 3 and 5).

SOLUBILITY AND SPECIATION DATA OF U, Sn, W IN HYDROTHERMAL SOLUTIONS IN THE RANGE 300°-500 °C

The amount of ore-mineral which can be precipitated from a fluid as the result of a change in physico-chemical conditions depends on : 1) the initial concentration of the metal in the fluid under the transport conditions (P, T, pH, fO_2, fS_2, ligand concentration) ; maximum concentration is usually fixed by the solubility (St) of the specific ore-mineral under these conditions ; 2) the solubility (Sd) of this ore mineral under the precipitation conditions ; 3) the amount of fluid

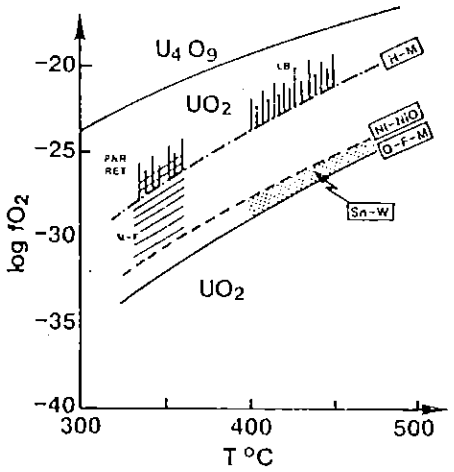

FIG. 5. — *Uranium oxides stability field* (Nguyen-Trung, 1985) *and fluids associated with U, Sn, W deposits in the log fO_2-temperature diagram at 1 kbar.*

Champ de stabilité des oxydes d'uranium (Nguyen-Trung, 1985) *et fluides associés aux minéralisations d'U, Sn, W, dans le plan log fO_2-température à 1 kbar.*

which is circulated in a given section of the hydrothermal system. In this paper, only the first two aspects will be considered. The higher the solubility difference (St-Sd), the larger the amount of ore mineral that can be precipitated. Therefore, the most favourable deposition conditions can be predicted if the parameters constraining the highest (St-Sd) values are known.

Both UO_2 and SnO_2 are oxides : this implies that the major rôle of other anions in the solution is only their ability to form complexes with these elements. In the next section, the change of valence between the element in solution and in the solid phases is emphasized, and is shown to be opposite for U and Sn for the P-T-pH-fO_2 conditions considered here. In contrast, tungsten precipitation in the form of tungstate minerals requires cations (Ca^{2+}, Fe^{2+}, Mn^{2+}) ; their bulk concentration and complexation in solution control the transport and deposition properties of the fluid with respect to tungsten.

UO_2

In aqueous solutions, uranium has three possible oxidation states (IV), (V) and (VI) at low

temperatures under natural conditions (Langmuir, 1978) and at high temperatures (Nguyen-Trung, 1985).

In the pure UO_2-H_2O system (Figure 6), the solubility of crystallized UO_2 varies as a function of pH at fixed temperature and fO_2. At the fO_2 conditions controlled by H-M or Ni-NiO buffers, minimum UO_2 solubility occurs probably near neutral pH (Nguyen-Trung, 1985). Higher fO_2 enhances the solubility only in acid to neutral solutions. Indeed, in this pH range, according to the experimental data of Nguyen-Trung (1985) UO_2 dissolves in water to form the pentavalent ion :

$$2UO_2(c) + 1/2O_2 + 2H^+ \rightleftharpoons 2UO_2^+ + H_2O \quad (1)$$

Reaction (1) shows that the solubility of UO_2 is fO_2-dependant for acid to neutral pH. In alkaline solution, by contrast, the dissolution of UO_2 only depends on pH as follows :

$$UO_2(c) + 3H_2O \rightleftharpoons U(OH)_5^- + H^+ \quad (2)$$

Experimental works show that reaction (2) occurs at oxidation states as high at H-M (Nguyen-Trung, 1985).

The uranium concentration can be enhanced by complexation with different inorganic ligands such as : sulphate, fluoride, chloride, carbonate and phosphate. Experimental works (Lietzke and Stoughton, 1960 ; Nikolaeva, 1971) show that U(VI) sulphate complexes are stable in acidic solutions (pH $\leq$ 5) in the temperature range 30°-200 °C (Nguyen-Trung, 1985). Their stability at higher temperature is still unknown but requires oxidizing fluids with fO_2 greater than values fixed by hematite-magnetite buffer, for SO_4^{--}/H_2S ratio > 1. According to theoretical calculations (Nguyen-Trung, 1985), U(IV) and U(VI) fluoride complexes predominate in acidic solution (pH $\leq$ 6) containing 10^{-4} molal F^- and at temperature up to 130 °C. At higher temperature, their existence requires high F^- concentration ($\Sigma F^- \geq 10^{-3}$ molal). Experimental works (Nikolaeva, 1977*a* and 1977*b*) and calculations (Nguyen-Trung, 1985) demonstrate that both U(IV) and U(VI) chloride complexes are stable in acidic solutions (pH $\leq$ 4) at room temperature. At moderate temperatures (T $\leq$ 200 °C), only U(VI) chloride complexe is stable. All these anions are expected to form uranium bearing complexes in oxidizing conditions (near H-M buffer) and in acidic solutions.

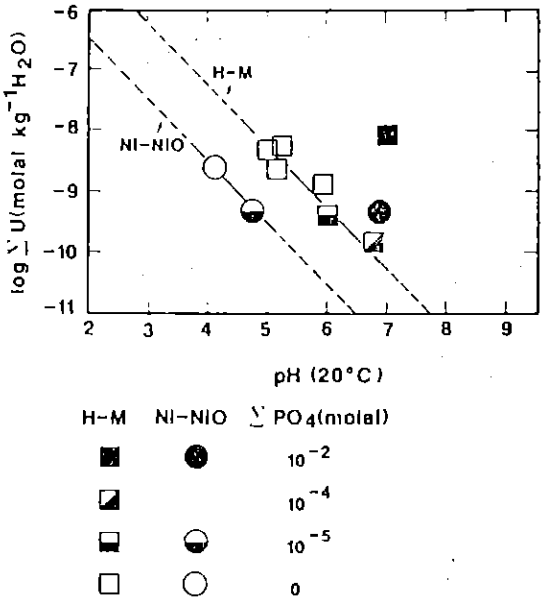

FIG. 6. — *UO_2 solubility at 400 °C as a function of room temperature pH with hematite-magnetite H-M and nickel-nickel oxide (Ni, NiO) buffers :* 1) In the pure water system : continuous and dashed lines established for different pH using boric acid (Nguyen-Trung, 1985). 2) In the H_2O-PO_4 system, the numbers give the bulk phosphate concentration in log molal unit.

Solubilité de UO_2 à 400 °C en fonction du pH mesuré à température ambiante, et des tampons d'oxydo-réduction hématite-magnétite (H-M) et nickel-nickel oxyde (Ni-NiO). 1) dans le système eau pure : lignes continues ou en tiretés établies pour différents pH en utilisant de l'acide borique (Nguyen-Trung, 1985). 2) dans le système H_2O-PO_4, les nombres donnent la concentration totale en phosphate exprimée en logarithme décimal de la molalité.

In the system UO_3-CO_2-H_2O, experimental results of Sergeyeva *et al.* (1972) show that the predominance of uranyl carbonate complexes also decreases with increasing temperature. At 300 °C, a minimal concentration of 0.5 molal carbonate is required for the U(VI) monocarbonate $[UO_2CO_3^0]$ to become significant in a solution containing $\Sigma U = 10^{-6}$ mole/kg H_2O (Nguyen-Trung, 1985). Therefore, in the temperature range of 300°-400 °C, the complexation of uranyl ions by carbonate ligand is possible in CO_2 rich, neutral pH and oxidized solutions ($fO_2 \geq fO_2$ fixed by H-M buffer). The U(V) or

U(VI) carbonate complexes at high temperatures ($T \geq 300$ °C) are still poorly known.

The U(IV) and U(VI) *phosphate* complexes are stable in the temperature range 25°-200 °C (Nguyen-Trung, 1985). Predictive calculations show that $UO_2(HPO_4)_2^{2-}$ is the most stable complex even at low phosphate concentration and in neutral pH and oxidized solutions ($fO_2 \geq fO_2$ of H-M). By constrast, U(IV) phosphate complexes predominate at high phosphate concentration and in acidic ($pH \leq 4$) and reduced solutions.

UO_2 solubility measurements in phosphate solutions at 400 °C, 0.7 kbar by Nguyen-Trung (Figure 6) show that :

1) the uranium solubility increases significantly only at high phosphate concentration ($\Sigma PO_4 \geq 10^{-2}$ molal),

2) at $\Sigma PO_4 \leq 10^{-4}$ molal, the uranium solubility is close to that in pure water,

3) the uranium solubility at fO_2 condition fixed by the Ni-NiO buffer is about one order of magnitude lower than that at fO_2 controlled by the H-M- buffer.

Because dissociation constants of boric acid and phosphate solution are still poorly known at 400 °C, 0.7 kbar, experimental results are presented with pH measured at room temperatures before and after experiments (both pH values are the same).

These experiments emphasize the control of fO_2 on UO_2 solubility at 400 °C. They also show that phosphate uranium complexes are far more stable than carbonate complexes in the 300°-400 °C temperature range, by comparison with those of Sergeyeva *et al.* (1972).

SnO_2

The valences of tin species in aqueous solutions are II and IV. In the temperature range 100°-400 °C, the measured solubility of SnO_2 in pure water shows that $Sn(OH_4)^0$ is the main tin species over a broad pH range (Klintsova and Barsukov, 1973 ; Dadze *et al.*, 1981). However, these experiments are questionable since fO_2 was not buffered. The predictive calculations by Jackson and Helgeson (1985) and the new SnO_2 solubility experiments by Eugster and Wilson (1985) show that the Sn (II) species are dominant at temperatures higher than 350 °C for a Ni-NiO buffer.

The possible tin ligands are F^-, Cl^-, OH^- and carbonate. However, the concentration of the Sn(IV) hydroxy-carbonate complex ($Sn((OH)_3CO_3)^-$) is significant only in the pH range 10.7-11.6 at 300 °C (Kurilchikova and Barsukov, 1971). Therefore, the tin speciation in H_2O-CO_2-salts solutions should be similar to that in H_2O-salts solutions for geologically realistic pH (generally lower than pH 9). Because of the presence of fluorine-bearing minerals associated with some SnO_2 mineralizations, fluorine has been considered as an efficient ligand for tin. However, the fluorine-bearing minerals such as fluorite and topaz, have limited solubilities in water and, therefore, maintain fluoride concentrations to a low level in hydrothermal fluids. Hence, the fluoride complexes are expected to be minor compared to chloro or hydroxy complexes (Jackson and Helgeson, 1985).

Below the critical point of water, the calculations of Jackson and Helgeson (1985) predict that the solubility of cassiterite is minimum between pH 5 and 6 (Figure 7). This results from the destabilization of Sn (II) chloride complexes as the pH is still too low to stabilize hydroxy Sn (II) complexes. Higher chloride concentrations also enhance SnO_2 solubility, especially for acid pH, as a result of stannous chloride complexes (Figure 7).

Since Sn (II) species dominate, SnO_2 solubility increases at lower fO_2, all other conditions being the same (Figure 8 ; Eugster and Wilson, 1985). These authors show that SnO_2 solubility increases also with temperature at pH controlled by the assemblage quartz-(K, Na) feldspar-muscovite as a result of tin chloride complexes formation.

Tungstates

Tungstates speciation. The solubility of tungstate minerals in water is controlled by the equilibrium $MeWO_4 = Me^{2+} + WO_4^{2-}$. The stability of Me^{2+} and WO_4^{2-}-bearing complexes is essential for understanding these solubilities. Potentiometric measurements of tungstate in sodium chloride solutions have shown three mononuclear species ($H_2WO_4^0$, HWO_4^-, WO_4^{2-}) and two polynuclear species ($H_{10}(WO_4)_6^{2-}$, $H_7(WO_4)_6^{5-}$ at 290 °C (Figure 9 ; Wesolowski *et*

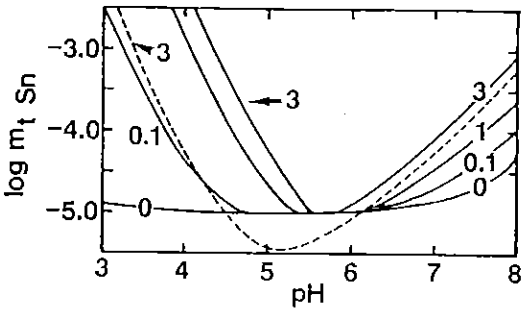

FIG. 7. — *Solubility of SnO_2 expressed as total molality of dissolved tin (m_{tSn}) in NaCl solutions (concentration is given in molal units along the curves) as a function of pH at 350 °C (continuous lines) and 300 °C (dashed curve) along the L-V equilibrium curve of H_2O (Psat) and at Ni-NiO fO_2 buffer* (from Jackson and Helgeson, 1985).

Solubilité de SnO_2 exprimé en molalité totale d'étain dissous (m_{tSn}) dans des solutions de NaCl (la concentration est donnée en molalité le long des courbes) en fonction du pH à 350 °C (les courbes continues) et 300 °C (courbe en tiretés) le long de la courbe d'équilibre L-V de l'eau (Psat). (d'après Jackson and Helgeson, 1985).

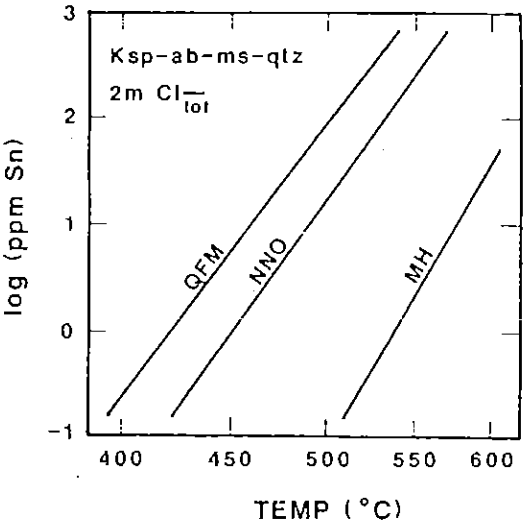

FIG. 8. — *SnO_2 solubility as a function of fO_2 and temperature above 400 °C with pH buffered by alkali feldspars-muscovite-quartz association and a 2 molar chloride solution* (from Eugster and Wilson, 1985).

Solubilité de SnO_2 en fonction de fO_2 et de la température au-dessus de 400 °C pour un pH tamponné par l'association minérale feldspaths alcalins-muscovite-quartz et une solution à 2 moles.l^{-1} de chlorure (d'après Eugster et Wilson, 1985).

al., 1984). WO_4^{2-} is the dominant species at pH greater than 4.8, whatever the bulk tungsten concentration and the temperature up to 300 °C (Figure 9). By contrast, other preliminary experiments on WO_3 solubility at 600 °C indicate that $H_2WO_4^0$ is the main tungstate species for pH ranging from 2 to 6 (Eugster and Wilson, 1985). The common association of tungstate minerals with apatite suggests the existence of phosphotungstic complexes. Such complexes have not yet been identified by Raman spectroscopy at temperatures below 250 °C (Bilal *et al.*, 1986), but this negative result might be due to the low temperatures of these experiments. W-deposits contain two main ore minerals : scheelite and wolframite, whose solubilities will be considered separately.

$CaWO_4$. Because both calcium and tungsten have a single valence in common geological

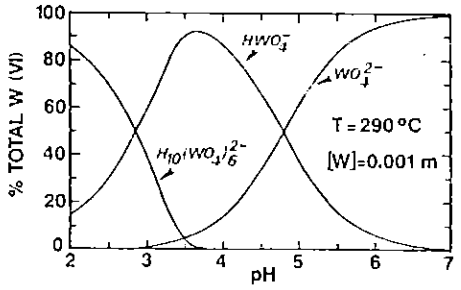

FIG. 9. — *Tungstate speciation at 290 °C as a function of pH at vapour pressure for a 0.001 molal total tungsten concentration in 1.014 NaCl molal solution* (from Wesolowski *et al.*, 1984).

Spéciation du tungstate à 290 °C en fonction du pH à la pression de vapeur saturante pour une concentration totale en tungstène de 0.001 mole.kg^{-1} H_2O dans une solution de 1.014 mole.kg^{-1} H_2O de NaCl (d'après Wesolowski *et al.*, 1984).

fluids, the fluid redox potential does not control scheelite solubility. For a given pressure and temperature, the solubility of scheelite increases with chloride and HCl concentrations according to the experimental data by Foster (1977) in the temperature range of 250° to 560 °C and the calculation by Rafal'skiy *et al.* (1984). This behaviour is due to : 1) an increase of calcium complexing by chloride. $CaCl_2^0$ is dominant over Ca^{++} and $CaCl^+$ ions at temperatures higher than 425 °C even at low chloride concentrations (0.02 Cl^- molal : Popp and Frantz, 1979) ; 2) an

increase of the concentration of polytungstate or $H_2WO_4^0$ at low pH. Figure 10 shows that the $CaWO_4$ solubility is minimum around neutral values for a given temperature and at a 1 molal NaCl concentration (Rafal'skiy *et al.*, 1984). At acid pH, calcium chloride complexes, HWO_4^-, $H_2WO_4^0$ and possibly tungstate polynuclear species are stable. At basic pH, $CaOH^+$ is stable. The minimum solubility between pH 4 and 7 is due to the increase of WO_4^{2-} concentration (Figure 9) as the disappearance of $CaCl_2^0$ complexes is not yet compensated by the calcium hydroxycomplexes. This emphasizes the important control of pH on scheelite solubility. In addition, high temperatures, enhancing $CaCl_2^0$ (Popp and Frantz, 1979) and $H_2WO_4^0$ stability, increase also the solubility of $CaWO_4$.

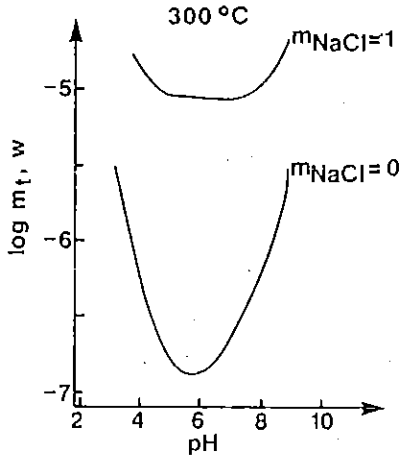

FIG. 10. — *Solubility of $CaWO_4$ at 300 °C as a function of pH and NaCl concentration (molal unit),* from Rafal'skiy *et al.* (1984).

Solubilité de $CaWO_4$ à 300 °C en fonction du pH et de la concentration de NaCl (exprimé en molalité) (d'après Rafal'skiy *et al.*, 1984).

$FeWO_4$. In the Fe-O-H system, the $Fe(OH)^+$ and $Fe(OH)_2^0$ species with valence II are dominant at 300 °C (Tremaine *et al.*, 1977). But in chloride-bearing aqueous solutions, $FeCl_2^0$ is dominant at high chloride concentrations and at neutral to acid pH) (Seward, 1977). In NaCl solutions at equilibrium with the buffer assemblage magnetite-pyrite-pyrrhotite, Crerar *et al.* (1978) found that Fe^{2+}, $FeCl^+$ and $FeCl_2^0$ at 300 °C and Fe^{2+} and $FeCl_2^0$ at 350 °C are the main species at neutral to acid pH. $FeCl_2^0$ is dominant even at low chloride concentration ($\leq$ 0.2 molal) at acid to neutral pH in the stability field of hematite (Boctor *et al.*, 1980) and of magnetite (Chou and Eugster, 1977). This iron chloride complexe accounts for observed magnetite solubility at T $\geq$ 400 °C (Eugster and Wilson, 1985). However, at basic pH, the $Fe(OH)_n^{2-n}$ species might easily predominate in NaCl-H_2O solutions. These results yield the following consequences : 1) in the normal fO_2 range of geological fluids from Q-F-M to H-M between 300° and 600 °C, the valency of complexed iron species is II which implies that the $FeWO_4$ solubility is not fO_2 controlled. 2) Wolframite solubility is expected to increase with chloride concentration as a result of formation of iron chloride complexes.

DISCUSSION

Uranium

Transport

70 % of uranium deposits occur in only three types of deposits formed at temperatures below 200 °C : sandstones, quartz-pebble conglomerates and unconformity types (Nash *et al.*, 1981). This suggests that the physico-chemical conditions which prevail at temperatures higher than 300 °C are not favourable to uranium transport. The neutral to weakly acid pH, derived from the stability of the quartz-K-feldspar- muscovite assemblage in the wall-rocks, indicates that uranium is likely to be transported by carbonate or phosphate complexes. The decreasing stability of uranium complexes with increasing temperature partly explains the fewer uranium deposits formed at temperatures higher than 300 °C. The nature of the ligand involved in the transport of uranium is not always clear from the study of uranium occurrences. Nevertheless recent studies of subsolidus granite alterations show that in some cases the leaching of uraninite occurs together with the dissolution of monazite or xenotime (Cathelineau, 1987). In addition, hematization of the associated wall-rock corroborates high fO_2. This suggests the formation of U-phosphate complexes in solutions as supported by the solubility experiments carried out on the UO_2-H_2O-PO_4 system at 400 °C and at fO_2

controlled by the H-M buffer (Figure 6). However, phosphate concentration in most geological fluids is probably buffered at low levels by apatite (Stausser, 1982), xenotime, and/or monazite. By contrast, the high total carbon dioxide of possible oxidized metamorphic fluids (with $CH_4/CO_2 \leqslant 10^{-5}$), shown from fluid inclusion studies may compensate for the lower stability of U-carbonate complexes relative to U-phosphate complexes.

At *Pen Ar Ran*, *Retail*, *Margnac-Fanay* and *Hyverneresse*, there is no clear indication about the U-transporting ligands. However, the general presence of hematite and pyrite in uranium deposits shows that high fO_2 characterizes the mineralizing fluids.

Both uranium occurrences and the available experimental data show that high fO_2 ($\geqslant$ H-M) is necessary for considerable U hydrothermal transport at weakly acid pH. Therefore, a key for understanding efficient U hydrothermal transport is the nature of homogeneous and/or heterogeneous reactions which control the fluid oxidation state. Among all the possible redox reactions, those of the C-O-H system are of prime importance whether they are homogeneous or heterogeneous (graphite-fluid equilibrium). But their control on hydrothermal metal transport depend strongly on their kinetics.

Experiments on carbon isotope exchange between CH_4 and CO_2 in a non-aqueous fluid show that isotopic equilibrium is not achieved at 500 °C up to 136 hours (Sackett and Chung, 1979). By contrast, isotope data on C-bearing aqueous geothermal fluids show that isotopic equilibrium is achieved above 320 °C (Sheppard, 1981). This indicates that homogeneous chemical equilibrium must also occur in such systems at temperatures higher than 320 °C. Fluid compositions in geothermal systems support this required minimal temperature (Giggenbach, 1982). However, in nature, the residence time of fluids is much more important than in experimental data and some minerals may catalyse chemical reactions. This may explain the apparent discrepancy between experimental and natural systems. Therefore, above 320 °C, the fO_2 of carbon-bearing aqueous fluids with more than 10^{-2} mole % CH_4 is fixed around and below the Ni-NiO buffer.

Graphite-fluid equilibrium was not achieved after 7 months at 700 °C in the experiments of Ziegenbein and Johannes (1980). But, the fluid inclusion data on the graphite bearing pelitic schists from South Massif Central (Ramboz, 1980*a* ; table II) support the hypothesis that heterogeneous graphite-fluid equilibrium occurs only at temperatures higher than 400 °C (Ramboz *et al.*, 1985). Thermodynamic calculations of graphite-fluid equilibrium show that fO_2 approximates the Q-F-M buffer in the 400°-500 °C temperature range (French, 1966 ; Ohmoto and Kerrick, 1977 ; Dubessy, 1984).

Consequently, temperatures above 350°-400 °C are expected to allow the fO_2 to be controlled at levels lower than the Ni-NiO buffer by homogeneous or/and heterogeneous redox reactions in the C-O-H system provided the fluid and/or rock composition and residence time are appropriate. Under these reduced conditions, uranium cannot be transported if the fluid is weakly acid. Below 350 °C-400 °C, these molecular equilibria probably do not control the oxidation state of the fluid and therefore are not the limiting factor for uranium transport. Geothermal systems exhibit a wide distribution of temperature through space and time. Consequently, the hotter fluids ($T \geqslant 400$ °C) of geothermal systems for which C-O-H equilibria are involved in the control of fluid oxidation state are not expected to be efficient for uranium transport but may favour its precipitation by mixing with oxidizing U-bearing fluids. By contrast, colder fluids ($T \leqslant 350$ °C) are generally more efficient for uranium transport.

Deposition

As indicated by theoretical calculations and solubility measurements, decreasing temperature enhances the formation of uranium-bearing complexes, all other conditions being equal. Therefore, cooling alone cannot account for uranium precipitation. At *Les Bombes*, the positive correlation between precipitation of phosphothorite, large quantities of fluoro-apatite and incorporation of uranium in phosphothorite show that uranium precipitation results mainly from the decrease in phosphate activity in the fluid phase. This agrees also with the experimental data showing an increase of UO_2 solubility with phosphate concentration at given P, T, pH, fO_2 conditions (Figure 6). At the *Margnac* and *Fanay* deposits, the spatial and temporal relation

between UO_2 deposition and CO_2-CH_4-rich aqueous fluids suggests that the latter cannot be the uranium transporting agents ; therefore, they are probably the reducing agent responsible for UO_2 deposition.

The decrease in the activity of a ligand involved in the uranium bearing complexes can initiate UO_2 precipitation as shown by the solubility experiments. However, the stoichiometry of the following reaction :

$$2UO_2^+ + H_2O \rightarrow 2UO_2(c) + 1/2O_2 + 2H^+$$

shows that if H^+ and O_2 are consumed, UO_2 crystallization will be enhanced. The quartz, K-feldspar, muscovite assemblage may account for the H^+ consumption. The consumption of O_2 may result from 1) oxidation reactions among species of the ore bearing fluid phase ($H_2S \rightarrow SO_2$ or $H_2S \rightarrow SO_4^{2-}$; $CH_4 \rightarrow CO_2$) ; 2) mixing with a fluid characterized by low fO_2 ; 3) precipitation of a mineral phase producing electrons such as pyrite : $Fe^{2-} + 2H_2S \rightarrow FeS_2 + 4H^- + 2e^-$.

Tin

Transport

Temperatures around 500°-600°C at the beginning of the hydrothermal episode provide one of the favourable conditions for tin transport as Sn (II) chloride complexes. In the South Massif Central, the CO_2 and CH_4 bearing fluids compatible with an equilibrium with graphite (Table II, figure 5) provide the low oxidation state necessary for a high SnO_2 solubility (Ramboz *et al.*, 1985). Similar redox potential has been suggested from bulk fluid inclusion analysis of the Komsomol'sk tin ore of USSR (Sushchevskaya *et al.*, 1978). These conditions are exactly those which prevent the hydrothermal transport of uranium in solution and this probably accounts for the inverse transport capacity of CH_4 bearing fluids relative to U and Sn.

Deposition

Precipitation of SnO_2 during cooling of the hydrothermal system is shown by fluid inclusion data and agrees with the decrease of cassiterite solubility with temperature (Figure 8). When no boiling occurs, a decrease in salinity is usually observed during the mineralizing hydrothermal evolution. Thus, the activity of the different stannous chloride complexes will decrease and this will favour SnO_2 precipitation. A pH increase is also mentioned by Volosov *et al.* (1981) and Sushchevskaya *et al.* (1985) at temperatures around 300°-350 °C. However, the pH given in these papers is suspected to be too high. This may partly result from the fact that NaOH° species, which are OH^- consuming, are not taken into account. However, the mineralogy of the different tin occurrences does not show any evidence of large-scale pH change during Sn stages in Cornwall.

According to numerical modelling by Drummond (1981), and Drummond and Ohmoto (1985) at temperatures below 350°C, adiabatic boiling produces a cooling, a pH increase and an increase in salinity of the liquid phase. The evolution of the two first parameters favours SnO_2 precipitation whereas the last one has an antagonist effect. In the case of an open boiling system, the fO_2 of the unmixed liquid increases as a result of the preferred partitioning of CH_4 into the vapour. The resultant increase of the redox potential has been suggested by Bannikova *et al.*, (1984) for the Komsomol'sk deposit. Therefore, even if the boiling effect on SnO_2 deposition below 350°C should be calculated in each case, this process seems favourable to SnO_2 precipitation as pointed out in the *Saint Cierge* tin occurrence (Ramboz, 1980*a*).

Tungsten

Transport

Tungstate minerals in the studied occurrences were always deposited in the range of 350°-500°C. In this temperature range, H_2WO_4 is the main tungstate species. On the other hand, the fluid salinity is always greater than one molal NaCl. This salinity and these temperatures enhance the stability of $FeCl_3^-$ and $CaCl_3^-$ species. All these conditions favour a high solubility of tungstate minerals. The fluid inclusion chemistry presented in this paper show that tungsten can be transported at low fO_2. The low fO_2 observed in the W occurrences is also required for Sn transport, but prevents U transport.

Deposition

The quasi-isobaric cooling which also occurs with a decrease of the CO_2-CH_4 content as a result of fluid mixing (Ramboz, 1980*a* ; Ramboz *et al.*, 1985) is expected to increase the dielectric constant of the fluid and correlatively the destabilization of neutral species $FeCl_2^0$, $CaCl_2^0$, H_2WO_4 in favour of Fe^{2+}, Ca^{2+} and WO_4^{2-} as discussed in the next section.

Scheelite precipitation is controlled by the supply of calcium to the fluid as a result of fluid-rock interaction. In granitic environments from the Alps, Poty (1969) and Poty *et al.* (1974) show that the albitization of plagioclase around the alpine clefts induced the increase of the calcium content of the inclusion fluid as confirmed by the experiments of Whitney *et al.* (1985).

The *Montredon* pegmatitic pods are devoid of any primary iron-bearing silicates, and scheelite is the only tungsten bearing mineral. Therefore, little iron was apparently mobilized by the hot carbonaceous solutions in this occurrence. In *Leucamp* and *Enguiales*, wolframite and apatite often precipitate at the same time. Therefore, there was probably a competition between tungstate and phosphate with respect to calcium.

The oxidation state of the fluid does not control directly the solubility of tungstate minerals, but might reflect the signature of W source rocks.

Physical and chemical controls on complex stabilities

In the previous discussion about the hydrothermal transport and deposition of U, Sn and W, the rôle of both fO_2 and temperature has been emphasized. Now the physico-chemical parameters which control the stability of metal bearing complexes is analysed.

Water is known at room temperature as a strong electrolytic solvent because of its high static dielectric constant ($\varepsilon = 78.3$ at $T = 25$ °C, $P = 1$ bar, Hasted, 1973). The hydration shell of water dipoles, especially around cations and to a less extent around anions, insulates cations and anions. But the static dielectric constant ε strongly depends on temperature and pressure. In the P-T range 1-2 kbar and 400-600 °C, ε is between 20 and 7 (Uematsu and Franck, 1980). These low values increase the formation of neutral or low charged chloride complexes : $NaCl^0$, KCl^0, $CaCl_2^0$, $PbCl_2^0$, $FeCl_2^0$, $CaCl_2^0$, $MgCl_2^0$, $SnCl_2^0$, (Franck, 1981 ; Seward, 1981, 1984 ; Crerar *et al.*, 1985). The predominance of $H_2WO_4^0$ over WO_4^{2-} at 600 °C over a wide pH range as shown by Eugster and Wilson (1985), may likely result from the same reason.

Dissolved gases are also expected to decrease the static dielectric constant as yet suggested by conductance measurements in the H_2O-KCl-Ar system (Hartmann and Franck, 1969 ; Franck, 1981). In addition, recent measurements of ε in water-benzene mixtures at 400 °C, 2 kbar show the following variations of ε as a function of the fluid composition : $X(C_6H_6) = 0$, $\varepsilon = 20$; $X(C_6H_6) = 0.2$, $\varepsilon = 7$; $X(C_6H_6) = 0.5$; $\varepsilon = 4$ (Deul, 1984 ; Franck, 1985). At temperatures above 400 °C, gases such as CO_2, CH_4 and N_2 can be produced by various metamorphic devolatilization reactions as shown by fluid inclusion chemistry in South Massif Central (Table II). Therefore, the low static dielectric constant of these gas bearing fluids favours the stability of chloride complexes and hence the transport of Sn, W. In contrast, isobaric cooling and decrease of gas content by fluid mixing may strongly favour Sn and W deposition. This shows a new rôle of temperature on metal speciations through gas producing reactions.

The decrease of the stability of phosphate and carbonate complexes with temperature is still poorly understood in terms of the electronic configuration of the complexes and of the physical properties of the fluid. This decrease of stability may result from the increase of the internal vibrations and rotations of the polyatomic ligands and the U-ligand oxygen bond vibrations. In addition, the increase of rotation of UO_2^{2+} or UO_2^{+} through its two equatorial axis is also expected to strongly destabilize the complexes by bringing near the negative charges, localized around the oxygen atoms, of UO_2^{2+} or UO_2^{+} and of the anionic ligands (CO_3^{2-}, PO_4^{3-}).

CONCLUSION

This work shows that fO_2, temperature and metal speciation have contrasting effects on the behaviour of U and Sn-W at the hydrothermal

stage around 300°-500 °C. This helps to explain the time, spatial and genetic separation of U and Sn-W deposits associated with peraluminous granite, although these metals tend to present a similar incompatible behaviour at the magmatic stage.

Iron mineralogy in U deposits, fluid inclusion chemistry in Sn-W occurrences from Massif Central, and solubility experiments show that fO_2 is the main discriminant parameter. This results from different changes of metal valence between the hydrothermal solution and the solid phase : U(V,VI) solution $\rightarrow$ U(IV)UO_2, Sn(II) solution $\rightarrow$ Sn(IV)SnO_2, no change for calcium, iron and tungsten.

Oxidation state estimated in uranium deposits indicates that the hematite-magnetite buffer fixes the minimal fO_2 for uranium transport and, hence, subsequent significant deposition.

The fO_2 estimated from fluid inclusion chemistry in Sn-W deposits from Massif Central is roughly that of the Q-F-M buffer. This results in the lack of cogenetic Sn-W and U mineralizations.

The indirect control of temperature on the contrasting behaviour of U and Sn-W at the hydrothermal stage has been emphasized. This includes the production of gases at high T and their correlative chemical and physical consequences on metal speciation. Temperatures greater than 400 °C allow redox equilibria in the C-O-H system to control the fluid oxidation state close to the Q-F-M buffer, especially if graphite or carbonaceous materials are present in the rocks. In such conditions, fluids are not able to transport uranium, but may favour its deposition, whereas they may be efficient for Sn and W transport.

The different metal-ligand structures of U, Sn, Fe, Ca, W bearing complexes result in opposite stability variations with temperature between U and Sn, Fe, Ca, W complexes. The decrease of the static dielectric constant of the fluid as a result of high temperature and high gas concentration combined with the different metal-ligand bonds of U and Sn, Fe, Ca, W bearing complexes, explain their opposite thermal stability. In addition, high temperatures favour CO_2, CH_4, N_2 producing reactions resulting in an important lowering of the fluid dielectric constant. Consequently the stabilization of Sn, Fe, Ca, W complexes as well as the fluid transport capacity with respect to Sn and W, are increased.

Such works involving paragenetic mineral studies and precise fluid inclusion chemistry for deriving T-pH-fO_2-fS_2 conditions have to be complemented by experimental determination of solubility and speciation of ore minerals at high temperature. Much still remains to be done on metal complex stability and stoichiometry, structure of complex gas bearing aqueous electrolytes and kinetics of redox equilibria at moderate to high temperature to understand the behaviour of metals in geological fluids.

ACKNOWLEDGMENTS

The authors thank John Frantz for fruitful discussions. Professors David Crerar, Gil Michard and E.U. Franck are acknowledged for their critical reviews.

APPENDIX

CALCULATION OF fO_2 AND fS_2 FROM FLUID INCLUSIONS

The fluid inclusions are analysed by microthermometry and micro-Raman spectrometry and their bulk $\overline{V}$-X properties are estimated using the methodology developed by Ramboz *et al.* (1985). The composition of inclusion fluids of the C-O-H system, determined at room temperature, does not differ significantly from their composition at chemical equilibrium in the P-T conditions of trapping. Consequently fO_2 can be calculated along the isochoric path of the inclusion from the $\overline{V}$-X properties measured by microthermometry and micro-Raman spectrometry (Dubessy, 1984). Data on carbon isotope exchange between CH_4 and CO_2 in natural samples suggest that the oxidation state of the fluids can be controlled by the equilibrium $CH_4 + 2O_2 \rightleftarrows CO_2 + 2H_2O$ at temperatures higher than 300 °C (Sheppard, 1981 ; Giggenbach, 1982). Therefore, in the 300-500 °C temperature range of interest, fO_2 can be calculated using the measured $\overline{V}$-X properties and the low mass action relative to the previous equilibrium. The calculation of the fugacity coefficients takes into account the concentration of dissolved salts in terms of equivalent NaCl (Dubessy, 1985). The sulfur fugacity is derived from the H_2S concentration, the fO_2 calculated previously and the chemical equilibrium : $2H_2S + O_2 \rightleftarrows 2H_2O + S_2$.

REFERENCES

BANNIKOVA, L.A., SUSHCHEVSKAYA, T.M., VOLKOV, V.V., MAKHOV, S.F. and BARSUKOV, V.L. (1984). — The rôle of redox reactions involving organic matter in producing tin deposits. *Geochem. Int., 21*, 105-115.

BARTON, P.B. and SKINNER, B.J. (1979). — Sulfide mineral stabilities. *In* "Geochemistry of Hydrothermal ore deposits", 2nd edition, H.C. Barnes ed., 278-403.

BILAL, B.A., HAUFE, P. and MOELLER, P. (1986). — Study of polymerization of tungsten (VI) in a hydrothermal solution up to 1 kbar and 200 °C. *Physica (B + C)*, 721-724.

BOCTOR, N.Z., POPP, R.K. and FRANTZ, J.D. (1980). — Mineral-solution equilibria. IV. Solubilities and the thermodynamic properties of $FeCl^0_2$ in the system Fe_2O_3-H_2-H_2O-HCl. *Geochim. Cosmochim. Acta, 44*, 1509-1518.

BOWERS, T.S., JACKSON, K.J. and HELGESON, H.C. (1984). — Equilibrium activity diagrams for coexisting minerals and aqueous solutions at pressures and temperatures to 5 kb and 600 °C. Springer Verlag, 397 p.

BRIL, H. (1985). — Conditions de stabilité des sulfures dans les filons de haute température du district de Brioude-Massiac. (Massif Central français). *Bull. Minéral., 108*, 161-171.

BRIL, H. and RAMBOZ, C. (1982). — Les concentrations stanno-wolframifères du district de Brioude-Massiac (Cantal) et du Sud du Massif Central : analyse comparée de la minéralogie et des phases fluides associées. *C.R. Acad. Sc., Paris, sér. II, 294*, 387-390.

BURNOL, L. (1974). — Different types of leucogranites and classification of the types of mineralization associated with acid magmatism in the Northwestern part in the French Massif Central. *In* "Metallization associated with acid magmatism", M. Stemprok, L. Burnol and C. Tischendorf, ed. vol. 3, 191-204, Prague.

CATHELINEAU, M. (1981). — Les gisements d'uranium liés spatialement aux leucogranites sud-armoricains et à leur encaissant métamorphique. *Sci. de la Terre*, Nancy, Fr., *Mém. 42*, 375 p.

CATHELINEAU, M. (1984). — Uranium veins in Western France : Mineralogy and geochemistry of uranium deposition *in* "Proceedings of ICAM 84 Congress", Los Angeles, TMS-AIME, 1083-1094.

CATHELINEAU, M. (1987). — U-Th-REE mobility during albitization and quartz dissolution in granitoids : evidence from South East French Massif Central. *Bull. Minéral., 110*, 249-259.

CHAROY, B. (1979*a*). — Définition et importance des phénomènes deutériques et des fluides associés dans les granites. Conséquences métallogéniques. *Sci. de la Terre*, Nancy, Fr., *Mém. 37*, 364 p.

CHAROY, B. (1979*b*). — Greisenisation, minéralisation et fluides associés à Cligga Head, Cornwall (Sud-Ouest de l'Angleterre). *Bull. Minéral., 102*, 633-641.

CHATTERJEE, A.K., STRONG, D.F. and MUECKE, G.K. (1983). — A multivariate approach to geochemical distinction between tin-specialized and uranium-specialized granites of southern Nova Scotia. *Canad. J. Earth Sci., 20*, 420-430.

CHAURIS, L. (1965). — Les minéralisations pneumatolytiques du Massif Armoricain. Mémoire B.R.G.M., *31*, 218 p.

CHOU, I.M. and EUGSTER, H.P. (1977). — Solubility of magnetite in supercritical chloride solutions. *Am. J. Sci., 277*, 1296-1314.

CRERAR, D.A., SUSAK, N.J., BORCSIK, M. and SCHWARTZ, S. (1978). — Solubility of the buffer assemblage pyrite-pyrrhotite-magnetite in NaCl solutions from 200 to 350 °C. *Geochim. Cosmochim. Acta, 42*, 1427-1438.

CRERAR, D., WOOD, S., BRANTLEY, S. and BOCARSLY, A. (1985). — Chemical controls on solubility of ore-forming minerals in hydrothermal solutions. *Canad. Mineral.*, Special issue on ore deposits, *23*, 333-352.

DADZE, T.P., SOROKHIN, V.I. and NEKRASOV, I. Ya (1981). — Solubility of SnO_2 in water and in aqueous solutions of HCl, HCl + KCl, and HNO_3 at 200-400 °C and 101.3 MPa. *Geochim. Int., 18*, 142-152.

DERRE, C. (1982). — Caractéristiques de la distribution des gisements à étain et tungstène dans l'Ouest de l'Europe. *Min. Deposita, 17*, 55-77.

DEUL, R. (1984). — Dielectric constant and density of water-benzene mixtures to 400 °C and 3 000 bar. Thesis Institute for Physical Chemistry, Karlsruhe University.

DRUMMOND, S.E. (1981). — Boiling and mixing of hydrothermal fluids : chemical effects on mineral precipitation. Unpub. Ph. D. Thesis, Penn state University, 380 p.

DRUMMOND, S.E. and OHMOTO, H. (1985). — Chemical evolution and mineral deposition in boiling hydrothermal systems. *Econ. Geol., 80*, 126-147.

DUBESSY, J. (1984). — Simulation des équilibres chimiques dans le système C-O-H. Conséquences méthodologiques pour les inclusions fluides. *Bull. Minéral., 107*, 155-168.

DUBESSY, J. (1985). — Contribution à l'étude des interactions entre paléo-fluides et minéraux à partir de l'étude des inclusions fluides par microspectrométrie Raman. Conséquences métallogéniques. Unpub. thesis, INPL, 198 p.

EUGSTER, H.P. and WILSON, G.A. (1985). — Transport and deposition of ore-forming elements in hydrothermal systems associated with granites. *In* : High heat production (HHP) granites, hydrothermal

circulation and ore genesis. *The Inst. Min. Metal.*, 87-98.

FOSTER, R.P. (1977). — Solubility of scheelite in hydrothermal chloride solutions. *Chem. Geol., 20*, 27-43.

FRANCK, E.U. (1981). — Survey of selected non-thermodynamic properties and chemical phenomena of fluids and fluid mixtures. *In* "Chemistry and geochemistry of solutions at high temperatures of the Earth. (D. Rickard and F.E. Wickman ed.), Pergamon Press, vol. 13 and 14, 65-88.

FRANCK, E.U. (1985). — Aqueous mixtures to supercritical temperatures at high pressures. *Pure and Appl. Chem., 57*, 8, 1065-1070.

FRENCH, B.M. (1966). — Some geological implications of equilibrium between graphite and a C-H-O gas phase at high temperatures and pressures. *Rev. Geophysics, 4*, 223-253.

FRIEDRICH, M. (1984). — Le complexe granitique hyperalumineux de Saint-Sylvestre, Nord Ouest du Massif Central français. *Geol. Geoch. Uranium. Nancy, 5*, 342 p.

FRIEDRICH, M.A., CUNEY, M. and POTY, B. (1987). — Uranium geochemistry in peraluminous leucogranites. *Uranium* (in press).

GEFFROY, J. (1971). — Les gîtes uranifères dans le Massif Central. *In* "Géologie, géomorphologie et structure profonde du Massif Central français". Symp. J. Jung., (Clermont : Plein Air Service ed.), 541-579.

GIGGENBACH, W.F. (1982). — Carbon-exchange between CO_2 and CH_4 under geothermal conditions. *Geochim. Cosmochim. Acta, 46*, 159-165.

HARTMANN, D. and FRANCK, E.U. (1969). — Electrische leitfähigkeit wässringer lösungen bei hohen temperaturen and drücken. III Kaliumchlorid in überkritisches wasser-argen-mischungen. *Ber. Bunsenges. Phys. Chemie , 73*, 514-521.

HASTED, J.B. (1973). — Liquid water : dielectric properties. *In* "Water a comprehensive treatise. Vol. 1. The physics and physical chemistry of water". Chap. 7, p. 255-309.

JACKSON, K.J. and HELGESON, H.C. (1985). — Chemical and thermodynamic constraints on the hydrothermal transport and deposition of tin. I. Calculation of the solubility of cassiterite at high pressures and temperatures. *Geochim. Cosmochim. Acta, 49*, 1-22.

KLINTSOVA, A.P. and BARSUKOV, V.L. (1973). — Solubility of cassiterite in water and in aqueous NaOH solutions at elevated temperatures. *Geochem. Int., 10*, 540-547.

KURILCHIKOVA, G. Ye and BARSUKOV, V.L. (1971). — Effects of CO_2 and sodium and potassium bicarbonates and carbonates on the formation of Sn(IV) complexes in solution. *Geochem. Int., 8*, 395-404.

LAGACHE, M. and WEISBROD, A. (1977). — The system : two alkali feldspars KCl-NaCl-H_2O at moderate to high temperatures and low pressures. *Contrib. Mineral. Petrol., 52*, 77-101.

LANGMUIR, D. (1978). — Uranium solution mineral-equilibria at low temperatures with applications to sedimentary ore deposits. *Geochim. Cosmochim. Acta, 42*, 547-569.

LA ROCHE, H. de, STUSSI, J.M. et CHAURIS, L. (1980). — Les granites à deux micas hercyniens français. Essais de cartographie et de corrélations géochimiques appuyés sur une banque de données. Implications pétrologiques et métallogéniques. *Sci. de la Terre*, Nancy, Fr., *24*, 1, 5-221.

LECERF, C. (1973). — Extraction et analyse par chromatographie gazeuse des fluides inclus dans les minéraux de roches. Rapport DEA, Université de Nancy I, 36 p.

LEROY, J. (1978). — The Margnac and Fanay uranium deposits of the La Crouzille district (Western Massif Central, France) : geologic and fluid inclusion studies. *Econ. Geol., 73*, 1611-1634.

LEROY, J. et CATHELINEAU, M. (1982). — Les minéraux philliteux dans les gisements hydrothermaux d'uranium. I. Cristallochimie des micas hérités et néoformés. *Bull. Minéral., 105*, 99-109.

LIETZKE, M.H. and STOUGHTON, R.W. (1960). — The solubility of silver sulfate in electrolyte solutions. Part 7. Solubility in uranyl sulfate solutions. *J. Phys. Chem., 64*, 816-820.

MARTIN, S. (1981). — Episyénitisation et minéralisation dans le leucogranite d'Hyvemeresse (Nord Millevaches). Unpub. thesis, Université de Clermont II, 222 p.

MONTOYA, J.W. and HEMLEY, J.J. (1975). — Activity relations and stabilities in alkali feldspar and mica alteration reactions. *Econ. Geol., 70*, 577-582.

NASH, J.T., GRANGER, H.C. and ADAMS, S.S. (1981). — Geology and concepts of genesis of important types of uranium deposits. *Econ. Geol., 75th anniversary volume*, 63-116.

NGUYEN-TRUNG, C. (1985). — Géochimie théorique et expérimentale des oxydes d'uranium dans les solutions aqueuses de 25 à 700 °C sous une pression de 1 à 6 000 bars. Synthèse hydrothermale de certains minéraux d'uranium VI et IV. Géologie et géochimie de l'uranium. Unpub. thesis, INPL, Nancy 479 p.

NIKOLAEVA, N.M. (1971). — The study of hydrolysis and complexing of uranyl ions in sulphate solutions at elevated temperatures. *Izv. Sib. Oct. Akad. Nauk SSSR. Ser. Khim. Nauk, 7(3)*, 61-67.

NIKOLAEVA, N.M. (1977*a*). — Complexing in the uranyl chloride solution at elevated temperature. *Izv. Sib. Otd. Akad. Nauk SSSR, Ser. Khim. Nauk*, 56-59.

NIKOLAEVA, N.M. (1977*b*). — The study of U(IV) complexing with chloride at the elevated temperature. *Izv. Sib. Otd. Akad. Nauk SSSR, Ser. Khim. Nauk, 3*, 114-120.

OHMOTO, H. and KERRICK, D. (1977). — Devolatili-

zation equilibria in graphitic systems. *Am. J. Sci.*, *277*, 1013-1044.

PAGEL, M. (1981). — Facteurs de distribution et de concentration de l'uranium et du thorium dans quelques granites de la chaine hercynienne d'Europe. Unpub. thesis, INPL, Nancy, 566 p.

PASCAL, M.L. (1984). — Nature et propriétés des espèces en solutions dans le système K_2O-Na_2O-SiO_2-Al_2O_3-H_2O-HCl : contribution expérimentale. Unpub. thesis, Orléans Univ., 151 p.

POPP, A.K. and FRANTZ, J. (1979). — Mineral solution equilibria. II. An experimental study of mineral solubilities and the thermodynamic properties of aqueous $CaCl_2$ in the system CaO-SiO_2-H_2O-HCl. *Geochim. Cosmochim. Acta*, *43*, 1777-1790.

POTY, B. (1969). — La croissance des cristaux de quartz dans les filons sur l'exemple du filon de La Gardette (Bourg d'Oisans) et des filons du massif du Mont Blanc. Unpub. thesis, Université de Nancy, 161 p.

POTY, B., LEROY, J., CATHELINEAU, M., CUNEY, M., FRIEDRICH, M., LESPINASSE, M. and TURPIN, L. (1986). — Uranium deposits spatially related to granites in the french part of the Hercynian orogen. IAEA, TECODS. *in* "Vein type uranium deposits", 215-246.

POTY, B., STALDER, H.A. and WEISBROD, A. (1974). — Fluid inclusions studies in quartz from fissures of Western Central Alps. *Schweiz. Mém., Petr., Mitt.*, *54*, 213, 717-752.

RAFAL'SKIY, R.P., BRYZGALIN, O.V. and FEDOROV, P.L. (1984). — Tungsten migration and scheelite deposition under hydrothermal conditions. *Geochem. Int.*, *21*, 1-13.

RAMBOZ, C. (1980*a*). — Géochimie et étude des phases fluides de gisements et indices d'étain-tungstène du Sud du Massif Central (France). Unpub. thesis, Nancy, 278 p.

RAMBOZ, C. (1980*b*). — Fluid phases associated with Sn-W deposits from South of Massif Central, France. 26th C.G.I., Paris, Abstr. 1, 80.

RAMBOZ, C., PICHAVANT, M. and WEISBROD, A. (1982). — Fluid immiscibility in natural processes : use and misuse of fluid inclusion data. Part II : Interpretation on fluid inclusion data in terms of immiscibility. *Chem. Geol.*, *37*, 29-48.

RAMBOZ, C., SCHNAPPER, D. and DUBESSY, J. (1985). — the P-$\overline{V}$-T-X-fO_2 evolution of H_2O-CO_2-CH_4-bearing fluid in a wolframite vein : reconstruction from fluid inclusion studies. *Geochim. Cosmochim. Acta*, *49*, 205-219.

SACKETT, W.M. and CHUNG, H.M. (1979). — Experimental confirmation of the lack of carbon isotope exchange between methane and carbon oxides at high temperatures. *Geochim. Cosmochim. Acta*, *43*, 273-276.

SERGEYEVA, E.I., NIKITIN, A.A., KHODAKOVSKIY, I.L. and NAUMOV, G.B. (1972). — Experimental investigation of equilibria in the system UO_3-CO_2-H_2O in the 25-200 °C temperature interval. *Geochem. Int.*, 900-910.

SEWARD, T.M. (1977). — Solubility of coexisting pyrite and pyrrhotite in the system NaHS-H_2S-NaCl-H_2O at elevated temperature and pressure. *In* "Geochemistry 1977", pp 44-48, New Zealand, Dept. of Scientific and Industrial Research, DSIR Bull. 218.

SEWARD, T.M. (1981). — Metal complex formation in aqueous solutions at elevated temperatures and pressures. *In* "Chemistry and geochemistry of solutions at high temperatures of the Earth (D. Rickard and F.E. Wickman ed.), Pergamon Press, vol. 13 and 14, 113-132.

SEWARD, T.M. (1984). — The formation of lead (II) chloride complexes to 300 °C. A spectrophotometric study. *Geochim. Cosmochim. Acta*, *48*, 121-134.

SHEPPARD, S.M.F. (1981). — Stable isotope geochemistry of fluids. *In* "Chemistry and geochemistry of solutions at high temperatures and pressures". Physics and chemistry of the Earth (D. Rickard and F.E. Wickman ed.), Pergamon Press vol. 13 and 14, 419-443.

SIMPSON, P.R., BROWN, G.C., PLANT, J. and OSTLE, D. (1979). — Uranium mineralization and granite magmatism in the British Isles. *Phil. Trans. R. Soc. Lond., A 291*, 385-412.

STAUSSER, R.E. (1982). — Fluorapatite and fluorite solubility controls on geothermal waters in Yellowstone National Park. *Geochim. Cosmochim. Acta*, *46*, 465-474.

SUSHCHEVSKAYA, T.M., LUCHITSKAYA, M.I., RYZHENKO, B.N. and BARSUKOV, V.L. (1985). — Acidity of the medium during hydrothermal cassiterite formation. *Geochem. Int.*, *21*, 77-87.

SUSHCHEVSKAYA, T.M., RYZHENKO, B.N., KNYAZEVA, S.N., MALAKHOV, V.V. and BARSUKOV, V.L. (1978). — Redox potential of tin-bearing hydrothermal solutions. *Geochem. Int.*, *15(4)*, 89-99.

SWART, P.K. and MOORE, F. (1982). — The occurrence of uranium in association with cassiterite, wolframite and sulphide mineralization in South-West England. *Mineral. Mag.*, *46*, 211-215.

TISCHENDORF, G. (1973). — The metallogenetic basis of tin exploration in the Erzgebirge. *Trans. Inst. Min. Metal.*, *82*, B9-B24.

TREMAINE, P.R., MASSON, R.V. and SHIERMAN, G.R. (1977). — A calculation of Gibbs free energies for ferrous ions and the solubility of magnetite in H_2O and D_2O to 300 °C. *Thermochim. Acta*, *19*, 287-300.

TREUIL, M., JORON, J.L., JAFFREZIC, H., VILLEMANT, et CALAS, G. (1979). — Géochimie des éléments hygromagmatophiles, coefficients de partage minéraux/liquides et propriétés structurales de ces éléments dans les liquides magmatiques. *Bull. Minéral.*, *102*, 402-409.

TURPIN, L. (1984). — Altérations hydrothermales et

caractérisation isotopique (O-H-C) des minéraux et des fluides dans le massif uranifère de St-Sylvestre. Extension à d'autres gisements intragranitiques d'uranium français. *Geol. Geoch. Uranium, Nancy, 6*, 190 p.

UEMATSU, M. and FRANCK, E.U. (1980). — Static dielectric constant of water and steam. *J. Phys. and Chem. Reference Data, 9*, 1291-1306.

VALENCIA HERRERA, J., PICHAVANT, M. and ESTEYRIES, C. (1984). — Le volcanisme ignimbritique peralumineux plio-quaternaire de la région de Macusani, Pérou. *C.R. Acad. Sci., Paris, sér. II*, 77-82.

VOLOSOV, A.G., BORISOV, M.V., SUSHCHEVSKAYA, T.M. and KNYAZEVA, S.N. (1981). — Deposition of cassiterite during formation of hydrothermal tin-ore deposits according to the results of physico-chemical modelling. *Geochem. Int., 18*, 49-66.

WESOLOWSKI, D., DRUMMOND, S.E., MESMER, R.E. and OHMOTO, H. (1984). — Hydrolysis equilibria of tungsten (VI) in aqueous sodium chloride solutions at 300 °C. *Inorg. Chemistry, 23*, 1120-1132.

WHITNEY, J.A., HEMLEY, J.J. and SIMON, O.F. (1985). — The concentration of iron in chloride solutions equilibrated with synthetic granitic compositions : the sulfur-free system. *Econ. Geol., 80*, 444-460.

ZIEGENBEIN, D. and JOHANNES, N.J. (1980). — Graphite in C-H-O fluids : an unsuitable compound to buffer fluid composition at temperatures up to 700 °C. *N. Jb. Miner. Abh., 7*, 280-305.

Contribution C.R.E.G.U. 115
Contribution C.R.P.G. 689